

Self-Assembly and Morphological Patterns in Drying Droplets of Bio-colloids

Anusuya Pal



A Dissertation
Submitted to the Faculty
of the
WORCESTER POLYTECHNIC INSTITUTE
In partial fulfillment of the requirements for the
Degree of Doctor of Philosophy
in
Physics
19 May 2021

APPROVED:

Germano Iannacchione

Prof. Germano S. Iannacchione,
(Ph.D. Supervisor)
Department of Physics, WPI

L. Ramdas Ram-Mohan

Prof. L. Ramdas Ram-Mohan,
Department of Physics, WPI

Padmanabhan Aravind

Prof. Padmanabhan K. Aravind,
Department of Physics, WPI

Mohan Srinivasarao

Prof. Mohan Srinivasarao,
School of Materials Science and Engineering,
Georgia Institute of Technology.

DECLARATION

I, Anusuya Pal, declare that this dissertation titled, "Self-Assembly and Morphological Patterns in Drying Droplets of Bio-colloids" and the work presented in it are my own. I confirm that:

- This work was done wholly or mainly while in candidature for a research degree at this University.
- No part of this dissertation has previously been submitted for a degree or any other qualification at this University or any other institution.
- I have consulted the published work of others to develop my theoretical understanding and framing the research gaps, and this has been clearly acknowledged and attributed in this dissertation.
- I have provided the sources of all the quotations cited in this work. With the exception of such quotations, this dissertation is entirely my own work.
- I have acknowledged all main sources of help.

Signed: Anusuya Pal

Date: 5th April 2021

*Dedicated to all those who sacrifice their LOVE for their professional
development...!!!*

Abstract

Understanding the drying evolution and morphological patterns of the colloidal fluids is very important and relevant to many industrial processes, pharmaceutical products, medical and forensic applications. This evolutionary process might look very straightforward; however, it is well accepted in the droplet community that the underlying physics is hard to comprehend. The final depositing patterns depend on several factors, including the solute particles' properties, nature of the solvent, geometry, substrate, environmental conditions, etc. The biological colloids (proteins, blood, etc.) attracted many researchers' significant attention due to the local self-assembling interactions between the constituent particles. This dissertation's principal thrust is to explore how and why different patterns are generated when these bio-colloids' native/initial properties vary as the droplets are dried under uniform conditions (surface, humidity, temperature, droplet diameter, etc.). In this work, the hierarchical complexity is systematically altered from one-component to multi-component systems. The findings of this dissertation reveal a unique drying pattern for (i) different globular proteins (the simplest hierarchical structure) with and without the bulk liquid crystals (LCs), and (ii) the whole human blood (the most complex hierarchical structure). These drying droplets' interfacial and self-assembling behavior are thoroughly examined using optical and scanning electron microscopic imaging, along with noble image processing protocols and contact angle measurements. Additionally, various statistical tests are employed to quantify a broad set of image data. The experimental work establishes the following outcomes: (i) the protein drying droplets confirms that the protein-protein interactions over the protein-substrate interactions play a substantial role in determining the morphological patterns, (ii) the LCs' texture are influenced by different protein droplets indicating that these bulk unaligned LCs are not always randomly distributed, and (iii) the experiments on the whole human blood approve that a concentration-driven phase transition may evolve in the bio-colloidal solution containing a large number of interacting components. Additionally, the effects of the saline water and the various substrate-controlled temperatures on the drying evolution and their resulting deposition patterns are examined in this dissertation. This work concludes that a series of simple experiments can track complex physical behavior unveiling new insights into the physics of pattern formation in a symmetric drying droplet.

Acknowledgments

It was the later part of 2016 when I received an official letter from the *Worcester Polytechnic Institute* (WPI) to be appointed as a Teaching Assistant (TA) at the Department of Physics. My journey as a *Ph.D.* graduate formally commenced in January 2017. Finally, I stepped into the world of my dreams after many deliberations of different levels, starting from convincing my parents to allow me to fly all the way to the USA to face all the administrative hurdles of acquiring the VISA! I always dreamt of pursuing a *Ph.D.* from a reputed institution in the *United States of America*. When it finally started, it was not easy to cope with all the hurdles in the first place. Every minor thing, starting with adapting the transition of the temperature from +15 to -15°C , to taking the graduate core courses, teaching 8-hours of labs per week, and preparing for the Qualifiers, appeared to be a lot difficult than I actually anticipated.

Fortunately, I was blessed enough to be surrounded by a bunch of kind people that ensured the whole transition of who I am today. I am indebted to many people who lived along with my *dream* of using *Dr.* before my name. I am specifically indebted to my ex-advisor, Prof. *Lyubov Titova*, for hiring me for the *Ph.D.* position in the first place and allowing me enough freedom and time to adjust to the US work culture. Unfortunately, my research thrusts and the research interests of *Titova* did not match, and I quickly had to find an alternate solution. Amidst all these, I got to explore the research interests and lab setup of Prof. *Germano S. Iannacchione* through one of my seniors, *Dr. Atanu Chatterjee*. (who was working under the supervision of Prof. *Germano* at that time). A conversation of only ~ 30 min with *Germano* settled down all my worries and made me realize the fundamental issues that I always wished to explore in my *Ph.D.* journey. As a matter of fact, I started my actual research endeavor in June 2017 in the *Order-Disorder Phenomena Laboratory* under the keen observation and guidance of Prof. *Germano*. And the journey turns out to be an eventful one!

I would like to express my immense gratitude to Prof. *Germano*, my *Ph.D.* advisor, for providing me so much independence in the lab. It was his trust and confidence that motivated me to grow into the person that I am today. His contribution as a mentor is beyond what I could ever imagine. He literally shaped my scientific thoughts, honed my research skills, gave directions to how I should approach and handle a problem (be it related to science or life in general), and helped me improve my communication skills. I shall always be grateful to you, *Germano*, for addressing tons of questions that I had throughout my journey!

Another person whose role is remarkable is Prof. *Amalesh Gope*. I got in touch with Prof. *Amalesh* in 2011 when I joined the *University of Hyderabad*, India, to pursue my *IM.Sc.* Since then, he has been my (personal) mentor and kindly agreed to collaborate with my *Ph.D.* project. A big thanks to you, *Amalesh*, for transforming me into a complete researcher from scratch. I sincerely appreciate your efforts and patience

in reading my series of drafts, highlighting the mistakes, and criticizing them whenever that was appropriate. I would also like to thank you for helping me and pulling me out from my (many of my) personal problems. Your advise and trust in me have always been a significant motivating factor that ensured that I did not deviate from realizing my goals and purpose in life. What a *dedicated* and *hard-working* person you are, and I *love* both these qualities.

I would also like to express my heartfelt thanks to my other collaborator, Prof. *John Obayemi* for training me on scanning electron microscopy and learning EDX analysis. Your suggestion and advise helped me to capture high-resolution images of the samples. A big thank to Prof. *Christopher R. Lambert* for allowing access to his lab for the contact angle measurements of the samples.

My humble thanks and gratitude are also due to all the defense committee members, Prof. *L. Ramdas Ram-Mohan*, Prof. *Padmanabhan K. Aravind*, and Prof. *Mohan Srinivasarao* for giving your valuable time in reading my dissertation. A special thanks to *PK* for writing so many recommendation letters for my Post-doc applications. On a personal note, I would like to specifically mention the contribution of *Mohan* for discussing, giving critical feedback, and sharing his valuable knowledge with me.

Thanks to Prof. *Sujata Tarafdar* and the entire *CMPRC* group members at *Jadavpur University*, Kolkata for inviting me for a colloquium talk. Also, a big thanks to Prof. *Tapati Dutta* at *St. Xavier's College*, Kolkata. Thanks to Dr. *Moutushi Dutta Choudhury* and Dr. *Somasri Hazra* for the fruitful comments and suggestions.

I would also like to thank the various communities at WPI who helped me financially and morally during this journey. First of all, I would like to thank Dr. *Abel Curtis* and Dr. *Levin Donna*, the Directors of *Foiesie Innovation Studio and Innovation & Entrepreneurship Integration*, for allowing me to uplift my research to a different level. Thanks for funding and appreciating the innovative idea of my *Ph.D.* project and awarding a seed funding of 12000\$ through the *Tinkerbox* program. Thanks are due to *Lusine Baghsarian*, the Executive Assistant of the *Innovation and Entrepreneurship* for preparing a beautiful video showcasing my *Ph.D.* journey. Without all of your contributions, I do not think I could have completed my journey so smoothly. Thanks a lot! Secondly, thanks to *Suzanne Sontgerath*, the Director of the *Pre-collegiate Outreach Programs*, for selecting me as a *Graduate Mentor* through the *Women Research and Mentoring Program (WRAMP)*. This program definitely shaped my mentoring and teaching skills to a large extent. Thanks for setting up an excellent network between the high-school, undergraduate, and the graduate students. Thanks to Dr. *Kathy Chen* for sending out all possible opportunities for additional funding to the graduate students. Finally, I would like to put it on record that it was an absolute honor to get an opportunity to work the entire summer as a *Graduate Liaison (GL)* with *Debra Boucher* through the *Early Research in E-term (EREE)* program in 2019.

Thanks for believing and selecting me as a GL. This opportunity provided me a much-needed exposure to administrative and logistic work.

Thanks to *Annie Grant*, the MOSTEC Program Administrator of Office of Engineering Outreach Programs at *Massachusetts Institute of Technology* (MIT) to select me as a *Course Instructor* for the project on *Image Processing and Pattern Recognition of Droplets*. This opportunity helped me designing a course for high-school students, and I really appreciate your guidance to be a better mentor and teacher.

Thanks to all of my students who worked with me and helped me to be a better mentor. Special thanks to *Maxi, Rumani, Cindy, Hamida, Hadiya, Emma, Ari, Mahia, Sammy*, and *Andrew*. I really liked your *momos* and *samosas, Rumani!* Thanks to *Hamida* and *Hadiya* for initiating the collaboration between Prof. *Kunta* and our lab on *microtubules*. Thanks to *Ari* for depositing perfectly circular droplets on the substrate and analyzing the droplets throughout the 2019 summer. What a patience level you have! Thanks to *Andrew* for helping me learn *machine learning algorithms*. I appreciate the interactions I have had with you all, and I *love you* all!

Finally, thanks to Prof. *Doug Petkie*, the Head of the *Department of Physics* and the *Graduate Committee*, for selecting me as a *Graduate Mentor* for the academic year 2018-19. Thanks to the *Dean of Graduate Studies* for awarding my research theme in the GRIE (*Graduate Research Innovation Exchange*) ceremony, 2020. Thank you for your constant support and for awarding the travel allowances each year. Thanks to *APS GSOFT* committee for selecting my talk and providing me a travel grant of 500\$ to present at the *APS March Meeting 2020*.

On a personal note, I would like to thank *Debanik* and *Atanu* for the long-hour conversation and providing *ample* opportunities to continue our conversations in *Bangla* here at WPI and to accompany me to the Indian Super Market. A special thanks to *Debanik*, without you, it was impossible to survive the last couple of months of my *Ph.D.* journey during the worst *COVID-19* situation. Thanks to *Yash*, the lab undergraduate, for staying late at nights and dropping me home sometimes. Thanks to *Anthony* and *Zhang* for helping me getting access to the Chemistry building. Thanks to all my *WhatsApp* friends for sharing and replying to my status, and initiating a conversation whenever I needed one. Many thanks to *Akash, Arabinda, Arindam, Bhargav, Bhargabi, Dip, Dwaipayyan, Joyita, Newton, Santu, Shantanu, Subhadip, and Subhasish!* Thanks for understanding me and my words and giving me a home-like feeling. Thanks to all the relatives for your appreciation and criticism. Your criticism helped me to improve myself as a better person. Your appreciation made me happy and motivated me to grow further. Thanks to *Choto Mama, Baban Mama, Baban Da, Didibhai, Boro, Papai, Jethu, Jemma, and Boudi* for loving me so much; you people are very close to my heart!

Last but not least, a big thank you to my *dikhaaguru, Sri Sri Satyanarayan*, for being a path demonstrator! Chanting Your *mantras* helped me accept the harsh reality and

forget the apparent emptiness in my life! Till now, You have helped me decide the right path for me, and I hope, You will do the same forever.

My humble thanks and appreciation are due to my parents, *Aparna Pal* and *Narayan Chandra Pal*, for giving me so much freedom, listening to me, and understanding my need! Thanks for taking all the family burdens and not involving me much during the tough times. Thanks for living my *dreams* with me. Thanks to both of you for always keeping me upfront while making any decisions about your happiness and life. Thanks to *ma* for not listening to the *gossips* of the relatives and not being too depressed with the tons of burdens of a typical low-income, middle-class Indian family. Without your efforts and mental support, it would not have been possible for me to make my *Ph.D.* journey a reality! *Baba*, now your daughter will be a Doctorate soon, *Dr. Anusuya*, the way you always wanted it to be! I am sure you are thrilled to see me succeed in life. It is an *aaha* moment for me as a *first-generation* student studying abroad and, of course, for you as well. I hope I fulfilled most of your desires and dreams. Yes, I know, you also want me to settle down in life soon! Please do not worry; I promise to make you proud very soon and be back home in a few months after starting my next journey as a *Post-doc* in the UK.

Ma and *baba*– thanks for loving me so much. Your *mona* loves you both!

Anu

Worcester Polytechnic Institute

Contents

Abstract	iii
Acknowledgments	iv
List of Figures	xii
List of Tables	xxix
1 Introduction	1
1.1 General Background	1
1.2 Outline of Dissertation	8
2 Fundamental Concepts related to Drying Droplets	10
2.1 Background	10
2.2 Surfaces and Interfaces	10
2.2.1 Surface tension	11
2.2.2 Laplace pressure	12
2.2.3 Wetting	12
Wetting states	13
Yong-Dupré equation	13
Contact angle hysteresis	14
2.3 Length scales and Dimensionless numbers	14
2.3.1 Capillary length	15
2.3.2 Bond number	15
2.3.3 Capillary number	16
2.3.4 Reynolds number	16
2.3.5 Péclet number	16
2.4 Insights of Drying Droplet	17
2.4.1 Different droplet configurations	17
2.4.2 Drying and its various modes	18
Concepts of Thermodynamics	18
Equations governing drying sessile droplet	19
Various modes of drying	21
2.4.3 Different flow mechanisms	22
Coffee-ring effect and Capillary flow	23

	Marangoni flow	24
2.4.4	Colloids and their interactions	24
	DLVO interaction	25
	Self-assembling interaction	26
2.5	Deposited Crack Patterns	28
2.6	Conclusions	30
3	Materials and Experimental Methodology	31
3.1	Background	31
3.2	Materials	31
	3.2.1 Proteins	31
	3.2.2 Liquid Crystals	33
	3.2.3 Human blood	35
	3.2.4 Solvents	38
3.3	Experimental Procedure	41
3.4	Image Acquisition	42
	3.4.1 Optical microscopy	42
	3.4.2 Contact angle goniometer	43
	3.4.3 Scanning electron microscopy	44
3.5	Image Processing Techniques	44
	3.5.1 Determining radius and ring width of the droplets	44
	3.5.2 Texture analysis	45
	First-order statistics	45
	Second-order statistics via GLCM approach	47
	3.5.3 Determining crack spacing of the dried films	48
3.6	Conclusions	49
4	Hierarchy I: Pattern Formation in Globular Protein Droplets	50
4.1	Background	50
4.2	Results and Discussions	51
	4.2.1 Time evolution of drying droplets	52
	Bovine Serum Albumin: BSA+DI	52
	Lysozyme: Lys+DI	54
	A physical mechanism	56
	4.2.2 Morphology of dried droplets	59
	Profilometry	60
	Quantification of the cracks	61
	A mechanical interpretation	64
4.3	Conclusions	67
5	Hierarchy II: Pattern Formation in Protein droplets with LCs	68
5.1	Background	68
5.2	Results and Discussions	69

5.2.1	Lys-LC: Drying droplets and patterns of dried films	69
	Temporal evolution of drying process	69
	Morphological study in dried droplets	72
	Textural analysis in dried droplets	75
	Statistical analysis of crack patterns in droplets	77
5.2.2	BSA-LC: Drying droplets and patterns of dried films	78
	Time evolution of the drying droplets	78
	Birefringence of the dried droplets	79
	Crack morphology of the dried droplets	81
5.3	Conclusions	82
6	Hierarchy II: Pattern Formation in Human Blood Droplets	83
6.1	Background	83
6.2	Results	86
6.2.1	Drying evolution of the blood droplets	86
6.2.2	Morphology of the dried blood film	91
6.3	Discussions	93
6.3.1	Microscopic structures of dried blood film	93
6.3.2	Concentration-driven phase transition in the drying droplets and the dried films	94
6.4	Conclusions	98
7	Drying Droplets in Phosphate Buffer Saline Solution	100
7.1	Background	100
7.2	Results	102
7.2.1	Drying evolution and morphology of Lys-saline droplets	102
7.2.2	Drying evolution and morphology of BSA-saline droplets	107
	Temporal study of the BSA-saline drying droplets	107
	FOS characterization of BSA-saline drying droplets	108
	GLCM characterization of BSA-saline drying droplets	109
7.2.3	Drying evolution and morphology of blood-saline droplets	114
	Time evolution of the blood-saline droplets	114
	Quantitative analysis of blood-saline droplets	117
	Micro-structural analysis of the dried blood-saline film	120
7.3	Discussions	122
7.3.1	Discussions on Lys-saline droplets	122
7.3.2	Discussions on BSA-saline droplets	123
	Qualitative analysis of BSA-saline droplets	123
	Quantitative analysis of BSA-saline droplets	124
7.3.3	Discussions on blood-saline droplets	128
7.4	Conclusions	131
8	Temperature and Concentration Dependent Pattern Formation	133

8.1	Background	133
8.2	Results	134
8.2.1	Qualitative analysis	135
	Human blood: The most complex bio-colloid	135
	BSA protein: The simplest bio-colloid	137
	Lys protein: The simplest bio-colloid	139
8.2.2	Quantitative analysis	141
	Drying evolution of the human blood	141
	Drying evolution of the BSA protein	145
	Drying evolution of the Lys protein	146
	Morphological patterns of the dried films	148
8.3	Discussions	151
8.4	Conclusions	155
9	Conclusions and Future Outlook	157
9.1	Conclusions	157
9.2	Future Outlook	160
	Bibliography	163
A	Directory of all the archived videos	173
A.1	Chapter 4	173
A.2	Chapter 5	173
A.3	Chapter 6	173
A.4	Chapter 7	174
B	List of Publications	175
B.1	Peer-reviewed Journals	175
B.2	Peer-reviewed Conference Proceedings	176
B.3	Peer-reviewed Book Chapters	176
B.4	In Preparations	176

List of Figures

- 1.1 Different forms of patterns observed in nature are illustrated in (I): (a) Branching patterns in leaves at a distinct hierarchy scale. (b) Schooling fish–circulating tori. (c) Buckling of spiral patterns. (d) Cloud patterns are arranged by atmospheric convection. (e) A network pattern formed in the river from erosion and deposition of particles. (f) Flocking and swarming of birds. Various examples of *soft matter* systems are displayed in (II): (a) Liquid crystals under crossed polarized light. (b) Water droplets spread on different surfaces. (c) A single layer of mostly hexagonal bubbles. (d) Mud cracks. (e) Dendrite growth in ice crystals. 3
- 1.2 Schematic diagram describing the various *soft matter* systems: (a) Deoxyribonucleic acid (DNA) (b) Patchy particles (c) Hydrogels (d) Human whole blood (e) Liquid crystals (f) Denatured proteins or polymeric chains. The different phenomena relevant to this dissertation involve wetting and geometry of the droplets on the substrates, phase separation, and self-assembling interactions between the particles, and finally leading to the pattern formation. These structures are drawn from <https://www.biorender.com/>. 4
- 1.3 (a) Schematic diagram describing the physical mechanism of a drying colloidal droplet where a system is relaxing from one equilibrium (initial state) to another equilibrium point (final state). (b) Bright-field images depicting different stages of a human whole blood droplet. Can the resulting macroscopic pattern (fingerprint) be connected to the native/initial state of the constituent particles present in the droplet? . . . 5
- 2.1 A partially-wet liquid droplet deposited on a solid substrate illustrating the balance between interfacial tensions at the three-phase contact line (TPCL: vapor, solid, liquid) are γ_{lv} (at liquid-vapor interface), γ_{sv} (at solid-vapor interface), and γ_{sl} (at solid-liquid interface). The θ_e is the equilibrium contact angle formed at the TPCL. This schematic is inspired by Gerber, 2020. 13
- 2.2 Different droplet configurations on the smooth solid substrate: (I) Sessile droplet, (II) Pendant droplet, (III) Vertical droplet, (IV) Inclined droplet. The diagrams are inspired by Zang et al., 2019. 17

2.3	Schematic of the sessile droplet's geometry and coordinate system. This schematic is inspired by Gorr, 2013.	19
2.4	Illustration of different modes of the drying process: (I) Constant Contact Radius (CCR), (II) Constant Contact Angles (CCA), and (III) Mixed Mode (MM). This schematic is inspired by Zang et al., 2019.	21
2.5	Schematic of different flows develop during the drying process when the droplet is deposited on the solid substrate. This illustration is inspired by Tarafdar et al., 2018.	23
2.6	Schematic of self-assembly in proteins.	27
2.7	Different modes of Crack propagation: (I) Mode I (Crack opening), (II) Mode II (In-plane), and (III) Mode III (Out-of plane). The arrows dictate the direction of the mechanical stress.	29
3.1	Schematic arrangement describing different phases: (I) solid (II) liquid crystal (LC), and (III) liquid. The gray-colored ellipsoids symbolize the molecules. The arrow in the LC phase dictates the average direction of the long axes or the molecules' preferred orientation. (IV) An example of nematic LC, 5CB (4-cyano-4'-pentylbiphenyl) drawn with Jmol (an open-source application for viewing and drawing the 3D chemical structures) http://www.jmol.org/	34
3.2	(I) Schematic diagram dictating the cellular components (RBCs, WBCs, and platelets) of the human blood transported through the blood vessel (artery/vein). The various types of WBCs (monocyte, echinophil, neutrophil, basophil) are also shown. (II) Illustration of the blood centrifuged into different layers. These images are drawn from https://biorender.com/	36
3.3	Schematic shapes of different forms of RBCs (erythrocytes) in the human blood: (a) Normal RBC (bi-concave shaped), (b) Flowing RBC (slipper shaped), (c) Flowing RBC (parachute shaped), (d) RBC in the hypotonic environment, (e) Echinocyte, (f) Sickled shaped RBC. These images are drawn from https://biorender.com/	37
3.4	Drying evolution of the droplets containing the only solvent at different initial concentrations of phosphate buffer saline (PBS): (I) 0x, and (II) 0.25x. The 0x means that the solvent is the de-ionized water.	39
3.5	Drying evolution of the droplets containing the only solvent at different initial concentrations of phosphate buffer saline (PBS): (I) 0.50x, and (II) 0.75x. The scale bar is of length 0.2 mm.	39
3.6	Drying evolution of the droplets containing the only solvent at different initial concentrations of phosphate buffer saline (PBS): (I) 1.00x, and (II) 2.00x.	40

3.7	Drying evolution of the droplets containing the only solvent at different initial concentrations of phosphate buffer saline (PBS): (I) 5.00x, and (II) 10.00x. The scale bar is of length 0.2 mm.	40
3.8	Schematic diagram describing the experimental procedure: (I) A required concentration of the sample solution is prepared. (IV) The solution is pipetted as a droplet on the substrate. (V) The substrate is kept on the sample stage of the optical microscope. (VI) A camera is attached to the microscope and the computer capturing the images of the drying droplets and dried films. It is to be noted that the steps of (II) and (III) are required only for the protein-LC solution. The LC is heated on the hot plate just above its transition temperature and added to the protein solution. (VII) is specific to the temperature study of the drying droplets, where the substrate temperature is tuned with the temperature controller. A hot stage is mounted on the microscope's sample stage, set to the desired observation temperature for a couple of hours before sample placement.	41
3.9	Schematic diagram describing the contact angle goniometer. The high-resolution camera, the light source, and the sample holder are placed on the undisturbed rail throughout the experiment. A computer is attached to the camera, and the installed software is used to measure the contact angle.	43
3.10	A representative processing of images of the dried state of BSA droplet to quantify the spacing between the cracks. a) The raw microscopic images. b) A stitched image. c) An 8-bit gray image. d) An adjusted brightness-contrast image. e) A high contrast image after filtering through variance filter. f) A final binary image depicting different regions, circular line-cut, and crack spacing (x_c).	48

- 4.1 Drying evolution of BSA droplet: (I) Top-view of the droplets through optical microscopy at ϕ of 5 wt% clicked during different time intervals (30 s, 140 s, 186 s, 290 s, 470 s and 530 s). The white dashed circle in (f) exhibits the “coffee-ring” formation. The scale bar represents a length of 0.2 mm. (II) The top panel shows the variation of contact angle ($\theta(t)$) at ϕ of 5 wt%. The solid line specifies the fitted function. The inset shows the variation of the characteristic fitting parameter ($1/\tau$) at different ϕ . The bottom panel displays the temporal variation of the normalized contact angle ($\theta(t)/\theta_0$). (III) The top panel reveals the variation of mean fluid front radius ($\bar{r}(t)$) at ϕ of 5 wt%. The error bars represent the standard deviation. A representative fit of two linear models is made; t_s signifies the time point where both the linear fits merge. The inset shows the dependence of the slope values of linear fit 1 (m_1) and 2 (m_2). The bottom panel indicates the temporal variation of normalized mean fluid front radius ($\bar{r}(t)/\bar{R}$) at different ϕ . t_d is the “dead” time up to which the fluid front radius ($r(t)$) is equal to the radius of the droplet (R). 53
- 4.2 Drying evolution of Lys droplet: (I) Top-view of droplets through optical microscopy at ϕ of 5 wt% during different drying intervals (55 s, 353 s, 563 s, 603 s, 617 s and 673 s). The white dashed circle in (f) shows the “coffee-ring” formation. The solid circle exhibits the “mound”-like structure. The scale bar represents a length of 0.2 mm. (II) The top panel confirms a variation of contact angle ($\theta(t)$) at ϕ of 5 wt%. The solid line shows the fitted function. The inset shows the variation of the characteristic fitting parameter ($1/\tau$) at different ϕ . The bottom panel displays the temporal variation of the normalized contact angle ($\theta(t)/\theta_0$). (III) The top panel reveals the variation of the mean fluid front radius ($\bar{r}(t)$) at ϕ of 5 wt%. The error bars represent the standard deviation. A representative fit of two linear models is made; t_s signifies the time point where both the linear fits merge. The inset represents the dependence of the slope values of linear fit 1 (m_1) and 2 (m_2). The bottom panel indicates the temporal variation of the normalized mean fluid front radius ($\bar{r}(t)/\bar{R}$) at different ϕ . t_d is the “dead” time up to which the fluid front radius ($r(t)$) is equal to the radius of the droplet (R). 55

- 4.3 Side view of the drying evolution: a) Initial mode is observed at an early stage of drying where only the contact angle decreases. The fluid front radius (r) remains unchanged during this time and equals to the radius (R) of the droplet. The protein particles interact with the substrate during this stage. b) In this mixed mode stage, along with the contact angle, the fluid front starts receding from the periphery of the droplet. The fluid front moves, deposits more particles, and forms a ring of width w . It moves further when the radius of fluid front just pass the ring width to the new position (r_2). r_1 indicates the movement towards the central region of the droplet, leading to a complimentary morphology. d) BSA+DI, without any "mound"-like structure and e) Lys+DI, the presence of a "mound" could be observed in the central region. 57
- 4.4 Gray images of two protein dried droplets: BSA at ϕ of a) 1, b) 3, c) 5, d) 7, e) 9, f) 11, and g) 13 wt%; Lys at ϕ of h) 1, i) 3, j) 5, k) 7, l) 9, m) 11, and n) 13 wt%. The images of the BSA droplets reveal the presence of the cracks near the periphery region, whereas, the images of Lys droplets confirm that the cracks are spread and connected from ϕ of 3 wt%. The "dimple" and the "mound"-structure can be observed in Lys droplets at every ϕ . The spirals are noticed in Lys droplets from ϕ of 9 wt%. The scale bar represents a length of 0.2 mm. 60
- 4.5 Profilometric measurements of protein droplets: Variation of the mean peripheral ring width (\bar{w}) normalized to the mean radius of the droplet (\bar{R}) with ϕ for (I) BSA+DI, and (II) Lys+DI. (III) Variation of the averaged area of "mound"-like structure (\bar{a}) normalized to \bar{R} with ϕ in Lys droplet. The error bars correspond to the standard deviation obtained from multiple measurements. 61
- 4.6 (I) Q-Q plot of BSA and Lys droplet at ϕ of 7 wt% displaying the skewed data points. (II) The histogram depicting the comparison of the mean crack spacing (\bar{x}_c) at different ϕ among the proteins in the peripheral regions. Significant pairs (BSA and Lys) are marked with an asterisk [*] at each ϕ . The error bars correspond to the standard error. (III) A characteristic linear fit of a spiral crack trajectory at ϕ of 13 wt% in Lys droplet. The upper inset shows the schematic diagram of the spiral cracks projected on the xy plane, in which $s(\theta)$ is the radial distance from the spiral center and θ is the angle starting from zero in an anticlockwise direction. The lower inset shows an example of spiral focused at $50\times$ magnification, with the scale bar of length $10\ \mu\text{m}$ 62
- 4.7 (a)-(d) show the spirals from 1 to 4 are shown at ϕ of 13 wt% respectively, with the scale bar of length $10\ \mu\text{m}$ 64

- 4.8 Schematic illustration explaining of the nature and propagation of cracks in both the protein droplets. (I) Top-view of a droplet shows radial and azimuthal cracks. A spiral crack is also shown in a polygonal crack domain. An element is focused on displaying crack propagation to get a notion of stress. Mode I (tensile mode) in which (II) stress (σ_θ) acting normal to the radial crack and (III) stress (σ_r) acting normal to the azimuthal crack. 65
- 5.1 Top panel: Time-lapse images of drying Lys-LC drop at the concentration of LCs (ϕ_{LC}) of 0.91 wt%. a) 193 s showed an initial stage of drying. A radial flow of the particles to the droplet edge at b) 403 s and c) 731 s are shown. Merging of large-sized LCs in the central region and filling of these LCs at the droplet edge were displayed at d) 791 s and e) 815 s. The self-assembled structures after visual drying process was observed at f) 1193 s. Bottom panel: Intensity variation with time of Lys-LC drop showing three regimes, an initial slower regime (I), a transition regime (II) and a saturation regime (III). The error bars correspond to the standard deviation. The microscopic images in I, II and III were taken at 301, 745 and 1193 s respectively. The crossed polarizing configuration is depicted by crossed double arrows. The white color in the right corner is a scale bar of 0.2 mm. 70
- 5.2 The morphology of drops after 24 hours. Top panel: Drops imaged in crossed polarizing configuration. The initial concentration of LC droplets (ϕ_{LC} in wt%) is a) 0, b) 0.23, c) 0.46 and d) 0.91. The drop without LC droplets (ϕ_{LC} of 0 wt%) showed very weak birefringence, therefore, lamp intensity was increased for clear visualization. Middle panel: e) and f) show a proposed mechanism for the evolution of the unique patterns. Bottom panel: Gray scaled drops imaged in bright field configuration, where ϕ_{LC} in wt% is g) 0, h) 0.23, i) 0.46 and j) 0.91. The scale bar corresponds to 0.15 mm. 72
- 5.3 Texture analysis of dried drops. Top panel: First order statistics (FOS) reveals the pixel distribution through Mean, Standard Deviation, Integrated Density, Skewness, and Kurtosis. Bottom panel: Gray level co-occurrence matrix (GLCM) reveals the interpixel relations through ASM (Angular Second Moment), Contrast, Correlation, IDM (Inverse Difference Moment) and Entropy. The exponential fit for the curves are shown in each graph. The error bars correspond to the standard error. 76

- 5.4 Top panel: An example of a binary image of a dried drop at ϕ_{LC} of 0.23 wt%. The scale bar corresponds to 0.15 mm. The yellow dashed line separates the drop into rim and central regions. Bottom panel: The histogram depicting the comparison of mean crack spacing (\bar{x}_c) between the regions at different ϕ_{LC} . Significant pairs are marked with an asterisk [*]. The error bars correspond to standard error. 77
- 5.5 (I) Time lapsed images of BSA-LC drying droplet in crossed polarizing configuration (crossed double arrows) at a) 117 s, b) 421 s, c) 677 s, d) 941 s, e) 1007 s and f) 1149 s. The white colored rectangle is a scale bar of 0.2 mm. (II) Intensity variation of BSA-LC droplet with drying time indicates three distinct regimes. The error bars correspond to the standard deviation. The microscopic images in the initial, transition and saturation regimes are taken at 415, 805 and 1149 s, respectively. 79
- 5.6 (I) The morphology of the dried droplets imaged in crossed polarizing configuration (crossed double arrows) after 24 hours: a) BSA-LC, and b) Lys-LC. The white colored rectangle is a scale bar of 0.15 mm. The orientation of LCs in each domain is shown in c) BSA-LC and d) Lys-LC. (II) One particular domain of the BSA-LC sample is rotated under crossed polarizers at a magnification of $10\times$. The yellow arrow indicates a reference point with respect to the four-fan brushes confirming the rotation of the patterns and reveals an *umbilical defect* with a strength of $[+1]$ 80
- 5.7 Dried droplets imaged in bright field configuration after 24 hours: a) Lys without LC, b) Lys with LC, c) BSA without LC, d) BSA with LC. The scale bar represents 0.15 mm. e) A histogram depicting the comparison of mean crack spacing \pm standard error in the protein droplets with and without LC. Significant pairs are marked with an asterisk [*]. 81
- 6.1 Time-lapse images of the blood droplets with different diluting concentration (ϕ) are captured during the drying process. These images dictate different stages: (I) from 100 to 62% (v/v), and (II) from 50 to 12.5% (v/v) (in respect to the original volume of the whole blood). The scale bar corresponds to 0.2 mm. 87

- 6.2 A normalized intensity of a 2-D plot profile along the horizontal diameter of the droplet (ρ) is shown for corresponding a-d depicted in Fig. 1(I-II). These plots captured during the drying process at each ϕ : (I) from 100 to 62% (v/v), and (II) from 50 to 12.5% (v/v). The intensity of the captured image rises along ρ when the dilution is increased (I-II)a. The movement of the fluid front from the periphery is illustrated by a hump in both the edges of the profile (I-II)b. An appearance of the hump in the central region of the profile is observed in (I)b, whereas its disappearance is evident in (II)b. The propagation of the cracks disturbs the uniformity of the plot profile from 100 to 62% (v/v) in (I)c-d; however, it is hardly visible in (II)c-d. The x ranges from -1.25 to 1.25 mm (with a step size of 0.5 mm), while the y axis varies from 0 to 1.1 arbitrary units (a.u.) (with step size of 0.2 a.u.). 88
- 6.3 Variations of the normalized contact angle ($\theta(t)/\theta_0$) during the drying process of the blood droplets at different ϕ ranging (I) from 100 to 62% (v/v), and (II) 50 to 12.5% (v/v) are shown. The normalization of $\theta(t)$ is done by dividing it with the angle at $t = 0$ (θ_0). A monotonic decrease in the contact angle measurements is associated with the presence of a peak-like feature (outlined with a green rectangle) is observed in (I). The disappearance of this feature in these measurements is depicted in (II). The macroscopic images are displayed at different time points (in seconds) points from 100 to 12.5% (v/v) [321s, 512s, 470s, 460s, 473s, 518s, and 617s respectively for different ϕ]. The instrumental limit is illustrated with dashed lines. 90
- 6.4 Statistical image analysis of the blood droplets at different ϕ from 100 to 12.5% (v/v) during the drying process. (I) and (II) show the drying evolution of the first order statistics (FOS) parameters (the mean on the left y axis and the standard deviation (SD) on the right y axis of the graph). The dashed lines in (I) display the time duration of the presence of the peak-like feature in the contact angle measurements from ϕ of 100 to 62% (v/v). The red rectangle and the red circle illustrate the first and the second peaks respectively in the SD. The star introduces the initial dip in the SD values observed from 62% (v/v) onwards. 91

- 6.5 Variation of the averaged corona width (\bar{w} measured in mm) is normalized to the averaged radius of the droplet (\bar{R} measured in mm). It is plotted in (I), the averaged crack spacing (\bar{x}_c) is depicted in (II), and the averaged crack width ($\bar{\lambda}_c$) is exhibited in (III) at different diluting concentrations (ϕ). The dashed line shows the linear fit for the whole range of ϕ from 100 to 12.5% (v/v). The solid lines display two linear fits- first one for the range from 100 to 62% (v/v); and the second one for 62 to 12.5% (v/v). The error bars correspond to the standard deviation. The macroscopic images illustrate the width of the corona (w), the radius of the droplet (R), the distance between the consecutive radial cracks (x_c), and the width between the consecutive radial cracks (λ_c). The dashed green circular line separates the corona from the central region in the droplet. 92
- 6.6 SEM images illustrating the microscopic structures of dried blood films at different length scales. The images at ϕ of 100, 75 and 12.5% (v/v) are, respectively, depicted in (I-III). The yellow, the orange and the black squares represent the blood structures at the periphery and the corona, the transition of the corona and central regions, and the central region, respectively. 93
- 6.7 Side view of the self-assembling mechanism in the whole blood ($\phi = 100\%$) during the drying evolution: (I) The *initial phase* starts when the droplet is deposited on the substrate. The evaporation rate is highest near the three-phase contact line (depicted with solid arrows). The components (RBCs, WBCs, platelets, and proteins) are distributed randomly. A dotted line indicates that a capillary flow is developed in the droplet. (II) The *middle phase* begins when these components are carried towards the periphery. These components initiate interactions as soon as they come in contact with each other. Meanwhile, a plasma-rich layer is developed on the substrate. (III) The segregation of these components takes place as the water continually evaporates from the droplet. During the *late phase*, the three distinct regions (the periphery, the corona, and the center) are developed. The proteins are mostly present in the periphery. The WBCs and the platelets are pushed towards the central region. The RBCs are stacked in the corona region. The trapped water in between two RBCs is marked as the "forbidden area". (IV) The deformation of the RBC and the WBC structures and the activation of the platelets take place during the *end phase*. These structures are drawn from <https://www.biorender.com/>. 96

- 7.1 Morphological patterns in the drying droplets of Lys are displayed. These patterns are shown for the various initial concentrations of Lys (ϕ_{Lys}) at the initial concentrations of salts present in the phosphate buffer saline (ϕ_{salts}). The $\phi_{salts} = 0$ wt% means that it is prepared in the de-ionized water. The scale bar is of length 0.15 mm. 103
- 7.2 Microscopic images of the dried Lys samples are displayed. (ϕ_{Lys}, ϕ_{salts}) = (1.0, 0.5) in (I), (ϕ_{Lys}, ϕ_{salts}) = (3.3, 0.5) in (II), (ϕ_{Lys}, ϕ_{salts}) = (4.8, 0.5) in (III), (ϕ_{Lys}, ϕ_{salts}) = (9.0, 0.5) in (IV), and (ϕ_{Lys}, ϕ_{salts}) = (9.0, 0.0) wt% in (V). The different length scales are shown as the scale bars in the upper-right corner of each image. 104
- 7.3 The time evolution of Lys droplets ($\phi_{Lys} = 9$ wt%) at various initial concentrations of salts in PBS (ϕ_{salts}) during the drying process is displayed in A-D. The $\phi_{salts} = 0$ wt% embodies the Lys solution prepared in the de-ionized water. The timestamps are shown at the left-bottom of each image. The white rectangle represents a scale bar of length 0.15 mm in the top-right. 105
- 7.4 Textural analysis of the Lys droplets ($\phi_{Lys} = 9$ wt%) at various initial concentrations of salts in PBS (ϕ_{salts}) during the drying process is displayed in (I-IV). The x-axis defines the drying time. The left-y (shown in back color squares) and right-y axes (shown in gray color circles) in each graph describe the mean gray values (I) and the standard deviation (SD) in arbitrary units (a.u.), respectively. The star symbol indicates the parameters' fluctuations. The optical image represents the droplets' morphology when significant changes in these parameters are observed. 106
- 7.5 BSA saline droplets at different initial salts concentration in PBS (ϕ_{salts}): The insets show the drying evolution of the droplets is displayed in a-e at ϕ_{salts} of (I) 0.9, (II) 1.8, and (III) 4.3 wt%. The first image is taken within ~ 90 seconds after their deposition on the substrate and is presented in a. The movement of the fluid front is indicated with the white dotted curved lines in b. The appearance of the radial cracks in the periphery and their inward propagation is mostly seen in c. The texture of the droplets changes due to the presence of the salts and is described in c-d. A dashed circular yellow line outlines the rim. The images are taken after completion of the process in e. The time at which the images are captured is shown at the left corner in every image. The scale bar corresponds to 0.2 mm. The different colored histograms depict the counts of the pixels along the y-axis, and the gray values along the x-axis of each image in a-e at various ϕ_{salts} 107

- 7.6 (I-IV) shows the time evolution of the first-order statistical (FOS) parameters [mean (I), standard deviation (SD), skewness ($SKEW$), and kurtosis (KUR)] in arbitrary units (a.u.), respectively in the BSA saline droplets as a function of drying time at the different initial salt concentrations in PBS (ϕ_{salts}) of 0.9 to 4.3 wt%. The different stages of the drying process are outlined with the dashed lines in I-IV. 109
- 7.7 (I-IV) show the comparison of the averaged gray level co-occurrence matrix (GLCM) parameters [angular second moment (ASM), correlation (COR), entropy (ENT), and inverse difference moment (IDM)] in arbitrary units (a.u.), respectively in the BSA-saline droplets at the different initial salt concentrations in PBS (ϕ_{salts}). The pixel displacements ranging from 1 to 1000, and the orientations [horizontal (0°) and vertical (90°)] are varied at each ϕ_{salts} . The significant pairs (0° and 90°) are marked with an asterisk (*). The error bars represent the standard deviation. 113
- 7.8 (I-IV) shows the time evolution of the gray level co-occurrence matrix (GLCM) parameters [angular second moment (ASM), correlation (COR), entropy (ENT), and inverse difference moment (IDM)] in arbitrary units (a.u.), respectively in the BSA saline droplets as a function of drying time at the different initial salt concentrations in PBS (ϕ_{salts}) of 0.9 to 4.3 wt%. The different stages of the drying process are outlined with the dashed lines in I-IV. 113

- 7.9 Time-lapse images of the diluted blood droplets during the drying process at ϕ_{blood} of 75% (v/v). These displayed images are cropped from the original ones for better visualization. The top panel illustrates the formation of the peripheral band (depicted with orange arrows) and the fluid front movement. The white dashed arc line shows that the front moves uniformly from the periphery of the droplet up to 467s. The texture in the central region becomes lighter, outlined with a white dashed circle. The middle panel captures the images from 479s to 587s. This panel emphasizes the non-uniform movement of the front and the appearance of the dendrite structure in the central region. The yellow dashed arc line separates the corona from the central region. The white arrows sketch the propagation of the radial cracks. The σ_l and σ_r demonstrate the symmetric stress fields of these cracks (depicted with yellow arrows). The bottom panel records the crack propagation from 591s to 653s. At the transition of the corona and the central regions, the cracks grow in both directions, and a kink is spotted (white dashed rectangles). The yellow dashed circles display the origin of the micro flaws around the radial crack, whereas the yellow dashed rectangles portray the widening of these radial cracks. The actual time (t in seconds) during the drying process is exhibited in the top-left corner of each image. The scale bar in the bottom-right corner at 653s corresponds to 0.2 mm. 114
- 7.10 Time-lapse images of the diluted blood droplets during the drying process at ϕ_{blood} varying from 62 to 12.5% (v/v). The first captured image after the deposition of the droplet on the coverslip is shown in (a). All the droplets show a homogeneous dark gray texture initially. (b) depicts the next stage that starts with the fluid front movement. Simultaneously, a peripheral band forms, and a light gray texture appears in the center in (b). The formation of different textures in the corona and the central regions is mostly observed in (c). The macroscopic crack patterns as the last stage of the drying process are exhibited in (d). The actual time (t in seconds) is shown in the left corner of every image. The scale bar in the right corner of 12.5(d) corresponds to 0.2 mm. 116

- 7.11 Time evolution of the first-order statistical (FOS) parameters: (I) the mean (I) and (II) the standard deviation (SD) at ϕ_{blood} varying from 100 to 12.5% (v/v). The δt is the shifted time computed by subtracting t_0 from t , where, t_0 is the time when the mean exhibits a rapid rise (indicated with an arrow) and t is the actual time (in seconds) of the drying process. The inset of (I) depicts the variation of t_0 with ϕ_{blood} . The FOS parameters of the first captured image during the drying process are plotted as a function of ϕ_{blood} in the inset of (II). The dashed line in (II) marks the time at which the mean rapidly rises. 117
- 7.12 Variation of the normalized contact angle ($\theta(\delta t)/\Theta$) and the normalized fluid front radius ($\bar{r}(\delta t)/\bar{R}$) as a function of δt is shown in (I) and (II), respectively at ϕ_{blood} of 100 to 12.5% (v/v). The inset of (I) displays the normalized contact angle as a function of δt for the range from -200 to 30 s. The shifted time, δt is defined as $t - t_0$ where t_0 is the time when the mean exhibits a rapid rise in Fig. 7.11(I). The Θ is the intercept value which is computed by plotting the experimental contact angle ($\theta(t)$) as a function of t . The normalization of the contact angle is done by dividing the $\theta(\delta t)$ with Θ . The $\bar{r}(\delta t)/\bar{R}$ is normalized by dividing the averaged fluid front radius [$\bar{r}(\delta t)$] with the averaged radius of the droplet (\bar{R}). 118
- 7.13 The variation of \bar{w}/\bar{R} and \bar{x}_c as a function of ϕ_{blood} is shown respectively in (I) and (II). The \bar{w} is the averaged width of the corona region, and the \bar{R} is the averaged radius of the droplet. The \bar{x}_c is the average crack spacing in the corona region. The error bars denote the standard deviation obtained from multiple measurements. The parameters, w , R , and x_c are illustrated in the macroscopic image captured at $\phi_{blood} = 50\%$ (v/v). 119
- 7.14 The SEM images illustrating the microscopic structures at different length scales are shown in (I) and (II) at ϕ_{blood} of 75% (v/v). The top, middle and bottom panels of (II) depicted with yellow, red and blue-colored rectangles detail the structures at the periphery and the corona, the transition of the corona and central regions, and the central region, respectively. The transition region is also specified with black dotted lines. An energy-dispersive X-ray (EDX) analysis consisting of the number of counts and the energy (keV) of different regions of the blood dried film is shown in (III). The signals are symbolized and colored to match the area from where these were collected. 120

- 7.15 The SEM images illustrating the microscopic structures at different length scales are shown in (I) and (II) at ϕ_{blood} of 12.5% (v/v). The yellow-colored rectangle in the top panel of (II) details the structures at the periphery and the corona. The light and dark blue colored rectangles in the middle and the bottom panels of (II) show different structures in the central regions. An EDX analysis shows the elemental composition of different regions of the blood film in (III). The signals are symbolized and colored to match the area from where these were collected. 121
- 7.16 The images of the dried films of BSA-saline are captured after 24 hours at various initial concentrations of salts in PBS (ϕ_{salts}) (a) 0.9, (b) 1.8, and (c) 4.3 wt%. The yellowed dashed circular lines separate the rim from the central regions. The scale bar has a length of 0.2 mm. The averaged rim width (\bar{w}) is divided with the averaged radius of the droplet (\bar{R}) and the normalized width (\bar{w}/\bar{R}) is shown in (d). The averaged crack spacing (\bar{x}_c) is displayed in (e). The error deviations represent the standard deviations. 124
- 7.17 Histograms depicting the counts of the pixels along the y-axis, and the gray values along the x-axis of each image taken at 440 s, 456 s, 472 s, 488 s, 504 s, and 540 s at $\phi_{salts} = 4.3$ wt% for (I) whole droplet, (II) rim region, and (III) central region. The gray values in x-axis ranges from 0 to 160 (a.u.) in the interval of 20. The pixel counts in y-axis ranges from 0 to 25 ($\times 10^4$) in the interval of 5 ($\times 10^4$). 127
- 7.18 Self-assembling mechanism of the diluted blood droplets at ϕ_{blood} of 75% (v/v) in (A) and 12.5% (v/v) in (B). (I) A capillary flow (indicated with dotted arrows) is established in both the droplets after it is deposited on the substrate. (II) Most of the components are moved towards the periphery of the droplet. (III-IV) The mechanical stress develops causing the structural alteration of the components present in these diluted blood. The droplet gets divided into three distinct regions, the periphery, the corona (the region between the periphery and the central regions), and the central region. 129
- 8.1 Morphology of the whole human blood film during 24 h at different initial concentrations (ϕ_{blood}) ranging from 100 to 12.5% (v/v) that are dried at various substrate temperatures (T) of 45, 35, and 25 °C. The scale bar of length 0.2 mm is represented by the white rectangle in the top-right panel. 135

8.2	Time evolution of the blood droplets during the drying process: (a-f) display the drying stages at the substrate temperature (T) of 45 and 25 °C at the initial concentration (ϕ_{blood}) of 100% (v/v) in (I) and 12.5% (v/v) in (II). The scale bar of length 0.2 mm is represented with the white rectangle in the top-right panel.	136
8.3	BSA film's morphology during the 24 h at different initial concentrations (ϕ_{BSA}) ranging from 20 to 1 wt% dried at various substrate temperatures (T) of 55, 45, 35, and 25 °C. The scale bar of length 0.3 mm is represented with the white rectangle in the top-right panel.	137
8.4	Time evolution of BSA droplets at different substrate temperature (T) during the drying process: (a-f) display different stages at the initial concentration (ϕ_{BSA}) of (I) 20 wt% for T of 55 and 25 °C, and (II) 1 wt% at T of 55 and 25 °C. The scale bar (0.2 mm length) is shown with the white rectangle in the top-right panel.	138
8.5	Morphology of dried lysozyme droplets captured within 24 hours at various initial concentrations (ϕ_{Lys}) diluted from 20 to 1 wt% at controlled substrate temperatures (T) of 25 to 55 °C The white rectangle represents a scale bar of length 0.2 mm in the top-right panel 55 °C.	139
8.6	Drying evolution of lysozyme droplets: (I) a-f displays ϕ_{Lys} of 1 wt% drying under 55 °C. (II) a-f shows the ϕ_{Lys} of 20 wt% drying at 55, 45, and 25 °C. The timestamps are shown at the left-bottom of each image. The white rectangle represents a scale bar of length 0.2 mm in the top-right.	141
8.7	Time evolution of the statistical image parameter, the mean [in arbitrary units, (a.u.)] of the blood droplets at the different initial concentrations (ϕ_{blood}) of 100 to 12.5% (v/v), respectively, in (a-f). The black and the red colors respectively represent the mean at 45 and 25 °C.	142
8.8	Time evolution of the statistical image parameter, the standard deviation [in arbitrary units, (a.u.)] of the blood droplets at the different initial concentrations (ϕ_{blood}) of 100 to 12.5% (v/v), respectively, in (a-f). The black and the red colors respectively represent the standard deviation at 45 and 25 °C.	143
8.9	Time evolution of the normalized fluid front radius ($\bar{r}(t)/\bar{R}$) at different initial concentration (ϕ_{blood}) ranging from 100 to 12.5% (v/v) in the whole blood droplets at various substrate temperatures (T) of 45 °C in (I) and 25 °C in (II). The initial (m_1) and final (m_2) slope values are calculated from ($\bar{r}(t)$) measurements in each region, whereas the slope values (m) are determined from the whole range. The variation of the slope with ϕ_{blood} is displayed in the insets of (I) and (II).	144
8.10	Time evolution of the normalized contact angle ($\theta(t)/\Theta$) in the BSA droplets at the different initial concentrations (ϕ_{BSA}) of 20 wt% in (I) and from 9 to 1 wt% in (II) for T = 25 °C.	145

- 8.11 Time evolution of the averaged fluid front radius ($\bar{r}(t)$) that is normalized with the averaged radius of the droplet (\bar{R}) at the different initial concentration (ϕ_{BSA}) ranging from 20 to 1 wt% in the BSA droplets at different substrate temperature (T) of 55 °C in (I) and 25 °C in (II). The initial (m_1) and final (m_2) slope values are calculated from ($\bar{r}(t)$) measurements in each region at T = 25 °C, whereas the slope values (m) are determined from the whole range at T = 55 °C. The variation of the slope with ϕ_{BSA} is displayed in the insets of (I) and (II). 146
- 8.12 Time evolution of the averaged fluid front radius, ($\bar{r}(t)$) normalized with the averaged radius of the droplet (\bar{R}) at an initial concentration (ϕ_{Lys}) ranging from 20 to 1 wt% at 55 °C in (I) and 25 °C in (II). The error bars represent the standard deviation obtained from multiple measurements (n = 3). The inset shows the concentration dependence of the initial (m_1) and final (m_2) slope values at T = 55 °C in (I) and 25 °C in (II). These values are determined from the time evolution of the $\bar{r}(t)$ 147
- 8.13 Concentration dependence of the normalized ring width (\bar{w}/\bar{R}) of the whole human blood film at different substrate temperatures (T) at (I) 45 °C, (II) 35 °C, and (III) 25 °C. The solid line depicts the linear fit over the whole range from 100 to 12.5% (v/v). The dotted and dash-dotted lines show the linear fit from 100 to 62%, and 62 to 12.5% (v/v), respectively. The dashed line at T = 45 °C is a line drawn to guide our eyes. 149
- 8.14 Concentration dependence of the averaged crack spacing (\bar{x}_c) of the whole human blood film at different substrate temperatures (T) at (I) 45 °C, (II) 35 °C, and (III) 25 °C. The solid green line depicts the linear fit done over the whole range from 100 to 12.5%. The dotted and dash-dotted lines show the linear fit from 100 to 62, and 62 to 12.5% (v/v). 150
- 8.15 (I) Concentration dependence of the normalized width of the ring (\bar{w}/\bar{R}) of the BSA film at different substrate temperatures (T) from 55 to 25 °C. The solid green line shows a master linear fit. (II) Concentration dependence of the averaged crack spacing (\bar{x}_c) of the BSA film at different T from 55 to 25 °C. The different colored dashed lines at different temperatures are drawn to guide our eyes. The x_c and w are shown on the dried BSA film at ϕ_{BSA} of 20 wt% and T = 25 °C. 150
- 8.16 (I) shows the averaged ring width (\bar{w}) normalized with the averaged radius of the droplet (\bar{R}). (II) exhibits the averaged crack spacing (\bar{x}_c), both at various T and ϕ_{Lys} . The error bars represent the standard deviation obtained from multiple measurements (n = 3). The inset of (I) displays a schematic droplet cartoon describing the radius of the fluid front (r) at an instant of time (t), the radius of the droplet (R), ring width (w), and crack spacing (x_c). 151

8.17	The BSA droplet's physical mechanism during the drying process at $\phi_{BSA} = 20$ wt% in (I)a-c and at $\phi_{BSA} = 1$ wt% in (II)a-c. The capillary flow is indicated with the dotted arrows in (I,II)a. The blue and the orange rectangles in (I, II)c display the microstructures in the central and the rim regions (both 20 and 1 wt%).	152
9.1	Schematic diagram describing different directions that could be explored in the near future.	160
9.2	Schematic diagram describing a mini set-up in the doctor's chamber to be used as a pre-diagnostic technique.	162

List of Tables

3.1	Differences between globular and fibrous proteins.	32
3.2	Differences between lysozyme (Lys) and bovine serum albumin (BSA) globular proteins.	33
3.3	It describes the amounts of salts (in mg mL ⁻¹) present in different initial concentrations of phosphate buffer saline (PBS).	38
4.1	Data from $\theta(t)$ vs. t graph of drying droplet at each ϕ (initial protein concentration in wt%) for BSA+DI with fitting parameters: θ_0 (contact angle at $t = 0$ in degrees), $1/\tau$ (characteristic rate in s ⁻¹), and R ² (adjusted R-square of the fit).	53
4.2	Data from $\bar{r}(t)$ vs. t graph of drying droplet at each ϕ (initial protein concentration in wt%) for BSA+DI with measured parameters: R (radius of droplet in mm), w (rim width in mm), t_d (time in seconds after which the contact line radius begins to shrink from droplet radius), t_s (time in seconds at which two linear fits merge); and fitting parameters: m_1 (slope of first linear fit in $\mu\text{m s}^{-1}$), R_1^2 (adjusted R-square of first linear fit), m_2 (slope of second linear fit in $\mu\text{m s}^{-1}$), R_2^2 (adjusted R-square of the second linear fit). The negative sign in the slope values corresponds to the decrease in the radius of the fluid front.	54
4.3	Data from $\theta(t)$ vs. t graph of drying droplet at each ϕ (initial protein concentration in wt%) for Lys+DI with fitting parameters: θ_0 (contact angle at $t = 0$ in degrees), $1/\tau$ (characteristic rate in s ⁻¹), and R ² (adjusted R-square of the fit).	56
4.4	Data from $\bar{r}(t)$ vs. t graph of drying droplet at each ϕ (initial protein concentration in wt%) for Lys+DI with measured parameters: R (radius of droplet in mm), w (rim width in mm), t_d (time in seconds after which the contact line radius begins to shrink from droplet radius), t_s (time in seconds at which two linear fits merge); and fitting parameters: m_1 (slope of first linear fit in $\mu\text{m s}^{-1}$), R_1^2 (adjusted R-square of first linear fit), m_2 (slope of second linear fit in $\mu\text{m s}^{-1}$), R_2^2 (adjusted R-square of second linear fit). The negative sign in the slope values corresponds to the decrease in the radius of the fluid front.	56
4.5	Outcome of Mann-Whitney U test with an asterisk [*] indicating significant interaction between Lys, and BSA in terms of x_c at different ϕ (wt %).	62

4.6	Characteristic fitting parameters of spiral cracks at ϕ of 11, and 13 wt% for $\ln s(\theta) = \ln a + b\theta$ are tabulated: "b" denotes the spiral tightness in $\mu\text{m rad}^{-1}$, and "a" denotes apparent length in μm . $s(\theta)$ is the distance from the spiral center, and θ is the angle which is not restricted to 2π .	64
7.1	Detailed report of Mann Whitney U test for <i>ASM</i> (angular second moment) at each initial concentration of salts in PBS (ϕ_{salts} of 0.9 to 4.3 wt%) and displacement (d) from 1 to 1000 (in pixels). The significant values are marked with an asterisk (*).	110
7.2	Detailed report of Mann Whitney U test for <i>COR</i> (correlation) at each initial concentration of salts in PBS (ϕ_{salts} of 0.9 to 4.3 wt%) and displacement (d) from 1 to 1000 (in pixels). The significant values are marked with an asterisk (*).	110
7.3	Detailed report of Mann Whitney U test for <i>ENT</i> (entropy) at each initial concentration of salts in PBS (ϕ_{salts} of 0.9 to 4.3 wt%) and displacement (d) from 1 to 1000 (in pixels). The significant values are marked with an asterisk (*).	111
7.4	Detailed report of Mann Whitney U test for <i>IDM</i> (inverse difference moment) at each initial concentration of salts in PBS (ϕ_{salts} of 0.9 to 4.3 wt%) and displacement (d) from 1 to 1000 (in pixels). The significant values are marked with an asterisk (*).	111
8.1	Data from $\bar{r}(t)$ vs. t graph of drying droplet at each ϕ_{blood} (initial blood concentration in (v/v)%) for diluted blood droplets with the fitting parameters: m_1 (slope of first linear fit in $\mu\text{m s}^{-1}$), m_2 (slope of second linear fit in $\mu\text{m s}^{-1}$), and m (slope of the linear fit for the whole range in $\mu\text{m s}^{-1}$) with R^2 (adjusted R-square of linear fit) at different substrate temperatures, 25 and 45 °C.	144
8.2	Data from $\bar{r}(t)$ vs. t graph of drying droplet at each ϕ_{BSA} (initial BSA concentration in wt %) for diluted BSA droplets with the fitting parameters: m_1 (slope of first linear fit in $\mu\text{m s}^{-1}$), m_2 (slope of second linear fit in $\mu\text{m s}^{-1}$), and m (slope of the linear fit for the whole range in $\mu\text{m s}^{-1}$) with R^2 (adjusted R-square of linear fit) at different substrate temperatures, 25 and 55 °C.	146
8.3	Data from $\bar{r}(t)$ vs. t graph of drying droplet at each ϕ_{Lys} (initial Lys concentration in wt %) for diluted Lys droplets with the fitting parameters: m_1 (slope of first linear fit in $\mu\text{m s}^{-1}$), m_2 (slope of second linear fit in $\mu\text{m s}^{-1}$), and m (slope of the linear fit for the whole range in $\mu\text{m s}^{-1}$) with R^2 (adjusted R-square of linear fit) at different substrate temperatures, 25 and 55 °C.	148

Chapter 1

Introduction

1.1 General Background

Nature is the home of a wide variety of complex and yet organized systems. Ant colonies, the organization of the human brain, bird flocks, growing ecosystem, river networks, etc., are a few representatives of nature's complex organized systems (Ball, 2021). Many of these systems are biological and yet are different in terms of unique physical realization. A common feature that these biological systems share involves the existence of a hierarchical structure (across length and time scales) and exhibiting collective behavior [see Figure 1.1(I)]. This feature is not simply the sum (or average) of individual microscopic actions. It involves the interactions and feedback mechanisms partially averaged over one length and/or time scale that sets the scale for the next larger/longer length and/or time scale. This phenomenon of macroscopic/mesoscopic patterns requires the interactions of the interconnecting sub-patterns without a centralized controller. The process relies on known physical mechanisms; however, this physical mechanism is applied in a complex recursive way. The biological systems (either living or in a biomaterial sense), therefore, generate a few fundamental questions that are worthy of exploring from a scientific point of view: Do we understand this pattern formation, if so, how? How does the hierarchy play an important role? Is there any single mechanism to anticipate their collective behavior? Does this pattern give rise to any order phenomena? If so, which systems do we need to focus on? What would be our *in-vitro* experiments/methods to understand this behavior?

The scientific field of “*soft matter*” or “*soft condensed matter*” caught the attention of the broader scientific communities during the 1990s when *Pierre-Gilles de Gennes*, the “founding father” of this emerging field, received the Nobel Prize in 1991 for discovering methods for studying these order phenomena (Gennes, 1992). This new field of science changed the vision of the way we address and explore *nature* around us. The daily observations include colorful swirling patterns in soap bubbles, the stickiness of melted cheese, sluggishness of honey, formation of snow crystals, mud cracks, and so on (Ball, 2021; McLeish, 2020) [see Fig. 1.1(II)]. Though we all are familiar with

such phenomena, it is pretty hard to comprehend the underlying physics. Fortunately, the findings of *soft matter* physics opened up new insights for the scientists to explore further. Moreover, this scientific field's emergence also generated a common scientific platform to reflect the coherency of otherwise fragmented scientific domains that include the colloidal physics, polymer physics, and liquid crystals (LCs). The *soft matter* physics, thus, includes a wide variety of systems- from colloids (systems consisting of large molecules where one substance dispersed through another), to polymers (possess a molecular structure which is bonded of a large number of similar units), to foams (form by trapping of air in a liquid or solid), to LCs (a class of materials which possesses fluidity and anisotropy), and finally to many bio-fluids (see Figure 1.2). The wider-scope of this field makes it an interdisciplinary field of research that caught the equal attention of physicists, biologists, chemists, material scientist, etc.

Not surprisingly, one can wonder what is so attractive in *soft matter* physics or how all such sub-systems fall within this domain? Is there any fundamental behavior that these *soft systems* possess? The answer lies in the fact that all these systems are *soft* enough that their interaction energy is in $\sim k_B T$, where k_B is the Boltzmann constant, and T is the absolute temperature. It implies that these systems are sensitive/delicate enough to be disturbed by a slight external perturbation. This also implies that these soft systems deform easily for having low elastic moduli ($G \sim \frac{k_B T}{l^3}$), where l is the characteristic length scale (Gennes, 1992; Fernandez-Nieves and Pueras, 2016). What makes these systems exciting is the co-existence of many phases, leading to an emerging structure or order. For example, LCs have the characteristics between the isotropic liquid and crystals. Interestingly, many researchers prefer to use soft materials as model systems to address many fundamental questions in hard condensed matter. On the other hand, some investigators feel the thrill of understanding the (unique) fundamental properties and phenomena in *soft matter* and focusing on synthesizing new building blocks and putting them together to study the systems' electrical, optical, and mechanical responses in the context of biomedical engineering. Compared to the hard condensed matter, these *soft matter* systems' emergent collective behavior does not depend on each building block's (atoms or electrons) properties. Therefore, the underlying physics can ignore the quantum effects while interpreting such behavior.

Another exciting aspect of these *soft matter* systems is the phase separation and phase transition. We can commonly find the emergence of two or more phases from a single homogeneous phase in the oil-water mixture. The melting of ice to water is a typical example of temperature-dependent phase transition. This transition of states is not limited to temperature but may also occur by tuning the system's concentration, such as changing the phases when the sunset yellow dye solution dries up (Davidson et al., 2017). However, what makes these systems challenging at the same time is their dependence on a vast parameter space to form connected, dynamic,

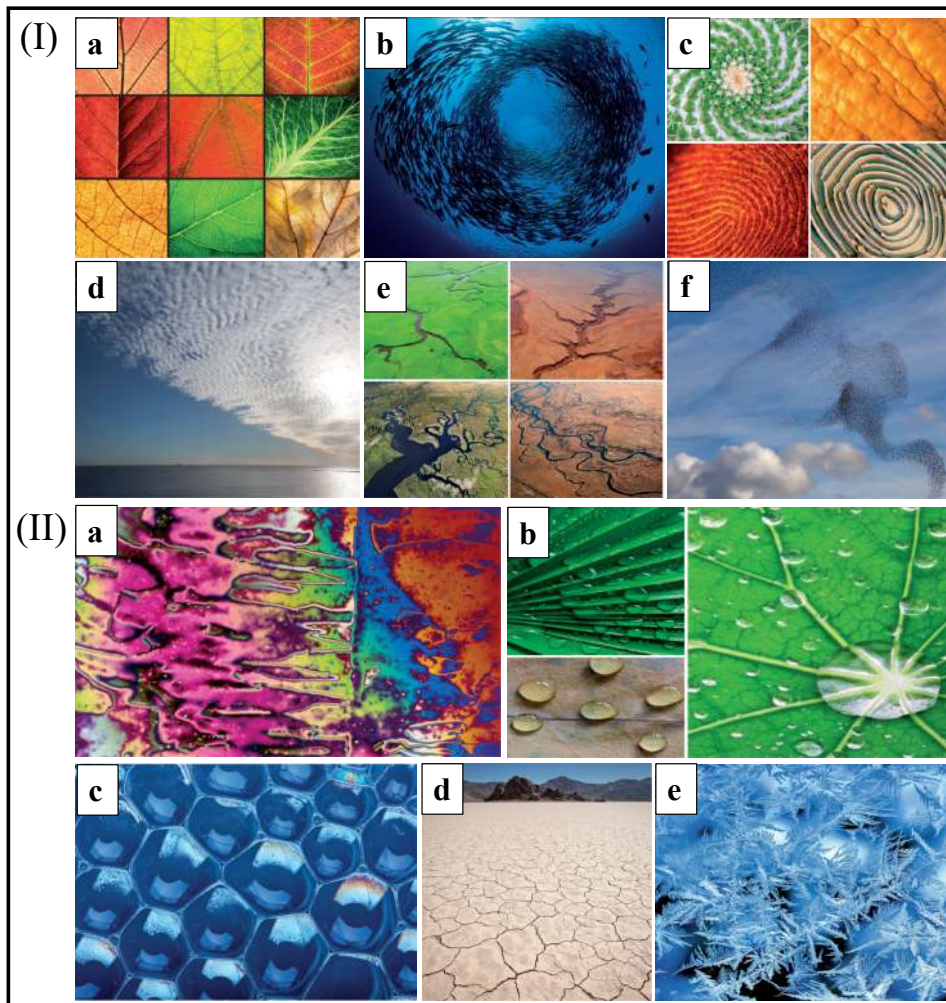


FIGURE 1.1: Different forms of patterns observed in nature are illustrated in (I): (a) Branching patterns in leaves at a distinct hierarchy scale. (b) Schooling fish–circulating tori. (c) Buckling of spiral patterns. (d) Cloud patterns are arranged by atmospheric convection. (e) A network pattern formed in the river from erosion and deposition of particles. (f) Flocking and swarming of birds. Various examples of *soft matter* systems are displayed in (II): (a) Liquid crystals under crossed polarized light. (b) Water droplets spread on different surfaces. (c) A single layer of mostly hexagonal bubbles. (d) Mud cracks. (e) Dendrite growth in ice crystals.

and hard-to-predict behaviors that are, in general, very sensitive to initial conditions and external perturbation. Researchers often consider exploring these problems in a systematic phase, i.e., changing one step or one parameter at a time. Different independent experiments are required to obtain an in-depth understanding of the complex behavior in such systems. Nonetheless, these experiments require careful modeling without rastering the whole parameter space. As mentioned above, these *soft systems* flow and deform the rheology has become an experimental tool over the past few decades. Since these systems are primarily multi-component, their characteristic relaxation time scales are in micro to milliseconds. We might not need to study the ultrafast relaxation, and in most cases, the observations through an optical microscope are enough to characterize their dynamics. The dynamic light scattering

technique can also be used to determine the particles' size and profile distributions (biomolecules or polymers) in the solution.

In the past few years, an area of *active matter* has appeared in *soft matter* physics in which the states of matter depend on the system being driven from equilibrium. One biologically relevant example involves being driven by microscopic entities (motors) that consume energy (either stored or externally supplied ATP) and generate forces in directions related to energy flow through the system (Das, Schmidt, and Murrell, 2020; Fodor et al., 2016). These systems would be considered both thermodynamically "open" and far-from-equilibrium systems because of the continuous exchange of energy and matter with the surrounding environment. The general hallmarks are that the emergent patterns are the resulting gradients due to the constituent particles' local self-assembling interactions.

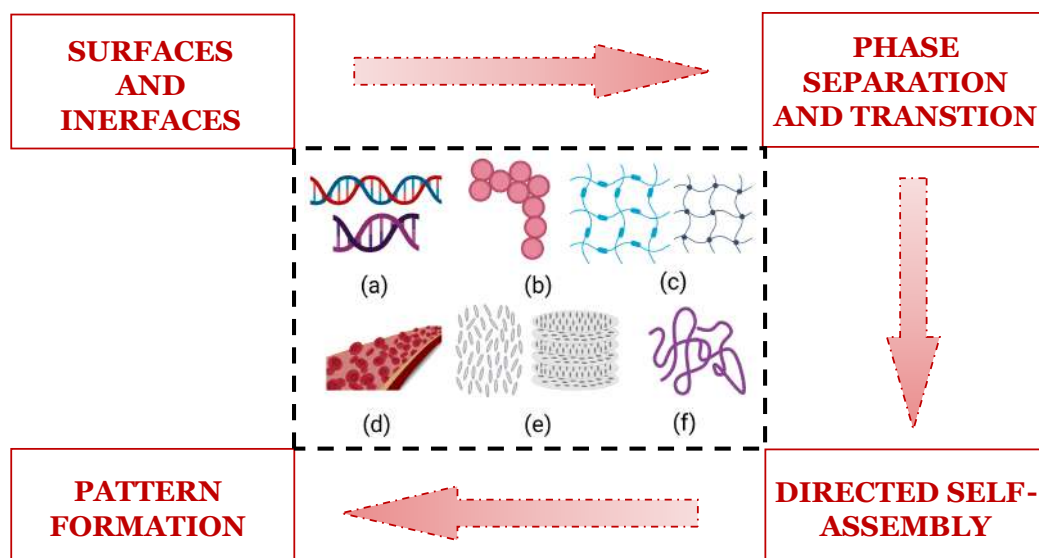


FIGURE 1.2: Schematic diagram describing the various *soft matter* systems: (a) Deoxyribonucleic acid (DNA) (b) Patchy particles (c) Hydrogels (d) Human whole blood (e) Liquid crystals (f) Denatured proteins or polymeric chains. The different phenomena relevant to this dissertation involve wetting and geometry of the droplets on the substrates, phase separation, and self-assembling interactions between the particles, and finally leading to the pattern formation. These structures are drawn from <https://www.biorender.com/>.

Another relevant example worth mentioning in connection to the findings of this dissertation is to consider the relaxation of a system from one state (initial fluid) to another (dried organized film) through a non-equilibrium process that exchanges energy and matter with the environment to drive the assembly between the particles and/or the substrate in order to reach the final state (pattern formation) [see Fig. 1.2]. The final state can be thought of as a frozen state, not in its lowest energy equilibrium state because of the inhomogeneous regular structures that formed. Many researchers have systematically conducted a series of experiments to understand the pattern formation of drying fluid droplets. This mechanism involves the differential evaporation of a solvent from a droplet across its surface that sets up

mass transport through an internal convective flow. It is worth mentioning that different non-biological (colloidal) systems that include liquid crystals, nanoparticles, polymers, etc., have attracted equal interests for their role in industrial applications, such as coatings, inkjet printing, spray cooling, etc. (Erbil, 2012; Deshmukh, Wagh, and Naik, 2016; Chu and Zussman, 2018; Poulard and Damman, 2007; Hu et al., 2013). More recently, systems with biological relevance have attracted interest to understand the constituent particles' self-assembling interactions, such as proteins, plasma, blood, etc. (Brutin et al., 2011; Brutin, Sobac, and Nicloux, 2012; Brutin, 2015; Brutin and Starov, 2018; Chen et al., 2019; Smith, Nicloux, and Brutin, 2020). Interestingly, the drying of bio-fluidal droplets has shown promise in biomedical applications by exhibiting distinctive patterns among the type of diseases, including the (near-perfect) detection of (different) stages of diseases (Mukhopadhyay et al., 2020; Bahmani, Neysari, and Maleki, 2017a; Brutin et al., 2011; Yakhno et al., 2005). Studies have revealed that the drying evolution and the dried state of any droplet (whether there is any biological relevance or not) depend on relatively simple factors: the size, composition, and concentration of the solute colloidal particles, hydrophobicity, or hydrophilicity (wetting conditions) of the substrates, geometry, and shape of the droplets, and evaporation rate driven by environmental conditions [temperature, relative humidity] (Pal, Gope, and Iannacchione, 2021; Iqbal, Shen, and Sen, 2020; Smith and Brutin, 2018; Sobac and Brutin, 2011; Zeid, Vicente, and Brutin, 2013; Zeid, and Brutin, 2014; Yakhno et al., 2010; Brutin, 2013).

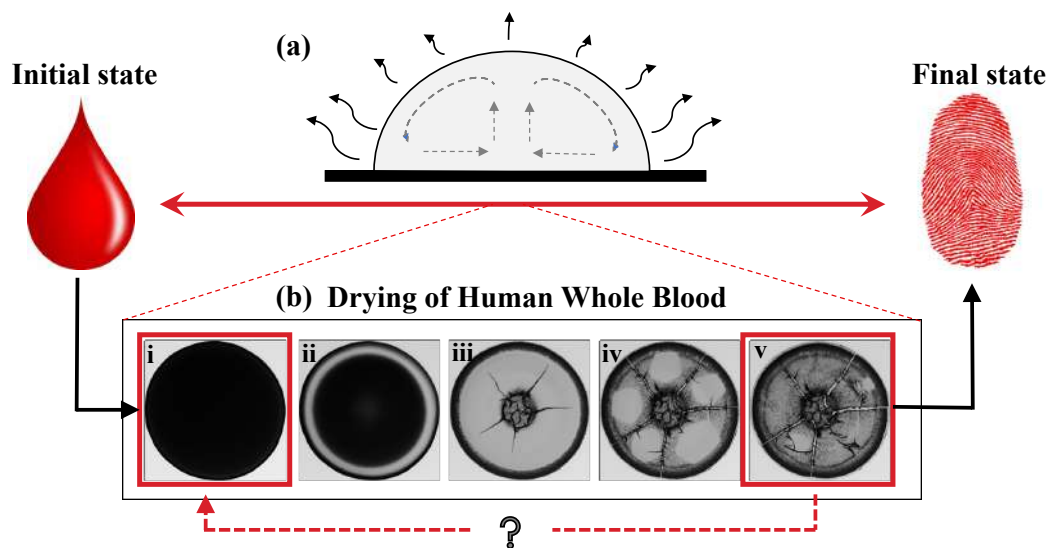


FIGURE 1.3: (a) Schematic diagram describing the physical mechanism of a drying colloidal droplet where a system is relaxing from one equilibrium (initial state) to another equilibrium point (final state). (b) Bright-field images depicting different stages of a human whole blood droplet. Can the resulting macroscopic pattern (fingerprint) be connected to the native/initial state of the constituent particles present in the droplet?

Figure 1.3(a) describes the physical mechanism of a colloidal drying droplet in general. When a droplet of any colloidal fluid solution is pipetted on a substrate, the

constituent particles are dispersed uniformly in the droplet, defining an initial equilibrium state. As the solvent evaporates from the droplet, the system is driven out of equilibrium, and gradients in concentration emerge, which generates convective flow within the droplet. This process acts as an engine and continues until the stored chemical potential of the solvent is exhausted as the system relaxes to another equilibrium-like state but with the suspended colloids organized onto the substrate. Specifically, due to the spherical-cap shape geometry, the solvent mass loss near the periphery is larger than the center. The capillary flow enables suspended particles to be carried towards the droplet's periphery to a degree depending on particle size to compensate for this loss, leading to the "coffee-ring" (Deegan et al., 1997; Goldstein, 2018). Since the droplet is pinned to the substrate, the deposited film's radius is constant throughout the drying process and experiences increasing mechanical stress as the fluid front shrinks. And finally, as the last of the solvent evaporates, and the film also shrinks, fractures occur to relieve the stresses, and a macroscopic pattern (fingerprint) emerges. When these droplets are dried under uniform conditions (shape, size, surface, temperature, humidity, etc.), the final pattern appears to be a unique fingerprint dependent on the initial state of the bio-colloid solution. For example, various stages of the drying evolution of human whole blood droplets are shown in Fig. 1.3(b)[i-v]. The top-view bright-field image of the blood droplet shows the uniform texture in Fig. 1.3(b)i. As time progresses, the fluid front starts moving from the periphery towards the central region (Fig. 1.3(b)ii). The random cracks develop in the central region and start propagating radially towards the periphery (Fig. 1.3(b)iii). The branching of these radial cracks and the change of the texture from light to dark gray is found in Fig. 1.3(b)iv. The dried blood droplet's final fingerprint can be observed in Fig. 1.3(b)v (Pal et al., 2020b). It should be noted that other physical parameters, which evolve during this drying process, also depend on the initial state of the bio-colloidal fluid, such as the wetting angle and the mass loss rate (a direct measure of the change in chemical potential). However, the drying evolution and the final configuration of the film are easily monitored by optical microscopy at different magnifications. Besides, smaller-scale structural information and distribution of material can be determined by scanning electron microscopy (SEM) imaging along with Energy Dispersive X-Ray (EDX) analysis. In-situ micro-rheological measurements would be particularly valuable as the deposited material evolves from a fluid to a gel to a solid to understand the mechanical behavior of the fracture failures of the film.

Because of the importance of images in such studies, the use of new and more sophisticated image processing techniques has become widespread (Dash et al., 2020; Pal, Gope, and Iannacchione, 2019b; Hamadeh et al., 2020; Mukhopadhyay et al., 2020; Baranov, Velichko, and Shariaty, 2020; Gorr, Xiong, and Barnard, 2014). The distance between the consecutive cracks in the droplets (crack spacing) is extracted using freely available software, such as ImageJ (Abràmoff, Magalhães, and Ram,

2004; Schindelin et al., 2012). The appropriate macros specific physical characteristics can be extracted from the images automatically, such as the evolution of cracks, their branching and length, the radius, area, and perimeter of the fluid front. In recent years, researchers [(Carreón et al., 2018b; Pal, Gope, and Iannacchione, 2019b; Pal, Gope, and Iannacchione, 2021)] started using first- and second-order statistics to specify textural image properties during the drying evolution that are capable of delivering another “fingerprint” for the final state of the film. The first-order statistics describe the gray level distribution of the image’s pixel intensity, whereas the second-order statistics are related to the interspatial correlation of pixel intensities. Finally, it should be remembered that the possible image analysis depends on the type of microscopy employed. Additional textural information can be extracted from cross-polarizing microscopy when one of the constituent materials in the bio-colloidal solution is birefringent, such as a liquid crystal (Pal et al., 2019; Pal, Gope, and Iannacchione, 2019a). Such analysis yields information on the orientational order of the LC-rich domains phase-separated from the solution during the drying process. The quantitative parameters can also be compared using data-driven statistical analysis. Recent work has found that when the bio-colloidal solution is blood, sweat, or even tears, the dried patterns exhibit distinctive features (fingerprints) that appear to be related to diseases (Yakhno et al., 2005; Yakhno et al., 2015; Muravlyova et al., 2014; Rapis, 2002; Yakhno et al., 2003). However, a large enough data set fully characterizing all the possible initial states of biomedically relevant fluids has yet to be established to invert the problem and use the fingerprints as a diagnostic tool. Progress is being made as very recently; this approach has been applied to thalassemia diseased patients and found that the interaction between blood cells affects the drying patterns (Bahmani, Neysari, and Maleki, 2017b; Mukhopadhyay et al., 2020). The current state of research aims to create an image corpus (as well as other physical characteristics of the drying sample) of the diseased biofluids and develop machine-learning algorithms to combine them for either fundamental science of colloidal systems or as a simple and easily implemented diagnostic tool. The dried blood samples are recently quantified to see the effects of the exercise-induced blood chemistry changes using such algorithms (Hamadeh et al., 2020). This potential application as an outgrowth from this research indicates the importance and need for understanding the emergence of complex patterns over a wide range of length scales driven by being out of equilibrium in active matter systems.

This dissertation is the outcome of a systematic study that explores the current research trends of the drying droplet community. This work primarily explored a one-component to multi-component bio-colloids. It showcased how image-processing and statistical techniques can be exploited as valuable tools in understanding the droplet phenomena. This dissertation’s goal is not limited to reviewing the state-of-the-art of this field (drying droplet) only. Instead, it aims to motivate future researchers to consider such bio-colloidal systems in a new light to understand (i) how the drying process in a droplet drives the self-assembly of complex structures? (ii)

Can the resulting macroscopic pattern be linked to the native/initial state of the constituent particles? (iii) How do the surfaces, interfaces, substrate temperature affect the pattern formation?

1.2 Outline of Dissertation

This dissertation consists of nine chapters. The work starts with the simplest bio-colloidal (one-component) protein system, and the complexity of such a system is increased hierarchically. This research expands from one-component to multi-component systems. In one direction, the multi-component system is synthetically prepared by adding an optically active material, such as an LC, into the protein solutions. In another direction, the investigation includes naturally occurring multi-component bio-fluid, i.e., the whole human blood. All the experiments' findings made it clear that the patterns become more complex as the variation (inhomogeneity) of the components increases. Different scientific questions are raised in each of these directions. Each chapter's outline is described below:

- After this introductory chapter, **Chapter 2** portrays the underlying concepts and physics involved in the drying droplet. The chapter begins with the concept of thermodynamics in the drying droplet. Then, it talks about different droplet configurations and the wetting behavior of these droplets. The governing equations of fluid behavior and physics of the coffee-ring effect are also elucidated. The various interactions between the colloidal particles and their behavior in the presence of (excess) salts are also explained. The transition of visco-elastic to elastic behavior is defined in the context of rheology. The origin of topological defects in LCs and their types are illuminated. Finally, this chapter ends with the physics of different types of crack patterns.
- **Chapter 3** illustrates different properties of proteins, LCs, and the human whole blood. It also describes the sample preparation and the detailed experimental procedure. Different types of microscopy, such as optical (both in bright-field and cross-polarizing configurations) and scanning electron microscopy, are discussed. The contact angle goniometer is explained for quantifying the wetting behavior during the drying process. The various image processing techniques: for example, determining crack spacing and textural analysis (both the first-order and second-order statistics), are explained using the ImageJ platform. The different solvents (de-ionized water and phosphate buffer saline) and their effect on the drying evolution and patterns are systematically examined and reported in this chapter.
- **Chapter 4** reveals the results and discussions in one-component protein solutions. An extensive study of the drying evolution and the final crack patterns is presented, highlighting the concentration dependence of two globular proteins, lysozyme (Lys) and bovine serum albumin (BSA), in de-ionized water. It

was attempted to describe how and why different patterns are generated when the protein properties vary. This study concludes that the protein-protein interactions play a significant role in deciding the patterns when these droplets are dried under uniform conditions (surface, humidity, temperature, droplet diameter, etc.).

- **Chapter 5** exposes the synthetically prepared multi-component system by adding bulk unaligned LCs into the Lys and BSA solutions. This chapter focuses on exploring the distributions of the LCs (i.e., whether these are always randomly distributed if not aligned, perpendicular or parallel to the substrate before the experiment). The chapter concludes that the LCs' textures and their distributions are influenced without changing the drying mechanism when added in different protein solutions.
- **Chapter 6** uncovers an experimental confirmation of an interesting sharp phase transition during the drying state (reported for the first time in the drying droplet community) and in the dried film as a function of diluting concentrations ranging from undiluted whole blood to diluted concentrations. A change in visco-elasticity is found to decrease with dilution, and it disappears at the dilution concentration for the observed phase transition. In this chapter, two crucial questions are explored. (i) How do the native states of the cellular components change when the mechanical stress emerges during the drying process? (ii) Is this phase transition limited to only blood (multi-component) drying droplets?
- **Chapter 7** reveals the drying process and the resulting morphological patterns when the de-ionized water is replaced with the saline water. Some insights to the scientific questions are exposed. For example, (i) do we still observe phase transition in the blood samples when the diluent is phosphate buffer saline (PBS)? (ii) What is the interplay between protein-protein and protein-salt interactions during the drying process?
- **Chapter 8** shows the effects on the drying evolution and the protein and blood samples' morphological patterns by changing the controlled substrate temperature. This chapter asks the following: (i) Whether the increase in temperature decreases the drying time only? (ii) Does it affect the patterns significantly in both the proteins? If not, why? (iii) Does this change the microstructures of the blood cellular components?
- **Chapter 9** summarizes this dissertation's significant findings and expands to the possible future avenues, which can extend this drying droplet research.

Chapter 2

Fundamental Concepts related to Drying Droplets

2.1 Background

Our previous chapter has provided a layout and the current state of your understanding of the soft matter-like systems in general and discussed how the various phenomena are involved in deciding the emerging patterns (see Figures 1.2 and 1.3). As our dissertation mainly focuses on how these patterns emerge when a system dries (i.e., relaxes from one equilibrium point to another) under a uniform set of conditions (surface, humidity, temperature, droplet diameter, etc.), it is important to understand some fundamental concepts related to the different types of droplet configurations, wetting, phase change, modes of drying, self-assembling interactions, and the deposited patterns. Therefore, this chapter briefly discusses the theoretical background relevant to this study.

2.2 Surfaces and Interfaces

An interface can be defined as the separation surface between two different phases. In a thermodynamic sense, a phase is a homogeneous part of a system that is under consideration or investigation. The term, "homogeneous" implies here that the part has the same thermodynamic state variables (such as pressure (P), volume (V), temperature (T), concentration (C), etc.). Any discontinuity in such variables implies that the phase boundary is reached or the interface of different phases. We assume the interface as an infinitely thin surface; however, it is to be noted that the real systems' interface is usually a transition zone with a few molecules thick. Capillarity is the interfacial study of two immiscible liquids (oil in water-like systems) and/or between liquid and/or air/solid (for example, a droplet sitting on a solid surface).

Since only the solid and flat substrate is used in this work, the physics of any soft substrate is not considered here. This section describes how the liquids interact with the substrate. Therefore, the concept of surface tension, wetting states, and

its dynamics are focused. Mainly this section is based on the book, "Capillarity and Wetting Phenomena" (De Gennes, Brochard-Wyart, and Qu  r  , 2013) and the Ph.D. dissertation (Gerber, 2020) unless otherwise stated.

2.2.1 Surface tension

It is well-known that some energy needs to be provided if we want to increase a given material's surface area. Suppose we want to distort a liquid for increasing its surface area by dA amount. Then, the work done by the system (liquid) should be proportional to its number of the molecules that must be brought to dA . Mathematically, we can express it as follows.

$$\delta W = \gamma dA \quad (2.1)$$

where γ is the proportionality constant called surface tension or interfacial tension.

Therefore, the mechanical definition of γ is the surface energy supplied to the system to increase the surface area by one unit. It is also viewed as the (capillary) force per unit length. The two aspects— force and energy depend mainly on the context. However, it is necessary to understand what it means thermodynamically. It is often related to any of the state functions (Helmholtz free energy (F), internal energy (U), etc.) because their variation depends on the initial and final states (defined by the intensive variables), not the path taken to come to the final state. If the work done against the external pressure P is PdV and to change the surface area is dA , the surface tension can be defined as

$$\gamma = \left. \frac{\partial F}{\partial A} \right|_{T,V,N} \quad (2.2)$$

The complete derivation of this relation can be found in (Rowlinson and Widom, 2013).

When this free energy is related to the surface tension, it is also called surface free energy (mostly used in the context of interface science); however, these terms ("surface free energy", "surface tension" and "surface stress") might be confused as these terms are widely used in different contexts. To provide a clear picture, we followed the article, "On surface stress and surface tension: I. Theoretical considerations" (Vermaak, Mays, and Kuhlmann-Wilsdorf, 1968). In general, we can relate the surface stress and the surface tension by,

$$f_{ij} = \delta_{ij}\gamma + \frac{\partial \gamma}{\partial e_{ij}} \quad (2.3)$$

where f_{ij} , δ_{ij} , and e_{ij} are the surface stress, Kronecker delta, and the strain.

Numerically, the f_{ij} is the force per unit length, which must be applied to an edge of the surface to keep it in equilibrium. The subscript i is the direction perpendicular to the exposed edge in the surface plane, and the subscript j directs where the force acts. In other words, it can be related to the eq. 2.1 by saying that $f_{ii}dA = \delta W$, i.e., the work required to increase the dA surface area in the i th direction.

It is clear from eq. 2.3 that the surface stress (f_{ij}) is different from the surface tension (γ) when there is definite value of strain (e_{ij}), i.e., the nature of the strain—either plastic or elastic. The strains, therefore, depend on the kind of stresses that are supported or considered by the material at the particular environment (P, T, μ , etc.). For example, the deformations in a free planar liquid surface are completely plastic as they do not change the average density or the configuration of the atomic arrangements. Therefore, $\frac{\partial \gamma}{\partial e_{ij}} = 0$ and the f_{ij} becomes identical to γ .

2.2.2 Laplace pressure

It is observed that the pressure jumps at any curved interface (surface). To get a mathematical expression, let us assume that there is a spherical droplet of liquid i is placed in another immisible liquid j , The radius of the droplet is R and it is displaced by dR amount at the interface. Then, the total work can be written as,

$$\delta W = -P_i dV_i - P_j dV_j + \gamma_{ij} dA \quad (2.4)$$

where the change of surface area is dA , and the volume of i th and j th liquids are dV_i and dV_j of the droplet, respectively. The dV_i is given by $-4\pi R^2 dR = dV_j$ and the dA is $8\pi R dR$. If P_i and P_j are the pressures of the i th and j th liquids and the system is in equilibrium mechanically ($\delta W = 0$), then, the pressure difference at the interface is called the Laplace pressure (ΔP_l), which is given by,

$$\Delta P_l = P_i - P_j = 2 \frac{\gamma_{ij}}{R} \quad (2.5)$$

Therefore, in general the the Laplace pressure is,

$$\Delta P_l = \gamma \left(\frac{1}{R_1} + \frac{1}{R_2} \right) \quad (2.6)$$

where R_1 and R_2 are the surface's radii of curvature. This implies that the pressure will be larger for a smaller droplet or a bubble.

2.2.3 Wetting

It is the study of the liquids' spreading when deposited on the solid or the liquid substrate. Since our study deals with the solid substrate, we will limit our discussion to the rigid substrate. Figure 2.1 shows an example of a liquid droplet sitting on the

solid substrate. It illustrates the balance between interfacial surface tensions at the three-phase contact line (TPCL). This interface is made from the vapor (v), solid (s), and liquid (l) phases. The interfacial γ is defined as γ_{lv} (at liquid-vapor interface), γ_{sv} (at solid-vapor interface), and γ_{sl} (at solid-liquid interface). The angle formed by these contact phases at equilibrium is given by θ_e , commonly known as the contact angle.

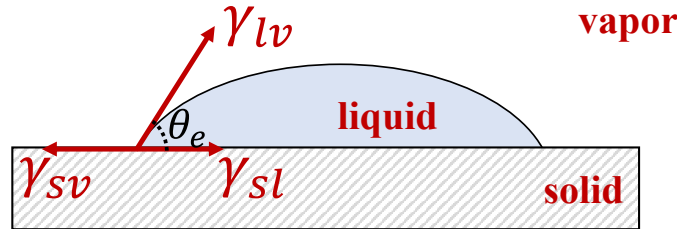


FIGURE 2.1: A partially-wet liquid droplet deposited on a solid substrate illustrating the balance between interfacial tensions at the three-phase contact line (TPCL: vapor, solid, liquid) are γ_{lv} (at liquid-vapor interface), γ_{sv} (at solid-vapor interface), and γ_{sl} (at solid-liquid interface). The θ_e is the equilibrium contact angle formed at the TPCL.

This schematic is inspired by Gerber, 2020.

Wetting states

Depending on the magnitude of the θ_e , experimentally, the substrate is classified as— (i) hydrophilic ($\theta_e < 90^\circ$), (ii) hydrophobic ($\theta_e > 90^\circ$), and (iii) superhydrophobic ($\theta_e > 150^\circ$). Sometimes, the substrate is called neutrally wet when the θ_e is exactly equal to 90° . The liquid can also spread completely on the substrate ($\theta_e = 0^\circ$) or not wet the substrate at all ($\theta_e = 180^\circ$). These various wetting states determine whether the evaporative-flux of these droplets is uniform or non-uniform, detailed later in this chapter.

Furthermore, a wetting/spreading parameter (S) can be defined that dictates the wetting regimes by measuring the difference of γ at the interface. The two regimes are total wetting (for $S > 0$) and partial wetting ($S < 0$). Within this partial wetting regime, we call it as “mostly wetting” state when $\theta_e < 90^\circ$, and “mostly non-wetting” when $\theta_e > 90^\circ$.

$$S = \gamma_{sv} - (\gamma_{lv} + \gamma_{sl}) \quad (2.7)$$

Yong-Dupré equation

The three interface surface tensions is also related to the equilibrium contact angle (θ_e) by the pioneering work done by Young in the year 1805. It states that the θ_e of a liquid droplet sitting on a smooth, rigid solid substrate is given by,

$$\gamma_{sv} - \gamma_{sl} = \gamma_{lv} \cos\theta_e \quad (2.8)$$

The complete derivation of eq. 2.8 is described in (De Gennes, Brochard-Wyart, and Quéré, 2013). It is to be noted that this equation needs to be modified if the substrate is rough and non-homogeneous or the substrate is inclined. Combining the eqs. 2.7 and 2.8, we get,

$$S = \gamma_{lv}(\cos\theta_e - 1) \quad (2.9)$$

Contact angle hysteresis

The eq. 2.9 is usually valid when the substrate is not rough and homogeneous; however, it is not the case for the real situation. There are two contact angles—advancing and receding. These angles are measured by tilting the substrate where a liquid droplet is deposited. The “downhill” droplet’s side will have a higher contact angle ($\theta_e = \theta_a$, known as advancing contact angle), and the “uphill” side will show the lower contact angle ($\theta_e = \theta_r$, known as receding contact angle). At a particular tilt angle, θ_a will be equal to θ_r , and the droplet will move on the substrate. However, for most of the cases, it is to be noted whether there is any significant difference in the contact angles measured at the left (θ_l) and right (θ_r) sides. If $|\theta_l - \theta_r| \leq 2^\circ$ for a droplet deposited on the substrate having $\theta_e \sim 30^\circ$ or above, we can use the θ_e for getting the insights at the three-phase. Like many researchers, we have also adopted this method and measured the contact angle evolution as the droplet dries. The detailed discussion about the contact angle measurement is described in chapter 3.

It is important to know that it is difficult (almost impossible) to measure θ_e accurately). There is often a precursor film (an extremely thin of \sim nm layer) at the TPCL (Zang et al., 2019). The contact angle goniometer (described in the next chapter) actually measures the apparent contact angle (θ^*) as the substrate is not perfectly smooth in a practical sense. Therefore, the contact angle measurements $\theta(t)$ throughout the dissertation is actually based on the θ^* , not the θ_e .

If the precursor film’s thickness is h^* , it is determined by the interaction between the surface tension and the van der Waals force. It is given by,

$$h^* = \sqrt{A/6\pi\gamma_{lv}} \quad (2.10)$$

where A is the *Hamaker* constant, which is a material property depending on the density and electronic polarisability.

2.3 Length scales and Dimensionless numbers

There are many length scales and dimensionless numbers that are used in different contexts—mostly in fluid mechanics. A few of the relevant numbers are described in

this section. The text is based on the review article, "Evaporation of a Droplet: From physics to applications" (Zang et al., 2019), unless otherwise stated.

2.3.1 Capillary length

As the droplet is deposited on the substrate, there could be some effects from the gravity. Therefore, the question remains– when do we ignore or consider such an effect? This is given by a particular length that is defined as,

$$l_c = \sqrt{\gamma_{lv}/\rho g} \quad (2.11)$$

where l_c , ρ , and g are the *capillary length*, the density of the liquid, and the acceleration due to gravity, respectively.

Comparing the *capillary length* with the droplet's radius (R), two regimes are found. When $R \ll l_c$, the surface tension will dominate over the gravity and vice-versa. This relation is not limited to the liquids but can be used for any colloidal systems. It also provides a clear distinction when to call a drop or droplet. When the surface tension dominates, we will say droplet; otherwise, drop (De Gennes, Brochard-Wyart, and Quéré, 2013). However, the terms drop and droplets are used interchangeably in the literature. Since we have maintained ~ 2 mm as the diameter, we will call these as "droplets" throughout our dissertation. Furthermore, in an intuitive sense, the droplets are the smaller-sized drops. These droplets tend to eat each other, and their coalescence (merging) leads to a larger droplet (termed as drop). The condition of $R \ll l_c$ also indicates that the droplet has a spherical-cap geometry, which will be described in details later in this chapter.

2.3.2 Bond number

There is also another parameter (dimensionless number), which is considered in the droplet community to know whether the surface tension or the gravity dominates. It is called *Bond number* (Bo) (Chen et al., 2016b), given by,

$$Bo = \rho g R h / \gamma_{lv} \quad (2.12)$$

where ρ is the fluid density, and R and h are the radius and the central height of the droplet, respectively. When $h = R$, Bo becomes $\rho g R^2 / \gamma_{lv}$ or $\rho g h^2 / \gamma_{lv}$. It is found in the literature (Chen et al., 2016b) that the surface tension influences much more than the gravity when the $Bo < 1$.

2.3.3 Capillary number

The wetting can be influenced by the viscosity in addition to the gravity and the surface tension. This is given by another dimensionless number, called *Capillary number* (Ca). The relation is described by,

$$Ca = \eta u / \gamma_{lv} \quad (2.13)$$

where u , and η are the TPCL velocity, and the dynamic viscosity, respectively. The droplet is dominated by surface tension over the viscosity force for the smaller values of Ca ($< 10^{-5}$).

2.3.4 Reynolds number

Another important parameter, Reynolds number (Re) is considered while studying the flow behavior (fluid dynamics) in the drying droplet community. It helps predicting the flow patterns. If Re is low ($Re < 1$), the flow will be sheet-like (parallel layers without any disturbance between those layers), i.e., dominated by the laminar flow over the turbulent flow (for high Re). The turbulent flow is characterized by the chaotic changes in the pressure (P) and flow velocity (u). Therefore, Re is defined as the ratio of the inertial forces to the viscous forces within a fluid (Eales et al., 2015).

$$Re = \frac{uL}{\nu} = \frac{\rho uL}{\eta} \quad (2.14)$$

where L , and ν are a characteristic length, and the kinematic viscosity (also called the momentum diffusivity), respectively. Therefore, the $\nu = \frac{\eta}{\rho}$.

2.3.5 Péclet number

It is relevant or used while studying the transport phenomena in a continuum. The Pe is defined as the ratio of the rate of advection to the rate of diffusion.

In the context of mass transfer, the Pe is defined as:

$$Pe = \frac{Lu}{D} \quad (2.15)$$

where D is the mass diffusion coefficient. For the negligible diffusion, the Pe is very large. In the context of the thermal fluids, it is defined as,

$$Pe = \frac{\rho Lu C_p}{\kappa} \quad (2.16)$$

where κ is the thermal conductivity, and C_p is the specific heat capacity.

In the droplet community for the sessile configuration, Pe is also written as,

$$Pe = \frac{Jh_0}{D} \quad (2.17)$$

where h_0 is the initial central height of the sessile droplet, D is the diffusion coefficient of the non-volatile particles present in the droplet, and J is the evaporation flux of the sessile droplet (Chen et al., 2016b). It is widely used to predict whether *skin* will form once the solvent starts leaving the system. Furthermore, the concentration of the particles increases and leads to solidification. If $Pe \ll 1$, the diffusion will be faster, and therefore, it can maintain a uniform concentrated film. For the weaker diffusion, $Pe \gg 1$ will produce the gradients in their concentration films (Goehring et al., 2015).

2.4 Insights of Drying Droplet

2.4.1 Different droplet configurations

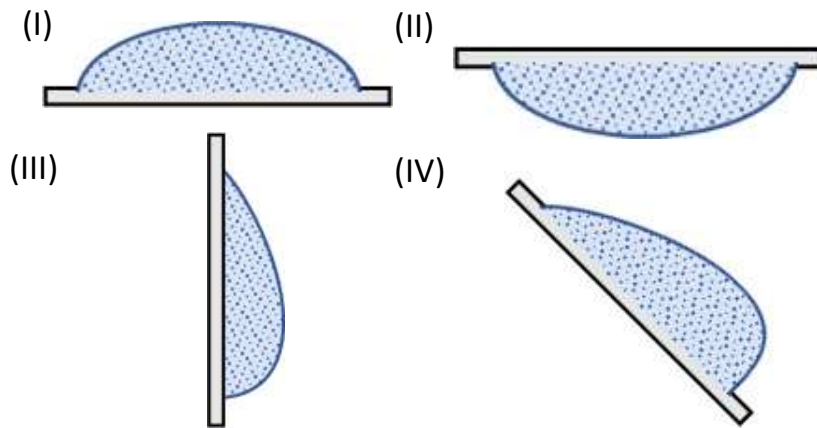


FIGURE 2.2: Different droplet configurations on the smooth solid substrate: (I) Sessile droplet, (II) Pendant droplet, (III) Vertical droplet, (IV) Inclined droplet. The diagrams are inspired by Zang et al., 2019.

The droplets can have different configurations; for example, the droplet sitting on the horizontal solid substrate is called the *sessile* droplet. This word is originated from the Latin word, “*sessilis*,” meaning fit for sitting on (Dictionary, 1989). This type of droplet exhibits axial symmetry and is only relevant to this dissertation. However, the other types of droplets form when the same substrate is rotated vertically. This breaks the symmetry of the droplets and is called vertical droplets. Further, the substrate can be tilted to create tilted droplets. If the system is turned upside down by rotating the substrate such that the droplet is suspended in a downward direction, it is defined as a pendant droplet [see Figure 2.2(I-IV)].

2.4.2 Drying and its various modes

Concepts of Thermodynamics

If the droplet is kept undisturbed under ambient conditions (at a fixed temperature, pressure, relative humidity, etc.), the solvent (liquid) from the system under the investigation (here is the droplet) will evaporate as time progresses. In other words, there will be removal of the liquid will make the system dry. Therefore, in the droplet community, the word drying or evaporation is used interchangeably. Just to maintain the consistency, we have used the word “drying” throughout our dissertation. It is good to know that these two words have separate definitions in different contexts. For example, “drying” typically refers to the loss of the moisture content from the phases (either solid, liquid, or gases). The word, “evaporation” in the thermal processing engineering <https://www.gunt.de/en/> implies a process to separate the solvent from the solution (a mixture of solute and solvent). In general terms, evaporation is a (phase) process that changes the liquid to the gaseous phase.

Thermodynamically, evaporation is a transitioning process in which the vapor pressure over the liquid is enhanced. In contrast, we can condensate the gas back to liquid by lowering its vapor pressure. Therefore, two phase transitions– evaporation and condensation involve either consuming or evolving enthalpy of transition and change in entropy. If the enthalpy of evaporation is ΔH_{vap} , the transition temperature is T_{tr} , and the changes in the vapor and entropy during the evaporation are ΔV_{vap} and ΔS_{vap} , respectively, the vapor pressure (P) at that temperature (T) is given by the *Claperyron equation*,

$$\frac{dP}{dT} = \frac{\Delta S_{vap}}{\Delta V_{vap}} = \frac{\Delta H_{vap}}{T_{tr}\Delta V_{vap}} \quad (2.18)$$

It is to be noted that this kind of transition occurs at constant atmospheric pressure. So, the latent heat of evaporation or condensation can be related to the enthalpy change as $\Delta Q = \Delta H_{vap}$ at constant pressure. Since the molecular arrangement and packing of the molecules get disturbed during this transition, this change is accompanied by ΔS_{vap} . Therefore, evaporation is an endothermic process as $\Delta H_{vap} > 0$ (heat is consumed), and condensation is an exothermic process as the heat is evolved. From eq. 2.18, we can write $\Delta S_{vap} = \frac{\Delta H_{vap}}{T_{tr}}$. This implies that $\Delta S_{vap} > 0$, i.e., the degree of molecular order decreases as the change of entropy increases during the evaporation process, and vice versa for the condensation process.

It is worth mentioning here that evaporation and condensation are examples of the first-order phase transitions. If the Gibbs free energy (G) is continuous but its first derivative to T , i.e., $(\frac{\partial G}{\partial T})$ is discontinuous across the phase transition, the slope of $G(T)$ in the solid region will be different from the liquid region. Therefore when the first derivative of any free energy w.r.t. any of the dependent thermodynamic

variables is discontinuous, it is called "first-order phase transition". The "second-order phase transition" is when the free energy and its first derivative is continuous but not its second derivative. One of the examples includes the transition of order-disorder in the paramagnetic materials.

To get insights of the drying (evaporation) process in a sessile droplet, it is important to understand what we mean by the term "vapor pressure". Above the surface of the liquid, there is always some amount of gaseous liquid. When the system is open, there are enough molecules at the liquid's surface that try to escape. Consequently, the number of escaping molecules becomes larger than the number of molecules coming back from the gaseous to the liquid phase. In this case, vapor pressure is small and far from saturation. As time progresses, the number of molecules escaping and returning becomes equal. At this point, we say that the vapor pressure over the liquid water is saturated.

Equations governing drying sessile droplet

The underlying mechanism in the drying droplets is modeled analytically and numerically by several researchers (Tarasevich and Ayupova, 2003; Tarasevich, 2005; Masoud and Felske, 2009; Barash et al., 2009; Maki and Kumar, 2011; Bouchenna et al., 2017; Hu and Larson, 2002; Popov, 2005; Hu and Larson, 2005). To do so, researchers often use lubrication approximation. It assumes a solid and flat substrate on which a partial-wet droplet is deposited. The fluid film is thin enough such that $\frac{R}{h} \ll 1$ (Eales et al., 2015). Nevertheless, it becomes a challenging task when these colloids self-interact (Tarasevich, 2004; Tarasevich and Ayupova, 2003). This self-assembly is typical in most of the bio-colloids, such as protein, serum, plasma, blood, etc. Since this dissertation is mainly focused on the experimental studies of the drying droplets, the mathematical derivation or finding the analytical solutions are beyond its scope. However, we will discuss some of the assumptions and end-results here. The following text is adopted from the Ph.D. dissertation, "Lysozyme pattern formation in evaporating droplets" (Gorr, 2013).

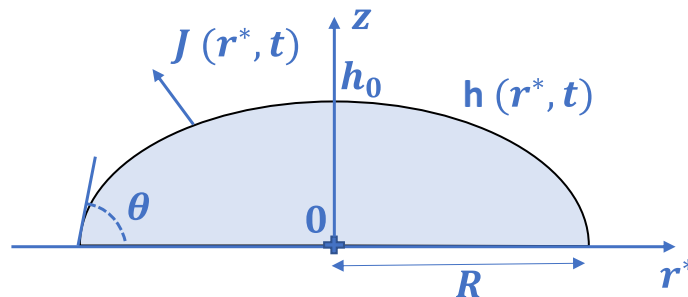


FIGURE 2.3: Schematic of the sessile droplet's geometry and coordinate system. This schematic is inspired by Gorr, 2013.

The evaporation model is based on the fact that the $Bo < 1$, which implies that the droplet initially has the shape of a spherical cap. The forces are mostly dominated

by the surface tension, and the gravitational force is negligible. This is the most acceptable model where the droplet is pinned to the substrate by maintaining constant contact radius, i.e., the radius of the droplet R stays the same, whereas the volume and the height changes with time (Deegan et al., 1997; Popov, 2005).

Figure 2.3 illustrates a schematic of a droplet deposited on the smooth substrate with a dynamic contact angle $[\theta(t)]$. Assuming spherical cap geometry, and r^* is the radial component of the coordinate system, the height of the droplet, $h(r^*, t)$ is,

$$h(r^*, t) = \sqrt{\frac{R^2}{\sin^2\theta(t)} - r^{*2}} - \frac{R}{\tan\theta(t)} \quad (2.19)$$

The volume of the droplet also varies with time. So, the $V(t)$ can be expressed by,

$$V = \int_0^R 2\pi R h(r^*, t) dr^* \quad (2.20)$$

This gives,

$$V = \frac{\pi R^3}{3 \sin^3\theta(t)} [1 - \cos\theta(t)]^2 [2 + \cos\theta(t)] \quad (2.21)$$

It is to be noted that we intentionally put r^* so that the readers don't confuse with the fluid front radius in the later chapters, which is denoted by r . The complete calculation for the volume and the surface area of the spherical-cap shaped droplet can be found in <https://mathworld.wolfram.com/SphericalCap.html>

To find the evaporation rate, we need to understand what happens at the liquid-vapor interface. The droplet is deposited and kept under ambient condition, so, the liquid evaporates into the ambient air. Because of the shape, the vapor concentration is not uniform, it has a nonuniform distribution. As discussed the thermodynamics concept of phase transition (i.e., evaporation), the local vapor concentration of liquid (c) need to be equal to its saturation value (c_{vap}) at the interface of the liquid-vapor. Far above the droplet, the vapor concentration approaches an ambient value Hc_{vap} , where H is the relative humidity of the ambient air. Therefore, the difference in their vapor concentrations (Δc) is given by,

$$\Delta c = c_{vap}(1 - H) \quad (2.22)$$

This drives the evaporation of liquid (here water) into the air, according to the diffusion equation,

$$\frac{\partial c}{\partial t} = D_v \Delta c \quad (2.23)$$

where D_v is the vapor diffusivity.

Since the time taken for the vapor concentration to saturated value is very less than the drying time, this process can be assumed it as the quasi-steady state. Therefore, we can neglect the term in the left hand side of eq. 2.23, and obtain the Laplace equation,

$$\Delta c = \nabla^2 c = 0 \quad (2.24)$$

If J is the vapor mass flux originated due to the drying process, i.e., the evaporative mass loss per unit surface area per unit time and its functional form depends on the rate limiting factor, the local evaporation flux ($\vec{J}(r^*, t)$) at the air-liquid interface is given by,

$$\vec{J}(r^*, t) = D_v \nabla c \quad (2.25)$$

This equation can be solved by using toroidal coordinates and special functions (Popov, 2005) or by finite element method (Hu and Larson, 2002; Hu and Larson, 2005), or by analytically (Deegan et al., 1997). Therefore, the evaporation rate can be computed as,

$$J(r^*) = \frac{2D_v}{\pi R_g T} \frac{M_w P_{vs}}{\sqrt{R^2 - r^{*2}}} \quad (2.26)$$

where M_w is the molar mass of water, P_{vs} is the saturation water vapor pressure, R_g is the ideal gas constant.

Various modes of drying

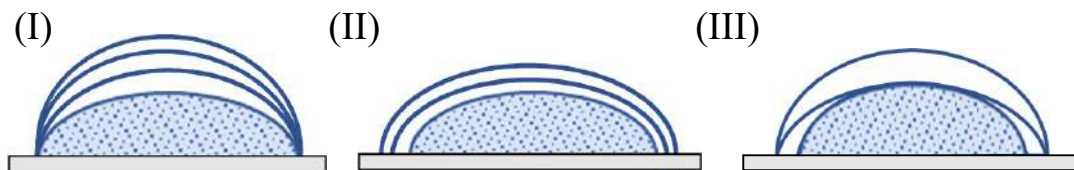


FIGURE 2.4: Illustration of different modes of the drying process: (I) Constant Contact Radius (CCR), (II) Constant Contact Angles (CCA), and (III) Mixed Mode (MM). This schematic is inspired by Zang et al., 2019.

Fig. 2.1 describes the different interfaces and TPCL of the droplet deposited on the solid substrate. According to the evolution of the contact angle and the TPCL, different drying modes are proposed [see Figure 2.4(I-III)]. For example, (I) Constant Contact Radius (CCR) mode in which only the contact angle reduces as time progresses. The diameter of the droplets (or the contact radius) remains constant during the drying process. (II) Constant Contact Angle (CCA) mode when the contact

radius of the droplet reduces with drying time without changing its contact angle. However, these CCA and CCR modes are the two extreme cases. We generally observe that both the contact angle and the contact radius move simultaneously as the drying process evolves. This mode is known as the Mixed Mode (MM).

It is worth mentioning that the colloidal droplets get pinned to the substrate, implying that the contact radius cannot shrink with drying time. In general, the bio-colloidal droplets show CCR mode. However, it is noticed in our studies that there is a "fluid front" that moves from the periphery to the central region despite having a constant contact radius. We believe that these modes could also be described based on the fluid front radius and the contact angle evolution [see one of our published papers (Pal et al., 2020a)]. We also have found different terminologies for this "fluid front". Sometimes, this front is also called a "sol-gel" front, "transition front", or "gelation front" depending on the system and its textural behavior. Therefore, the terminology is contextual, and the reader should pay attention while defining it. We find the "fluid front" is more appropriate in our studies as this front carries solute particles/materials with it as the solvent (water) leaves from the system.

2.4.3 Different flow mechanisms

In general, convection is a process for transferring the mass or heat due to the bulk movement of the molecules in the fluid. The convection might involve diffusion (non-directional heat or mass transport), advection (directional heat or mass transport), or both. Depending on the droplet type and its wettability to the substrate, the convection can be caused for different reasons. For example, in the pendant droplets and the sessile droplets deposited on the superhydrophobic substrate ($\theta > 150^\circ$), the convective currents can be generated due to the vertical gradients. This makes sense (in the sessile droplet configurations) because the circulation of the currents will be generated more due to the greater droplet height ($h \gg R$) near the center. Due to this high curvature-shaped droplets, the evaporation flux is non-uniform—the highest near the apex and the lowest near the periphery. This kind of convection arising due to temperature is known as "buoyancy convection". In such situations, a characteristic dimensionless number, "Rayleigh number" (Ra) is widely used by the fluid dynamics community.

$$Ra = \frac{g\beta}{\nu D_T} (T_s - T_\infty) L^3 \quad (2.27)$$

where Ra is the Rayleigh number, D_T is the thermal diffusion coefficient, β is the thermal expansion coefficient, T_s is the surface temperature, and T_∞ is the temperature very very far from the surface.

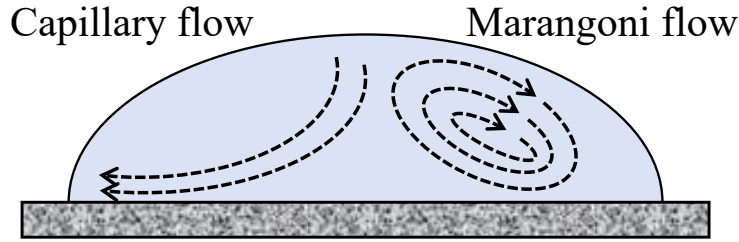


FIGURE 2.5: Schematic of different flows develop during the drying process when the droplet is deposited on the solid substrate. This illustration is inspired by Tarafdar et al., 2018.

Coffee-ring effect and Capillary flow

Another type of convection is the “capillary convection” where a gradient of the Laplace pressure generates when there is any change (distortion) in the droplet shape. This convection can generate both inward and outward flow inside the droplet. A new quantity, the Laplace number (La) is introduced that is defined as the ratio of the γ to the momentum transport in a fluid.

$$La = \frac{\rho l \gamma_{lv}}{\eta^2} \quad (2.28)$$

The “coffee-ring” effect is a well-known physical mechanism in a drying sessile colloidal droplet after the paper. “Capillary flow as the cause of ring stains from dried liquid drops” was published (Deegan et al., 1997). The study, including the mathematical analysis, shows that the evaporation rate is the highest near the periphery due to the curvature of the droplet. The colloidal particles present in the droplet are transported towards the periphery by the outward radial flow [also known as “capillary convection” (see Figure 2.5)] to compensate for the excessive mass-loss. This transport will deposit more particles near the periphery than the central region. This deposition of the particles will develop a ring, called “coffee-ring” effect. Though this study provided a concrete analytical analysis, this observation is not that new. Ray Goldstein, the Professor at the University of Cambridge, UK described in his paper (Goldstein, 2018) that the botanist Robert Brown, who is well-known for the Brownian motion, scooped ~ 170 years ago that the drop evaporation leads to outward flows transporting the particles near the periphery.

However, this coffee-ring effect becomes a problem as it is not recommended for industrial applications, such as printing, microarrays, etc. Therefore, this inhomogeneous particle deposition needs to be prevented. In other words, the effect needs to be suppressed. We can achieve this by using hydrophobic substrates, electrowetting, generating solutal and thermal Marangoni flows or introducing external fields (Hu and Larson, 2006; Eral et al., 2011; Li et al., 2015; Mampallil et al., 2015).

Marangoni flow

The capillary convection can also originate from the surface tension gradient along the surface of the droplet. This is known as “Bénard–Marangoni convection” (or Marangoni flow). This gradient of surface tension can be induced by either temperature (referred as “thermal Marangoni”) or the solute concentration (referred as “solutal Marangoni”). The thermal Marangoni number (Ma_T) and the solutal Marangoni number (Ma_c) for thermal and the solutal Marangoni flow are used respectively. Ma_T is defined as the ratio of the surface tension (γ_{lv}) induced by a temperature gradient along the free surface to the adhesive force. The temperature (T) is just replaced by c in Ma_c .

$$Ma_T = -\frac{d\gamma_{lv}}{dT} \frac{L\Delta T}{\eta D_T} \quad (2.29)$$

$$Ma_c = -\frac{d\gamma_{lv}}{dc} \frac{L\Delta c}{\eta D_c} \quad (2.30)$$

Besides these flows, the interfacial flows are observed in the drying sessile droplets for $\theta > 90^\circ$. Due to the high contact angles, the evaporation rate is higher at the droplet apex when compared to its periphery. The particles at the air-liquid interface prefer to move from the apex (higher curvature) to the periphery (lower curvature), and the particles accumulate near the periphery (Mondal et al., 2018). There is another interesting study found in the literature which implies that the diffusion (here, non-directional bulk-flow for mass transport), advection (here horizontal mass transport towards the periphery), and the capillary attraction (the ordered arrangement of the particles particularly induced by the capillary forces near the three-phase interface)– all three are responsible for emerging the patterns in the drying droplets which are partially-wet to the substrate ($\theta < 90^\circ$) (Kolegov and Barash, 2019). These studies imply that more experimental data is needed to understand the sessile droplets’ underlying flow mechanisms.

2.4.4 Colloids and their interactions

Since our work involves bio-colloidal samples, it is good to know some colloidal interactions, which play an important role in deciding the patterns. This text is mainly adopted from the Ph.D. dissertation (Gerber, 2020) and <http://www.colloid.ch/>.

A dispersion forms when the particles (either solid, liquid, or gas) disperse (distribute) in a continuous phase (solid, liquid, or gas). The term “colloid” refers to the particles that range from ~ 1 nm to ~ 0.1 μm . Depending on the phase or the particle types, we observe different colloidal dispersions. For example, when the solid particles are dispersed in the liquid, it is called a suspension. The liquid-liquid dispersion is commonly known as emulsions. In contrast, when the gaseous particles

are dispersed in the liquid phase, we have foams. The aerosol is made with solid-gas dispersion. In our studies, the colloidal particles are dissolved/suspended to form a uniform homogeneous mixture.

It is to be noted that the dispersion is thermodynamically unstable because the free energy of the system (dispersed solution) is higher than that of the corresponding bulk material. If there is no energy barrier, the dispersed phase can transit to a lower free energy state spontaneously to minimize its surface energy. During this, the particles randomly collide with each other (popularly known as Brownian motion) in the medium. The average energy is on the order of $\sim k_B T$, where k_B is the Boltzmann constant, and T is the absolute temperature. If the energy barrier is higher than $\sim k_B T$, the dispersion will remain unstable indefinitely.

The stability depends on various factors; for instance, the particles might sediment depending on the viscosity, size (due to their aggregation), and/or density. The light scattering technique is mostly used to determine the stability by measuring the size distribution of the particles dispersed in the system. Therefore, it is important to know how to stabilize these colloidal dispersions. The colloidal stability is mainly contributed by the interparticle interactions and their aggregation processes.

DLVO interaction

This assumes that the total energy (W_d) can be written as the addition of the two interaction terms, namely, van der Waals (W_v) and double layer interactions (W_l). This is first developed by B. Derjaguin. The work was extended by L. Landau, E. Verwey and J. Overbeek, which popularly known as Derjaguin Landau Vervey Overbeek (DLVO) interaction. Therefore,

$$W_d = W_v + W_l \quad (2.31)$$

The van der Waals interactions are the long range interactions (when compared to the particle radius), mostly present in all the colloidal systems. The movement of electrons around the nuclei forms fluctuating dipoles, which in turn affects the neighboring molecules due to the coupling between each other. This develops to an attraction force (London dispersion force). It can be defined as,

$$W_v = -\frac{A}{12\pi s^2} \quad (2.32)$$

where s is the surface separation of the two colloidal particles on which the force is acting. The negative sign indicates that the interaction is attractive as the Hamaker constant (A) is a positive value. It is clear from eq. 2.10 that the surface roughness might affect (reduce) the interaction. The other contribution is important to encounter the charging effects. The surface charges (i.e., the charges which are

distributed on the surface of the colloidal particles) are typically balanced by the counter-ions (i.e., the oppositely charged ions present in the media or solution). This balance occurs by diffusion forming an ionic atmospheres surrounding each particle, called the diffuse double layer. This layer overlaps when these particles come very close to each other. Ideally, two extreme cases can happen: the surface charges changes and the surface potential remains constant or vice-versa. Therefore, the double layer interaction can be approximated as

$$W_l = -\frac{2\lambda_d\sigma_+\sigma_-}{\epsilon_0\epsilon} \exp\left(\frac{-s}{\lambda_d}\right) \quad (2.33)$$

where σ_+ and σ_- are the surface charge densities per unit area of the two particles, ϵ_0 and ϵ are the permittivity of vacuum, and the dielectric constant of water, respectively. λ_d is the Debye length or Debye screening length, which is given by,

$$\lambda_d = \sqrt{\frac{k_B T \epsilon_0 \epsilon}{2q^2 N_A I}} \quad (2.34)$$

where N_A is the Avogadro constant, q is elementary charge, and I is the ionic strength of the solution. This λ_d reduces in the process of the aggregation of the particles when the droplet contains salts or ions. It is to be noted that λ_d is the distance from a particle where the electrostatic interaction falls to $1/e$. Therefore, a high salt concentrated solution has a smaller λ_d , and vice versa. The I is given by

$$I = \frac{1}{2} \sum_i z_i^2 c_i \quad (2.35)$$

where z_i and c_i are the valence and concentration of the i th ion present in the solution, respectively.

This ionic strength (I) is widespread when we work with the protein-saline solution. Though the system's properties rely on the protein nature, pH, temperature, the main contribution is the salts' ionic strength. While performing experiments, two scenarios are generally observed— either the solubility of proteins increases slightly or drops sharply. The former is known as the “salting-in” effect, and the latter is “salting-out”. Therefore, it is often recommended to choose the concentration of the salts (or buffer) while making the protein-saline solutions; otherwise, these proteins can precipitate out in the solution.

Self-assembling interaction

Self-assembly is defined as the organization of the structures (patterns) without any guidance or intervention from outside or humans. It can be classified into different types based on the criteria (such as static or dynamic, spontaneous or directed,

etc.). Since it varies from molecular, mesoscopic to macroscopic length scales (Whitesides and Grzybowski, 2002), it is often classified into molecular and mesoscopic, and macroscopic self-assembly. It is worth mentioning here that these concepts are very interconnected and contextual. Therefore, it is not obvious to have a concrete definition for each class of self-assembly; however, we will try to provide a clear picture by limiting ourselves to the context of biology. One type of self-assembly to the biological relevance is commonly known as “molecular self-assembly” (Whitesides and Boncheva, 2002). It involves a spontaneous assembling mechanism where the costable structured aggregates can form through non- or weak-covalent interactions. The electrostatic and van der Waals interactions mostly govern this kind of self-assembly. In this class, the aggregated structures and properties are determined by the individual molecules’ nature and state. It can be further divided into intra- and intermolecular self-assembly. The classic example of intra-molecular self-assembly is the protein folding forming the secondary and tertiary structures [see the schematic of Figure 2.6 (McManus et al., 2016)]. In contrast, the micelle formation by surfactant solution is a well-known example of inter-molecular self-assembly. In a different context, the same molecular self-assembly can be divided into static and dynamic. The formation of the ordered structures in the static self-assembly often requires energy, whereas the dynamic self-assembly occurs only when the system dissipates the energy.

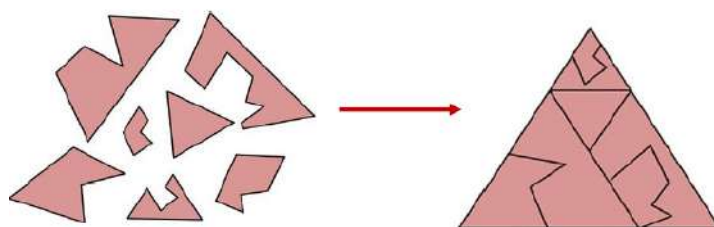


FIGURE 2.6: Schematic of self-assembly in proteins.

There is another class of self-assembly, called “assisted or directed self-assembly” (Whitesides and Boncheva, 2002; Whitesides and Grzybowski, 2002). These are mostly thermodynamically irreversible processes where the final products (once formed), can’t be reversed back to the intermediate states. Here, the aggregated self-assembled structures might be different from the initial components present in the system. These systems are exciting to study as the controlling factors are not often rationalized and could explain the hierarchical structures observed in nature. In this dissertation, we view the self-assembling interactions as the directed self-assembly and at the higher length scales (which also falls under the category of mesoscopic and macroscopic self-assemblies). This kind of high-length scaled assemblies are not spontaneous and are often directed, i.e., induced or assisted by external factors, such as capillary, magnetic forces, etc. However, it is worth mentioning that the reader should not be confused with the evaporation-induced self-assembly (EISA) that is a commonly used method to obtain mesophase of ordered crystalline structures at

various length scales. In our study, different flow mechanisms direct the particles to self-assemble between each other and to form assembled structures on the substrate. For example, we are interested in knowing how the aggregated structures (at the mesoscopic and macroscopic length scales) are related to the native states (properties) of the individual components; for example, the formation of the dendrite structures in the drying droplet of protein-saline solution. Therefore, in our dissertation, we will try to understand: (i) how the capillary flow during the drying process directs or assists the formation of these self-assembled structures, and (ii) how these structures depend on the particle-particle and particle-substrate interactions provided that the droplets (systems of interest) are dried under uniform conditions (relative humidity, temperature, substrate, droplet size, etc.).

2.5 Deposited Crack Patterns

The formation or the evolution of the cracks could be described as a part of the drying process. However, it is considered separately because we are more interested in different morphological crack patterns (once the droplet completely dries). This section is based on the book, "Desiccation Cracks and their Patterns" (Goehring et al., 2015), unless stated. We will briefly describe the fracture mechanics but limit ourselves to the mechanical interpretations. Since we could not measure the heights of the dried bio-colloidal films, it is beyond our dissertation's scope to experimentally verify the scaling laws and/or dependent factors that we will describe in this section.

As mentioned earlier in Chapter 1, the pinning of the droplet to the substrate near the periphery develops frustration and mechanical stress in the film. When the energy exceeds the critical energy, a crack nucleate. The nature of stress and strain energy determines the properties of the cracks. These cracks or crack patterns are understood mostly by making the analogy with the cracks in the brittle materials; however, it is to be noted that the origin of the cracks in these two cases is different. In the colloidal dried film, the cracks originate from releasing the underlying developed stress induced due to excessive loss of solvent from the pinned droplet. In contrast, the cracks nucleate from the pre-existing flaw in the brittle solid.

We observe different types of crack patterns in the colloidal deposited films, such as linear, radial, orthoradial, spiral, wavy, etc. We will study some of these cracks in our later chapters in the context of different drying colloidal droplets. However, studying these (crack) patterns, it is found that we can measure them quantitatively to understand their origin and propagation. Some of them include the distance between two consecutive cracks [crack spacing (x_c)], thickness or height of the cracks (h_c), crack length (l_c), the width of the cracks (λ_c), and so on.

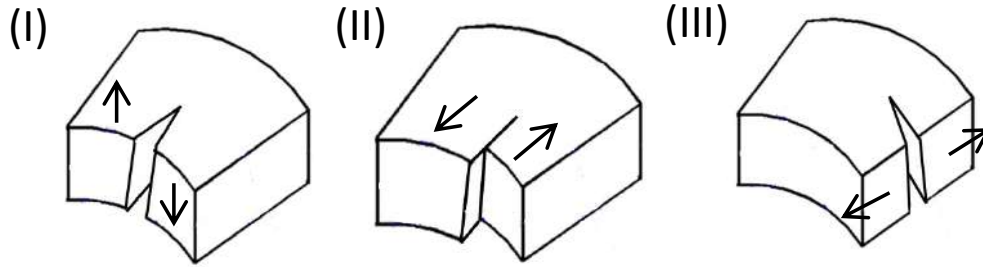


FIGURE 2.7: Different modes of Crack propagation: (I) Mode I (Crack opening), (II) Mode II (In-plane), and (III) Mode III (Out-of plane). The arrows dictate the direction of the mechanical stress.

Many researchers studied the fracture mechanics in detail and provided different theories and interpretations to gain some physical insights into these crack formations. Around 1957, G. Irwin came up with the possible ways (modes) by which the stress tensor can be applied if the crack's direction is defined on the crack surface. Figure 2.7(I-III) shows the three modes: Mode I (also called "opening" mode), where the tensile stress acts normal to the plane of the crack. Mode II (also known as "sliding" mode), where the shear stress acts parallel to the plane of the cracks but perpendicular to the crack front. Mode III (also called "tearing" mode), where the shear stress acts parallel to both the plane of crack and crack front.

Now that we know the cracking modes, we need to know how the path is selected for the crack propagation. Again there are different theories, but here will only discuss Griffith's criterion. Let us try to understand the crack propagation thermodynamically. He pointed out that the energy required for any fracture usually comes from the stored strain energy around the crack. The crack has to release the tension accumulated at the crack vicinity. By now, it is clear that the strain energy release rate depends on several factors such as the path history, position of the crack, the orientation of the path, etc. Therefore, each path (no matter which one is being taken: growing straight, curving, waving, etc.) will have a particular energy release rate and energy cost.

Let us define the rate of change of the strain energy for an increase of the crack surface area (A) as G , and the energy cost as G_c . Then, three different situations are possible.

$$G - G_c < 0 \quad (2.36)$$

$$G - G_c = 0 \quad (2.37)$$

$$G - G_c > 0 \quad (2.38)$$

If the eq. 2.36 holds, the crack has not enough strain energy to propagate. Since the

propagation will lower the free energy, the crack will prefer not to grow, and the crack stops. The eq. 2.37 is the situation where just the boundary condition is made. At this point, the crack will neither prefer to grow or shrink. That's why G_c is also called the critical strain energy release rate. However, before we interpret anything, we need to see whether the crack is stable or unstable. We can easily find this out by determining the second derivative of free energy. As obvious, the crack will grow if eq. 2.38 is satisfied. Therefore, we can conclude that Griffith's criteria for crack propagation are,

$$G = G_c \quad (2.39)$$

$$\frac{\partial G}{\partial A} > 0 \quad (2.40)$$

Experimentally, there is a characteristic length scale that can be easily measured or quantified. This is called the "critical cracking thickness", denoted by h_c . The underlying concept is the same as discussed above. Though this thickness is dependent on the nature of the material, especially dominated by film homogeneities, any film cannot crack if the layer or the film thickness (h) is less than h_c . When the $h \sim h_c$, interestingly, different class of crack patterns are observed; for example, crack nucleate around flaw and joins symmetrically at 120° .

It is worth mentioning here that we can connect these crack patterns to many directions. One can use these morphological patterns for fractal studies. The percolation and network theory can also be related as a function of the colloidal samples. We can also extend it towards topological defects and network connectivity of the cracks.

2.6 Conclusions

Therefore, the intention of this chapter is not to be exhaustive in reviewing the concepts of the wetting, phase separation, colloidal interactions, cracks, etc. but more to motivating the readers to consider this chapter in terms of the broader general sense to understand the underlying physics of the bio-colloidal drying droplets. In the next chapter, we will describe the materials (bio-colloids) that are used in our studies. We will also emphasize the protocols adopted to make the samples, different experimental setups, and the image processing techniques to acquire and analyze the images during drying and dried films.

Chapter 3

Materials and Experimental Methodology*

3.1 Background

This chapter starts with the detailed characteristics of the colloids that are used in this dissertation. This involves globular proteins [lysozyme (Lys) and bovine serum albumin (BSA)], human whole blood, and thermotropic liquid crystals (5CB). This study has used two different solvents [de-ionized water and phosphate buffer saline (PBS)] for preparing their colloidal solutions. We will discuss the experimental procedure. For image acquisition, the optical microscopy is used to capture the images during the drying process, and the dried films. The scanning electron microscopy is used for investigating the microstructures of the dried films. The wetting of these droplets on the substrate and their evolution is studied through a contact angle goniometer. Finally, the chapter ends with the image processing techniques, such as determining the crack spacing, fluid front radius, texture evolution, etc.

3.2 Materials

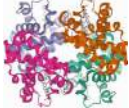

3.2.1 Proteins

Amino acids are the organic compounds containing amino ($-NH_2$) and carboxyl ($-COOH$) functional groups with different side chain (R group) specific to the particular amino acid. A polypeptide is usually made up of a linear chain of the amino acid residues. The polypeptide can be long or short. If the polypeptide contains 20-30 residues, it is denoted as the peptide or oligopeptide (rarely denoted as protein). Therefore, the protein can be defined as one of the macromolecules (biomolecules) which contains at least one long polypeptide, and its characteristics depends on the amino acid sequence. There are various types of proteins based on their structure

*The part of this work is published. **Pal, A., Gope, A. and Iannacchione, G.S., 2019, December.** Image-Based Analysis of Patterns Formed in Drying droplets. In *International Conference on Pattern Recognition and Machine Intelligence* (pp. 567-574). Springer, Cham. (Online ISBN 978-3-030-34869-4). https://doi.org/10.1007/978-3-030-34869-4_62.

and functions. The differences between the globular and fibrous proteins are tabulated in Table 3.1.

TABLE 3.1: Differences between globular and fibrous proteins.

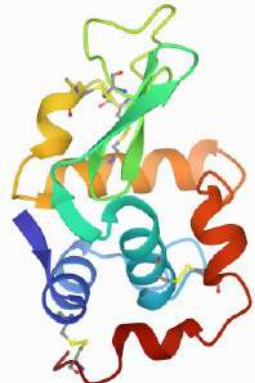
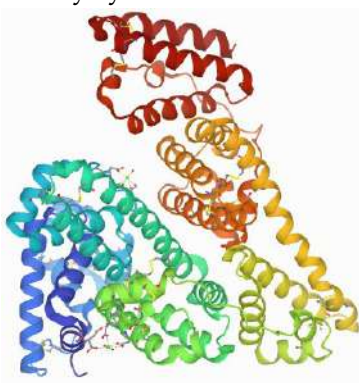
Globular Proteins	Fibrous Proteins
<ul style="list-style-type: none"> • These are compact and spherical and folded in nature • Most of their hydrophobic residues are buried inside and charged residues are at surface • Mainly involved in the metabolic functions • Mostly soluble in water • Highly sensitive to the changes in pH, temperature, etc. • Examples: lysozyme, BSA, HSA, haemoglobin, etc. 	<ul style="list-style-type: none"> • These are elongated and have helical or sheet like structures • Each site of these proteins is exposed to interact with other particles • Mainly constitute structural element • Mostly insoluble in water • Less sensitive to the changes in pH, temperature, etc. • Examples: actin, myosin, collagen, keratin, etc.
	
<ul style="list-style-type: none"> • Protein structure of haemoglobin from Donkey, DOI: 10. 2210/pdb1S0H/pdb 	<ul style="list-style-type: none"> • Protein structure of the type IX collagen from human, DOI: 10. 2210/pdb5CVA/pdb

As stated above, there are many different types of globular proteins. In this dissertation, the *lysozyme* (*Lys*) and *bovine serum albumin* (*BSA*) are studied in details. Though both show the globular nature, their physical characteristics are unique. It is to be noted that these proteins can be obtained from the various organisms. We purchased BSA that is a blood protein derived from cows (Genetic name: *Bos taurus*), and Lys from chicken egg white (Genetic name: *Gallus gallus*). The commercial lyophilized BSA and the Lys are obtained from Sigma Aldrich, USA (Catalog A2153 and L6876 respectively). We can find the exact structure of these proteins from the protein data bank (PDB) at <https://www.rcsb.org/>. Each protein has its own PDB ID and DOI to maintain the catalog of the huge number of proteins. The globular shape and stability of these proteins are attributed to the disulfide bridges, hydrogen bonds, and hydrophobic interactions among the amino acids. Interestingly, BSA is chemically identical to the globular albumin protein present in human blood (HSA) (Carter and Ho, 1994).

It is to be noted that the protein solution can be considered as a complex fluid in the context of rheology as its concentration and protein characteristics determine whether it is a non-Newtonian or Newtonian fluid. For example, the same protein at low concentration behaves like a Newtonian fluid, whereas it becomes non-Newtonian at the high concentration. This is why many recommend studying the viscosity as a function of the protein's initial concentration and nature to understand

these protein solutions better. However, it is not our study's motivation; therefore, it is beyond the scope of this dissertation. Our present study assume that the globular nature (or the overall tertiary structure) of these proteins is maintained. The key differences between these proteins are tabulated in Table 3.2.

TABLE 3.2: Differences between lysozyme (Lys) and bovine serum albumin (BSA) globular proteins.

Lys	BSA
<ul style="list-style-type: none"> • Each Lys has molecular mass of ~ 14.3 kDa • It has roughly spherical shape • Its dimension is $3.0 \times 3.0 \times 4.5$ nm³ • It has 129 amino acids in a single polypeptide chain • Lys' isoelectric point of 11.1 allows it to carry a net positive charge under the present conditions of the study (pH of ~ 7) • Lys has 4 disulfide bridges • Its denaturing temperature is ~ 75 °C • Lys can also be observed in human mucosal secretions such as saliva, tears, etc. 	<ul style="list-style-type: none"> • Each BSA has molecular mass of ~ 66.5 kDa • It has ellipsoid shape • Its dimension is $4.0 \times 4.0 \times 14.0$ nm³ • It has 581 amino acids in a single polypeptide chain • BSA's isoelectric point is 4.7 allows it to carry a net negative charge under the present conditions of the study (pH of ~ 7) • BSA has 17 disulfide bridges • Its denaturing temperature is ~ 65 °C • BSA predominantly acts as a transporter protein in the circulatory system
	
<p>The DOI of the Lys structure: 10. 2210/pdb1HSW/pdb</p>	<p>The DOI of the BSA structure: 10. 2210/pdb3V03/pdb</p>

3.2.2 Liquid Crystals

The liquid crystals (LCs) are the phases whose properties lie between the solid crystalline and the (isotropic) liquid state (De Gennes and Prost, 1993). The molecules in the solid phase consist of both positional and orientational order. When the solid changes into the LC phase, these molecules possess orientational order but not the long-range positional order [see Figure 3.1(I-IV)]. This enables the molecules to flow

or coalesce like the liquid but simultaneously exhibit anisotropy in their optical and electrical properties like the solid crystal. However, the liquid phase exists without having any of these positional and orientational orders [see Fig. 3.1(III)]. However, it is to be noted that the LC phase has specific electro-optical behavior, which is neither found in solid and liquid phases. Since the orientational order of LCs is related to the macroscopic properties, their magnetic, optical, or magnetic properties could be easily changed by just aligning these LCs in different directions.

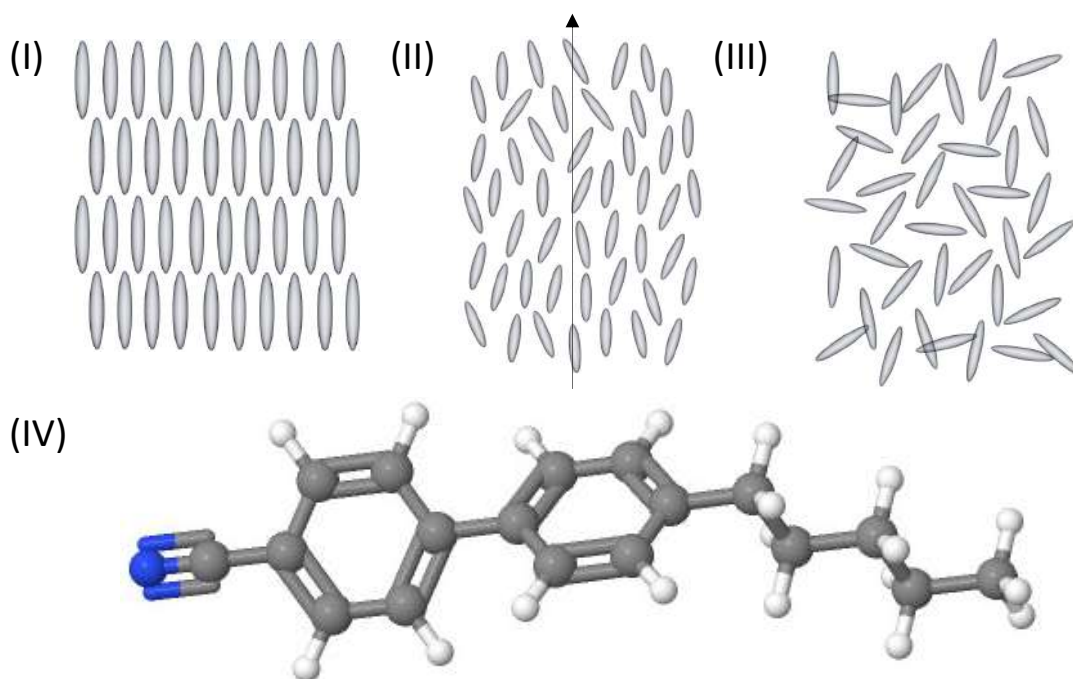


FIGURE 3.1: Schematic arrangement describing different phases: (I) solid (II) liquid crystal (LC), and (III) liquid. The gray-colored ellipsoids symbolize the molecules. The arrow in the LC phase dictates the average direction of the long axes or the molecules' preferred orientation. (IV) An example of nematic LC, 5CB (4-cyano-4'-pentylbiphenyl) drawn with Jmol (an open-source application for viewing and drawing the 3D chemical structures) <http://www.jmol.org/>.

There are two classes of LCs. The molecules changed to LC phases by changing the temperature are called *thermotropic* LCs. In contrast, *lyotropic* LC phases are formed by varying the concentration or both temperature and concentration. Most of the thermotropic LCs are made up of organic molecules that have (i) a rigid core such as aromatic benzene rings and their derivatives, heterocyclics, sterols, etc., (ii) side-chains and terminal groups, such as alkyl, alkoxy, carbonyl, nitro, and cyano groups, etc., and (iv) linkage groups attached between the rings which could be either simple bonds or groups, such as ester, tolane, etc. Generally, the *lyotropic* LCs are formed by amphiphilic molecules containing a hydrophilic head and a hydrophobic tail group. It is to be noted that the core can be straight (often referred to as calamitic or rod-like LCs), disc- or bent-shaped. Typically the LCs are ~ 20 Å long and ~ 5 Å wide. Furthermore, another class of *lyotropic* LCs are found called *chromonic* LCs formed by water-soluble molecules containing planar aromatic rings.

Some examples are drugs, dyes, nucleic acids (Lydon, 1998). Interestingly, these *lyotropic* LC phases are commonly observed in the living cells that spontaneously try to align themselves in the response of the visco-elasticity, micro-phase separation, or induced mechanical stress near the boundary.

Conventionally, the LC is sandwiched between a glass slide and a coverslip and imaged under crossed polarizing microscopy to identify the phases. The homeotropic oriented LC is obtained when the long axes of the LC molecules (on average) are found to be perpendicular to the surface of the glass substrate, whereas homogeneous or planar alignment is obtained when their long axes lie parallel to the substrate. It is to be noted that the dark brushes (lines of extinction) may appear as *schlieren* defect when the nematic LCs are aligned with one of the polarizers under the crossed polarizing configuration. This defect could be understood when both the polarizer and analyzer are rotated simultaneously. The black brushes should rotate without any movement of the extinction point. Typically, two types of point singularities occur— one having four brushes and another having two brushes. Whichever is the case, it is always recommended to characterize the sign and charge (s) of such defect. The s is defined as the number of the brushes/4. Therefore, for four-brush defects, $s = 1$, and for two-brush defects, $s = 1/2$. The effective way to determine the sign of s is to rotate the sample stage of the polarizing microscope either clockwise or anticlockwise keeping the polarizer and analyzer undisturbed. If the brushes rotate in the same direction, s is positive, otherwise s is negative. Thus, s becomes $+1$ and -1 for four-brush defects, and $+1/2$ and $-1/2$ for two-brush defects (Kléman, 1989).

In this dissertation, we have used a well-studied *thermotropic* nematic LC, i.e., 5CB (Catalog 328510, Sigma Aldrich, USA) whose structure is shown in Fig. 3.1(IV). The chemical name is 4-cyano-4'-pentylbiphenyl, also known as 4'-amyl-4-biphenylcarbonitrile, 4'-pentyl-4-biphenylcarbonitrile, 4-amyl-4'-cyanobiphenyl. The phase transition of 5CB from the crystalline to the nematic phase is ~ 24 °C, and from nematic LC to liquid is ~ 35 °C. The chemical formula is $C_{18}H_{19}N$, the molecular mass is ~ 249 gmol $^{-1}$. It mostly appears cloudy white when it stays in the LC phase but becomes colorless in the liquid phase. The density in its LC phase is ~ 1.008 g mL $^{-1}$.

3.2.3 Human blood

Figure 3.2(I) shows the schematic of the blood components transported through the vessel (vein/artery). It is the most complex hierarchical structural non-Newtonian fluid consisting of plasma (composed of mostly 93% water carrying ions, nutrients, and 7% proteins) and many cellular components [red blood cells (RBCs) or erythrocytes, white blood cells (WBCs) or leukocytes, platelets or thrombocytes] (Flormann, 2017). The RBCs are primarily responsible for oxygen supply to the blood cells, WBCs guard the body against infections and foreign invaders, and platelets are mainly involved in blood clotting. However, different types of WBCs such as

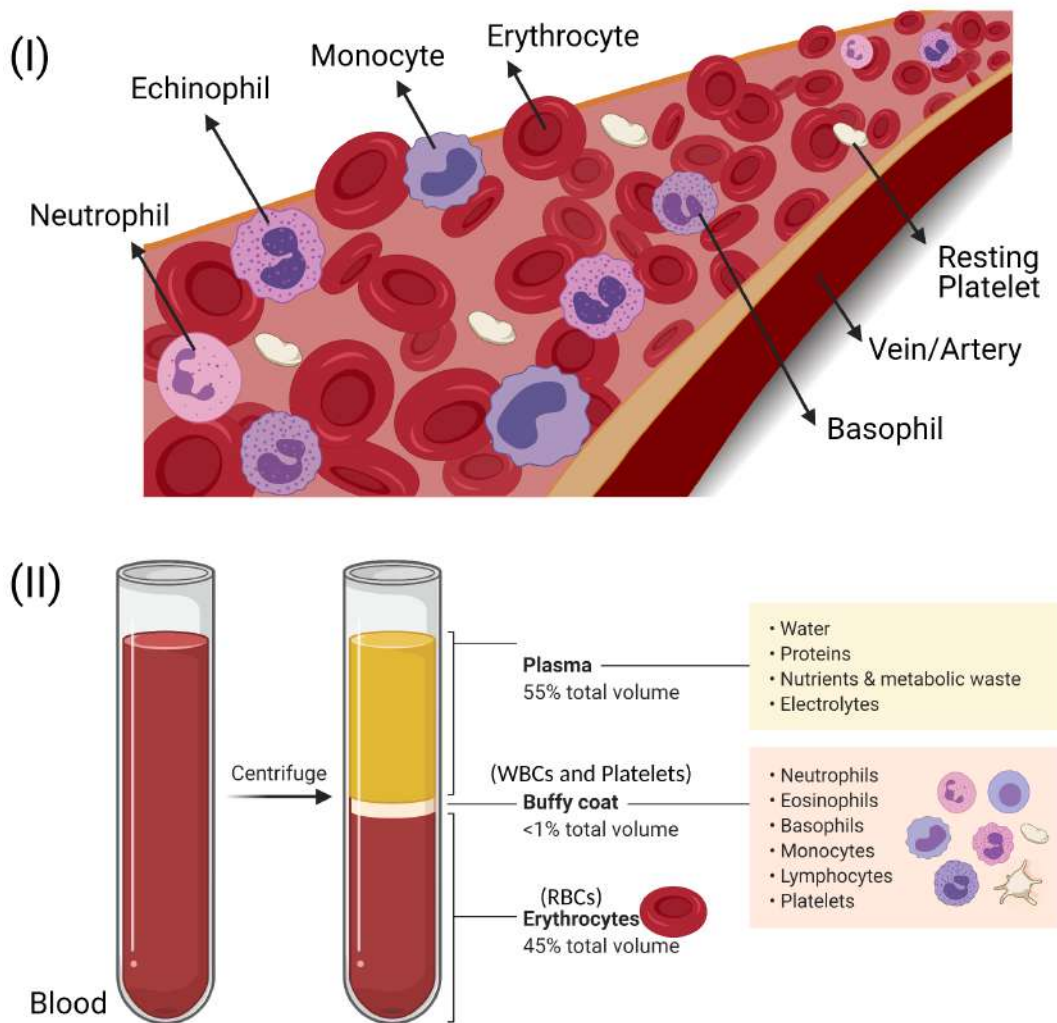


FIGURE 3.2: (I) Schematic diagram dictating the cellular components (RBCs, WBCs, and platelets) of the human blood transported through the blood vessel (artery/vein). The various types of WBCs (monocyte, echinophil, neutrophil, basophil) are also shown. (II) Illustration of the blood centrifuged into different layers. These images are drawn from <https://biorender.com/>.

monocyte, neutrophils, basophils, echinophils, etc., are present in our blood for protecting different activities in protecting our cells. A $1 \mu\text{L}$ of whole blood contains 400 to 500×10^4 of RBCs, 0.5 to 1×10^4 of WBCs, 14 to 40×10^4 of platelets, depending on the pathological condition of a donor, along with a small amount of plasma proteins (fibrinogen, immunoglobulins, albumin) and salt ions (Brutin et al., 2011). The typical size of RBCs, WBCs, and platelets are 6 to $8 \mu\text{m}$, $\sim 15 \mu\text{m}$, and 2 to $3 \mu\text{m}$ respectively (Bain, 2004). The RBCs are red in color due to the presence of the iron-containing protein, hemoglobin. Furthermore, RBCs contain a membrane as well. A membrane is made of 19.5% water, 39.6% proteins, 35.1% lipids and 5.8% (w/w) carbohydrates (Yawata, 2006). It is to be noted that the “whole” term signifies that the human whole blood consists of both plasma and cellular components. However, in reality, the whole blood could separate into three parts if kept undisturbed in the test tubes due to their density differences. The common method used for the *in-vitro*

experiments is the centrifugation [see Fig. 3.2(II)]. This process results in three different layers: plasma in the top, buffy coat (containing WBCs and platelets) in the middle, and RBCs in the bottom (Flormann, 2017).

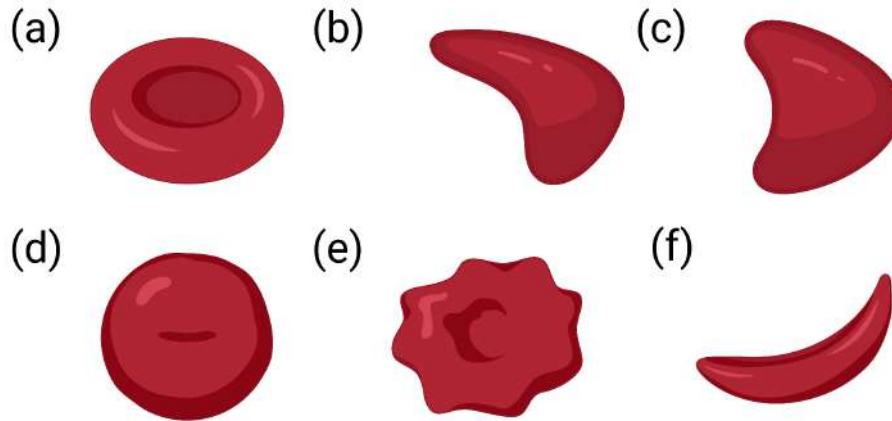


FIGURE 3.3: Schematic shapes of different forms of RBCs (erythrocytes) in the human blood: (a) Normal RBC (bi-concave shaped), (b) Flowing RBC (slipper shaped), (c) Flowing RBC (parachute shaped), (d) RBC in the hypotonic environment, (e) Echinocyte, (f) Sickled shaped RBC. These images are drawn from <https://biorender.com/>.

It is also important to know that these cellular components in the blood can alter their shapes in response to the toxicity or pH (hypertonic or hypotonic environment) or shear stress (Gregory, Stevens, and Fraser, 2017). For example, the healthy RBCs are of bi-concave or discoid shape; however, these transform into different forms such as ellipsoidal, echinocyte (a round shape with short blunt spicules), sickle (crescent moon), teardrop, etc. (Yawata, 2006) [see Figure 3.3(a-f)]. For the *in-vitro* experiments, it is found that the transformation of discoid to echinocyte shape could be due to the contact of the RBCs with substrates like glass or plastics. This change is not yet known; however, one could argue the reason as the electrostatic interactions (which will be discussed in chapter 6 in detail). For the *in-vivo* case, such a variation is observed when the person undergoes a cardiopulmonary bypass or decompression phase (Flormann, 2017).

On the other hand, the WBCs are white in color and generally contain irregular and nucleated structures. These structures can transform themselves into different functional forms, irregular troughs and ridges (microvilli structures) (Newell, Roath, and Smith, 1976; Yang, 1989). The platelet, when inactivated (or in resting phase), follows a discoid and an anuclear structure but changes into its spread form with extended filopodia on its activation [see Fig. 3.2(I-II)]. The cytoskeleton of platelets is composed of actin and actin-binding proteins; these can polymerize and activate those platelets in response to the environmental or chemical signals (Gregory, Stevens, and Fraser, 2017).

The whole human blood used in this dissertation is already mixed with Na-Citrate anticoagulant (Catalog 7203706, Lampire Biological Laboratories, USA). These blood samples are used without any further chemical processing except for dilution with de-ionized water (DI) or phosphate buffer saline (PBS). The anticoagulants inhibit most of the platelets from aggregation and prevent the coagulation of the blood. It must be noted that the dilution of the whole blood could change the native environment of the blood's components. It is beyond the scope of this dissertation if any changes in their structures happen prior to the drying process. Therefore, the images are captured soon after the sample preparation to avoid further complications (if any). It is also important to know that the dilution of the whole blood can make it Newtonian fluid as the dilution reduces the number of cellular components in the blood. We understand that testing the viscosity at different shear rates can provide us the complete picture; however, it is beyond the scope of this dissertation.

3.2.4 Solvents

Two different solvents are used in our study of drying droplets of the colloids. One is the de-ionized water (Millipore, a resistivity of 18.2 M Ω .cm, viscosity of 0.897 mPa s, density of 0.9970 g mL⁻¹ at 25 °C). Another one is phosphate buffer saline (PBS), containing a mixture of different salts. The Table 3.3 describes the salt concentrations (in mg mL⁻¹) for each of the PBS (from 0.25 to 10x). Different concentrations are prepared by adding the de-ionized water to the PBS. For example, 1x PBS has an initial concentration of 0.137 M NaCl, 0.0027 M KCl, and 0.119 M phosphates that maintains a pH of 7.3 – 7.5. 1x and 10x (Catalog No BP243820, and BP39920, respectively) are purchased from Fisher BioReagents, USA. 1x is used to prepare 0.25x, 0.5x, 0.75x, whereas 10x is used for 2x and 5x.

TABLE 3.3: It describes the amounts of salts (in mg mL⁻¹) present in different initial concentrations of phosphate buffer saline (PBS).

Salts	0.25x	0.50x	0.75x	1.00x	2.00x	5.00x	10.00x
<i>NaCl</i>	2.00	4.00	6.00	8.00	16.00	40.00	80.00
<i>KCl</i>	0.05	0.10	0.15	0.20	0.40	1.00	2.00
<i>Na₂HPO₄</i>	0.36	0.71	1.07	1.42	2.84	7.10	14.20
<i>KH₂PO₄</i>	0.06	0.12	0.18	0.24	0.48	1.20	2.40

The drying evolution of the droplets at various initial concentrations of PBS from 0x to 10x are imaged under the bright-field optical microscopy [see Figures 3.4-3.7(I-II)]. The water evaporates from all these droplets during the drying evolution. The 0x means that the solvent is the de-ionized water. As expected, it does not show any residue, whereas the deposits' formation changes from 0.25x to 10x. The appearance of the salts and their crystal formation vary as the initial concentration increases.

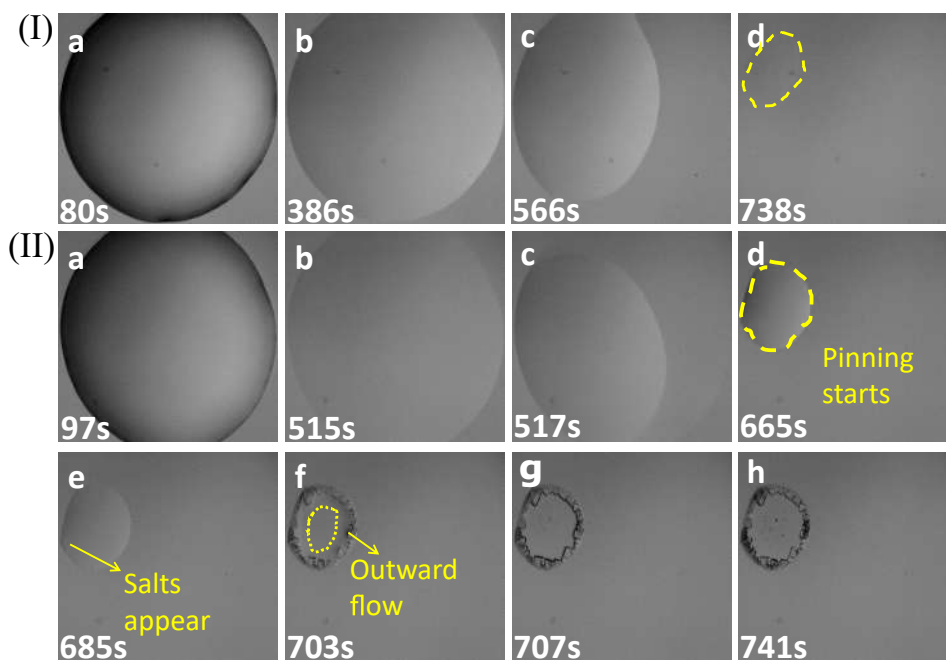


FIGURE 3.4: Drying evolution of the droplets containing the only solvent at different initial concentrations of phosphate buffer saline (PBS): (I) 0x, and (II) 0.25x. The 0x means that the solvent is the de-ionized water.

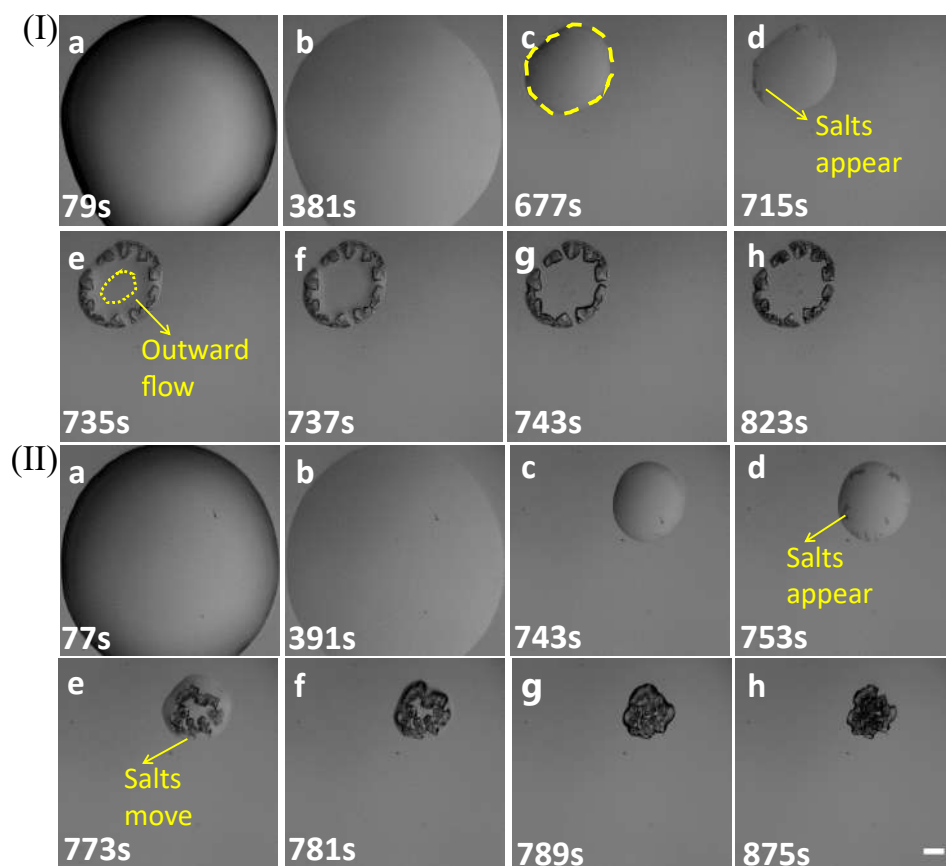


FIGURE 3.5: Drying evolution of the droplets containing the only solvent at different initial concentrations of phosphate buffer saline (PBS): (I) 0.50x, and (II) 0.75x. The scale bar is of length 0.2 mm.

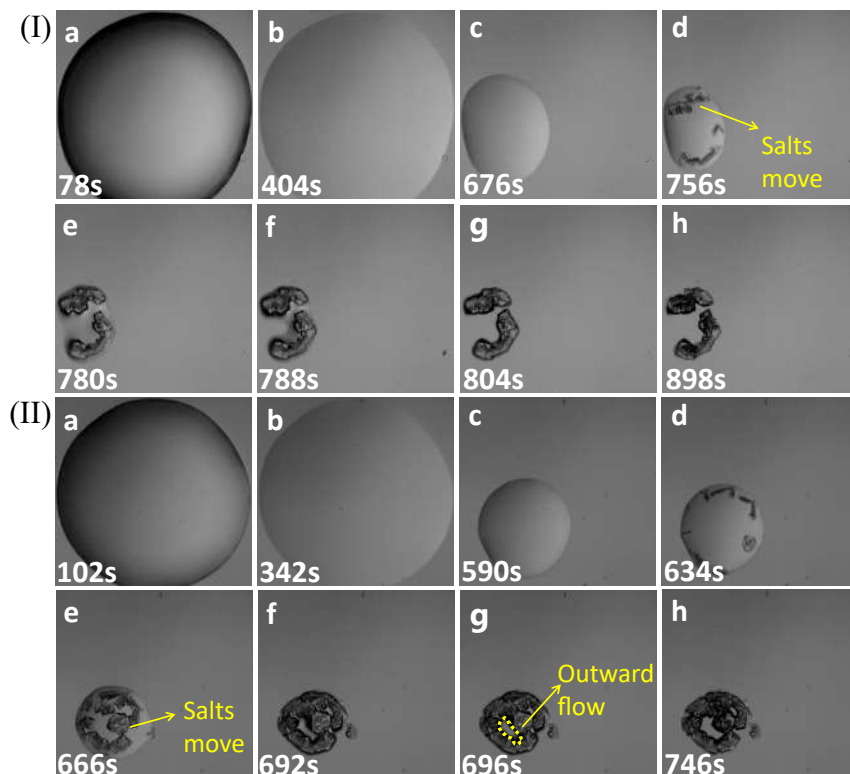


FIGURE 3.6: Drying evolution of the droplets containing the only solvent at different initial concentrations of phosphate buffer saline (PBS): (I) 1.00x, and (II) 2.00x.

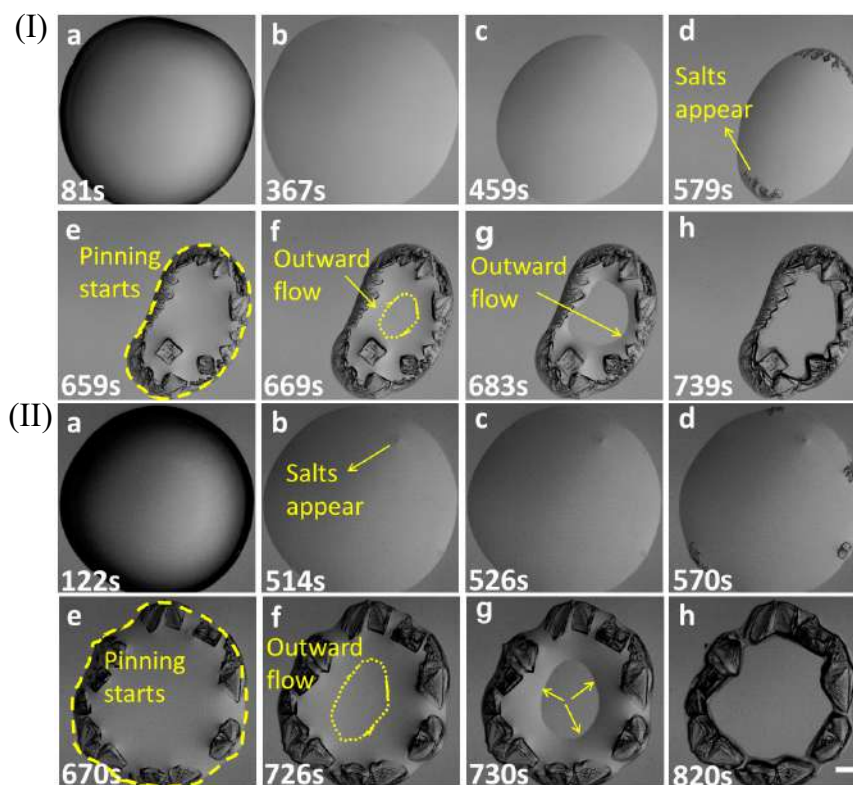


FIGURE 3.7: Drying evolution of the droplets containing the only solvent at different initial concentrations of phosphate buffer saline (PBS): (I) 5.00x, and (II) 10.00x. The scale bar is of length 0.2 mm.

3.3 Experimental Procedure

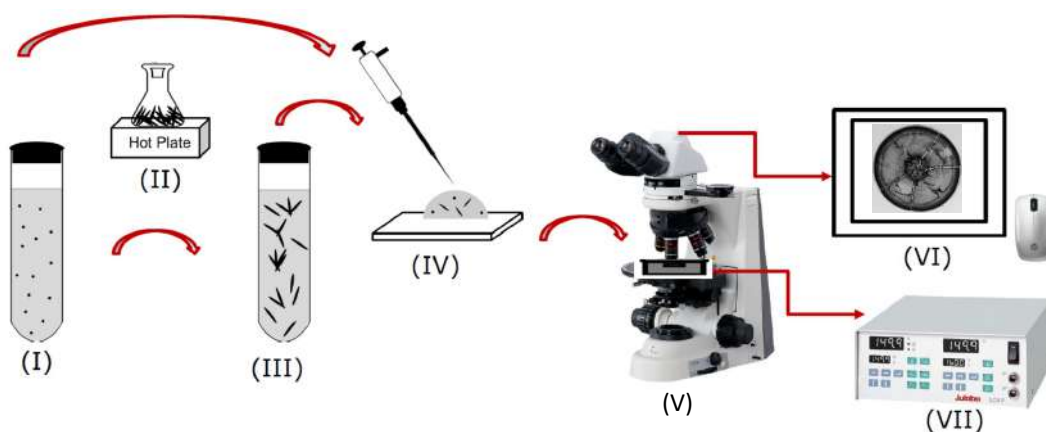


FIGURE 3.8: Schematic diagram describing the experimental procedure: (I) A required concentration of the sample solution is prepared. (IV) The solution is pipetted as a droplet on the substrate. (V) The substrate is kept on the sample stage of the optical microscope. (VI) A camera is attached to the microscope and the computer capturing the images of the drying droplets and dried films. It is to be noted that the steps of (II) and (III) are required only for the protein-LC solution. The LC is heated on the hot plate just above its transition temperature and added to the protein solution. (VII) is specific to the temperature study of the drying droplets, where the substrate temperature is tuned with the temperature controller. A hot stage is mounted on the microscope's sample stage, set to the desired observation temperature for a couple of hours before sample placement.

Different initial concentrations of the protein solutions are prepared by weighing various amounts of proteins with a weighing balance and dissolving it with different volumes of solvents (either de-ionized water or PBS). It is to be noted that these bio-colloidal systems might depend on the history of the sample preparation. Therefore, it is always kept the same throughout the dissertation, i.e., the solvent is prepared, and the solute is dissolved in that solvent. The initial concentration of these samples is quantified as weight percentage (denoted as wt%). It is calculated as the mass of the solute divided by the mass of the solution and converted into a percentage by multiplying it by 100. For preparing the blood samples, different volumes of the blood are prepared by adding de-ionized water or PBS into the whole blood. These samples' initial concentration is quantified as volume percentage (denoted as (v/v)%). The whole blood is considered as 100 (v/v)% and the blood is diluted from 85 to 12.5 (v/v)% [see Figure 3.8(I)].

Once the protein solution is prepared, the LC is heated just above the LC-liquid transition temperature ($> 35\text{ }^{\circ}\text{C}$) and added to the protein solution. Different volumes of LC are added into the protein solutions [see Figs. 3.8(II-III)]. It is to be noted that these LCs were used in bulk without any prior alignment to the substrate (either parallel or perpendicular). Further, an LC and de-ionized water solution are also made. Only the the LC-protein and LC-DI samples are ultrasonicated before pipetting the droplets on the substrate.

A volume of $\sim 1 \mu\text{L}$ of sample is pipetted on a fresh microscopic coverslip (Catalog 48366-045, VWR, USA) to form a circular droplet of radius $\sim 1 \text{ mm}$ at the room temperature of $\sim 25^\circ\text{C}$, and relative humidity of $\sim 50\%$ [see Fig. 3.8(IV)]. This procedure ensured that every droplet is precisely exposed to the same substrate conditions, and environmental conditions, and helped achieve uniform reproducibility of 3-4 repetitions. The time-point when the droplets are deposited on the coverslip is marked as the start-time of image acquisition. It is to be noted that the samples are prepared immediately before imaging under optical microscopy.

The substrate is placed on the optical microscope sample stage [see Fig. 3.8(V)]. A camera is attached to the microscope which captures the images, and visualized in the computer [see Fig. 3.8(VI)]. For temperature-controlled studies, a hot stage mounted on the same microscope which had been set to the desired observation temperature for a couple of hours prior to the sample placement. These pipetted droplets are transferred to the hot stage within ~ 45 seconds and equilibrated to the set temperature within about 10 seconds. The temperature controller (Model 340, Lake Shore Cryotronics, MA, USA) is set at different temperatures [see Fig. 3.8(VII)]. It is worthwhile to mention that the T should be less than the denaturing temperature (T_d) of the sample as their structures and functions might get transformed above T_d . The T_d of the human blood, BSA, and Lys is $\sim 45^\circ\text{C}$ (Huang et al., 2017), $\sim 65^\circ\text{C}$ (Giancola et al., 1997), and $\sim 75^\circ\text{C}$ (Gorr, 2013).

3.4 Image Acquisition

3.4.1 Optical microscopy

The optical microscopy technique is the oldest but considered a powerful technique to date to visualize soft matter-like systems (Born and Wolf, 2013; Fernandez-Nieves and Puertas, 2016). It uses light and a group of lenses to generate the magnified images of the small objects, here, $\sim 2 \text{ mm}$ diameter droplets. Typically, the crossed polarizing configuration is used for observing different phases and measuring the birefringence of the anisotropic materials (such as LCs). In most optical microscopes (including ours— Leitz Wetzlar, Germany), the incident light comes from the tungsten microscope bulb. The light then passes through a linear polarizer (an optical filter that allows the light of a specific polarization) and condenser (a set of lenses that converges and aligns the light with being passed through the microscope aperture and the sample). It then hits the sample, and the light transmitted from the sample progresses through an analyzer (another linear polarizer). Finally, the image is captured by the camera attached to the microscope. It is to be noted that when the analyzer and the polarizer are perpendicular to each other, it is called crossed polarizing configuration (Fernandez-Nieves and Puertas, 2016). In contrast, if we remove any of the polarizers, the same microscope can be used as the bright-field configuration. The images of the samples containing LCs are taken between crossed

polarizers, whereas the samples without LCs are imaged under the bright-field configuration.

The time-lapse images are captured at every two seconds in a transmission mode polarizing optical microscope using a $5\times$ magnification or objective lens (with numerical aperture, $NA = 0.10$). An 8-bit digital camera (MU300, Amscope, USA) attached to the microscope captured images at a fixed resolution of 2048×1536 pixels. This camera in color profile mode assigns intensity values from 0 to 255 in each color of red, green, and blue (RGB) pixels for the image acquisition. It is to be noted that the lamp intensity needs to be kept fixed throughout the experiment to minimize the fluctuations in the background (coverslip) intensity. The morphology of the final dried samples is always captured after 24 hours (Gorr, 2013).

3.4.2 Contact angle goniometer

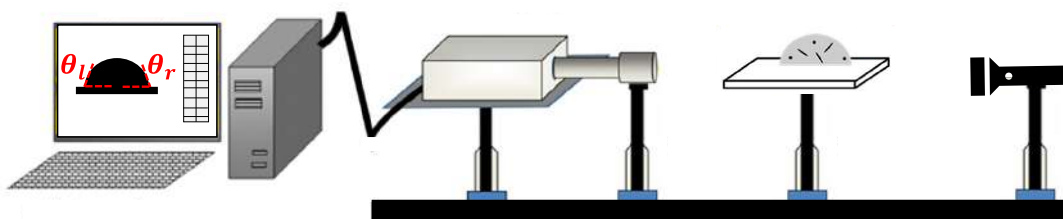


FIGURE 3.9: Schematic diagram describing the contact angle goniometer. The high-resolution camera, the light source, and the sample holder are placed on the undisturbed rail throughout the experiment. A computer is attached to the camera, and the installed software is used to measure the contact angle.

The contact angle of the prepared samples is measured during the drying process by the contact angle goniometer (Model 90, Ramé-hart Instrument Company, USA) to check the wettability of these droplets at the room temperature of $\sim 25^\circ\text{C}$, and relative humidity of $\sim 50\%$. Figure 3.9 shows the schematic arrangement of the setup. The high-resolution camera is used to capture the side-view of the drying droplets. A light source is placed opposite the sample for clear visualization. The sample holder, camera, and light source are placed on the rail that is undisturbed throughout the experiment. A computer is attached to the camera where the software is installed from the Ramé-hart Instrument Company. To determine the contact angle (θ), a baseline (shown by red dashed line on the surface of the droplet in Fig. 3.9) needs to be created on the computer screen. For acquiring the angles from both sides of the droplet, two vertical baselines need to be drawn in the center of the droplets. The time-lapse data is collected out every two seconds. Since the θ_l and θ_r do not show any significant differences, the average of two values is used as $\theta(t)$ throughout our study. Each experiment is repeated twice to ensure the reproducibility of the contact angles and the radius of the droplets. We also ensured that the different events occur around the same time during the drying process and kept a record of the total drying time. It is important because we have used this contact angle

data and the fluid front data (calculated from the optical microscopy images under ambient conditions) to reveal different modes of the drying process.

3.4.3 Scanning electron microscopy

Unlike optical microscopy, the scanning electron microscope (SEM) uses a focused high-energy electron beam to generate different signals at the sample surface. Therefore, the image is formed by rastering the sample space deriving from the electron-sample interactions. Different signals such as secondary electrons, backscattered electrons (BSE), diffracted backscattered electrons (EBSD), photons, etc. are used for different purposes. In our case, the microstructural analysis of the dried films is performed using the secondary electrons at an accelerating voltage of 3 kV and probe current of 5 mA (JEOL-7000F, JEOL Inc. MA, USA). For this, the conductive carbon adhesive tab (Catalog JN56592, Ted Pella, Inc., USA) is put on the specimen mount. The same coverslip containing the ~ 2 mm diameter dried film (observed under optical microscope) is very carefully placed and attached to this conducting tab. Prior to using SEM, these are sputter-coated with a ~ 4 nm thick layer of gold nanoparticles using EMS sputter coater to improve the quality of the sample surface's conductivity. An energy-dispersive X-ray (EDX) analysis is conducted at an accelerating voltage of 10 kV to extract the information about the chemical composition of these microstructures. The point detection mode is selected in the EDX analysis so that the detection area is less than $1 \mu\text{m}^2$.

3.5 Image Processing Techniques

The captured images are converted to an 8-bit gray images prior to using any image processing techniques.

3.5.1 Determining radius and ring width of the droplets

To quantify the radius of the fluid front during the drying process, a circular region of interest (ROI) is drawn on the image covering the area in the droplet using the *Oval tool* in ImageJ (Abràmoff, Magalhães, and Ram, 2004). The pixel locations are converted into a mm-length scale using a length calibration slide. It needs to be checked whether the *centroid* is checked in the *Set Measurements* in the *Analyze* in ImageJ. This gives the (x, y) coordinate points for the center of the droplet. Once this point is selected using the *Point tool*, the fluid front radius (\bar{r}) is extracted by drawing a line from the edge of that line to the central point. The averaged front radius is calculated by taking the mean of the measurements taken at five different positions throughout the droplet. This step is needed so that we can estimate the standard deviation of the front radius. Similarly, the averaged radius (\bar{R}) of the droplet is calculated. The width of the ring (\bar{w}) is measured by drawing the line from the droplet edge to the inner ring. This peripheral ring is at a greater height than the

central region, and the greater height in the dried films can be viewed from the one-sided dark shadowy shade molded due to side illumination. The \bar{w} is normalized by dividing it with the averaged radius of the droplet (\bar{R}). The parameter, \bar{w}/\bar{R} is plotted as a function of the initial concentration of the samples.

3.5.2 Texture analysis

The word, “*texture*” is used in our everyday life. Whenever we need to point out the topological information about the material, we say whether it is rough, silky, smooth, etc., just by touching the surface. The material can be anything, say, paper, cloth, furniture. And we determine its texture by touching with our fingers or fingertips. We call it rough if a large difference in the respective areas is found spatially. Similarly, the texture of an image works, except now the difference is based on the gray level values. Instead of just touching (which can give a qualitative sense of the material texture), we can quantify the image’s texture by different parameters. The image is a grid of pixels. We have adopted two approaches for analyzing the texture of the images captured during the drying process. The first approach is the first-order statistics, which is based on the gray level distribution of the pixel values without intervening in the interpixel relationships. The second one is extracting the GLCM (Gray Level Co-occurrence Matrix) parameters, also known as the second-order statistics. These parameters are calculated from the spatial relationship between two neighboring pixels (Haralick, Shanmugam, and Dinstein, 1973). Therefore, this makes GLCM parameters complicated and different from the first-order statistics (FOS), which solely depends on the individual pixel values (Carreón et al., 2018b; Athanasiou, Fotiadis, and Michalis, 2017).

First-order statistics

We extracted first-order statistics parameters, such as the mean (I) and the standard deviation (SD), skewness ($SKEW$), and kurtosis (KUR) from the time-lapse images for both the droplet and background (coverslip) captured in both bight-field and crossed polarizing configurations. Mathematically, these parameters can be defined as follows; where, $I(i, j)$ is the gray scale value of the pixel at location (i, j) in the image, and N is the number of pixels in the image (Carreón et al., 2018b).

$$Mean = \frac{1}{N} \sum_{i,j=0}^N I(i, j) \quad (3.1)$$

$$SD = \sqrt{\frac{\sum_{i,j=0}^N (I(i, j) - Mean)^2}{N - 1}} \quad (3.2)$$

$$Skewness = \frac{\sum_{i,j=0}^N (I(i, j) - Mean)^3}{(SD)^3} \quad (3.3)$$

$$Kurtosis = \frac{\sum_{i,j=0}^N (I(i,j) - Mean)^4}{(SD)^4} \quad (3.4)$$

A circular region of interest (ROI) is drawn on the image covering the area in the droplet, and another ROI is drawn on the image covering the background (cover-slip) using the *Oval tool* in ImageJ (Abràmoff, Magalhães, and Ram, 2004). Once the ROI is selected, the mean gray values of that ROI is measured. To ensure that the different size of ROI in the sample and the background do not affect the intensity measurement, *mean gray value* (the sum of the values of the pixels in the selection divided by the area of the pixels in the selection, i.e., I) in ImageJ (Abràmoff, Magalhães, and Ram, 2004) is chosen. A script is written for an automated image-processing algorithm which measures the *mean gray value* for each ROI in the images during the drying process. However, the differences in the *mean gray values* during image recording might affect both the background and the sample. To counter this, a correction (calibration) with the background i.e., a correction factor is determined. It could be done by subtracting the background gray values; however, it wouldn't have fixed an uneven background in the series of images. So, the ROI with the lowest background *mean gray value* is chosen from the whole set of images during the drying process as a reference. The lowest is also selected to avoid into running the risk of generating overexposed images (otherwise the correction factors would be smaller than 1). The corrected intensity of the sample (I_c) is then determined for each sample by dividing the mean gray values with the correction factor. The intensity is averaged over a range of 30 seconds and also averaged for three droplets. Good reproducibility is found in the intensity profile, though the time is shifted (added or subtracted) to make the profile nearly overlap to each other. Note that the lamp intensity is kept fixed throughout the whole experiment done with each protein droplet. And finally, the averaged corrected intensity values (\bar{I}_c) is plotted with time. In addition to \bar{I}_c , another textural parameter i.e., standard deviation (SD) is calculated and are averaged over 30 seconds to understand the emerging complexity during the drying process.

We calibrated the intensity with the background for quantifying the birefringence of the LCs (imaged under crossed polarizers) during the drying process. In contrast, it is found that the fluctuations of background are minimal for the blood samples (imaged under bright-field configuration). For example, the I and the SD of the background image for all initial concentrations are 94.56 ± 1.20 arbitrary units (a.u.) and 2.48 ± 0.14 a.u., respectively. Therefore, the raw data without any pre-processing and the average is reported in these samples.

The mean (I) represents the average value of the pixels in an image. In one case, we can use it to determine the LCs' birefringence intensity in any solution where LC is only optically-active, imaged under crossed polarizing configuration. On the other hand, the same I can give information about the disturbances due to particle dispersion under bright-field microscopy. The standard deviation (SD) tells us how

much the intensity varies around the mean. SD 's larger value is related to the roughness/complexity of the image surface. Therefore, these two parameters are widely used in physics communities in different contexts. The higher-order moments such as skewness and kurtosis are used less compared to these parameters. These values measure whether the distribution is asymmetric and flat, respectively. In this dissertation, these parameters are used to study the evolution of the drying process. It is to see how the distribution of the particles affects these first-order statistical parameters.

Second-order statistics via GLCM approach

As mentioned before, these GLCM parameters are based on the interpixel relations. Therefore, before establishing any relationship between two neighboring pixels, it is crucial to address a few questions. For example, what will be the displacement between the neighboring pixels? Should the displacement be close/far to each other? What are the directions of the pixels? Which pixels should be counted- the pixels which are placed horizontally or vertically, or their average? To answer these questions, we will examine the influence of horizontal (0°) and vertical (90°) orientations and pixel displacements (1,10, 50, and 1000) on the GLCM parameters, such as angular second moment (ASM), correlation (COR), inverse difference moment (IDM), and entropy (ENT) in this dissertation.

Let us assume that the central or the reference pixel is i_c, j_c , and the displacement d is the distance from that reference. Then, the direction is determined by the θ as $D_x = D\cos\theta$ and $D_y = D\sin\theta$. If $C_D(i, j)$ is the number of occurrences at location (i, j) at particular D and θ , and N is the number of pixels in the image, then the probability [$p_D(i, j)$] for the changes occurring between i and j at a particular D and θ . The $p_D(i, j)$ is defined as $\frac{C_D(i, j)}{\sum_{i,j=0}^N C_D(i, j)}$. If we need to take different directions into account, the probability becomes $p_D(x) = \sum_{j=0}^N p_D(x, j)$ and $p_D(y) = \sum_{i=0}^N p_D(i, y)$. Various GLCM parameters are defined as follows (Tuceryan and Jain, 1993).

$$ASM = \sum_{i,j=0}^N p(i, j)^2 \quad (3.5)$$

$$COR = \sum_{i,j=0}^N \frac{(i - \mu_x)(j - \mu_y)p_D(i, j)}{\sigma_x\sigma_y} \quad (3.6)$$

where, (μ_x, μ_y) and (σ_x, σ_y) are the means and the standard deviations of $(p_D(x), p_D(y))$, respectively.

$$IDM = \sum_{i,j=0}^N \frac{p_D(i, j)}{1 + |i - j|} \quad (3.7)$$

$$ENT = - \sum_{i,j=0}^N p_D(i,j) \log p_D(i,j) \quad (3.8)$$

For this, a circular region of interest (ROI) is drawn on the image covering the area in the droplet, and another ROI is drawn on the image covering the background (coverslip) using the *Oval tool* in ImageJ (Abràmoff, Magalhães, and Ram, 2004). Once the ROI is selected, these parameters are computed for each step size and direction using *Texture Analyzer* plugin in ImageJ (<https://imagej.nih.gov/ij/plugins/texture.html>). The *ASM* (also called energy sometimes) measures the homogeneity or uniformity globally, whereas *IDM* dictates the local inhomogeneity in an image. The *COR* determines how the two are related to each other. The lower value of *COR* indicates that there is a difference in the gray tones. Like *SD*, the *ENT* determines the heterogeneity and the complexity of the images.

3.5.3 Determining crack spacing of the dried films

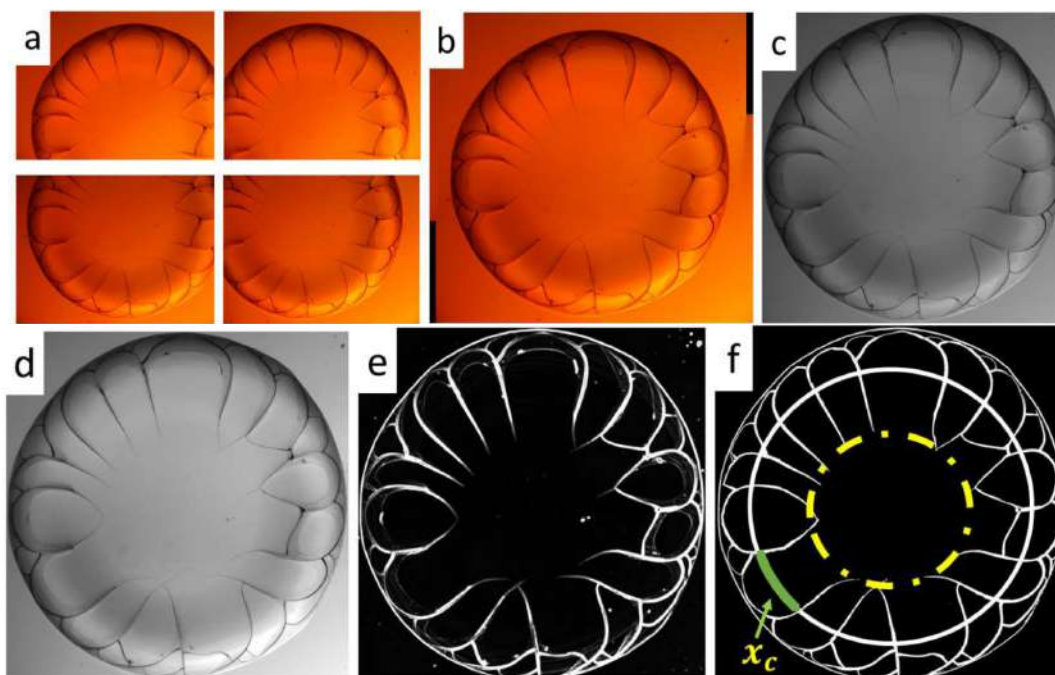


FIGURE 3.10: A representative processing of images of the dried state of BSA droplet to quantify the spacing between the cracks. a) The raw microscopic images. b) A stitched image. c) An 8-bit gray image. d) An adjusted brightness-contrast image. e) A high contrast image after filtering through variance filter. f) A final binary image depicting different regions, circular line-cut, and crack spacing (x_c).

Since it is challenging to view the entire ~ 2 mm diameter droplet using a $5\times$ magnification, different sections of the dried droplets are imaged separately (Figure 3.10a). Each section is stitched together (Fig. 3.10b) by using *Stitching* plugin (Preibisch,

Saalfeld, and Tomancak, 2009) in Fiji (Schindelin et al., 2012). We propose a semi-automated image-processing algorithm on the stitched images to determine the spacing between the consecutive cracks (x_c) in ImageJ (Abràmoff, Magalhães, and Ram, 2004). The pixel locations are also converted into a mm-length scale using a length calibration slide. We converted stitched bright-field images into gray (Fig. 3.10c). For these gray images, the range of monochromatic shades from black to white are displayed from 0 to 255 without partitioning into RGB sets of pixels. Then, the bright and contrast of the image are adjusted (Fig. 3.10d) and filtered with a variance filter (Fig. 3.10e), and processed into an 8-bit binary image (255 for pixels depicting the crack lines and 0 for pixels elsewhere else) (Fig. 3.10f). However, the filtering is not enough to process the images into exact binary images. The artifacts are, therefore manually removed by comparing (overlapping) the processed images on to the original images. However, future work will automate this procedure.

The morphology of the dried droplet is such that it can be divided into two regions: rim and central. The rim is near the edge depicted by yellow dashed line in Fig. 3.10f. We converted all the images of the dried droplets into a scaled stack. Three circular-cut lines (shown by white circular line in Fig. 3.10f) of different radii are made in each region by using *Oval Profile* plugin in ImageJ. The intensity values are plotted along each circular line at every 0.1° as a function of arc-length along each circle. A script using '*Array.findMaxima*' is used to determine the positions of maximum intensity values. An estimate of the crack spacing, x_c (outlined by green color in Fig. 3.10f) is calculated by the consecutive maxima difference. All the intensity values along the crack lines are cross-checked manually to see if there is an artifact. If found, are corrected to the consistent (and fixed) values to maintain uniformity along the crack lines. A threshold of ± 0.005 mm are used as a standard range and x_c values outside this range is recorded and aggregated in each region to obtain an average (\bar{x}_c). However, there may be cracks that propagate along the drawn circle, leading to some uncertainty in the extracted crack distributions [also found in one of our papers (Pal, Gope, and Iannacchione, 2019b)].

3.6 Conclusions

This chapter describes the materials and the experimental protocols used throughout our studies. The next chapter, i.e., Chapter 4 starts with the results and discussions of the protein samples prepared in the de-ionized water (the simplest hierarchical fluid in the context of complexity). It is to be noted that this chapter (Chapter 3) has detailed the general procedure. The sample sets and any particular procedure adopted for studying the drying droplets are discussed separately in each chapter (from Chapter 4 to 8).

Chapter 4

Hierarchy I: Pattern Formation in Globular Protein Droplets*

4.1 Background

Owing to the significance of the patterns resulting from the drying process in many potential applications as stated in our introduction (Chapter 1), this chapter aims to provide a systematic study on a one-component bio-colloidal system. This chapter's primary objective is to explore the fundamental understanding of the drying evolution and morphological patterns in the simplest bio-colloid, i.e., an aqueous solution of protein drying droplets. It is to be noted that this protein solution (prepared in de-ionized water) is more straight-forward, and the presence of ions in the fluids will influence the patterns to a great extent. However, the principal thrusts of this chapter lie in setting a baseline for understanding the complex multi-component systems such as proteins with the addition of various salts (ions) and liquid crystals, whole human blood, etc. (described in the following chapters, Chapters 5-7) when dried under uniform conditions (surface, humidity, temperature, droplet diameter, etc.).

For the record, the commercially available high-quality globular proteins such as bovine serum albumin (BSA) and lysozyme (Lys) have also attracted many researchers' attention. Many studies investigated the temporal drying process and their resulting patterns. Despite the intense research, most of the work on protein-solvent systems is primarily confined to either a dilute regime of protein concentration and/or the involvement of the salts into the systems (Gorr, Zueger, and Barnard, 2012; Gorr et al., 2013; Chen and Mohamed, 2010; Annarelli et al., 2001; Carreón et al., 2018b). The dilute regime of the initial protein concentration is well explored in the drying droplets; however, not beyond the range of 60 mg mL^{-1} . Researchers also attempted to explore the drying evolution and the crack distribution of these proteins dissolved in (de-ionized) water under the ambient conditions (Gorr, Zueger, and

*This work is published. Pal, A., Gope, A., Athair A.S. and Iannacchione, G.S., 2020. A comparative study of the drying evolution and dried morphology of two globular protein and de-ionized water solutions. *RSC Advances*, 10(29), pp.16906-16916. <https://doi.org/10.1039/D0RA01748E> (Pal et al., 2020a). Thanks to the *Tinkerbox* community at WPI for spending ~1000\$ as the article processing fees for publishing in the journal.

Barnard, 2012; Carreón et al., 2018a). Gorr et al. (Gorr, Zueger, and Barnard, 2012) studied the time evolution and the morphological patterns of Lys dissolved in water, varying the initial concentration from 0.1 (1 mg mL⁻¹) to 1 wt% (10 mg mL⁻¹). This study concluded that all the drops exhibit a “coffee-ring” effect (Deegan et al., 1997; Gorr, Zueger, and Barnard, 2012). The volume fraction of the lysozyme is found to be linearly dependent on its initial concentration; however, the morphology does not show any significant changes in the ring’s height and width. They also reported a “mound”-like feature in the central region and observed a few surface cracks in the given concentration range. Carreón et al. investigated the mixture of BSA and Lys dissolved in water and mainly focused on their interactions. They also conducted experiments with denatured BSA and Lys proteins and their mixtures at different relative concentrations. The folding and unfolding of these proteins and their structural (morphological) alternation are also discussed in their paper. They concluded that the formation of the crystal clusters and dendrite structures are independent of the external salts (Carreón et al., 2018a). In a recent study, the drying droplets of raw egg-white protein solutions have been explored that validates the dependence of daisy and wavy-ring crack patterns on the initial protein concentrations (Gao, Huang, and Zhao, 2018).

In this chapter, two fundamental questions about the drying evolution and the resulting patterns of the dried droplets of aqueous solutions of commercially available globular proteins, are addressed. This article aims to explore (i) the role of the protein properties (in terms of mass, composition, configuration, and size); and examine, (ii) the effect of higher initial protein concentration (above 60 and up to 150 mg mL⁻¹) on the aggregation process. The inclusion of the higher-initial protein concentration is essential since the higher concentrations enable us to explore how the excessive aggregation of these proteins play a role in relieving mechanical stress during the drying process, and the crack formation patterns. It is worth mentioning that no studies till date attempted to investigate these fundamental queries at the concentration ranges we considered in this study. To the best of our knowledge, we did not come across any experimental evidence that compares the drying evolution of the protein droplets in terms of the contact angle and the fluid front. To address this gap, two proteins, BSA and Lys, are chosen in this study. The droplets are prepared using de-ionized water (DI) that avoids ion-mediated effects and exposes the protein-protein interactions. Furthermore, the inclusion of DI under ambient conditions ensures that the functionality of the proteins is not affected by any external factors such as pH, temperature, etc.

4.2 Results and Discussions

The protein samples are used without any further purification. ~150 mg of each BSA and Lys were massed and separately dissolved in 1 mL of de-ionized water to create the protein stock solutions, BSA+DI and Lys+DI at a concentration of 13 wt%. Each

stock solution was diluted to prepare the concentrations of 1, 3, 5, 7, 9, and 11 wt%. In this study, we didn't differentiate the notation for the initial concentrations of BSA (ϕ_{BSA}) and Lys (ϕ_{Lys}) and denoted it as ϕ . It is to be noted that we used the factory-fresh microscopic glass slides (Catalog 2947-75x25, Corning, NY, USA) as the substrates (for this study only), which have minimal exposure to the environment prior to the actual experiments. These slides were rinsed with ethanol and dried subsequently. Thus, every droplet precisely contained the same substrate conditions and a uniform reproducibility in terms of the circularity of the droplets and their pinning effects was observed. The drying evolution and the emerging patterns are then examined at the initial protein concentration ranging from 1 (10 mg mL⁻¹) to 13 wt% (150 mg mL⁻¹). The spiral crack study was conducted at 50× magnification.

4.2.1 Time evolution of drying droplets

Bovine Serum Albumin: BSA+DI

Fig. 4.1(I) shows the top view of the drying evolution of BSA droplet at the initial concentration (ϕ) of 5 wt% captured through the optical microscopy. As soon as the first image of the deposited droplet is captured, a symmetrical dark (black) shade is observed near the periphery of the droplet. With the progression of time, the dark shade changes to the bright (gray) shade (Fig. 4.1(I)a-c). The periphery of the droplet is found to be pinned to the glass substrate throughout the drying process. After ~3 minutes, the fluid front starts receding from the periphery to the center of the droplet. The radius (r) of this front is measured with the progression of time, (t) (Fig. 4.1(I)d,e). The movement allows the particles to be deposited along each receding line and eventually forms a peripheral ring (shown by a white dashed circle in Fig. 4.1(I)f). It is to be noted that a few cracks in the BSA droplets up to ϕ of 5 wt% are formed during 24 hours, which are shown in the following section.

Fig. 4.1(II) depicts the side view of the drying evolution of BSA droplet at different ϕ observed with the contact angle goniometer. θ and height at the center of the droplet (h) are found to be $37 \pm 2^\circ$ and 0.35 ± 0.20 mm respectively within ~50 seconds of the deposition of the droplet. The radius (R) of the droplets is 1.1 ± 0.2 mm, and therefore, the gravitational effects can be negligible. Furthermore, the macroscopic shape of the droplet can be approximated as the spherical-cap geometry, which is based on the assumption that $h \ll R$. The black shade, observed at ϕ of 5 wt% in Fig. 4.1(I) is due to the spherical-cap shape of the droplet. The change from the black to the gray shade occurs when the contact angle (θ) reaches to a threshold value. The top panel of Fig. 4.1(II) shows the variation of θ at ϕ of 5 wt%, and $\theta(t)$ is found to be monotonously reducing with time. This suggests that the drying process occurs in a continuous evaporation limit. To validate this limit, $\theta(t)$ is fitted with a linear function: $\theta(t) = \theta_0(1 - t/\tau)$, where, θ_0 is the initial θ at $t=0$, and $1/\tau$ is a characteristic rate. For ϕ of 5 wt%, θ_0 and $1/\tau$ are found to be $39.96 \pm 0.08^\circ$ and $0.001500 \pm 0.000005s^{-1}$ respectively, with $R^2 = 0.995$. The $1/\tau$ is observed

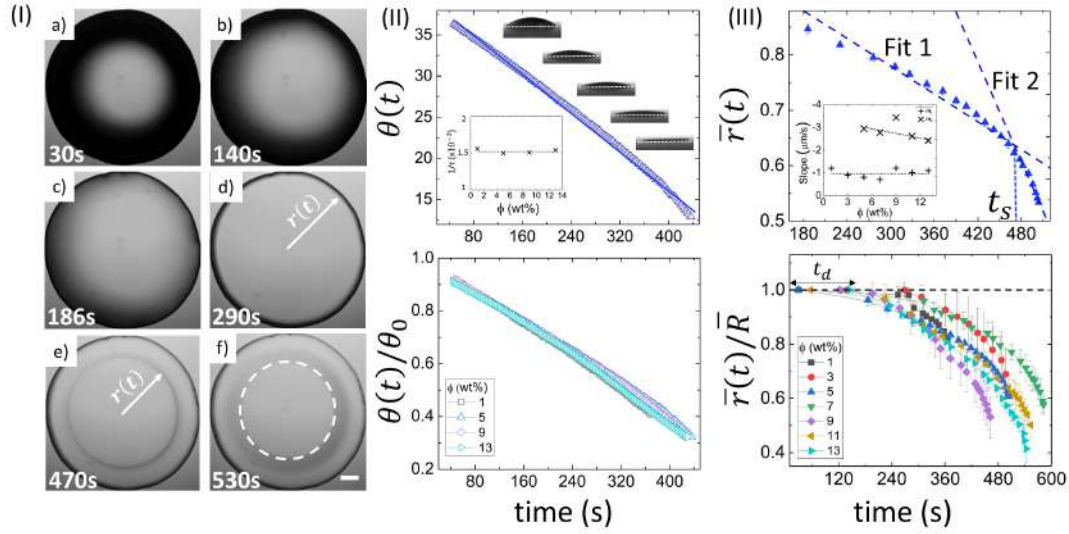


FIGURE 4.1: Drying evolution of BSA droplet: (I) Top-view of the droplets through optical microscopy at ϕ of 5 wt% clicked during different time intervals (30 s, 140 s, 186 s, 290 s, 470 s and 530 s). The white dashed circle in (f) exhibits the “coffee-ring” formation. The scale bar represents a length of 0.2 mm. (II) The top panel shows the variation of contact angle ($\theta(t)$) at ϕ of 5 wt%. The solid line specifies the fitted function. The inset shows the variation of the characteristic fitting parameter ($1/\tau$) at different ϕ . The bottom panel displays the temporal variation of the normalized contact angle ($\theta(t)/\theta_0$). (III) The top panel reveals the variation of mean fluid front radius ($\bar{r}(t)$) at ϕ of 5 wt%. The error bars represent the standard deviation. A representative fit of two linear models is made; t_s signifies the time point where both the linear fits merge. The inset shows the dependence of the slope values of linear fit 1 (m_1) and 2 (m_2). The bottom panel indicates the temporal variation of normalized mean fluid front radius ($\bar{r}(t)/R$) at different ϕ . t_d is the “dead” time up to which the fluid front radius ($r(t)$) is equal to the radius of the droplet (R).

to be independent of ϕ [inset of Fig. 4.1(II)]. A complete description of all the fit parameters is tabulated in Table 4.1.

TABLE 4.1: Data from $\theta(t)$ vs. t graph of drying droplet at each ϕ (initial protein concentration in wt%) for BSA+DI with fitting parameters: θ_0 (contact angle at $t = 0$ in degrees), $1/\tau$ (characteristic rate in s^{-1}), and R^2 (adjusted R-square of the fit).

ϕ (wt%)	θ_0 ($^\circ$)	$1/\tau \times 10^{-3}$ (s^{-1})	R^2
1	31.43 ± 0.04	1.560 ± 0.004	0.998
5	39.96 ± 0.08	1.500 ± 0.005	0.995
9	39.10 ± 0.07	1.510 ± 0.005	0.996
13	42.90 ± 0.07	1.540 ± 0.004	0.997

The normalized contact angle is calculated by dividing $\theta(t)$ with the θ_0 (obtained from the fitting equation). The individual normalized θ decay curves at different ϕ are found to collapse to a master curve when the data is plotted. This is shown in the bottom panel of Fig. 4.1(II).

In this context, it is interesting to compute the fluid front radius and its dependence on ϕ . Fig. 4.1(III) shows the evolution of the fluid front radius in BSA droplet at different ϕ . The top panel of Fig. 4.1(III) shows the variation of mean fluid front radius

($\bar{r}(t)$) at ϕ of 5 wt% exhibiting two distinct regimes: a slow, initial linear regime, and a subsequent non-linear, fast regime. Two linear fits are made on the respective linear and non-linear regimes, and a characteristic time t_s (the time point at which two linear fits intersect) is introduced. It is to be noted that the linearity of $\bar{r}(t)$ deviates after the peripheral ring formation [Fig. 4.1(I)e and top panel of Fig. 4.1(III)]. The inset of Fig. 4.1(III) compares the slope values (m_1 and m_2) obtained from the linear fits in the respective regimes at each ϕ . The negative sign in the slope values confirms the reduction of the mean radius ($\bar{r}(t)$) with time. For 1 and 3 wt%, the linear fit in the non-linear regime can't be achieved due to a swift and non-uniform movement, resulting in less number of data points to quantify. On average, the velocity of the fluid front in the linear and non-linear regime is found to be $0.99 \pm 0.20 \mu\text{m s}^{-1}$ and $2.83 \pm 0.38 \mu\text{m s}^{-1}$ respectively. m_2 decreases from ~ 3 to $\sim 2 \mu\text{m s}^{-1}$ with the increase of ϕ . The bottom panel of Fig. 4.1(III) displays the normalized radius (obtained by dividing the $\bar{r}(t)$ with the mean radius of the droplet, \bar{R}). In the early stage of the drying evolution, i.e., up to ~ 240 seconds, the radius remains constant, ($\bar{r}(t)/\bar{R} = 1$) for all the ϕ . This time is labeled as the "dead" time (t_d) where only the contact angle changes without disturbing the radius. A complete description of all the measured and fit parameters is tabulated in Table 4.2.

TABLE 4.2: Data from $\bar{r}(t)$ vs. t graph of drying droplet at each ϕ (initial protein concentration in wt%) for BSA+DI with measured parameters: R (radius of droplet in mm), w (rim width in mm), t_d (time in seconds after which the contact line radius begins to shrink from droplet radius), t_s (time in seconds at which two linear fits merge); and fitting parameters: m_1 (slope of first linear fit in $\mu\text{m s}^{-1}$), R_1^2 (adjusted R-square of first linear fit), m_2 (slope of second linear fit in $\mu\text{m s}^{-1}$), R_2^2 (adjusted R-square of the second linear fit). The negative sign in the slope values corresponds to the decrease in the radius of the fluid front.

ϕ	R	w	$t_d \pm 30$	$t_s \pm 20$	m_1	R_1^2	m_2	R_2^2
1	1.265 ± 0.025	0.319 ± 0.043	254	<i>n/a</i>	-1.2	0.960	<i>n/a</i>	<i>n/a</i>
3	1.129 ± 0.025	0.292 ± 0.072	307	<i>n/a</i>	-0.9	0.980	<i>n/a</i>	<i>n/a</i>
5	1.215 ± 0.028	0.507 ± 0.051	186	470	-0.8	0.979	-2.9	0.978
7	1.135 ± 0.036	0.465 ± 0.071	312	524	-0.7	0.983	-2.8	0.967
9	0.814 ± 0.017	0.378 ± 0.029	224	429	-1.2	0.977	-3.4	0.993
11	1.080 ± 0.016	0.543 ± 0.022	225	503	-1.0	0.996	-2.6	0.967
13	0.854 ± 0.014	0.462 ± 0.021	235	477	-1.1	0.983	-2.4	0.970

Lysozyme: Lys+DI

Akin to BSA, Lys droplet at ϕ of 5 wt% also shows a dark shade near the periphery of the droplet (Fig. 4.2(I)a). The dark shade diminishes, the fluid front starts receding from the periphery after ~ 6 minutes, and forms a ring (Fig. 4.2(I)b-d). Interestingly, a sharp spot around the center appears and forms a "mound"-like structure. The water starts drying from that mound, and finally, a "dimple" appears in the existing structure. Simultaneously, the radial cracks grow near the periphery and come in

each other's contact through the orthoradial cracks (Fig. 4.2(I)d-f). The white dashed circle displays the peripheral ring and the solid circle depicts the mound and the dimple structures (Fig. 4.2(I)f). Unlike BSA, most of the cracks appeared during the visible drying process at ϕ of 5 wt%.

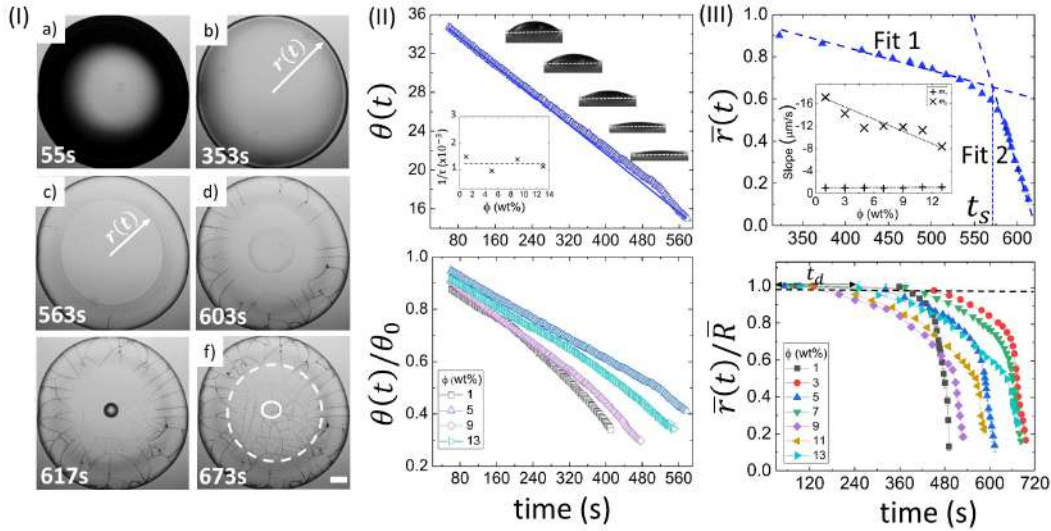


FIGURE 4.2: Drying evolution of Lys droplet: (I) Top-view of droplets through optical microscopy at ϕ of 5 wt% during different drying intervals (55 s, 353 s, 563 s, 603 s, 617 s and 673 s). The white dashed circle in (f) shows the “coffee-ring” formation. The solid circle exhibits the “mound”-like structure. The scale bar represents a length of 0.2 mm. (II) The top panel confirms a variation of contact angle ($\theta(t)$) at ϕ of 5 wt%. The solid line shows the fitted function. The inset shows the variation of the characteristic fitting parameter ($1/\tau$) at different ϕ . The bottom panel displays the temporal variation of the normalized contact angle ($\theta(t)/\theta_0$). (III) The top panel reveals the variation of the mean fluid front radius ($\bar{r}(t)$) at ϕ of 5 wt%. The error bars represent the standard deviation. A representative fit of two linear models is made; t_s signifies the time point where both the linear fits merge. The inset represents the dependence of the slope values of linear fit 1 (m_1) and 2 (m_2). The bottom panel indicates the temporal variation of the normalized mean fluid front radius ($\bar{r}(t)/\bar{R}$) at different ϕ . t_d is the “dead” time up to which the fluid front radius ($r(t)$) is equal to the radius of the droplet (R).

Fig. 4.2(II) shows the side view of the drying evolution of Lys droplet at different ϕ . It is to note that different Lys concentrations might affect the surface tension of the solutions. However, our first measured value of θ during the contact angle measurements at all ϕ is found to be $37.0 \pm 1.6^\circ$. This measurement tempted us to conclude that the effect is not significant enough for the unique pattern formation. The θ at ϕ of 5 wt% during the drying process reduces monotonously [top panel of Fig. 4.2(II)]. θ_0 and $1/\tau$ are found to be $36.66 \pm 0.01^\circ$ and $0.0009740 \pm 0.0000007s^{-1}$ respectively, with $R^2 = 0.999$. Similar to BSA, the characteristic rate ($1/\tau$) is found to be independent of ϕ . A complete description of all fit parameters is tabulated in Table 4.3.

Unlike BSA, the normalized contact angle data shows that the individual decay curves at different ϕ start deviating from each other towards the very end of the

TABLE 4.3: Data from $\theta(t)$ vs. t graph of drying droplet at each ϕ (initial protein concentration in wt%) for Lys+DI with fitting parameters: θ_0 (contact angle at $t = 0$ in degrees), $1/\tau$ (characteristic rate in s^{-1}), and R^2 (adjusted R-square of the fit).

ϕ (wt%)	θ_0 ($^\circ$)	$1/\tau \times 10^{-3}$ (s^{-1})	R^2
1	43.83 ± 0.15	1.500 ± 0.008	0.987
5	36.64 ± 0.01	0.900 ± 0.001	0.999
9	41.89 ± 0.10	1.400 ± 0.005	0.994
13	40.38 ± 0.08	1.140 ± 0.004	0.994

process [bottom panel of Fig. 4.2(II)].

The top panel of Fig. 4.2(III) displays the evolution of the $\bar{r}(t)$ at ϕ of 5 wt% in Lys droplet. And, the bottom panel depicts the evolution of the normalized mean fluid front radius ($\bar{r}(t)/\bar{R}$) at different ϕ . It is to be noted that this movement in BSA droplets could be tracked only till the point where the radius just passes through the peripheral ring. Unlike BSA, this movement in the Lys droplets could be tracked till the "mound"-like structure around the central region of the droplet. This causes the range of the $\bar{r}(t)/\bar{R}$ data from 1 to ~ 0.1 . The presence of a linear and a subsequent non-linear regime is commonly observed in the fluid front movement at every ϕ in both the Lys and BSA droplets. On average, the velocity of the fluid front in the linear and non-linear regime is found to be $1.00 \pm 0.08 \mu\text{m s}^{-1}$ and $12.36 \pm 2.73 \mu\text{m s}^{-1}$ respectively. A sharp dependence of the slope values in regime 2 with ϕ is observed, m_2 decreases from ~ 17 to $\sim 8 \mu\text{m s}^{-1}$. A complete description of all the measured and fit parameters is tabulated in Table 4.4.

TABLE 4.4: Data from $\bar{r}(t)$ vs. t graph of drying droplet at each ϕ (initial protein concentration in wt%) for Lys+DI with measured parameters: R (radius of droplet in mm), w (rim width in mm), t_d (time in seconds after which the contact line radius begins to shrink from droplet radius), t_s (time in seconds at which two linear fits merge); and fitting parameters: m_1 (slope of first linear fit in $\mu\text{m s}^{-1}$), R_1^2 (adjusted R-square of first linear fit), m_2 (slope of second linear fit in $\mu\text{m s}^{-1}$), R_2^2 (adjusted R-square of second linear fit). The negative sign in the slope values corresponds to the decrease in the radius of the fluid front.

ϕ	R	w	$t_d \pm 30$	$t_s \pm 20$	m_1	R_1^2	m_2	R_2^2
1	0.803 ± 0.017	0.195 ± 0.037	395	459	-1.0	0.987	-17.2	0.974
3	0.895 ± 0.014	0.320 ± 0.043	492	655	-1.0	0.973	-14.2	0.971
5	0.919 ± 0.020	0.383 ± 0.033	320	569	-1.0	0.974	-11.7	0.987
7	1.213 ± 0.028	0.411 ± 0.073	427	642	-0.9	0.978	-12.0	0.999
9	1.149 ± 0.034	0.491 ± 0.048	199	490	-0.9	0.941	-11.8	0.989
11	1.095 ± 0.016	0.481 ± 0.075	213	526	-1.1	0.955	-11.3	0.964
13	1.153 ± 0.016	0.438 ± 0.061	303	639	-1.1	0.948	-8.4	0.985

A physical mechanism

The underlying physical mechanism of the drying evolution and the visible difference in terms of the morphology of the droplets is demonstrated in Fig. 4.3. The deposited droplet goes through a convective flow where the constituent particles tend

to interact (adsorb) with the substrate during the early drying stage. The evaporation rate is observed to be highest at the three-phase contact line (solid-vapor-liquid) due to the curvature of the circular droplet. This process drives the flow to compensate the higher rate of mass loss near the periphery compared to the central part of the droplet. This early stage depicted in Fig. 4.3a shows the time duration (t_d) in which no fluid front movement is observed; however, the height and the contact angle get considerably reduced. During this time frame, the protein particles form an inhomogeneous film and (subsequently) a fluid front starts moving on this film from the periphery to the center which marks the beginning of the next stage. The mixed mode i.e., the movement of both the contact angle and the fluid front is found at this stage. The front seems to deposit some more protein particles as it moves (Fig. 4.3b). A bulge [popularly known as “coffee ring” effect (Deegan et al., 1997)] at the periphery of the droplet is noticed during this fluid front movement. The bulge is believed to form due to the excess deposition of the particles which could be seen in Fig. 4.3c. The drying process till this point, i.e., the formation of this peripheral ring is observed to be similar for both the protein droplets (Figs. 4.1 and 4.2). However, the formation of a “mound”-like structure (Fig. 4.3d,e) in Lys droplets [a similar phenomenon is observed in (Carreón et al., 2018a; Gorr, Zueger, and Barnard, 2012)] creates a visible difference in the drying evolution of both the protein droplets. The comparison of the drying rates of these different sized protein particles may reveal new insights. To map the rate of water loss with the change in morphology during the drying process, it is vital to explore the possible reasons behind the similarities and dissimilarities for both the protein droplets in terms of the parameters (t_d , t_s , m_1 , and m_2) extracted from the fluid front movement.

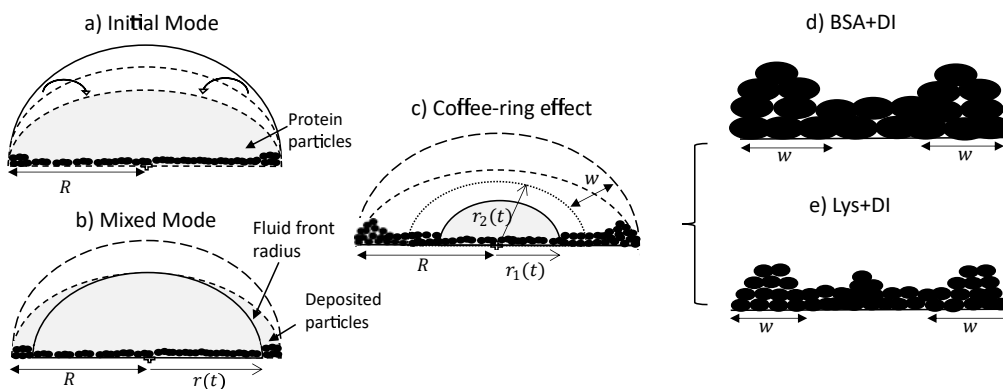


FIGURE 4.3: Side view of the drying evolution: a) Initial mode is observed at an early stage of drying where only the contact angle decreases. The fluid front radius (r) remains unchanged during this time and equals to the radius (R) of the droplet. The protein particles interact with the substrate during this stage. b) In this mixed mode stage, along with the contact angle, the fluid front starts receding from the periphery of the droplet. The fluid front moves, deposits more particles, and forms a ring of width w . It moves further when the radius of fluid front just pass the ring width to the new position (r_2). r_1 indicates the movement towards the central region of the droplet, leading to a complimentary morphology. d) BSA+DI, without any “mound”-like structure and e) Lys+DI, the presence of a “mound” could be observed in the central region.

t_d indicates the (early stage) time point of the drying process where the protein particles in both droplets experience the convective flow. During this flow, these particles first tend to interact (adsorb) with the substrate. The usage of de-ionized water in the present study enables us to avoid the ion-mediated effects and does not influence the conformational states (or the functionality) of these proteins. This means that the globular nature of the overall protein structure during the drying process is maintained. During adsorption of these proteins on the glass substrate, one can expect different BSA-glass and Lys-glass interactions. This expectation can be due to the fact that the BSA and the Lys proteins carry an opposite net charge whereas, the glass (substrate) is negatively charged. However, we also need to consider that the hydrophobic residues are buried inside the protein core, and numerous positively and negatively charged residues in a protein's surface are exposed. Though the overall charge of BSA (or Lys) is negative (or positive), it is the fact that the BSA (or Lys) will prefer to adsorb on the negatively charged glass substrate with its positively charged residues. Therefore, the overall interaction of BSA-glass or Lys-glass might not be altered, while there is a high probability of having different BSA-BSA or Lys-Lys interactions. It is because these charged residues help in orientating these protein particles in such a way that one particle gets influenced by the neighboring particle. With time, the protein-protein interactions tempt to be dominant over the protein-substrate interactions, assist in forming the protein film on the substrate, and finally could be responsible for determining these unique patterns. So, t_d is the time in which protein particles interact with the substrate and interact with other proteins to form a film. The constant rate of the evaporation validates of having a similar trend in this initial mode till the time point t_d .

As time passes during the drying process, we observed a fluid front to recede from the periphery to the center of the droplet. We quantified the velocity of the front movement. The average speed of first linear fit (m_1) is found to be $0.99 \pm 0.14 \mu\text{m s}^{-1}$, which is independent of the initial concentration and the type of protein. Considering the trends observed in m_1 , it could be concluded that similar mass transfer mechanisms have emerged in the linear regime. This assumption makes sense because there is enough water on the front surface at this stage, and the front behaves as if it is a water-pool and hardly feels the presence of any protein particles. Subsequently, we have observed a transition from the linear to the non-linear regime in the front movement (Figs. 4.1(III) and 4.2(III). A linear fit on the linear and non-linear regimes was made. t_s signifies the time point where both these linear fits merge. Interestingly, it can be physically interpreted as the time when the fluid front moves from r_2 to r_1 (Fig. 4.3c), i.e., the time point of the movement from the edge of the peripheral ring towards the central region of the droplet. The t_s for all ϕ is found to be within ± 20 s from this ring formation.

Once the fluid front passes this peripheral ring, the fluid no longer resembles a water-pool. The continuation of water evaporating process leads to the presence

of more protein particles than water. In this context, we observed that the velocity of the second linear fit (m_2) is dependent on the initial concentration and it is different for both the protein droplets. The differences observed in m_2 are probably due to different self-assembling interactions, which is dependent on the unique physical characteristics of these proteins. Given the globular nature of these proteins, we know that these proteins are different in terms of their net charged states, molecular shape, weight and disulfide bridges. Since the pH of the system is unchanged, it is beyond the scope of this study to conclude the mobility effects that emerged due to the individual charged residues present in the protein during the fluid front movement. However, this mobility can easily be interpreted in terms of their weight, shape and bridges. BSA particles are mostly restricted to flow with the fluid front due to high molecular weight (~ 66.5 kDa) and high aspect ratio (major/minor axis = 3.5). Moreover, the presence of 17 disulfide bridges in BSA provides a compact network between BSA-BSA particles; it will prefer to be deposited within the existing film-layer in the droplet. This results in a few left-over BSA particles to be carried with the water during the later stage of the fluid front movement. In contrast, Lys could be thought of a squishy sphere (aspect ratio = 1.5) with a low molecular weight (~ 14.3 kDa). The presence of the lower disulfide bridges (17 for BSA and 4 disulfide bridges for Lys) results in a weak network among these Lys particles, and, it triggers the Lys particles to be carried away with the fluid front. The water content of the fluid decreases with the progression of time, and a large number of Lys particles is left behind. These (left out) particles eventually gets accumulated around the center and forms the "mound"-like structure. We believe that some water is trapped in the mound. Therefore, a dimple is noticed when the Lys particles fall out of the solution as this entrapped water evaporates.

The movement of the fluid front appears to slow down with the increase of ϕ (number of particles), even though the movement continues to carry and deposit the Lys particles at each line of the fluid front. The concentration dependence of the mound and the peripheral ring on different protein types will be discussed later. At the final stage of the drying process, the water-loss in the droplet induces high mechanical stress leading to the formation of different crack patterns, which will be discussed in the next subsection.

4.2.2 Morphology of dried droplets

Fig. 4.4a-g and Fig. 4.4h-n represent the morphology of the dried droplets in BSA and Lys respectively, and both the common and distinctive properties are identified. A few common characteristics of both the dried droplets include (1) the presence of a peripheral ring at a greater height than the central region. This greater height can be viewed from the one-sided dark shadowy shade molded due to side illumination. (2) The cracks are observed in both the droplets; however, the distribution and the nature of the cracks differ to a large extent.

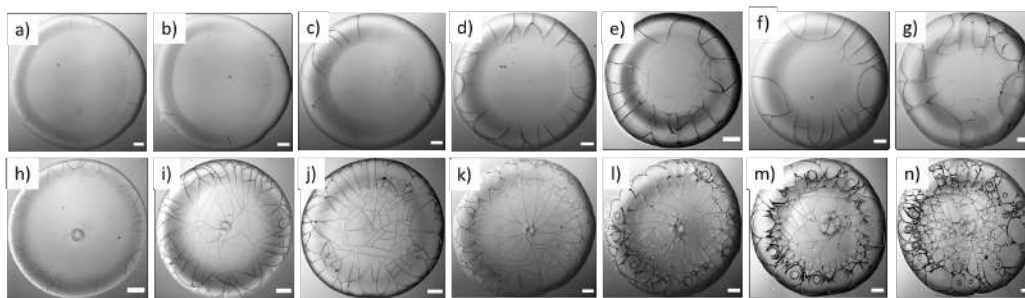


FIGURE 4.4: Gray images of two protein dried droplets: BSA at ϕ of a) 1, b) 3, c) 5, d) 7, e) 9, f) 11, and g) 13 wt%; Lys at ϕ of h) 1, i) 3, j) 5, k) 7, l) 9, m) 11, and n) 13 wt%. The images of the BSA droplets reveal the presence of the cracks near the periphery region, whereas, the images of Lys droplets confirm that the cracks are spread and connected from ϕ of 3 wt%. The “dimple” and the “mound”-structure can be observed in Lys droplets at every ϕ . The spirals are noticed in Lys droplets from ϕ of 9 wt%. The scale bar represents a length of 0.2 mm.

A few distinct morphological patterns observed in both the protein droplets are (1) In BSA droplets, mostly the radial cracks are observed; whereas, different types of cracks such as radial, wavy, spiral, etc. makes Lys droplets a chaotic system. (2) There are almost no cracks in the central region of the BSA droplet, whereas, the cracks are present throughout the Lys droplets. The cracks are found only in the periphery of the Lys droplets at ϕ of 1 wt%. (3) There is a complimentary morphology in the central region, with the mound and the dimple structures in Lys and without any such structures in the BSA droplet. (4) The number of cracks increases with the increase of ϕ is clearly observed in BSA. The cracks are mostly equally spaced and countable. (5) A thin hair-like structure is observed at the termination of each crack (from 7 to 13 wt%) in BSA droplets. In contrast, the cracks are well-connected and form a uniform domain in every Lys droplet (except the ϕ of 1 wt%). (6) The presence of (few) circular and (many) spiral cracks in Lys droplets from 9 to 13 wt% makes the morphology very different at the high concentrated regime from that in BSA droplets. The possible reasons are discussed in the mechanical interpretation section.

Profilometry

Figs. 4.5(I) and (II) show the variation of dimensionless quantity, mean peripheral ring width (\bar{w}) divided by the mean radius of the droplet (\bar{R}) with ϕ for BSA and Lys droplets respectively. It is observed that the ring width is directly proportional to ϕ , i.e., with the increase of ϕ , this ring width is expanded further [Fig. 4.5(I)]. The number of BSA particles increases with the evaporation of water. This process triggers additional deposition of the particles at the droplet periphery with the upsurge of ϕ . In contrary, the Lys droplet is found to be constant and independent of the variation of ϕ . An almost equal quantity of Lys particles is deposited in the ring, and most of the free particles are carried towards the center (and forms a mound structure). Fig. 4.5(III) shows the areal dependence of this mound structure. The mean area \bar{a} is

normalized with \bar{R} , and the \bar{a}/\bar{R} at different ϕ in Lys droplet is plotted. The linear dependence with ϕ makes it evident that most of the Lys particles are carried and deposited towards the center.

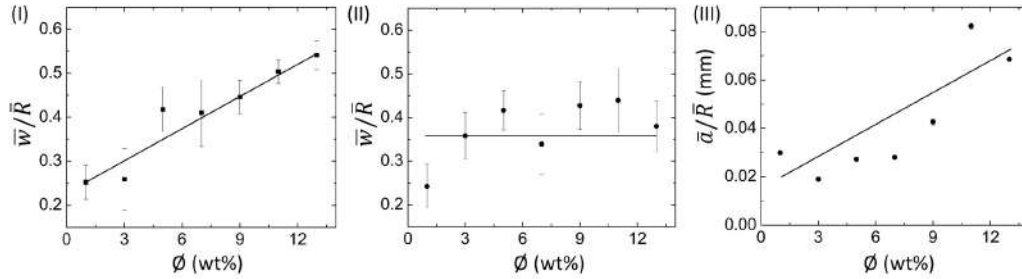


FIGURE 4.5: Profilometric measurements of protein droplets: Variation of the mean peripheral ring width (\bar{w}) normalized to the mean radius of the droplet (\bar{R}) with ϕ for (I) BSA+DI, and (II) Lys+DI. (III) Variation of the averaged area of “mound”-like structure (\bar{a}) normalized to \bar{R} with ϕ in Lys droplet. The error bars correspond to the standard deviation obtained from multiple measurements.

As we have mentioned already, the mound structure is formed by carrying and depositing the free Lys particles during the fluid front movement. As such, the increase of ϕ also triggers the upsurge of the overall number of particles, resulting in the piling of these particles to a height. The formation of a dimple (depression) is probably when the Lys particles falls out of the solution. The presence of this dimple is not reported in any of the earlier works (Gorr, Zueger, and Barnard, 2012; Carreón et al., 2018a) probably due to usage of relatively low concentration range. One can anticipate the dimple or the mound as the optical illusion, nonetheless, this is not the case. We did the height profile-like imaging with the sensofar microscopy to confirm the mound and dimple structures; however, we could not calibrate sufficiently to get the exact height measurements. It is also observed that the mound structure is situated almost at the center. It is due to the fact that the circular droplet shape prefers the symmetry for the fluid front movement. To confirm this fact, we pipetted the solutions in a strip-like geometry on the glass substrate. We followed the fluid front movement from both the ends of the strips; however, we did not observe any mound and dimple structures. Furthermore, we assumed that this structure is likely to be shifted to some extent (not forming perfectly at center of the droplet) due to the droplet’s circularity. However, no general trend is observed while measuring it in the asymmetrical (or oval) droplets.

Quantification of the cracks

Fig. 4.6(I) displays the Q-Q plot at ϕ of 7 wt% and confirms the non-normal distribution of the mean crack spacing (x_c). The representative plots also suggest that the cracks are not equally distributed in different protein droplets. The figures indicate that the outliers have surfaced in the form of skewed data points. The outliers (depicted by three circles deviate from the reference line in the Q-Q plot) are not

ideal consideration from a statistical perspective since these violate one of the assumptions for t-test (parametric); nonetheless, in our case, there is no good reason to consider these outliers as invalid samples. To counter the non-normal distributions of the mean crack spacing, a non-parametric Mann-Whitney U test (an alternative to the parametric t-test) was preferred to examine the (significant) differences in terms of x_c values among the different protein droplets at different ϕ . In this study, the mean rank test is chosen over the median (for the visual inspection) because (a) the number of cracks are observed to be different in both the protein droplets; and, (b) the number of samples is relatively large.

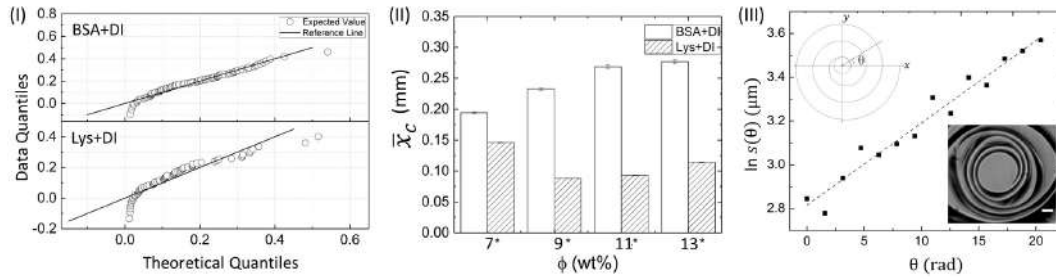


FIGURE 4.6: (I) Q-Q plot of BSA and Lys droplet at ϕ of 7 wt% displaying the skewed data points. (II) The histogram depicting the comparison of the mean crack spacing (\bar{x}_c) at different ϕ among the proteins in the peripheral regions. Significant pairs (BSA and Lys) are marked with an asterisk [*] at each ϕ . The error bars correspond to the standard error. (III) A characteristic linear fit of a spiral crack trajectory at ϕ of 13 wt% in Lys droplet. The upper inset shows the schematic diagram of the spiral cracks projected on the xy plane, in which $s(\theta)$ is the radial distance from the spiral center and θ is the angle starting from zero in an anticlockwise direction. The lower inset shows an example of spiral focused at $50\times$ magnification, with the scale bar of length $10\ \mu\text{m}$.

In the Mann-Whitney U test, the protein was kept as the categorized factor (independent factor, with two levels, BSA and Lys) and x_c as a dependent variable at different ϕ . All the histograms are expressed as the mean \pm standard error (SE). The differences where $p \leq 0.05$ are considered to be significant in this study. A detailed report of the statistical test (U, z, and p values) is shown in Table 4.5.

TABLE 4.5: Outcome of Mann-Whitney U test with an asterisk [*] indicating significant interaction between Lys, and BSA in terms of x_c at different ϕ (wt %).

ϕ (wt%)	Mann-Whitney U	Z	p value
7	2893.500	-2.119	0.034*
9	2666.500	-5.331	$\leq 0.001^*$
11	1732.500	-5.752	$\leq 0.001^*$
13	1643.500	-5.439	$\leq 0.001^*$

Fig. 4.6(II) shows \bar{x}_c for BSA and Lys droplets at each ϕ . The results confirm our morphological observations that the crack patterns in BSA and Lys droplets are different from each other, resulting in a significant difference in \bar{x}_c in the peripheral regions at every ϕ (the presence of crack spacing at every ϕ is significantly higher in Lys). The visual observations could be considered as an effective way to determine

the differences in terms of \bar{x}_c ; however, the statistical test helps us to distinguish the data fluctuations borne out due to the experimental conditions. It is observed that \bar{x}_c in the Lys droplets varies from 0.08 to 0.15 mm without any trend when the ϕ is increased. In contrast, \bar{x}_c in the BSA droplet varies from 0.19 to 0.27 mm, and suggests a proportionate distribution; i.e., x_c increase with the increased ϕ . The release of the available stress is mostly unidirectional in the BSA droplets, resulting in a uniform crack pattern in the peripheral ring. The uniform crack spacing resulted in an increased x_c when ϕ is also increased. However, in Lys droplets, the stress is relieved from all the directions resulting in the distribution of small to large cracks spread throughout the droplet, affecting \bar{x}_c at each ϕ .

Fig. 4.6(III) shows a characteristic linear fit of a spiral crack trajectory at ϕ of 13 wt% in the Lys droplet. The domains containing the spiral cracks in the Lys droplets are three dimensional and it is not possible to observe all the spiral lines simultaneously with the droplet surface. The lack of information about the z plane prompted us to represent these spirals on the xy plane (in the form of 2D). The expression of the logarithmic spiral in polar coordinates: $s(\theta) = ae^{b\theta}$. Assumption of this logarithm leads to $\ln s(\theta) = \ln a + b\theta$ where, $s(\theta)$ is the distance from the spiral center, and θ is the angle which is in an anti-clockwise direction from the x axis, not restricted to 2π . The final theta corresponds to the angle made by the x axis and the outermost spiral line. The schematic diagram of a two-dimensional spiral is shown in the upper inset. The logarithmic parameters are “a”, which is the apparent length of the spiral, and “b”, which controls the tightness and predicts the direction of the spiral. A lower value of “b” means the spiral has more revolutions and hence, more tightness in the spiral shape. No preference of clockwise or counter-clockwise direction in the spirals is observed in any of these droplets. This prompted us to generalize the direction by flipping all the required images so that the spirals would be consistent every time with the starting spiral revolution line lying at zero degrees as shown in the lower inset. The linear fit between $\ln s(\theta)$ and θ with R^2 of 0.957 confirms that the spirals in Lys droplets are in the form of logarithmic spirals. An oscillation of the data points is obtained due to the presence of the irregular, polygonal-shaped domains. The overall shape of the spirals for different ϕ is almost the same; however, the trajectories are influenced by the material and fracture properties [a similar phenomenon is observed in (Neda, Jozsa, Ravasz, et al., 2002; Sendova and Willis, 2003)]. The spirals at ϕ of 13 wt% are shown in Fig. 4.7.

The various parameters of the spiral crack analysis at ϕ of 11 and 13 wt% are reported in Table 4.6. Spirals with a very few revolutions in ϕ of 13 wt% are also observed. The value of “b” is found to be in the range of 0.0376 to 0.0548 $\mu\text{m rad}^{-1}$ - a narrow range implying that the tightness is probably insensitive to the concentration of proteins; however, a detailed trend of “b” requires to examine more levels ϕ .

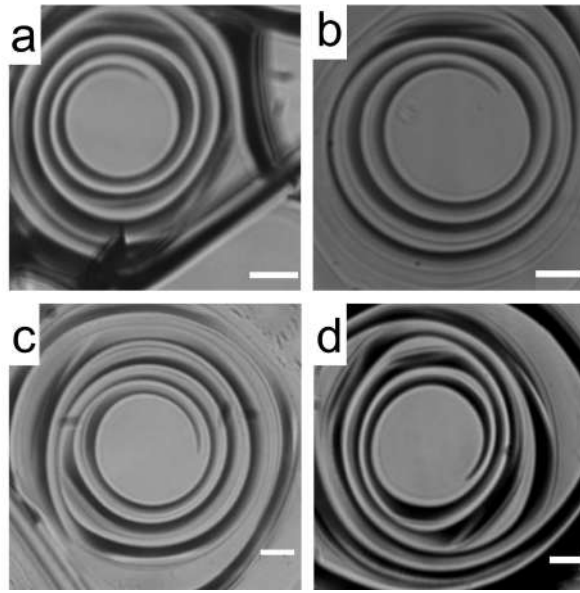


FIGURE 4.7: (a)-(d) show the spirals from 1 to 4 are shown at ϕ of 13 wt% respectively, with the scale bar of length $10 \mu\text{m}$.

TABLE 4.6: Characteristic fitting parameters of spiral cracks at ϕ of 11, and 13 wt% for $\ln s(\theta) = \ln a + b\theta$ are tabulated: "b" denotes the spiral tightness in $\mu\text{m rad}^{-1}$, and "a" denotes apparent length in μm . $s(\theta)$ is the distance from the spiral center, and θ is the angle which is not restricted to 2π .

ϕ (wt%)	Spiral no	b	a	R^2
11	1	0.0548	13.1800	0.9460
13	1	0.0398	12.3407	0.9002
13	2	0.0437	13.3631	0.9373
13	3	0.0359	14.8322	0.9521
13	4	0.0376	16.7049	0.9569

A mechanical interpretation

It is reported in the earlier subsection that each droplet is pinned to the substrate throughout the drying process. The particles in the droplet are adsorbed on the substrate, and simultaneously are carried towards the periphery. With further water-loss from the droplet, the protein particles are deposited in such a way that it creates a film. These particles are accumulated in the layers and might be influenced by a shear-mode or mode II (the stress is applied parallel to the plane). However, this influence is almost negligible as the top surface of the film still contains enough water to evaporate. This water evaporates during the fluid front movement, and the tensile stressed fields are generated when the droplet is almost devoid of water.

Fig. 4.8 indicates that two types of tensile stresses (mode I) are involved in propagating the radial and azimuthal cracks in the protein droplets. σ_θ and σ_r are the stress that normally acts to the radial crack and azimuthal crack, respectively. In both the droplets, a directional growth, i.e., a radial crack, was initially observed to propagate

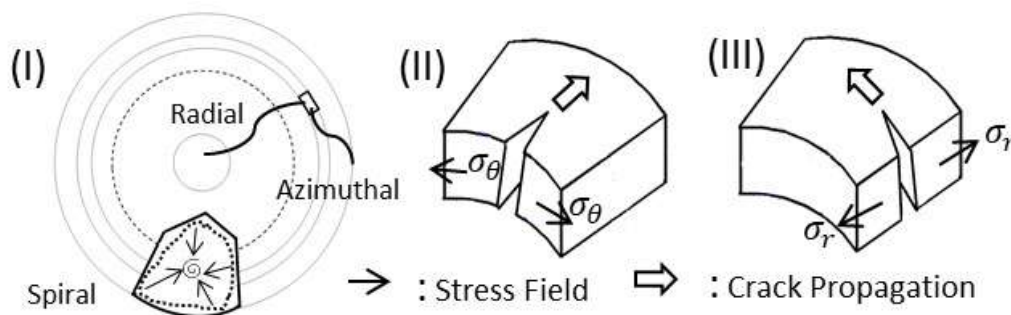


FIGURE 4.8: Schematic illustration explaining of the nature and propagation of cracks in both the protein droplets. (I) Top-view of a droplet shows radial and azimuthal cracks. A spiral crack is also shown in a polygonal crack domain. An element is focused on displaying crack propagation to get a notion of stress. Mode I (tensile mode) in which (II) stress (σ_θ) acting normal to the radial crack and (III) stress (σ_r) acting normal to the azimuthal crack.

from the periphery of the droplet (for example, see Fig. 4.2(I)c). Therefore, it indicates that the stress acts along the fluid front, normal to the radial crack, i.e., σ_θ is dominant initially. It is known from Griffith's hypothesis that the moment when the available stress in the film exceeds the critical stress, the excess stress is released by virtue of the crack propagation (Katzav, Adda-Bedia, and Arias, 2007; Goehring et al., 2015). This film height could be one of the reasons for the cracks appearing in the peripheral ring first and then proceeds towards the central region in every protein droplet in general. We attempted the height profile-like imaging with the sensorfar microscopy; however, we could not calibrate sufficiently to get the exact height measurements. The crack propagation could also be characterized based on the opening of the cracks and the distance of the crack tip as a function of ϕ . However, this is not possible with the current set-up as the time-lapse images are captured with an 8-bit camera and can only be taken every two seconds.

After the formation of the radial cracks, a few are curved azimuthally and the remaining ones join the neighboring cracks. However, it is observed that the stressed fields are dependent on the nature of protein particles. The crack propagation is stopped in BSA droplets, and a hair-like crack is developed without invading the central region of the droplet (Fig. 4.4d-g). The cracks form almost no connected domains. Our assumption is that the propagation of the cracks is stopped when the film thickness is less than the critical crack thickness resulting in zero cracks in the central region of every BSA droplet.

Lys, on the other hand, is a loosely-compacted and a low molecular weighted protein. The cracks are spread all over the droplet at all ϕ except 1 wt%. The presence of mound and dimple structures in the central region creates a thick gradient (highest at the periphery, lower at the center, and lowest at the middle region) during the drying process. This thickness gradient is enough to meet the crack propagation criteria and joins the crack lines from the center to the periphery. The stress

fields act from all the directions (σ_r and σ_θ) leading to a chaotic system. No cracks are observed in the central region at 1 wt% (Fig. 4.4h) due to the presence of a few Lys particles in the middle region, which reduces the film thickness from the critical crack thickness. There are mostly well-connected polygonal domains in the Lys droplets at ϕ of 3 wt% and above (Fig. 4.4i-n). The cracking leads to a subsequent process of delamination at ϕ of 5 wt% and 7 wt% near the periphery of the droplet (Fig. 4.4j,k). Adhesion energy persists between the protein particles and the glass (substrate). As soon as the stored elastic energy in the domain overcomes this adhesion energy, each domain buckled- curving outwards like a bowl [a similar process is observed in other studies as well (Sobac and Brutin, 2014; Giorgiutti-Dauphiné and Pauchard, 2015; Lazarus and Pauchard, 2011)]. The interference fringes of each fragmented domain imply that there is an air gap between the detached film and the substrate that forms a non-uniform adhering region in each domain present in the Lys droplet. This phenomenon is observed in high-magnification images of Lys droplets represented in Fig. 4.4j-n.

A spiral path, thus, is initiated in the well-connected polygonal domain of the Lys droplets at ϕ from 9 wt% onwards (Fig. 4.4l-n). The spirals propagate to release the elastic energy stored in the fragmented domain. This phenomenon is observed from ϕ of 9 wt% in Lys droplet, implying that there is not enough stored elastic energy in the fragmented domains below ϕ of 9 wt%. The formation of the spirals on the irregular (polygonal) domains in Lys droplets has no radial cracks intersecting the spiral cracks, i.e., no splitting of the spiral cracks is observed in the Lys droplet (Fig. 4.4m,n). It indicates that the size domains turn so small that there is no available energy for the radial cracks to propagate. At ϕ of 9 and 11 wt% in Lys droplets, it is observed that the corners of the domains act as the precursor (Fig. 4.4l,m). It means that a high-stress area is achieved; however, due to lack of sufficient energy, the spirals fail to form the shape of those observed at ϕ of 13 wt% (Fig. 4.4n). Most of the spirals are present on the peripheral ring of the droplet at ϕ of 11 and 13 wt% (Figs. 4.4m,n). This implies that the film height could be one of the necessary criteria to have spiral cracks only at specific ϕ in the Lys droplet.

Though the increase of the protein concentration directly increases the film thickness, the heavy weighted protein (BSA of ~ 66.5 kDa) contains less number of particles forming thinner film height than that observed in Lys (~ 14.3 kDa) at the same initial concentration. We argue that the absence of well-connected domains makes it hard to buckle the protein film. As a result, the stored elastic energy can not be applied from all the directions on the delamination front to propagate in the BSA droplet. Interestingly, a hierarchy is only observed in the Lys protein droplets. At the lowest ϕ (1 wt%), the cracks are present in the peripheral ring of Lys droplet. The cracks are observed throughout the film from 3 to 13 wt%; however, there is no delamination process involved until the ϕ of 3 wt%. At ϕ of 5 and 7 wt%, the delaminated cracks are observed, particularly in the ring. As ϕ increased from 9 to

13 wt%, the circular and spiral cracks appeared in the ring in addition to the delamination (Fig. 4.4h-n). Observation of these spirals might be a common phenomenon in polymeric systems (Dillard et al., 1994; Behnia, Buttlar, and Reis, 2017; Neda, Jozsa, Ravasz, et al., 2002); however, such phenomenon observed in Lys droplets is yet to be reported. This proves a similar unstructured, amorphous reminiscent behavior of the Lys protein.

This mechanical interpretation, thus, reveals the differences in the type of crack patterns observed in the BSA and Lys droplets and throws light on the reason behind the existence of spirals in the Lys droplets at specific ϕ . Further, this mechanical interpretation can also be used in explaining the crack patterns in the dried droplets of any bio-molecules.

4.3 Conclusions

This work showcased the self-assembly of proteins driven by the drying process. The findings of these experiments confirm that the nature of protein plays an important role in deciding the drying evolution and the subsequent morphology. The monotonous reduction of the contact angle during the drying process helps in identifying different modes of the evaporation. The relatively higher initial protein concentration used in this study facilitated in identifying a "dimple" on the mound-structure in the dried lysozyme droplets. This study further establishes the presence of a spiral crack pattern at the specific initial protein concentration in lysozyme droplets. The non-parametric statistical tests facilitate the crack spacing quantification and confirm the visual observations.

In the next chapter (Chapter 5), the hierarchy is increased in terms of complexity. These drying protein droplets are examined with the thermotropic liquid crystals (LCs). Since these LCs were not aligned to the substrate before doing any experiments, Chapter 5 specifically aims at exploring how the bulk LCs affect these protein droplets' pattern formation. It is to be noted that this kind of work has not been arrested in the literature so far. Therefore, the next chapter does not follow the conventional way of quantifying the LC textures, such as the birefringence study in the crossed polarizing configuration. It provides a new way of extracting information about the self-assembled structures.

Chapter 5

Hierarchy II: Pattern Formation in Protein droplets with LCs*

5.1 Background

Liquid crystals (LCs) are a unique class of anisotropic materials those can explore a wide range of ordered phases. The latest experimental developments consider LCs as a promising tool for sensing biological and chemical events due to their label-free detection, phase-separation and easy visualization (Kato, 2002). LC-based bio-sensing systems are typically used to detect the interaction among the biomolecules by utilizing an aligned nematic state of the LCs (Hu and Jang, 2012b; Hu and Jang, 2012a; Liu, Hu, and Jang, 2013; Marin et al., 2013; Shehzad et al., 2015; Lee, Chang, and Lee, 2017).

Apparently, the self-assembled drying mechanism of a combined system consisting of protein and LC (without any prior alignment) has not attracted any attention. This work bridges the gap between LC and drying protein droplet research by introducing a conventional, thermotropic LC at the initial concentrations of LCs into a protein-water system. In the previous chapter (Chapter 4) we have used Lys (Lys) and bovine serum albumin (BSA) as the archetypes to understand the drying mechanism and pattern formation of these protein solutions prepared in de-ionized water. Therefore, adding bulk LCs in the simplest Lys-water and BSA-water systems helps us to identify the effects of these droplets in the form of emerging patterns. The main findings of this study include (1) a temporal study providing a qualitative description of the collective motion and the inter-particle interactions of the protein particles and the LCs. The main advantage is that the self-assembled structures are formed in the absence of any external field- either electric or magnetic, and induced due to

*This work is published as two journal papers. (i) Pal, A., Gope, A., Kafle, R. and Iannacchione, G.S., 2019. Phase separation of a nematic liquid crystal in the self-assembly of Lys in a drying aqueous solution drops. *MRS Communications*, 9(1), pp.150-158. <https://doi.org/10.1557/mrc.2019.18>. (Pal et al., 2019) (ii) Pal, A., Gope, A. and Iannacchione, G.S., 2019. A comparative study of the phase separation of a nematic liquid crystal in the self-assembling drying protein drops. *MRS Advances*, 4(22), pp.1309-1314. <https://doi.org/10.1557/adv.2019.209>. (Pal, Gope, and Iannacchione, 2019a). Thanks to WRAMP at WPI for spending money in purchasing the samples.

evaporative flow; (2) a birefringence intensity profile for both Lys-LC and BSA-LC systems; (3) the concentration dependence textural study using the first order statistics (FOS) and gray level co-occurrence matrix (GLCM), and lastly; (4) performing statistical tests to compare the mean crack spacing (\bar{x}_c) between (a) peripheral ring and the central regions at different concentrations of the Lys-LC systems, and (b) Lys and BSA systems with and without LCs.

5.2 Results and Discussions

The lysozyme-water (Lys+DI) and bovine serum albumin-water (BSA+DI) solutions were prepared by weighing 100 mg of proteins and dissolving them separately in 1 mL of de-ionized water. The LC (5CB) was heated just above its transition temperature ($T \geq 35$ °C) and added to the protein solutions. Different volumes (2, 5, 10 μ L, respectively) of LC were added to the Lys+DI solution to make the initial concentration of LCs (ϕ_{LC}) as 0.23, 0.46 and 0.91 wt%. Keeping the $\phi_{LC} = 0.91$ wt%, the BSA-LC system is also made. Further, these different volumes of LC were added to 1 mL of de-ionized water to make LC+DI system. It is to be noted that the LCs are not aligned to the substrate prior to the experiment. The bulk LCs were used throughout this study.

5.2.1 Lys-LC: Drying droplets and patterns of dried films

Temporal evolution of drying process

A sessile drying droplet generally features a curved air-fluid interface. Time dependence of the drying Lys-LC droplets at a concentration of LCs (ϕ_{LC}) of 0.91 wt% between crossed polarizers is shown in the top panel of Fig. 5.1. The droplets was pinned to the coverslip and a convective flow took place in the droplets. These droplets were bright in the cross-polarizing configuration due to their birefringence nature. Similar to the Lys+DI system (ϕ_{LC} of 0 wt%), this system too decreased along the contact angle (revealing a blur to prominent bright spots, Figs. 5.1a-c). As soon as the contact angle reached to a smaller value, a fluid front started moving from the edge to the center (similar to the Lys+DI system). An outline at the curved interface (Fig. 5.1b) was observed indicating a starting effect of the "coffee-ring" (alternatively called rim). The solvent loss was highest near the droplets edge, as a result, all particles were rushed with the flow to compensate the non-uniform evaporation rate. The big LCs (small LCs clustered together) were mostly observed in the central region (these were originally found there, while depositing the droplets). The small LCs were spread (easily flowed by the convective and radial flow) throughout the droplets, mostly near the droplets edge (Fig. 5.1c). The restrictive movement of the big LCs was possibly due to their viscous nature, resulting in space confinement by flow-induced shear force. However, big LCs went through a little orientation, alignment, or tumbling as induced by inherent non-uniform fluid front flow due to the

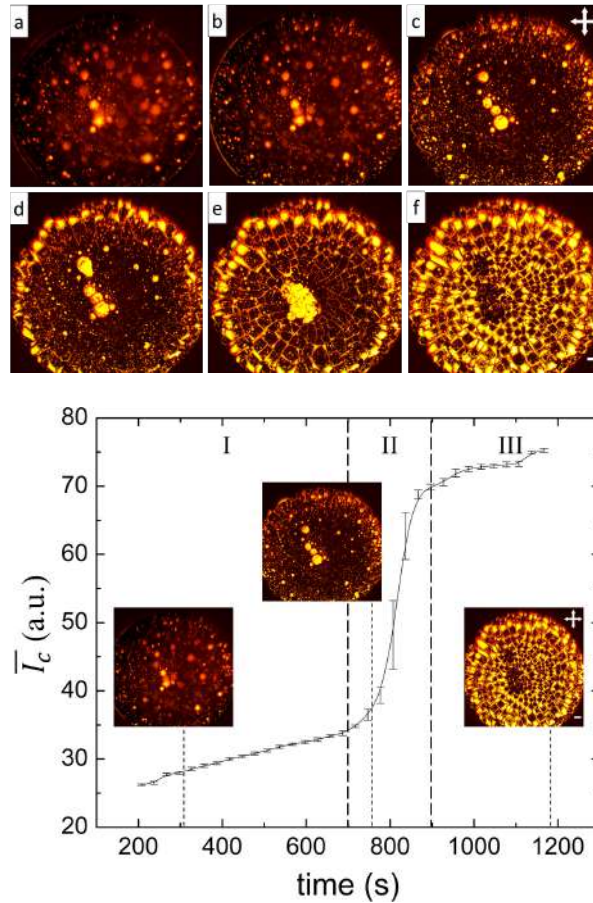


FIGURE 5.1: Top panel: Time-lapse images of drying Lys-LC drop at the concentration of LCs (ϕ_{LC}) of 0.91 wt%. a) 193 s showed an initial stage of drying. A radial flow of the particles to the droplet edge at b) 403 s and c) 731 s are shown. Merging of large-sized LCs in the central region and filling of these LCs at the droplet edge were displayed at d) 791 s and e) 815 s. The self-assembled structures after visual drying process was observed at f) 1193 s. Bottom panel: Intensity variation with time of Lys-LC drop showing three regimes, an initial slower regime (I), a transition regime (II) and a saturation regime (III). The error bars correspond to the standard deviation. The microscopic images in I, II and III were taken at 301, 745 and 1193 s respectively. The crossed polarizing configuration is depicted by crossed double arrows. The white color in the right corner is a scale bar of 0.2 mm.

attractive forces (capillary, van der Waals and dipolar interactions) between adjacent LCs (Fig. 5.1d) (Jeong et al., 2015). The individual big LCs further merged and coalesced into bigger LCs, resulting in increasing the optical intensity (Fig. 5.1e). Like Lys+DI system (described in Chapter 4), this system also showed the rim which was at a greater height from the central region due to the deposition of most of the Lys particles.

Finally, a mechanical stress originated due to the solvent loss and the pinning of the droplets leading to the formation of cracks (starting from the droplets edge). The crack lines started forming like the Lys+DI system; however, a slow and ordered way was observed in this system. Subsequently, a fast follow-up process of LCs took place in the crack lines (all lines become bright, Fig. 5.1e). A simultaneous process

of filling of domains (created by the cracks) with LCs started at the droplets edge, unlike Lys+DI system (described in Chapter 4). This whole process of LC-filling completed within a time span of ~ 2 minutes (starting from ~ 745 to ~ 865 seconds). The final step of the drying process was the formation of the self-assembled patterns of the Lys particles in the presence of a small fraction of LCs (Fig. 5.1f). The miscibility of the solutes (LCs and Lys particles) is the key to obtain this pattern after the water evaporates from the system. The LCs were found to be partially soluble in the de-ionized water; whereas, the Lys particles without LCs, form a homogeneous solution with water. However, the inclusion of LCs into Lys without water was not possible as we have used lyophilized Lys. The striking feature of this study is the phase separation of LCs induced by the convective flow of solutes and the loss of water during the drying process.

The bottom panel of Fig. 5.1 illustrates a typical intensity response of LCs (since only LCs are birefringent) varying with drying time in Lys-LC droplets at ϕ_{LC} of 0.91 wt%. Furthermore, a clear correlation between the top and bottom panels of Fig. 5.1 was made. Initially, the intensity didn't change much for a certain period (up to ~ 700 s). The movement of LCs and the change in the intensity were not quite visible during this period (regime I) due to the spherical-cap shape of the droplets. However, this shape got reduced by the decrease of the contact angle and finally reached a minimum value. In regime II, by maintaining the smaller contact angle configuration, the onset of LC activities (such as merging and filling up the crack domains) increased resulting in a rapid increase of intensity. This transition period (regime II) was only found for ~ 200 s, in which the intensity varied from ~ 35 to ~ 69 a.u., i.e. an increase by a factor of two: the rate of change in intensity with time is ~ 0.17 . The standard deviation was higher in the transition than all other regimes due to the presence of different sized big LCs in different droplets. As this regime was solely dependent on the LC activities, it resulted in the change of the intensity (values) for three different droplets and hence, a higher standard deviation was observed. It was followed by regime III in which the intensity saturated as the droplets was about to complete the drying process.

The drying system of LC+DI was also explored, and we observed a slow movement of bulk LCs towards the droplets edge. A non-uniform evaporation of water was observed in the LC+DI droplets and the LCs remained at the surface (coverslip) due to LC-surface interaction. Contrary to the LC+DI system, in the Lys+DI system (concentration of LCs (ϕ_{LC}) of 0 wt%), the Lys particles were distributed on the coverslip to form a protein film during the convective flow. It followed by a radial flow of particles towards the droplets edge which helped to deposit most of the particles. Then, the fluid front started moving from the edge and rest of the particles were carried to the center resulting in the formation of 'mound'-like structure (Figs. 5.2a, g). The averaged intensity (\bar{I}_c) was measured for both LC+DI and Lys+DI systems in which no variation of intensity in drying time was observed. However, LC+DI showed

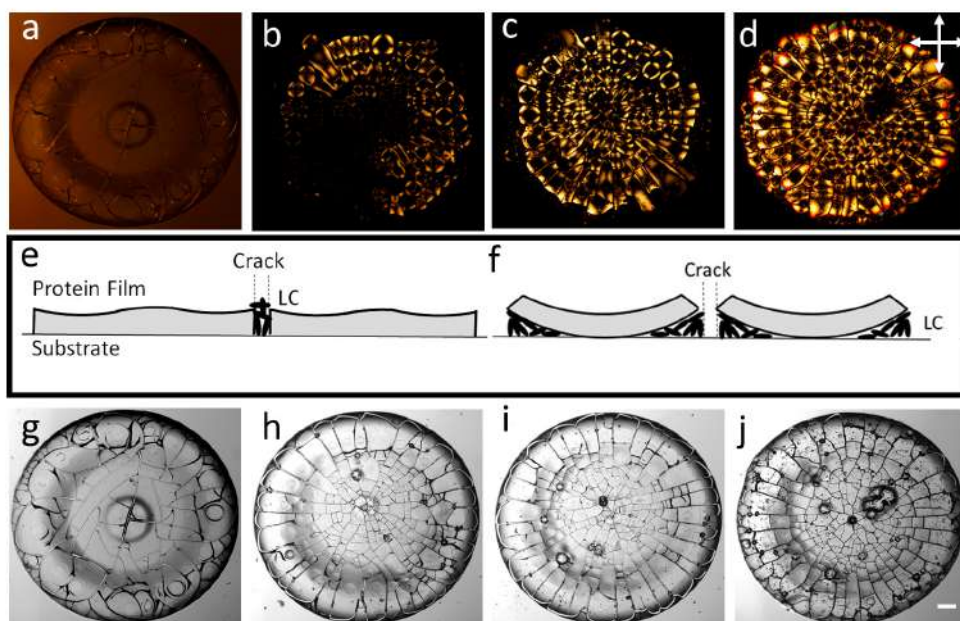


FIGURE 5.2: The morphology of drops after 24 hours. Top panel: Drops imaged in crossed polarizing configuration. The initial concentration of LC droplets (ϕ_{LC} in wt%) is a) 0, b) 0.23, c) 0.46 and d) 0.91. The drop without LC droplets (ϕ_{LC} of 0 wt%) showed very weak birefringence, therefore, lamp intensity was increased for clear visualization. Middle panel: e) and f) show a proposed mechanism for the evolution of the unique patterns. Bottom panel: Gray scaled drops imaged in bright field configuration, where ϕ_{LC} in wt% is g) 0, h) 0.23, i) 0.46 and j) 0.91. The scale bar corresponds to 0.15 mm.

a higher value of intensity than Lys+DI system due to the birefringence nature of LCs. A significant difference was noticed between LC+DI and Lys+DI or Lys-LC droplets i.e. there was no coffee-ring or no self-assembled patterns in absence of Lys (protein) particles. This reveals that the significant contributions to the final patterns were Lys-Lys and Lys-LC interactions. Furthermore, protein in general, has a non-uniform surface, with most of the hydrophobic regions sheltered inside and with exposed charged or polar residues. This helps in making it available for new points of attraction with either neighboring protein particles or LCs (Paul et al., 2008). LC has its own dipole moment due to the presence of cyano group at its one end (De Gennes and Prost, 1993). The accumulation of LCs into the protein solution has a tendency to form Lys-LC complexes. These complexes were formed by attracting the exposed parts of the protein to the cyano group of 5CB. At this point, the electrostatic attraction is almost zero due to non-involvement of external salts/ions. Nonetheless, this attraction may not have a large contribution owing to the presence of cyano groups at one end of the LCs and due to the overall positive charge of Lys.

Morphological study in dried droplets

The available stress in the dried droplets (after visible evaporation) was relieved by the increase in the number of cracks. Also, the flow of LCs was found to be affected

in the droplets (Fig. 5.1f which was taken after visible evaporation and Fig. 5.2d which was taken after 24 hours at the concentration of LCs (ϕ_{LC}) of 0.91 wt%). We observed that some regions in the dried droplets initially had more LCs (bright regions) and then, uniformly distributed towards the end of the day. Hence, all the dried samples were imaged after 24 hours.

Figs. 5.2a-d show the images of the dried Lys droplets with and without LCs imaged in the crossed polarizing configuration. The lamp intensity of the dried Lys droplets without any LCs (concentration of LCs (ϕ_{LC}) of 0 wt%) was increased for a clear visualization. It is well known that Lys in crystal form shows birefringence and scatter light depending on the domain size (Singer et al., 2006). However, our perception is that only the evaporation process (the loss of water) from the Lys solution without LCs may not be able to form crystals completely. The scattering of light was mostly visible near the crack lines once the lamp intensity was increased to maximum. These lines were the areas without any Lys particles or LCs and were just the bare coverslips leaking the light from the microscope probably. Hence, comparing ϕ_{LC} of 0 wt% to other concentrations, it could be inferred that Lys+DI system exhibits a very weak birefringence. This indicates that, the optical activity in cross-polarizing imaging was mostly due to the activities of the LCs. Contrary to the Lys+DI system, Lys-LC systems showed a dark region in the interior and bright regions at each corner of every crack domains. In this context, a physical mechanism is proposed to understand the self-assembled patterns in the Lys droplets due to phase separation of LCs (Figs. 5.2e-f). During the convective flow of the drying process, most of the Lys particles were distributed on the coverslip and resulted in a protein film.

However, it is possible to have some LCs to get trapped in the film or to be on the top of the Lys film. The external stress increased due to solvent loss and the droplets cracked resulting in different sized interconnected domains. A simultaneous process of buckling in every domain took place. Two scenarios were possible; (i) the presence of the LCs was on the top of the Lys film; and/or (ii) the presence of these droplets was underneath the film. It was found in Fig. 5.1d-f that LCs were following the crack lines (channels) for their distributions in every domain, starting from the droplets edge. Moreover, after completing the visible evaporation, the LCs distributed in the crack lines depicted by bright color (Fig. 5.1f), but within 24 hours the crack lines became dark (Fig. 5.2d). If the LCs were present on the top of the film, then, their flowing through the crack lines would not be possible because the protein film is at a greater height near the droplets edge (compared to the central region). The change of the bright crack lines into dark within 24 hours would also be baffling. In addition to this, the air-LC interface is known to have weak homeotropic anchoring, hence, all the domains would have shown a radial point defect in the form of the Maltese cross (a cross always lining up with the polarizer and analyzer); but here, that was not the case. The dried droplets in presence of LCs showed a dark region which likely to be the attached Lys film to the coverslip (substrate) and

most of the bright regions were the randomly oriented LCs underneath the protein film; suggesting being the second scenario (mentioned above). Within 24 hours, the Lys domains were more uplifted (buckled) and the LCs flowed inside the domains from the crack lines through the capillary action. The representative of most of the domains in the dried droplets with LCs show randomly oriented LCs in the bright regions. However, in some of the domains, a perfect radial configuration (Maltese cross) was observed probably due to the presence of the LCs at the air-LC interface. On the other hand, some of the crosses often seem to align with what was likely a radial flow during the drying process. In addition to this, most of the crack domains contained a single dark region at the center, some were found to be off-centered probably due to the domain shape and the unstable buckling mode. The centered configuration would evolve from that off-centering when buckling start to develop fully (Islam et al., 2005; Zou and Fang, 2010). To ensure that each of the domain had a distribution of LCs with random orientations, the domains were rotated with a sample angle for a complete revolution, and we did not observe any optical change in the patterns. All crack lines appeared dark even when the sample angle was varied for a complete revolution and no uniformed angular dependence with the intensity was found when compared among different domains.

In Figs. 5.2b-c an uncertainty arose in the count of the bright regions in the droplets as LCs were partially soluble in the water. But these droplets were the most repetitive ones and we concluded that LCs were not enough to fill the whole surface of the droplets. The LC concentration up to 0.91 wt% was chosen which was just enough to fill the whole droplets of radius ~ 1 mm. It was also observed that further increase of LC concentration (for eg. 1.82 wt%, or more) made bright blob like structures which restricted the smooth flow of LCs within the droplets. A minute observation of Figs. 5.2c-d confirmed the presence of ripples in some dark regions of the domains. These were formed because of an air gap between the protein film and packing of LCs. These domains had a non-uniform thickness and these small (unavoidable) variations were depicted by different colors (reddish, yellowish, greenish) in the droplets (Heo and Park, 2017; Ohzono et al., 2017).

In the bright field imaging, the gray images with and without LCs were shown in Figs. 5.2g-j. Following the observation of the morphology at ϕ_{LC} of 0 wt% (Fig. 5.2g), it could be argued that the stress was built not only along the fluid front movement, but, applied from all directions. The gradient in the protein-film thickness (a thick sheet in rim, a thin sheet in the center and an extremely thin sheet in between the regions) resulted in a chaotic system. Therefore, it could be concluded that a random (chaotic) crack is a response to the lack of dominant stress in any specific direction. Unlike Fig. 5.2g, the presence of viscous, denser particles (here LCs) enabled the cracks to experience mostly azimuthal tensile stress (the stress along the fluid front), leading to radial and highly ordered cracks. Fine radial, regularly spaced cracks appeared first near the droplets edge (rim), then the big LCs tried to fill in the large

crack domains, and a further flaw was developed with the propagation of desiccation. Due to these flaws, the long and large radial cracks were developed throughout the droplets. However, the orthoradial cracks appeared in the rim to release the available local strain energy in the domains created by the radial cracks. This helped the cracks to curve and join the consecutive radial cracks. Furthermore, both orthoradial and radial cracks continuously appeared in the central region to release the remaining stress in the droplets resulted in forming the small domains (when compared with the domains in the rim). Further, a prominent 'mound'-like structure in the central region of the droplets in the absence of LCs (ϕ_{LC} of 0 wt%) was observed, however, the presence of LCs was likely to prevent or disturb this formation. This structure was likely to be 'free' Lys particles that were light enough for the fluid front to carry to the center (Gorr, Zueger, and Barnard, 2012). The out-of-equilibrium drying of this system and the increased viscosity, density and surface tension gradients (LC-coverslip, Lys-LC, Lys-coverslip interfaces) helped in the protein aggregation throughout the whole droplets. In addition to this, LCs were affected in forming the small domains in the central region and big domains (highly ordered, uniform radial cracks) in the rim. The perception is that LCs in the central region didn't get to relax to a smooth uniform state owing to the in-homogeneous, fast fluid front movement as soon as the front part touched the big LCs while propagating from droplets edge. On the other hand, in the rim, the absence of big LCs helped the fluid front to move in an uniform way. As a result, the smaller LCs gathered enough time to anneal into the homogeneous structures, resulting in the big domains (Davidson et al., 2017). Moreover, in all systems, the curved and wavy-ring patterns were found near the droplets edge possibly due to the stress originating from the boundaries created by the radial cracks (Pal et al., 2020a). A minute observation of Figs. 5.2h-j showed a gelation between central and rim regions in presence of LCs. This region believed to be a transition region in the protein film thickness and we conclude that the dispersion of LCs within the film trapped some water during the fluid front movement and formed this gelation. Interestingly, no rim width dependence was observed with varying concentration of LCs (ϕ_{LC}). This expanded our knowledge that the rim was only affected by the concentration of protein particles and not from the added amount of LCs. The independence of rim width on ϕ_{LC} (due to the dispersion of LCs into different crack domains) supported the physical mechanism proposed in this chapter.

Textural analysis in dried droplets

The FOS (first order statistics) parameters depend on the pixel distribution of the selected ROI, whereas GLCM (gray level co-occurrence matrix) parameters rely on the interpixel relations. Though these are complimentary measurements to evaluate droplets texture, interestingly all the parameters followed a simple exponential law when varied with the concentration of LCs (ϕ_{LC}) (Carreón et al., 2018b). The

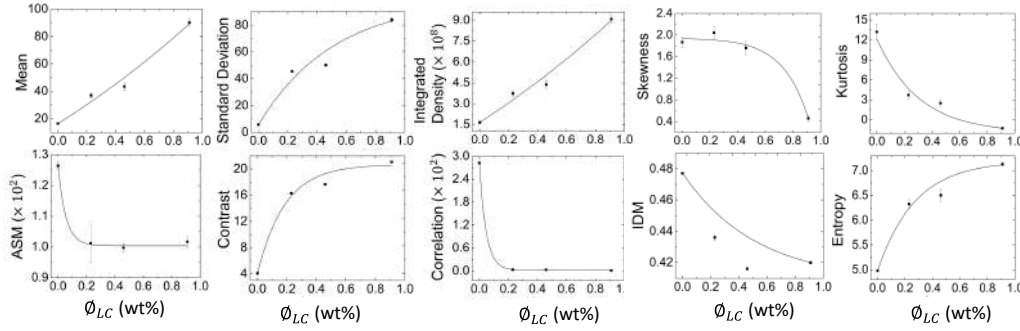


FIGURE 5.3: Texture analysis of dried drops. Top panel: First order statistics (FOS) reveals the pixel distribution through Mean, Standard Deviation, Integrated Density, Skewness, and Kurtosis. Bottom panel: Gray level co-occurrence matrix (GLCM) reveals the interpixel relations through ASM (Angular Second Moment), Contrast, Correlation, IDM (Inverse Difference Moment) and Entropy. The exponential fit for the curves are shown in each graph. The error bars correspond to the standard error.

equation stated as:

$$\delta = \delta_0 e^{(-\phi_{LC}/k)} + \delta_s \quad (5.1)$$

where δ is the textural parameter, δ_0 is an initial textural parameter, δ_s is the saturated parameter and k is the characteristic concentration at which the parameter diminishes by the $1/e$ factor.

The variation of ϕ_{LC} affected the textural patterns (morphology) in the dried droplets (Fig. 5.2). The top panel of Fig. 5.4 showed FOS parameters in which the mean determines the intensity per pixel of the selected region of interest (ROI) within the droplets, standard deviation determines the variation around the mean values relating to the roughness of the image texture and integrated density determines the total pixel intensity of the ROI. All grew exponentially due to the increase of LC-dominating regions resulting in an increase of the brightness (hence, the pixel intensity of the image) (Pal, Gope, and Iannacchione, 2019b; Carreón et al., 2018b). Both the skewness and kurtosis, in contrast, decreased with the increase of LC-dominating regions possibly due to the intensity distribution (histograms changed from asymmetrical to symmetrical tailed). The lowest values of skewness and kurtosis were found at the highest ϕ_{LC} . The bottom panel of Fig. 5.4 showed GLCM parameters varying with ϕ_{LC} i.e. ASM measures global homogeneity in the texture, correlation measures the degree of similarity in a row or column direction of the image texture and IDM measures local homogeneity of the selected ROI. All these displayed an exponential decrease due to the decrease in the uniformity of the texture with the increase of ϕ_{LC} . On the other hand, contrast and entropy increased in terms of the number of pixels and the heterogeneous regions formed. An increase in the diversity of the self-assembled structures occurred when ϕ_{LC} was varied through the increase of bright LC-dominating regions in the dried textures (Pal, Gope, and Iannacchione, 2019b; Carreón et al., 2018b).

It can be hypothesized that these analyses (FOS and/or GLCM) in the final deposits

of any drying droplets will follow simple exponential laws. Our perception is that these structural changes following the exponential laws are not due to any contribution of external salts, as our experiments were conducted by varying LC concentrations only.

Statistical analysis of crack patterns in droplets

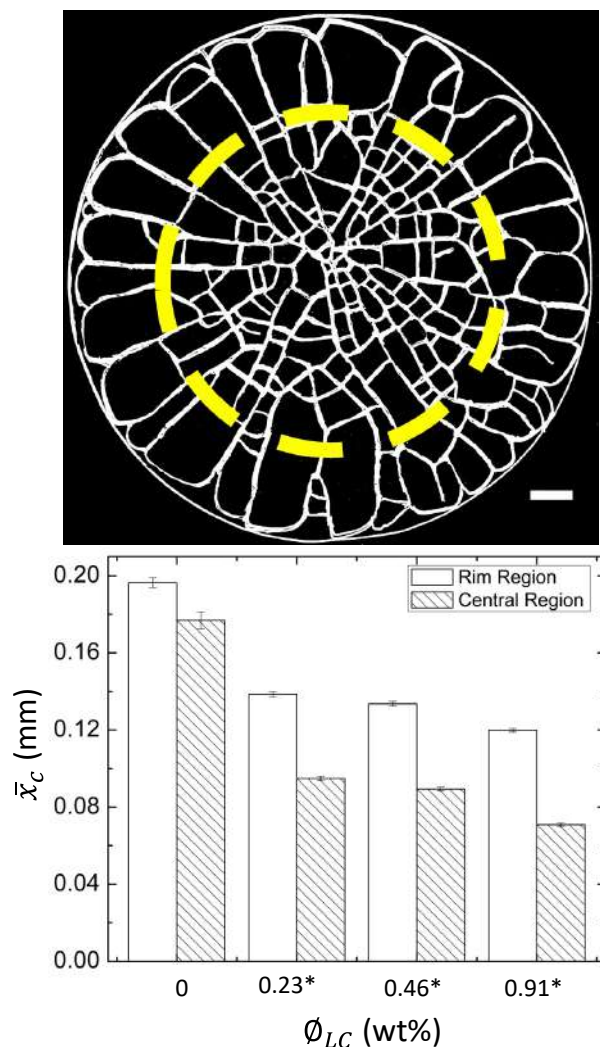


FIGURE 5.4: Top panel: An example of a binary image of a dried drop at ϕ_{LC} of 0.23 wt%. The scale bar corresponds to 0.15 mm. The yellow dashed line separates the drop into rim and central regions. Bottom panel: The histogram depicting the comparison of mean crack spacing (\bar{x}_c) between the regions at different ϕ_{LC} . Significant pairs are marked with an asterisk [*]. The error bars correspond to standard error.

The visual observations showed the differences in terms of crack spacing between two different regions at each concentration of LCs (ϕ_{LC}). However, the visual observations may not be able to distinguish the data fluctuations borne out due to the experimental conditions or quantify the trend of \bar{x}_c with increasing ϕ_{LC} . We observed that the aggregated data in different regions at each ϕ_{LC} was not normally

distributed (positively skewed). Therefore, we conducted a non-parametric Mann-Whitney U test using SPSS (version 22.0). The difference is said to be statistically significant if $p \leq 0.05$. The 'region' was kept as the categorical factor (independent factor, with two levels: rim and central) and ' x_c ' as the dependent variable. The yellow dashed line in the binary image depicts an example separating the droplets into rim and central regions (top panel of Fig. 5.4). The comparison of \bar{x}_c between the regions at different ϕ_{LC} is shown in the bottom panel of Fig. ?? . The statistical test quantified the morphological observations that \bar{x}_c in two regions were almost identical in absence of LCs, but their presence made two regions significantly different. The \bar{x}_c wasn't found to be significantly different i.e. ~ 0.20 mm in the rim and ~ 0.18 mm in central regions at ϕ_{LC} of 0 wt%. It significantly decreased from ~ 0.20 to ~ 0.12 mm in the rim and to ~ 0.07 mm in the central region as ϕ_{LC} increased in the presence of LCs. The central region was found to contain small domains, resulting in a smaller value in \bar{x}_c when compared to that of the rim in presence of LCs. The absence of LCs enabled the stress to act from all the directions resulting in similar cracks in both the regions. The 'mound'-like structure further facilitated the crack to propagate from all the directions. The presence of LCs produced the uniform and radial cracks in the rim (big domains) resulting in larger \bar{x}_c values. Many radial and orthoradial cracks were observed leading to small domains in the central region of the droplets. These were possibly due to the presence of the thin sheet of the protein film in the central region resulting in smaller \bar{x}_c values.

The presence of LCs and their partial phase-separation facilitated the uniform crack formation in the rim region (the reason is explained in detail in the previous section). Moreover, \bar{x}_c was decreased with the increase of ϕ_{LC} in both the regions. It was because the number of LCs increased with the increase of ϕ_{LC} , resulting in more stress, more cracks and subsequently resulted in a decrease in the \bar{x}_c . The results of the statistical test were found to be consistent with the visual observations and the differences in \bar{x}_c between the regions of a droplets were derived by varying the concentration of LCs.

5.2.2 BSA-LC: Drying droplets and patterns of dried films

Time evolution of the drying droplets

Similar to Lys-LC system, Figure 5.5(I) shows the drying evolution of the deposited droplet containing BSA, DI, and LC in the crossed polarizing configuration. In the first regime, the droplet got pinned on the substrate (coverslip) and the contact angle started decreasing. The transformation of the intensity (from blur to prominent spots, Figs. 5.5a-c) indicates a decreased contact angle. During this regime, the convective and radial flow of both BSA particles and tiny LCs were observed (see Fig. 5.5(I)a-b) in the time span of ~ 11 minutes. This resulted in depositing most of the BSA particles near the edge displaying a "coffee-ring" effect (Deegan et al., 1997). A few big LC (clustered small LC) droplets merged with other droplets, whereas a

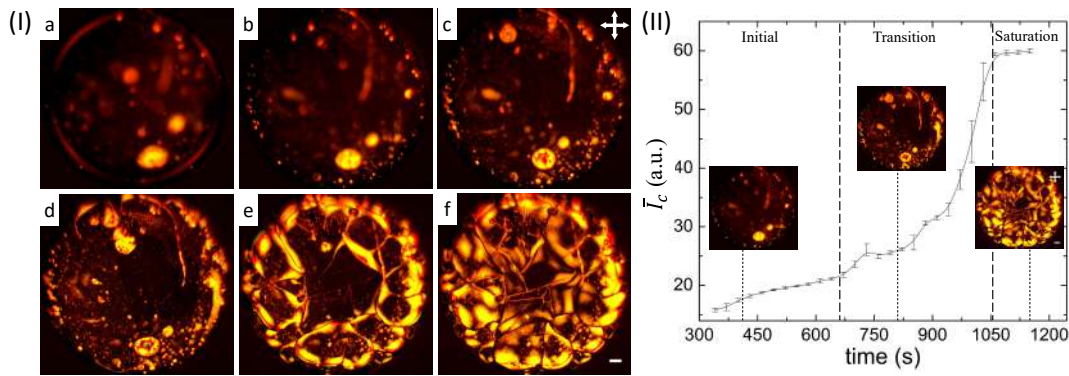


FIGURE 5.5: (I) Time lapsed images of BSA-LC drying droplet in crossed polarizing configuration (crossed double arrows) at a) 117 s, b) 421 s, c) 677 s, d) 941 s, e) 1007 s and f) 1149 s. The white colored rectangle is a scale bar of 0.2 mm. (II) Intensity variation of BSA-LC droplet with drying time indicates three distinct regimes. The error bars correspond to the standard deviation. The microscopic images in the initial, transition and saturation regimes are taken at 415, 805 and 1149 s, respectively.

few LCs popped up, and spread individually (Fig. 5.5(I)b-c). The concentration of these droplets and BSA particles were mostly observed near the edge (Fig. 5.5(I)d). The mechanical stress was built as not much water was left and the droplet started cracking to relieve the available stress. The filling of LCs took place in the crack lines and started spreading on the domains created by the cracks. Most of the LCs were spread near the boundary of each domain in the droplet (Fig. 5.5(I)e-f) showing the morphology after the visible evaporation (Fig. 5.5(I)f).

Figure 5.5(II) depicts the intensity profile of the drying process. The profile started with a slow increase of the intensity due to spherical-cap shape of the droplet, an initial regime up to ~ 670 s. Once the contact angle reached the minimum, the LCs became prominent, and a rapid rise of the intensity was found in the transition regime. It raised from ~ 22 to ~ 54 a.u. and found till ~ 1030 s, i.e., for ~ 6 minutes. Finally, it saturated when the droplet completed the process. This intensity profile was only possible due to the birefringence nature of LC droplets, and so the protein droplets without LC didn't show any variation. Though the activities of LCs in Lys (Fig. 5.1) were different from BSA, the intensity variation of BSA-LC couldn't account the minor details and revealed three regimes (initial, transition and saturation) like Lys-LC.

Birefringence of the dried droplets

It is to be noted that LCs (bright regions) in BSA-LC droplet redistributed themselves in each domain towards the end of the day (Figs. 5.5(I)f and 5.6(I)a). As most of the LCs were present near the edge after visible drying process, each domain in the rim showed four-fan like structures and bright crack lines in the central region of the dried BSA-LC droplet are observed (Fig. 5.6a). In contrast, all the domains were bright at the corners and dark in the center, separated by dark crack lines in the dried Lys-LC droplet (Fig. 5.6(I)b). This observed behavior may be due to the protein-LC interactions that affects the wettability of the LCs during the drying process. Lys

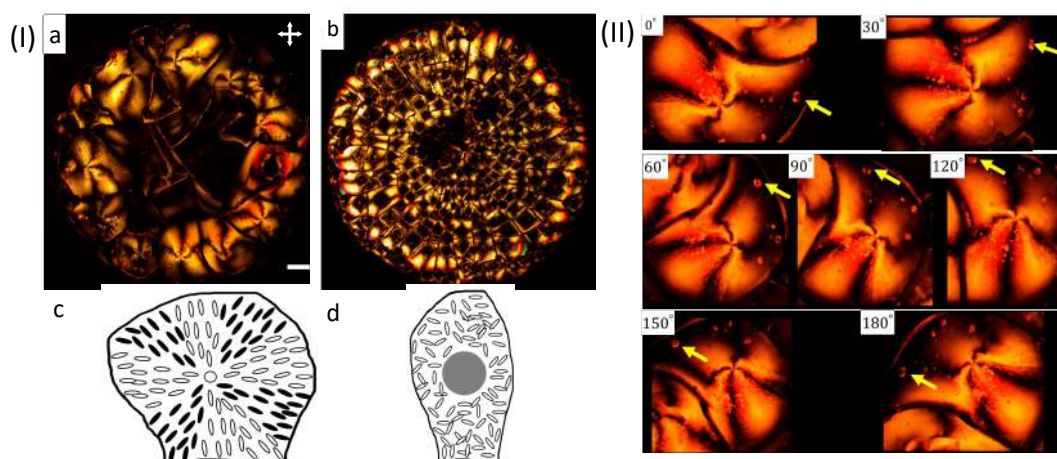


FIGURE 5.6: (I) The morphology of the dried droplets imaged in crossed polarizing configuration (crossed double arrows) after 24 hours: a) BSA-LC, and b) Lys-LC. The white colored rectangle is a scale bar of 0.15 mm. The orientation of LCs in each domain is shown in c) BSA-LC and d) Lys-LC. (II) One particular domain of the BSA-LC sample is rotated under crossed polarizers at a magnification of $10\times$. The yellow arrow indicates a reference point with respect to the four-fan brushes confirming the rotation of the patterns and reveals an *umbilical defect* with a strength of $[+1]$.

is a more compact, stable and four times lighter protein particle compared to BSA. The viscous nature of the LCs allows those to prefer beneath the Lys protein film. The (initial) process of cracking induces the flow of these droplets through the crack lines. Each domain attached to the coverslip buckled (uplifted) from the corner to the central region (dark in the morphology). The randomly distributed droplets (bright in the morphology) were rearranged by the capillary action (Fig. 5.6(I)d). On the other hand, in case of BSA-LC, the droplets were present at every corner of the domains and spread over each BSA domain for 24 hours.

Between crossed polarizers, the characteristic fourfold brushes (lines of extinction) with a defect core appeared in BSA-LC droplet after 24 hours. The distribution of LCs as the radial director configuration is illustrated in Fig. 5.6(I)c. A typical texture of the unaligned nematic phase under crossed polarizers is the Schlieren defect which exhibits two and fourfold brushes. Here, only the fourfold brushes were observed and termed as *umbilical defect* (Dierking et al., 2005) where each self-assembled protein domain contains only one defect. The four dark brushes in the BSA-LC droplet indicated that the director of the LC nearly matches either the polarizer or analyzer in the crossed polarizing configuration. When the sample was rotated in an anti-clockwise direction (the yellow arrows shown in the Fig. 5.6(II) provided a reference point) keeping the polarizer and the analyzer fixed, the brushes were observed to rotate in the same direction, whereas the defect core of the brushes continued in a fixed position indicating a $[+1]$ strength defect.

The droplets were found to be aligned anisotropically with respect to the shape of the domains as a minimum energy configuration. The domain boundary confines these droplets and the preferred alignment of the LCs considers the shape of the

domain and whether the anchoring energy and the domain size are large enough to accommodate their elastic energy (Dierking et al., 2005). Ideally, the core defect should be observed to be at the highest height and in the middle of the domain. However, the distortion of the brushes provides the evidence that the nematic director follows the contour in each protein domain. Based on these observations, it can be inferred that most of the LCs form a layer on the top of the BSA film revealing a radial defect in each domain at the air-LC interface, with some droplets trapped in the film during the drying process.

Crack morphology of the dried droplets

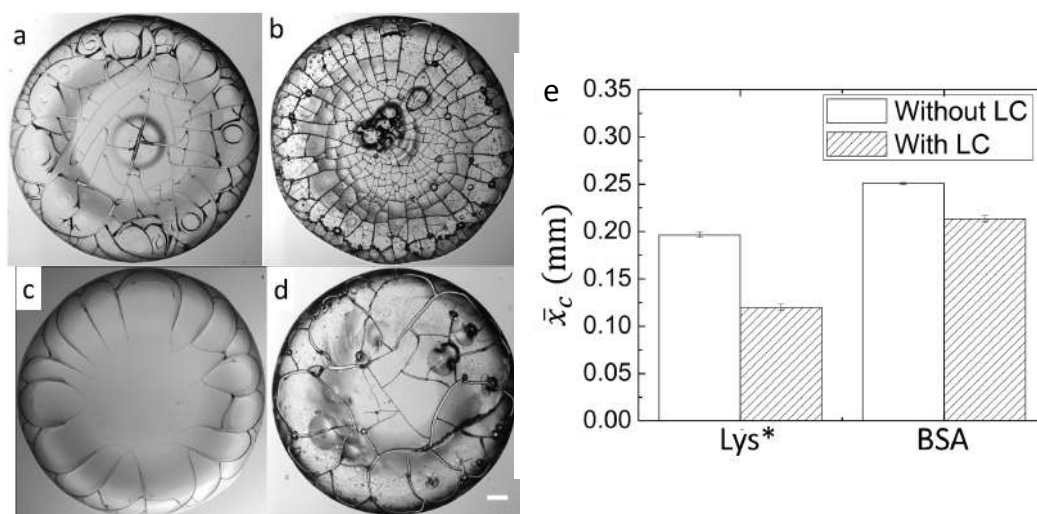


FIGURE 5.7: Dried droplets imaged in bright field configuration after 24 hours: a) Lys without LC, b) Lys with LC, c) BSA without LC, d) BSA with LC. The scale bar represents 0.15 mm. e) A histogram depicting the comparison of mean crack spacing \pm standard error in the protein droplets with and without LC. Significant pairs are marked with an asterisk [*].

The bright field images of each protein droplet with and without LC are shown in Figure 5.7a-d. The common feature noticed in all the droplets is the presence of the rim at a higher height compared to the central region confirming the favored “coffee-ring” effect in the droplets. Nonetheless, the presence of LCs made the surface of the droplets rough probably due to phase separation during the drying process. The inclusion of LCs also increased the stress in the droplets resulting in increasing the number of cracks. The comparison of Lys droplet with and without LC revealed that the ‘mound’-like structure was disturbed; the presence of LCs enabled ordered cracks in the rim [discussed in detail in the previous section, and our published work in (Pal et al., 2019)]. The comparison of BSA droplet with and without LC (Fig. 5.7c and 5.7d) revealed that the cracks were only present in the rim in the absence of these droplets. Moreover, most of the cracks were not connected at their terminals in BSA droplet without LC. In contrast, cracks are seen to be connected with other resulting in the formation of the domains and spread in the whole BSA droplet with LC. The comparison of Lys and BSA droplets with LC (Figs. 5.7b and 5.7d) indicates

a smaller domain size of Lys than that of BSA. Hence, it could be inferred that the domain size in BSA droplet with LC was probably one of the reasons which provided the necessary criteria to form radial director configuration.

The non-parametric Mann-Whitney U statistical test was conducted to quantify the cracks concerning mean crack spacing (\bar{x}_c) in the rim region of the droplet. The 'Lys' ('BSA') was kept as a categorical factor with two levels, without and with LC and ' x_c ' as a dependent variable. The comparison of \bar{x}_c with and without LC for different proteins was shown in Fig. 5.7e. In Lys droplet without LC, \bar{x}_c was found to be ~ 0.20 and reduce to ~ 0.12 mm in the presence of LC droplets. The Mann-Whitney U test indicates a significant interaction in Lys. A large crack spacing is observed in Lys without LC (depicted by [*]), agreeing to the morphological observations. In contrast, no significant difference in terms of x_c was observed in BSA droplet with and without LC. The \bar{x}_c without LC was found to be ~ 0.25 and ~ 0.21 mm with LC. This indicates a non-significant interaction in BSA providing an extra dimension not clearly observed morphologically. Hence, it could be concluded that LCs drastically affected the crack formation in Lys droplet since most of these droplets were beneath the Lys film. On the other hand, LC didn't alter the crack spacing in BSA droplet significantly supporting our claims that most of these droplets were present on the top of the BSA film.

5.3 Conclusions

The major finding of this chapter is that different morphological patterns evolved through phase separation of bulk liquid crystal (LC) and self-assembly of globular proteins (Lys and BSA) induced by evaporation of the solvent (de-ionized water) only. The intensity study during the drying process for both Lys-LC and BSA-LC systems revealed three regimes: a slow increase, a transition phase and a saturation of the intensity in the presence of LCs whereas, no variation was observed when the LCs were absent. Furthermore, the dried BSA droplet showed *umbilical defects* with a strength of [+1] in different domains and is observed only near the edge. In contrast, each domain of the dried Lys droplet appeared to be bright with dark central regions.

The protein-LC study discussed in this chapter provide clues on how the synthesized complex multi-component bio-colloid behaves and affects the morphological patterns in the presence of optically active material. In the next chapter (Chapter 6), we will be exploring the drying process in a naturally occurring complex multi-component system such as human blood. The primary motivation is to understand the influence of the water loss in the pinned droplet on the microstructural behavior and connect with the macroscopic patterns.

Chapter 6

Hierarchy II: Pattern Formation in Human Blood Droplets*

6.1 Background

Phase transition refers to a physical process where a substance experiences a state transformation (Landau and Lifshitz, 2013). The alteration of ice (solid) to water (liquid) and eventually to vapor (gas) due to heat is a typical example of the phase transition. Besides, the appearance of zero electrical resistivity in the superconductivity state, or the transformation of the liquid crystalline into the crystalline phase are just a few other well-studied phase transition examples in the field of condensed matter physics (Landau and Lifshitz, 2013; Singh, 2000). In a similar way, the state of phase transitions in the biological systems equally attracted considerable research attention, where the ideas of statistical mechanics have been applied on many applications, including order parameters, fluctuations, and universality classes. For example, the phase transition of various biomolecules (from a liquid crystalline to gel state) such as lipids, cholesterol, proteins, etc. is found to play an essential role in the selective trafficking and signaling activities across the cell plasma membrane (Simons and Ikonen, 1997; Boeynaems et al., 2018). Another vital instance of phase transition includes the sol-gel transformation that modifies the assembling mechanism of the platelets (one of the cellular components of the whole blood) and various fibrin proteins. This particular transition state of the sol-gel is considered to be crucial to healing an injury during the process of blood clotting (Tablin et al., 1996). Furthermore, the ion-selectivity in nerve fibers alters their structures from the swollen to the shrinking state and influences the process of nerve excitation and conduction. All these biological phase transitioning examples are at the cellular or the molecular

*The work described in this chapter is published. Pal, A., Gope, A., Obayemi, J.D. and Iannacchione, G.S., 2020. Concentration-driven phase transition and self-assembly in drying droplets of diluting whole blood. *Scientific Reports*, 10(1), pp.1-12. <https://doi.org/10.1038/s41598-020-76082-6> (Pal et al., 2020b)–I am indebted to WPI *Tinkerbox* program sponsored by WIN (Women Impact Network) at WPI for awarding me the essential funding to conduct all the experiments and bear the article processing fees of ~1800\$.

level and are driven by both physical and chemical processes (Jacobs and Frenkel, 2017; Pollack and Chin, 2008).

Understanding the drying phases of a multi-component bio-colloidal droplet, such as the whole human blood has attracted many researchers. For example, the spreading, the wetting and the cracking phenomena of the drying droplets of blood (varying in different parameters including substrate, wetting, relative humidity, etc.) have been examined in detail to develop an understanding of the evolving patterns (Brutin, Sobac, and Nicloux, 2012; Zeid, Vicente, and Brutin, 2013; Zeid, and Brutin, 2014; Sobac and Brutin, 2014; Chen et al., 2016a; Chen, Zhang, and Shen, 2018; Choi, Kim, and Kim, 2020). The presence of various cells [red blood cells (RBCs or erythrocytes), white blood cells (WBCs or leukocytes), and platelets (thrombocytes)] make the whole blood a complex bio-colloidal fluid (Brutin et al., 2011). These cells are suspended in the blood plasma and usually contains water (92% by volume) along with a minute amount of plasma proteins, ions, and hormones in them (Sobac and Brutin, 2011). The process of drying evolution of the blood droplet starts as soon as a droplet gets deposited on a substrate. The constituent components are dispersed uniformly in the droplet that defines an initial equilibrium state. As the solvent (water) starts evaporating from the droplet, the drying process drives the system out of the equilibrium. The wetting conditions on the substrate enables the evaporation-driven convective flow. Further, water-loss in the droplet concentrates the components facilitating their self-assembling interactions. A signature pattern evolves, and the droplet reaches a new equilibrium state as soon as the drying process is completed.

Recently, diluted blood samples (into different concentration ranges) have shown insightful drying patterns in blood pattern analysis (BPA) (Ramsthaller et al., 2016; Ramsthaller et al., 2017; Van den Berge et al., 2019; San Pietro and Steelberg, 2019). Sen et al. (Iqbal, Shen, and Sen, 2020), in a different study, examined the effects of diluted blood droplets at a fixed saline concentration by changing the substrate conditions. The study concluded that the transition of the cracking to the non-cracking regime exists for the droplets deposited on the hydrophilic substrate. On the other hand, when the droplet dries on the hydrophobic substrate, the buckling regime is merged to this transition phase. The study primarily focused on the decrease of the RBCs in diluted blood samples, and how the reduction of RBCs affects the mechanical stress developed due to the water loss. Despite the intense research on drying blood droplets, the range of dilution and the use of several experimental techniques (optical microscopy detailing the drying evolution and the final morphology, scanning electron microscopy exploring the deformed blood structures in the dried samples, contact angle measurements giving the idea of the wetting) do not reveal any concentration-driven phase transition region for these diluted blood droplets. In fact, no study is performed on the diluted blood samples to understand the characteristic changes and aim to examine the fundamental understanding of such phase transition and self-assembly (Whitesides and Grzybowski, 2002) during their drying

process and the resulting morphology. The implication of diluted blood samples is crucial and makes this study different from others' report. The diluted blood samples lead to changes in the initial equilibrium state that results in reducing the interaction between various components as well as minimizing the biological activities within such multi-colloidal system.

This investigation reveals a unique mesoscopic phase transition that is solely driven by the physical process, drying at different concentrations. Exploring the phase transition and the self-assembly patterns in such a multi-component system may reveal much significant information. Keeping these notions in mind, this article aims to address the following vital questions: (i) What are the factors those stimulate a phase transition in the drying droplet of the whole blood?, (ii) What are the different drying mechanisms leading to the phase transition?, (iii) Is it possible to explain the complexity of the microscopic structures of the cellular components following the phase transition? If so, to what extent is it possible to do so? And finally, (iv) How do the wettability and the interfacial properties of the droplets influence the different environment during the drying process?

Furthermore, the outcome of this research also has the potentiality in applications related to disease diagnosis (Rapis, 2002; Yakhno et al., 2003; Yakhno et al., 2005; Yakhno et al., 2015; Tarasevich, 2004; Muravlyova et al., 2014; Bel'skaya, Sarf, and Solonenko, 2019; Bahmani, Neysari, and Maleki, 2017b; Mukhopadhyay et al., 2020). Several studies have revealed that the resulting final patterns of the drying droplets appear correlated to the initial state (Sobac and Brutin, 2014; Chen et al., 2016a). Researchers also concluded that patients with chronic kidney disease usually suffer from overhydration or an overload of extracellular water (Onofriescu et al., 2015). Moreover, patients in receipt of hemodialysis (a therapy for patients with poorly functioning kidneys) often continue to have low cellular counts after treatments (Hsieh et al., 2009; Hung et al., 2014). In some cases, this therapy tends to create a low supply of RBCs, which in turn leads to possible anemia cases. Thus, the initial concentration of the whole blood (whether diluted or concentrated) is an important parameter correlated to these pathologies. The conventional method includes the complete blood count (CBC) of almost every patient; however, this alternative drying process proposed in this study may reflect the (actual) different stages of critical diseases in a more convenient way in the near future. Our proposed method is an initiative to explore their physiological activities.

We attempted to investigate the drying process of the whole blood macroscopically (*mm* scale) using a bright-field optical microscopy and a contact angle goniometer of the droplet. The statistical image parameters of the microscopy, such as the first-order statistics (mean and standard deviation) are characterized during the drying process (Pal, Gope, and Iannacchione, 2021). The morphological quantities of the final dried state such as the crack width, spacing, etc. are extracted from the optical images at the end of the drying process. Besides, different regions of the morphology

of the dried film such as the periphery, the corona (between the periphery and the center), and the central regions are examined in detail (μm scale) using a scanning electron microscopy (SEM). For this, the whole blood ($\phi = 100\%$ (v/v)) is diluted by adding different volumes of de-ionized water ranging from 85 to 12.5% (v/v) in respect to the original concentration of the whole blood. The time-lapse images are captured in bright field microscopy (Amscope, USA) at a magnification of $5\times$ at a fixed resolution of 3664×2748 pixels.

6.2 Results

6.2.1 Drying evolution of the blood droplets

Figure 6.1(I-II) shows the time evolution of the blood droplets diluted at different concentration levels (ϕ) ranging from 85 to 12.5% (v/v) in respect to the original concentration of the whole blood ($\phi = 100\%$). The texture of this first image appears to be dark within the concentration range of 100 to 62% (v/v) [Fig. 6.1(I)a]. However, the dark texture eventually turns out to be gray following the increase of dilution levels [Fig. 6.1(I-II)a]. The physical mechanism of its occurrence is explained in the discussion section. Moreover, a thick peripheral band is observed from 100 to 62% (v/v) [Fig. 6.1(I)a], which becomes thinner with further dilution from 50 to 12.5% (v/v) [Fig. 6.1(II)a]. Subsequently, a fluid front starts receding from the periphery towards the central region (Fig. 6.1(I-II)b).

As time progresses, the central region becomes devoid of water. The appearance of the light gray texture confirms the evaporation of the water in the central region. This (light gray) texture is prominently observed in samples from 100 to 75% (v/v) dilution; however, it cannot be clearly differentiated in samples from 62 to 12.5% (v/v). This is because the texture of the first image is already light gray at this range of ϕ , and there is not enough contrast between the two (Fig. 6.1(II)a-b). The evaporation of the water and the concentration/assembly of the constituent components promotes the build up of internal stress as the droplet periphery is still pinned to the substrate (coverslip). Fig. 6.1(I-II)c marks the evolution of the cracks (similar to the prior observations discussed in (Brutin et al., 2011; Lanotte et al., 2017; Smith and Brutin, 2018)). The green dashed circular lines separate the corona from the central regions at each ϕ . The random (small and large) cracks in the central region are first observed from 100 to 75% (v/v). Some of these radial cracks begin propagating towards the periphery, and some towards central regions at ϕ of 100 to 62% (v/v) [the points A-E in Fig. 6.1(I-II)c]. In contrast, their propagation from the periphery towards the central regions is predominantly observed in the diluted samples ranging from 62 to 12.5% (v/v) [the points F-J in Fig. 6.1(I-II)c]. The radial cracks separate the film into large domains in the corona region as the remaining water evaporates from the droplet during the final drying stage, as shown for ϕ from 100 to 75% (v/v) [Fig. 6.1(I)c]. Subsequently, some micro-cracks start originating from these radial

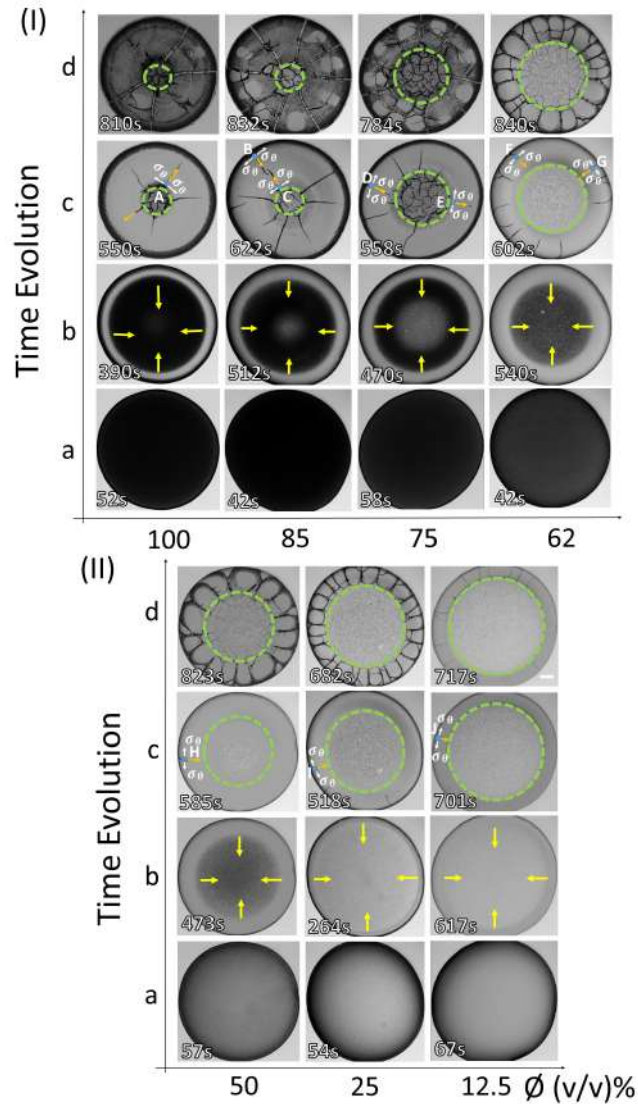


FIGURE 6.1: Time-lapse images of the blood droplets with different diluting concentration (ϕ) are captured during the drying process. These images dictate different stages: (I) from 100 to 62% (v/v), and (II) from 50 to 12.5% (v/v) (in respect to the original volume of the whole blood). The scale bar corresponds to 0.2 mm.

cracks in the corona region. However, these micro-cracks cannot propagate in re-joining the dominant cracks in responding to the dominant orthoradial stress field (σ_θ). These domains start then begin separating from each other and widening of the radial cracks are observed (Fig. 6.1(I)d). This process indicated how the film domains detach (delaminate) from the substrate. At this point in the process, the sliding of these films in the radial direction indicates that the energy to adhere to the film is costlier than the sliding energy. This process is predominantly observed from ϕ of 100 to 75% (v/v); however, with more dilution, the film adheres more strongly to the substrate. Moreover, the domains which are formed by these radial cracks become narrower with the dilution. The central region of the dried films is found to have the random small crack domains, which are observed for samples from 100 to

50% (v/v). For 25 and 12.5% (v/v), no cracks are detected by the optical microscope (under $5\times$ magnification) in the central region, where these radial cracks are mostly observed in the corona (Fig. 6.1(I-II)d). A comparison of these dried films textures at each ϕ indicates that the whole corona region is of dark gray at ϕ of 100% (v/v), whereas, this region is only partially covered by dark gray at ϕ of 85 and 75% (v/v). Furthermore, the texture is observed to be of light gray at ϕ of 62 to 12.5% (v/v). It should be noted that the optical microscope illumination was nearly constant during the experiments. During this time, the width of the corona region decreases with increasing dilution (decreasing ϕ). The “coffee-ring” behavior (Deegan et al., 1997) (similar to what is typically observed in other protein aqueous solutions (Pal et al., 2020a)) becomes evident in samples from ϕ of 62 to 12.5% (v/v).

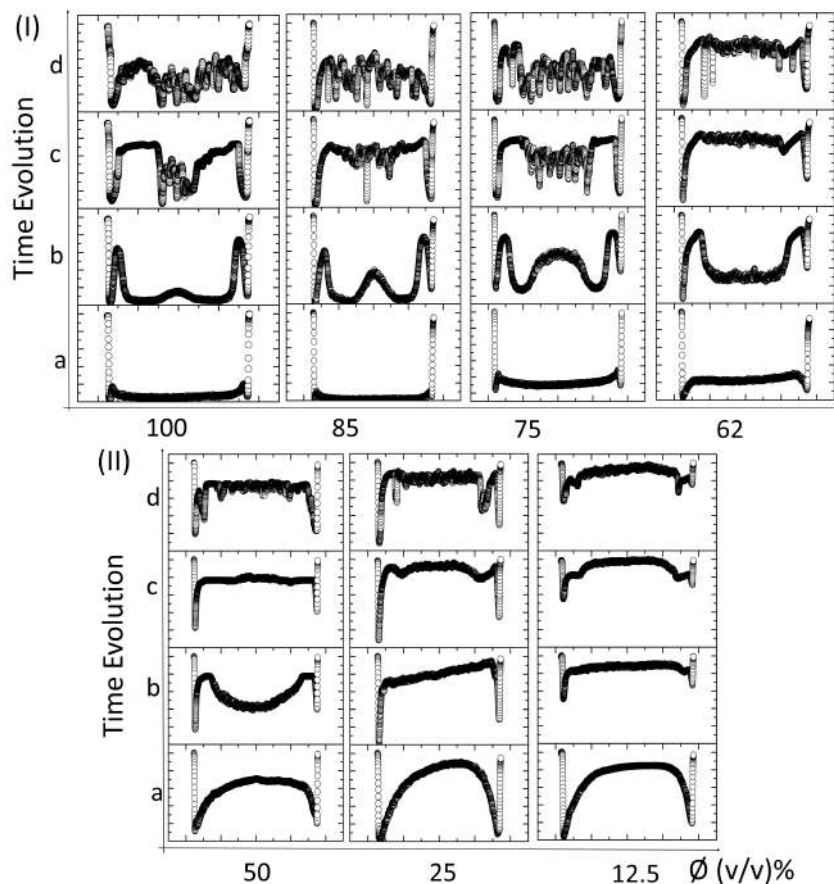


FIGURE 6.2: A normalized intensity of a 2-D plot profile along the horizontal diameter of the droplet (ρ) is shown for corresponding a-d depicted in Fig. 1(I-II). These plots captured during the drying process at each ϕ : (I) from 100 to 62% (v/v), and (II) from 50 to 12.5% (v/v). The intensity of the captured image rises along ρ when the dilution is increased (I-II)a. The movement of the fluid front from the periphery is illustrated by a hump in both the edges of the profile (I-II)b. An appearance of the hump in the central region of the profile is observed in (I)b, whereas its disappearance is evident in (II)b. The propagation of the cracks disturbs the uniformity of the plot profile from 100 to 62% (v/v) in (I)c-d; however, it is hardly visible in (II)c-d. The x ranges from -1.25 to 1.25 mm (with a step size of 0.5 mm), while the y axis varies from 0 to 1.1 arbitrary units (a.u.) (with step size of 0.2 a.u.).

The change in the textures of the images [shown in Fig. 6.1(I-II)] is directly mapped with the normalized plot in Fig. 8.9(I-II). A rectangle (containing a width of ~ 0.6 mm) along the diameter was drawn on the images in such a way that a small portion covers the background (coverslip) on both sides to complete the normalization process. In this plot, the x-axis illustrates the distance along the horizontal diameter (ρ) of the droplet, and the y-axis displays the vertically normalized averaged pixel intensity. For the first captured image at ϕ varying from 100 to 62% (v/v), only the 20% of the total intensity value in the plot profile (Fig. 8.9(I)a) indicates the uniformity of the dark texture (Fig. 6.1(I)a). The texture of these images turns lighter gray (Fig. 6.1(II)a) with the increasing dilution [from 50 to 12.5% (v/v)]. It is evident if we notice the plot profile which shows the intensity as 60 – 80% of the total value (Fig. 8.9(II)a). The texture of the droplet changes to gray as soon as the front moves from the periphery towards the center (Fig. 6.1(I-II)b). It is indicated by the increasing normalized intensity near the edge of the droplet (Fig. 8.9(I-II)b). In the next phase, the gray texture appears in the central region of the droplet shown in Fig. 6.1(I-II)b. This appearance is predominantly marked with a broad hump-like feature at the center of the plot profile from 100 to 75% (v/v). However, this feature starts disappearing from 62 to 12.5% (v/v) [Fig. 8.9(I-II)b]. The next stage is identified with the propagation of the radial cracks and their widening and branching (Fig. 6.1(I-II)c-d). The plot profile in Fig. 8.9(I-II)c-d shows the way the depth of the cracks decreases with the (increased) dilution by tracking the spikes from 100 to 12.5% (v/v). This observation indicates the thinning of the dried film and the decrease in the depth of their intervening cracks.

Figure 6.3(I-II) depicts the time evolution of the normalized contact angle of the blood droplets. The normalization of the contact angle ($\theta(t)$) is done in respect to the angle at $t = 0$ (θ_0). The θ_0 is determined by a linear extrapolation of the first 200 seconds of θ varying with time, where it appears linear. The y -intercept provides the normalization in θ . The average slope of this linear extrapolation of the contact angle for all ϕ are computed and found to be $-0.14^\circ/s$ with $R^2 = 0.996$ with very little variation between the samples. The contact angle then shows non-monotonic behavior after 200 seconds that exhibits a peak marked by a green rectangle in Fig. 6.3(I)a-d before saturating to a nearly constant with increasing dilution (decreasing ϕ) from 100 to 62% (v/v). The peak decreases in magnitude and shifts to a later time from 100 to 62% (v/v). No peak is observed with further dilution from 50 to 12.5% (v/v) [Fig. 6.3(II)a-c]. Similar saturation and monotonic behavior are commonly observed in the aqueous protein solutions (Pal et al., 2020a). The peak is observed from 250 to 400 seconds at $\phi = 100\%$ (v/v) [Fig. 6.3(I)a]; and from 400 to 500 seconds for ϕ varying from 85 to 62% (v/v) [Fig. 6.3(I)b-d] (denoted with vertical dashed lines). The corresponding macroscopic images during the emergence of this peak are displayed in Fig. 6.3(I)a-d. The images indicate that the peak originates during the appearance of the fluid front or the gray texture from the periphery and it continues to evolve

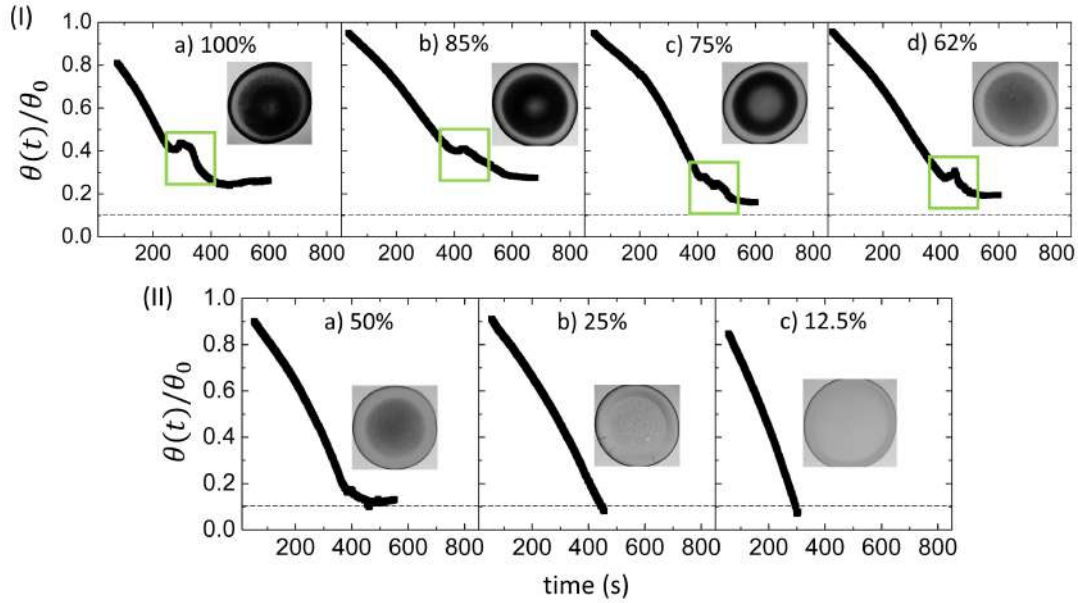


FIGURE 6.3: Variations of the normalized contact angle ($\theta(t)/\theta_0$) during the drying process of the blood droplets at different ϕ ranging (I) from 100 to 62% (v/v), and (II) 50 to 12.5% (v/v) are shown. The normalization of $\theta(t)$ is done by dividing it with the angle at $t = 0$ (θ_0). A monotonic decrease in the contact angle measurements is associated with the presence of a peak-like feature (outlined with a green rectangle) is observed in (I). The disappearance of this feature in these measurements is depicted in (II). The macroscopic images are displayed at different time points (in seconds) points from 100 to 12.5% (v/v) [321s, 512s, 470s, 460s, 473s, 518s, and 617s respectively for different ϕ]. The instrumental limit is illustrated with dashed lines.

when the texture starts growing in the central region. In contrast, this peak is not observed for samples from 50 to 12.5% (v/v). The macroscopic images in Fig. 6.3(II)a-c are captured once the contact angle advances to steadiness. It is to note that the contact angle becomes constant when it is $\sim 25\%$ for ϕ of 100 and 85% (v/v), $\sim 15\%$ for ϕ of 75 and 62% (v/v), $\sim 10\%$ for ϕ of 50% (v/v), and $< \sim 10\%$ of the total value for ϕ of 25 and 12.5% (v/v). This suggests that the thickness of the film at the end of the drying process decreases with the diluting concentration (ϕ).

Figure 6.4(I-II) illustrates the parameters of the first-order statistics (FOS). The left y -axis of the graph shows the mean intensity and its right y -axis exhibits the standard deviation. These parameters are extracted from the captured time-lapse images of the droplets at different ϕ during the drying process. The dashed lines of Fig. 6.4(I) denote the time range of the peak-like feature in the contact angle measurements. Note that the mean intensity shown in Fig. 6.4(I) depends on the average pixel distribution of the images. These data display three distinct phases- a slow increase, a rapid rise, and a saturation from ϕ of 100 to 75% (v/v). The first and second of these three phases; however, could not be distinguished in the 62 to 12.5% (v/v) samples. The large area under the peak is observed in the mean intensity at about 600 seconds for 100% sample, which continuously decreases with increasing dilution, nearly disappearing in the 12.5% (v/v) sample. The SD measurement [gray

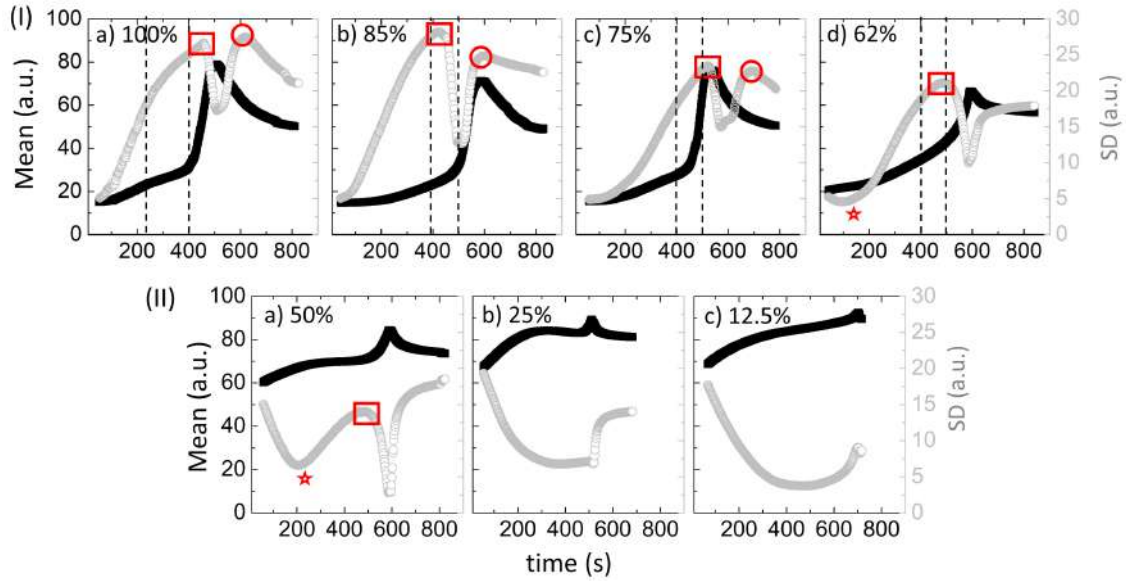


FIGURE 6.4: Statistical image analysis of the blood droplets at different ϕ from 100 to 12.5% (v/v) during the drying process. (I) and (II) show the drying evolution of the first order statistics (FOS) parameters (the mean on the left y axis and the standard deviation (SD) on the right y axis of the graph). The dashed lines in (I) display the time duration of the presence of the peak-like feature in the contact angle measurements from ϕ of 100 to 62% (v/v). The red rectangle and the red circle illustrate the first and the second peaks respectively in the SD. The star introduces the initial dip in the SD values observed from 62% (v/v) onwards.

circles in Fig. 6.4(II)] depends on the global heterogeneity of the images, and is a measure of the image complexity. It exhibits an initial dip (outlined by a red-colored star) from 62% (v/v) onwards. The behavior of these FOS (the mean intensity and especially the SD) parameters changes abruptly at about 62% (v/v) dilution.

6.2.2 Morphology of the dried blood film

Figure 6.5(I) illustrates the variation of the averaged corona width (\bar{w}) that is normalized to the averaged radius of the droplet (\bar{R}). The macroscopic image in Fig. 6.5(I) illustrates the width of the corona (w) and the radius of the droplet (R). The increased dilution [ϕ from 100 to 12.5% (v/v)] systematically decreases the corona width. The \bar{w}/\bar{R} is plotted for the whole range of ϕ , i.e., from 100 to 12.5% (v/v). The slope value (m) is found to be $0.0055 \pm 0.0006 \phi^{-1}$ with $R^2 = 0.931$. A first linear curve is fixed from 100 to 62% (v/v). Subsequently, a second curve is fitted from 62 to 12.5% (v/v). The slope value of the first linear fit (m_1) is found to be $0.0095 \pm 0.0019 \phi^{-1}$, with $R^2 = 0.894$. In contrast, the slope value of the second linear fit (m_2) is $0.0051 \pm 0.0008 \phi^{-1}$, with $R^2 = 0.928$. The variation of the averaged crack spacing (\bar{x}_c) with ϕ is shown in Fig. 6.5(II). The distance between the consecutive radial cracks (x_c) is illustrated in the macroscopic image. The parameter, m [the slope value of the linear fit for the range of 100 to 12.5% (v/v)], m_1 [the slope value of the linear fit for the range of 100 to 62% (v/v)], and m_2 [the slope value of the linear

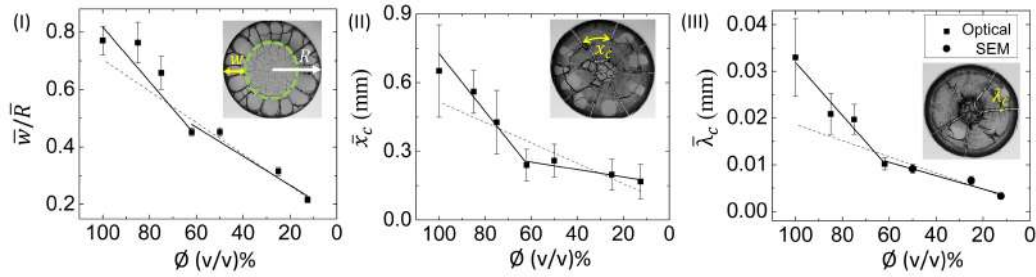


FIGURE 6.5: Variation of the averaged corona width (\bar{w} measured in mm) is normalized to the averaged radius of the droplet (\bar{R} measured in mm). It is plotted in (I), the averaged crack spacing (\bar{x}_c) is depicted in (II), and the averaged crack width ($\bar{\lambda}_c$) is exhibited in (III) at different diluting concentrations (ϕ). The dashed line shows the linear fit for the whole range of ϕ from 100 to 12.5% (v/v). The solid lines display two linear fits- first one for the range from 100 to 62% (v/v); and the second one for 62 to 12.5% (v/v). The error bars correspond to the standard deviation. The macroscopic images illustrate the width of the corona (w), the radius of the droplet (R), the distance between the consecutive radial cracks (x_c), and the width between the consecutive radial cracks (λ_c). The dashed green circular line separates the corona from the central region in the droplet.

fit for the range of 62 to 12.5% (v/v)] are found to be $0.0045 \pm 0.0012 \text{ mm } \phi^{-1}$ with $R^2 = 0.668$, $0.013 \pm 0.0014 \text{ mm } \phi^{-1}$ with $R^2 = 0.965$, and $0.0016 \pm 0.0005 \text{ mm } \phi^{-1}$ with $R^2 = 0.736$ respectively. Fig. 6.5(III) displays the averaged crack width ($\bar{\lambda}_c$) variations of each ϕ . The width between the consecutive radial cracks (λ_c) is exhibited in the macroscopic image. The optical microscopy at $5\times$ magnification has the resolution to measure the $\bar{\lambda}_c$ down to the 62% (v/v) sample. For the $\bar{\lambda}_c$, the m_1 is extracted as $0.00057 \pm 0.00008 \text{ mm } \phi^{-1}$ (with $R^2 = 0.938$). To overcome the limitations of the optical microscopy, the SEM images are used to calculate λ_c for ϕ from 50 to 12.5% (v/v), where m_2 at this range yields $0.00014 \pm 0.00002 \text{ mm } \phi^{-1}$ (with $R^2 = 0.920$). Finally, over the whole range of ϕ , the slope (m) for $\bar{\lambda}_c$ is $0.00017 \pm 0.00003 \text{ mm } \phi^{-1}$ (with $R^2 = 0.835$).

Figure 6.6(I-III)a shows the regions of interest at ϕ of 100, 75, and 12.5% (v/v) respectively. The yellow, the orange, and the black squares display the zoomed view at the periphery and the corona, the interface of the corona and the central regions, and the central region, respectively. Fig. 6.6b exhibits a smooth film in the corona region, and becomes more uniform with the increasing dilution of the blood sample. The cracks of the peripheral region at ϕ of 100 and 62% (v/v) [Fig. 6.6(I-II)b] consist of some ellipsoidal structures which lead to inhomogeneity within the cracks, whereas no such peripheral region is found at ϕ of 12.5% (v/v) [Fig. 6.6(III)a]. At the interface of the corona and the central regions, some irregular troughs and ridges are revealed from the images of Fig. 6.6(I-II)c-d. A complex image is visible in Fig. 6.6(I-II)d, where the crack lines are not sharp and contain hair-like structures. which smoothly diminish in appearance in the diluted blood sample. Interestingly, these results show that the dilution at ϕ of 75% (v/v) [Fig. 6.6(II)] doesn't exhibit any significant changes in the distribution of these structures from the whole blood [Fig. 6.6(I)]. However, a

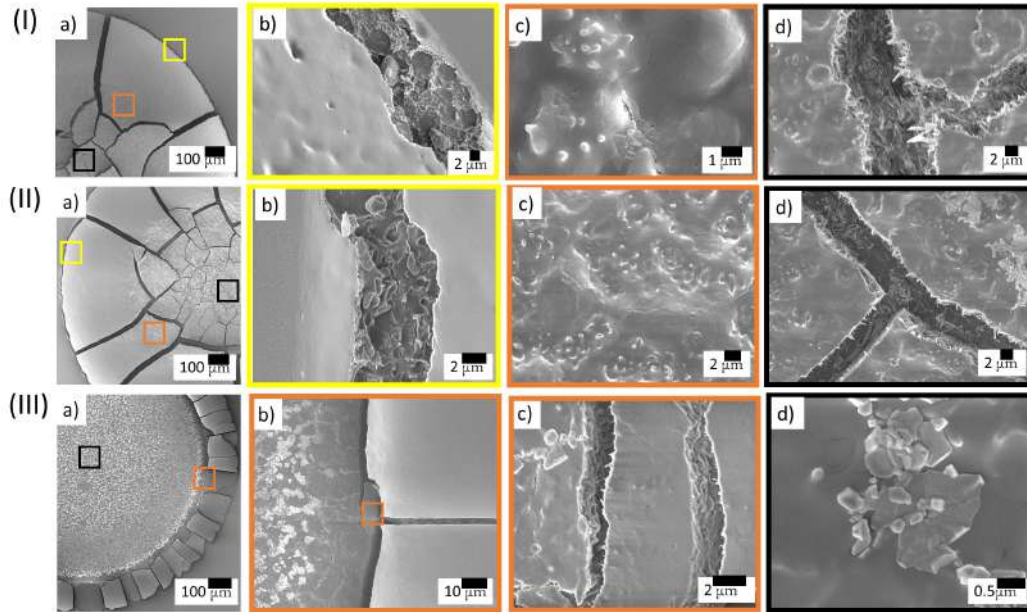


FIGURE 6.6: SEM images illustrating the microscopic structures of dried blood films at different length scales. The images at ϕ of 100, 75 and 12.5% (v/v) are, respectively, depicted in (I-III). The yellow, the orange and the black squares represent the blood structures at the periphery and the corona, the transition of the corona and central regions, and the central region, respectively.

marked difference can be seen at 12.5% (v/v) [Fig. 6.6(III)]. Unlike other concentrations, some unique blunt spicules are present on the film (Fig. 6.6(III)b-c), and some aggregated sickle or oblate shaped structures are observed in the central region in Fig. 6.6(III)d.

6.3 Discussions

6.3.1 Microscopic structures of dried blood film

The SEM images in Fig. 6.6(I-III) allow us to determine the distribution of various components in the dried film. The components that can be distinguished from these images are plasma proteins, red blood cells (RBCs), white blood cells (WBCs), and platelets. The periphery of the film and the textures within the cracks indicate that the plasma proteins interact with the substrate and form a plasma-rich layer as soon as the droplet is deposited.

Most of these cracks in the peripheral region consist of fragmented or ellipsoidal RBCs (Fig. 6.6(I-II)b). None of the samples [ϕ of 100, 75, and 12.5% (v/v)] show any blunt spicules (which resembles echinocyte, a deformed structural form of RBCs reported in (Mukhopadhyay et al., 2018)) in these cracks. This indicates that RBCs do not interact with the substrate directly; however, it does with the plasma-rich layer. Had these RBCs adsorbed on this substrate, their membranes would have different electrostatic interactions and might have led to the echinocytes, which are

not (obviously) observed here. At the upper film surface, the corona region reveals smooth fragmented sheets. This suggests that the RBCs are stacked in a packed fashion such that their membranes form this sheet, a similar phenomenon reported in (Chen et al., 2017). The compressed RBCs are raptured, as could be seen in the crack walls due to the mechanical stress curving the cracks (shown in Fig. 6.6(I-II)b).

Close observation of the film from the thin periphery region across the corona and into the central region indicates that the RBCs are predominantly in the corona. Any of these platelets and WBCs are not present in the periphery and in the corona. Moving from the corona to the central region, we see the concentration of the WBCs, the platelets and some residual RBCs. Fig. 6.6(I-II)c displays the irregular troughs and ridges which would resemble the different functional forms of the WBCs (microvilli structures reported in (Newell, Roath, and Smith, 1976; Yang, 1989)) and some of the residual echinocytes. The crowdedness of the RBCs, the WBCs, and the plasma proteins is clearly illustrated by the fact that the dried film at ϕ of 100% (v/v) [Fig. 6.6(I)a] contains $\sim 500 \times 10^4$ of RBCs, $\sim 1 \times 10^4$ of WBCs, and $\sim 40 \times 10^4$ of platelets, in addition to the initial salts and other molecular blood factors (Brutin et al., 2011). The crack lines are not sharp enough and contain hairy structures. These hairy structures are believed to be the activated form (a spreading structure with extended filopodia mentioned in (Gregory, Stevens, and Fraser, 2017)) of the platelets (Fig. 6.6(I-II)d). It confirms the existence of a complex combination of interactions among these components which can activate these platelets in response to the mechanical stress.

At ϕ of 12.5% (v/v), the film only contains $\sim 60 \times 10^4$ of RBCs, $\sim 0.12 \times 10^4$ of WBCs, and $\sim 5 \times 10^4$ of platelets, a decrease of about a factor of 10. This significant reduction in their counts influences the morphology of the film, and is denoted in Fig. 6.6(III)a. The peripheral region does not appear in these images. Furthermore, the fragmented sheets in the corona region appear to be smoother, and its width gets reduced compared to other ϕ . Some spicule-like structures are identified in the transitional region from the corona to the central regions (Fig. 6.6(III)b-c); and, some sickle and oblate-shaped structures are observed near the center (Fig. 6.6(III)d). The reduction (of RBCs, WBCs and platelets) concentrations decreases their interaction among themselves and with each other such that different functional forms of these components are observed. Moreover, as dilution increases, any interaction among the components within blood becomes negligible such that the inactivated form of these platelets are preserved, mostly observed in the central region.

6.3.2 Concentration-driven phase transition in the drying droplets and the dried films

The outcome of three experimental observations support the presence of the phase separation in the samples of a multi-colloid self-interacting solution, such as the whole blood. Our observations (drawn based on these three experimental outcomes)

are independent of each other and facilitate measuring different aspects of the drying process including the final dried film morphology.

The first observation is related to the contact angle (θ) measurements as a function of time during the drying process. The θ is found to decrease monotonically. Subsequently, a peak is observed for the whole blood. This pattern is observed in the dilution ranging from 100 to 62% (v/v) [Figs. 6.3(I)]. The peak, however, starts disappearing in the diluted samples starting from 50 to 12.5% (v/v) [Figs. 6.3(II)]. During this stage, θ exhibits a steep monotonic decrease. The third independent measurement is done on the morphology of the dried film. The mean width of the corona (\bar{w}), the mean crack spacing (\bar{x}_c) and the mean crack widening ($\bar{\lambda}_c$) are found to be the highest for the whole blood [$\phi = 100\%$ (v/v)]. All these parameters; however, are reduced as the initial concentration of the blood sample is diluted [Fig. 6.5(I-III)]. Interestingly, a smooth gradual decrease in these extracted parameters (\bar{w}/\bar{R} , \bar{x}_c , and $\bar{\lambda}_c$) is not observed when varying with ϕ . Had that been the case it could have assumed that the droplets experience a universal mechanism throughout the drying process, which is not the case here. Instead, a pronounced break in the trends of the parameters is seen at about 62% (v/v). Comparing the R-squared values for the double linear fits with a single linear fit clearly favors the use of two linear fits- one from 100 to 62% (v/v) samples, and, the other for 62 to 12.5% (v/v). This behavior for the parameter \bar{w}/\bar{R} is found to be weakest, but still present, and is likely due to the fact that the width formation is the result of the deposition of the components during the convective flow, especially in the early stages of drying. Dilution of the whole blood (whether DI water or PBS) lowers the number of the components, and so reduces the corona's width. Moreover, the formation of the corona is strongly influenced by the drying-driven fluid circulation, the droplet geometry, and its wetting. It is; however, not so dependent on the type of the components, but just the amount. In contrast, \bar{x}_c and $\bar{\lambda}_c$ show a much stronger break and evidence for two linear regimes from 100 to 12.5% (v/v).

All these three measurements indicate that there are two classes of the mechanisms involved. These mechanisms could be interpreted in the following way. A large number of components (such as RBCs, WBCs, platelets, proteins, etc.) are present in ~ 2 mm diameter droplet at $\phi = 100\%$ (v/v) [the whole blood]. These components are randomly distributed as soon as the droplet of the whole blood is deposited on the substrate [Fig. 6.7(I)]. In this *initial phase*, the evaporation rate is observed to be highest near the three-phase contact line [indicated with solid arrows in Fig. 6.7(I)]. A capillary flow [marked with dotted lines in Fig. 6.7(I)] is observed to develop and most of these components are carried towards the periphery. Subsequently, a plasma-rich layer is developed on the substrate. Soon after, all these components start moving closer to each other, which indicates the beginning of the *middle phase* in Fig. 6.7(II). In this phase, these components experience compression, or stretch, and shear at the same time near the periphery. The concentration of these components

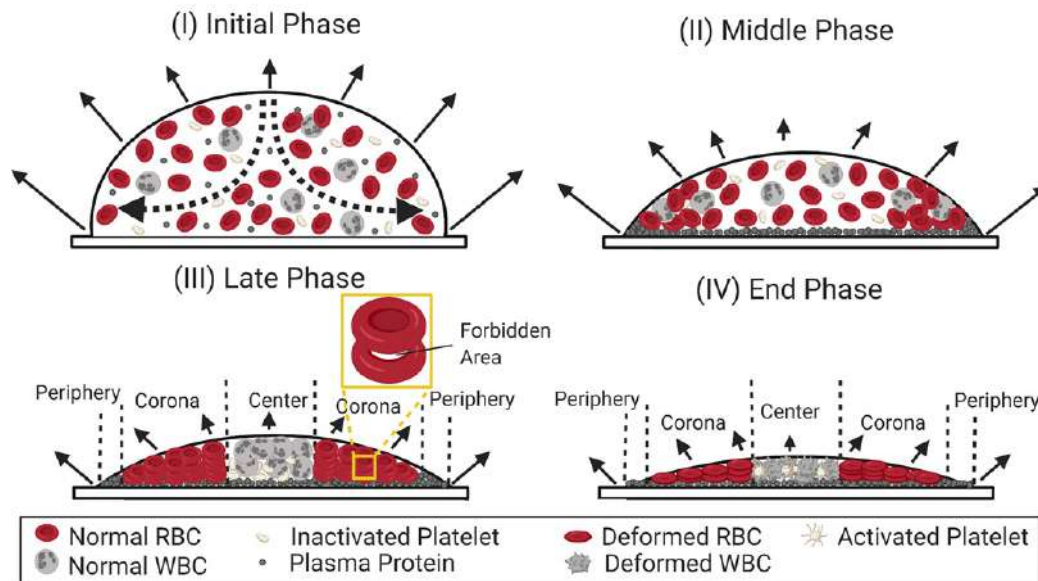


FIGURE 6.7: Side view of the self-assembling mechanism in the whole blood ($\phi = 100\%$) during the drying evolution: (I) The *initial phase* starts when the droplet is deposited on the substrate. The evaporation rate is highest near the three-phase contact line (depicted with solid arrows). The components (RBCs, WBCs, platelets, and proteins) are distributed randomly. A dotted line indicates that a capillary flow is developed in the droplet. (II) The *middle phase* begins when these components are carried towards the periphery. These components initiate interactions as soon as they come in contact with each other. Meanwhile, a plasma-rich layer is developed on the substrate. (III) The segregation of these components takes place as the water continually evaporates from the droplet. During the *late phase*, the three distinct regions (the periphery, the corona, and the center) are developed. The proteins are mostly present in the periphery. The WBCs and the platelets are pushed towards the central region. The RBCs are stacked in the corona region. The trapped water in between two RBCs is marked as the “forbidden area”. (IV) The deformation of the RBC and the WBC structures and the activation of the platelets take place during the *end phase*. These structures are drawn from <https://www.biorender.com/>.

within the droplet increases as the water constantly evaporates. The confinement in the droplet diameter and the presence of the huge number of these components is likely to influence the activity of one component on others. Such interactions may result in a strong, complex combination of the potential chemicals amongst these various components. For example, a few of these components may try to arrange themselves in their original shape (elastic behavior); however, their arrangement would then create negative stress on other components. These other components may then rearrange (viscous behavior) themselves to accompany the accumulated stress. The elastic behavior can be modeled as $\sigma = E\epsilon$ where σ , E , and ϵ is the stress, averaged elastic modulus resulted from the arrangements of these components and the strain which occurs under the accumulated stress respectively. The visco-elastic behavior can be re-modeled by adding the Kelvin-Voigt element, i.e., $\sigma = E\epsilon + \eta\dot{\epsilon}$, where, η is the viscosity, and $\dot{\epsilon}$ is the change of strain in respect to time t . This speculated viscous behavior is most likely governed by the interacting capabilities of the WBCs (with the other components viz., the RBCs and the platelets) owing to its

largest size ($\sim 15 \mu\text{m}$) compared to the other components (the RBCs and the platelets are of $\sim 7 \mu\text{m}$, and $\sim 2 \mu\text{m}$ respectively). The large peak that was noticed at ϕ of 100% (v/v) [Figs. 6.3(I)], the presence of a similar peak has also been reported in (Iqbal, Shen, and Sen, 2020), may have some correlation to this viscous behavior during the drying process. However, the experiments reported in (Iqbal, Shen, and Sen, 2020) did not concentrated on diverse ranges of dilution; and hence the study failed to observe the transition at 62%. The current study, thus, contributes a crucial information related to phase transition. It would be interesting to conduct an in-situ rheology and mass measurements to directly probe these mechanisms; however, this is beyond the scope of this present study. The segregation of these components takes place during the *late phase* of the drying process [Fig. 6.7(III)]. The confinement of their sizes does not allow both the RBCs and the WBCs to be present within the periphery [evident from the SEM results shown in Fig. 6.6(I)a-b]. Most of the RBCs are organized in stacks in the corona region, and the WBCs and the platelets are pushed towards the central region [Fig. 6.7(III)]. There is a possibility that some of the water is trapped between two RBCs during the stacking of the RBCs, [marked as the "forbidden areas" in Fig. 6.7(III)]. The change of the texture from the light to dark gray texture (Fig. 6.1(I)c-d) might be related to the final evaporation of this entrapped water. The loss of water in these droplets during the drying process creates a hypotonic environment to the cellular components present in the blood. The blood cells are more likely to undergo hemolysis inducing a fundamental change in their composition. Furthermore, the developing mechanical stress evolved due to the loss of the water from the droplet deforms the structures of RBCs and the WBCs in the *end phase* [Fig. 6.7(IV)]. The inactive platelets are activated in response to the mechanical stress and are observed as the hairy structures along the crack lines (indicated in Fig. 6.6(I)d).

As mentioned already, the whole blood sample is diluted by adding different volumes of de-ionized water. Obviously, the initial concentration of these components in the diluted blood samples [ϕ ranging from 85 to 12.5% (v/v)] becomes less compared to the whole blood. The addition of de-ionized water rather than PBS (the buffered saline) is likely to trigger a hypotonic environment to these cellular components prior to the drying process. However, it is to be noted that the changes (if any) occur in the initial mixtures before deposition but may be balanced as the water evaporates. Exploring this effect would be interesting but is beyond the scope of this study. Additional measurements were carried out in a parallel way but diluting with PBS, in order to maintain the native environment of the cells and the fundamental changes (hemolysis) in the blood composition (from intact to fragments) could be avoided. These results appear consistent with the DI water dilution and so minimizes this mechanism. However, it is worth mentioning that the dilution of the blood by PBS (at its fixed concentration) will increase the appearance of salts residues or crystals (Iqbal, Shen, and Sen, 2020), which influences the statistics derived from the optical images, and lead to artifacts in the scanning electron

microscopy images.

The drying process of the diluted blood samples exhibits similar phases [from *initial* to the *end phase* shown in Fig. 6.7(I-IV)]. Fig. 6.1(I-II)a indicates a change in the texture (from dark to light gray) as soon as the first image during the drying process is captured. The normalized plot in Fig. 8.9(I-II)a shown in the supplementary information directly illustrates this change in the texture. At ϕ from 100 to 62% (v/v), the mean intensity value of the first image is $\sim 20\%$ of the total value, further dilutions of the concentration leads the mean intensity to be at $\sim 80\%$ of the total value. It is to be noted that RBCs contain hemoglobin protein (which is responsible for the redness). The change of texture, or the rise in the normalized plot, indicates that the number of RBCs reduces with the diluted concentrations. The decrease of RBCs also ensures that the other components will also minimize to maintain their relative initial concentrations. The number of these components gradually decreases with the diluted concentrations [in ϕ ranging from 85 to 62% (v/v)] and leads to a reduction in the chemical potential amongst them. The shrinkage and disappearance of peak in the contact angle measurements supports this mechanism. In addition, the observed shift in the peak to the later time (depicted by green rectangles in Fig. 6.3(I)a-d) indicates that these diluted samples require more time (greater concentration and assembly) to reach the visco-elastic tipping point of the system. Furthermore, the wetting angle peak at the concentration range of 100 to 62% (v/v) is found to be present in spite of varying the physiological and environmental conditions (described in Chapter 7).

The presence of WBCs also seems to act as a mediator which favors the interactions between various components, rather than the interaction between these components and the substrate. This process results in sliding of the cracked domains over the attachment of these domains with the substrate in the samples ranging from 100 to 62% (v/v). Furthermore, this process shows a sharp decrease in \bar{x}_c and $\bar{\lambda}_c$. In contrast, for ϕ from 50 to 12.5% (v/v), the number of these various components is reduced enough that the chemical potential related to WBCs becomes negligible. This results in the switching of the mechanism from the visco-elastic to elastic behavior. No peak observed at this concentration range in the contact angle measurements [Figs. 6.3(II)]. Moreover, the attachment of the film to the substrate becomes stronger, the sliding of the crack domains stops, and more radial cracks appear on the film surface [Fig. 6.1(II)].

6.4 Conclusions

Our findings, thus, clearly establish the existence of a sharp phase transition in the whole blood through a simple physical drying process. This transition relied on the concentration of the various components present in the droplet. It reveals essential information about the self-assembling mechanism in a multi-component

bio-colloid, such as the whole human blood. Our systematic study of the dilution range also ensures that the concentration-driven phase transition is not specific to the blood-water system only; rather it is a general phenomenon of drying-driven diluting blood droplets. Finally, this study demands theoretical attention for such a multifaceted phase transition that relies on the complex combination of interacting chemical potentials for unearthing the hierarchical structures present in nature.

So far, we have discussed (Chapters 4-6) that how the drying evolution influence the resulting morphological patterns in the bio-colloidal drying droplets at different complexity levels. For instance, the fundamental understanding of the patterns evolved in the simple bio-colloids: globular proteins [lysozyme (Lys) and bovine serum albumin (BSA)] prepared in de-ionized water is described in Chapter 4. The artificially synthesized complex bio-colloidal system is studied in Chapter 5. In contrast, this chapter [Chapter 6] focuses on the most complex naturally-occurring bio-colloid, such as human blood. It provides new physical insights and reports how the concentration-driven phase transition develops when the blood is diluted in the de-ionized water. However, it is to be noted that all the samples are studied without adding any external salts in the solutions. The next chapter [Chapter 7] focuses on understanding how the morphological patterns of such bio-colloidal drying droplets change in the buffered saline solutions.

Chapter 7

Drying Droplets in Phosphate Buffer Saline Solution

7.1 Background

This section specifically emphasizes the studies done in the droplet community to understand the colloid-colloid and colloid-saline interactions during the drying process and the resulting morphological patterns. The Lys protein at various concentrations of NaCl was studied Gorr et al. (Gorr et al., 2013) that reported the presence of three distinct regions in the presence of NaCl. The first one is formed in the peripheral ring, where most of the Lys is present. The second one forms different salts structures that occupy the secondary ring area (observed adjacent to the ring), and the final one is observed in the central regions. A much like observation is also reported in BSA-saline protein drying droplets by Yakhno (Yakhno, 2008). This study infers that the salt crystals are phase-separated by forming different zones from homogeneous protein film near the periphery to the salt crystals in the central region. The BSA proteins in the presence of different phosphate buffer saline (PBS) and observed two distinct drying modes during the interaction phase with the salt residues (Chen and Mohamed, 2010). The quicker drying rate is detected near the droplets' edge when the initial salt concentration is low. This evaporation rate is greater at the center of the droplets at higher salt concentrations. Recently, it was investigated the effects of multiple salts ($MgCl_2$ and KCl) on the BSA patterns. This study reveals that the crystal structures depend on the initial tuning ratio of these salts (Pathak et al., 2020). The standard assessment protocols of both the drying evolution and the resulting morphological patterns are indicated through mass loss, contact angle, contact line, fluid front progression, etc. Despite intense research on the protein drying droplets, only a few studies exploited the image processing techniques to explore the drying mechanism. For instance, the pattern recognition tools, such as k-means clustering and k-nearest neighbor algorithm, were applied by Gorr et al. (Gorr, Xiong, and Barnard, 2014). It shows that these tools are powerful enough to differentiate the Lys-NaCl deposits based on the salts' initial concentration. The first-

and second-order statistics (GLCM) were applied to specify textural image properties and explored information about the evolution of the final state of drying BSA-Lys films in NaCl salts' presence (Carreón et al., 2018b). The study reports that this textural analysis can capture structural changes due to the formation of the complex dendrite, rosette, and scalloped-like structures in such drying droplets.

The evolving morphological patterns are also studied in the plasma serum in the presence of the NaCl salts by Chen et al. (Chen et al., 2019). It is done to examine the crystal-like structures' chemical compositions and their effects on the crack patterns. However, it is to keep in mind that plasma lacks cellular components (RBCs, WBCs, platelets). Therefore, this study did not allow us to draw any conclusions on these components' aggregation process by adding salts. Very recently, Sen et al. (Iqbal, Shen, and Sen, 2020) have studied the effects of the dilution on the blood patterns by changing the substrate conditions. They concluded that the cracking transition to the non-cracking regime exists for the droplets deposited on the hydrophilic substrate. On the other hand, the buckling regime adds to this transition when the droplet dries on the hydrophobic substrate. They mainly focused on the decrease of the RBCs in the process of the dilution. They showed how reducing their counts affects the mechanical stress developed due to the water loss during the drying evolution. It is to be noted that this study does not reveal any information about different deformed structures of the blood components and their self-assembling interactions.

Despite the intense research on protein-saline drying droplets, to our best knowledge, no systematic study is being performed to understand multiple salts' effects on various concentrated Lys protein solutions. This chapter investigates the drying droplet consisting of Lys in different phosphate buffer saline solution using bright-field and scanning electron microscopy. A morphological grid is displayed by changing the initial concentration of Lys (ϕ_{Lys}) along the x-axis and varying the initial concentration of the salts (ϕ_{salts}) present in the buffered saline along the y-axis. To better understand these morphological patterns, the microstructural analysis is done by varying ϕ_{Lys} and fixing ϕ_{salts} . Furthermore, the drying evolution of different initial concentrations of Lys at a fixed ϕ_{salts} is investigated and quantified using textural image processing techniques. Therefore, this paper attempts to answer a few fundamental questions; do we always observe three regions in Lys-saline droplets? If not, why? What are the effects of multiple salts on Lys droplets? Does it behave similarly as reported in the BSA droplet? Can the texture analysis reveal information about the protein-protein and protein-salt interactions?

Since the GLCM of an image is highly dependent on its orientation and pixel displacement (Cai et al., 2019; Zhou et al., 2017), to our best knowledge, no study to date has attempted to examine these (initialized) factors of the GLCM parameters. Furthermore, the gray values in terms of the pixel counts are not explored for the drying droplets. Therefore, this chapter also focuses on the physics associated with

different pattern formations by exploiting the FOS and GLCM textural image parameters on BSA-saline droplets. Our principal motivation is to explore the effects of different ϕ_{salts} on the time evolution and the morphological properties of BSA protein during the drying process using optical bright-field microscopy. Additionally, we also wish to develop a mechanism that can interpret the pixel distribution of the images acquired during the drying process. Our final goal is to examine the influence of horizontal (0°) and vertical (90°) orientations and pixel displacements (1, 10, 50, and 1000) on such GLCM parameters using suitable statistical tests. The FOS parameters [viz., the mean (I), standard deviation (SD), kurtosis (KUR), and skewness ($SKEW$)], and the GLCM parameters (viz., angular second moment (ASM), correlation (COR), inverse difference moment (IDM), and entropy (ENT)) are thoroughly examined in this chapter.

Furthermore, this chapter's initiative is to comprehend the effects of the salts in the most-complex bio-fluid, i.e., whole human blood. It explores the self-assembling mechanisms as the number of the blood's cellular components reduces in the presence of a fixed concentration of the salts. It investigates how the diluent PBS affects the components' microstructures (RBCs, WBCs, and platelets) present in the blood and the macroscopic patterns of the droplets. It is also to see whether the concentration-driven phase transition is affected due to the addition of external salts.

7.2 Results

For the Lys-saline study, the different concentrations of the phosphate buffer saline (PBS) were prepared by diluting 1x to 0.75, 0.5, and 0.25x. The various amounts, i.e., 100, 75, 50, 35, 25, and 10 mg of Lys, are weighed and mixed separately in 1 mL of these PBS solutions. Therefore, the samples were prepared with the initial concentrations of Lys ($\phi_{Lys} = 9.0, 6.9, 4.8, 3.3, 2.4,$ and 1.0 wt%) at the various salts' initial concentrations ($\phi_{salts} = 0.9, 0.7, 0.5, 0.2,$ and 0.0 wt%) present in PBS. The $\phi_{salts} = 0$ wt% means that the Lys solution is prepared without dissolving it in any PBS but in the de-ionized water. For the BSA-saline study, 10x PBS was diluted to different of 5, 2, and 1x. The 100 mg of BSA is weighed and mixed separately in 1 mL of these PBS solutions to prepare the initial concentrations of $\phi_{salts} = 4.3, 1.8,$ and 0.9 wt%. For the blood-saline study, the whole human blood [100 (v/v)%] is diluted by adding phosphate buffer saline (PBS) at a fixed initial concentration of 1x. The initial concentration of blood diluted by PBS is ϕ_{blood} , which ranges from 75 to 12.5% (v/v).

7.2.1 Drying evolution and morphology of Lys-saline droplets

Figure 7.1 displays a morphological grid of the samples varying the initial concentrations of Lys (ϕ_{Lys}) from 9.0 to 1.0 and the initial concentrations of various salts present in the PBS (ϕ_{salts}) from 0.9 to 0.2 wt%. The $\phi_{salts} = 0$ wt% embodies the

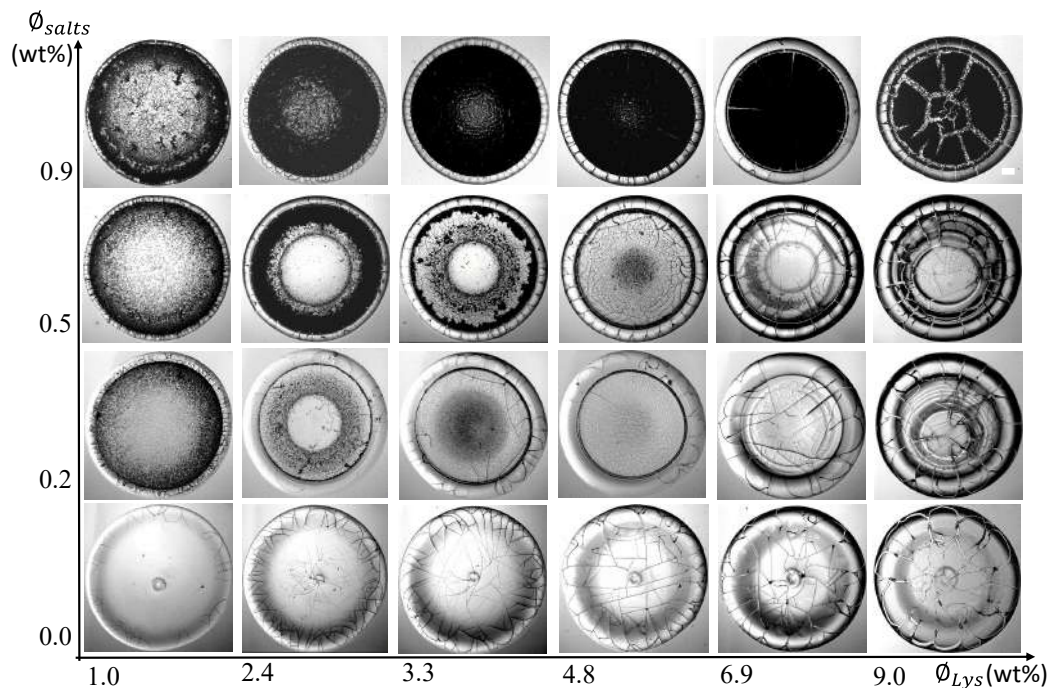


FIGURE 7.1: Morphological patterns in the drying droplets of Lys are displayed. These patterns are shown for the various initial concentrations of Lys (ϕ_{Lys}) at the initial concentrations of salts present in the phosphate buffer saline (ϕ_{salts}). The $\phi_{salts} = 0$ wt% means that it is prepared in the de-ionized water. The scale bar is of length 0.15 mm.

Lys solution prepared in the de-ionized water. Though all these deposits show the “coffee-ring” effect (Deegan et al., 1997), the diverse patterns are observed for each ϕ_{Lys} and ϕ_{salts} . The Lys films show a mound-like structure when the solution is prepared without any external salts. A dimple (or depression) is also noticed within this mound. The mound area gets wider as the ϕ_{Lys} increases. The random cracks are only observed in the peripheral ring at $(\phi_{Lys}, \phi_{salts}) = (1.0, 0.0)$ wt%. However, these cracks are spread throughout the film as the ϕ_{Lys} increases. The radial and ortho-radial cracks promote well-connected (small and large) domains in these droplets. Some fringes appear in the concentrated Lys samples at $\phi_{salts} = 0$ wt%. Many domains in the ring get delaminated, which are predominantly observed at $(\phi_{salts}, \phi_{Lys}) = (0.0, 9.0)$ wt%. The concentration dependence of these Lys droplets in the salts’ absence is detailed in our previous chapter. A comparison of these patterns reveals that the mound diminishes in the salts’ presence. However, no general trend in these patterns is observed at a fixed ϕ_{salts} . Interestingly, such a trend is noticed when ϕ_{Lys} is fixed and ϕ_{salts} is varied. For example, at $\phi_{Lys} = 1.0$ wt%, the ring width decreases with the increasing ϕ_{salts} . The central region becomes grainy. The texture becomes darker, and some thread-like structures appear in the central region. The samples at $\phi_{salts} = 0.9$ wt% display a dark texture in the central region and a gray texture in the peripheral ring. The various textural regions are observed in the central region. The multiple rings are also found in the highly concentrated Lys samples. The random small cracks are observed at $\phi_{Lys} = 1.0$ wt% whereas, mostly radial cracks are found

in the peripheral ring as ϕ_{Lys} increases in the salts' presence. In contrast, no overall drift is found whether these cracks intervene in the central region. For instance, the sample at $(\phi_{Lys}, \phi_{salts}) = (9.0, 0.9 \text{ wt}\%)$ shows crack patterns, whereas other samples at $\phi_{salts} = 0.9 \text{ wt}\%$ do not. In the presence of the low salt concentrations, different cracks are observed in the Lys droplets in the central region at $\phi_{Lys} \geq 6.9 \text{ wt}\%$. Though these optical images showcase these patterns globally, it is to be noted that these do not reveal any microstructural information.

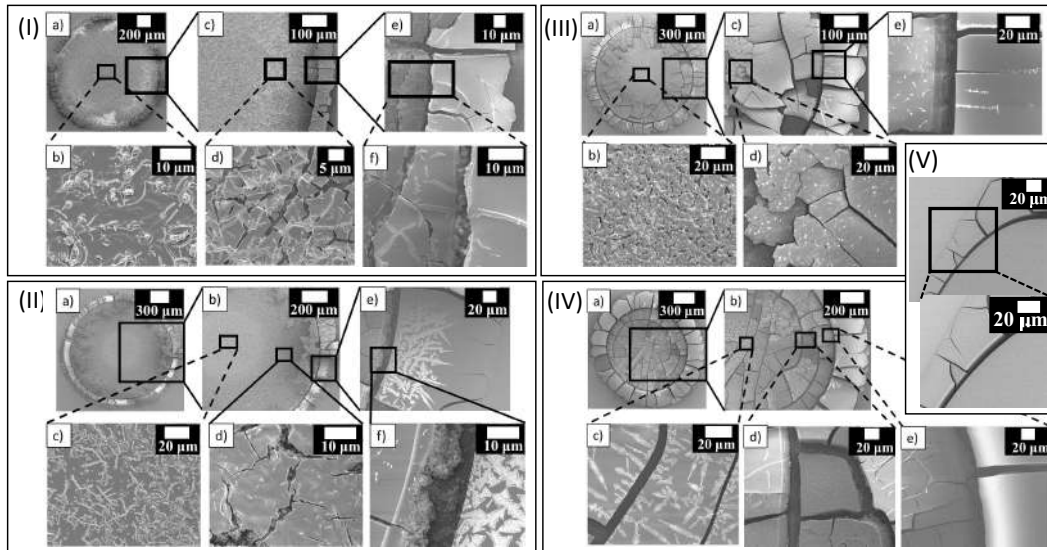


FIGURE 7.2: Microscopic images of the dried Lys samples are displayed. $(\phi_{Lys}, \phi_{salts}) = (1.0, 0.5)$ in (I), $(\phi_{Lys}, \phi_{salts}) = (3.3, 0.5)$ in (II), $(\phi_{Lys}, \phi_{salts}) = (4.8, 0.5)$ in (III), $(\phi_{Lys}, \phi_{salts}) = (9.0, 0.5)$ in (IV), and $(\phi_{Lys}, \phi_{salts}) = (9.0, 0.0)$ in (V). The different length scales are shown as the scale bars in the upper-right corner of each image.

Figure 7.2(I-IV) exhibits the microstructures of the various concentrated Lys samples at $\phi_{salts} = 0.5 \text{ wt}\%$. The sample at $(\phi_{Lys}, \phi_{salts}) = (9.0, 0.0) \text{ wt}\%$ is displayed in Fig. 7.2(V). The different regions in the central and peripheral regions were emphasized in all these samples. The sample shows a uniform homogeneous texture in the absence of any external salts [see Fig. 7.2(V)]. In contrast, the distinct texture is observed at different regions in the salts' presence [see Fig. 7.2(IV)]. Not only that, but some non-uniform structures are also uncovered in the crack lines separating the periphery and the central regions. Comparing the central and the peripheral regions, the smooth texture is mostly found in the peripheral ring. However, some snowflakes-like structures appear in the inner ring of the periphery at $(\phi_{Lys}, \phi_{salts}) = (3.3, 0.5) \text{ wt}\%$ [see Fig. 7.2(II)]. The crystal-like structures are discovered in the zone between the central and peripheral regions at $(\phi_{Lys}, \phi_{salts}) = (1.0, 0.5) \text{ wt}\%$ [see Fig. 7.2(I)]. These structures are not so prominent as we move towards the central region of the film. The central region is mostly replaced with different forms of the dendrite structures; long but thin structures at $(\phi_{Lys}, \phi_{salts}) = (3.3, 0.5) \text{ wt}\%$ whereas shorter but thicker structures at $(\phi_{Lys}, \phi_{salts}) = (9.0, 0.5) \text{ wt}\%$ [see Figs. 7.2(II) and (IV)]. The middle region (between peripheral and the central regions) is mostly occupied with a grainy amorphous layer in these samples. On the other hand, it is

hard to differentiate this layer between the middle and the central regions at $(\phi_{Lys}, \phi_{salts}) = (4.8, 0.5)$ wt% [see Fig. 7.2(III)].

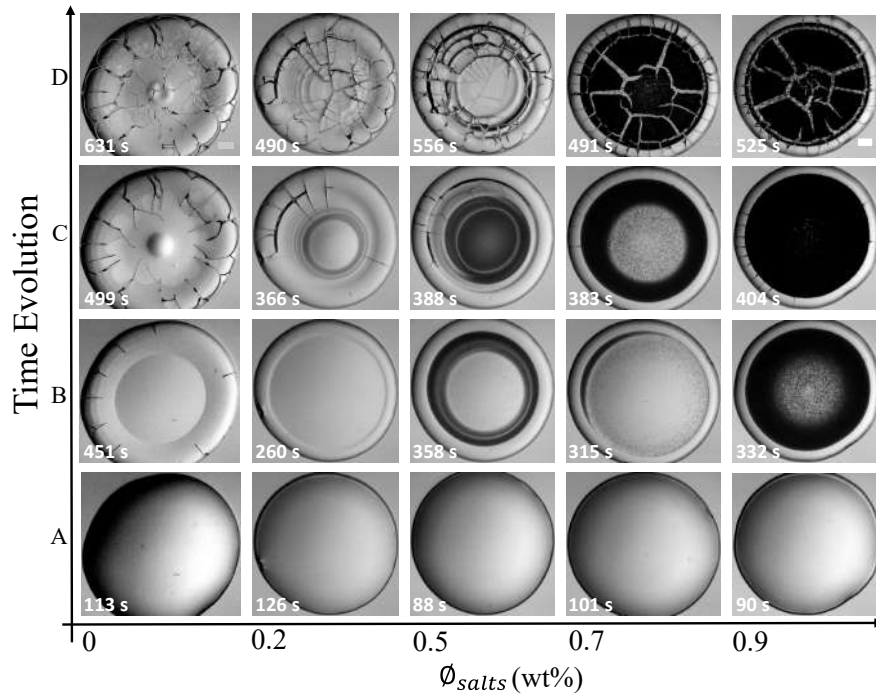


FIGURE 7.3: The time evolution of Lys droplets ($\phi_{Lys} = 9$ wt%) at various initial concentrations of salts in PBS (ϕ_{salts}) during the drying process is displayed in A-D. The $\phi_{salts} = 0$ wt% embodies the Lys solution prepared in the de-ionized water. The timestamps are shown at the left-bottom of each image. The white rectangle represents a scale bar of length 0.15 mm in the top-right.

To understand how these distinct structures appear in different regions, we examined the drying evolution and dried morphology by keeping ϕ_{Lys} at 9.0 wt%, and only the ϕ_{salts} is varied from 0.2 to 0.9 wt%. Figure 7.3(A-D) describes the drying evolution of the Lys droplets, where the first set of images were captured for the solution prepared in the de-ionized water ($\phi_{salts} = 0$ wt%). A uniform gray texture with a dark peripheral band is observed in all the droplets when the first image is captured of the drying process [see Fig. 7.3(A)]. As time progresses, the fluid front moves from the periphery to the central region [see Fig. 7.3(B)]. Surprisingly, the texture of the front movement changes in the salts' presence. Once the peripheral ring emerges, the grainy texture starts developing in the central region. Clearly, a distinction is visible at the interface of the inner peripheral ring. At $\phi_{salts} = 0.2$ wt%, the development of the dark texture is not predominantly observed, whereas the darkness increases as the ϕ_{salts} rises. Simultaneously, the cracks propagate from the periphery towards the center. However, the propagation is not smooth, unlike $\phi_{salts} = 0$ wt% and found to be interrupted in the presence of the salts. The mound-like structure begins in the last stage of this fluid front movement, but the salts' presence diminishes its formation in the central region. The multiple rings are found as the front's radius gets smaller [see Fig. 7.3(B-C)]. The final morphological patterns after the visible drying process are captured in Fig. 7.3(D).

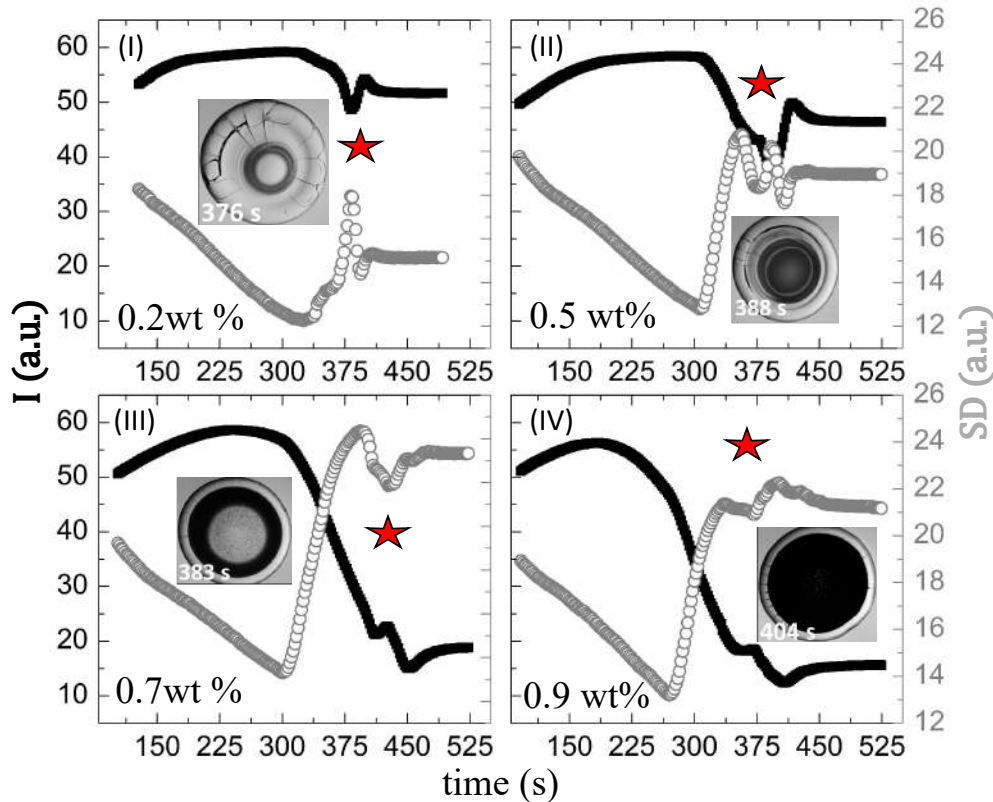


FIGURE 7.4: Textural analysis of the Lys droplets ($\phi_{Lys} = 9$ wt%) at various initial concentrations of salts in PBS (ϕ_{salts}) during the drying process is displayed in (I-IV). The x-axis defines the drying time. The left-y (shown in back color squares) and right-y axes (shown in gray color circles) in each graph describe the mean gray values (I) and the standard deviation (SD) in arbitrary units (a.u.), respectively. The star symbol indicates the parameters' fluctuations. The optical image represents the droplets' morphology when significant changes in these parameters are observed.

Figure 7.4(I-IV) shows the quantitative analysis of the textural evolution during the drying process. The first-order statistical parameters, the mean gray values (I), and the standard deviation (SD) are displayed as a function of the drying time (in seconds) at ϕ_{salts} ranging from 0.2 to 0.9 wt%. It is to be noted that these parameters describe the gray level distribution of the image's pixel intensity. The I defines the averaged values, whereas the SD illustrates the textural complexity. The I stays nearly constant at the beginning of the drying process. It reduces and then fluctuates [marked with a star in Fig. 7.4(I-IV)]. In contrast, the SD starts decreasing linearly till ~ 300 s and rapidly rises till ~ 375 s. It decreases, grows again [marked with a star in Fig. 7.4(I-IV)]. Finally, both the I and SD saturate in the later phase of the drying evolution. Interestingly, both the I and SD exhibit significant changes for ~ 150 s, i.e., between ~ 300 and ~ 450 s. The I varies within ~ 15 a.u. at $\phi_{salts} = 0.2$ wt%. This change in I increases with the rise of ϕ_{salts} ; for instance, the I reduces from ~ 50 to ~ 20 a.u. at $\phi_{salts} = 0.9$ wt%. The images [shown in Fig. 7.4(I-IV)] show that the variation in these textural parameters (I and SD) occurs considerably when the dark textured fluid front moves in the central region.

7.2.2 Drying evolution and morphology of BSA-saline droplets

Temporal study of the BSA-saline drying droplets

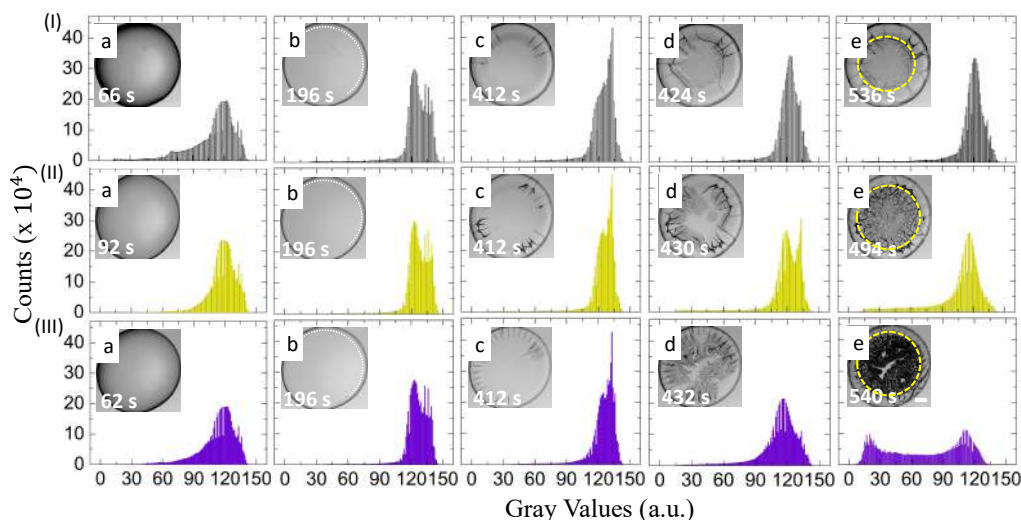


FIGURE 7.5: BSA saline droplets at different initial salts concentration in PBS (ϕ_{salts}): The insets show the drying evolution of the droplets is displayed in a-e at ϕ_{salts} of (I) 0.9, (II) 1.8, and (III) 4.3 wt%. The first image is taken within ~ 90 seconds after their deposition on the substrate and is presented in a. The movement of the fluid front is indicated with the white dotted curved lines in b. The appearance of the radial cracks in the periphery and their inward propagation is mostly seen in c. The texture of the droplets changes due to the presence of the salts and is described in c-d. A dashed circular yellow line outlines the rim. The images are taken after completion of the process in e. The time at which the images are captured is shown at the left corner in every image. The scale bar corresponds to 0.2 mm. The different colored histograms depict the counts of the pixels along the y-axis, and the gray values along the x-axis of each image in a-e at various ϕ_{salts} .

Figure 7.5(I-III) shows the pixel counts as a function of gray values for BSA-saline droplets at different ϕ_{salts} of 0.9, 1.8, and 4.3 wt%. The images of the time evolution during the drying process are displayed in the insets of Fig. 9.1(I-III) a-e. The first image was captured within ~ 1.5 minutes after the deposition of these droplets on the substrate (coverslip). The droplets show dark gray shade near the periphery. The light gray texture covers most of the droplet's area at each ϕ_{salts} (Fig. 7.5(I-III) a). The histograms [black in (I), yellow in (II), violet in (III)] extracted from the images (Fig. 7.5(I-III) a) indicate a Gaussian distribution between ~ 90 and ~ 130 gray values with a flatter tail on the left side of the distribution. The fluid front recedes from the periphery towards the center within ~ 1 minute of the droplets' deposition. The movement continues for ~ 3 minutes. The white dashed curved lines in Fig. 7.5(I-III) b mark its movement from the periphery to the center. The distribution in the tail is reduced. Moreover, the symmetry in the distribution disappears when the histogram is compared between Fig. 7.5(I-III) a and b. As time progresses, more water evaporates from these droplets. A bulged ring near the periphery is observed. Two different regions (the rim and the center) are established. These regions are marked with a dashed yellow circular line. Furthermore, the equally spaced radial

cracks and a few orthoradial cracks near the periphery are noticed (Fig. 7.5(I-III) c).

The fluid front continues to move while the radial cracks propagate, and intervene through the rim to the central region at each ϕ_{salts} . Interestingly, a spike at a gray value of ~ 200 is observed (Fig. 7.5(I-III) c). The grainy structures start forming near the rim's inner edge, and these structures cover the entire central region (Fig. 7.5(I-III) d). As the salt crystals grow more and more, the texture becomes dark, and the pixel values decrease. The pixel counts also reduce when the saline concentration (ϕ_{salts}) increases from 0.9 to 4.3 wt%. The final morphology is presented at the end of the visible drying process (Fig. 7.5(I-III) e). The texture of the rim is transparent at $\phi_{salts} = 0.9$ wt% (Fig. 1(I) e) and does not contain any optically visible structures like what observed in the BSA film prepared with only de-ionized water (Pal et al., 2020a). This texture becomes less transparent with the increase of the saline concentration from 1.8 to 4.3 wt% (Fig. 7.5(II-III) e). The central region appears to be grainy near the dashed yellow line and (mostly) gray in the center at $\phi_{salts} = 0.9$ wt%. In contrast, this region turns out to be inhomogeneous, and the texture becomes dark gray with the upsurge of ϕ_{salts} . The radial cracks are observed to propagate towards the central region at ϕ_{salts} of 0.9 and 1.8 wt%; however, it is hard to conclude anything for 4.3 wt% (Fig. 7.5(III) e). The pixel distribution changes to Gaussian at 0.9 and 1.8 wt% (Fig. 7.5(I-II) e). Surprisingly, a bi-modal distribution is observed at 4.3 wt%, where the first and second peaks are observed at 20 and 120 gray values, respectively (Fig. 7.5(III) e).

FOS characterization of BSA-saline drying droplets

Figure 7.6(I-IV) exhibits the first-order statistics (FOS) parameters (mean (I), standard deviation (SD), skewness ($SKEW$), and kurtosis (KUR)] respectively as a function of drying time at the different initial saline concentration (ϕ_{salts}) of 0.9 to 4.3 wt%. The I in Fig. 7.6(I) increases from ~ 50 arbitrary units (a.u.) to ~ 65 a.u. till ~ 200 seconds. It remains the same for the next 200 seconds (~ 200 to ~ 400 seconds, outlined with dashed lines). Interestingly, the I does not indicate any significant change for different ϕ_{salts} until ~ 400 seconds. After that, it starts decreasing from ~ 65 to ~ 50 a.u. for 0.9 and 1.8 wt%, whereas it reduces to ~ 10 a.u. at $\phi_{salts} = 4.3$ wt%. The SD , on the other hand, depends on different ϕ_{salts} before ~ 400 seconds unlike the I [Fig. 7.6(I-II)]. The SD initially displays a decrease from ~ 20 to ~ 10 a.u., whereas an upsurge is observed in the later time from ~ 400 seconds [Fig. 7.6(II)]. The $SKEW$ in Fig. 7.6(III) illustrates the negative values that decrease from -1.5 to -4.5 a.u. till 400 seconds; however, it starts increasing afterward. On the other hand, the KUR in Fig. 7.6(IV) shows an increasing trend until ~ 350 seconds. It declines as the drying process ends. It is worthy to mention that the I shows three ubiquitous stages (illustrated with dotted lines at ~ 200 seconds and ~ 400 seconds). In contrast, the other parameters (SD , $SKEW$, and KUR) reveals multiple peaks and dips throughout the drying process.

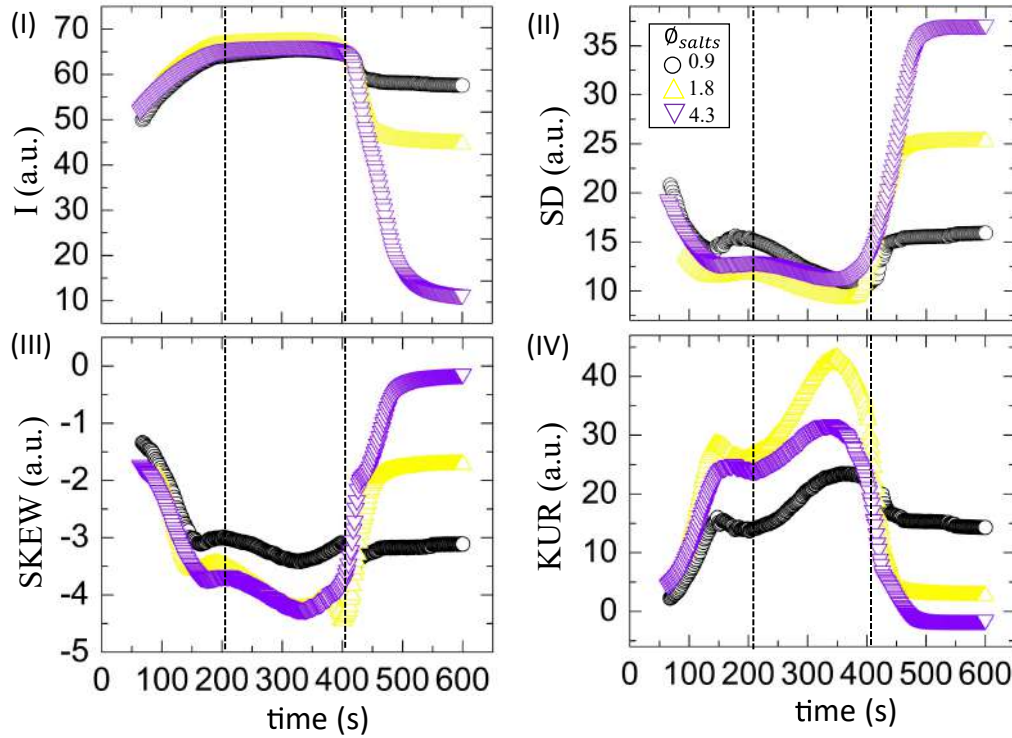


FIGURE 7.6: (I-IV) shows the time evolution of the first-order statistical (FOS) parameters [mean (I), standard deviation (SD), skewness ($SKEW$), and kurtosis (KUR)] in arbitrary units (a.u.), respectively in the BSA saline droplets as a function of drying time at the different initial salt concentrations in PBS (ϕ_{salts}) of 0.9 to 4.3 wt%. The different stages of the drying process are outlined with the dashed lines in I-IV.

GLCM characterization of BSA-saline drying droplets

The GLCM (Gray Level Co-occurrence Matrix) parameters are the second-order statistics calculated from the spatial relationship between two neighboring pixels (Carreón et al., 2018b). This makes GLCM parameters complicated and different from the first-order statistics (FOS), which solely depends on the individual pixel values (Zhou et al., 2017; Cai et al., 2019). Before establishing any relationship between two neighboring pixels, it is crucial to address a few things. For example, what will be the displacement between the neighboring pixels? Should the displacement be close at each other? What if the displacement between the pixels is far enough? Are there any limitations? What are the directions of the pixels? Which pixels should be counted- the pixels which are placed horizontally or vertically, or their average? In our study, we examined how the directions can be used in extracting the GLCM parameters such as the angular second moment (ASM), correlation (COR), entropy (ENT), and inverse difference moment (IDM) at various initial concentrations (ϕ_{salts}) from 0.9 to 4.3 wt%. Furthermore, a non-parametric Mann-Whitney U test is performed to see whether these GLCM parameters are rotationally invariant along the horizontal (0°) and the vertical (90°) orientations for the BSA-saline droplets. In the test, the rotation was kept as the independent factor, with two levels, 0° , and 90° . The GLCM parameters are chosen as the dependent variables. The

mean over the median rank in the test is chosen as the number of time points during the drying process is observed to be relatively large. The $p \leq 0.05$ is considered to be significant interaction [indicated with an asterisk]. The detailed report of the statistical test (Mann-Whitney U, Wilcoxon W, Z, and Asymptotic Significant (2-tailed) p-values) is shown in the Tables 7.1-7.4.

TABLE 7.1: Detailed report of Mann Whitney U test for *ASM* (angular second moment) at each initial concentration of salts in PBS (ϕ_{salts} of 0.9 to 4.3 wt%) and displacement (d) from 1 to 1000 (in pixels). The significant values are marked with an asterisk (*).

ϕ_{salts} (wt%)	d (pixels)	Mann-Whitney U	Wilcoxon W	Z	p value
0.9	1	33231.000	69546.000	-1.636	.102
0.9	10	33215.500	69530.500	-1.645	.100
0.9	50	31300.500	67615.500	-2.707	.007*
0.9	100	30750.000	67065.000	-3.012	.003*
0.9	1000	194.000	36509.000	-19.961	.000*
1.8	1	42802.500	87055.500	-.623	.534
1.8	10	41722.000	85975.000	-1.139	.255
1.8	50	39085.000	83338.000	-2.400	.016*
1.8	100	39288.000	83541.000	-2.303	.021*
1.8	1000	6857.500	51110.500	-17.810	.000*
4.3	1	43900.000	88153.000	-.098	.922
4.3	10	43633.000	87886.000	-.225	.822
4.3	50	40752.000	85005.000	-1.603	.109
4.3	100	40508.000	84761.000	-1.720	.085
4.3	1000	15612.000	59865.000	-13.624	.000*

TABLE 7.2: Detailed report of Mann Whitney U test for *COR* (correlation) at each initial concentration of salts in PBS (ϕ_{salts} of 0.9 to 4.3 wt%) and displacement (d) from 1 to 1000 (in pixels). The significant values are marked with an asterisk (*).

ϕ_{salts} (wt%)	d (pixels)	Mann-Whitney U	Wilcoxon W	Z	p value
0.9	1	33647.000	69962.000	-1.405	.160
0.9	10	22395.500	58710.500	-7.646	.000*
0.9	50	319.000	36634.000	-19.892	.000*
0.9	100	.000	36315.000	-20.069	.000*
0.9	1000	.000	36315.000	-20.071	.000*
1.8	1	43863.500	88116.500	-.115	.908
1.8	10	42994.000	87247.000	-.531	.595
1.8	50	42123.500	86376.500	-.947	.344
1.8	100	27318.500	71571.500	-8.026	.000*
1.8	1000	.000	44253.000	-21.096	.000*
4.3	1	41866.500	86119.500	-1.070	.285
4.3	10	33796.500	78049.500	-4.929	.000*
4.3	50	22389.500	66642.500	-10.383	.000*
4.3	100	21090.000	65343.000	-11.005	.000*

4.3	1000	10918.000	55171.000	-15.870	.000*
-----	------	-----------	-----------	---------	-------

TABLE 7.3: Detailed report of Mann Whitney U test for *ENT* (entropy) at each initial concentration of salts in PBS (ϕ_{salts} of 0.9 to 4.3 wt%) and displacement (d) from 1 to 1000 (in pixels). The significant values are marked with an asterisk (*).

ϕ_{salts} (wt%)	d (pixels)	Mann-Whitney U	Wilcoxon W	Z	p value
0.9	1	34067.000	70382.000	-1.172	.241
0.9	10	33818.000	70133.000	-1.310	.190
0.9	50	31579.000	67894.000	-2.552	.011*
0.9	100	31043.000	67358.000	-2.850	.004*
0.9	1000	14081.000	50396.000	-12.258	.000*
1.8	1	42874.000	87127.000	-.588	.556
1.8	10	41343.000	85596.000	-1.320	.187
1.8	50	39717.000	83970.000	-2.098	.036*
1.8	100	42385.000	86638.000	-2.822	.041*
1.8	1000	29060.000	73313.000	-7.194	.000*
4.3	1	41857.000	86110.000	-1.075	.283
4.3	10	43664.000	87917.000	-.211	.833
4.3	50	41925.500	86178.500	-1.042	.297
4.3	100	40075.000	84328.000	-1.927	.054
4.3	1000	27657.000	71910.000	-7.865	.000*

TABLE 7.4: Detailed report of Mann Whitney U test for *IDM* (inverse difference moment) at each initial concentration of salts in PBS (ϕ_{salts} of 0.9 to 4.3 wt%) and displacement (d) from 1 to 1000 (in pixels). The significant values are marked with an asterisk (*).

ϕ_{salts} (wt%)	d (pixels)	Mann-Whitney U	Wilcoxon W	Z	p value
0.9	1	31820.000	68135.000	-2.419	.061
0.9	10	29329.000	65644.000	-3.800	.000*
0.9	50	25264.000	61579.000	-6.055	.000*
0.9	100	23918.000	60233.000	-6.802	.000*
0.9	1000	7871.000	44186.000	-15.703	.000*
1.8	1	41822.000	86075.000	-1.091	.275
1.8	10	36134.000	80387.000	-3.811	.000*
1.8	50	35133.000	79386.000	-4.290	.000*
1.8	100	42703.000	86956.000	-.670	.043*
1.8	1000	13886.000	58139.000	-14.449	.000*
4.3	1	42020.500	86273.500	-.996	.319
4.3	10	39893.500	84146.500	-2.014	.044*
4.3	50	34924.000	79177.000	-4.390	.000*

4.3	100	34434.000	78687.000	-4.624	.000*
4.3	1000	26440.000	70693.000	-8.447	.000*

Figure 7.7(I-IV) maps the histograms of the averaged GLCM parameters at various rotations (0° and 90°), displacements (1, 10, 50, 100, and 1000), and initial saline concentrations ($\phi_{salts} = 0.9, 1.8, \text{ and } 4.3 \text{ wt\%}$). The error bars represent the standard deviation. These deviations are large as the GLCM parameters change as the droplets dry under ambient conditions. All these parameters show non-significant results (rotationally invariant) when the displacement between the neighboring pixels is 1 at each ϕ_{salts} . The *ASM* and *ENT* are only rotationally invariant when the displacement increases to 10 [Fig. 7.7(I, III)]. These parameters are found to be non-significant when the displacement becomes 50 and 100 only at $\phi_{salts} = 4.3 \text{ wt\%}$. All the GLCM parameters show significant results when the displacement is 1000. The *COR* at displacement of 1000 pixels in Fig. 7.7(II) shows negative values for every ϕ_{salts} . It suggests that the relation between the pixels' ceases when the displacement is 1000. Fig. 7.7(IV) exhibits that the *IDM* is significantly different for 0° and 90° at all the displacements except 1. This indicates that it is the most sensitive parameter when its values are compared between two different directions. All the parameters except *ENT* show a decreasing trend in their values when the displacement increases from 1 to 1000. This suggests that the magnitude of the *ENT* get weakly influenced by the displacement values. Surprisingly, the *ASM* oriented along 90° at the pixel displacement of 1000 is significantly larger than 0° . It can be concluded that these GLCM parameters at 0° and 90° are not significantly different at the displacement of 1 pixel. It suggests that these parameters cannot be averaged for these two orientations except displacement of 1 pixel. Therefore, the averaged GLCM parameters at 1 pixel are presented for the drying evolution at different ϕ_{salts} in Figure 7.8(I-IV).

The *ASM* and the *COR* increase until ~ 400 seconds and start decreasing from ~ 400 seconds onwards [Fig. 7.8(I-II)]. All the GLCM parameters except *COR* show a master curve till ~ 400 seconds. These curves get differentiated after ~ 400 seconds for the various ϕ_{salts} . On the other hand, the *COR* shows its dependency throughout the drying process. Interestingly, the *ENT* [Fig. 7.8(III)] and the *IDM* [Fig. 7.8(IV)] behave differently than the other two parameters. The *ENT* decreases, whereas the *IDM* is found to be nearly constant until ~ 400 seconds. While the *ENT* starts increasing, the *IDM* reduces for the duration of 400 to ~ 600 seconds. All these parameters, except *ENT* of the dried films (after the visible drying process ends), show that the values are highest at ϕ_{salts} of 0.9 wt\% , followed by 1.8 and 4.3 wt\% . Interestingly, the *ENT* shows a complementary behavior compared to the *ASM* during the drying process and in the dried states [Fig. 7.8(I, III)].

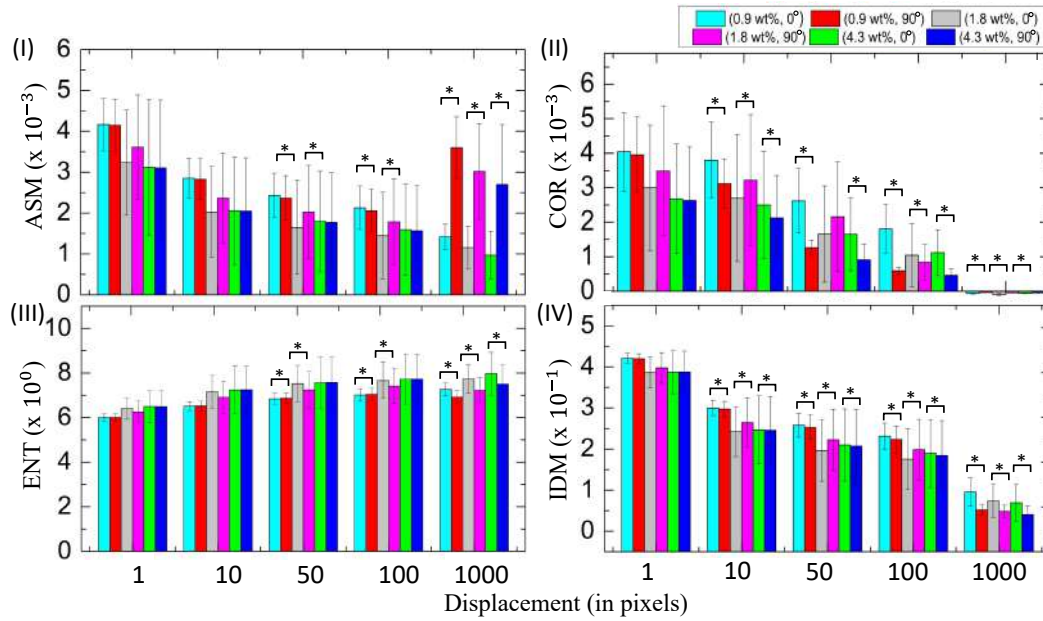


FIGURE 7.7: (I-IV) show the comparison of the averaged gray level co-occurrence matrix (GLCM) parameters [angular second moment (ASM), correlation (COR), entropy (ENT), and inverse difference moment (IDM)] in arbitrary units (a.u.), respectively in the BSA-saline droplets at the different initial salt concentrations in PBS (ϕ_{salts}). The pixel displacements ranging from 1 to 1000, and the orientations [horizontal (0°) and vertical (90°)] are varied at each ϕ_{salts} . The significant pairs (0° and 90°) are marked with an asterisk (*). The error bars represent the standard deviation.

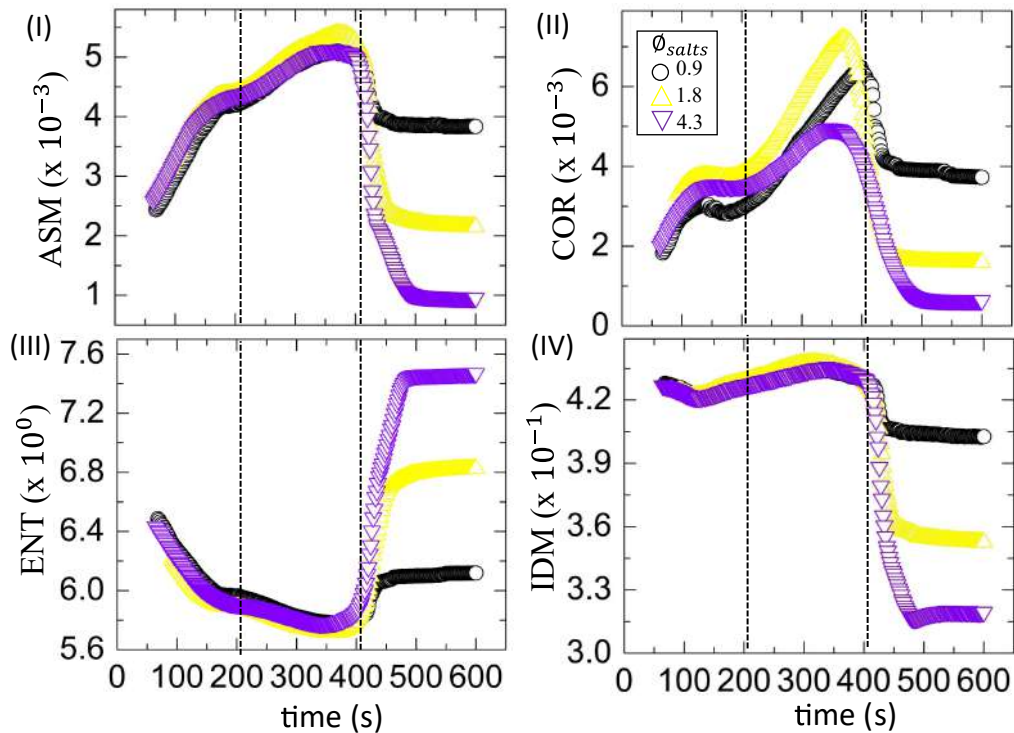


FIGURE 7.8: (I-IV) shows the time evolution of the gray level co-occurrence matrix (GLCM) parameters [angular second moment (ASM), correlation (COR), entropy (ENT), and inverse difference moment (IDM)] in arbitrary units (a.u.), respectively in the BSA saline droplets as a function of drying time at the different initial salt concentrations in PBS (ϕ_{salts}) of 0.9 to 4.3 wt%. The different stages of the drying process are outlined with the dashed lines in I-IV.

7.2.3 Drying evolution and morphology of blood-saline droplets

Time evolution of the blood-saline droplets

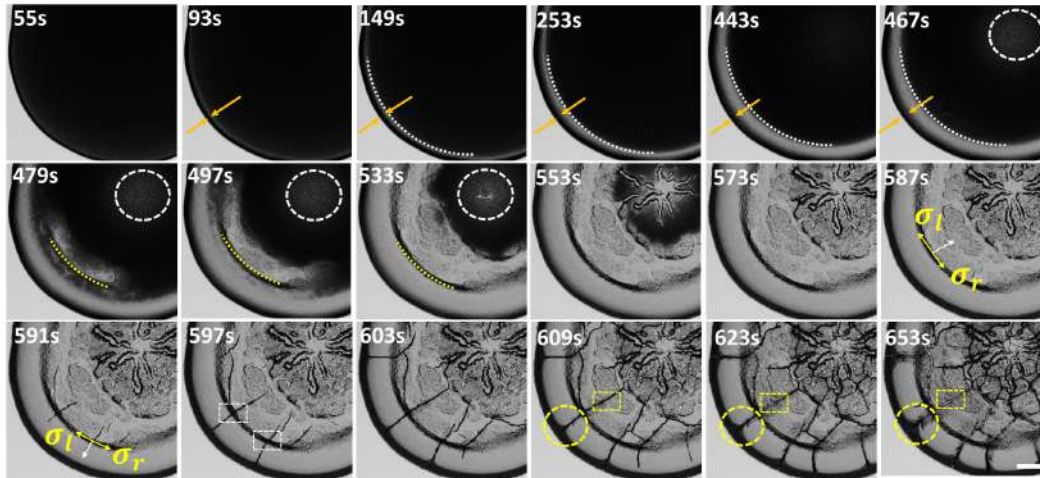


FIGURE 7.9: Time-lapse images of the diluted blood droplets during the drying process at ϕ_{blood} of 75% (v/v). These displayed images are cropped from the original ones for better visualization. The top panel illustrates the formation of the peripheral band (depicted with orange arrows) and the fluid front movement. The white dashed arc line shows that the front moves uniformly from the periphery of the droplet up to 467s. The texture in the central region becomes lighter, outlined with a white dashed circle. The middle panel captures the images from 479s to 587s. This panel emphasizes the non-uniform movement of the front and the appearance of the dendrite structure in the central region. The yellow dashed arc line separates the corona from the central region. The white arrows sketch the propagation of the radial cracks. The σ_l and σ_r demonstrate the symmetric stress fields of these cracks (depicted with yellow arrows). The bottom panel records the crack propagation from 591s to 653s. At the transition of the corona and the central regions, the cracks grow in both directions, and a kink is spotted (white dashed rectangles). The yellow dashed circles display the origin of the micro flaws around the radial crack, whereas the yellow dashed rectangles portray the widening of these radial cracks. The actual time (t in seconds) during the drying process is exhibited in the top-left corner of each image. The scale bar in the bottom-right corner at 653s corresponds to 0.2 mm .

The time-lapse images are captured in bright field microscopy (Amscope, USA) at a magnification of $5\times$ at a fixed resolution of 3664×2748 pixels. Figure 7.9 shows the drying process of the diluted blood droplet at ϕ_{blood} of 75% (v/v). These images were cropped from the original images to 1812×1656 pixels. The formation of the peripheral band, the uniform movement of the fluid front, and the appearance of the central light gray texture occur from 55s to 467s. All these events are found to be common at ϕ_{blood} of 100 and 75% (v/v) [shown in the top panel of Figs. 7.9].

The next stage of the drying evolution begins with the non-uniform movement of the fluid front. The front in the whole blood droplet [100% (v/v)] (described in the earlier chapter) completely disappears after which the corona (the region between the periphery and the central regions) and the central regions could be identified. In contrast, at ϕ_{blood} of 75% (v/v), a transition line appears (marked with yellow dashed arc line in the snapshot captured at 479s) while the front still moves non-uniformly.

This line continues developing until it fully grows to a ring. Finally, it separates the corona and the central regions similar to the whole blood droplet (middle panel of Figs. 7.9). It is to be noted that the corona at $\phi_{blood} = 75\%$ (v/v) covers a smaller area than that of the whole blood droplet. Interestingly a dendrite structure starts appearing in the center of the droplet at ϕ_{blood} of 75% (v/v). The growth of such a structure is evident for the time intervals between 533s and 573s. Its presence makes the drying evolution very different from that of the whole blood. The crack propagation initiates from the transition region at 587s. The white and the yellow arrows show the direction of the cracks and the symmetric stress fields, respectively (snapshots at 587s and 591s). Unlike the 100% (v/v) [described in the earlier chapter], some cracks grow towards the central region whereas, some propagate towards the periphery. It is to be noted that the crack lines in the transition region are not straight. A kink around the transition line is spotted (white dashed rectangles at the snapshot of 597s). The cracks propagating towards the central region, join the dendrite structure as the time advances. In contrast, the cracks in the corona region divide it into different domains, similar to the human whole blood.

Akin to whole blood droplet, the branching and the widening of the radial cracks are found at ϕ_{blood} of 75% (v/v) from 609s to 653s. The yellow dashed circles display the origin of the micro flaws around the radial crack whereas, the yellow dashed rectangles portray the widening of these radial cracks in the snapshots captured from 609 s. However, the texture within the crack domains in the corona region does not become dark gray fully. Furthermore, the droplet's periphery is observed in the same position throughout the drying process, unlike the whole blood droplet (bottom panel of Figs. 7.9). Therefore, it is clear that the presence of the salts affects the events of the drying process and the resulting crack patterns.

Figure 7.10a-d displays different image snapshots during the drying process in the diluted blood droplets at ϕ_{blood} of 62 to 12.5% (v/v). The first image is captured within ~ 90 s after the deposition of the droplets on the coverslip (Fig. 7.10a). Initially, these images have a homogeneous dark texture, which is found to be independent of the dilution concentration (ϕ_{blood}). In the next stage, the droplets show the formation of the peripheral band. It is followed by the uniform and the non-uniform movement of the fluid front. These events are observed within ~ 600 s at ϕ_{blood} of 62 to 25% (v/v). However, the droplet at ϕ_{blood} of 12.5% (v/v) takes ~ 740 s for these events to occur (Fig. 7.10b-c). The texture of the droplets at ϕ_{blood} of 62 to 50% (v/v) is homogeneous light gray. This becomes non-homogeneous and grainy for 25 and 12.5% (v/v). The center at all ϕ_{blood} of 62 to 12.5% (v/v) is found to have a patchy dark gray shade (Fig. 7.10c). The snapshots at the end of the drying process in Fig. 7.10d show the final macroscopic patterns. Interestingly, no dendrite structure is evolved in any of these ϕ_{blood} . Akin to ϕ_{blood} of 75% (v/v), the radial cracks are present in the corona at ϕ_{blood} of 62 to 25% (v/v). These cracks divide the corona into different domains. However, at 12.5% (v/v), only one or two cracks are visible

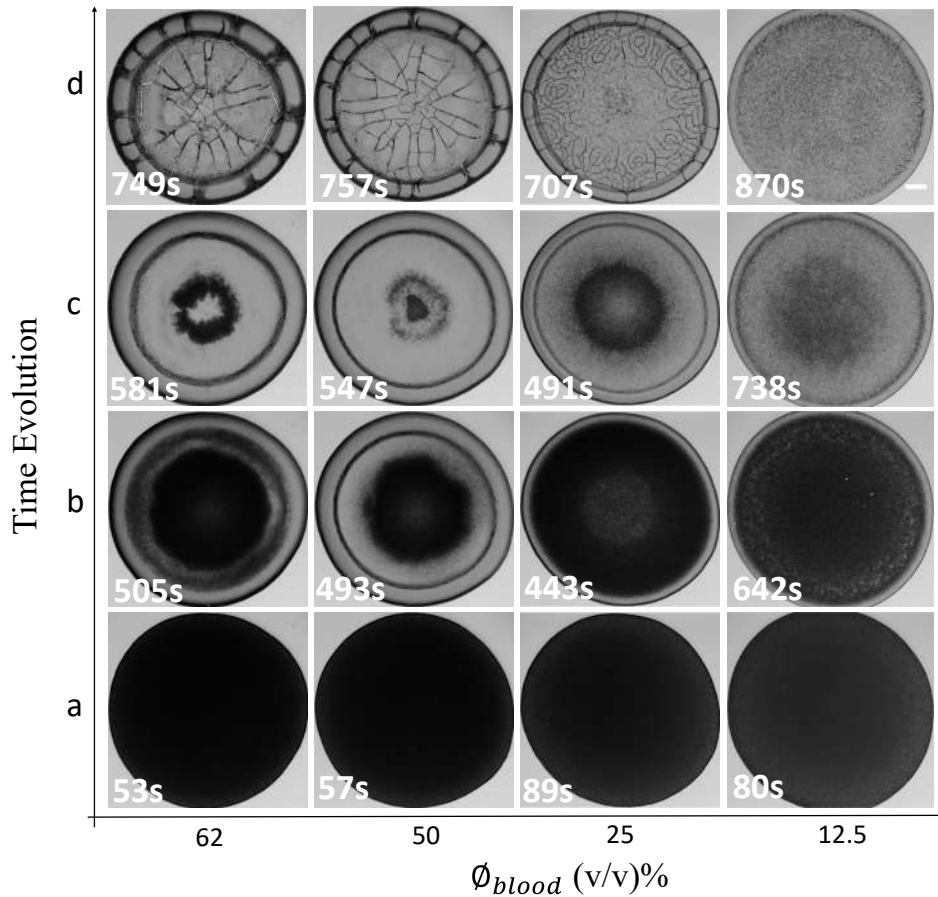


FIGURE 7.10: Time-lapse images of the diluted blood droplets during the drying process at ϕ_{blood} varying from 62 to 12.5% (v/v). The first captured image after the deposition of the droplet on the coverslip is shown in (a). All the droplets show a homogeneous dark gray texture initially. (b) depicts the next stage that starts with the fluid front movement. Simultaneously, a peripheral band forms, and a light gray texture appears in the center in (b). The formation of different textures in the corona and the central regions is mostly observed in (c). The macroscopic crack patterns as the last stage of the drying process are exhibited in (d). The actual time (t in seconds) is shown in the left corner of every image. The scale bar in the right corner of 12.5(d) corresponds to 0.2 mm.

under the present resolution ($5\times$ magnification). Furthermore, the corona is not covered fully with the dark gray texture. This coverage becomes less with the increase of the dilution. The transition region is thick at ϕ_{blood} of 62% but, turns out to be thin enough at 12.5% (v/v). The central region is drastically changed as the samples are diluted. At ϕ_{blood} of 62 and 50% (v/v), the cracks are radially extended. However, there are long branches at some of the radial cracks (orthoradial cracks) which join these consecutive radial cracks. Surprisingly, no radial cracks are observed at $\phi_{blood} = 25\%$ (v/v). A ring-like pattern is found around the edges of the central region. No cracks are visible at the center. At ϕ_{blood} of 12.5% (v/v), the central region exhibits a heterogeneous (grainy) texture without any cracks.

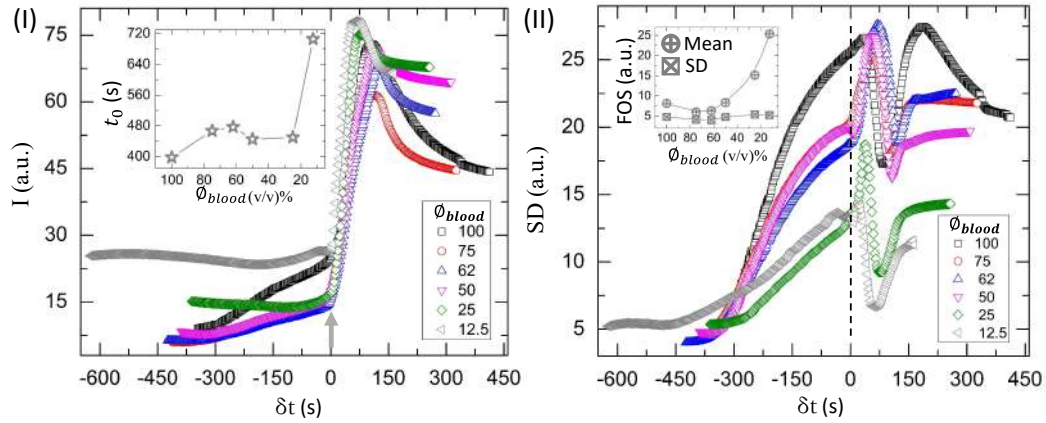


FIGURE 7.11: Time evolution of the first-order statistical (FOS) parameters: (I) the mean (I) and (II) the standard deviation (SD) at ϕ_{blood} varying from 100 to 12.5% (v/v). The δt is the shifted time computed by subtracting t_0 from t , where, t_0 is the time when the mean exhibits a rapid rise (indicated with an arrow) and t is the actual time (in seconds) of the drying process. The inset of (I) depicts the variation of t_0 with ϕ_{blood} . The FOS parameters of the first captured image during the drying process are plotted as a function of ϕ_{blood} in the inset of (II). The dashed line in (II) marks the time at which the mean rapidly rises.

Quantitative analysis of blood-saline droplets

Fig. 7.11(I-II) illustrates the temporal variation of the first-order statistical (FOS) parameters (the mean and the standard deviation) of the image at the different diluting concentrations (ϕ_{blood}) from 100 to 12.5% (v/v). The time in the x axis is the shifted time (δt) which is computed as $t - t_0$, where, t_0 is the time when the mean exhibits a rapid rise (indicated with an arrow in [Fig. 7.11(I)] and t is the actual time (in seconds) of the drying process. The mean is defined as the sum of the gray values of all the pixels divided by the number of the pixels. And, the SD is a measure of the range of pixel values deviated from the mean. The inset of (I) plots t_0 as a function of diluting concentration (ϕ_{blood}). The mean and the SD of the first image during the drying process is displayed in the inset of (II) as a function of ϕ_{blood} .

The mean (I) in Fig. 7.11(I) exhibits a universal behavior independent of the initial dilution concentration (ϕ_{blood}). It shows four different phases: a slow increase, a rapid rise, a gradual decrease, and a saturation. The first phase varies within 10 – 20 arbitrary units (a.u.). This phase stays up to the time at which the fluid front moves uniformly. As soon as the gray texture of the central region starts appearing, the I rapidly rises from ~ 25 to ~ 75 a.u. The I gradually decreases once the radial cracks begin, and the dark gray texture of the corona region initiates. Finally, it becomes constant once the droplets approach towards the end of the drying process. The saturated mean values at ϕ_{blood} of 100 and 75% (v/v) is ~ 50 a.u. whereas it is found within 60 – 70 a.u. as the dilution increases. Interestingly, the time taken by the droplets to reach the rapid rise phase (t_0) is different for ϕ_{blood} [inset of Fig. 7.11(I)]. t_0 varies within 380 – 480s for all ϕ_{blood} except 12.5% (v/v), the highest dilution concentration of this study. It takes the longest time of ~ 720 s to reach the rapid rise

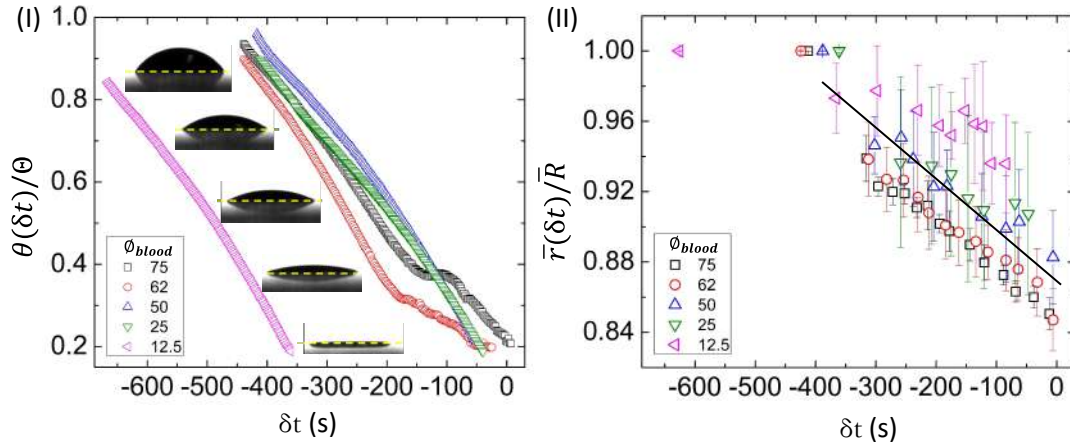


FIGURE 7.12: Variation of the normalized contact angle ($\theta(\delta t)/\Theta$) and the normalized fluid front radius ($\bar{r}(\delta t)/\bar{R}$) as a function of δt is shown in (I) and (II), respectively at ϕ_{blood} of 100 to 12.5% (v/v). The inset of (I) displays the normalized contact angle as a function of δt for the range from -200 to 30 s. The shifted time, δt is defined as $t - t_0$ where t_0 is the time when the mean exhibits a rapid rise in Fig. 7.11(I). The Θ is the intercept value which is computed by plotting the experimental contact angle ($\theta(t)$) as a function of t . The normalization of the contact angle is done by dividing the $\theta(\delta t)$ with Θ . The $\bar{r}(\delta t)/\bar{R}$ is normalized by dividing the averaged fluid front radius [$\bar{r}(\delta t)$] with the averaged radius of the droplet (\bar{R}).

phase.

The temporal variation of the SD in Fig. 7.11(II) shows a strong dependency on ϕ_{blood} . At ϕ_{blood} of 100% (v/v), it increases to a first peak at the time when $\delta t = 0$ s. It decreases from ~ 26 to ~ 17 a.u. at $\delta t \sim 75$ s. It again rises to reach a second peak at $\delta t \sim 160$ s. Finally, it decreases and saturates to ~ 20 a.u. at $\delta t \sim 375$ s. For the ϕ_{blood} ranging from 75 to 12.5% (v/v), no second peak is observed. It slowly increases to ~ 20 a.u. up to the time, $\delta t = 0$ s. Subsequently, it rapidly rises to a peak and decreases to a minimum value. Finally, it rises again to reach saturation. It is to be noted that the phases from 75 to 12.5% (v/v) are similar. However, the SD values for 25 and 12.5% (v/v) are lower than that of others. The dependency of the SD and the independent behavior of the I on ϕ_{blood} indicate that the I cannot capture the finer textural details due to its averaging criteria; however, the SD does (Pal et al., 2020b). The inset of Fig. 7.11(II) shows the I and the SD of the first captured image. It is found that I rises from ~ 5 to ~ 25 a.u. as we dilute the ϕ_{blood} . On the other hand, the SD remains nearly constant.

The experimental contact angle (θ) is plotted with the drying time (t). The Θ is computed by a linear extrapolation of the first 100 seconds of θ varying with t , where it appears linear. Subsequently, the θ is plotted as a function of δt . The normalized contact angle is measured by dividing the $\theta(\delta t)$ with Θ . Fig. 7.12(I) displays the variation of the $\theta(\delta t)/\Theta$ with respect to δt at different ϕ_{blood} . For ϕ_{blood} of 100 to 62% (v/v), the $\theta(\delta t)/\Theta$ reduces monotonically till the time at which $\delta t \sim 200$ s. A peak-like feature is observed before it stops varying [inset of Fig. 7.12(I)]. This peak becomes broader as we dilute the ϕ_{blood} from 100 to 62% (v/v). Surprisingly, no

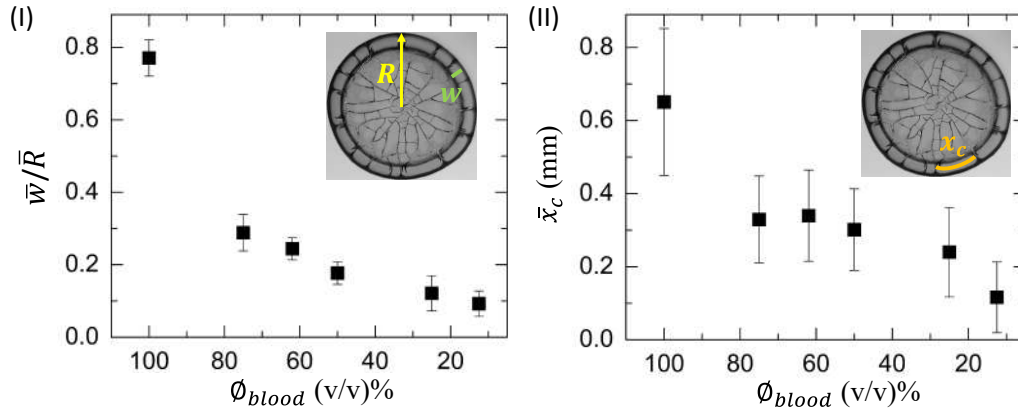


FIGURE 7.13: The variation of \bar{w}/\bar{R} and \bar{x}_c as a function of ϕ_{blood} is shown respectively in (I) and (II). The \bar{w} is the averaged width of the corona region, and the \bar{R} is the averaged radius of the droplet. The \bar{x}_c is the average crack spacing in the corona region. The error bars denote the standard deviation obtained from multiple measurements. The parameters, w , R , and x_c are illustrated in the macroscopic image captured at $\phi_{blood} = 50\%$ (v/v).

such peak is found when $\theta(\delta t)/\Theta$ is plotted as a function of δt for the range from 50 to 12.5% (v/v). Furthermore, all the curves follow a master curve except $\phi_{blood} = 12.5\%$ (v/v). The $\theta(\delta t)/\Theta$ shows a steep monotonic behavior and becomes constant at $\delta t \sim -350$ s for 12.5% (v/v).

Fig. 7.12(II) shows the evolution of the normalized fluid front radius ($\bar{r}(\delta t)/\bar{R}$) as a function of δt for the given range of ϕ_{blood} . This parameter is computed by dividing the averaged fluid front radius [$\bar{r}(\delta t)$] with the averaged radius of the droplet (\bar{R}). It could be measured till the front moves uniformly. The front radius reduces only $\sim 20\%$ from the droplet's periphery. The average slope of the $\bar{r}(t)$ vs t is found to be $-0.22 \pm 0.13 \mu\text{m/s}$. The negative sign indicates that the radius decreases with time. It exhibits a universal monotonic decrease for all ϕ_{blood} unlike the contact angle measurements. A comparison of both these measurements [Fig. 7.12(I-II)] indicates that the contact angle decreases without any fluid front movement initially. Interestingly, both the contact angle and the fluid front moves from $\delta t = -350$ s to 0s at ϕ_{blood} of 100 to 25% (v/v). It is to be noted that the front moves uniformly in this phase. Afterwards, the front moves non-uniformly, and the contact angle stops varying. Though this non-uniform movement could not be quantified, it is evident from the time lapse images in Figs. 7.9-7.10. On the other hand, $\phi_{blood} = 12.5\%$ (v/v) behaves uniquely. Both the fluid front and the contact angle do not vary simultaneously. The fluid front starts moving after the contact angle reduces to the minimum value.

Fig. 7.13(I-II) reveals the concentration dependence of the crack spacing, and the width of the corona region in the dried blood film at different diluting initial concentrations (ϕ_{blood}). Fig. 7.13(I) shows the variation of the normalized width of the corona region (\bar{w}/\bar{R}). The averaged width of the corona (\bar{w}) is found to be reduced with an increase of ϕ_{blood} . It is to note that the whole blood film shows a higher value when compared to the other ϕ_{blood} . In the presence of the salts, the \bar{w}/\bar{R} varies up

to ~ 0.3 , i.e., the width covers only $\sim 30\%$ of the radius of the droplet (Figs. 7.9-7.10). The \bar{w} decreases monotonically with the increase of ϕ_{blood} . On the other hand, this width is $\sim 80\%$ of the total value at 100% (v/v) in the absence of any salts. The variation of the averaged spacing between the radial cracks (\bar{x}_c) in the corona region is exhibited in Fig. 7.13(II). The \bar{x}_c at all ϕ_{blood} except 12.5% (v/v) is computed from the optical images. As the present resolution was not enough to measure x_c at 12.5% (v/v), it is done through the scanning electron microscopy. Similar to the corona width, the \bar{x}_c also reduces its length. The image depicting all the parameters (w , R , and x_c) in Fig. 7.13(I-II) is the dried blood film captured at $\phi_{blood} = 50\%$ (v/v). In the presence of the salts, it decreases from ~ 0.4 to ~ 0.1 mm (Figs. 7.9-7.10) whereas, it is ~ 0.6 mm for the whole blood dried film [100% (v/v)]. The standard deviation at 100% (v/v) is also larger than others. This indicates that the radial crack domains are not equal sized in the whole blood film.

Micro-structural analysis of the dried blood-saline film

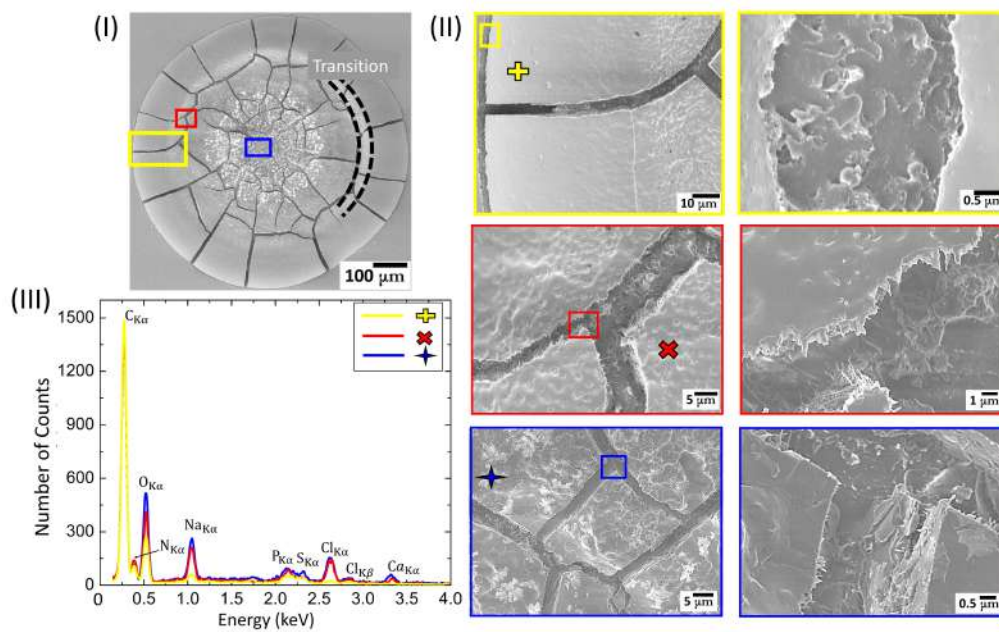


FIGURE 7.14: The SEM images illustrating the microscopic structures at different length scales are shown in (I) and (II) at ϕ_{blood} of 75% (v/v). The top, middle and bottom panels of (II) depicted with yellow, red and blue-colored rectangles detail the structures at the periphery and the corona, the transition of the corona and central regions, and the central region, respectively. The transition region is also specified with black dotted lines. An energy-dispersive X-ray (EDX) analysis consisting of the number of counts and the energy (keV) of different regions of the blood dried film is shown in (III). The signals are symbolized and colored to match the area from where these were collected.

Fig. 7.14(I-II) shows the different micro-structures in the diluted blood droplet at ϕ_{blood} of 75% (v/v). The smooth fragmented sheet in the corona region, the ruptured structures in the peripheral cracks, the presence of the troughs and ridges in the transition region, and the presence of the hair-like structures in the crack edges are

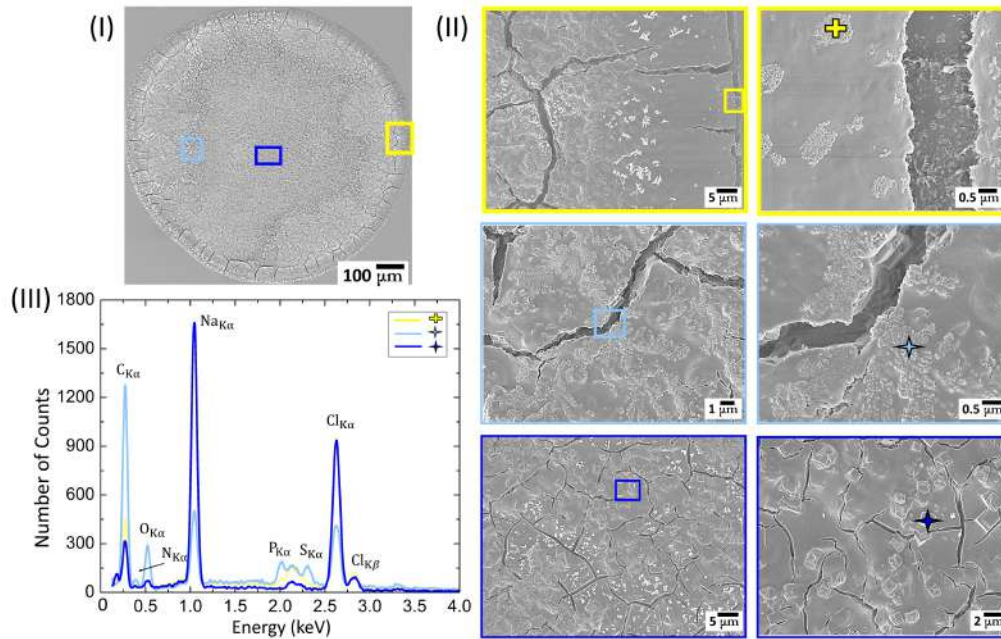


FIGURE 7.15: The SEM images illustrating the microscopic structures at different length scales are shown in (I) and (II) at ϕ_{blood} of 12.5% (v/v). The yellow-colored rectangle in the top panel of (II) details the structures at the periphery and the corona. The light and dark blue colored rectangles in the middle and the bottom panels of (II) show different structures in the central regions. An EDX analysis shows the elemental composition of different regions of the blood film in (III). The signals are symbolized and colored to match the area from where these were collected.

found common in both the dried films at ϕ_{blood} of 100 and 75% (v/v) [Figs. 7.14(II)]. Interestingly, the central region at ϕ_{blood} of 75% (v/v) displays the crystal-like structures in addition to the ridges and the toughs. The cracks in the central regions are comparatively sharper. The regions within these cracks are more homogeneous when compared to that of the whole blood droplet. The energy-dispersive X-ray (EDX) analysis is exhibited in Fig. 7.14(III). The different symbols are presented to identify the specific area from where the counts are collected. A graph of the number of counts and the energy (in keV) is plotted. The significant peaks are observed at 0.28, 0.53, 1.06, and 2.64 keV characterizing the presence of the elements, Carbon (C), Oxygen (O), Sodium (Na), and Chlorine (Cl) respectively.

The micro-structures at ϕ_{blood} of 12.5% (v/v) are shown in Fig. 7.15(I-III). These structures are unique and very different than that of 100 and 75% (v/v). A transition region between the corona and the central regions is not observed at $\phi_{blood} = 12.5\%$ (v/v). Fig. 7.15(I-II) marks different regions of interest. The yellow-colored rectangle in the top panel of Fig. 7.15(II) details the structures at the periphery and the corona. The light and dark blue-colored rectangles in the middle and the bottom panels of Fig. 7.15(II) show different structures in the central regions. The corona region is smooth like what we observed at other ϕ_{blood} ; however, it contains discoid-shaped aggregated structures. Almost no ruptured structures is found within the cracks of the peripheral region. A closer view in the central region indicates the presence of

different crystal-like structures [the middle and the bottom panels of Fig. 7.15(II)]. There are no troughs and ridges throughout the film at $\phi_{blood} = 12.5\%$ (v/v). Similar to $\phi_{blood} = 75\%$ (v/v), Fig. 7.15(III) also shows the significant presence of C, O, Na, and Cl elements.

However, it is to be noted that the number of counts for the elements changes as we dilute the initial concentration of blood (ϕ_{blood}) from 75 to 12.5% (v/v). For example, the counts of C decreases from ~ 1500 to ~ 450 in the corona region for ϕ_{blood} of 75 and 12.5% (v/v), respectively. It is found to be ~ 300 for Na and Cl at ϕ_{blood} of 75% (v/v) in the central region of the film. These counts of Na and Cl turn out to be more than ~ 900 at $\phi_{blood} = 12.5\%$ (v/v).

7.3 Discussions

7.3.1 Discussions on Lys-saline droplets

As soon as the droplets are pipetted on the coverslip, the height and the contact angle start reducing (checked with the contact angle goniometer). The non-uniform textural gradient in the optical images [Fig. 7.3(A)] and the images captured using the goniometer show that these droplets are partially wetted (the contact angle is ~ 50 degrees within ~ 45 s of their deposition) and are of the spherical-cap shape. The curvature of these droplets induces the highest mass-loss near the periphery compared to the central region. The droplets get pinned to the coverslip, and the Lys particles are transported through the outward capillary radial flow to compensate for this loss. The process leads to a well-known “coffee-ring effect” (Deegan et al., 1997) like other bio-colloids (Pal et al., 2020a; Chen and Mohamed, 2010; Pal et al., 2020b). As time progresses, it is observed that the fluid front recedes from the periphery to the central region, and simultaneously, the contact angle reduces, unlike the result reported in (Gorr, 2013). The deposits in the crack lines (Fig. 7.2) suggests that there exists a discontinuity at the ring interface [also evident in Fig. 7.3(B-C)]. It could be speculated that a significant amount of water gets evaporated by this time, and the salts start crystallizing. Since the images were taken in the transmission mode, the thick film gives rise to the dark texture. The dark textured front starts engulfing the central region (a similar phenomenon of the phase transition reported in (Yakhno, 2008)). The significant fluctuations in the textural evolution [Fig. 7.4(I-IV)] are also observed at this phase. The complexity (SD) increases as the salt crystals (inhomogeneities) begin to appear. As these droplets are pinned, the mechanical stress is relieved by virtue of crack propagation. The appearance of the salt crystals in different Lys concentrations affects crack formation [Fig. 7.1]. It also alters the interaction between the Lys particles and changes their aggregation and precipitation processes (samples with and without adding external salts, evident from Figs. 7.1-7.2). It also demonstrates that the three prominent regions may or may not be found

in the Lys droplets in the salts' presence (unlike reported in (Gorr et al., 2013)). Furthermore, the exclusive variation of the salt content might not provide us a clear picture. The chemistry between multiple salts and Lys at various initial concentrations is the crucial factor. It is not merely a sum (or average) of individual microscopic actions [Fig. 7.2]. It appears to involve both protein-protein and protein-salt interactions partially averaged over one length/time scale that sets the next larger/longer length/time scale in such drying droplets.

7.3.2 Discussions on BSA-saline droplets

Qualitative analysis of BSA-saline droplets

The first image of the drying BSA droplets at different initial saline concentrations (ϕ_{salts} of 0.9, 1.8, and 4.3 wt%) is captured soon after their deposition on the substrate (Fig. 7.5(I-III) a). A higher water loss is observed near the periphery (compared to the central region) due to its hemispherical-cap shape. A capillary flow develops in these droplets. The particles are carried towards the periphery to compensate for this rapid mass loss. This particles relocation continues till the three-phase (solid-liquid, liquid-vapor, and solid-vapor) contact angle reduces significantly. The BSA particles continue to adsorb on the substrate in this initial stage of the drying process. The fluid front recedes from the periphery towards the central region as time advances (Fig. 7.5(I-III) b), and marks the second stage of the drying process. The two regions, viz., the rim and the central regions become prominent as the front passes and specifies the "coffee-ring effect" (Deegan et al., 1997). The distinct textures of the regions confirm a greater height of the rim than the central regions. Furthermore, we observed that the width of the rim decreases as the saline concentration rises. Most of the water evaporates from these droplets with the advancement of the drying process. These droplets turn to films, and a mechanical stress develops. Since these droplets are pinned to the substrate (coverslip), these dried films are unable to shrink. The radial cracks originate from the periphery and propagate inwards to relieve the stress from these films (Fig. 7.5(I-III) c). A few orthoradial cracks also join these radial cracks. This indicates that a dominant stress direction is present in the rim. These events are commonly observed in the BSA droplets (both) in presence and absence of the salts (Pal et al., 2020a; Yakhno, 2008). Hence, it can be argued that the fluid front movement and the developing cracks form the components of the pinned bio-colloidal droplets. We did not observe any evident influence of any salts. The next stage begins with the growing of grainy structures near the dashed line. The grainy structures subsequently cover the entire central region. The dendrite and rosette structures also develop during this stage. The formation of the salt crystals starts towards the later stage of the drying process (Fig. 7.5(I-III) c-d). This evidently suggests that the drying mechanism is different in the rim and the central regions, and a similar observation is also reported in (Yakhno, 2008). The central region is found to be of light gray at ϕ_{salts} of 0.9 wt%. However, this region turns out

to be inhomogeneous, and becomes dark gray with the upsurge of ϕ_{salts} from 1.8 to 4.3 wt%. With the increasing numbers of salt crystals, the texture becomes dark gray as the film becomes thick and opaque to pass the light under the transmission mode of the bright-field microscopy. The final morphology is presented at the end of the visible drying process in Fig. 7.5(I-III) e. It is to be noted that the minute change in the textures is noticed after 24 hours [Figs. 7.5(I-III) e and 7.16(a-c)]. The texture of the films becomes darker. This indicates that some water could be trapped in the salt crystals. The evaporation of water after the visible drying process might have caused the textural changes in the dried films.

Quantitative analysis of BSA-saline droplets

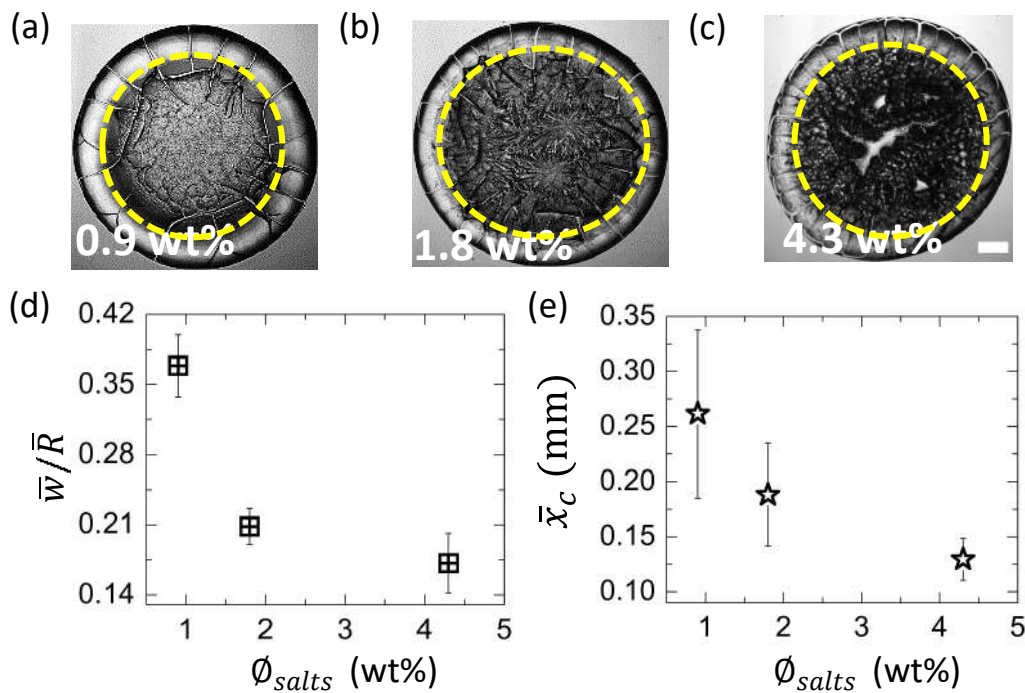


FIGURE 7.16: The images of the dried films of BSA-saline are captured after 24 hours at various initial concentrations of salts in PBS (ϕ_{salts}) (a) 0.9, (b) 1.8, and (c) 4.3 wt%. The yellowed dashed circular lines separate the rim from the central regions. The scale bar has a length of 0.2 mm. The averaged rim width (\bar{w}) is divided with the averaged radius of the droplet (\bar{R}) and the normalized width (\bar{w}/\bar{R}) is shown in (d). The averaged crack spacing (\bar{x}_c) is displayed in (e). The error deviations represent the standard deviations.

The crack spacing and the ring width are quantified and found to be reduced with the increase of ϕ_{salts} . Figure 7.16(d-e) shows the variation of \bar{w}/\bar{R} and \bar{x}_c in the BSA-saline dried films as a function of ϕ_{salts} . Both these parameters decrease with the increment of ϕ_{salts} . The reduction of the rim width predominantly takes place due to the drop of the BSA-BSA interactions in these droplets. As we increase the ϕ_{salts} , the BSA-salt interaction becomes dominant in the formation of the crystal complex structures over the BSA-BSA interactions. Furthermore, the standard deviation of \bar{x}_c is observed to be reduced with the upsurge of ϕ_{salts} . This confirms that the different sized crack domains are present at the low saline concentration (for example, ϕ_{salts}

= 0.9 wt%). Their increased number makes the crack domains uniform when the ϕ_{salts} changes from 0.9 to 4.3 wt%. However, it does not mean that the number of cracks increases due to the increase of the saline concentrations. It must be noted that these radial cracks develop only in the rim region, where only the BSA particles are predominantly present. Their number increases because the energy required for the propagation of the smaller cracks is less than the larger cracks.

The FOS parameters (I , SD , $SKEW$, and KUR) are the spatial moments of order 1 to 4, respectively (Carreón et al., 2018b). These parameters are extracted during the drying evolution of the BSA-saline droplets at ϕ_{salts} of 0.9, 1.8, and 4.3 wt% [Fig. 7.6(I-IV)]. The I is defined as the sum of the gray values of all pixels divided by the number of pixels. It depicts the average values within the selected area (in our case, it is the circular droplet). The SD indicates the amount that the pixel values stray away from the mean. Interestingly, the I shows three ubiquitous stages when the images captured during the drying process are compared (Fig. 7.5(I-III) a-e). The I grows initially where the contact angle is significantly reduced, and the droplet changes from its spherical-cap shape. In contrast, the uniformity increases, and the SD decreases during this stage. The dark texture of the image changes into bright, and this maps up to ~ 200 seconds. In the second stage, no change in the I is observed, whereas the SD differentiates the fluid front movement and the origin of the cracks [Fig. 7.6(I-II)]. It is to be noted that the SD captures most of the textural details even if many complex phenomena assemble them. Both the I and the SD lines up to ~ 400 seconds that marks the next stage, i.e., the crystal growth. Till this stage, both these parameters are mostly independent of ϕ_{salts} . As the crystals start appearing, the texture transforms (from light) to dark gray. While the I decreases, the complexity increases through the upsurge of the SD .

The $SKEW$ and the KUR of the FOS parameters reveal the information about the distribution of the pixels. The $SKEW$ of an image describes the symmetry of the normal distribution of the pixels in the selected area (in our case, it is the circular droplet). The $SKEW$ of any normal (symmetric) distribution is zero, whereas the negative (positive) values of $SKEW$ indicate that the pixel data are skewed in the left (right) of the distribution. This also implies that the left (right) tail is relatively long than the right (left) tail of its pixel distribution. Comparison of the Figs. 7.5(I-III) a-e and 7.6(III) reveal that the distribution of the pixels is asymmetric towards the left throughout the drying process. However, their values change during different stages of drying. In the first stage (within ~ 200 seconds), the $SKEW$ decreases from -1 to -4 a.u. The value remains the lowest during the second stage, where the fluid front moves and most of the radial cracks form. With the growth of the crystals in the central region, the $SKEW$ starts increasing, and it reaches to zero only at ϕ_{salts} of 4.3 wt%. The change in the Gaussian distributions from a single to two peaks at gray values of ~ 15 and ~ 117 in Fig. 1(III) e is directly connected with the increasing $SKEW$ value towards the end of the drying process. In contrast, the KUR of the

image indicates the peak or flatness of the data under consideration. In our case, the *KUR* shows two peaks at ~ 150 and ~ 350 seconds, only to be reduced and reach at a constant value during the drying evolution [Fig. 7.6(IV)]. These peaks highlight the transition of the first to the second and second to the third drying stages, respectively. More interestingly, the second peak of *KUR* becomes sharper as the saline concentration (ϕ_{salts}) increases. Since the droplet size is the same for all ϕ_{salts} , the crystals proliferate at $\phi_{salts} = 4.3$ wt%, resulting in a sharp peak during drying.

All these parameters differentiate their values at different ϕ_{salts} as the drying process completes. Nonetheless, the sensitivity of these FOS parameters increases as the higher ranks are computed. This could be a possible reason why only the *I* displays a uniform distribution, whereas a few peaks and dips are observed in *KUR* measurements. The FOS parameters are obtained from the pixel values, it ignores all the tonal and structural properties. In contrast, the tone of the GLCM parameters is based on the pixel intensity (or the gray values). The structure is determined by the spatial relationship between two neighboring pixels. The GLCM parameters, therefore, are based on the local tonal and structural properties that are dependent on each other. The different parameters adopted to extract the FOS and the GLCM properties disable them to compare with each other.

The GLCM parameters (*ASM*, *COR*, *ENT*, and *IDM*) are extracted during the drying evolution of the BSA-saline droplets at different saline concentrations (ϕ_{salts} of 0.9, 1.8, and 4.3 wt% [Fig. 7.8(I-IV)]). However, it can be concluded from Fig. 7.7(I-IV) that all the GLCM parameters depend on the orientations and the pixel displacements. Since these are specific to the drying droplets, these parameters need to be checked before making any choice of their computations. The *ASM* measures the global uniformity of the textures. The uniformity (or the *ASM*) increases until the salts crystallize in the central region from 400 seconds. On the other hand, the *ENT* measures the global heterogeneity of the image. The *ASM* and *ENT* are found to be inversely proportional to each other [Fig. 7.8(I, III)]. The *ASM*, *COR*, and *IDM* parameters show greater uniformity and similarity in the gray regions before the crystallization of the salts occurs. On the other hand, these parameters reduce when the salt crystals start forming due to the appearance of different heterogeneous regions [Fig. 7.8(I-II, IV)]. This results in decreasing the similarity index between the pixels in a horizontal or vertical orientation. This means that the presence of more salts in the droplets (or the increasing ϕ_{salts}) give rise to more heterogeneity. This leads to the highest value of *ENT* at $\phi_{salts} = 4.3$ wt% followed by 1.8 and 0.9 wt%. Similar arguments also hold for other parameters (*ASM*, *COR*, and *IDM*). The ϕ_{salts} of 4.3 wt% shows the lowest values than 1.8 or 0.9 wt% when *ASM*, *COR*, and *IDM* are computed towards the end of the drying process.

To understand the physical mechanism of the appearance of such a bi-modal distribution at $\phi_{salts} = 4.3$ wt%, we plotted its progression from ~ 440 to ~ 540 seconds [Figure 7.17(I-III)]. It is clear from Fig. 7.5(III) d-f that these two peaks origin during

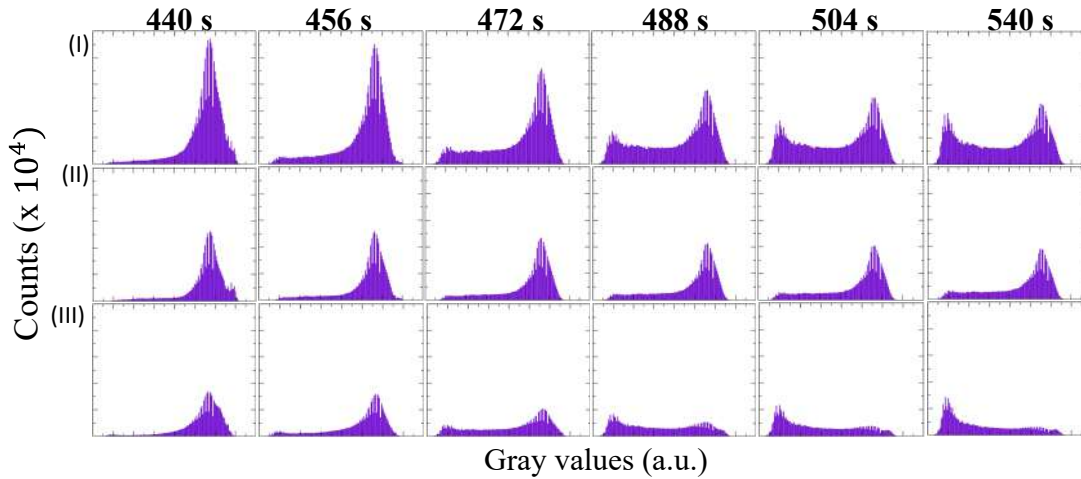


FIGURE 7.17: Histograms depicting the counts of the pixels along the y-axis, and the gray values along the x-axis of each image taken at 440 s, 456 s, 472 s, 488 s, 504 s, and 540 s at $\phi_{salts} = 4.3$ wt% for (I) whole droplet, (II) rim region, and (III) central region. The gray values in x-axis ranges from 0 to 160 (a.u.) in the interval of 20. The pixel counts in y-axis ranges from 0 to 25 ($\times 10^4$) in the interval of 5 ($\times 10^4$).

the crystal growth stage, somewhat at the very end of the drying process. This is the stage when almost all the water evaporates from these droplets. The salt layer is formed in the central region during this time. More crystals-like structures appear as the trapped water evaporates from these droplets. It means that the equilibrium-like regions start emerging locally, whereas the whole system (drying droplet) is still out of the equilibrium. Two local equilibrium-like regions (one in the rim, and the other in the central region) appear when the droplets approach the steady-state (end of the drying process). However, these two regions seem to be weakly correlated. To validate this assumption, we extracted the pixel counts as a function of the gray values only for the rim [Fig. 7.17(II)] and the central regions [Fig. 7.17(III)]. It is observed that the second peak decreases to the minimum and the first peak appears at 472 seconds when the counts are computed for the central region. In contrast, the rim does not show any such behavior and consistently show the second peak. This implies that the gray value of ~ 15 (first peak) is due to the emergence of the crystal structures in the central region. The second peak at gray value of ~ 117 confirms the origin of the rim region. If these regions were uncorrelated, zero values in their interaction terms should have emerged. However, we observed a finite value between the peaks when the pixel counts are plotted for the whole droplet [Fig. 7.17(I)]. This confirms that the BSA-BSA interactions are dominant (recessive) over the BSA-saline interactions in the rim (central) regions that results in the phase separated aggregation of the BSA particles in presence of the salts. It is also understood that the saline concentration, in principle, should have been enough for the BSA-saline interactions to be dominant over the BSA-BSA interactions. This is probably the reason that we did not observe any bimodal distributions in the lower saline concentrations. Furthermore, it also validates why ϕ_{salts} of 4.3 wt% behaves uniquely when the FOS and GLCM parameters are extracted during the drying evolution.

7.3.3 Discussions on blood-saline droplets

A spherical-cap shape is exhibited as soon as the droplet is deposited on the substrate (coverslip). The first image is captured within ~ 90 s of its deposition. The mean intensity of the first image shows an increase from ~ 5 a.u. to ~ 25 a.u. with the increasing dilution. In contrast, the image's standard deviation (SD) remains nearly constant [inset of Fig. 7.11(II)]. This suggests that the texture of the image becomes lighter with the dilution while maintaining the uniformity of the image (Figs. 7.9-7.10). Since RBCs carry hemoglobin (an iron-containing protein responsible for the redness), and every other component is colorless, it can be inferred that the effect on this texture is solely due to the reduction of RBCs in the droplet.

The curvature of the droplet near the periphery increases the drying rate. A capillary flow [indicated with dotted arrows in Fig. 7.18A-B(I)] is developed to compensate for the excessive mass loss. Most of the blood components are moved towards the periphery. This is evident by the appearance of the peripheral band. Its width decreases as the number of the components reduces with the increasing dilution (Figs. 7.9-7.10). Meanwhile, the plasma proteins tend to interact with the substrate and form a protein-rich layer. The height of the droplet reduces [Fig. 7.18A-B(II)]. The fluid front starts receding from the periphery towards the central region. The lowering of the contact angle (the angle formed at the interfaces of substrate-fluid, fluid-air, and air-substrate) also occurs during this time.

The mapping of the contact angle measurements with the fluid front radius data [Fig. 7.12(I-II)] reveals that both the contact angle and the fluid front vary when δt changes from -350 s to 0 s at ϕ_{blood} of 100 to 25% (v/v). The δt is defined as the shifted time computed by subtracting t_0 from t , where t_0 is the time when the mean intensity exhibits a rapid rise, and t is the actual time of the drying process. On the other hand, the fluid front starts moving after the contact angle reduces to the minimum value at ϕ_{blood} of 12.5%. Furthermore, the mean at $\phi_{blood} = 12.5\%$ (v/v) takes the longest time to reach the rapid rise phase during its evolution. It takes ~ 140 s more than the others [inset of Fig. 7.11(I)]. It suggests that a large amount of the salts [$\phi_{blood} = 12.5\%$ (v/v)] change the wetting and the interfacial properties of the droplet. Their presence can serve as a hygroscopic agent resulting in a long time for the underneath water to evaporate. The elastic network formed by the salts [Fig. 7.15(II)] might attribute to the delay of the rapid rise phase at ϕ_{blood} of 12.5% (v/v).

Interestingly, a peak-like feature is observed in the contact angle measurements during the time interval (δt) of -250 s to -50 s. The peak becomes broader and gets delayed as we dilute the ϕ_{blood} from 100 to 62% (v/v) [inset of Fig. 7.12(I)]. No such peak is found for the range from 50 to 12.5% (v/v). As the number of RBCs decreases, it is obvious that the other components (WBCs, platelets, etc.) also minimize to maintain their relative initial concentrations. To confirm whether the broadening

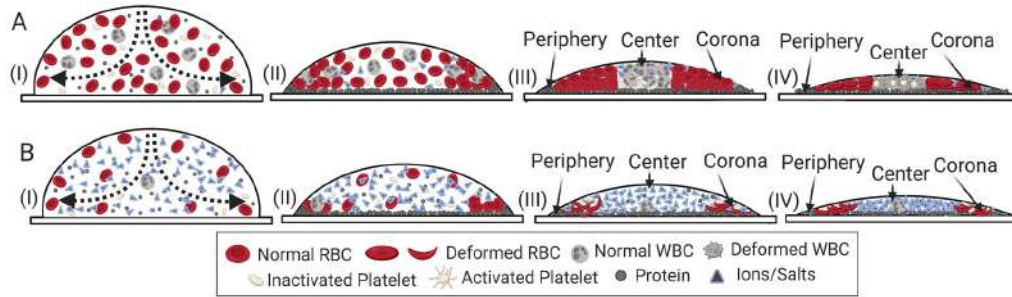


FIGURE 7.18: Self-assembling mechanism of the diluted blood droplets at ϕ_{blood} of 75% (v/v) in (A) and 12.5% (v/v) in (B). (I) A capillary flow (indicated with dotted arrows) is established in both the droplets after it is deposited on the substrate. (II) Most of the components are moved towards the periphery of the droplet. (III-IV) The mechanical stress develops causing the structural alteration of the components present in these diluted blood. The droplet gets divided into three distinct regions, the periphery, the corona (the region between the periphery and the central regions), and the central region.

and the disappearance of the peak are due to the increased salt residues, we diluted the whole blood with the de-ionized water instead of PBS. Surprisingly, these peaks are found to be present in the diluted blood samples, which do not contain any salts (described in previous chapter). This suggests that the space confinement (~ 2 mm droplet's diameter) and the presence of a large number of these components near the periphery influence their distributions. It appears that the RBCs try to arrange themselves (elastic behavior), while their arrangements create negative stress to other components, such as the WBCs, and the platelets. Since the WBCs are the largest (~ 15 μm) among all the components (RBCs are ~ 7 μm , and the platelets are ~ 2 μm), the rearrangement of these WBCs causes the viscous behavior to accompany the accumulated stress. The presence of the peak confirms the visco-elastic behavior of these components. The broadening and the delaying of this peak indicate that these diluted samples at this range now take more time to reach a critical concentration at which the visco-elasticity of these components (mostly the competition between RBCs and WBCs) can build up. Most likely, the number of WBCs is just enough for the range of ϕ_{blood} from 100 to 62% (v/v) for exhibiting the viscous properties. From 50 to 12.5% (v/v), their number becomes so less that the elastic behavior is dominant. This indicates that a phase transition at 62% (v/v) takes place. However, this transition is only driven by the concentration of the blood's components, not contributed by the presence of the salts. The crowd still exists at 12.5% (v/v) due to a large number of salts; however, no peak-like feature (aka visco-elasticity) is observed. This concludes that the self-assembling interactions between the components in the blood is one of the necessary criteria for the visco-elasticity to appear.

As more water leaves during the drying process, the mechanical stress develops. The blood film is unable to shrink due to its pinning to the substrate. The ellipsoidal or the ruptured structures within the cracks of the peripheral region are found in both undiluted [100% (v/v)] and diluted [$\phi_{blood} = 75\%$ (v/v)] droplets. These are the

RBCs altered in response to the stress (reported in (Pal et al., 2020b; Mukhopadhyay et al., 2018)). Most of the RBCs are packed in a stacked fashion in the corona region. The phospholipids of their membranes form a lipid bilayer, which appears to be a smooth sheet under scanning electron microscopy [Fig. 7.14(II)]. Furthermore, the stress triggers the WBCs and alters the biological activity of the platelets. The troughs and the ridges in the central region are the deformed (Yang, 1989) structures of the WBCs. The stress also activates the platelets by changing their discoid shapes to extended filopodia (reported in (Gregory, Stevens, and Fraser, 2017)). The hairy structures along the crack edges in the central region are the activated form of these platelets [Fig. 7.18A(III-IV)]. As the ϕ_{blood} changes from 75 to 12.5% (v/v), the amount of the salts increases with the decreasing number of the components. The film at 12.5% (v/v) looks very different from the whole blood [100% (v/v)] or the diluted blood at 75% (v/v) [Figs. 7.14(I-II), and 7.15(I-II)]. Some discoid structures and sickle-shaped RBCs are found in the corona region. No trough and ridges are found in the central region. In addition to the sharp crack lines, different crystal structures are observed in this region [Figs. 7.15(I-II)]. This indicates that the platelets could not be activated once the ϕ_{blood} is reduced below the critical concentration. The reduction of the blood components at 12.5% (v/v) makes the film as a sea of salts [Fig. 7.18B(III-IV)]. It is to be noted that Fig. 7.18A-B(IV) is not the schematic for the final morphology of the dried film, rather of the self-assembling mechanism. It is clear from the optical images [Figs. 7.9 and 7.10] that the corona is at higher height than the central region. The increment of the salts' presence at 12.5% (v/v) is also evident from the micro-structural EDX analysis of the dried films at ϕ_{blood} of 75 and 12.5% (v/v) [Figs. 7.14(III) and 7.15(III)]. Moreover, the higher counts of Na and Cl than other ions in EDX micrographs confirm the excess concentrations of NaCl in the diluent, PBS.

While the structural deformation of these components provides a local response to the stress, the global response is achieved by the cracking of the blood film. The presence of the WBCs, the platelets, and some of the residual RBCs make the central region at 100% (v/v) crowded. The inhomogeneity of this region can be understood by comparing the texture of the central and the corona regions. The random cracks appear in this central region due to the lack of any dominant stress. The radial cracks are observed in the corona region. These cracks divide the film into different sized domains. Once these radial cracks form, the texture around the corners of the cracked domains changes into dark gray. This is because the stacking of the RBCs have pores, and these pores could contain some trapped water (Chen et al., 2017; Iqbal, Shen, and Sen, 2020). As the water evaporates from these pores, the residual stress is relieved through the branching (micro-flaws) of the cracks. The widening of the radial cracks occurs due to the sliding of these cracked domains. This indicates that a stronger interaction between the components exists over the interaction between the substrate and the blood film.

As we dilute the blood samples, we observe distinct crack patterns. For example, the random cracks are replaced with the dendrite structure at 75% (v/v). The ring-like cracks are observed at 25% (v/v), whereas the ϕ_{blood} of 12.5% (v/v) does not show any cracks in the central region under $5\times$ magnification (Figs. 7.9-7.10). This suggests that the various amount of salts creates different physio-chemical environments to release the mechanical stress in the central region. However, we didn't find any such behavior in the corona region. While computing its averaged width (\bar{w}) and the averaged crack spacing (\bar{x}_c), the width covers 80% of the total film area at 100% (v/v). In the presence of the salts, the higher shrinkage of the width is observed. The corona covers only 30% of the total area at $\phi_{blood} = 75%$ (v/v), and it gradually decreases with increasing dilution [Fig. 7.13(I)]. Similarly, \bar{x}_c is found to be ~ 0.6 mm at 100% (v/v), and it reduces uniformly from ~ 0.4 to ~ 0.1 mm in the presence of the salts [Fig. 7.13(II)]. The number of cracks increases in the salt-added diluted blood than the whole blood. However, this does not indicate that more stress has developed. It is just the fact that the energy cost of forming multiple shorter cracks (due to small corona width) is less than that of the single long crack [due to large corona width at 100% (v/v)]. Interestingly, the sliding of the crack domains is only observed in the absence of the salts (described in earlier chapter). This suggests that the elastic network formed by the salts and the reduction of the blood's components result in the attachment of the film with the substrate.

7.4 Conclusions

This study on Lys-saline drying droplets reveals that their tuning with salts is essential in determining the morphological patterns. The textual evolution indicates that the interactions between different Lys particles during the drying process are dependent on the amount of salts present in phosphate buffer saline. It also shows that the occurrence of three distinct regions is not the general characteristic of Lys-saline droplets; rather, it depends on the relative initial concentrations of Lys and salts. It rasters the parameter space by varying their initial concentrations and portraying a morphological grid. These protein model systems would benefit us to understand the complexity in other bio-fluids.

This chapter also reveals that we can use image processing techniques to understand and quantify textural features. The horizontal and the vertical orientations of the GLCM parameters show a non-significant effect when the pixel displacement is ≤ 1 . The entropy and the angular second moment of GLCM appeared to be inversely proportional during the evolution process. The distribution changes from single to bimodal as the initial saline concentration increases. This helps us to understand the aggregation process of the BSA particles in the presence of the salts.

Furthermore, this chapter confirms that the blood components' interactions drive the phase transition in diluted blood droplets. The salts or the ions of PBS do not play

any crucial role in this transition. While the structural deformation of these components provides a local response to the mechanical stress developed due to significant water loss in these droplets, the global response is achieved by cracking these blood films. Various amounts of salts in the diluent change the physio-chemical environment in these droplets influencing the macroscopic patterns to a great extent. However, the salts' presence does not have any significance for altering the structures of these components.

Till now, we have studied the drying patterns dried under ambient conditions. The next chapter [Chapter 8] discusses the results by varying the samples' initial concentrations, and the solutions are dried under various controlled substrate temperatures. It is to study whether the temperature only reduces the drying time? Or it substantially changes the patterns? For this, the whole human blood is targeted as the most complex bio-colloid system, whereas bovine serum albumin (BSA) and lysozyme are the simplest. Therefore, the next chapter focuses on the drying characteristics and the final morphology of these bio-colloids dried under different temperatures.

Chapter 8

Temperature and Concentration Dependent Pattern Formation*

8.1 Background

In the previous chapters, we discussed the findings of systematic experiments on the most complex bio-colloid, blood, and discussed the self-assembling mechanisms borne out during the drying process. The study in Chapters 6 [published in (Pal et al., 2020b)] and 7 reveal a concentration-driven phase transition when the blood is precisely diluted in de-ionized water and phosphate buffer saline (PBS). The analysis of three different independent measurements (textural analysis, contact angle measurements, and morphology) confirmed that the complex combinations of the chemical potentials among the cellular components are responsible for such origin. The progress made so far on the drying evolution and the resulting morphological patterns in the diluted blood samples lead to some consequent exciting questions that are addressed in this chapter. These questions include understanding what happens to the phase transition when a one-component system replaces the multi-component? What kind of interactions plays a role in this type of transition? Does the wettability of the droplet change for a one-component system? How does it change during the drying process? Does the temperature effect differently for one and multi-component drying droplets?

Furthermore, the systematic studies on the bio-colloidal droplets (from globular proteins to human blood) indicate that the initial parameters (geometry, wetting condition, substrate, environmental conditions (relative humidity (RH), temperature, etc.) are essential for linking the morphological patterns to the initial states of the constituent particles. Recently, the influence of RH on the spreading dynamics of the blood droplets is studied (Zeid, and Brutin, 2014). It is observed that the spreading time and dynamics depend on the RH and are related to the interactions between

*Part of the work described in this chapter is published. Pal, A., Gope, A. and Iannacchione, G.S., 2021. Concentration and Temperature dependence of Protein and Blood Drying Droplets. *Biomolecules*, 11(2), pp.231. <https://doi.org/10.3390/biom11020231> (Pal, Gope, and Iannacchione, 2021).

the cellular components and substrate. Though the effects of the temperature are focused on many drying colloidal systems, to our best knowledge, only the aqueous solution of lysozyme (Lys) in the context of bio-colloids is explored at different substrate temperatures (Gorr, 2013). It is concluded that the coffee-ring width depends on the initial concentration when droplets are dried under different elevated temperatures. However, it is to be noted that the studied samples were at very low concentrations than ours ($\phi_{Lys} \leq 1$ wt%). Therefore, it is essential to check whether the higher initial concentrations have a similar impact. Recently, the effects of the substrate temperature is observed on the protein-saline drying droplets. Different morphology is found in the various ranges of protein solutions and the substrate temperatures. For example, the “functional” patterns are observed from 25 to 37 °C. The range of 44 to 50 °C shows a “transition” pattern. Very interestingly, the “eye” patterns are detected from 58 to 63 °C (Carreón et al., 2021).

This chapter presents results that shed light on (i) the self-assembling mechanism where both the (relatively higher) initial concentration and temperature changes, (ii) whether it is possible to tune the final morphology by changing the dependent factors. For this, the drying evolution and final morphology of the complex (multi-component–human blood) and the simplest (one-component–BSA and Lys) drying droplets are studied by varying the initial concentrations at different controlled substrate temperatures. The comparison between these two systems also reveals the influence of multiple components’ interactions versus features that depend on single-molecule self-interactions. This chapter, thus, seeks to answer a few fundamental questions; is it possible to suppress the formation of the mound-like feature in the Lys droplets? If so, how? Does the coffee-ring effect always be observed? What is the interaction between temperature and initial concentration? How does this interaction (if any) affect the final dried morphological patterns?

8.2 Results

The various amounts of BSA were dissolved in de-ionized water to prepare the initial BSA concentration (ϕ_{BSA}) of 20, 9, 5, 3, and 1 wt%. Different Lys solution was prepared by dissolving the needed amounts of Lys in de-ionized water to prepare the initial concentration (ϕ_{Lys}) of 20, 17, 13, 9, 5, 3, and 1 wt%. The blood is diluted by adding different volumes of de-ionized water to prepare a different range of initial blood concentrations (ϕ_{blood}) of 75, 62, 50, 25, and 12.5% (v/v). The hot stage mounted on a transmission mode bright-field optical microscope had been set to the desired observation temperature for a couple of hours prior to sample placement. These pipetted droplets were transferred to the stage within ~ 45 seconds and equilibrated to the set temperature within about 10 seconds. The temperature controller was set at different temperatures (T) with ± 0.2 °C of uncertainty. The T of 25, 35, and 45 °C was used to run the blood samples’ experiments. The T = 55 °C is added for the BSA and Lys samples.

8.2.1 Qualitative analysis

Human blood: The most complex bio-colloid

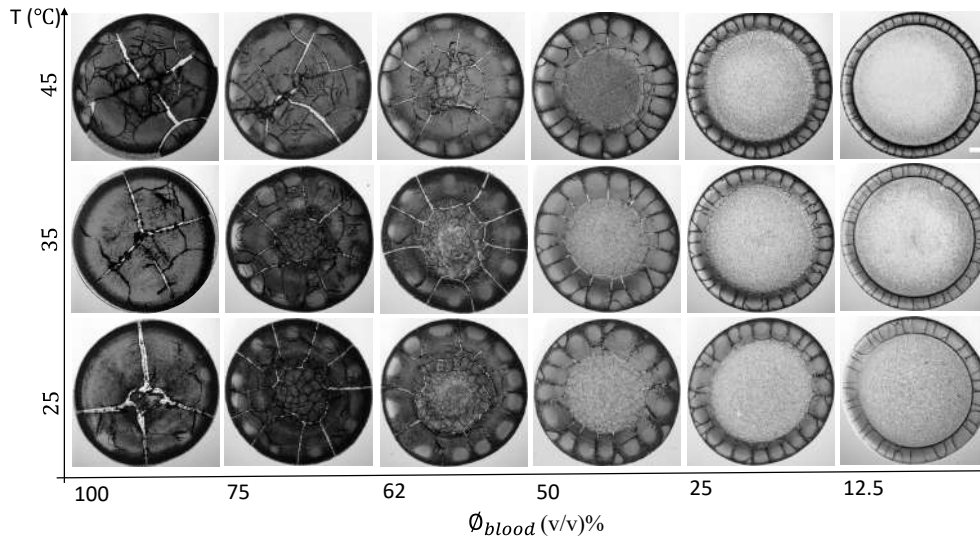


FIGURE 8.1: Morphology of the whole human blood film during 24 h at different initial concentrations (ϕ_{blood}) ranging from 100 to 12.5% (v/v) that are dried at various substrate temperatures (T) of 45, 35, and 25 °C. The scale bar of length 0.2 mm is represented by the white rectangle in the top-right panel.

Figure 8.1 shows the morphology of the whole human blood droplet dried during 24 h at different substrate temperatures (T) ranging from 25 to 45 °C. The various initial concentrations of blood (ϕ_{blood}) from 100 (undiluted whole blood) to 12.5% (v/v) (diluted whole blood) are also studied at this temperature range. The whole blood texture changes from dark (at ϕ_{blood} of 100%) to light gray (at ϕ_{blood} of 12.5%) as we dilute its initial concentration. A ring-like feature is found at all ϕ_{blood} at $T = 25$ °C; however, it can be prominently observed at ϕ_{blood} of 50 to 12.5% (v/v). It is to be noted that the ring (or the rim) terminology is the same as the blood's corona in this study. The ring's width (w) decreases, and the central region's width increases as ϕ_{blood} is diluted. Both of these regions are found in all the samples except 100% (v/v) at $T = 35$ and 45 °C as well as 75% (v/v) at $T = 45$ °C. A uniform dark-gray texture is found in both of these regions for the samples ranging from 100 to 62% (v/v). The difference in their textures gets visible from 50 to 12.5% (v/v). The central region becomes lighter than the ring at this range. It indicates that the ring and the central regions are at different heights from 50 to 12.5% (v/v) (Pal et al., 2020b). Interestingly, the elevated temperatures (T of 35 and 45 °C) show a sharp-edged ring compared to $T = 25$ °C, independent of their initial concentration.

The ϕ_{blood} of 100% (v/v) at $T = 25$ °C has four radial cracks. These cracks divide the ring (or the corona) into large-sized domains [a similar behavior is observed in (Chen et al., 2017; Brutin et al., 2011)]. Some of the micro-flaws are noticed in these domains. The crack lines are thick. The number of these cracks is increased as we dilute the sample. It is to be noted that the length of these cracks is directly

proportional to the ring's width. The thick crack lines become thin as the sample is diluted. Looking around the edges at ϕ_{blood} of 100% (v/v) suggests that these cracked domains are not firmly attached to the substrate. Some of these domain sheets are moved towards the center, and some are away. These misplaced sheets are profoundly exhibited at $T = 45^\circ\text{C}$. These dried films' high magnified images display that these films firmly adhere to the substrate (coverslip) at ϕ_{blood} of 50 to 12.5% (v/v). The small-sized random cracks in the central region are only seen at ϕ_{blood} of 100 to 62% (v/v) under our study's present resolution. Surprisingly, the blood samples' crack morphology does not significantly change at the elevated temperatures (T of 35 and 45°C).

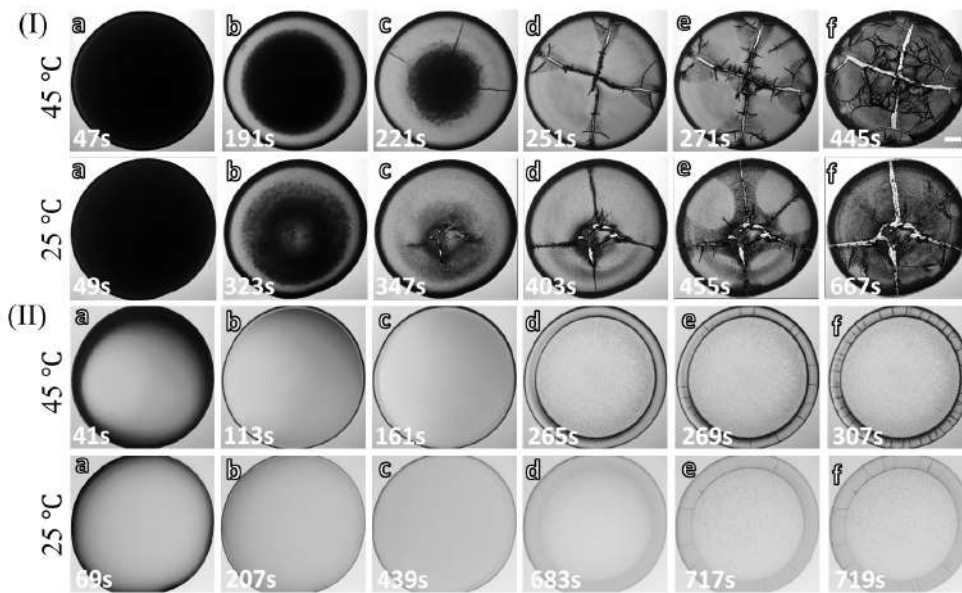


FIGURE 8.2: Time evolution of the blood droplets during the drying process: (a-f) display the drying stages at the substrate temperature (T) of 45 and 25°C at the initial concentration (ϕ_{blood}) of 100% (v/v) in (I) and 12.5% (v/v) in (II). The scale bar of length 0.2 mm is represented with the white rectangle in the top-right panel.

Figure 8.2(I,II)a-f examines the drying evolution of the blood droplet at ϕ_{blood} of 100 and 12.5% (v/v), respectively, at the substrate temperature (T) of 45 and 25°C . The first image is captured within ~ 70 s after the droplet's deposition on the substrate (Fig. 8.2(I,II)a). The images at 12.5% (v/v) are lighter than 100% (v/v) under ambient and elevated temperatures. The first stage of the drying process started when the fluid front moves from the periphery towards the central region exhibited in Fig. 8.2(I,II)b,c. The light gray texture starts appearing as the front moves, which is observed predominantly at 100% (v/v). However, the change of the texture is not notable at 12.5% (v/v) as the first captured image is already of light gray shade (Fig. 8.2(I,II)a,b). Soon after this movement, the droplet is found to have two distinct regions, the ring (or the corona) and the central regions at $T = 25^\circ\text{C}$. Interestingly, the corona's edge is found to be sharp at $T = 45^\circ\text{C}$.

The second stage of the drying process marks the propagation of the cracks. The

morphological difference between the undiluted and the diluted blood droplets begins from this stage (Fig. 8.2(I,II)c,d). The cracks propagate radially from the center to the periphery in the undiluted blood sample [100% (v/v)]. In contrast, these cracks move from the periphery to the corona (or the ring) at $\phi_{blood} = 12.5\%$ (v/v). Subsequently, the cracked domains get detached from the substrate, whereas the central region still adheres to the substrate at ϕ_{blood} of 100% (v/v) and $T = 25$ °C. The radial cracks propagate throughout the droplet at $T = 45$ °C, leading to the absence of the central region. The increased number of the micro-flaws and an additional sliding of the sheets are also observed at $T = 45$ °C (Fig. 8.2(I)e,f).

The third stage involves changing the texture (from the light to the dark gray), the appearance of the micro flaws from these radial cracks, and the widening of these radial cracks. However, this stage is found to be absent at 12.5% (v/v) [Fig. 8.2(II)e,f].

BSA protein: The simplest bio-colloid

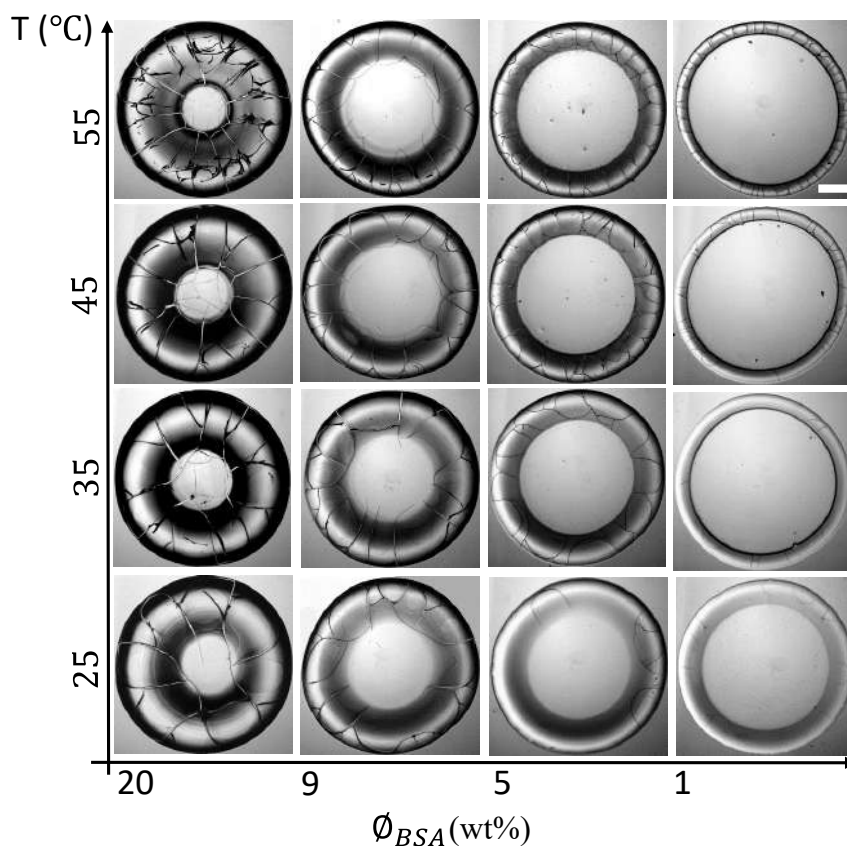


FIGURE 8.3: BSA film's morphology during the 24 h at different initial concentrations (ϕ_{BSA}) ranging from 20 to 1 wt% dried at various substrate temperatures (T) of 55, 45, 35, and 25 °C. The scale bar of length 0.3 mm is represented with the white rectangle in the top-right panel.

Figure 8.3 shows the morphology of the bovine serum albumin (BSA) droplet dried for 24 h at different substrate temperatures (T) of 25 to 55 °C and various initial concentrations (ϕ_{BSA}) ranging from 20 to 1 wt%. Unlike the blood sample (Fig. 8.1), all BSA's dried films show a uniform light gray texture. The "coffee-ring" (Deegan

et al., 1997) like behavior is seen at every ϕ_{BSA} (Pal et al., 2020a; Carreón et al., 2018a). These films exhibit a shadowy dark texture around the inner edge of the ring. This texture differentiates the film into two separate regions, the rim (or the ring), and the central regions. It also indicates that the ring is at a higher height than the central region. The shadowy texture is prominent at 20 as compared to 1 wt%. This suggests that their heights' differences are more profound with the increase of BSA's initial concentration. A peripheral dark band is noticed at $\phi_{BSA} = 20$ wt% and minimized as we dilute the samples to 1 wt%. Similar to the whole blood dried film (Fig. 8.1), the ring's width (w) is found to be dependent (decreased) as ϕ_{BSA} is diluted from 20 to 1 wt% at every temperature.

Furthermore, the sharp-edged ring is found at elevated temperatures (T from 35 to 55 °C). Unlike the blood samples, the cracks in BSA films are mostly observed in the ring. These cracks intervene from the ring to the central regions at ϕ_{BSA} of 20 and 9 wt%. No cracks are found in the central region from 5 to 1 wt%. Most of the cracks are radial, dividing the ring into large-sized domains. The orthoradial cracks are mainly observed to join the consecutive radial cracks [reported in our Chapter 4 and published paper, (Pal et al., 2020a)]. Interestingly, the number of radial cracks in the blood increases, whereas its number reduces as the BSA's initial concentration is diluted. In contrast, the radial cracks' length reduces in both the blood and the BSA samples with dilution. Interestingly, some curved flaws are noticed around the corners of these domains at ϕ_{BSA} of 20 wt% and T = 55 °C.

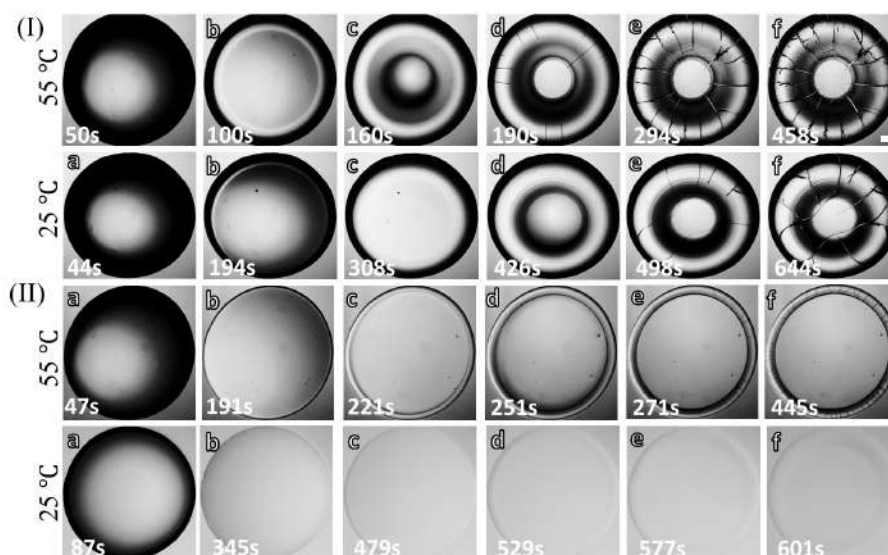


FIGURE 8.4: Time evolution of BSA droplets at different substrate temperature (T) during the drying process: (a-f) display different stages at the initial concentration (ϕ_{BSA}) of (I) 20 wt% for T of 55 and 25 °C, and (II) 1 wt% at T of 55 and 25 °C. The scale bar (0.2 mm length) is shown with the white rectangle in the top-right panel.

Figure 8.4(I,II)a-f illustrates the various stages of the BSA droplets' drying process. The concentrated (ϕ_{BSA} of 20 wt% in Fig. 8.4(I)a-f) and the most diluted (1 wt% in Figure 8.4(II)a-f) samples are selected for studying the drying evolution at T of 55,

and 25 °C. After the droplets are pipetted (Fig. 8.4(I,II)a), the fluid front recedes from the periphery towards the central region (Fig. 8.4(I,II)b-d); similar to what is also observed in the blood droplets (Fig. 8.2 (I,II)b,c) (Pal et al., 2020a; Pal et al., 2020b). This indicates that the first stage is a characteristic of a drying bio-colloidal droplet, which does not depend on the constituent particles' type. Along with the fluid front movement, a prominent dark peripheral band is observed at $\phi_{BSA} = 20$ wt%. No such band is found in 1 wt% at $T = 25$ °C; however, a thin dark circular line is exhibited at $T = 55$ °C. The distinct regions (the ring and the central) are noticed as the fluid front movement approaches its end. Simultaneously, the cracks propagate from the periphery towards the central region like the diluted blood droplet at ϕ_{blood} of 12.5% (v/v). The cracks mostly appear in all the samples except for ϕ_{BSA} of 1 wt% and $T = 25$ °C. The long radial cracks generate, and, subsequently, the orthoradial cracks join these radial cracks (Fig. 8.4(I,II) d-f). Some of the curved flaws also start forming at ϕ_{BSA} of 20 wt% and $T = 55$ °C. The ϕ_{BSA} of 1 wt% at $T = 55$ °C shows that the cracks do not propagate in the central region, whereas these cracks intervene at 20 wt%.

Lys protein: The simplest bio-colloid

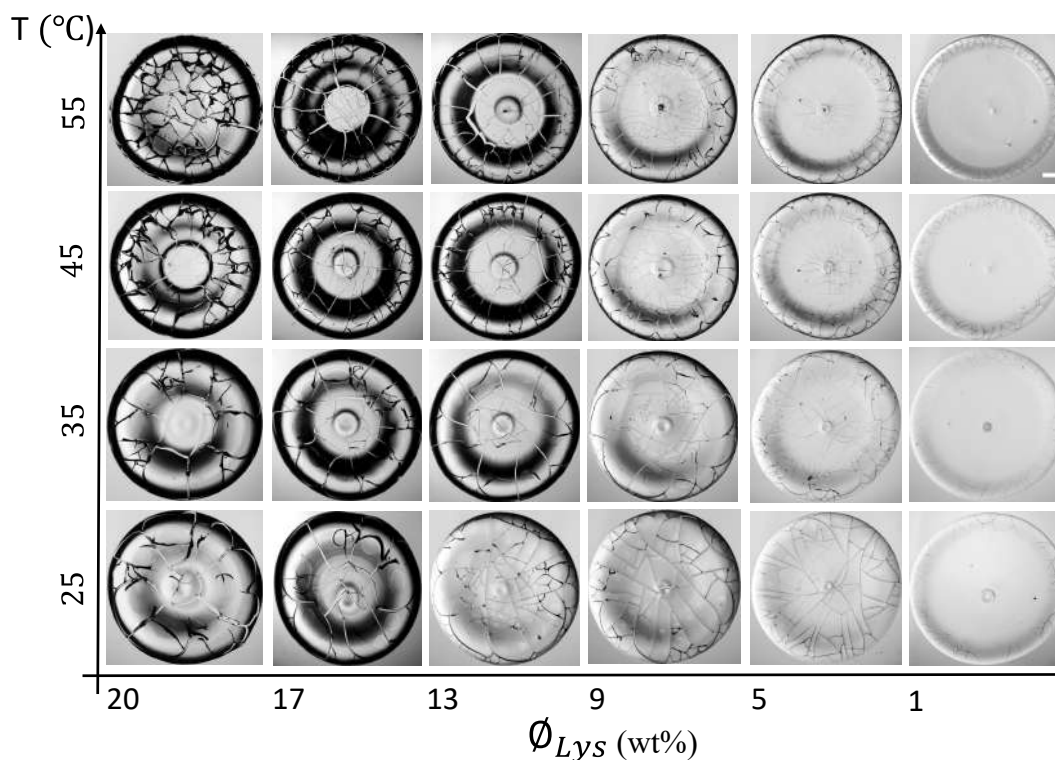


FIGURE 8.5: Morphology of dried lysozyme droplets captured within 24 hours at various initial concentrations (ϕ_{Lys}) diluted from 20 to 1 wt% at controlled substrate temperatures (T) of 25 to 55 °C. The white rectangle represents a scale bar of length 0.2 mm in the top-right panel 55 °C.

Figure 8.5 shows the morphological patterns of Lys dried droplets at different initial

concentrations (ϕ_{Lys}) from 20 to 1 wt% dried under controlled substrate temperatures (T) of 25 to 55 °C. The ϕ_{Lys} is divided into three regimes, ultra-concentrated ($20 < \phi_{Lys} \leq 17$ wt%), concentrated ($17 < \phi_{Lys} \leq 9$ wt%) and dilute ($9 < \phi_{Lys} \leq 1$ wt%). It should be noted that the morphological patterns shown here are somewhat different from our previous work [8], especially at the higher ϕ_{Lys} , because a different substrate was used resulting in a different wetting angle, which plays an important role in determining these patterns.

A common trend observed is that the thick dark peripheral of the dried droplet in the ultra-concentrated regime becomes thin in the concentrated regime, and further diminishes in the diluted regime irrespective of temperature. The characteristic feature in all these samples at T = 25 °C is the presence of the central mound with a dimple (see the bottom panel of Fig. 8.5) (Pal et al., 2020a). However, the crack (fracture) patterns depend strongly on both T and ϕ_{Lys} . In the ultra-concentrated regime, most of these radial cracks create large-sized domains. Some dark curved cracks are noticed near these radial cracks in this regime. In contrast, the random large and small-sized cracks are observed in the concentrated regime throughout the film. With more dilution, these random cracks are found only in the ring. The images at an elevated temperature of 35 °C are quite similar to those at 25 °C; however, the shadowy dark shade becomes sharper (mid panel of Fig. 8.5). An enlarged spot in the dimple is detected in various samples at elevated temperatures and ϕ_{Lys} of 9 to 1 wt%. Interestingly, no mound is observed at (T, ϕ_{Lys}) = (45 and 55 °C, 20 wt%) and (55 °C, 17 wt%). Furthermore, the suppression of coffee-ring behavior and a unique crack pattern are seen at (T, ϕ_{Lys}) = (55 °C, 20 wt%) [top panel of Fig. 8.5].

Figure 8.6(I-II) a-f describes the drying evolution of the selected lysozyme samples at (T, ϕ_{Lys}) = (55 °C, 1 wt%) and (55, 45, and 25 °C, 20 wt%). A comparison of Figs. 8.6(I-II)f reveals that the time required to complete the drying process at 55 and 45 °C (~290 seconds) is less than half that at 25 °C (~700 seconds). For all the samples shown in Fig. 8.6(I-II) a-c, the same initial drying characteristics are seen, irrespective of T and ϕ_{Lys} . Note that the time between the droplet deposition onto the coverslip and the first captured image is ~55 seconds. These first images show a textural gradient, i.e., the dark texture near the periphery and bright near the center (see Fig. 8.6(I-II) a). However, the dark texture area is larger at 20 than that of 1 wt%. As time progresses, the fluid front starts moving from the periphery to the center for all samples. A peripheral band is developed that is thickest for $\phi_{Lys} = 20$ wt% (see Fig. 8.6(I-II) c). The front still moves inward when the cracks begin in the rim width regime (see Fig. 8.6(I-II) d-e). Only for the (T, ϕ_{Lys}) = (55 °C, 1 wt%) sample and only in the ring area do small random cracks emerge. Interestingly, the 20 wt% sample shows a unique crack pattern for various T. Here, the cracks appear near the periphery and start propagating towards the center for (T, ϕ_{Lys}) = (25 °C, 20 wt%) but reverses for the 20 wt% sample at T = 45 and 55 °C. Some of the curved cracks also develop to join these radial cracks at 25 °C. Almost no curved cracks are found at T

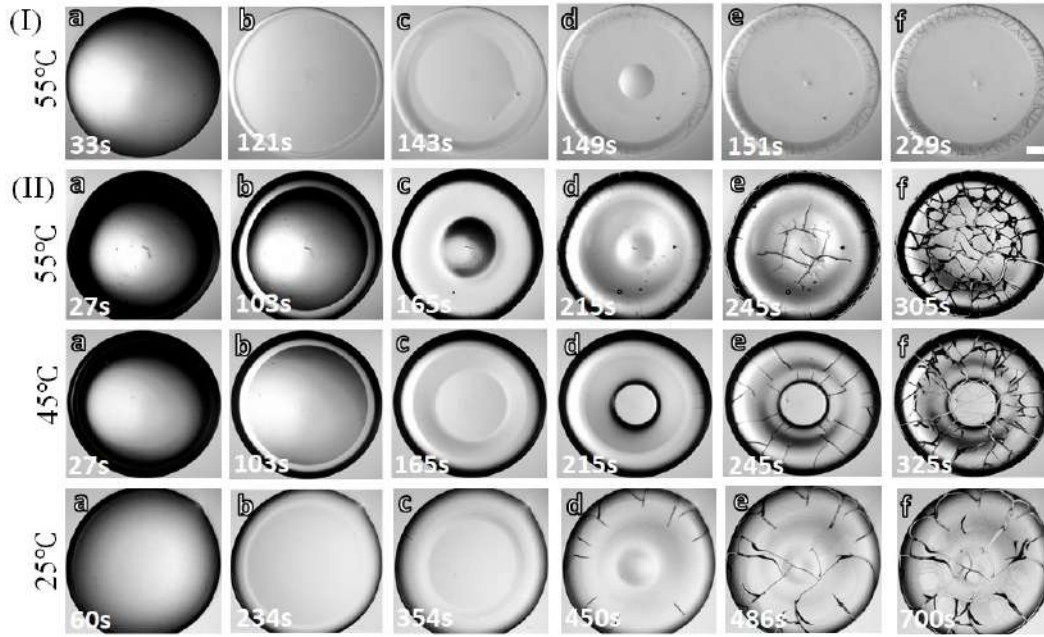


FIGURE 8.6: Drying evolution of lysozyme droplets: (I) a-f displays ϕ_{Lys} of 1 wt% drying under 55 °C. (II) a-f shows the ϕ_{Lys} of 20 wt% drying at 55, 45, and 25 °C. The timestamps are shown at the left-bottom of each image. The white rectangle represents a scale bar of length 0.2 mm in the top-right.

= 45 °C. As T increases to 55 °C, the random various sized cracks originate near the center. Furthermore, the mound-like structure and the depression (dimple) within the mound appears are seen at $(T, \phi_{Lys}) = (25 \text{ }^\circ\text{C}, 20 \text{ wt}\%)$ [a similar observation is reported in (Pal et al., 2020a)]. This mound then disappears at $(T, \phi_{Lys}) = (45 \text{ }^\circ\text{C}, 20 \text{ wt}\%)$, and a spot is noticed in the mound at $(T, \phi_{Lys}) = (55 \text{ }^\circ\text{C}, 1 \text{ wt}\%)$ [see Fig. 8.6(I-II) d-e]. The final morphology is displayed in Fig. 8.6(I-II) f.

8.2.2 Quantitative analysis

Drying evolution of the human blood

Figures 8.7a-f and 8.8a-f show the drying evolution of the statistical image parameters, the mean and the standard deviation [in arbitrary units, (a.u.)] of the blood droplets at the different initial concentrations (ϕ_{blood}) of 100 to 12.5% (v/v), respectively. The substrate temperature (T) of 45 °C is presented in the left y -axis, and $T = 25 \text{ }^\circ\text{C}$ is displayed in the right y -axis. The x -axis exhibits the drying times in seconds for both temperatures.

The mean (I) is defined as the sum of the pixel values divided by the number of the pixels (Carreón et al., 2018b; Pal, Gope, and Iannacchione, 2019b). The I shows three distinct phases: a rapid rise follows the initial increase, after which a peak appears and, finally, decreases to reach the saturation stage. The initial rise of the I is when the fluid front starts moving from the periphery to the central region. When the gray texture starts appearing significantly, the pixel values increase, resulting in the mean

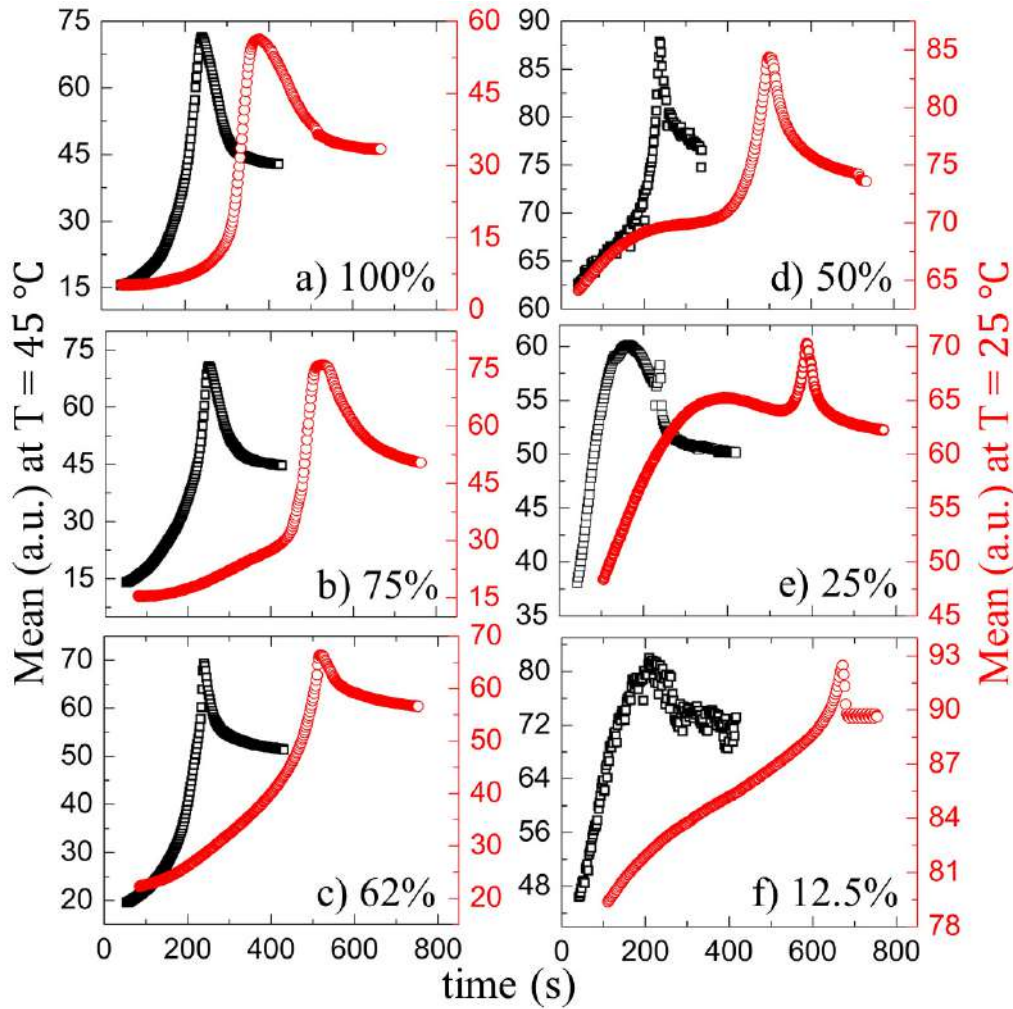


FIGURE 8.7: Time evolution of the statistical image parameter, the mean [in arbitrary units, (a.u.)] of the blood droplets at the different initial concentrations (ϕ_{blood}) of 100 to 12.5% (v/v), respectively, in (a-f). The black and the red colors respectively represent the mean at 45 and 25 °C.

rapid rise (Figs. 8.7a,f and 8.2(I,II)a-f). Soon after reaching the maximum values, the mean begins to decrease when the cracks propagate. The standard deviation (SD) ranges from 100 to 50% (v/v) at both temperatures starts with a rapid rise, followed by a dip. Finally, it increases to reach saturation. The SD measuring the image texture's complexity can capture the finer textural details (Carreón et al., 2018b; Pal, Gope, and Iannacchione, 2019b). The uniformity of the image after the deposition of the droplet is the highest. The dark gray texture of the image for the range from 100 to 62% (v/v) signifies the low value of the SD . It follows a rise and a dip when the mean increases. The pixel values increase (the mean expands) in the process of changing the texture; however, the image's uniformity is reduced (or the complexity is escalated). As soon as the front progresses significantly, it results in a dip of the SD values. The growth of these cracks breaks the uniformity, and the SD shoots up. Interestingly, the SD starts with a high value and reduces at ϕ_{blood} of 25 and 12.5% (v/v)

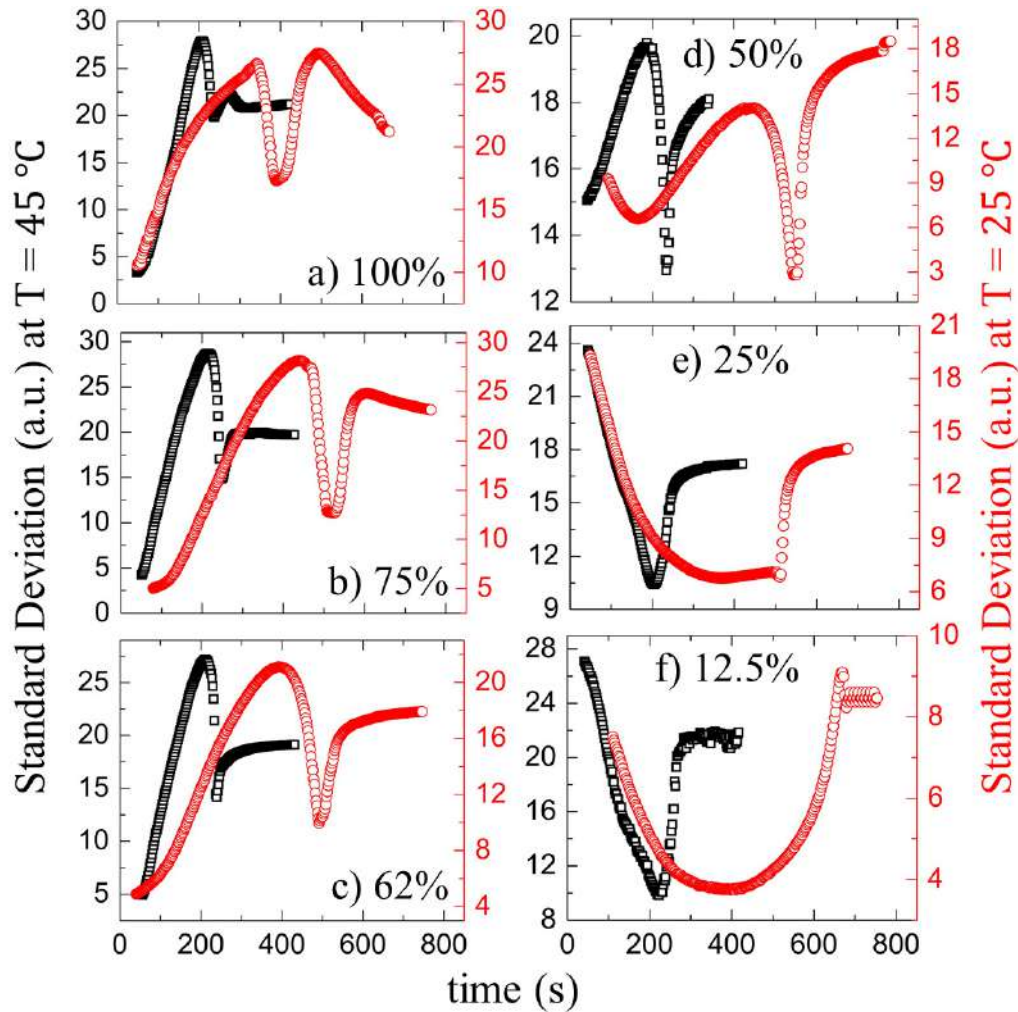


FIGURE 8.8: Time evolution of the statistical image parameter, the standard deviation [in arbitrary units, (a.u.)] of the blood droplets at the different initial concentrations (ϕ_{blood}) of 100 to 12.5% (v/v), respectively, in (a-f). The black and the red colors respectively represent the standard deviation at 45 and 25 °C.

(Fig. 8.8e-f). The uniformity of the images deteriorates due to the presence of the lower pixel values in the light gray textured images at this concentration range. It exhibits a broad dip during the fluid front movement. The crack propagation leads to an increase in their values. In addition, finally, it gets saturated at every ϕ_{blood} as the drying process ends. It is to be noted that the substrate temperature does not induce any significant changes in their behavior (Figs. 8.7 and 8.8).

Figure 8.9(I,II) shows the time evolution of the averaged fluid front radius [$\bar{r}(t)$] that is normalized with the averaged radius of the droplet (\bar{R}) at different diluting concentrations (ϕ_{blood}) ranging from 100 to 12.5% (v/v). The parameter, $\bar{r}(t)/\bar{R}$, is plotted at T of 45 °C in Fig. 8.9(I) and 25 °C in Fig. 8.9(II). The $\bar{r}(t)/\bar{R}$ at 45 °C shows an initial slow linear and a later fast nonlinear regime for all the samples except the most diluted cases, ϕ_{blood} of 25 and 12.5% (v/v). The averaged fluid front radius [$\bar{r}(t)$] is plotted as a function of time at both temperatures. Subsequently, the velocity (or

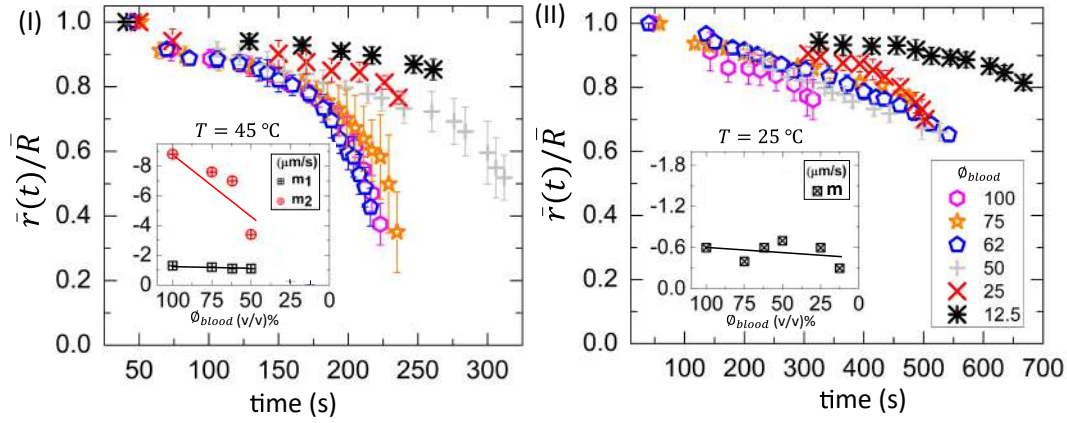


FIGURE 8.9: Time evolution of the normalized fluid front radius ($\bar{r}(t)/\bar{R}$) at different initial concentration (ϕ_{blood}) ranging from 100 to 12.5% (v/v) in the whole blood droplets at various substrate temperatures (T) of 45 °C in (I) and 25 °C in (II). The initial (m_1) and final (m_2) slope values are calculated from ($\bar{r}(t)$) measurements in each region, whereas the slope values (m) are determined from the whole range. The variation of the slope with ϕ_{blood} is displayed in the insets of (I) and (II).

TABLE 8.1: Data from $\bar{r}(t)$ vs. t graph of drying droplet at each ϕ_{blood} (initial blood concentration in (v/v)%) for diluted blood droplets with the fitting parameters: m_1 (slope of first linear fit in $\mu\text{m s}^{-1}$), m_2 (slope of second linear fit in $\mu\text{m s}^{-1}$), and m (slope of the linear fit for the whole range in $\mu\text{m s}^{-1}$) with R^2 (adjusted R-square of linear fit) at different substrate temperatures, 25 and 45 °C.

ϕ_{blood}	T = 45 °C				T = 45 °C		T = 25 °C	
	m_1	R^2	m_2	R^2	m	R^2	m	R^2
100	-1.3	0.932	-8.8	0.932	n/a	n/a	-0.6	0.927
75	-1.2	0.893	-7.6	0.893	n/a	n/a	-0.4	0.994
62	-1.1	0.897	-7.0	0.897	n/a	n/a	-0.6	0.986
50	-1.1	0.991	-5.5	0.991	n/a	n/a	-0.7	0.985
25	n/a	n/a	n/a	n/a	0.8	0.911	-0.6	0.876
12.5	n/a	n/a	n/a	n/a	0.6	0.984	-0.3	0.828

the slope) of the fluid front is analyzed. The initial slope values (m_1) are calculated when a linear fit is done in the linear regime. The m_1 is found to be almost independent of the initial concentration (ϕ_{blood}). The \bar{m}_1 is found to be $-1.17 \pm 0.09 \mu\text{m s}^{-1}$. The negative sign indicates that the radius of the fluid front reduces with the drying time. The later slope values (m_2) are extracted by doing a linear fit in the nonlinear regime. When compared to m_1 , a weak dependency of m_2 on ϕ_{blood} is found. It reduces from -8.8 to $-5.5 \mu\text{m s}^{-1}$ as ϕ_{blood} is diluted [inset of Fig. 8.9(I)]. The \bar{m}_2 is $-5.4 \pm 3.1 \mu\text{m s}^{-1}$. It is to be noted that the samples of 25 and 12.5% (v/v) at 45 °C do not show enough data points for two separate regimes. The \bar{m} at 45 °C is found to be $0.7 \pm 0.1 \mu\text{m s}^{-1}$. At $T = 25^\circ\text{C}$, all the samples show a weak non-linear regime. Therefore, the slope values (m) are determined from the whole range. The \bar{m} at $T = 25^\circ\text{C}$ is $-0.5 \pm 0.2 \mu\text{m s}^{-1}$, which is again weakly dependent on ϕ_{blood} . It is to be noted that the radius of the fluid front could only be measured when it covers $\sim 20\%$ of the whole droplet at 25 °C, whereas it covers $\sim 60\%$ of the total droplet area at

45 °C. A complete description of all the fitting parameters is tabulated in Table 8.1.

Drying evolution of the BSA protein

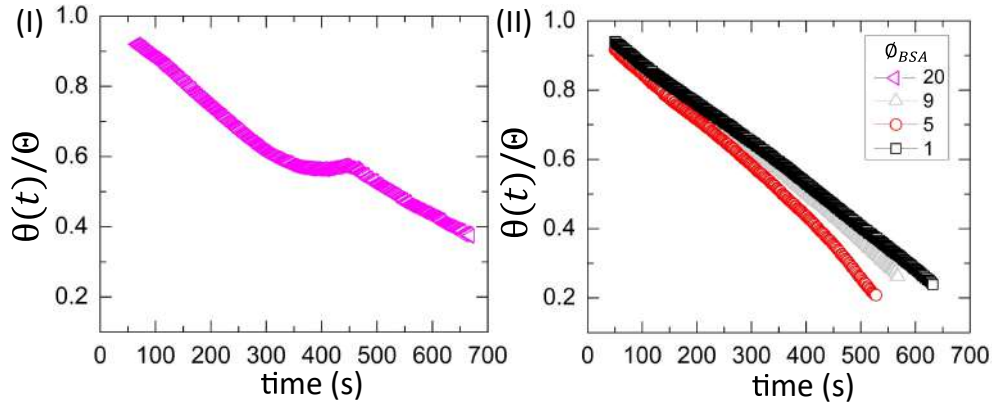


FIGURE 8.10: Time evolution of the normalized contact angle ($\theta(t)/\Theta$) in the BSA droplets at the different initial concentrations (ϕ_{BSA}) of 20 wt% in (I) and from 9 to 1 wt% in (II) for $T = 25$ °C.

Figure 8.10(I,II) shows the drying evolution of the normalized contact angle ($\theta(t)/\Theta$) in the BSA droplets at ϕ_{BSA} of 20 wt% in Fig. 8.10(I). It shows a non-monotonic decrease with a small peak at 20 wt% [Fig. 8.10(I)]. The peak occurs from ~ 350 to ~ 450 s during the contact angle movement. It is found that this duration is the time when the fluid front moves from the periphery towards the central region [Fig. 8.4(I)a-f]. The monotonic decrease (without the presence of any peak) is found at ϕ_{BSA} of 9 to 1 wt% [also reported in the earlier chapter Chapter 4 and our work (Pal et al., 2020a)]. The $\theta(t)$ is plotted as a function of time, and the velocity (or the slope) of the contact angle is measured. The slope for 9, 5, and 1 wt% is found to be -0.0731 ± 0.0002 ° s $^{-1}$ (with $R^2 = 0.998$), -0.0876 ± 0.0004 ° s $^{-1}$ (with $R^2 = 0.996$), and -0.0674 ± 0.0001 ° s $^{-1}$ (with $R^2 = 0.999$), respectively. Interestingly, the contact angle varies monotonically for both the blood droplets at ϕ_{blood} of 50 to 12.5% (v/v) and the BSA droplets at ϕ_{BSA} of 9 to 1 wt%. However, their slope values differ, suggesting that the variation is steeper in the blood rather than the BSA droplets.

Figure 8.11(I,II) shows the drying evolution of the normalized fluid front radius [$\bar{r}(t)/\bar{R}$] at ϕ_{BSA} ranging from 20 to 1 wt% in the BSA droplets at a different substrate temperature (T) of 55 °C in Fig. 8.11(I) and 25 °C in Fig. 8.11(II). The mapping of the contact angle and the fluid front radius measurements [Figs. 8.11(II) and 8.10(I,II)] of the BSA droplets reveal that all ϕ_{BSA} show a similar trend. Only the contact angle reduces without any fluid front movement in the initial ~ 200 s, whereas the simultaneous movement of both the contact angle and the fluid front is found afterward.

Unlike the blood samples, the separate initial slow and later fast fluid front velocities are not apparent in these BSA samples at 55 °C, where only a single rate is seen being m decreases from -4.6 to -1.4 $\mu\text{m s}^{-1}$. On the other hand, the \bar{m}_1 and \bar{m}_2 are found

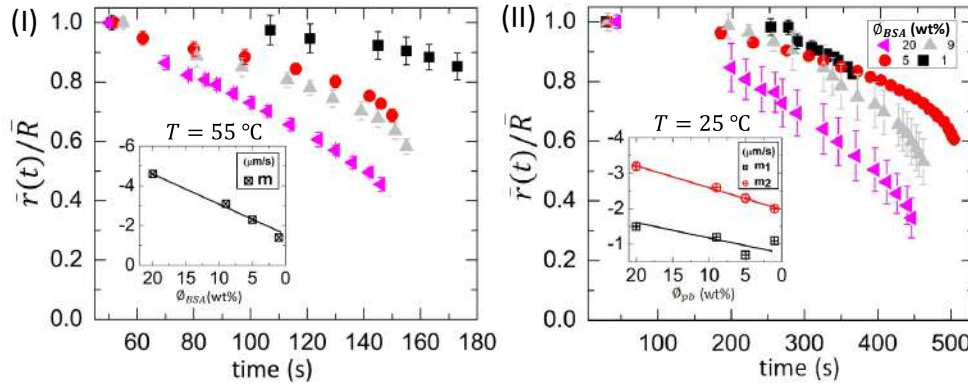


FIGURE 8.11: Time evolution of the averaged fluid front radius ($\bar{r}(t)$) that is normalized with the averaged radius of the droplet (\bar{R}) at the different initial concentration (ϕ_{BSA}) ranging from 20 to 1 wt% in the BSA droplets at different substrate temperature (T) of 55 °C in (I) and 25 °C in (II). The initial (m_1) and final (m_2) slope values are calculated from ($\bar{r}(t)$) measurements in each region at $T = 25$ °C, whereas the slope values (m) are determined from the whole range at $T = 55$ °C. The variation of the slope with ϕ_{BSA} is displayed in the insets of (I) and (II).

to be -1.1 ± 0.3 (with $R^2 = 0.968$) and -2.5 ± 0.5 (with $R^2 = 0.966$), respectively at $T = 25$ °C. A complete description of all the fitting parameters is tabulated in Table 8.2. It indicates that the initial concentration does not have a strong effect on these slope values, i.e., the onset of depositing particles along the line during the fluid front movement is weakly dependent on the initial concentration of both blood and BSA samples.

TABLE 8.2: Data from $\bar{r}(t)$ vs. t graph of drying droplet at each ϕ_{BSA} (initial BSA concentration in wt %) for diluted BSA droplets with the fitting parameters: m_1 (slope of first linear fit in $\mu\text{m s}^{-1}$), m_2 (slope of second linear fit in $\mu\text{m s}^{-1}$), and m (slope of the linear fit for the whole range in $\mu\text{m s}^{-1}$) with R^2 (adjusted R-square of linear fit) at different substrate temperatures, 25 and 55 °C.

ϕ_{BSA}	T = 25 °C				T = 55 °C	
	m_1	R^2	m_2	R^2	m	R^2
1	-1.1	0.929	-2.0	0.982	-1.4	0.959
5	-0.7	0.972	-2.3	0.970	-2.3	0.945
9	-1.2	0.977	-2.6	0.968	-3.1	0.949
20	-1.5	0.995	-3.2	0.943	-4.6	0.992

Drying evolution of the Lys protein

Now that a comparison between the fluid front measurements for both blood and BSA samples at different substrate temperatures has been drawn, it would be interesting to explore the Lys sample's fluid front movement. Like all these samples, the $\bar{r}(t)/\bar{R}$ is plotted as a function of drying time at 55 °C in Fig. 8.12(I) and 25 °C in Fig. 8.12(II) for the Lys droplets. Surprisingly, an intense concentration and temperature dependence for the Lys samples (unlike the blood and BSA samples) was observed at a delayed time point (later) in both substrate temperatures (25 and 55 °C).

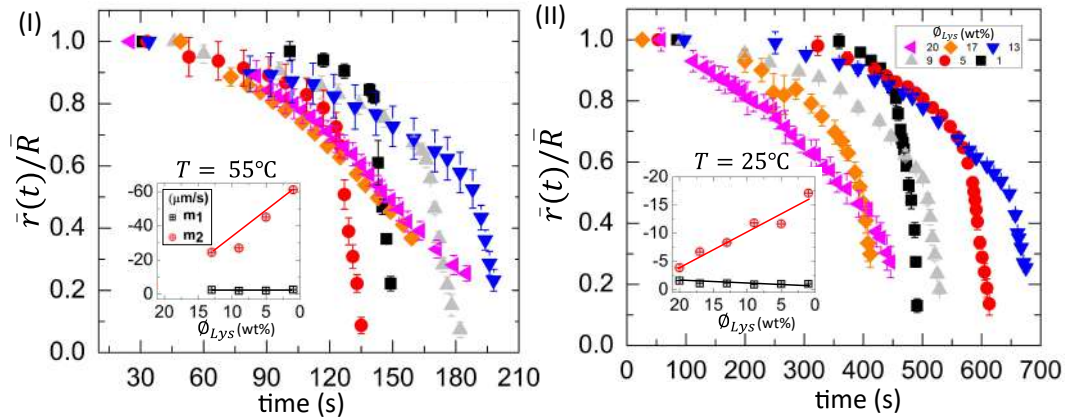


FIGURE 8.12: Time evolution of the averaged fluid front radius, $(\bar{r}(t))$ normalized with the averaged radius of the droplet (\bar{R}) at an initial concentration (ϕ_{Lys}) ranging from 20 to 1 wt% at 55°C in (I) and 25°C in (II). The error bars represent the standard deviation obtained from multiple measurements ($n = 3$). The inset shows the concentration dependence of the initial (m_1) and final (m_2) slope values at $T = 55^\circ\text{C}$ in (I) and 25°C in (II). These values are determined from the time evolution of the $\bar{r}(t)$.

The fluid front moves slowly and linearly and then crosses over to a much faster movement in both diluted and concentrated regimes [reported in our earlier chapter (Chapter 4) and work (Pal et al., 2020a)]. Interestingly, the fluid front ($\bar{r}(t)/\bar{R}$) moves almost linearly with nearly the same behavior over the entire time evolution for the ultra-concentrated samples at $T = 55^\circ\text{C}$. In contrast, there is a strong temperature dependence and two apparent rates for the lower concentration samples. The overall time until the disappearance of the droplet, for the fluid front to move towards the center and vanish, is almost three times shorter at 55°C compared to that at 25°C . Two linear fits are done in the initial evolution and for the later time regime of the fluid front ($\bar{r}(t)$) data to estimate this front's velocity. The inset of Fig. 8.12(I-II) shows the concentration dependence of the initial slope (m_1) and later slope (m_2) values at $T = 25$ and 55°C . The averaged slope over all concentrations gives $m_1 = -1.12 \pm 0.25 \mu\text{m s}^{-1}$ at 25°C (with $R^2 = 0.962$) and $-2.35 \pm 0.35 \mu\text{m s}^{-1}$ at 55°C (with $R^2 = 0.965$). The averaged m is only weakly dependent on ϕ_{Lys} similar to blood and BSA samples [Figs. 8.9(I-II) and 8.11(I-II)]. The negative sign indicates the reduction of the front radius with the progression of time. On the other hand, the extracted m_2 values increase linearly with increasing ϕ_{Lys} . Note that the separate initial slow and later fast fluid front velocities are not apparent in the ultra-concentrated regime at 55°C , where only a single rate is seen being $\bar{m} = -5.7 \mu\text{m s}^{-1}$ ($R^2 = 0.991$) for the 20 wt% sample and a similar $-5.1 \mu\text{m s}^{-1}$ ($R^2 = 0.987$) for the 17 wt% sample. A complete description of all the fitting parameters is tabulated in Table 8.3. It indicates that the onset of depositing these Lys particles along the line during the fluid front movement is strongly affected by the substrate temperature and initial concentration.

TABLE 8.3: Data from $\bar{r}(t)$ vs. t graph of drying droplet at each ϕ_{Lys} (initial Lys concentration in wt %) for diluted Lys droplets with the fitting parameters: m_1 (slope of first linear fit in $\mu\text{m s}^{-1}$), m_2 (slope of second linear fit in $\mu\text{m s}^{-1}$), and m (slope of the linear fit for the whole range in $\mu\text{m s}^{-1}$) with R^2 (adjusted R-square of linear fit) at different substrate temperatures, 25 and 55 °C.

ϕ_{Lys}	T = 25 °C				T = 55 °C			
	m_1	R^2	m_2	R^2	m_1	R^2	m_2	R^2
1	-1.0	0.987	-17.15	0.974	-2.7	0.940	-61.2	0.984
5	-1.0	0.974	-11.67	0.987	-2.1	0.930	-45.1	0.992
9	-0.9	0.941	-11.83	0.989	-2.0	0.965	-27.0	0.960
13	-1.1	0.948	-8.35	0.985	-2.6	0.979	-24.5	0.990
17	-1.1	0.936	-6.70	0.943	-4.8	0.987	-13.8	0.962
20	-1.6	0.987	-3.90	0.981	-5.3	0.986	-5.3	0.995

This fluid front analysis for the various samples (the one-component systems– proteins such as BSA and Lys; and the multi-component system– human blood) at different initial concentrations and substrate temperatures strongly emphasizes that the drying evolution dictates the morphological patterns. For example, the Lys' morphological patterns show diversity (Fig. 8.5) compared to blood (Fig. 8.1) and BSA samples (Fig. 8.3). Therefore, it encourages researchers in this field to examine both the drying evolution and resulting patterns to draw any conclusive remark in any of these bio-colloidal samples. The forthcoming section of this chapter examines all these samples' dried films and initiates to explore the origin of different crack patterns.

Morphological patterns of the dried films

Figure 8.13(I-III) shows the normalized ring width (\bar{w}/\bar{R}) of the blood film as a function of ϕ_{blood} at T of 45 to 25 °C. The solid line depicts the linear fit over the whole range from 100 to 12.5% (v/v). The dotted and dash-dotted lines show the linear fit from 100 to 62 and 62 to 12.5% (v/v). The linear fits for the range from 100 to 12.5% and from 100 to 62% (v/v) are not possible at T = 45 °C. Therefore, a dashed line is drawn for the guide to our eyes. The slope values were extracted for the different ranges of ϕ_{blood} . The slope for the range 100 to 12.5, 100 to 62, and 62 to 12.5% (v/v) is denoted by m , m_1 , and m_2 . The m is found to be $0.0096 \pm 0.0003 \phi_{blood}^{-1}$ ($R^2 = 0.995$) and $0.0054 \pm 0.0006 \phi_{blood}^{-1}$ ($R^2 = 0.936$), respectively at T = 35 and 25 °C. On the other hand, the m_1 is $0.0123 \pm 0.0002 \phi_{blood}^{-1}$ ($R^2 = 0.999$), and $0.0089 \pm 0.0021 \phi_{blood}^{-1}$ ($R^2 = 0.891$), respectively, at T = 35 and 25 °C. In addition, m_2 is $0.0094 \pm 0.0020 \phi_{blood}^{-1}$ ($R^2 = 0.873$), $0.0067 \pm 0.0006 \phi_{blood}^{-1}$ ($R^2 = 0.999$), and $0.0051 \pm 0.0008 \phi_{blood}^{-1}$ ($R^2 = 0.928$), respectively, at T = 45, 35, and 25 °C. The higher R^2 value of m compared to that of m_1 and m_2 indicates that the linear fit is better suited for the whole range of ϕ_{blood} instead of splitting the fits at 62% (v/v).

The variation of the averaged crack spacing (\bar{x}_c) of the blood film as a function of

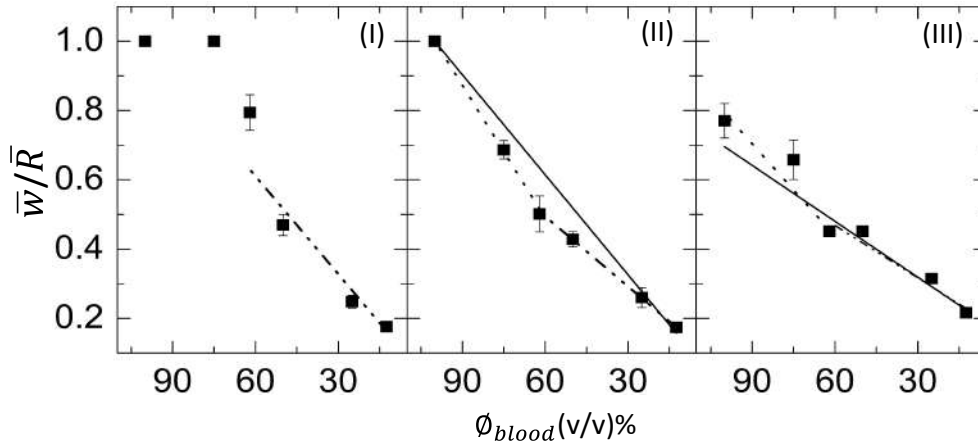


FIGURE 8.13: Concentration dependence of the normalized ring width (\bar{w}/\bar{R}) of the whole human blood film at different substrate temperatures (T) at (I) 45 °C, (II) 35 °C, and (III) 25 °C. The solid line depicts the linear fit over the whole range from 100 to 12.5% (v/v). The dotted and dash-dotted lines show the linear fit from 100 to 62%, and 62 to 12.5% (v/v), respectively. The dashed line at $T = 45$ °C is a line drawn to guide our eyes.

ϕ_{blood} at 45, 35, and 25 °C is presented in Figure 8.14(I-III), respectively. Similar to Fig. 8.13(I-III), the slope values (m , m_1 , and m_2) are extracted for various concentration ranges. The m is found to be 0.0056 ± 0.0006 mm ϕ_{blood}^{-1} ($R^2 = 0.942$) at $T = 45$ °C. As we decrease the temperature to 35 °C, the m reduces and is observed to be 0.0049 ± 0.0013 mm ϕ_{blood}^{-1} ($R^2 = 0.721$). Finally, the m becomes 0.0034 ± 0.0012 mm ϕ_{blood}^{-1} ($R^2 = 0.579$) at room temperature of 25 °C. In contrast, the m_1 is 0.0081 ± 0.0008 mm ϕ_{blood}^{-1} ($R^2 = 0.982$), and 0.0081 ± 0.0015 mm ϕ_{blood}^{-1} ($R^2 = 0.934$) at the elevated temperatures, 45 and 35 °C, respectively. At $T = 25$ °C, the m_1 is 0.0011 ± 0.0015 mm ϕ_{blood}^{-1} ($R^2 = 0.960$). The m_2 is 0.0039 ± 0.0005 ϕ_{blood}^{-1} ($R^2 = 0.958$), 0.0029 ± 0.0007 ϕ_{blood}^{-1} ($R^2 = 0.844$), and 0.0016 ± 0.0005 ϕ_{blood}^{-1} ($R^2 = 0.736$), respectively, at $T = 45, 35,$ and 25 °C. Unlike the \bar{w}/\bar{R} , R^2 values of m_1 and m_2 at all temperatures increases compared to m when \bar{x}_c is plotted as a function of ϕ_{blood} . The slope values change for different ranges of the linear fits done from 100 to 62, and 62 to 12.5% (v/v). A kink is observed at 62% (v/v) in all temperatures; however, it reduces with the increase of the temperature [Fig. 8.14(I-III)].

Figure 8.15(I,II) shows the variation of the normalized ring width (\bar{w}/\bar{R}) and the averaged crack spacing (\bar{x}_c), respectively, as a function of ϕ_{BSA} in the BSA film at T ranging from 55 to 25 °C. The solid green line depicts that the width of the ring decreases with the dilution. The slope values of \bar{w}/\bar{R} at $T = 55, 45, 35,$ and 25 °C are 0.033 ± 0.004 ϕ_{BSA}^{-1} ($R^2 = 0.960$), 0.029 ± 0.006 ϕ_{BSA}^{-1} ($R^2 = 0.893$), 0.033 ± 0.007 ϕ_{BSA}^{-1} ($R^2 = 0.866$), and 0.026 ± 0.004 ϕ_{BSA}^{-1} ($R^2 = 0.945$), respectively. These values indicate that the \bar{w}/\bar{R} is independent on the temperature. In contrast, the \bar{x}_c exhibits a strong dependency on the temperature. The different colored dashed lines guide us to understand the variation of the \bar{x}_c with the substrate temperature. The straight line of \bar{x}_c suggests that it is nearly independent of ϕ_{BSA} at $T = 55$ °C. As T decreases

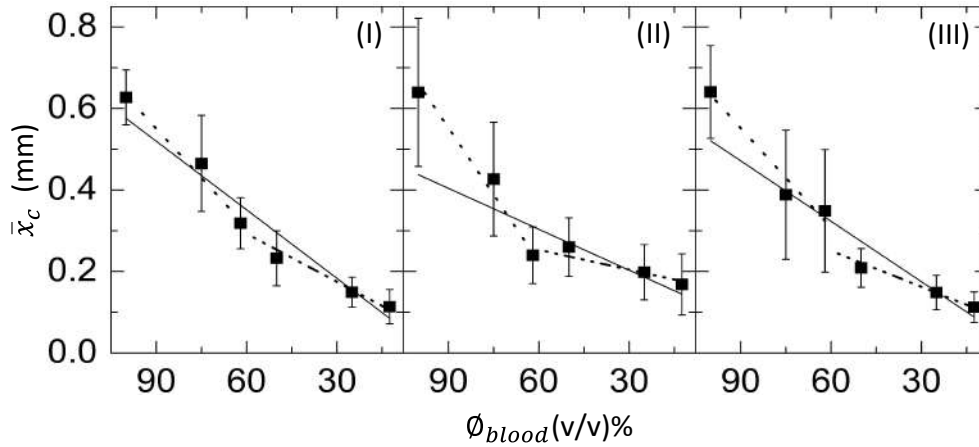


FIGURE 8.14: Concentration dependence of the averaged crack spacing (\bar{x}_c) of the whole human blood film at different substrate temperatures (T) at (I) 45 °C, (II) 35 °C, and (III) 25 °C. The solid green line depicts the linear fit done over the whole range from 100 to 12.5%. The dotted and dash-dotted lines show the linear fit from 100 to 62, and 62 to 12.5% (v/v).

from 55 to 25 °C, the \bar{x}_c reduces from ~ 0.45 mm to ~ 0.21 mm.

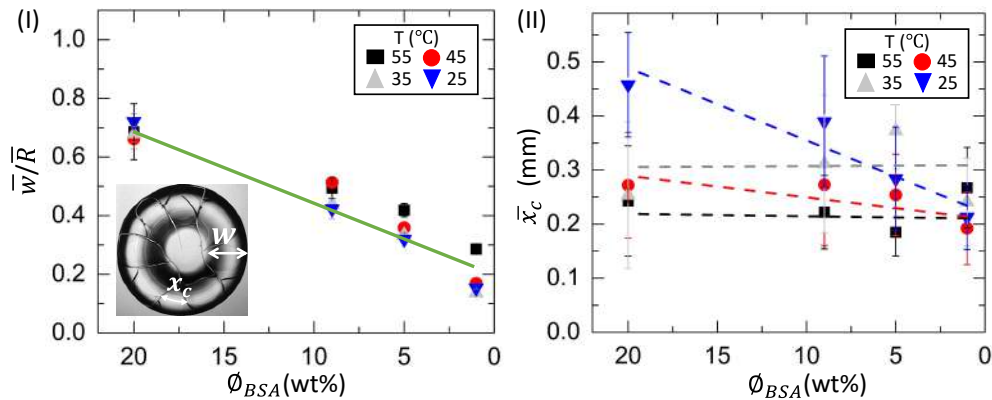


FIGURE 8.15: (I) Concentration dependence of the normalized width of the ring (\bar{w}/R) of the BSA film at different substrate temperatures (T) from 55 to 25 °C. The solid green line shows a master linear fit. (II) Concentration dependence of the averaged crack spacing (\bar{x}_c) of the BSA film at different T from 55 to 25 °C. The different colored dashed lines at different temperatures are drawn to guide our eyes. The x_c and w are shown on the dried BSA film at ϕ_{BSA} of 20 wt% and $T = 25$ °C.

Figure 8.16(I-II) exhibits the concentration dependence of the normalized ring width (\bar{w}/R) [Fig. 8.16(I)] and the averaged spacing between the consecutive radial cracks (\bar{x}_c) [Fig. 8.16(II)] at different T for Lys samples. It is observed that both these parameters decrease with increasing ϕ_{Lys} , similar to BSA samples. However, the standard deviation of \bar{w}/R is not as large as \bar{x}_c when plotted as a function of T and ϕ_{Lys} . It is also to be noted that the quantification of the ring width is not possible at $(T, \phi_{Lys}) = (55 \text{ °C}, 20 \text{ wt}\%)$. It seems that the temperature does not play a strong role for the ring width shown in Fig. 8.16(I) as the data overlay each other closely. Similarly, the \bar{x}_c behavior is also weakly dependent on temperature. However, it is far more scattered, with larger uncertainties for higher concentrations. It thus showed the largest

separation between the two highest and the two lowest temperatures.

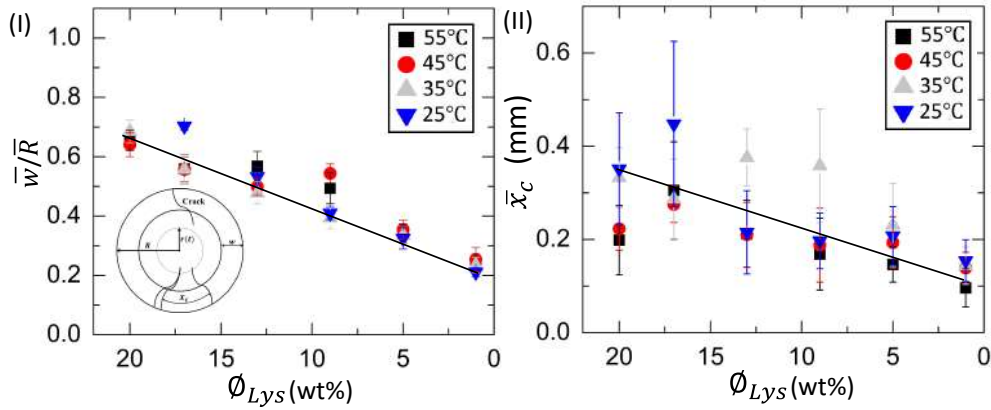


FIGURE 8.16: (I) shows the averaged ring width (\bar{w}) normalized with the averaged radius of the droplet (\bar{R}). (II) exhibits the averaged crack spacing (\bar{x}_c), both at various T and ϕ_{Lys} . The error bars represent the standard deviation obtained from multiple measurements ($n = 3$). The inset of (I) displays a schematic droplet cartoon describing the radius of the fluid front (r) at an instant of time (t), the radius of the droplet (R), ring width (w), and crack spacing (x_c).

8.3 Discussions

Figures 8.17(I-II)a-c show the physical mechanism of BSA droplets (please refer to Chapters 4 and 6 and our previous publications (Pal et al., 2020a; Pal et al., 2020b) for detailed discussion on protein and blood process). The images are taken from the top in transmission mode and capture the droplets' entire hemispherical-cap shape. Thus, the uniformity of the drying conditions across the droplet is confirmed by the symmetrical fluid front radial movement and by the textural radial gradients (the dark region near the periphery and the bright region in the central region) seen in protein droplets (Figs. 8.4a and 8.6a). However, this non-uniformity is observed in a specific range of blood samples only. For instance, it is predominantly observed in the droplets diluted at ϕ_{blood} of 62 to 12.5% v/v to due to the reduced number of RBCs (Figs. 8.2(II)a). Due to droplet curvature, the evaporative mass loss is most significant near the three-phase contact line (interface between coverslip, droplet, and air) than the droplet top. This loss drives the convective flow within the droplet during drying. The capillary flow (Fig. 8.17(I,II)a) drives the BSA particles towards the droplet periphery. As time progresses, a BSA-rich layer is observed to form in the one-component system (Fig. 8.17(I,II)b). Similar steps are observed in the Lys drying droplets (Fig. 8.6(I,II)b). On the other hand, a plasma protein-rich layer develops in the multi-component system. With the advancement of time, more water starts evaporating from these droplets, leading to an interaction of the droplet particles. The BSA and the Lys particles interact in the respective protein droplets,

whereas the cellular components (WBCs, RBCs, and platelets) (significantly) interact in the blood droplets. We assumed that many of these particles and their interactions near the periphery disturb the contact angle measurements. For example, the non-monotonic decrease of the contact angle is observed at ϕ_{blood} of 100 to 62% (v/v) in blood droplets and at ϕ_{BSA} of 20 wt% in the BSA droplets [Fig. 8.10(I)]. Please refer to Chapter 4 and (Pal et al., 2020b) for a detailed discussion on the origin of such non-monotonic property. The drying mechanism of the one component (simplest) BSA and the multi-component (complex) blood bio-colloidal droplets discussed in this chapter indicates that the non-monotonic property (i.e., the presence of the peak-like feature) could be a universal property that can be observed across any high-concentrated colloidal samples. A similar observation (i.e., the presence of such non-monotonic property) has recently been reported in the polymeric system (Kumar, Katz, and Schroeder, 2017) that further supports our claims. However, to establish these claims, the Lys and other globular proteins need to be thoroughly examined. Its origin might also be dependent on the molecular weight of the particles present in the droplets. Since the average molecular weight of these latex spheres is $\sim 1 \times 10^6$ g (for particles of diameter ≤ 100 nm) which is much higher than the protein's average weight (~ 14.3 kDa and ~ 64.5 kDa for BSA, and Lys, respectively).

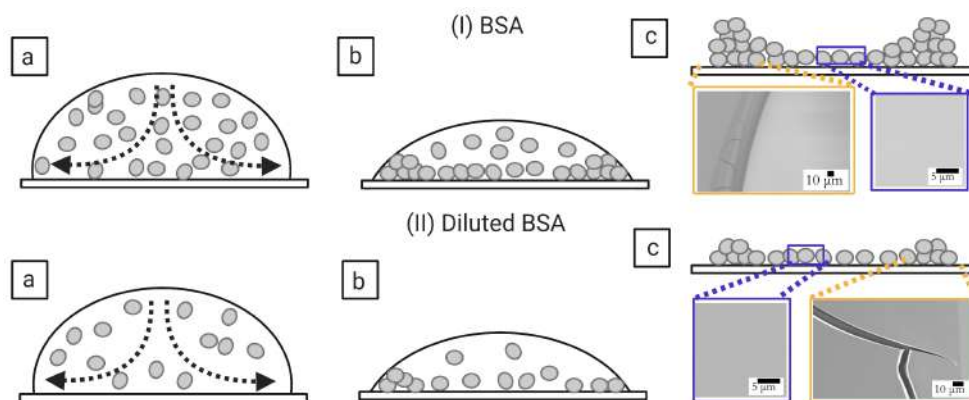


FIGURE 8.17: The BSA droplet's physical mechanism during the drying process at $\phi_{BSA} = 20$ wt% in (I)a-c and at $\phi_{BSA} = 1$ wt% in (II)a-c. The capillary flow is indicated with the dotted arrows in (I,II)a. The blue and the orange rectangles in (I, II)c display the microstructures in the central and the rim regions (both 20 and 1 wt%).

A comparison amongst the macroscopic images of the drying process (Figs. 8.2(I,II) a-f and 8.4(I,II) a-f) confirms that the peak-like feature obtained from the contact angle measurements (non-monotonic property) appears only during the fluid front movement. This indicates that a sufficient amount of water is still present in the droplet to preserve these particles' native states. Both these droplets, however, experience mechanical stress as soon as the water reduces significantly. Please refer to (Pal et al., 2020b) and Chapter 6 for a detailed microstructural discussion on these diluted blood droplets. Interestingly, BSA dried films' micrographs show a uniform texture (Fig. 8.17(I,II)c). This indicates that these BSA structures are at a shallow

length scale (unlike blood dried films), and the magnification is not enough to analyze at those length scales.

It is worth mentioning that the morphological texture and the (crack) patterns significantly affect the blood and Lys droplets (Figs. 8.1 and 8.5), but not the BSA droplets (Fig. 8.3). The sliding of the cracked films is observed at ϕ_{blood} of 100 to 62% (v/v); it is, however, absent at ϕ_{blood} of 50 to 12.5% (v/v) [Fig. 8.1, reported in (Pal et al., 2020b)]. On the other hand, all the protein samples show that the dried films firmly adhere to the substrate (Figs. 8.3 and 8.5), reported in (Pal et al., 2020a). Furthermore, the ring's height is higher than the central region at ϕ_{BSA} or $\phi_{Lys} = 20$ wt%, and it reduces as we dilute to 1 wt%. The corona region of the blood film at the highest dilution [ϕ_{blood} of 12.5% (v/v)] nearly mimics the homogeneous texture of the BSA blood films [Figs. 8.1 and 8.3]. The dried films of both simplest and complex bio-colloidal films show a gradual decrease when the ring's normalized width is plotted with the initial concentration [Figs. 8.13(I-III), 8.15(I), and 8.16(I)]. This trend indicates that the width of the ring measures the deposition of the particles. When the number of particles is high, the ring's width is more (reported in one of our papers in (Pal et al., 2020a) and earlier chapters 4 and 6). As the number reduces, the ring's width decreases; however, the self-assembling mechanism is different during their deposition. The different self-interacting mechanism (of a large number of components) is observed for other complex multi-component systems (Carreón et al., 2018a; Carreón et al., 2018b; Pal et al., 2019), not specifically to the blood. Contrary to these blood samples, the \bar{x}_c is found to have a weak concentration dependence in the proteins films [Figs. 8.15(II) and 8.16(II)].

One could suggest changing the ratio of blood components and plasma proteins by decreasing RBCs' concentration using the centrifugation method instead of diluting it with de-ionized water. This particular method is used to study the morphological alteration of RBCs recently (Mukhopadhyay et al., 2018). While we understand that a systematic study is required to understand how each cellular component behaves and contributes to the drying process, we must admit that this is beyond the scope of the current study. The visco-elastic to elastic transition is developed during the drying process when the concentration of the blood components increases. Therefore, starting with the different initial concentrations, i.e., changing the ratio of blood components and plasma proteins, will affect the transition concentration reported in the series of study.

In addition to the concentration study, the substrate temperature (T) is varied. The droplets are pipetted on the coverslip at 25 °C outside the hot microscope stage and then transferred to the hot stage well within ~ 45 s. So, it is likely that the temperature fluctuations might be present in these droplets, especially when the set temperature is ≥ 25 °C for the initial ~ 10 s after closure. After the initial first minute of deposition and mounting, the subsequent imaging should also be affected by the temperature gradients driven by evaporative cooling and convective flow of the drying

process. Interestingly, the statistical mean and the standard deviation extracted from the images of the blood samples indicate that the temperature only reduces the total drying time (Figs. 8.7a-f and 8.8a-f). Furthermore, the fluid front measurements of both the blood and BSA samples suggest that the fluid's velocity gets increased with the increase of the temperature; however, the deposition of the particles is weakly dependent on both temperature and initial concentration [Figs. 8.9(I,II) and 8.11(I,II)] compared to the Lys samples [Figs. 8.12(I,II)].

One of the best possible ways to understand the observed drying and final dried patterns evolved under an elevated temperature is to examine the mass flow generated inside the droplet. The flow could be capillary, surface tension, and temperature-induced Marangoni flow. It is reported in the literature that if the Marangoni flow exceeds the outward radial flow, the ring-like behavior is suppressed (Majumder et al., 2012). However, all of our samples at each T show the ring-like behavior except 100% (v/v) at T = 35 and 45 °C as well as 75% (v/v) at T = 45 °C in the blood samples, and (T, ϕ_{Lys}) = (55 °C, 20 wt%) in Lys samples (see Figs. 8.1 and 8.5). Interestingly, we observed a dark peripheral band in each sample. This feature indicates that this suppression might not conclude the Marangoni flow's dominance for every case. Therefore, we speculate that most of these particles near the three-phase contact line are transported with the capillary flow. Energizing the system by increasing the T above the room temperature (here, up to 55 °C for protein samples and 45 °C for blood samples) might not dominate one flow over the other. The suppression of ring-like behavior at elevated substrate temperature remained because there is not enough time to segregate (high T promotes the evaporation of water quickly) these large number of particles during the drying process. The thickness of this peripheral band is observed to be dependent on the samples' initial concentrations (ϕ_{blood} , ϕ_{BSA} , and ϕ_{Lys}). For example, in Lys sample, the thickest band is seen at $\phi_{Lys} = 20$ wt%, and it becomes thin with the decreasing ϕ_{Lys} (see Fig. 8.5). This suggests that more material would be transported to the periphery for a larger initial concentration. The leftover particles fall out of the solution giving rise to the mound-like structure in the central region. A depression (dimple) is also found, indicating the trapped water's evaporation within that mound. It is to be noted that all the Lys samples do not form this mound structure. As this structure can be turned off by supplying enough energy (increasing T) to the system, it should not be considered the Lys' fingerprint in general. The T was just enough that most of the particles at ϕ_{Lys} of 20 and 17 wt% are carried by the fluid front, and there are no leftover particles by the end of its movement. This suppression is due to an interaction between the T and ϕ_{Lys} . This also indicates a phase diagram between T and ϕ_{Lys} ; however, two points are not enough to draw any conclusive claim. More samples need to be examined to attest to this observation. The absence of the non-linearity in the fluid front measurements for the ultra-concentrated regime at 55 °C also indicates some interaction between the T and ϕ_{Lys} that exist in these Lys samples.

The evaporation of a large amount of water resulted in mechanical stress development due to the pinning effect. The droplet is unable to shrink any further. The film cracks to relieve this stress. However, this crack propagation depends on when the available film stress exceeds the critical stress (popularly known as Griffith's criterion). For example, $\phi_{Lys} = 1$ wt% does not show any cracks in the middle region (between the mound and the ring) [please see the previous chapter for a detailed discussion (Chapter 4)]. The cracks are throughout the Lys film in the concentrated samples. The morphological patterns are different in the ultra-concentrated samples since the thickness gradient throughout the film differs at elevated T (see Figs. 8.5 and 8.6(I-II) d,e). Interestingly, the images captured during the drying process and the dried films of both the BSA and the blood show that the morphological (crack) patterns do not significantly differ from those captured under the ambient temperature (Figs. 8.1-8.4). The mean crack spacing (\bar{x}_c) shows a gradual decrease in both the protein samples (BSA and Lys) [Fig. 8.15(II) and 8.16(II)]. On the other hand, the kink at 62% (v/v) gets reduced when the temperature is increased in blood samples [Fig. 8.14(I-III)].

The study of these bio-colloidal samples (blood, BSA, and Lys) at ambient and elevated temperatures suggests two main points. First, there exists an interaction between the initial concentration and the substrate temperature. The second one is that this interaction is unique for different samples and could be linked to the native states of the constituent particles present in these droplets. It would be more interesting to examine these samples under infrared microscopy. This technique will allow us to understand the physics better by observing the isotherms on the droplet-air interface, the substrate's surface and mapping this temperature distribution at each timestamp during the drying process. It will also be interesting to examine the effects of the relative humidity and/or its coupling with the temperature on the pattern formation of such diluted bio-colloidal droplets since relative humidity directly affects the drying mechanism.

8.4 Conclusions

This chapter explored the physical phenomena of different patterns formed during different phases of the drying process in one of the most complex (the whole human blood) and the simplest bio-colloidal droplets (the aqueous solution of the globular proteins, BSA and Lys). The captured images, the statistical image analysis, the fluid front, the contact angle measurements during the drying process, and the dried films' microstructural sketches are described for both the blood and the BSA samples. The findings confirm that the samples' visco-elasticity depends on the self-interacting mechanism of a large number of components, not specifically to the blood. The sample prepared by extreme dilution of the whole blood behaves like the BSA droplet. Thus, this current study initiates a theoretical effort to examine how the dilution and the substrate temperature interact in characterizing these bio-colloidal

droplets. This study offers new macroscopic and microscopic insights connecting the hierarchical structures that are evolved as the drying process advances through a new phase transition mechanism. The next chapter describes the general conclusion of studying these drying droplets systematically, starting from the simplest to naturally-occurring bio-colloids.

Chapter 9

Conclusions and Future Outlook

9.1 Conclusions

Pattern formation in drying bio-colloidal droplets has attracted considerable research attention recently since it can easily be linked to specific colloid-colloid and colloid-substrate interactions. The evolution and the final pattern display a fingerprint of the initial state when dried under uniform conditions (surface, humidity, temperature, droplet diameter, etc.). In this dissertation, a series of systematic experiments are conducted to comprehend the macroscopic patterns related to the constituent particles' microscopic native states by allowing the system to relax (dry) under controlled conditions. The findings of the drying droplet experiments reveal a unique drying pattern for different globular proteins (Pal et al., 2020a) (the simplest hierarchical structure) (i) with and (ii) without liquid crystals (LCs- a class of materials that possess both liquid and crystal-like phases) (Pal et al., 2019; Pal, Gope, and Iannacchione, 2019a; Pal, Gope, and Iannacchione, 2019b), and (iii) the whole blood (the most complex hierarchical structural fluid, i.e., plasma in the presence of cellular components) (Pal et al., 2020b; Pal, Gope, and Iannacchione, 2021). It must be noted that the blood samples used in this thesis are acquired from healthy people. Furthermore, this work specifically explained how external salts and the controlled substrate temperature affect the drying process and resulting morphological patterns in proteins and blood. The interfacial and self-assembling behavior of the drying droplets is thoroughly examined using optical and scanning electron microscopic imaging, along with new image processing protocols and contact angle measurements. Moreover, various statistical tests were employed to quantify a broad set of image data. All the protein and blood samples are imaged under bright-field microscopy. In contrast, the protein-LC samples are examined and imaged using both bright-field and cross-polarizing configurations.

This dissertation highlights the concentration dependence of two globular proteins, lysozyme (Lys) and bovine serum albumin (BSA), in both de-ionized water and phosphate buffer saline (PBS). The coffee-ring behavior is observed in all these bio-colloidal samples. It also reveals its dependence when the whole human blood is diluted in the presence of water and PBS. Interestingly, the high dilution of blood

behaves like the BSA solution. All the samples show significantly different morphological patterns with and without salts. The common characteristics observed in salts' presence is the phase separation of the salts and proteins, i.e., the protein particles are primarily distributed in the rim, whereas the salt deposits in the inner central region. While the structural deformation of the blood's cellular components provides a local response to the mechanical stress developed due to significant water loss in these droplets, the global response is achieved by cracking these bio-colloidal films. Various amounts of salts in the diluent change the physio-chemical environment in these bio-colloidal droplets influencing the macroscopic patterns to a great extent. However, the salts' presence does not have any significance for altering the structures of the blood's cellular components.

Apart from qualitative observations, the drying evolution in these samples is quantified by extracting the fluid front radius. However, the fluid front radius extraction is possible only when these samples are prepared in the de-ionized water. The front moves uniformly from the periphery to the ring, enabling the possible tracking movement until the inner ring (only) in the salts samples. It implies that there are not enough data to quantify its drying evolution compared to samples without salts. The findings further indicate that different image processing techniques are needed to quantify the drying evolution. The textural analysis adopted in this dissertation and other work (Carreón et al., 2018b; Pal et al., 2019; Pal, Gope, and Iannacchione, 2019a; Pal, Gope, and Iannacchione, 2019b; Pal, Gope, and Iannacchione, 2021) is indeed valuable for quantifying the changes at different saline concentrations and dictating the ubiquitous stages of the drying process. The first-order statistical parameters such as the standard deviation capture the textural complexity, whereas the mean averages the textural details.

Contrary to the first-order statistical analysis, the gray level co-occurrence matrix (GLCM) summarizes both the tonal and structural relationships between the image's neighboring pixels. Thus, it demonstrates the versatility and usefulness of this textural analysis, and we can adopt a similar methodology in other (related) bio-colloidal systems. Furthermore, this analysis leads to large data sets, which are used statistically to identify whether the (horizontal and the vertical) orientations show any significant effect when the pixel displacement is varied for different saline concentrations. This analysis also reveals that the tuning between bio-colloid and salts is essential in determining the morphological patterns. The textual evolution indicates that the interactions between different bio-colloidal particles during the drying process are dependent on the quantity of salts present in PBS. It also needs to keep in mind that enough contrast in the images is essential for an 8-bit camera to capture the textural details. This implies why this analysis might not be helpful in protein samples without salts. Interestingly, this same analysis is applied in the different contexts when we study the patterns evolved through phase separation of bulk LC (an optically active material) and self-assembly of protein induced by evaporation

of the de-ionized water. Though the first-order statistical parameters (mean and standard deviation) reveal unique regimes like protein-saline or blood-saline samples, here, the mean profile provides information about the birefringence of LCs. It would be interesting to expand this research on emerging pattern formation where the LCs are anchored to the substrate (either perpendicular or parallel). The protein droplets are pipetted on these LC-coated substrates.

Another concluding remark from this Ph.D. work is the evidence of a surprisingly sharp concentration-driven phase transition. This transition relied on the competition among the various components present in the droplet. Our systematic study of the dilution range also ensures that this transition is not specific to the blood-water system only. It can also be concluded that the salts or the ions of PBS do not play any crucial role in this transition. This work also indicates that this transition behavior is not limited to multi-component bio-colloid (blood with and without external salts) only but may be a phenomenon of a colloidal solution containing a large number of interacting components.

This work concludes that the samples have enough time to segregate and deposit onto the substrate under ambient conditions. However, there is insufficient time for evaporative-driven segregation to occur at elevated temperatures. The drying evolution, ring-like deposition, and the crack morphology in the protein and the blood samples prepared in de-ionized water suggest that both the initial concentration and substrate temperature lead to surface tension and temperature gradients across the droplet, affecting the final dried patterns. Comparing the Lys' patterns under ambient and elevated temperature, it is found to be affected significantly. In contrast, the total drying time gets reduced without much change in the blood and BSA samples. Though this study provides clues for the interplay of the substrate temperature and initial sample concentration affecting the final morphology, it would be interesting to study these samples under infrared microscopy. The proposed technique may enable us to better understand the physics by observing the isotherms on the droplet-air interface, the substrate's surface and mapping this temperature distribution at each timestamp during the drying process.

Therefore, this dissertation work reveals that a simple physical mechanism (drying) can easily track the complex physical behavior and presents new insights on the self-assembly of colloidal structures in a symmetric droplet. However, many results yielded are in their developing stage and demand an in-depth exploration to address the fundamentals for many other complex fluids by rastering through the vast parameter space to establish a general understanding of this emerging field of research. This research aims to create a predictable route for the deposition/segregation of multi-component complex systems by tuning their self-assembly at different (nano to micrometers) length scales. Furthermore, this *in-vitro* drying study might help us understand the condensation of the cells due to the changes in their intermolecular

interactions and what kind of physio-chemical environmental change triggers the phase transition from liquid to gel (or liquid crystal) for *in-vivo* configurations.

9.2 Future Outlook

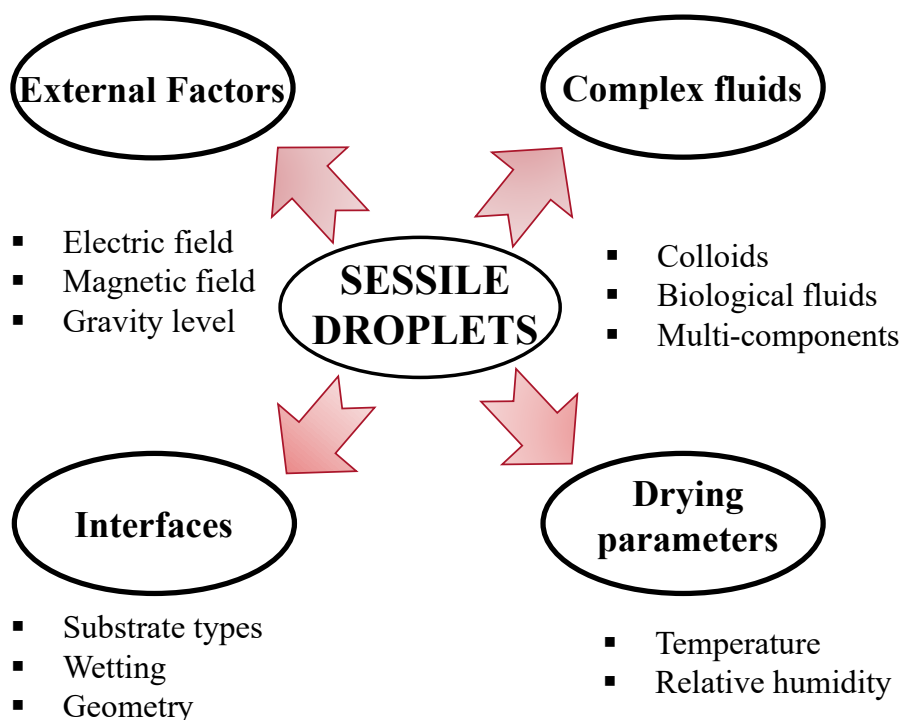


FIGURE 9.1: Schematic diagram describing different directions that could be explored in the near future.

This work further looks forward to creating a corpus of image-databank of the resulting macroscopic patterns. Different aspects can be explored in any soft matter systems, such as examining the deposition patterns, the formation of coffee-ring behavior, or the droplets' flow behavior by varying environmental factors, external perturbations, and substrates or the complex fluids (see Figure 9.1). The simple systems such as mono- and polydisperse lyotropic colloidal LCs, different globular proteins (myoglobin, hemoglobin), etc., could be explored, creating a baseline to understand their interfacial optical, mechanical properties. The dilution of whole human blood can exactly be performed on the human plasma samples. Since there are no cellular components, one can expect no such concentration-driven phase transition; however, no related work (to my best knowledge) is reported so far in the literature. Future studies can also increase the systems' complexity by performing experiments on essential biomolecule, lipid, a structural element for signal transduction across the cell membranes. The target of lipids is attractive because of their amphipathic nature, i.e., they contain both hydrophilic regions (polar head groups) and long hydrophobic chains. In aqueous solutions, these lipid molecules can either form micelles or a bilayer sheet. Besides, we could also study structural protein

(for example, microtubules). It is to be noted that each site of these structural proteins is exposed to interact with other particles. Though most of the studies aim to understand the growing and shrinking mechanisms of microtubules, this could evolve in a new direction if we use these structural proteins as the drying droplets. We hypothesize that their interactions in such a system will help us comprehend the formation of lyotropic LC phases in *in-vivo* conditions and apply to a wide variety of similar biological serums. The proposed research's general hypothesis is that the different morphologies/patterns could be templated/dictated. Combining different bio and non-biological components might help mediate the constituents' deposition/organization and guide their self-assembling interactions. Such insights are crucial for exploring a new direction in the whole experimental physics community or the drying droplet community, particularly for templating purposes, and encourages theorists to develop a new framework for far-from-equilibrium-like behavior.

This study also encourages us to understand the emerging behavior in living biological systems such as bacteria-like microorganisms (see Figure 9.1). It would be interesting to answer a few questions at the fundamental level: (i) How do bacteria communicate to form colonies? (ii) How do they respond to the external convective flow during the drying process? (iii) what is the role of bacterial flagella in the drying dynamics? (iv) How does the substrate wetting affect the resulting patterns? (v) How does the shape of a droplet alter bacterial patterns? Nonetheless, this proposed idea requires robust experiments in a lab set-up to acquire the necessary at a fundamental level to achieve the desired goal. We should learn the microbes' encapsulation and how to keep them hydrated with the correct nutrients first. Some preliminary work on drying droplets of bacteria (*E. coli*, *P. phosphoreum*, and *P. aeruginosa*) is available in the literature (Sempels et al., 2013; Dunstan et al., 2018; Andac et al., 2019); however, the scope of this work is minimal, and many primary questions remain to be explored. To this end, the first set of experiments could involve the drying mechanism of different bacterial samples (both dead and alive) dried under uniform experimental conditions- the initial concentration, the type of solvent, substrate, geometry, and drying conditions (temperature, pH, relative humidity, etc.). The second set of experiments could be focused on any particular bacterial species to understand how substrate wettability, patterned substrate, and different geometric configurations affect the resulting morphology. It is more to understand how these variables can be tailored to characterize these microbial behaviors and model their growth by suppressing/encouraging them to communicate and form their colonies.

There are folklores and scientific claims that drying droplets of complex biofluids exhibit distinctive patterns of diseases under different stages of development (Rapis, 2002; Yakhno et al., 2005; Yakhno et al., 2015). This is clearly an overstatement, but the essence lies in the fundamental and practical significance of "drying bio-fluid droplets". The current state of research is pointing to two things. First of all, it is to

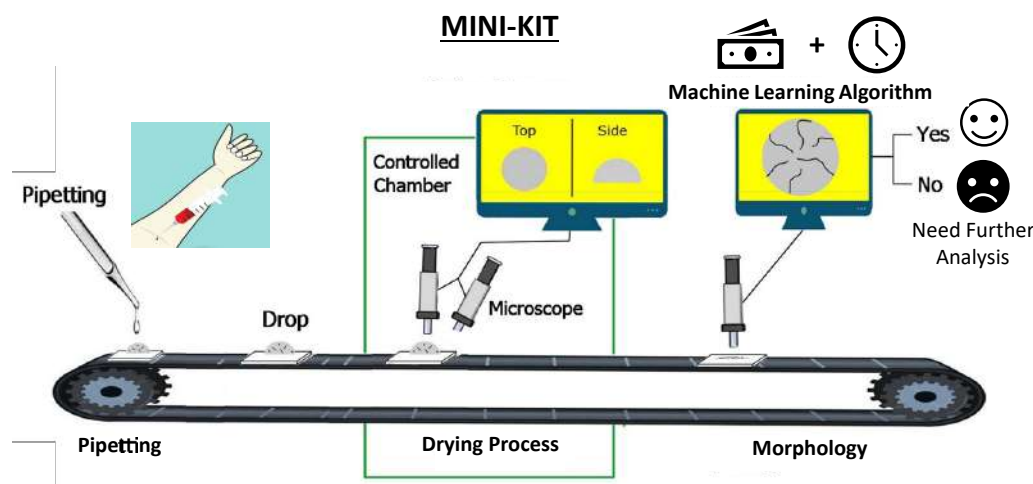


FIGURE 9.2: Schematic diagram describing a mini set-up in the doctor's chamber to be used as a pre-diagnostic technique.

create a corpus of an image-databank (and other physical characteristics of the drying sample) of the diseased bio-fluids' fingerprints. Secondly, to develop machine-learning tools to mine these data for either the fundamental science of colloidal systems or as a simple and easily implemented diagnostic tool. For this, various diseased serum samples (saliva, nasal fluid, plasma, blood) taken from patients suffering from later stages of various diseases, including cancer, diabetes, or Alzheimer's, could be studied as a drying droplet configuration. This is to test whether image analysis gives zero false-negative results of these targeted diseases. The aim is to explore the preliminary data and extensively examine the patterns that evolved during those initial stages. It checks significantly how physical parameters influence the final dried morphological patterns and investigate the underlying fundamental mechanisms. This understanding of different diseased samples will help us explore the effect of different compositions of available antimicrobial drugs. The drying droplet pattern recognition can be automated using image processing techniques and statistical modeling. We can also invert the problem by providing unknown serum samples and setting up training image sets using machine-learning tools to identify different diseases at different stages. As the drying droplet patterns have the potential to be used as a pre-diagnostic technique (see the schematic in Figure 9.2, the proposed pathological method may simplify and revolutionize the health and pharmaceutical sector in particular and could be used as a cost-effective method in remote locations in the near future*.

*This innovative and creative idea was received considerable praise from various research communities at WPI. It was duly acknowledged by the GRIE (Graduate Research Innovation Exchange) and awarded me with a seed funding of 12000\$ from the Tinkerbox community to initiate the research activities that aim to prepare 'A pre-diagnostic Marker for Future Clinicians' using the pattern formations of bio-colloidal droplets.

Bibliography

- Abràmoff, Michael D, Paulo J Magalhães, and Sunanda J Ram (2004). "Image processing with ImageJ". In: *Biophotonics International* 11.7, pp. 36–42.
- Andac, Tugba et al. (2019). "Active matter alters the growth dynamics of coffee rings". In: *Soft Matter* 15.7, pp. 1488–1496.
- Annarelli, CC et al. (2001). "Crack patterns in drying protein solution drops". In: *European Physical Journal E* 5.5, pp. 599–603.
- Athanasiou, Lambros S., Dimitrios I. Fotiadis, and Lampros K. Michalis (2017). "4 - Plaque characterization methods Using intravascular ultrasound imaging". In: *Atherosclerotic Plaque Characterization Methods Based on Coronary Imaging*. Ed. by Lambros S. Athanasiou, Dimitrios I. Fotiadis, and Lampros K. Michalis. Oxford: Academic Press, pp. 71–94. ISBN: 978-0-12-804734-7.
- Bahmani, Leila, Mahdi Neysari, and Maniya Maleki (2017a). "The study of drying and pattern formation of whole human blood drops and the effect of thalassaemia and neonatal jaundice on the patterns". In: *Colloids and Surfaces A: Physicochemical and Engineering Aspects* 513, pp. 66–75.
- (2017b). "The study of drying and pattern formation of whole human blood drops and the effect of thalassaemia and neonatal jaundice on the patterns". In: *Colloids and Surfaces A: Physicochemical and Engineering Aspects* 513, pp. 66–75. ISSN: 0927-7757.
- Bain, Barbara J (2004). *A Beginner's Guide to Blood Cells*. John Wiley Sons, Ltd. ISBN: 9781119367871.
- Ball, Philip (2021). *Patterns in Nature*. University of Chicago Press.
- Baranov, Maksim, Elena Velichko, and Faridoddin Shariaty (2020). "Determination of geometrical parameters in blood serum films using an image segmentation algorithm". In: *Optical Memory and Neural Networks* 29.4, pp. 330–335.
- Barash, L Yu et al. (2009). "Evaporation and fluid dynamics of a sessile drop of capillary size". In: *Physical Review E* 79.4, p. 046301.
- Behnia, Behzad, William G Buttlar, and Henrique Reis (2017). "Spiral cracking pattern in asphalt materials". In: *Materials & Design* 116, pp. 609–615.
- Bel'skaya, Lyudmila V, Elena A Sarf, and Anna P Solonenko (2019). "Morphology of dried drop patterns of saliva from a healthy individual depending on the dynamics of its surface tension". In: *Surfaces* 2.2, pp. 395–414.
- Boeynaems, Steven et al. (2018). "Protein phase separation: a new phase in cell biology". In: *Trends in Cell Biology* 28.6, pp. 420–435.

- Born, Max and Emil Wolf (2013). *Principles of optics: electromagnetic theory of propagation, interference and diffraction of light*.
- Bouchenna, Chafea et al. (2017). "Generalized formulation for evaporation rate and flow pattern prediction inside an evaporating pinned sessile drop". In: *International Journal of Heat and Mass Transfer* 109, pp. 482–500.
- Brutin, David (2013). "Influence of relative humidity and nano-particle concentration on pattern formation and evaporation rate of pinned drying drops of nanofluids". In: *Colloids and Surfaces A: Physicochemical and Engineering Aspects* 429, pp. 112–120.
- (2015). *Droplet Wetting and Evaporation: from Pure to Complex Fluids*. Academic Press.
- Brutin, David, Benjamin Sobac, and Céline Nicloux (2012). "Influence of substrate nature on the evaporation of a sessile drop of blood". In: *Journal of Heat Transfer* 134.6.
- Brutin, David and Victor Starov (2018). "Recent advances in droplet wetting and evaporation". In: *Chemical Society Reviews* 47.2, pp. 558–585.
- Brutin, David et al. (2011). "Pattern formation in drying drops of blood". In: *Journal of Fluid Mechanics* 667, pp. 85–95.
- Cai, Jie et al. (2019). "Osteoporosis recognition in rats under low-power lens based on convexity optimization feature fusion". In: *Scientific Reports* 9.1, pp. 1–14.
- Carreón, Yojana JP et al. (2018a). "Patterns produced by dried droplets of protein binary mixtures suspended in water". In: *Colloids and Surfaces B: Biointerfaces* 161, pp. 103–110.
- Carreón, Yojana JP et al. (2018b). "Texture analysis of protein deposits produced by droplet evaporation". In: *Scientific Reports* 8.1, pp. 1–12.
- Carreón, Yojana J.P. et al. (2021). "Effects of substrate temperature on patterns produced by dried droplets of proteins". In: *Colloids and Surfaces B: Biointerfaces* 203, p. 111763. ISSN: 0927-7765. DOI: <https://doi.org/10.1016/j.colsurfb.2021.111763>. URL: <https://www.sciencedirect.com/science/article/pii/S0927776521002071>.
- Carter, Daniel C and Joseph X Ho (1994). "Structure of serum albumin". In: *Advances in Protein Chemistry*. Vol. 45. Elsevier, pp. 153–203.
- Chen, Guofang and Gideon J Mohamed (2010). "Complex protein patterns formation via salt-induced self-assembly and droplet evaporation". In: *European Physical Journal E* 33.1, pp. 19–26.
- Chen, Ruoyang, Liyuan Zhang, and Wei Shen (2018). "Controlling the contact angle of biological sessile drops for study of their desiccated cracking patterns". In: *Journal of Materials Chemistry B* 6.37, pp. 5867–5875.
- Chen, Ruoyang et al. (2016a). "Blood drop patterns: Formation and applications". In: *Advances in Colloid and Interface Science* 231, pp. 1–14.
- (2016b). "Wetting and drying of colloidal droplets: Physics and pattern formation". In: *Advances in Colloid Science*, pp. 3–25.

- Chen, Ruoyang et al. (2017). "Understanding desiccation patterns of blood sessile drops". In: *Journal of Materials Chemistry B* 5.45, pp. 8991–8998.
- Chen, Ruoyang et al. (2019). "Desiccation patterns of plasma sessile drops". In: *ACS Sensors* 4.6, pp. 1701–1709.
- Choi, Junhee, Wonjung Kim, and Ho-Young Kim (2020). "Crack density in blood-stains". In: *Soft Matter* 16 (24), pp. 5571–5576.
- Chu, Guang and Eyal Zussman (2018). "From chaos to order: evaporative assembly and collective behavior in drying liquid crystal droplets". In: *Journal of Physical Chemistry Letters* 9.16, pp. 4795–4801.
- Das, Moumita, Christoph F Schmidt, and Michael Murrell (2020). "Introduction to Active Matter". In: *Soft Matter* 16.31, pp. 7185–7190.
- Dash, Amitosh et al. (2020). "An image processing method to measure droplet impact and evaporation on a solid surface". In: *Sādhanā* 45.1, pp. 1–10.
- Davidson, Zoey S et al. (2017). "Deposition and drying dynamics of liquid crystal droplets". In: *Nature Communications* 8.1, pp. 1–7.
- De Gennes, Pierre-Gilles, Françoise Brochard-Wyart, and David Quéré (2013). *Capillarity and Wetting Phenomena: Drops, Bubbles, Pearls, Waves*. Springer Science & Business Media.
- De Gennes, Pierre-Gilles and Jacques Prost (1993). *The Physics of Liquid Crystals*. Vol. 83. Oxford university press.
- Deegan, Robert D et al. (1997). "Capillary flow as the cause of ring stains from dried liquid drops". In: *Nature* 389.6653, p. 827.
- Deshmukh, Rameshwar, Pankaj Wagh, and Jitendra Naik (2016). "Solvent evaporation and spray drying technique for micro-and nanospheres/particles preparation: A review". In: *Drying Technology* 34.15, pp. 1758–1772.
- Dictionary, Oxford English (1989). "Oxford english dictionary". In: *Simpson, JA & Weiner, ESC*.
- Dierking, I et al. (2005). "Annihilation dynamics of umbilical defects in nematic liquid crystals under applied electric fields". In: *Physical Review E* 71.6, p. 061709.
- Dillard, David A et al. (1994). "Spiral Tunneling Cracks Induced by Environmental Stress Cracking in LaRC™-TPI Adhesives". In: *Journal of Adhesion* 44.1-2, pp. 51–67.
- Dunstan, Jocelyn et al. (2018). "Evaporation-driven convective flows in suspensions of nonmotile bacteria". In: *Physical Review Fluids* 3.12, p. 123102.
- Eales, Adam D et al. (2015). "Evaporation of pinned droplets containing polymer—an examination of the important groups controlling final shape". In: *AIChE Journal* 61.5, pp. 1759–1767.
- Eral, H. B. et al. (2011). "Suppressing the coffee stain effect: how to control colloidal self-assembly in evaporating drops using electrowetting". In: *Soft Matter* 7 (10), pp. 4954–4958.
- Erbil, H Yildirim (2012). "Evaporation of pure liquid sessile and spherical suspended drops: A review". In: *Advances in colloid and interface science* 170.1-2, pp. 67–86.

- Fernandez-Nieves, Alberto and Antonio Manuel Puertas (2016). *Fluids, Colloids, and Soft Materials: An Introduction to Soft Matter Physics*. Vol. 7. Wiley Online Library.
- Flormann, Daniel Amadeus Dominic (2017). "Physical characterization of red blood cell aggregation". PhD thesis. Universität des Saarlandes.
- Fodor, Étienne et al. (2016). "How far from equilibrium is active matter?" In: *Physical Review Letters* 117.3, p. 038103.
- Gao, MengNi, XianFu Huang, and YaPu Zhao (2018). "Formation of wavy-ring crack in drying droplet of protein solutions". In: *Science China Technological Sciences* 61.7, pp. 949–958.
- Gennes, Pierre-Gilles de (1992). "Soft matter (Nobel lecture)". In: *Angewandte Chemie International Edition in English* 31.7, pp. 842–845.
- Gerber, Julia (2020). "Wetting, bouncing, drying and freezing of drops on soft materials". PhD thesis. ETH Zurich.
- Giancola, Concetta et al. (1997). "DSC studies on bovine serum albumin denaturation effects of ionic strength and SDS concentration". In: *International journal of Biological Macromolecules* 20.3, pp. 193–204.
- Giorgiutti-Dauphiné, F and L Pauchard (2015). "Striped patterns induced by delamination of drying colloidal films". In: *Soft Matter* 11.7, pp. 1397–1402.
- Goehring, Lucas et al. (2015). *Desiccation Cracks and their Patterns: Formation and Modelling in Science and Nature*. John Wiley & Sons.
- Goldstein, Raymond E. (2018). "Coffee stains, cell receptors, and time crystals: Lessons from the old literature". In: *Physics Today* 71.9, pp. 32–38.
- Gorr, Heather Meloy (2013). "Lysozyme pattern formation in evaporating droplets". PhD thesis. University of Pittsburgh.
- Gorr, Heather Meloy, Ziyue Xiong, and John A Barnard (2014). "Pattern recognition for identification of lysozyme droplet solution chemistry". In: *Colloids and Surfaces B: Biointerfaces* 115, pp. 170–175.
- Gorr, Heather Meloy, Joshua M Zueger, and John A Barnard (2012). "Lysozyme pattern formation in evaporating drops". In: *Langmuir* 28.9, pp. 4039–4042.
- Gorr, Heather Meloy et al. (2013). "Salt-induced pattern formation in evaporating droplets of lysozyme solutions". In: *Colloids and Surfaces B* 103, pp. 59–66.
- Gregory, Shaun, Michael Stevens, and John F Fraser (2017). *Mechanical Circulatory and Respiratory Support*. Academic Press.
- Hamadeh, Lama et al. (2020). "Machine learning analysis for quantitative discrimination of dried blood droplets". In: *Scientific Reports* 10.1, pp. 1–13.
- Haralick, R. M., K. Shanmugam, and I. Dinstein (1973). "Textural features for image classification". In: *IEEE Transactions on Systems, Man, and Cybernetics* SMC-3.6, pp. 610–621.
- Heo, In-Seok and Soo-Young Park (2017). "Smart shell membrane prepared by microfluidics with reactive nematic liquid crystal mixture". In: *Sensors and Actuators B: Chemical* 251, pp. 658–666.

- Hsieh, Matthew M et al. (2009). "Allogeneic hematopoietic stem-cell transplantation for sickle cell disease". In: *New England Journal of Medicine* 361.24, pp. 2309–2317.
- Hu, Hua and Ronald G Larson (2002). "Evaporation of a sessile droplet on a substrate". In: *Journal of Physical Chemistry B* 106.6, pp. 1334–1344.
- (2005). "Analysis of the microfluid flow in an evaporating sessile droplet". In: *Langmuir* 21.9, pp. 3963–3971.
- (2006). "Marangoni effect reverses coffee-ring depositions". In: *Journal of Physical Chemistry B* 110.14, pp. 7090–7094.
- Hu, Qiong-Zheng and Chang-Hyun Jang (2012a). "A simple strategy to monitor lipase activity using liquid crystal-based sensors". In: *Talanta* 99, pp. 36–39.
- (2012b). "Imaging trypsin activity through changes in the orientation of liquid crystals coupled to the interactions between a polyelectrolyte and a phospholipid layer". In: *ACS Applied Materials & Interfaces* 4.3, pp. 1791–1795.
- Hu, Yin-Chun et al. (2013). "Peculiar surface profile of poly (ethylene oxide) film with ring-like nucleation distribution induced by Marangoni flow effect". In: *Colloids and Surfaces A: Physicochemical and Engineering Aspects* 428, pp. 39–46.
- Huang, Lien-Hung et al. (2017). "The effects of storage temperature and duration of blood samples on DNA and RNA qualities". In: *PloS One* 12.9.
- Hung, Szu-Chun et al. (2014). "Volume overload correlates with cardiovascular risk factors in patients with chronic kidney disease". In: *Kidney International* 85.3, pp. 703–709.
- Iqbal, R., Amy Q. Shen, and A.K. Sen (2020). "Understanding of the role of dilution on evaporative deposition patterns of blood droplets over hydrophilic and hydrophobic substrates". In: *Journal of Colloid and Interface Science* 579, pp. 541–550. ISSN: 0021-9797.
- Islam, MF et al. (2005). "Cracks and topological defects in lyotropic nematic gels". In: *Physical Review Letters* 95.14, p. 148301.
- Jacobs, William M and Daan Frenkel (2017). "Phase transitions in biological systems with many components". In: *Biophysical Journal* 112.4, pp. 683–691.
- Jeong, Joonwoo et al. (2015). "Liquid crystal Janus emulsion droplets: preparation, tumbling, and swimming". In: *Soft Matter* 11.34, pp. 6747–6754.
- Kato, Takashi (2002). "Self-assembly of phase-segregated liquid crystal structures". In: *Science* 295.5564, pp. 2414–2418.
- Katzav, E, M Adda-Bedia, and Rodrigo Arias (2007). "Theory of dynamic crack branching in brittle materials". In: *International Journal of Fracture* 143.3, pp. 245–271.
- Kléman, Maurice (1989). "Defects in liquid crystals". In: *Reports on Progress in Physics* 52.5, p. 555.
- Kolegov, KS and L Yu Barash (2019). "Joint effect of advection, diffusion, and capillary attraction on the spatial structure of particle depositions from evaporating droplets". In: *Physical Review E* 100.3, p. 033304.

- Kumar, Subhalakshmi, Joshua S Katz, and Charles M Schroeder (2017). "Heterogeneous drying and nonmonotonic contact angle dynamics in concentrated film-forming latex drops". In: *Physical Review Fluids* 2.11, p. 114304.
- Landau, Lev Davidovich and Evgenii Mikhailovich Lifshitz (2013). *Course of Theoretical Physics*. Elsevier.
- Lanotte, Luca et al. (2017). "Role of red cells and plasma composition on blood sessile droplet evaporation". In: *Physical Review E* 96.5, p. 053114.
- Lazarus, V and L Pauchard (2011). "From craquelures to spiral crack patterns: influence of layer thickness on the crack patterns induced by desiccation". In: *Soft Matter* 7.6, pp. 2552–2559.
- Lee, Mon-Juan, Chung-Huan Chang, and Wei Lee (2017). "Label-free protein sensing by employing blue phase liquid crystal". In: *Biomedical Optics Express* 8.3, pp. 1712–1720.
- Li, Yanshen et al. (2015). "From coffee rings to coffee eyes". In: *Soft Matter* 11 (23), pp. 4669–4673.
- Liu, Dingdong, Qiong-Zheng Hu, and Chang-Hyun Jang (2013). "Orientational behaviors of liquid crystals coupled to chitosan-disrupted phospholipid membranes at the aqueous–liquid crystal interface". In: *Colloids and Surfaces B: Biointerfaces* 108, pp. 142–146.
- Lydon, John (1998). "Chromonic liquid crystal phases". In: *Current opinion in Colloid & Interface Science* 3.5, pp. 458–466.
- Majumder, Mainak et al. (2012). "Overcoming the "coffee-stain" effect by compositional Marangoni-flow-assisted drop-drying". In: *Journal of Physical Chemistry B* 116.22, pp. 6536–6542.
- Maki, Kara L and Satish Kumar (2011). "Fast evaporation of spreading droplets of colloidal suspensions". In: *Langmuir* 27.18, pp. 11347–11363.
- Mampallil, Dileep et al. (2015). "Acoustic suppression of the coffee-ring effect". In: *Soft Matter* 11 (36), pp. 7207–7213.
- Marin, Luminita et al. (2013). "Chitosan as matrix for bio-polymer dispersed liquid crystal systems". In: *Carbohydrate Polymers* 95.1, pp. 16–24.
- Masoud, Hassan and James D Felske (2009). "Analytical solution for inviscid flow inside an evaporating sessile drop". In: *Physical Review E* 79.1, p. 016301.
- McLeish, Tom (2020). *Soft Matter: A Very Short Introduction*. Oxford University Press.
- McManus, Jennifer J et al. (2016). "The physics of protein self-assembly". In: *Current Opinion in Colloid & Interface Science* 22, pp. 73–79.
- Mondal, Ranajit et al. (2018). "Patterns in drying drops dictated by curvature-driven particle transport". In: *Langmuir* 34.38, pp. 11473–11483.
- Mukhopadhyay, Manikuntala et al. (2018). "Surface property induced morphological alterations of human erythrocytes". In: *Soft Matter* 14.36, pp. 7335–7346.
- Mukhopadhyay, Manikuntala et al. (2020). "Interfacial energy driven distinctive pattern formation during the drying of blood droplets". In: *Journal of Colloid and Interface Science* 573, pp. 307–316. ISSN: 0021-9797.

- Muravlyova, LE et al. (2014). "Structure-forming properties of blood plasma of patients with interstitial lung diseases". In: *World Journal of Medical Sciences* 10.4, pp. 478–483.
- Neda, Z, L Jozsa, M Ravasz, et al. (2002). "Spiral cracks in drying precipitates". In: *Physical Review Letters* 88.9, p. 095502.
- Newell, DG, S Roath, and JL Smith (1976). "The scanning electron microscopy of normal human peripheral blood lymphocytes". In: *British Journal of Haematology* 32.3, pp. 309–316.
- Ohzono, Takuya et al. (2017). "Uncovering different states of topological defects in schlieren textures of a nematic liquid crystal". In: *Scientific Reports* 7.1, pp. 1–13.
- Onofriescu, Mihai et al. (2015). "Overhydration, cardiac function and survival in hemodialysis patients". In: *PLoS One* 10.8, e0135691.
- Pal, Anusuya, Amalesh Gope, and Germano S Iannacchione (2019a). "A comparative study of the phase separation of a nematic liquid crystal in the self-assembling drying protein drops". In: *MRS Advances* 4.22, pp. 1309–1314.
- (2019b). "Image-based analysis of patterns formed in drying drops". In: *Pattern Recognition and Machine Intelligence*. Ed. by Bhabesh Deka et al. Cham: Springer International Publishing, pp. 567–574.
- (2021). "Temperature and concentration dependence of human whole blood and protein drying droplets". In: *Biomolecules* 11.2. ISSN: 2218-273X.
- Pal, Anusuya et al. (2019). "Phase separation of a nematic liquid crystal in the self-assembly of lysozyme in a drying aqueous solution drop". In: *MRS Communications* 9.1, pp. 150–158.
- Pal, Anusuya et al. (2020a). "A comparative study of the drying evolution and dried morphology of two globular proteins in de-ionized water solutions". In: *RSC Advances* 10.29, pp. 16906–16916.
- Pal, Anusuya et al. (2020b). "Concentration-driven phase transition and self-assembly in drying droplets of diluting whole blood". In: *Scientific Reports* 10.1, pp. 1–12.
- Pathak, Binita et al. (2020). "Complex pattern formation in solutions of protein and mixed salts using dehydrating sessile droplets". In: *Langmuir* 36.33, pp. 9728–9737.
- Paul, Sharmistha et al. (2008). "Studies of adsorption and viscoelastic properties of proteins onto liquid crystal phthalocyanine surface using quartz crystal microbalance with dissipation technique". In: *Journal of Physical Chemistry C* 112.31, pp. 11822–11830.
- Pollack, Gerald H and Wei-Chun Chin (2008). *Phase transitions in Cell Biology*. Springer.
- Popov, Yuri O (2005). "Evaporative deposition patterns: spatial dimensions of the deposit". In: *Physical Review E* 71.3, p. 036313.
- Poulard, C and P Damman (2007). "Control of spreading and drying of a polymer solution from Marangoni flows". In: *EPL (Europhysics Letters)* 80.6, p. 64001.
- Preibisch, Stephan, Stephan Saalfeld, and Pavel Tomancak (2009). "Globally optimal stitching of tiled 3D microscopic image acquisitions". In: *Bioinformatics* 25.11, pp. 1463–1465.

- Ramsthaller, Frank et al. (2016). "The ring phenomenon of diluted blood droplets". In: *International Journal of Legal Medicine* 130.3, pp. 731–736.
- Ramsthaller, Frank et al. (2017). "Effect of anticoagulation therapy on drying times in bloodstain pattern analysis". In: *International Journal of Legal Medicine* 131.4, pp. 955–961.
- Rapis, E (2002). "A change in the physical state of a nonequilibrium blood plasma protein film in patients with carcinoma". In: *Technical Physics* 47.4, pp. 510–512.
- Rowlinson, John Shipley and Benjamin Widom (2013). *Molecular Theory of Capillarity*. Courier Corporation.
- San Pietro, D and R Steelberg (2019). "A preliminary assessment of the correlation of drying time and the peripheral rim thickness of perimeter bloodstains". In: *Journal of Forensic Research* 10.442, p. 2.
- Schindelin, Johannes et al. (2012). "Fiji: an open-source platform for biological-image analysis". In: *Nature Methods* 9.7, pp. 676–682.
- Sempels, Wouter et al. (2013). "Auto-production of biosurfactants reverses the coffee ring effect in a bacterial system". In: *Nature Communications* 4.1, pp. 1–8.
- Sendova, M and K Willis (2003). "Spiral and curved periodic crack patterns in sol-gel films". In: *Applied Physics A* 76.6, pp. 957–959.
- Shehzad, Muhammad Arslan et al. (2015). "Nematic liquid crystal on a two dimensional hexagonal lattice and its application". In: *Scientific Reports* 5.1, pp. 1–8.
- Simons, Kai and Elina Ikonen (1997). "Functional rafts in cell membranes". In: *Nature* 387.6633, pp. 569–572.
- Singer, Wolfgang et al. (2006). "Orientation of optically trapped nonspherical birefringent particles". In: *Physical Review E* 73.2, p. 021911.
- Singh, Shri (2000). "Phase transitions in liquid crystals". In: *Physics Reports* 324.2-4, pp. 107–269.
- Smith, FR and David Brutin (2018). "Wetting and spreading of human blood: Recent advances and applications". In: *Current Opinion in Colloid & Interface Science* 36, pp. 78–83.
- Smith, FR, Céline Nicloux, and David Brutin (2020). "A new forensic tool to date human blood pools". In: *Scientific Reports* 10.1, pp. 1–12.
- Sobac, Benjamin and David Brutin (2011). "Structural and evaporative evolutions in desiccating sessile drops of blood". In: *Physical Review E* 84.1, p. 011603.
- (2014). "Desiccation of a sessile drop of blood: Cracks, folds formation and delamination". In: *Colloids and Surfaces A: Physicochemical and Engineering Aspects* 448, pp. 34–44.
- Tablin, Fern et al. (1996). "Membrane phase transition of intact human platelets: correlation with cold-induced activation". In: *Journal of Cellular Physiology* 168.2, pp. 305–313.
- Tarafdar, Sujata et al. (2018). "Droplet drying patterns on solid substrates: from hydrophilic to superhydrophobic contact to levitating drops". In: *Advances in Condensed Matter Physics* 2018.

- Tarasevich, Yu Yu and AK Ayupova (2003). "Effect of diffusion on the separation of components in a biological fluid upon wedge-shaped dehydration". In: *Technical Physics* 48.5, pp. 535–540.
- Tarasevich, Yuri Yu (2005). "Simple analytical model of capillary flow in an evaporating sessile drop". In: *Physical Review E* 71.2, p. 027301.
- Tarasevich, Yurii Yur'evich (2004). "Mechanisms and models of the dehydration self-organization in biological fluids". In: *Physics-Uspokhi* 47.7, pp. 717–728.
- Tuceryan, Mihran and Anil K Jain (1993). "Texture analysis". In: *Handbook of Pattern Recognition and Computer Vision*, pp. 235–276.
- Van den Berge, M. et al. (2019). "Determining how diluted bloodstains were derived: Inferring distinctive characteristics and formulating a guideline". In: *Forensic Science International* 302, p. 109918. ISSN: 0379-0738.
- Vermaak, J.S., C.W. Mays, and D. Kuhlmann-Wilsdorf (1968). "On surface stress and surface tension: I. Theoretical considerations". In: *Surface Science* 12.2, pp. 128–133. ISSN: 0039-6028.
- Whitesides, George M and Mila Boncheva (2002). "Beyond molecules: Self-assembly of mesoscopic and macroscopic components". In: *Proceedings of the National Academy of Sciences* 99.8, pp. 4769–4774.
- Whitesides, George M and Bartosz Grzybowski (2002). "Self-assembly at all scales". In: *Science* 295.5564, pp. 2418–2421.
- Yakhno, TA et al. (2003). "On the existence of regular structures in liquid human blood serum (plasma) and phase transitions in the course of its drying". In: *Technical Physics* 48.4, pp. 399–403.
- Yakhno, TA et al. (2010). "Drops of biological fluids drying on a hard substrate: Variation of the morphology, weight, temperature, and mechanical properties". In: *Technical Physics* 55.7, pp. 929–935.
- Yakhno, Tatiana (2008). "Salt-induced protein phase transitions in drying drops". In: *Journal of Colloid and Interface Science* 318.2, pp. 225–230.
- Yakhno, Tatiana A et al. (2005). "The informative-capacity phenomenon of drying drops". In: *IEEE Engineering in Medicine and Biology Magazine* 24.2, pp. 96–104.
- Yakhno, Tatiana A et al. (2015). "Drying drop technology as a possible tool for detection leukemia and tuberculosis in cattle". In: *Journal of Biomedical Science and Engineering* 8.01, p. 1.
- Yang, SC (1989). "Scanning electron microscopy of normal human peripheral blood cells." In: *Journal of the Formosan Medical Association* 88.11-12, pp. 1128–1132.
- Yawata, Yoshihito (2006). *Cell Membrane: The Red Blood Cell as a Model*. John Wiley & Sons.
- Zang, Duyang et al. (2019). "Evaporation of a Droplet: From physics to applications". In: *Physics Reports* 804, pp. 1–56.
- Zeid, W Bou, and David Brutin (2014). "Effect of relative humidity on the spreading dynamics of sessile drops of blood". In: *Colloids and Surfaces A: Physicochemical and Engineering Aspects* 456, pp. 273–285.

- Zeid, W Bou, J Vicente, and David Brutin (2013). "Influence of evaporation rate on cracks' formation of a drying drop of whole blood". In: *Colloids and Surfaces A: Physicochemical and Engineering Aspects* 432, pp. 139–146.
- Zhou, Jingjing et al. (2017). "The Effects of GLCM parameters on LAI estimation using texture values from Quickbird Satellite Imagery". In: *Scientific Reports* 7.1, pp. 1–12.
- Zou, Jianhua and Jiyu Fang (2010). "Director configuration of liquid-crystal droplets encapsulated by polyelectrolytes". In: *Langmuir* 26.10, pp. 7025–7028.

Appendix A

Directory of all the archived videos

A.1 Chapter 4

All the diluting concentrations (ϕ) are prepared by weighing ~ 50 mg protein and mixing it with 1 mL of de-ionized water. Two different proteins [bovine serum albumin (BSA) and lysozyme (Lys)] are used. All the videos can be accessed through [Anusuya/Ph.d.thesis/Videos/chapter4](#)

1. V1_BSA is the video that shows the drying evolution of the BSA at ϕ of 5 wt%.
2. V2_Lys is the video that shows the drying evolution of the Lys at ϕ of 5 wt%.

A.2 Chapter 5

All the diluting concentrations (ϕ_{LC}) are prepared by adding 10 μL of 5CB liquid crystal (LC) into the aqueous solution of protein. The protein solution is prepared by weighing ~ 100 mg protein and mixing it with 1 mL of de-ionized water. All the videos can be accessed through [Anusuya/Ph.d.thesis/Videos/chapter5](#)

1. V1_BSA+LC is the video that shows the drying evolution of the BSA droplet in the presence of LCs at ϕ_{LC} of 0.9 wt%.
2. V2_Lys+LC is the video that shows the drying evolution of the BSA droplet in the presence of LCs at ϕ of 0.9 wt%.

A.3 Chapter 6

All the diluting concentrations (ϕ) are prepared by adding different volumes of de-ionized water with the whole human blood. All the videos can be accessed through [Anusuya/Ph.d.thesis/Videos/chapter6](#)

1. V1_100% is the video that shows the drying evolution of the whole human blood at ϕ of 100%.

2. V2_85% is the video that shows the drying evolution of the diluted human blood at ϕ of 85%.
3. V3_75% is the video that shows the drying evolution of the diluted human blood at ϕ of 75%.
4. V4_62% is the video that shows the drying evolution of the diluted human blood at ϕ of 62%.
5. V5_50% is the video that shows the drying evolution of the diluted human blood at ϕ of 50%.
6. V6_25% is the video that shows the drying evolution of the diluted human blood at ϕ of 25%.
7. V7_12.5% is the video that shows the drying evolution of the diluted human blood at ϕ of 12.5%.

A.4 Chapter 7

All the diluting concentrations (ϕ_{blood}) are prepared by adding different volumes of 1x phosphate buffer saline with the whole human blood. All the videos can be accessed through [Anusuya/Ph.d.thesis/Videos/chapter7](#)

1. V1_75% is the video that shows the drying evolution of the diluted human blood at ϕ_{blood} of 75%.
2. V2_62% is the video that shows the drying evolution of the diluted human blood at ϕ_{blood} of 62%.
3. V3_50% is the video that shows the drying evolution of the diluted human blood at ϕ_{blood} of 50%.
4. V4_25% is the video that shows the drying evolution of the diluted human blood at ϕ_{blood} of 25%.
5. V5_12.5% is the video that shows the drying evolution of the diluted human blood at ϕ_{blood} of 12.5%.

Appendix B

List of Publications

B.1 Peer-reviewed Journals

- **Pal, A.** and Iannacchione, G.S., 2021. Bio-colloidal Drying Droplets: Current Trends and Future Perspectives on Image Processing Applications. *Academia Letters* (Under Review).
- **Pal, A.**, Gope, A. and Iannacchione, G.S., 2021. Concentration and Temperature dependence of Protein and Blood Drying Droplets. *Biomolecules*, 11(2), pp.231. <https://doi.org/10.3390/biom11020231>.
- **Pal, A.**, Gope, A., Obayemi, J.D. and Iannacchione, G.S., 2020. Concentration-driven phase transition and self-assembly in drying droplets of diluting whole blood. *Scientific Reports*, 10(1), pp.1-12. <https://doi.org/10.1038/s41598-020-76082-6>.
- **Pal, A.**, Gope, A., Athair A.S. and Iannacchione, G.S., 2020. A comparative study of the drying evolution and dried morphology of two globular protein and de-ionized water solutions. *RSC Advances*, 10(29), pp.16906-16916. <https://doi.org/10.1039/D0RA01748E>.
- **Pal, A.**, Gope, A. and Iannacchione, G.S., 2019. A comparative study of the phase separation of a nematic liquid crystal in the self-assembling drying protein drops. *MRS Advances*, 4(22), pp.1309-1314. <https://doi.org/10.1557/adv.2019.209>.
- **Pal, A.**, Gope, A., Kafle, R. and Iannacchione, G.S., 2019. Phase separation of a nematic liquid crystal in the self-assembly of lysozyme in a drying aqueous solution drop. *MRS Communications*, 9(1), pp.150-158. <https://doi.org/10.1557/mrc.2019.18>.

B.2 Peer-reviewed Conference Proceedings

- **Pal, A.**, Gope, A. and Iannacchione, G.S., 2021. Exploring the Pattern Formation of Lysozyme Drying Droplets in Phosphate Buffer Saline Solution (International Conference on Advanced Physics IEMPHYS 2021) (Accepted).
- **Pal, A.**, Gope, A. and Iannacchione, G.S., 2021. Temperature-dependent Pattern Formation in Drying Aqueous Droplets of Lysozyme. (International Conference on Current Trends in Materials Science and Engineering CTMSE2021) (Accepted).

B.3 Peer-reviewed Book Chapters

- **Pal, A.**, Gope, A. and Iannacchione, G.S., 2021, Statistical Image Analysis of Drying Bovine Serum Albumin Droplets in Phosphate Buffered Saline. In *Information Retrieval Models for Biomedical and Health Informatics, Artificial Intelligence and Soft Computing for Industrial transformation*, Scrivener Wiley Publishing. (In Press).
- **Pal, A.**, Gope, A. and Iannacchione, G.S., 2019, December. Image-Based Analysis of Patterns Formed in Drying Drops. In *International Conference on Pattern Recognition and Machine Intelligence* (pp. 567-574). Springer, Cham. (Online ISBN 978-3-030-34869-4), https://doi.org/10.1007/978-3-030-34869-4_62.

B.4 In Preparations

- **Pal, A.**, Gope, A. and Iannacchione, G.S., 2021. Morphological Pattern Formation of 5CB Nematic Liquid Crystal Droplets in Protein-saline Drying Drops (1st draft in progress).
- **Pal, A.**, Gope, A. and Iannacchione, G.S., 2021. Self-Assembly in Drying Droplets of Human Blood: A Dilution by Phosphate Buffer Saline (Final draft in progress).



Image-Based Analysis of Patterns Formed in Drying Drops

Anusuya Pal¹, Amalesh Gope², and Germano S. Iannacchione¹(✉)

¹ Department of Physics, Worcester Polytechnic Institute, Worcester, USA
{apal,gsiannac}@wpi.edu

² Department of EFL, Tezpur University, Tezpur, Assam, India
amalesh@tezu.ernet.in

Abstract. Image processing and pattern recognition offer a useful and versatile method for optically characterizing drops of a colloidal solution during the drying process and in its final state. This paper exploits image processing techniques applied to cross-polarizing microscopy to probe birefringence and the bright-field microscopy to examine the morphological patterns. The bio-colloidal solution of interest is a mixture of water, liquid crystal (LC) and three different proteins [lysozyme (Lys), myoglobin (Myo), and bovine serum albumin (BSA)], all at a fixed relative concentration. During the drying process, the LC phase separates and becomes optically active detectable through its birefringence. Further, as the protein concentrates, it forms cracks under strain due to the evaporation of water. The mean intensity profile of the drying process is examined using an automated image processing technique that reveals three unique regimes- a steady upsurge, a speedy rise, and an eventual saturation. The high values of standard deviation show the complexity, the roughness, and inhomogeneity of the image surface. A semi-automated image processing technique is proposed to quantify the distance between the consecutive cracks by converting those into high contrast images. The outcome of the image analysis correlates with the initial state of the mixture, the nature of the proteins, and the mechanical response of the final patterns. The paper reveals new insights on the self-assembly of the macromolecules during the drying mechanism of any aqueous solution.

Keywords: Image processing · Drying drops · Liquid crystals

1 Introduction

Image processing and automated pattern recognition techniques are crucial elements in advance of (optical) imaging technology. As image acquisition has become more precise (in time and spatial resolution) and ubiquitous, the need to extract information from these images has grown exponentially. One of the many scientific areas impacted by such processing is in observing the drying drops of some complex fluids. Specifically, one such class of complex colloidal fluid relevant to forensics and medical sciences is biological fluid such as blood,

plasma serum, tear, urine, or simple protein solutions [1]. Recent research findings [2,3] have found that dried drops of serums can differentiate the state of health of a patient. Furthermore, the whole dried pattern appears to be connected to the initial state of the material present in these complex fluids [4,5]. For example, Deegan et al. have studied colloidal drops and found that the drops get pinned after depositing on the substrate. The particles start concentrating near the edge more than the central region, forming a ring called “coffee-ring effect” [6]. Due to this pinning and solvent loss, the drops are no longer able to shrink and ultimately, form cracks (patterns) under strain during the drying process.

This paper exploits image processing techniques applied to the cross-polarizing microscopy to probe birefringence and the bright-field microscopy to examine the crack patterns. The bio-colloidal solution of interest is a mixture of water, and three different proteins [lysozyme (Lys), myoglobin (Myo), and bovine serum albumin (BSA)], all at a fixed relative concentration with and without a nematic liquid crystal (LC). The patterns are characterized using three different criteria, (a) the optical outcome, (b) the textural dynamics, and, (c) statistical significance. This work uses both automated and semi-automated image processing techniques to quantify drying dynamics and dried morphology. Our analysis reveals that the topmost part of the BSA film is coated with LC droplets, whereas, the same LC droplets are randomly distributed underneath the Lys and Myo films. This paper demonstrates the versatility and usefulness of these image processing techniques and is adaptable to any similar imaging system.

2 Materials, Sample Preparation and Image Acquisition

Lysozyme (Lys), myoglobin (Myo) and bovine serum albumin (BSA) are globular proteins differing in mass, charge, and properties [4]. The presence of a heme group helps Myo to serve as an oxygen-binding protein. Lys and Myo have similar molecular masses of ~ 14.3 , and ~ 17.0 kDa respectively, whereas BSA contains a higher molecular mass of ~ 66.5 kDa [4]. The net charge of Lys, BSA, and Myo is positive, negative, and neutral respectively. The commercial powdered proteins were purchased from Sigma Aldrich, USA. Myo (Catalog no. M0630), Lys (L6876), and BSA (A2153) were used without any further purification. Distinct protein solutions containing each of Lys, Myo, and BSA (100 mg each) were prepared by dissolving those separately in 1 mL of de-ionized water. Following that, an optically active and polar LC, 5CB (328510) was heated above the transition temperature (35°C), and $10\ \mu\text{L}$ was added as a third component to the solution. A $\sim 1.3\ \mu\text{L}$ of the solution was pipetted on the coverslip in the form of a circular drop, which was allowed to dry under ambient conditions [4].

A polarizing microscopy (Leitz Wetzlar, Germany) with a $5\times$ objective lens at a fixed resolution of 2048×1536 pixels was used to capture the images [4,5]. An 8-bit digital camera (Amscope MU300) in color profile mode assigns intensity values from 0 to 255 in each color of red, green, and blue (RGB) pixels for image acquisition. After the deposition of the drop on the coverslip, the time-lapse

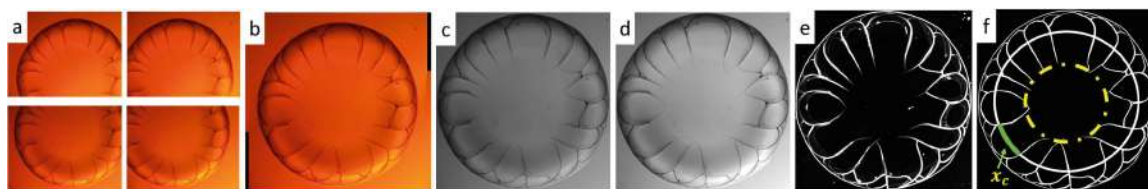


Fig. 1. A representative processing of images of the dried state of BSA drop to quantify the spacing between the cracks. (a) The raw microscopic images. (b) A stitched image. (c) An 8-bit gray image. (d) An adjusted brightness-contrast image. (e) A high contrast image after filtering through variance filter. (f) A final binary image depicting different regions, circular line-cut, and crack spacing (x_c). (Color figure online)

images in crossed polarizing configuration were recorded at every two seconds to monitor LC droplets' birefringence during the drying process. Each drop was deposited three times from the same sample to ensure the reproducibility. The final dried state was examined in bright-field configuration to understand different crack patterns in different protein drops with and without inclusion of LC droplets. Since it was challenging to view the entire ~ 2 mm diameter drop using a $5\times$ objective lens, different sections of the dried drops were imaged separately (Fig. 1a). Each section is stitched together (Fig. 1b) by using *Stitching* plugin [7] in Fiji [8]. We propose a semi-automated image-processing algorithm on the stitched images to determine the spacing between the consecutive cracks (x_c) in ImageJ [9]. We converted stitched bright-field images into gray (Fig. 1c). For these gray images, the range of monochromatic shades from black to white are displayed from 0 to 255 without partitioning into RGB sets of pixels. Then, the bright and contrast of the image were adjusted (Fig. 1d) and filtered with a variance filter (Fig. 1e), and processed into an 8-bit binary image (255 for pixels depicting the crack lines and 0 for pixels elsewhere else) (Fig. 1f) [4, 5]. However, the filtering was not enough to process the images into exact binary images. The artifacts were, therefore manually removed by comparing (overlapping) the processed images on to the original images. However, future work will automate this procedure.

The morphology of the dried drop is such that it can be divided into two regions: rim and central. The rim is near the edge depicted by yellow dashed line in Fig. 1f. We converted all the images of the dried drops into a scaled stack. Three circular-cut lines (shown by white circular line in Fig. 1f) of different radii were made in each region by using *Oval Profile* plugin in ImageJ [4, 5]. The intensity values were plotted along each circular line at every 0.1° as a function of arc-length along each circle. A script using '*Array.findMaxima*' was used to determine the positions of maximum intensity values. An estimate of the crack spacing, x_c (outlined by green color in Fig. 1f) is calculated by the consecutive maxima difference [4, 5]. All the intensity values along the crack lines were cross-checked manually to see if there is an artifact. If found, were corrected to the consistent (and fixed) values to maintain uniformity along the crack lines. A threshold of ± 0.005 mm were used as a standard range and x_c values outside

this range was recorded and aggregated in each region to obtain an average (\bar{x}_c) [4,5]. However, there may be cracks that propagate along the drawn circle, leading to some uncertainty in the extracted crack distributions.

To quantify the birefringence of the LC droplets during the drying process, a circular region of interest (ROI) was drawn on the image covering the area in the drop, and another ROI was drawn on the image covering the background (coverslip) using the *Oval tool* in ImageJ [9]. Once the ROI was selected, the birefringence intensity of that ROI was measured. To ensure that the different size of ROI in the sample and the background do not affect the intensity measurement, *mean gray value* (the sum of the values of the pixels in the selection divided by the area of the pixels in the selection) in ImageJ [9] was chosen. A script was written for an automated image-processing algorithm which measures the *mean gray value* for each ROI in the images during the drying process. However, the differences in the *mean gray values* during image recording might affect both the background and the sample. To counter this, a correction (calibration) with the background i.e., a correction factor was determined. It could be done by subtracting the background gray values; however, it wouldn't have fixed an uneven background in the series of images. So, the ROI with the lowest background *mean gray value* was chosen from the whole set of images during the drying process as a reference. The lowest was also selected to avoid into running the risk of generating overexposed images (otherwise the correction factors would be smaller than 1). The corrected intensity of the sample (I_c) was then determined for each sample by dividing the mean gray values with the correction factor. The intensity was averaged over a range of 30s and also averaged for three drops. Good reproducibility was found in the intensity profile, though the time was shifted (added or subtracted) to make the profile nearly overlap to each other. Note that the lamp intensity was kept fixed throughout the whole experiment done with each protein drop. And finally, the averaged corrected intensity values (\bar{I}_c) was plotted with time. In addition to \bar{I}_c , another textural parameter i.e., standard deviation (SD) was calculated and were averaged over 30s to understand the emerging complexity during the drying process.

3 Results and Discussions

The upper panel of Fig. 2 reveals the variation of birefringence intensity (\bar{I}_c) of LC droplets during the drying process. The standard deviation ($n = 3$) is higher in all the transition compared to the other regimes due to the presence of different sized LC droplets in different drops. It demonstrates an archetypal response of LC droplets dissolved in protein solutions and displays three distinct regimes: (I) the initial process of getting a minimum contact angle configuration with a gradual increase of intensity, (II) the intensity gets amplified due to LC activities, and (III) the intensity is saturated in the final regime once the drop completes the evaporation process. It also suggests that the birefringence nature is independent of types of proteins and less efficient to capture the minute details of the LC activities during the drying process. The stage I completes in 11–14 min, and the

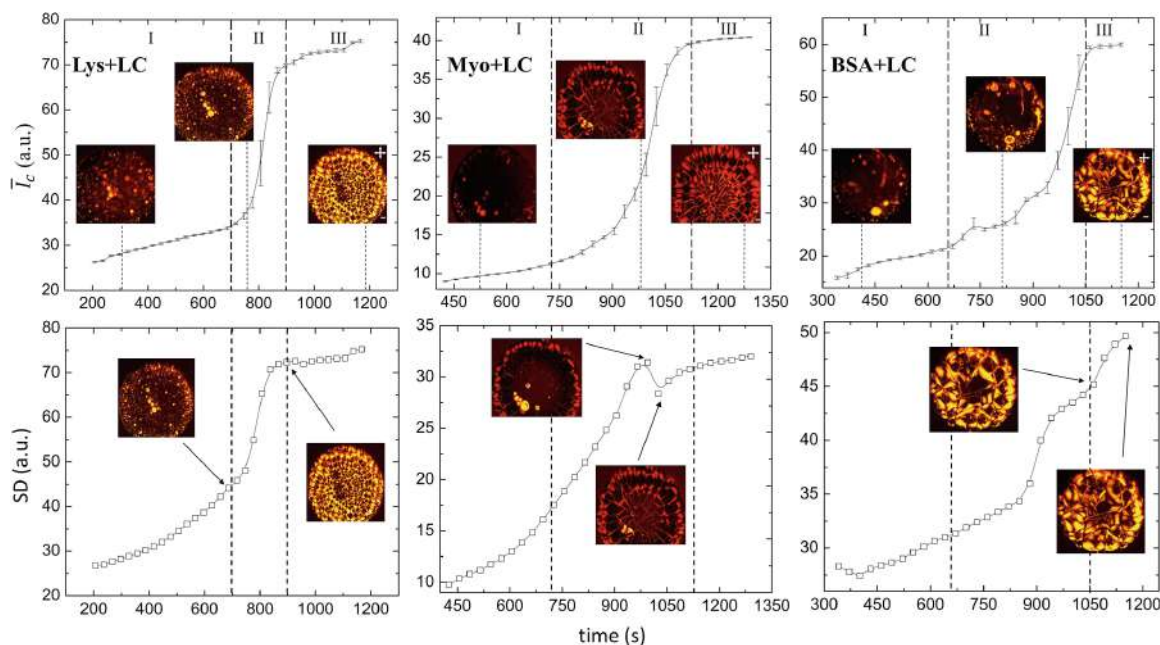


Fig. 2. Upper panel: Variation of birefringence intensity (\bar{I}_c) of LC droplets during the drying process. Three unique regimes are observed: (I) a steady upsurge, (II) a speedy rise, and, (III) an eventual saturation of intensity. Lower panel: variation of standard deviation (SD) of the images during different drying stages. (Color figure online)

rate of intensity in stage II is ~ 0.28 (for Lys), ~ 0.09 (for Myo), and ~ 0.08 (for BSA). A smooth transition regime in both Lys and Myo is observed, but not in BSA drops indicating a distinct final morphology in BSA. As mentioned earlier, BSA contains a higher molecular weight (~ 66.5 KDa) and the increase of mass in proteins decreases the rate of intensity change (one surprising finding is the drastic decrease from 0.28 to 0.09 in similar weighted proteins of Lys and Myo respectively). It is to note that LC has a strong dipole moment (polar) and the presence of a heme group without any disulfide bonds in Myo could interrupt the local interactions of Myo-LC differently than Lys-LC. Moreover, LC droplets wet the substrate (coverslip) differently for different proteins because of their difference in nature (mass, size, charges of proteins). Hence, it indicates that the mass is not only the contributing factor but involves many other interactions such as self-assembly among protein particles (protein-protein interaction), phase separation and self-assembly of LC droplets (protein-LC, LC-substrate), etc. [4].

The lower panel of Fig. 2 shows the SD (standard deviation of the image) of the same drops depicting a similar trend as a function of time. The \bar{I}_c captures the whole process such as phase separation, formation of protein film, movement of fluid, water evaporation, etc., whereas, the SD is sensitive to changes in the image complexity [10]. The SD gives additional insights into the morphology in terms of changes in inhomogeneity and complexity. In Myo, it shows a difference in the evolution pattern from \bar{I}_c by observing a dip and rise in the transition region. Though Myo protein film is faint red in color under cross-polarizing microscopy, it doesn't mean that it is optically active like the LC droplets (yellow

in color). It means that Myo reflects a particular wavelength (red), and absorbs rest of the colors in the visible spectrum. This becomes advantageous over other proteins in our study i.e., Lys and BSA because the inhomogeneity is clearly distinguishable by calculating SD. The flow of the LC droplets through the Myo film promotes a dip, and the process of turning the film (into reddish) indicates a difference in SD. On the other hand, BSA shows a rise in the complexity of regime III. At this stage, the texture (SD) is found to be changing while distributing the LC droplets, whereas, the \bar{I}_c fails to display such details and shows constant values. In spite of these differences, a common characteristic is observed in both \bar{I}_c and SD by their increase through the drying process and saturation when the drops are fully dried. This is consistent with the process of droplet drying, phase separation, film formation, stain, and finally, film cracking.

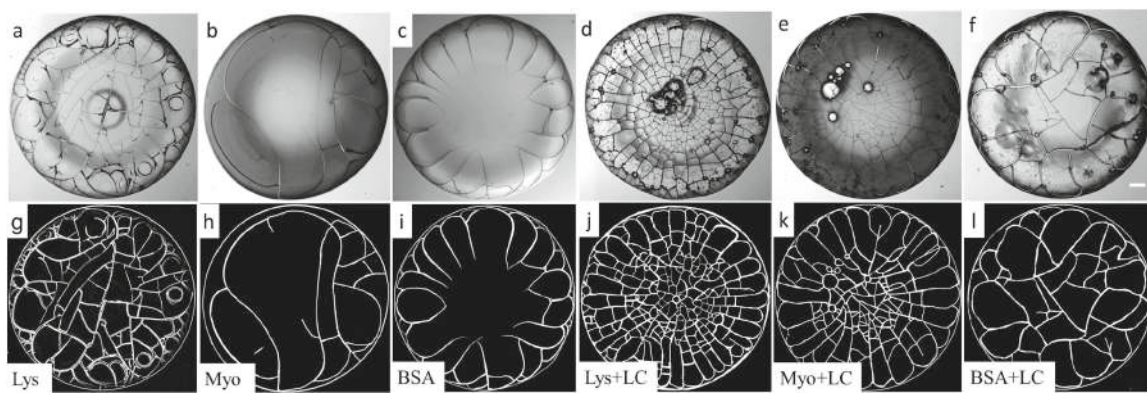


Fig. 3. Upper panel: After 24 hours, the images were captured in the bright-field configuration in the presence and absence of LC droplets (a–f). Lower panel: the processed binary images (g–l). The scale bar of 0.15 mm is shown in the right corner of [f].

Figure 3 shows the crack patterns and their processed binary images (in presence and absence of LC droplets). The common feature noticed in all the drops is the presence of “coffee-ring” [6] (upper panel of Fig. 3) confirming the general mechanism of the drying colloidal drops. The inclusion of the LC droplets affects the cracks’ nature, and makes a rough protein film’s surface. LC is believed to increase the stress in all the drops and the stress in turns produces more number of cracks. The central region of both Myo and BSA does not contain any cracks in the absence of the LC droplets (Fig. 3b, c). Contrary to that, the inclusion of the LC droplets in the protein drops leads to - (i) an ordered crack distribution and disturbs a ‘mound’-like structure in the Lys drops (Fig. 3a, d), (ii) a formation of well-connected large and small crack domains in the Myo (Fig. 3b, e), and (iii) an overall increase of the cracks in the BSA and the formation of a few cracks in the central region (Fig. 3c, f).

To quantify the crack spacing (x_c) and to develop a physical mechanism of the underlying process of crack distributions, a non-parametric Mann-Whitney U and Kruskal Wallis tests were conducted. Any statistical difference in mean crack spacing (\bar{x}_c) is considered to be significant when $p < 0.05$. The significant

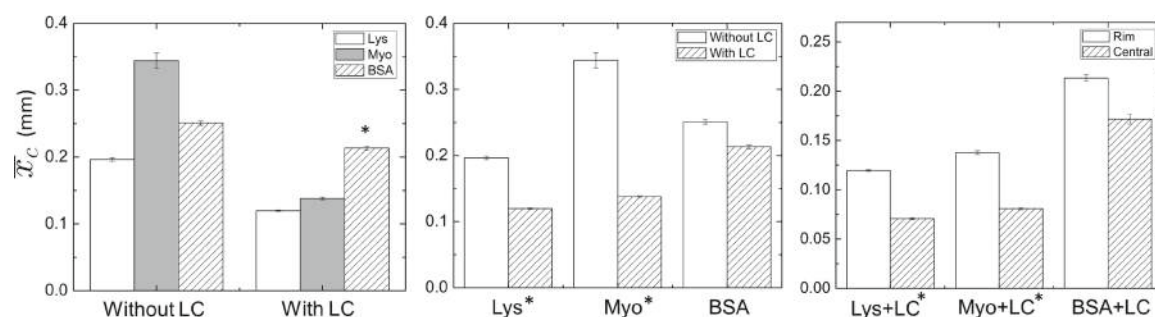


Fig. 4. The comparison of mean crack spacing (\bar{x}_c) in different conditions and environment. Left panel: comparison of \bar{x}_c with and without LC droplets observed in the rim region. Middle panel: overall effect of the LC droplets in relation to \bar{x}_c in all the protein drops. Right panel: comparison of \bar{x}_c in the rim and the central region in different protein drops in presence of LC droplets. An asterisk [*] indicates significant pairs.

pairs are marked with an asterisk [*] in Fig. 4. All the experimental data are expressed as mean \pm standard error (SE). The crack morphology discussed in Fig. 3 confirmed that the rim region of all the protein drops is specified for more number of cracks compared to the central region. We, therefore, conducted a series of statistical tests to examine the (significant) effects of LC droplets on all the proteins. The left panel of Fig. 4 shows the way LC droplets affect the x_c distributions in the rim region of all proteins. We did not observe any significant difference related to x_c distributions. The distribution is observed to be equally large in all the protein solutions without LC droplets. However, x_c is observed to be reduced (i.e., there is more number of cracks) when LC droplets are added. A pairwise comparison (using Dunn's procedure with a Bonferroni correction) of the proteins in the presence of LC droplets reveals that BSA still has significantly larger x_c compared to the other two protein drops (Lys and Myo). In other words, LC droplets do not have a significant effect in terms of x_c distributions on BSA even though the morphology shows a reduced x_c when LC is added (Fig. 3f, 1). The middle panel of Fig. 4 further reveals that the presence of LC considerably reduces the x_c distributions (a large number of uniformed cracks) in all the proteins, however, the difference is found to be statistically significant in both Lys and Myo, but not in the BSA. Finally, we examined the way (inclusion of) LC droplets affect the x_c distributions in the rim and the central regions of all the protein drops (right panel of Fig. 4). The results confirm that the presence of LC considerably reduces the x_c in the central region of all the proteins. However, this reduction of x_c is observed to be significant in both Lys and Myo (but not in BSA). This outcome is evident as we have already seen that LC does not affect the BSA (in terms of x_c reduction). The quantification of x_c and the outcome of the statistical tests provide a convincing indication about the effect of LC on the proteins (under study) which otherwise is slightly misleading if the morphological observations are considered alone.

Following these findings discussed above, a physical mechanism is proposed. Our findings confirm that Lys and Myo follow a similar process of crack forma-

tion, unlike BSA. Each domain in these two proteins is buckled up, and most of the LC droplets are moved underneath the film from the cracks through the capillary action. The dark region at the center of each of these regions is the film attached to the coverslip. In contrast, BSA shows a radial defect (four-fan brushes) which is commonly observed at the LC-air interface confirming that the LC droplets are spread at the top of the BSA film [4].

4 Conclusions

Sessile drop drying is popularly used to explore the self-assembly and the phase separation of the particles in the colloidal drops. In this paper, we proposed an automated image-based mechanism to calculate birefringence of the optically active material and can be applied to any such colloidal drops. Further, the proposed semi-automated image processing mechanism of quantifying crack patterns can be applied to any drying system (with similar crack patterns) helping to understand the underlying physical mechanism. These methods have a broad range of applications quantifying image morphology in an efficient and economical way.

References

1. Brutin, D., Starov, V.: Recent advances in droplet wetting and evaporation. *Chem. Soc. Rev.* **47**(2), 558–585 (2018)
2. Chen, R., Zhang, L., Zang, D., Shen, W.: Blood drop patterns: formation and applications. *Adv. Colloid Interface Sci.* **231**, 1–14 (2016)
3. Bel'skaya, L.V., Sarf, E.A., Solonenko, A.P.: Morphology of dried drop patterns of saliva from a healthy individual depending on the dynamics of its surface tension. *Surfaces* **2**(2), 395–414 (2019)
4. Pal, A., Gope, A., Iannacchione, G.S.: A comparative study of the phase separation of a nematic liquid crystal in the self-assembling drying protein drops. *MRS Adv.* **4**(22), 1309–1314 (2019)
5. Pal, A., Gope, A., Kafle, R., Iannacchione, G.S.: Phase separation of a nematic liquid crystal in the self-assembly of lysozyme in a drying aqueous solution drop. *MRS Commun.* **9**(1), 150–158 (2019)
6. Deegan, R.D., Bakajin, O., Dupont, T.F., Huber, G., Nagel, S.R., Witten, T.A.: Capillary flow as the cause of ring stains from dried liquid drops. *Nature* **389**(6653), 827 (1997)
7. Preibisch, S., Saalfeld, S., Tomancak, P.: Globally optimal stitching of tiled 3D microscopic image acquisitions. *Bioinformatics* **25**(11), 1463–1465 (2009)
8. Schindelin, J., et al.: Fiji: an open-source platform for biological-image analysis. *Nat. Methods* **9**(7), 676–682 (2012)
9. Abràmoff, M.D., Magalhães, P.J., Ram, S.J.: Image processing with ImageJ. *Biophotonics Int.* **11**(7), 36–42 (2004)
10. Carreón, Y.J., Ríos-Ramírez, M., Moctezuma, R., González-Gutiérrez, J.: Texture analysis of protein deposits produced by droplet evaporation. *Sci. Rep.* **8**(1), 9580 (2018)


 Cite this: *RSC Adv.*, 2020, 10, 16906

A comparative study of the drying evolution and dried morphology of two globular proteins in de-ionized water solutions†

 Anusuya Pal,^a Amalesh Gope,^b Ari S. Athair^a and Germano S. Iannacchione^a

Pattern formation in drying protein droplets continues to attract considerable research attention because it can be linked to specific protein–protein interactions. An extensive study of the drying evolution and the final crack patterns is presented, highlighting the concentration dependence (from 1 to 13 wt%) of two globular proteins, lysozyme (Lys) and bovine serum albumin (BSA), in de-ionized water. The drying evolution starts with a constant contact radius mode and shifts to a mixed mode where both fluid front and contact angle changes. The contact angle monotonically decreases, whereas, the fluid front exhibits two regimes: an initial linear regime and a later non-linear regime. Unlike the linear regime, the non-linear regime is faster for Lys droplets. This results in the formation of a “mound”-like structure in the central region. A new feature, a “dimple” is observed in this mound which is found to be dependent on the initial concentration. The different crack morphology of BSA and Lys depends strongly on the initial state of the solution and can be interpreted using a simple mechanical model. In fact, when dried under uniform conditions (surface, humidity, temperature, droplet diameter, etc.), the evolution and the final pattern displays as a fingerprint of the initial state.

Received 23rd February 2020

Accepted 15th April 2020

DOI: 10.1039/d0ra01748e

rsc.li/rsc-advances

1 Introduction

A colloidal droplet deposited on a surface either spreads over the surface or remains as it is depending on the wettability of the surface. Whatever the case, the droplet endures a whole range of interfacial phenomena (wetting dynamics, adsorption, and adhesion), internal flow (diffusion and convection), and particle–substrate interactions during the solvent evaporation (drying).^{1,2} The pattern formation of a bio-colloidal droplet, even on an ideal surface, is exposed to additional complexity during the drying process. This complexity arises primarily due to strong and potentially competing interparticle interactions that govern the particle aggregation and self-assembly. Furthermore, some bio-colloidal droplets such as blood and plasma serum are ubiquitous, and, most notably, are used in medical diagnostics and forensics analysis.^{3–6} Studies on drying droplets reveal that the evolution and the emerging patterns depend on multiple factors including the nature of the solute particles (size, chemical composition initial concentration), different type of substrates (hydrophilic, hydrophobic), geometry, substrate wetting, and various drying conditions (temperature, pH, relative humidity).^{7–11} Accordingly, it turns out to be

essential to understand the effects of these factors on the drying and dried bio-colloidal droplets in order to compare (and explain) the macroscopically observed behavior with the initial microscopic state of the constituent particles.

Owing to its significance in many potential applications, the drying evolution and the morphological patterns of dried plasma and blood have been examined by several researchers.^{3,4,6} Essential mechanisms of spreading, gelation, and crack formation of these droplets are presented in recent review articles by Brutin *et al.*¹² and Chen *et al.*¹³ An aqueous solution of protein drying droplets may similarly be substantiated as a prolific system of biological relevance. The aqueous solution of proteins is far less complicated than blood and plasma. In a recent study, the drying droplets of raw egg-white protein solutions have been explored which validate the dependence of daisy and wavy-ring crack patterns on the initial protein concentrations.¹⁴

It is worth mentioning that commercially available high-quality globular proteins such as bovine serum albumin (BSA) and lysozyme (Lys) have also attracted the attention of many researchers. Many studies investigated the temporal drying process and their resulting patterns. Despite the intense research, most of the work on protein–solvent systems is primarily confined to either a dilute regime of protein concentration and/or the involvement of the salts into the systems.^{15–19} The dilute regime of the initial protein concentration is well explored in the drying droplets; however, not beyond the range of 60 mg mL^{−1}. Researchers also attempted to explore the

^aDepartment of Physics, Order-Disorder Phenomena Laboratory, Worcester Polytechnic Institute, Worcester, MA, 01609, USA. E-mail: apal@wpi.edu

^bDepartment of English, Tezpur University, Tezpur, Assam, 784028, India

† Electronic supplementary information (ESI) available. See DOI: 10.1039/d0ra01748e



drying evolution and the crack distribution of these proteins dissolved in (de-ionized) water under ambient conditions.^{15,20} Gorr *et al.*¹⁵ studied the time evolution and the morphological patterns of Lys dissolved in water, varying the initial concentration from 0.1 (1 mg mL⁻¹) to 1 wt% (10 mg mL⁻¹). This study concluded that all the drops exhibit a “coffee-ring” effect.^{15,21} The volume fraction of the Lys is found to be linearly dependent on its initial concentration; however, the morphology does not show any significant changes in the ring’s height and width. They also reported a “mound”-like feature in the central region and observed a few surface cracks in the given concentration range. Carreón *et al.*²⁰ investigated the mixture of BSA and Lys dissolved in water and mainly focused on their interactions. They also conducted experiments with denatured BSA and Lys proteins and their mixtures at different relative concentrations. The folding and unfolding of these proteins and their structural (morphological) alternation are also discussed in their paper. They concluded that the formation of the crystal clusters and dendrite structures are independent of the external salts.

In this paper, two fundamental questions about the drying evolution and the resulting patterns of the dried droplets of aqueous solutions of commercially available globular proteins, are addressed. This article aims to explore (i) the role of the protein properties (in terms of mass, composition, configuration, and size); and examine, (ii) the effect of higher initial protein concentration (above 60 mg mL⁻¹ and up to 150 mg mL⁻¹) on the aggregation process. The inclusion of the higher-initial protein concentration is essential since the higher concentrations enable us to explore how the excessive aggregation of these proteins play a role in relieving mechanical stress during the drying process, and the crack formation patterns. It is worth mentioning that no studies to date have attempted to investigate these fundamental queries at the concentration ranges we considered in this paper. To the best of our knowledge, we did not come across any experimental evidence that compares the drying evolution of the protein droplets in terms of the contact angle and the fluid front. To address this gap, two proteins, BSA and Lys, are chosen in this study. The droplets are prepared using de-ionized water (DI) that avoids ion-mediated effects and exposes the protein–protein interactions. Furthermore, the inclusion of DI under ambient conditions ensures that the functionality of the proteins is not affected by any external factors such as pH, temperature, *etc.*

The drying evolution and the emerging patterns are then examined at the initial protein concentration ranging from 1 (10 mg mL⁻¹) to 13 wt% (150 mg mL⁻¹). Each solution sample is deposited as a ~2 mm diameter droplet on a glass slide to record the temporal variation of contact angle, fluid front, and to capture the image of the final dried state. An image processing technique is employed to extract the distribution of the distance between consecutive cracks (crack spacing) in the protein droplets. To ensure the reliability of the visual observations, an appropriate statistical test is used on the obtained crack-spacing data. A physical mechanism is proposed in this paper to relate the dried morphology with the nature of the initial protein solutions. Finally, the crack patterns are

interpreted in terms of a simple mechanical stress model to explain the presence of a crack hierarchy in the Lys (not seen in BSA) droplets.

The paper is structured as follows. Following this introduction, section 2 describes the materials and the experimental methodology adopted in this paper. Section 3 presents the process of the drying evolution, the morphology, the physical and mechanical mechanism, and the statistical findings on the dried crack patterns in both protein droplets. The results and the significant findings of this paper are discussed in this section. Finally, the results are concluded in section 4.

2 Materials and experimental methodology

BSA and Lys are well-studied water-soluble globular proteins. BSA is a representative blood protein primarily derived from cows. It is four times heavier than Lys. BSA has a molecular mass of ~66.5 kDa with an ellipsoid shape of dimensions 4.0 × 4.0 × 14.0 nm³.²² Lys, on the other hand, can be observed in human mucosal secretions such as saliva, tears, *etc.* It consists of a molecular mass of ~14.3 kDa, and a roughly ellipsoid shape of dimensions 3.0 × 3.0 × 4.5 nm³.²³ Lys is made up of 129 amino acids whereas, this blood protein contains 581 amino acids in a single polypeptide chain. The isoelectric point of BSA is 4.7 which enables it to carry a net negative charge under the present conditions of the study (pH of ~7). The isoelectric point of 11.1 in Lys, on the other hand, allows it to carry a net positive charge. The globular shape and stability of these proteins are attributed to the disulfide bridges (17 in BSA and 4 in Lys), hydrogen bonds, and hydrophobic interactions among the amino acids.²⁴ It is to be noted that the globular nature of the overall tertiary structure of these proteins is maintained in this present study. The synthetic polymer-based colloidal behavior of these proteins is only possible when these are completely denatured (or their structures are relaxed). Therefore, this study is much more complicated and difficult to interpret than other polymer-based droplet studies.

The commercial lyophilized BSA and the Lys are obtained from Sigma Aldrich, USA (Catalog no. A2153 and L6876 respectively). The protein samples are used without any further purification. ~150 mg of each BSA and Lys were measured and separately dissolved in 1 mL of de-ionized water (Millipore, resistivity of 18.2 MΩ cm) to create the protein stock solutions, BSA + DI and Lys + DI at a concentration of 13 wt%. Each stock solution was diluted to prepare concentrations of 1, 3, 5, 7, 9, and 11 wt%. To make samples combining protein and liquid crystal (LC), 4-cyano-4'-pentyl-biphenyl was purchased from Sigma Aldrich, USA (Catalog no. 328510). The LC was heated at ~39 °C, and a volume of ~10 μL was added to the prepared protein solutions of 9 wt%. The sample sets were used in the next few hours of their preparation time. We used the factory-fresh microscopic glass slides as the substrates, which have minimal exposure to the environment prior to the actual experiments. These slides were rinsed with ethanol and dried. Thus, every droplet precisely contained the same substrate



conditions and a uniform reproducibility in terms of the circularity of the droplets and their pinning effects was observed. A volume of $1 \pm 0.2 \mu\text{L}$ of the sample was pipetted to form a circular droplet of $\sim 2 \text{ mm}$ diameter. For strip-like geometry, two carbon tapes were placed in parallel on the glass substrate by keeping a separating distance of $\sim 2 \text{ mm}$, and a volume of $\sim 5 \mu\text{L}$ of the protein samples was pipetted. The samples were left to dry under a bright-field microscope (Leitz Wetzlar, Germany) with a $5\times$ objective lens in ambient conditions (room temperature of $\sim 25^\circ\text{C}$ and relative humidity of $\sim 50\%$). The total time of the drying process for all droplets was roughly around 10–20 minutes.

The captured images were analyzed using ImageJ²⁵ software. The time-lapsed images of the drying process were obtained every two seconds. The start time of the clock was the time of the deposition point of the droplet on the glass slide. The fluid front radius ($r(t)$) was measured by tracking the distance from the center to the edge of the front under the microscopy during the drying evolution. These radii were measured repeatedly ten times at each time (t), and the averaged values ($\bar{r}(t)$) were computed. The spiral crack study was conducted using a $50\times$ objective lens. The images of dried droplets were captured over 24 hours using side-illuminated bright-field microscopy (since a few cracks appeared after the visible drying process²⁶). The *stitching plugin*²⁷ of ImageJ was used to redraw the complete image of the dried droplets. The stitched bright-field images were converted into high contrast images. The circular cut lines were drawn using the *oval profile* plugin of ImageJ. The intensity values (255 for pixels depicting crack lines and 0 for elsewhere)

were plotted as a function of arc-length. A script with “Array and Maxima” was used to determine the positions of the maximum intensity values to estimate the spacing between the consecutive cracks (x_c). The detailed processing can be found in our previous paper.²⁸ The same process was repeated for two other droplets deposited from the same sample set at each concentration (ϕ) to ensure the reproducibility of the final morphology. The data were aggregated to yield an overall crack spacing x_c at each ϕ . It is to be noted that this crack spacing analysis is conducted only at the peripheral region where the cracks of both protein droplets are present. Furthermore, the contact angle goniometer (Model 90, Ramé-hart Instrument Co. USA) was used to monitor the contact angle ($\theta(t)$) measurements of the prepared protein samples during the drying process.

3 Results and discussion

3.1 Time evolution of drying droplets

3.1.1 Bovine serum albumin: BSA + DI. Fig. 1(I) shows the top view of the drying evolution of a BSA droplet at the initial concentration (ϕ) of 5 wt% captured through optical microscopy. As soon as the first image of the deposited droplet is captured, a symmetrical dark (black) shade is observed near the periphery of the droplet. With the progression of time, the dark shade changes to the bright (gray) shade (Fig. 1(I)a–c). The periphery of the droplet is found to be pinned to the glass substrate throughout the drying process. After ~ 3 minutes, the fluid front starts receding from the periphery to the center of the droplet. The radius (r) of this front is measured with the

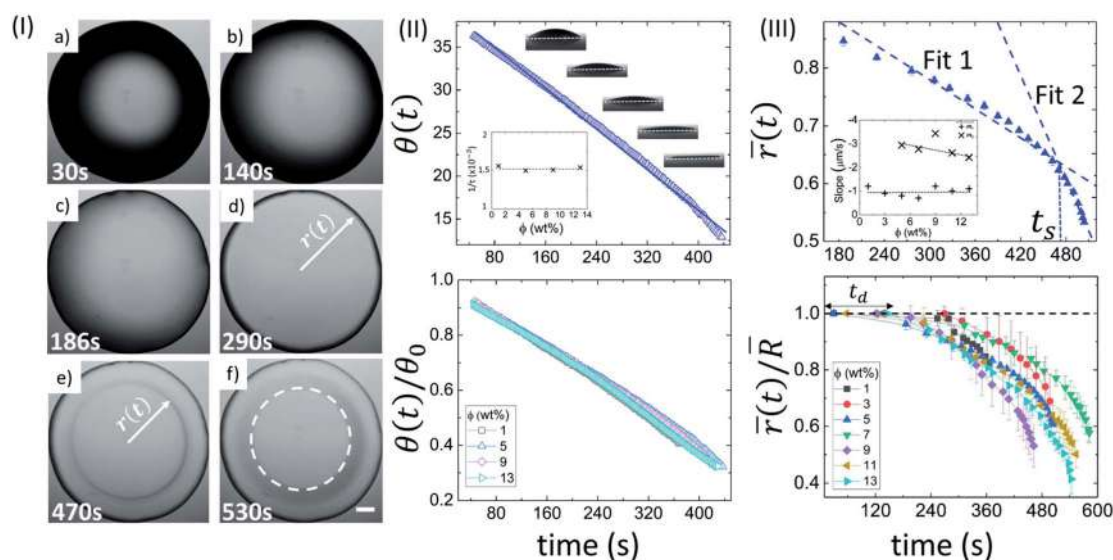


Fig. 1 Drying evolution of a BSA droplet: (I) top-view of the droplet through optical microscopy at ϕ of 5 wt% obtained during different time intervals (30 s, 140 s, 186 s, 290 s, 470 s and 530 s). The white dashed circle in (f) exhibits the “coffee-ring” formation. The scale bar represents a length of 0.20 mm. (II) The top panel shows the variation of contact angle ($\theta(t)$ in degrees) at ϕ of 5 wt%. The solid line specifies the fitted function. The inset shows the variation of the characteristic fitting parameter ($1/\tau$ in s^{-1}) at different ϕ . The bottom panel displays the temporal variation of the normalized contact angle ($\theta(t)/\theta_0$). (III) The top panel reveals the variation of mean fluid front radius ($r(t)$ in mm) at ϕ of 5 wt%. The error bars represent the standard deviation. A representative fit of two linear models is made; t_s signifies the time point where both the linear fits merge. The inset shows the dependence of the slope values of linear fit 1 (m_1) and 2 (m_2). The bottom panel indicates the temporal variation of normalized mean fluid front radius ($r(t)/R$) at different ϕ . t_d is the “dead” time up to which the fluid front radius ($r(t)$) is equal to the radius of the droplet (R).



progression of time, (t) (Fig. 1(I)d and e). The movement allows the particles to be deposited along each receding line and eventually forms a peripheral ring (shown by a white dashed circle in Fig. 1(I)f). It is to be noted that a few cracks in the BSA droplets up to ϕ of 5 wt% are formed within 24 hours, which are shown in the following section.

Fig. 1(II) depicts the side view of the drying evolution of a BSA droplet at different ϕ observed with the contact angle goniometer. The contact angle (θ) and the height at the center of the droplet (h) are found to be $37 \pm 2^\circ$ and 0.35 ± 0.20 mm, respectively, within ~ 50 seconds of the deposition of the droplet. The radius (R) of the droplets is 1.1 ± 0.2 mm, and therefore, the gravitational effects can be negligible. Furthermore, the macroscopic shape of the droplet can be approximated as the spherical-cap geometry, which is based on the assumption that $h \ll R$. The black shade, observed at ϕ of 5 wt% in Fig. 1(I) is due to the spherical-cap shape of the droplet. The change from the black to the gray shade occurs when the contact angle (θ) reaches a threshold value. The top panel of Fig. 1(II) shows the variation of θ at ϕ of 5 wt%, and $\theta(t)$ is found to consistently reduce with time. This suggests that the drying process occurs under a continuous evaporation limit. To validate this limit, $\theta(t)$ is fitted to a linear function: $\theta(t) = \theta_0(1 - t/\tau)$, where, θ_0 is the initial θ at $t = 0$, and $1/\tau$ is a characteristic rate. For ϕ of 5 wt%, θ_0 and $1/\tau$ are found to be $39.96 \pm 0.08^\circ$ and $0.001500 \pm 0.000005 \text{ s}^{-1}$, respectively, with $R^2 = 0.995$. The $1/\tau$ is observed to be independent of ϕ (inset of Fig. 1(II)). A complete description of all the fit parameters is tabulated in Table T1 of the ESI.† The normalized contact angle is calculated by dividing $\theta(t)$ with the θ_0 (obtained from the fitting equation). The individual normalized θ decay curves at different ϕ are found to collapse to a master curve when the data is plotted. This is shown in the bottom panel of Fig. 1(II).

In this context, it is interesting to compute the fluid front radius and its dependence on ϕ . Fig. 1(III) shows the evolution of the mean fluid front radius ($\bar{r}(t)$) in a BSA droplet at different ϕ . The top panel shows the variation of $\bar{r}(t)$ at ϕ of 5 wt% exhibiting two distinct regimes: a slow, initial linear regime, and a subsequent non-linear, fast regime. Two linear fits are made on the respective linear and non-linear regimes, and a characteristic time, t_c (the time point at which two linear fits intersect) is introduced. It is to be noted that the linearity of $\bar{r}(t)$ deviates after the peripheral ring formation (Fig. 1(I)e and top panel of Fig. 1(III)). The inset of Fig. 1(III) compares the slope values (m_1 and m_2) obtained from the linear fits in the respective regimes at each ϕ . The negative sign in the slope values confirms the reduction of the mean radius ($\bar{r}(t)$) with time. For 1 and 3 wt%, the linear fit in the non-linear regime cannot be achieved due to a swift and non-uniform movement, resulting in a lower number of data points to quantify. On average, the velocity of the fluid front in the linear and non-linear regime is found to be $0.99 \pm 0.20 \mu\text{m s}^{-1}$ and $2.83 \pm 0.38 \mu\text{m s}^{-1}$ respectively. m_2 decreases from ~ 3 to $\sim 2 \mu\text{m s}^{-1}$ with the increase of ϕ . The bottom panel of Fig. 1(III) displays the normalized radius (obtained by dividing the $\bar{r}(t)$ with the mean radius of the droplet, \bar{R}). In the early stage of the drying evolution, *i.e.*, up to ~ 240 seconds, the radius remains constant, ($\bar{r}(t)/\bar{R} = 1$) for all the ϕ . This time is labeled as

the “dead” time (t_d) where only the contact angle changes without disturbing the radius. A complete description of all the measured and fit parameters is tabulated in Table T2 of the ESI.†

3.1.2 Lysozyme: Lys + DI. Akin to BSA, a Lys droplet at ϕ of 5 wt% also shows a dark shade near the periphery of the droplet (Fig. 2(I)a). The dark shade diminishes, as the fluid front starts receding from the periphery after ~ 6 minutes, and forms a ring (Fig. 2(I)b–d). Interestingly, a sharp spot around the center appears and forms a “mound”-like structure. The water starts drying from that mound, and finally, a “dimple” appears in the existing structure. Simultaneously, the radial cracks grow near the periphery and come into contact with each other through the orthoradial cracks (Fig. 2(I)d–f). The white dashed circle displays the peripheral ring and the solid circle depicts the mound and the dimple structures (Fig. 2(I)f). Unlike BSA, most of the cracks appeared during the visible drying process at ϕ of 5 wt%.

Fig. 2(II) shows the side view of the drying evolution of a Lys droplet at different ϕ . It is to note that different Lys concentrations might affect the surface tension of the solutions. However, our first measured value of θ during the contact angle measurements at all ϕ is found to be $37.0 \pm 1.6^\circ$. This measurement tempted us to conclude that the effect is not significant enough for the unique pattern formation. The θ at ϕ of 5 wt% during the drying process reduces consistently (top panel of Fig. 2(II)). θ_0 and $1/\tau$ are found to be $36.66 \pm 0.01^\circ$ and $0.0009740 \pm 0.0000007 \text{ s}^{-1}$, respectively, with $R^2 = 0.999$. Similar to BSA, the characteristic rate ($1/\tau$) is found to be independent of ϕ . A complete description of all fit parameters is tabulated in Table T3 of the ESI.† Unlike BSA, the normalized contact angle data shows that the individual decay curves at different ϕ start deviating from each other towards the very end of the process (bottom panel of Fig. 2(II)).

The top panel of Fig. 2(III) displays the evolution of the ($\bar{r}(t)$) at ϕ of 5 wt% in Lys droplet. And, the bottom panel depicts the evolution of the normalized mean fluid front radius ($\bar{r}(t)/\bar{R}$) at different ϕ . It is noted that this movement in BSA droplets could be tracked only up to the point where the radius just passes through the peripheral ring. Unlike BSA, this movement in the Lys droplets could be tracked till the “mound”-like structure around the central region of the droplet formed. This causes the range of the $\bar{r}(t)/\bar{R}$ data to be 1 to ~ 0.1 . The presence of a linear and a subsequent non-linear regime is commonly observed in the fluid front movement at every ϕ in both the Lys and BSA droplets. On average, the velocity of the fluid front in the linear and non-linear regime of these Lys droplets is found to be $1.00 \pm 0.08 \mu\text{m s}^{-1}$ and $12.36 \pm 2.73 \mu\text{m s}^{-1}$, respectively. A sharp dependence of the slope values in regime 2 with ϕ is observed, m_2 decreases from ~ 17 to $\sim 8 \mu\text{m s}^{-1}$. A complete description of all the measured and fit parameters is tabulated in Table T4 of the ESI.†

3.1.3 A physical mechanism. The underlying physical mechanism of the drying evolution and the visible difference in terms of the morphology of the droplets is demonstrated in Fig. 3. The deposited droplet goes through a convective flow where the constituent particles tend to interact (adsorb) with the substrate during the early drying stage. The evaporation rate



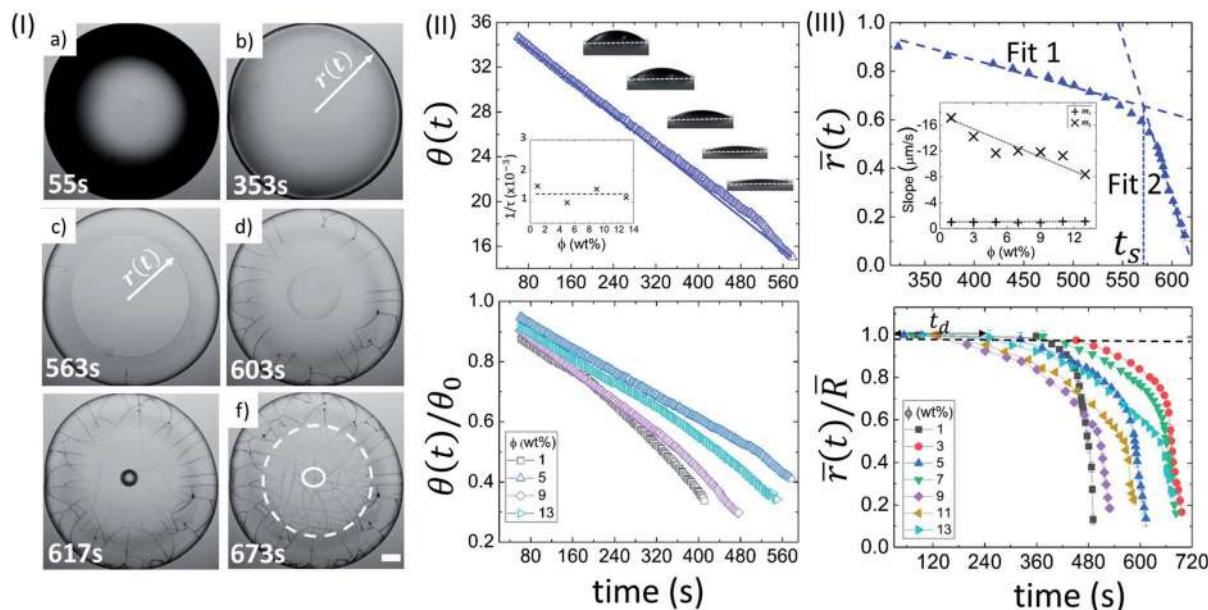


Fig. 2 Drying evolution of a Lys droplet: (I) top-view of the droplet through optical microscopy at ϕ of 5 wt% during different drying intervals (55 s, 353 s, 563 s, 603 s, 617 s and 673 s). The white dashed circle in (f) shows the “coffee-ring” formation. The solid circle exhibits the “mound”-like structure. The scale bar represents a length of 0.20 mm. (II) The top panel confirms a variation of contact angle ($\theta(t)$ in degrees) at ϕ of 5 wt%. The solid line shows the fitted function. The inset shows the variation of the characteristic fitting parameter ($1/\tau$ in s^{-1}) at different ϕ . The bottom panel displays the temporal variation of the normalized contact angle ($\theta(t)/\theta_0$). (III) The top panel reveals the variation of the mean fluid front radius ($\bar{r}(t)$ in mm) at ϕ of 5 wt%. The error bars represent the standard deviation. A representative fit of two linear models is made; t_s signifies the time point where both the linear fits merge. The inset represents the dependence of the slope values of linear fit 1 (m_1) and 2 (m_2). The bottom panel indicates the temporal variation of the normalized mean fluid front radius ($\bar{r}(t)/\bar{R}$) at different ϕ . t_d is the “dead” time up to which the fluid front radius ($r(t)$) is equal to the radius of the droplet (R).

is observed to be the highest at the three-phase contact line (solid-vapor-liquid) due to the curvature of the circular droplet. This process drives the flow to compensate the higher rate of mass loss near the periphery compared to the central part of the droplet. This early stage depicted in Fig. 3a shows the constant

contact radius mode (CCR) in which no fluid front movement is observed; however, the height and the contact angle get considerably reduced. During this time-frame, the protein particles form an inhomogeneous film and (subsequently) a fluid front starts moving on this film from the periphery to the

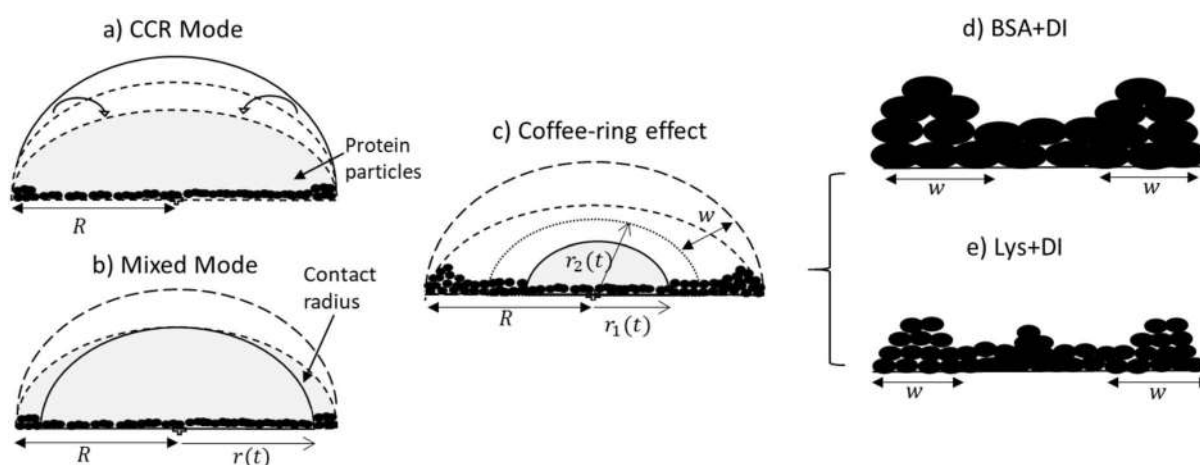


Fig. 3 Side view of the drying evolution: (a) CCR mode is observed at an early stage of drying where only the contact angle decreases. The fluid front radius (r) remains unchanged during this time and is equal to the radius (R) of the droplet. The protein particles interact with the substrate during this stage. (b) In this mixed mode stage, along with the contact angle, the fluid front starts receding from the periphery of the droplet. (c) The fluid front moves, deposits more particles, and forms a ring of width w . It moves further when the radius of the fluid front just passes the ring width to the new position (r_2). r_1 indicates the movement towards the central region of the droplet, leading to a complimentary morphology. (d) BSA + DI, without any “mound”-like structure and (e) Lys + DI, the presence of a “mound” could be observed in the central region.



center which marks the beginning of the next stage. The mixed mode *i.e.*, the movement of both the contact angle and the fluid front is found at this stage. The front seems to deposit more protein particles as it moves (Fig. 3b). A bulge (popularly known as “coffee ring” effect²¹) at the periphery of the droplet is noticed during this fluid front movement. The bulge is believed to form due to the excess deposition of the particles which could be seen in Fig. 3c. The drying process up to this point, *i.e.* the formation of this peripheral ring, is observed to be similar for both protein droplets (Fig. 1 and 2). However, the formation of a “mound”-like structure (Fig. 3d and e) in the Lys droplets (a similar phenomenon is observed in ref. 15 and 20) creates a visible difference in the drying evolution of both protein droplets. The comparison of the drying rates of these different-sized protein particles may reveal new insights. To map the rate of water loss with the change in morphology during the drying process, it is vital to explore the possible reasons behind the similarities and dissimilarities for both protein droplets in terms of the parameters (t_d , t_s , m_1 , and m_2) extracted from the fluid front movement.

t_d indicates the (early stage) time point of the drying process where the protein particles in both droplets experience convective flow. During this flow, these particles first tend to interact (adsorb) with the substrate. The usage of de-ionized water in the present study enables us to avoid ion-mediated effects and does not influence the conformational states (or the functionality) of these proteins. This means that the globular nature of the overall protein structure during the drying process is maintained. During adsorption of these proteins on the glass substrate, one can expect different BSA-glass and Lys-glass interactions. This expectation can be due to the fact that the BSA and the Lys proteins carry an opposite net charge whereas, the glass (substrate) is negatively charged. However, we also need to consider that the hydrophobic residues are buried inside the protein core, and numerous positively and negatively charged residues in a protein's surface are exposed. Though the overall charge of BSA (or Lys) is negative (or positive), means that the BSA (or Lys) will prefer to adsorb on the negatively charged glass substrate with its positively charged residues. Therefore, the overall interaction of BSA-glass or Lys-glass might not be altered, while there is a high probability of having different BSA–BSA or Lys–Lys interactions. This is because these charged residues help orient these protein particles in such a way that one particle gets influenced by the neighboring particle. With time, the protein–protein interactions start to become dominant over the protein–substrate interactions, and assist in forming the protein film on the substrate, and finally could be responsible for determining these unique patterns. So, t_d is the time in which protein particles interact with the substrate and interact with other proteins to form a film. The constant rate of the evaporation validates the similar trend in this CCR mode up to the time point t_d .

As time passes during the drying process, we observed a fluid front to recede from the periphery to the center of the droplet. We quantified the velocity of the front movement. The average speed of first linear fit (m_1) is found to be $0.99 \pm 0.14 \mu\text{m s}^{-1}$,

which is independent of the initial concentration and the type of protein. Considering the trends observed in m_1 , it could be concluded that similar mass transfer mechanisms have emerged in the linear regime. This assumption makes sense because there is enough water on the front surface at this stage, and the front behaves as if it is a water-pool and hardly feels the presence of any protein particles. Subsequently, we have observed a transition from the linear to the non-linear regime in the front movement (Fig. 1(III) and 2(III)). A linear fit on the linear and non-linear regimes was made. t_s signifies the time point where both these linear fits merge. Interestingly, it can be physically interpreted as the time when the fluid front moves from r_2 to r_1 (Fig. 3c), *i.e.*, the time point of the movement from the edge of the peripheral ring towards the central region of the droplet. The t_s for all ϕ is found to be within ± 20 s from this ring formation.

Once the fluid front passes this peripheral ring, the fluid no longer resembles a water-pool. The continuation of the water evaporation process leads to the presence of more protein particles than water. In this context, we observed that the velocity of the second linear fit (m_2) is dependent on the initial concentration and this is different for both protein droplets. The differences observed in m_2 are probably due to different self-assembling interactions, which is dependent on the unique physical characteristics of these proteins. Given the globular nature of these proteins, we know that these proteins are different in terms of their net charged states, molecular shape, weight and disulfide bridges. Since the pH of the system is unchanged, it is beyond the scope of this paper to conclude the mobility effects that emerged due to the individual charged residues present in the protein during the fluid front movement. However, this mobility can easily be interpreted in terms of their weight, shape and bridges. BSA particles are mostly restricted to flow with the fluid front due to high molecular weight (~ 66.5 kDa) and a high aspect ratio (major/minor axis = 3.5). Moreover, the presence of 17 disulfide bridges in BSA provides a compact network between BSA–BSA particles; it will prefer to be deposited within the existing film-layer in the droplet. This results in a few left-over BSA particles to be carried with the water during the later stage of the fluid front movement. In contrast, Lys could be thought of as a squishy sphere (aspect ratio = 1.5) with low molecular weight (~ 14.3 kDa). The presence of the lower disulfide bridges (17 for BSA and 4 for Lys) results in a weak network among these Lys particles, and it triggers the Lys particles to be carried away with the fluid front. The water content of the fluid decreases with the progression of time, and a large number of Lys particles are left behind. These (left-out) particles eventually accumulate around the center and forms the “mound”-like structure. We believe that some water is trapped in the mound. Therefore, a dimple is noticed when the Lys particles fall out of the solution as this entrapped water evaporates.

The movement of the fluid front appears to slow down with the increase of ϕ (number of particles), even though the movement continues to carry and deposit the Lys particles at each line of the fluid front. The concentration dependence of the mound and the peripheral ring on different protein types will be discussed later. At the final stage of the drying process, the water-loss in the droplet induces high mechanical stress



leading to the formation of different crack patterns, which will be discussed in the next subsection. The movies of the drying process in both protein droplets are available in the ESI,† V1 for BSA + DI and V2 for Lys + DI; both videos are recorded at ϕ of 5 wt%.

3.2 Morphology of dried droplets

Fig. 4a–g and h–n represent the morphology of the dried droplets in BSA and Lys, respectively, both the common and distinctive properties are identified. A few common characteristics of both dried droplets include: (1) the presence of a peripheral ring at a greater height than the central region. This greater height can be viewed from the one-sided dark shadowy shade due to side illumination; (2) the cracks are observed in both the droplets; however, the distribution and the nature of the cracks differ.

A few distinct morphological patterns are observed in the protein droplets: (1) in BSA droplets, mostly the radial cracks are observed, whereas different types of cracks such as radial, wavy, spiral, *etc.* make the Lys droplets a chaotic system. (2) There are almost no cracks in the central region of the BSA droplet, whereas the cracks are present throughout the Lys droplets. However, cracks are found only in the periphery of the Lys droplets at ϕ of 1 wt%. (3) The morphology of the central region has a mound and dimple structures in Lys, but no such structures in the BSA droplet. (4) The increase of cracks with the increase of ϕ is clearly observed in BSA. The cracks are mostly equally spaced and countable. (5) A thin hair-like structure is observed at the termination of each crack (from 7 to 13 wt%) in BSA droplets. In contrast, the cracks are well-connected and form a uniform domain in every Lys droplet (except the ϕ of 1 wt%). (6) The presence of (few) circular and (multiple) spiral cracks in Lys droplets from 9 to 13 wt% makes the morphology very different in the highly concentrated regime, from that in BSA droplets. The possible reasons are discussed in the mechanical interpretation section.

3.2.1 Profilometry. Fig. 5(I) and (II) show the variation of a dimensionless quantity, the mean peripheral ring width (\bar{w})

divided by the mean radius of the droplet (\bar{R}) with ϕ for BSA and Lys droplets, respectively. It is observed that the ring width is directly proportional to ϕ , *i.e.*, with the increase of ϕ , this ring width is expanded further in these BSA droplets (Fig. 5(I)). The number of BSA particles increases with the evaporation of water. This process triggers additional deposition of the particles at the droplet periphery with the upsurge of ϕ . On the contrary, the Lys droplet is found to be constant and independent of the variation of ϕ . An almost equal quantity of Lys particles is deposited in the ring, and most of the free particles are carried towards the center (and form a mound structure). Fig. 5(III) shows the areal dependence of this mound structure. The mean area \bar{a} is normalized with \bar{R} , and the \bar{a}/\bar{R} at different ϕ in the Lys droplet is plotted. The linear dependence with ϕ makes it evident that most of the Lys particles are carried and deposited towards the center.

As we have mentioned already, the mound structure is formed by carrying and depositing the free Lys particles during the fluid front movement. As such, the increase of ϕ also triggers the upsurge of the overall number of particles, resulting in the piling of these particles. The formation of a dimple (depression) is probably when the Lys particles fall out of the solution. The presence of this dimple is not reported in any of the earlier works,^{15,20} probably due to the use of a relatively low concentration range. One can anticipate the dimple or the mound as the optical illusion, nonetheless, this is not the case. We did the height profile-like imaging with Sensofar microscopy to confirm the mound and dimple structures; however, we could not calibrate sufficiently to get the exact height measurements. It is also observed that the mound structure is situated almost at the center. This is due to the fact that the circular droplet shape prefers the symmetry for the fluid front movement. To confirm this fact, we pipetted the solutions in a strip-like geometry on the glass substrate. We followed the fluid front movement from both ends of the strips; however, we did not observe any mound or dimple structure. Furthermore, we assumed that this structure is likely to be shifted to some extent (not forming perfectly at the center of the droplet) due to

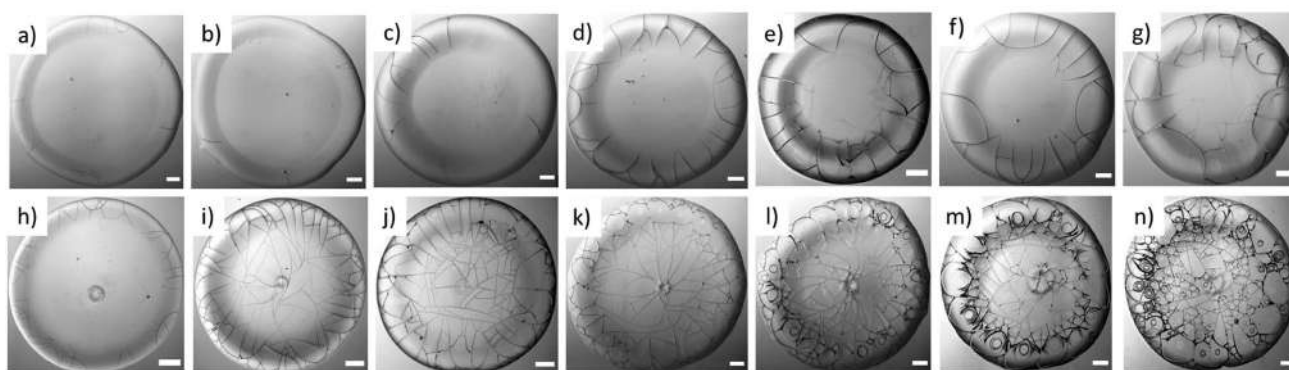


Fig. 4 Gray images of the protein dried droplets: BSA at ϕ of (a) 1, (b) 3, (c) 5, (d) 7, (e) 9, (f) 11, and (g) 13 wt%; Lys at ϕ of (h) 1, (i) 3, (j) 5, (k) 7, (l) 9, (m) 11, and (n) 13 wt%. The images of the BSA droplets reveal the presence of the cracks near the periphery region, whereas, the images of the Lys droplets confirm that the cracks are spread and connected from ϕ of 3 wt%. The "dimple" and the "mound"-structure can be observed in the Lys droplets at every ϕ . The spirals are noticed in the Lys droplets from ϕ of 9 wt%. The scale bar represents a length of 0.20 mm.



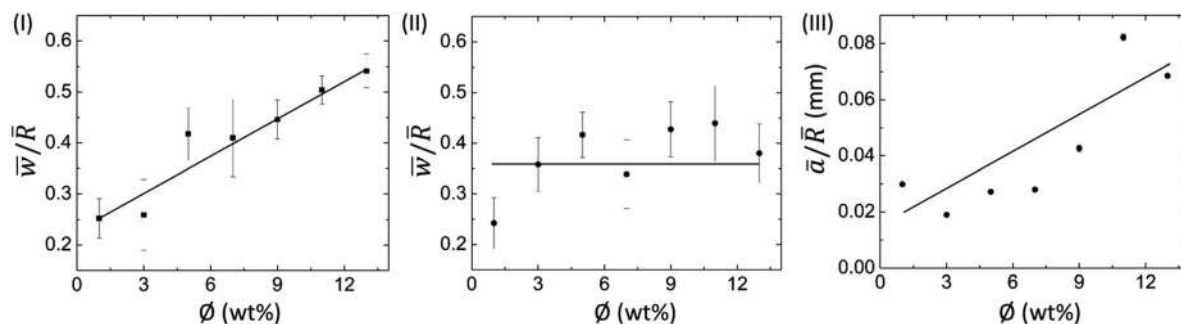


Fig. 5 Profilometric measurements of protein droplets: variation of the mean peripheral ring width (w) normalized to the mean radius of the droplet (R) with ϕ for (I) BSA + DI, and (II) Lys + DI. (III) Variation of the mean area of the "mound"-like structure (\bar{a}) normalized to R with ϕ in the Lys droplet. The error bars correspond to the standard deviation obtained from multiple measurements.

the droplet's circularity. However, no general trend is observed while measuring it in the asymmetrical (or oval) droplets.

3.2.2 Quantification of the cracks. Fig. 6(I) displays the Q–Q plot at ϕ of 7 wt% and confirms the non-normal distribution of the mean crack spacing (x_c). The representative plots also suggest that the cracks are not equally distributed in different protein droplets. The figures indicate that the outliers have surfaced in the form of skewed data points. The outliers (depicted by three circles deviating from the reference line in the Q–Q plot) are not ideal considerations from a statistical perspective since these violate one of the assumptions for the t -test (parametric); nonetheless, in our case, there is no good reason to consider these outliers as invalid samples. To counter the non-normal distributions of the mean crack spacing, a non-parametric Mann–Whitney U test (an alternative to the parametric t -test) was preferred to examine the (significant) differences in terms of x_c values among the different protein droplets at different ϕ . In this study, the mean rank test is chosen over the median (for the visual inspection) because (a) the number of cracks are observed to be different in both protein droplets; and, (b) the number of samples is relatively large.

In the Mann–Whitney U test, the protein was kept as the categorized factor (independent factor, with two levels, BSA and Lys) and x_c as a dependent variable at different ϕ . All the

histograms are expressed as the mean \pm standard error (SE). The differences where $p \leq 0.05$ are considered to be significant in this study. A detailed report of the statistical test (U , z , and p values) is shown in Table T5 of the ESL.† Fig. 6(II) shows \bar{x}_c for the BSA and Lys droplets at each ϕ . The results confirm our morphological observations that the crack patterns in the BSA and Lys droplets are different from each other, resulting in a significant difference in \bar{x}_c in the peripheral regions at every ϕ (the presence of crack spacing at every ϕ is significantly higher in Lys). The visual observations could be considered an effective way to determine the differences in terms of \bar{x}_c ; however, the statistical test helps us to distinguish the data fluctuations borne out due to the experimental conditions. It is observed that \bar{x}_c in the Lys droplets varies from 0.08 to 0.15 mm without any trend when the ϕ is increased. In contrast, \bar{x}_c in the BSA droplet varies from 0.19 to 0.27 mm, and suggests a proportionate distribution; *i.e.*, x_c increase with increasing ϕ . The release of the available stress is mostly unidirectional in the BSA droplets, resulting in a uniform crack pattern in the peripheral ring. The uniform crack spacing resulted in an increased x_c when ϕ is also increased. However, in Lys droplets, the stress is relieved from all directions resulting in the distribution of small to large cracks spread throughout the droplet, affecting \bar{x}_c at each ϕ .

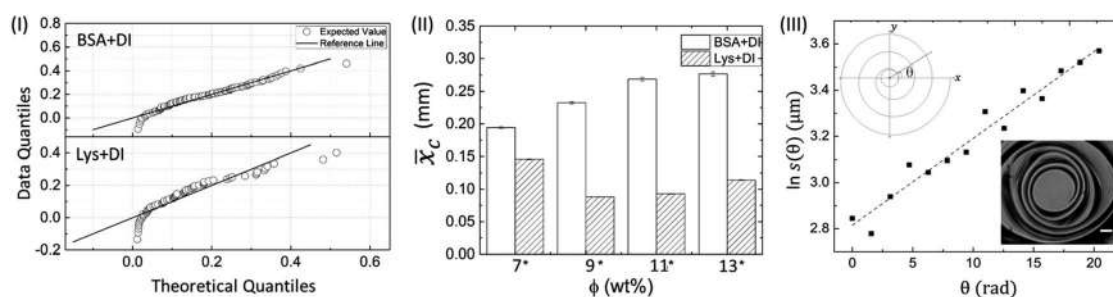


Fig. 6 (I) Q–Q plot of BSA and Lys droplet at ϕ of 7 wt% displaying the skewed data points. (II) The histogram depicting the comparison of the mean crack spacing (\bar{x}_c) at different ϕ among the proteins in the peripheral regions. Significant pairs (BSA and Lys) are marked with an asterisk [*] at each ϕ . The error bars correspond to the standard error. (III) A characteristic linear fit of a spiral crack trajectory at ϕ of 13 wt% in Lys droplet. The upper inset shows the schematic diagram of the spiral cracks projected on the xy plane, in which $s(\theta)$ is the radial distance from the spiral center and θ is the angle starting from zero in an anticlockwise direction. The lower inset shows an example of a spiral focused at 50 \times objective lens, with a scale bar of length 10 μm .



Fig. 6(III) shows a characteristic linear fit of a spiral crack trajectory at ϕ of 13 wt% in the Lys droplet. The domains containing the spiral cracks in the Lys droplets are 3D and it is not possible to observe all the spiral lines simultaneously with the droplet surface. The lack of information about the z plane prompted us to represent these spirals on the xy plane (2D). The expression of the logarithmic spiral is in polar coordinates: $s(\theta) = ae^{b\theta}$. The assumption of this logarithm leads to $\ln s(\theta) = \ln a + b\theta$ where, $s(\theta)$ is the distance from the spiral center, and θ is the angle which is in an anti-clockwise direction from the x axis, not restricted to 2π . The final theta corresponds to the angle made by the x axis and the outermost spiral line. The schematic diagram of a 2D spiral is shown in the upper inset. The logarithmic parameters are “ a ”, which is the apparent length of the spiral, and “ b ”, which controls the tightness and predicts the direction of the spiral. A lower value of “ b ” means the spiral has more revolutions and hence, more tightness in the spiral shape. No preference of clockwise or counter-clockwise direction in the spirals is observed in any of these droplets. This prompted us to generalize the direction by flipping all the required images so that the spirals would be consistent every time with the starting spiral revolution line lying at zero degrees as shown in the lower inset. The linear fit between $\ln s(\theta)$ and θ with R^2 of 0.957 confirms that the spirals in the Lys droplets are in the form of logarithmic spirals. An oscillation of the data points is obtained due to the presence of the irregular, polygonal-shaped domains. The overall shape of the spirals for different ϕ is almost the same; however, the trajectories are influenced by the material and fracture properties (a similar phenomenon is observed in ref. 29 and 30). The spirals at ϕ of 13 wt% are shown in Fig. S1 of the ESI,† and various parameters of the spiral crack analysis at ϕ of 11 and 13 wt% are reported in Table T6 of the ESI.† Spirals with very few revolutions in ϕ of 13 wt% are also observed. The value of “ b ” is found to be in the range of 0.0376 to $0.0548 \mu\text{m rad}^{-1}$ – a narrow range implying that the tightness is probably insensitive to the concentration of proteins; however, a detailed trend of “ b ” requires the examination of more levels ϕ .

3.2.3 A mechanical interpretation. It is reported in the earlier subsection that each droplet is pinned to the substrate throughout the drying process. The particles in the droplet are

adsorbed on the substrate, and simultaneously are carried towards the periphery. With further water-loss from the droplet, the protein particles are deposited in such a way that it creates a film. These particles are accumulated in the layers and might be influenced by a shear-mode or mode II (the stress is applied parallel to the plane). However, this influence is almost negligible as the top surface of the film still contains enough water to evaporate. This water evaporates during the fluid front movement, and the tensile stressed fields are generated when the droplet is almost devoid of water.

Fig. 7 indicates that two types of tensile stress (mode I) are involved in propagating the radial and azimuthal cracks in the protein droplets. σ_θ and σ_r are the stresses that act normal to the radial crack and azimuthal crack, respectively. In both the droplets, a directional growth, *i.e.*, a radial crack, was initially observed to propagate from the periphery of the droplet (for example, see Fig. 2(I)c). Therefore, it indicates that the stress acts along the fluid front, normal to the radial crack, *i.e.*, σ_θ is dominant initially. It is known from Griffith's hypothesis that the moment when the available stress in the film exceeds the critical stress, the excess stress is released by virtue of the crack propagation.^{31,32} This film height could be one of the reasons for the cracks appearing in the peripheral ring first, and then proceeding towards the central region in every protein droplet in general. We attempted height profile-imaging with Sensofar microscopy; however, we could not calibrate sufficiently to get the exact height measurements. The crack propagation could also be characterized based on the opening of the cracks and the distance of the crack tip as a function of ϕ . However, this is not possible with the current set-up as the time-lapse images are captured with an 8 bit camera and can only be taken every 2 s.

After the formation of the radial cracks, a few are curved azimuthally and the remaining ones join the neighboring cracks. However, it is observed that the stressed fields are dependent on the nature of protein particles. The crack propagation is stopped in BSA droplets, and a hair-like crack is developed without invading the central region of the droplet (Fig. 4d–g). The cracks form almost no connected domains. Our assumption is that the propagation of the cracks is stopped when the film thickness is less than the critical crack thickness resulting in zero cracks in the central region of every BSA droplet.

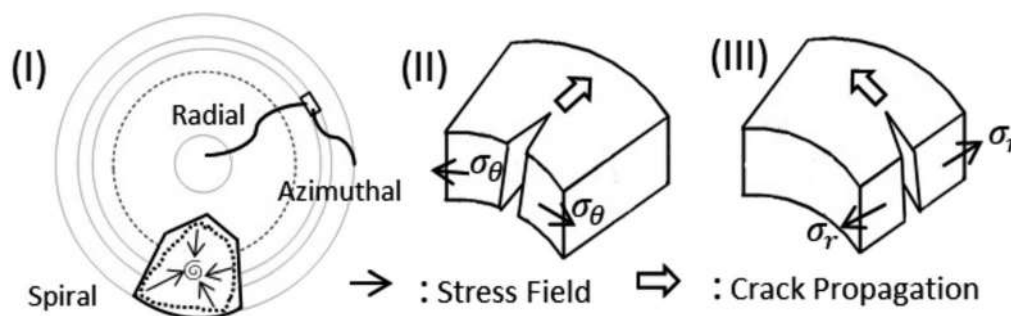


Fig. 7 Schematic illustration explaining the nature and propagation of cracks in both protein droplets. (I) Top-view of a droplet shows radial and azimuthal cracks. A spiral crack is also shown in a polygonal crack domain. An element is focused on displaying crack propagation to get a notion of stress. Mode I (tensile mode) in which (II) stress (σ_θ) acts normal to the radial crack and (III) stress (σ_r) acts normal to the azimuthal crack.



Lys, on the other hand, is a loosely-compacted and a low molecular weighted protein. The cracks are spread all over the droplet at all ϕ except 1 wt%. The presence of mound and dimple structures in the central region creates a gradient in the film thickness (highest at the periphery, lower at the center, and lowest at the middle region) during the drying process. This thickness gradient is enough to meet the crack propagation criteria and joins the crack lines from the center to the periphery. The stress fields act from all directions (σ_r and σ_θ) leading to a chaotic system. No cracks are observed in the central region at 1 wt% (Fig. 4h) due to the presence of a few Lys particles in the middle region, which reduces the film thickness from the critical crack thickness. There are mostly well-connected polygonal domains in the Lys droplets at ϕ of 3 wt% and above (Fig. 4i–n). The cracking leads to a subsequent process of delamination at ϕ of 5 wt% and 7 wt% near the periphery of the droplet (Fig. 4j and k). Adhesion energy persists between the protein particles and the glass (substrate). As soon as the stored elastic energy in the domain overcomes this adhesion energy, each domain buckled – curving outwards like a bowl (a similar process is observed in other studies as well^{33–35}). The interference fringes of each fragmented domain imply that there is an air gap between the detached film and the substrate that forms a non-uniform adhering region in each domain present in the Lys droplet. This phenomenon is observed in highly-magnified images of the Lys droplets presented in Fig. 4j–n.

Thus, a spiral path, is initiated in the well-connected polygonal domain of the Lys droplets at ϕ from 9 wt% onwards (Fig. 4l–n). The spirals propagate to release the elastic energy stored in the fragmented domain. This phenomenon is observed from ϕ of 9 wt% in the Lys droplet, implying that there is not enough stored elastic energy in the fragmented domains below ϕ of 9 wt%. The formation of the spirals on the irregular (polygonal) domains in the Lys droplets has no radial cracks intersecting the spiral cracks, *i.e.*, no splitting of the spiral cracks is observed in the Lys droplet (Fig. 4m and n). This indicates that the size domains become so small that there is no available energy for the radial cracks to propagate. At ϕ of 9 and 11 wt% in the Lys droplets, it is observed that the corners of the domains act as the precursor (Fig. 4l and m). This means that a high-stress area is achieved; however, due to lack of sufficient energy, the spirals fail to form the shape of those observed at ϕ of 13 wt% (Fig. 4n). Most of the spirals are present on the peripheral ring of the droplet at ϕ of 11 and 13 wt% (Fig. 4m and n). This implies that the film height could be one of the necessary criteria to have spiral cracks only at specific ϕ in the Lys droplet.

Although the increase of the protein concentration directly increases the film thickness, the heavy weighted protein (BSA of ~66.5 kDa) contains a lower number of particles forming a thinner film height than that observed in Lys (~14.3 kDa) at the same initial concentration. We argue that the absence of well-connected domains makes it hard to buckle the protein film. As a result, the stored elastic energy can not be applied in all directions on the delamination front to propagate in the BSA droplet. This is evident when we studied these proteins at ϕ of

9 wt% in the presence of 5CB liquid crystal (LC). None of the LC was present in the crack lines, and all were carried underneath the domains in Lys. The center of each domain adhered to the substrate and therefore appeared black under crossed polarizing configuration.²² In contrast, some of the LC was found in the crack lines and was mostly distributed on the top of the BSA film.²³ These studies indicate that the domains of the BSA adhered to the substrate, but, Lys did not do so.

Interestingly, a hierarchy is only observed in the Lys protein droplets. At the lowest ϕ (1 wt%), the cracks are present in the peripheral ring of the Lys droplets. The cracks are observed throughout the film from 3 to 13 wt%; however, there is no delamination process involved until ϕ of 3 wt%. At ϕ of 5 and 7 wt%, the delaminated cracks are observed, particularly in the ring. As ϕ increased from 9 to 13 wt%, the circular and spiral cracks appeared in the ring in addition to the delamination (Fig. 4h–n). Observation of these spirals might be a common phenomenon in polymeric systems;^{29,36,37} however, such phenomenon observed in Lys droplets is yet to be reported. This proves a similar unstructured, amorphous reminiscent behavior of the Lys protein.

This mechanical interpretation, thus, reveals the differences in the type of crack patterns observed in the BSA and Lys droplets and throws light on the reasons behind the existence of spirals in the Lys droplets at specific ϕ . Further, this mechanical interpretation can also be used to explain the crack patterns in the dried droplets of any bio-molecules.

4 Conclusions

This work showcases the self-assembly of proteins and demonstrates that the process of self-assembly is driven by the drying process. The findings of the experiments confirm that the nature of a protein plays an important role in deciding the drying evolution and the subsequent morphology. The consistent reduction of the contact angle during the drying process helps in identifying the different modes of evaporation. The relatively higher initial protein concentration used in this study facilitated the identification of a “dimple” on the mound-structure in the dried Lys droplets. This study further establishes the presence of a spiral crack pattern at the specific initial protein concentration in Lys droplets, which has not been reported in the literature so far. The non-parametric statistical tests facilitated the crack spacing quantification and confirmed the visual observations. This procedure of quantification may be used in broad disciplines to quantify different parameters and their effects.

It is to be noted that all the experiments in this paper have been performed in DI water, and the presence of ions in body fluids will influence the patterns to a great extent. However, this study can set a baseline for understanding multi-component systems such as proteins with the addition of various salts (ions), whole human blood, plasma serum, *etc.* when dried under uniform conditions (surface, humidity, temperature, droplet diameter, *etc.*). The resulting pattern of the drying droplets is expected to be a signature of the initial state, as observed in our study. Thus, the findings of this paper ensure



that such information may potentially be used for diagnostic screening in the near future.

Conflicts of interest

There are no conflicts to declare.

Acknowledgements

This work was supported by the Department of Physics at WPI. The authors would also like to thank the Tinkerbox (Innovation and Entrepreneurship) Grant sponsored by the Women Impact Network (WIN) at WPI for financial assistance and moral support.

References

- M. Parsa, S. Harmand and K. Sefiane, *Adv. Colloid Interface Sci.*, 2018, **254**, 22–47.
- D. Brutin and V. Starov, *Chem. Soc. Rev.*, 2018, **47**, 558–585.
- D. Brutin, B. Sobac, B. Loquet and J. Sampol, *J. Fluid Mech.*, 2011, **667**, 85–95.
- R. Chen, L. Zhang, D. Zang and W. Shen, *J. Mater. Chem. B*, 2017, **5**, 8991–8998.
- R. Chen, L. Zhang and W. Shen, *J. Mater. Chem. B*, 2018, **6**, 5867–5875.
- R. Chen, L. Zhang, H. He and W. Shen, *ACS Sens.*, 2019, **4**, 1701–1709.
- N. D. Patil, P. G. Bange, R. Bhardwaj and A. Sharma, *Langmuir*, 2016, **32**, 11958–11972.
- V. R. Dugyala, H. Lama, D. K. Satapathy and M. G. Basavaraj, *Sci. Rep.*, 2016, **6**, 30708.
- P. Sáenz, A. Wray, Z. Che, O. Matar, P. Valluri, J. Kim and K. Sefiane, *Nat. Commun.*, 2017, **8**, 14783.
- P. Retailleau, M. Ries-Kautt and A. Ducruix, *Biophys. J.*, 1997, **73**, 2156–2163.
- G. Dunn, S. Wilson, B. Duffy, S. David and K. Sefiane, *J. Fluid Mech.*, 2009, **623**, 329–351.
- F. Smith and D. Brutin, *Curr. Opin. Colloid Interface Sci.*, 2018, **36**, 78–83.
- R. Chen, L. Zhang, D. Zang and W. Shen, *Adv. Colloid Interface Sci.*, 2016, **231**, 1–14.
- M. Gao, X. Huang and Y. Zhao, *Sci. China: Technol. Sci.*, 2018, **61**, 949–958.
- H. M. Gorr, J. M. Zueger and J. A. Barnard, *Langmuir*, 2012, **28**, 4039–4042.
- H. M. Gorr, J. M. Zueger, D. R. McAdams and J. A. Barnard, *Colloids Surf., B*, 2013, **103**, 59–66.
- G. Chen and G. J. Mohamed, *Eur. Phys. J. E: Soft Matter Biol. Phys.*, 2010, **33**, 19–26.
- C. Annarelli, J. Fornazero, J. Bert and J. Colombani, *Eur. Phys. J. E: Soft Matter Biol. Phys.*, 2001, **5**, 599–603.
- Y. J. Carreón, M. Ríos-Ramírez, R. Moctezuma and J. González-Gutiérrez, *Sci. Rep.*, 2018, **8**, 9580.
- Y. J. Carreón, J. González-Gutiérrez, M. Pérez-Camacho and H. Mercado-Urbe, *Colloids Surf., B*, 2018, **161**, 103–110.
- R. D. Deegan, O. Bakajin, T. F. Dupont, G. Huber, S. R. Nagel and T. A. Witten, *Nature*, 1997, **389**, 827–829.
- A. Pal, A. Gope, R. Kafle and G. S. Iannacchione, *MRS Commun.*, 2019, **9**, 150–158.
- A. Pal, A. Gope and G. S. Iannacchione, *MRS Adv.*, 2019, **4**, 1309–1314.
- D. C. Carter and J. X. Ho, *Adv. Protein Chem.*, 1994, **45**, 153–203.
- M. D. Abràmoff, P. J. Magalhães and S. J. Ram, *Biophot. Int.*, 2004, **11**, 36–42.
- H. M. Gorr, PhD thesis, University of Pittsburgh, 2013.
- S. Preibisch, S. Saalfeld and P. Tomancak, *Bioinformatics*, 2009, **25**, 1463–1465.
- A. Pal, A. Gope and G. S. Iannacchione, *International Conference on Pattern Recognition and Machine Intelligence*, 2019, pp. 567–574.
- Z. Neda, L. Jozsa, M. Ravasz, *et al.*, *Phys. Rev. Lett.*, 2002, **88**, 095502.
- M. Sendova and K. Willis, *Appl. Phys. A: Mater. Sci. Process.*, 2003, **76**, 957–959.
- E. Katzav, M. Adda-Bedia and R. Arias, *Int. J. Fract.*, 2007, **143**, 245–271.
- L. Goehring, A. Nakahara, T. Dutta, S. Kitsunezaki and S. Tarafdar, *Desiccation cracks and their patterns: Formation and Modelling in Science and Nature*, John Wiley & Sons, 2015.
- B. Sobac and D. Brutin, *Colloids Surf., A*, 2014, **448**, 34–44.
- F. Giorgiutti-Dauphiné and L. Pauchard, *Soft Matter*, 2015, **11**, 1397–1402.
- V. Lazarus and L. Pauchard, *Soft Matter*, 2011, **7**, 2552–2559.
- D. A. Dillard, J. A. Hinkley, W. S. Johnson and T. L. S. Clair, *J. Adhes.*, 1994, **44**, 51–67.
- B. Behnia, W. G. Buttlar and H. Reis, *Mater. Des.*, 2017, **116**, 609–615.



Phase separation of a nematic liquid crystal in the self-assembly of lysozyme in a drying aqueous solution drop*

Anusuya Pal, Order-Disorder Phenomena Laboratory, Department of Physics, Worcester Polytechnic Institute, Worcester, MA 01609, USA

Amalesh Gope, Department of English and Foreign Languages, Tezpur University, Tezpur, Assam 784028, India

Rumani Kafle, Massachusetts Academy of Math and Science at WPI, Worcester, MA 01605, USA

Germano S. Iannacchione, Order-Disorder Phenomena Laboratory, Department of Physics, Worcester Polytechnic Institute, Worcester, MA 01609, USA

Address all correspondence to Germano S. Iannacchione at gsiannac@wpi.edu

(Received 31 October 2018; accepted 23 January 2019)

Abstract

This paper discusses the unique patterns evolved through phase separation of a bulk liquid crystal (LC) from the self-assembly of lysozyme induced by evaporation of de-ionized water only. Each domain shows a central dark region surrounded by bright regions (randomly oriented LC droplets). The birefringence intensity reveals three regimes (a slow increase, rapid rise, then saturation) not seen without LC droplets. The textural study exhibits a simple exponential behavior that changes as a function of LC concentration. Furthermore, in the presence of LC, the crack patterns are found to be different near the drop edge than those in the central region.

Introduction

Liquid crystals (LC) are a unique class of anisotropic materials those can explore a wide range of ordered phases. The latest experimental developments consider LC droplets as a promising tool for sensing biological and chemical events due to their label-free detection, phase-separation, and easy visualization.^[1] LC-based bio-sensing systems are typically used to detect the interaction among the biomolecules by utilizing an aligned nematic state of the LC droplets.^[2–7] Concurrently the interest in studying the drying drops is growing in the recent years and has attracted the attention of bio-medical and forensic applications. The drying systems include suspension of colloids, proteins (lysozyme, bovine serum albumin), LC, nanocrystals, biofluids, etc.^[8–15]

Apparently, the self-assembled drying mechanism of a combined system consisting of protein and LC (without any prior alignment) has not attracted any attention. This work bridges the gap between LC and drying protein droplet research by introducing a conventional, thermotropic LC at the initial concentrations of LC droplets (\emptyset) into a lysozyme–water system. Lysozyme is often used as an archetype in studying the drying mechanism of the protein solutions. Therefore, adding bulk LC droplets in a simplest lysozyme–water system helps us to identify the effects of these droplets in the form of emerging patterns. The main findings of this paper include (1) a temporal study providing a qualitative description of the collective

motion and the inter-particle interactions of the protein particles and the LC droplets. The main advantage is that the self-assembled structures are formed in the absence of any external field—either electric or magnetic, and induced due to evaporative flow; (2) a birefringence intensity profile of the temporal study reveals three regimes in the lysozyme drops with LC droplets, first with a slow increase of intensity, followed by a rapid rise in the transition regime and finally the saturation of the intensity when the evaporation of the water in the drop is about to complete; (3) the textural study [first-order statistics (FOS) and gray level co-occurrence matrix (GLCM)] is performed on the images of the dried drops. It reveals that the structural changes at various concentration of LC droplets (\emptyset) follow simple exponential laws^[16]; and lastly (4) it is observed with statistical evidences that the mean crack spacing (\bar{x}_c) near the edge of the drop appears to be larger in the presence of LC droplets than that in central region at different \emptyset .

Experimental methods

Lysozyme, mostly found in human mucosal secretions, has a molecular mass of ~ 14.3 kDa with a roughly ellipsoid shape of dimensions $3.0 \text{ nm} \times 3.0 \text{ nm} \times 4.5 \text{ nm}$.^[17] The commercial lysozyme powder (Sigma Aldrich, USA, L6876) of 100 mg was massed and dissolved in 1 ml of de-ionized water (Millipore, a resistivity of $18.2 \text{ M}\Omega\cdot\text{cm}$, density of 0.9970 g/mL at 25°C) to prepare an initial protein solution. The nematic LC 4-cyano-4'-pentyl-biphenyl (5CB, Sigma Aldrich, 328510) has a nematic to isotropic phase transition temperature of $\sim 35^\circ\text{C}$. The LC was heated just above the transition

* A video of the time evolution of the drying process is available in Supplementary section.

temperature and added to the protein solution. Different volumes of LC were added to make the initial concentration of LC droplets (\varnothing) as 0.23, 0.46 and 0.91 wt%. Further, an LC and de-ionized water solution were also made. All the samples were ultrasonicated, a circular drop of volume $\sim 1.3 \mu\text{L}$ was created and allowed it to dry under ambient conditions (room temperature of 25°C and relative humidity of 30%).^[18]

The drops were observed using an optical microscopy (Leitz Wetzlar, Germany) with a $5\times$ objective lens, 8-bit digital camera (Amscope MU300) at a resolution of 2048×1536 pixels and analyzed with ImageJ.^[19] The time lapsed images were taken between crossed polarizers for the duration of the drying process. A circular region of interest (ROI) was drawn on the gray images with the *Oval tool* of ImageJ. In the next step, the mean intensity (intensity per pixel) was determined for all the sample drops and background (coverslip) with ImageJ. A calibration of the image was conducted in respect to the coverslip and the corrected intensity for each sample (I_c) was measured. Drops from the same sample set were deposited three times by keeping the lamp intensity fixed. The whole procedure was repeated and the averaged intensity (\bar{I}_c) was plotted against time. To study the morphology of the dried drops, different sections of each drop were imaged separately as the ~ 2 mm diameter drop could not be captured under $5\times$. The image of the whole drop was extracted with the *Stitching* plugin^[20] of ImageJ. For the crack analysis, only bright-field images were converted into gray, filtered with a variance filter, and processed into binary images. All the images of the dried drops were converted into a scaled stack and three circular-cut lines were drawn in each region (near the drop edge and the central region) using the *Oval Profile* plugin of ImageJ. The 8-bit intensity values (255 for pixels depicting the crack lines and 0 for pixels elsewhere) were plotted as a function of arc-length along each circle at every 0.1° . A script employing “Array.findMaxima” was used to determine the positions of maximum intensity values. The consecutive maxima difference provided an estimate of the spacing between cracks (x_c) along each circular line. The x_c values which did not fall within ± 0.005 mm were considered in respect to the reference circular line in order to avoid double-counting. The data were aggregated to yield an average (\bar{x}_c) in each region as a function of the different concentration of LC droplets (\varnothing).^[18] FOS and GLCM parameters were extracted from 8-bit images of the dried drops for the textural analysis. The images were taken between the crossed polarizers using the *Texture Analyzer* plugin of ImageJ. These analyses indicated a uniform (high) reproducibility for each sample.

Results and discussions

Temporal study in drying drops

A sessile drying drop generally features a curved air–fluid interface. Time dependence of a drying LC–lysozyme drop at a concentration of LC droplets (\varnothing) of 0.91 wt% between crossed polarizers is shown in the top panel of Fig. 1. The drop was pinned to the coverslip and a convective flow of both the

protein particles and LC droplets took place. These droplets were bright in the cross-polarizing configuration due to their birefringence nature. Similar to the lysozyme–water system (\varnothing of 0 wt%), this system too decreased along the contact angle [revealing a blur to prominent bright spots, Figs. 1(a)–1(c)]. As soon as the contact angle reached a minimum configuration, a fluid front started moving from the edge to the center (similar to the lysozyme–water system). An outline at the curved interface [Fig. 1(b)] was observed indicating a starting effect of the “coffee-ring” (alternatively called rim). The solvent loss was highest near the drop edge; as a result, all particles were rushed with the flow to compensate the non-uniform evaporation rate. The big LC droplets (small LC droplets clustered together) were mostly observed in the central region (these were originally found there, while depositing the drop). The small LC droplets were spread (easily flowed by the convective and radial flow) throughout the drop, mostly near the drop edge [Fig. 1(c)]. The restrictive movement of the big LC droplets was possibly due to their viscous nature, resulting in space confinement by flow-induced shear force. However, big LC droplets went through a little orientation, alignment, or tumbling as induced by inherent non-uniform fluid front flow due to the attractive forces (capillary, van der Waals, and dipolar interactions) between adjacent LC droplets [Fig. 1(d)].^[21] The individual big LC droplets further merged and coalesced into bigger LC droplets, resulting in increasing the optical intensity [Fig. 1(e)]. Like lysozyme–water system, this system also showed the rim which was at a greater height from the central region due to the deposition of most of the lysozyme particles. Finally, a mechanical stress originated due to the solvent loss and the pinning of the drop leading to the formation of cracks (starting from the drop edge). The crack lines started forming like the lysozyme–water system; however, a slow and ordered way was observed in this system. Subsequently, a fast follow-up process of LC droplets took place in the crack lines [all lines become bright, Fig. 1(e)]. A simultaneous process of filling of domains (created by the cracks) with LC droplets started at the drop edge, unlike lysozyme–water system. This whole process of LC-filling completed within a time span of ~ 2 min (starting from ~ 745 to ~ 865 s). The final step of the drying process was the formation of the self-assembled patterns of the lysozyme particles in the presence of a small fraction of LC droplets [Fig. 1(f)]. The miscibility of the solutes (LC droplets and lysozyme particles) is the key to obtain this pattern after the water evaporates from the system. The LC droplets were found to be partially soluble in the de-ionized water; whereas, the lysozyme particles without LC droplets form a homogeneous solution with water. However, the inclusion of LC droplets into lysozyme without water was not possible as we have used lyophilized lysozyme. The striking feature of this study is the phase separation of LC droplets induced by the convective flow of solutes and the loss of water during the drying process. A complete video of drying LC–lysozyme drop is available in the Supplementary section.

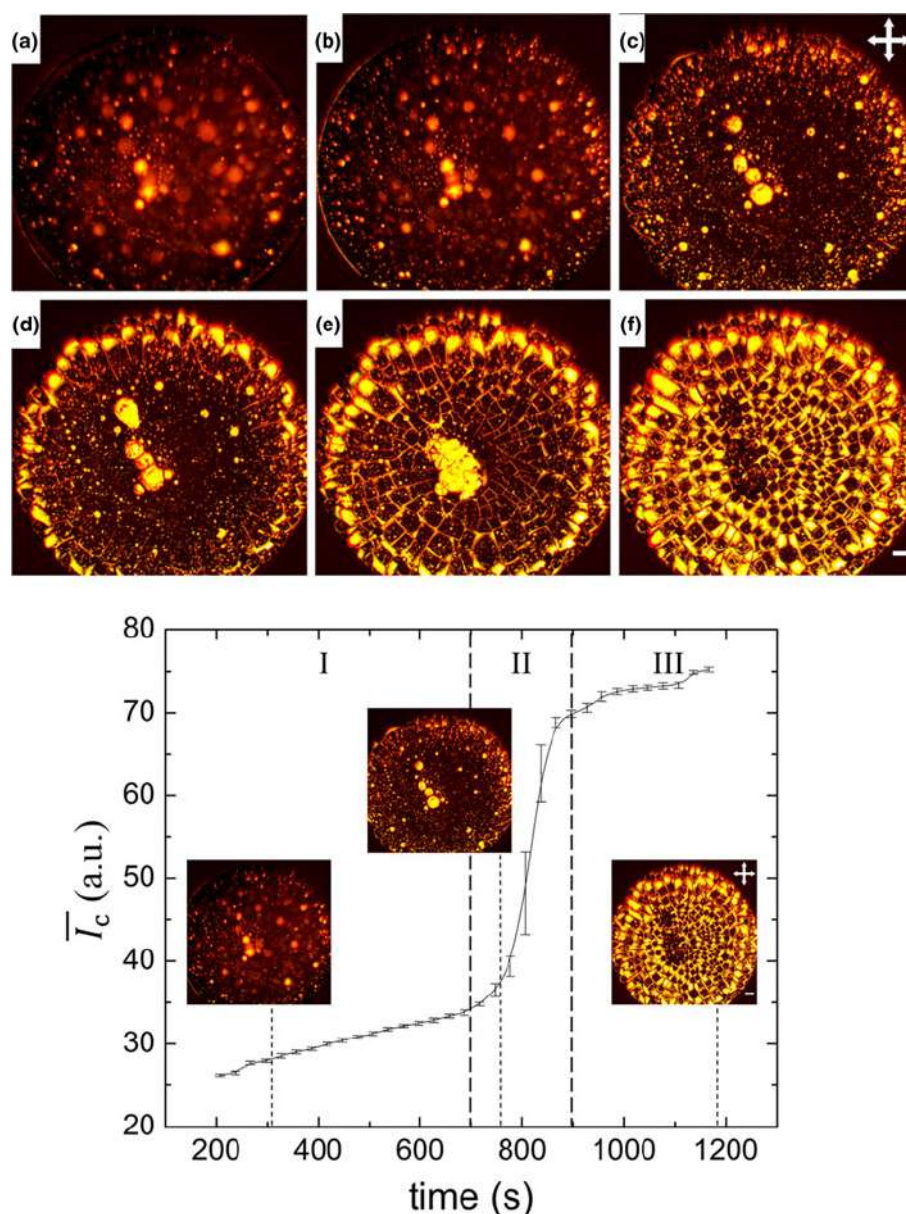


Figure 1. Top panel: Time-lapse images of drying LC-lysozyme drop at the concentration of LC droplets (ϕ) of 0.91 wt%. (a) 193 s showed an initial stage of drying where the contact angle started to decrease. A radial flow of the particles to the drop edge at (b) 403 s and (c) 731 s are shown. Merging of big sized LC droplets in the central region and filling of LC droplets at the drop edge were displayed at (d) 791 s and (e) 815 s. The self-assembled structures after visual evaporation was observed at (f) 1193 s. Bottom panel: Intensity variation with time of LC-lysozyme drop showing three regimes, an initial slower regime (I), a transition regime (II), and a saturation regime (III). The error bars correspond to the standard deviation. The microscopic images in I, II, and III were taken at 301, 745, and 1193 s, respectively. The crossed polarizing configuration is depicted by crossed double arrows. The white color in the right corner is a scale bar of 0.20 mm.

The bottom panel of Fig. 1 illustrates a typical intensity response of LC droplets (since only LC droplets are birefringent) varying with drying time in LC-lysozyme drop at ϕ of 0.91 wt%. Furthermore, a clear correlation between the top and bottom panels of Fig. 1 was made. Initially, the intensity did not change much for a certain period (up to ~ 700 s). The movement of LC droplets and the change in the intensity

were not quite visible during this period (regime I) due to spherical-“cap” shape of the drop. However, this shape got reduced by the decrease of the contact angle and finally reached a minimum value. In regime II, by maintaining the minimum contact angle configuration, the onset of LC activities (such as merging and filling up the crack domains) increased resulting in a rapid increase of intensity. This transition period (regime

II) was only found for ~ 200 s, in which the intensity varied from ~ 35 to ~ 69 a.u., i.e., an increase by a factor of two: the rate of change in intensity with time is ~ 0.17 . The standard deviation was higher in the transition than all other regimes due to the presence of different sized big LC droplets in different drops. As this regime was solely dependent on the LC activities, it resulted in the change of the intensity (values) for three different drops and hence, a higher standard deviation was observed. It was followed by regime III in which the intensity saturated as the drop was about to complete the drying process.

The drying system of LC–water was also studied in this paper and we observed a slow movement of bulk LC droplets toward the drop edge. A non-uniform evaporation of water was observed in the LC–water drop and the LC droplets remained at the surface (coverslip) due to LC–surface interaction. Contrary to the LC–water system, in the lysozyme–water system [concentration of LC droplets (\varnothing) of 0 wt%], the lysozyme particles were distributed on the coverslip to form a protein film during the convective flow. It followed by a radial flow of particles toward the drop edge which helped to deposit most of the particles. Then, the fluid front started moving from the edge and rest of the particles were carried to the center resulting in the formation of “mound”-like structure [Figs. 2 (a) and 2(g)]. The averaged intensity \bar{I}_c was measured for

both LC–water and lysozyme–water systems in which no variation of intensity in drying time was observed. However, LC–water showed a higher value of intensity than lysozyme–water system due to the birefringence nature of LC droplets. A significant difference was noticed between LC–water and lysozyme–water or lysozyme–LC drop, i.e., there was no coffee-ring or no self-assembled patterns in the absence of lysozyme (protein) particles. This reveals that the significant contributions to the final patterns were lysozyme–lysozyme and LC–lysozyme interactions. Furthermore, protein in general has a non-uniform surface, with most of the hydrophobic regions sheltered inside and with exposed charged or polar residues. This helps in making it available for new points of attraction with either neighboring protein particles or LC droplets.^[22] LC has its own dipole moment due to the presence of cyano group at its one end.^[23] The accumulation of LC droplets into the protein solution has a tendency to form lysozyme–LC complexes. These complexes were formed by attracting the exposed parts of the protein to the cyano group of 5CB. At this point, the electrostatic attraction is almost zero due to non-involvement of external salts/ions. Nonetheless, this attraction may not have a large contribution owing to the presence of cyano groups at one end of the LC droplets and due to the overall positive charge of lysozyme.

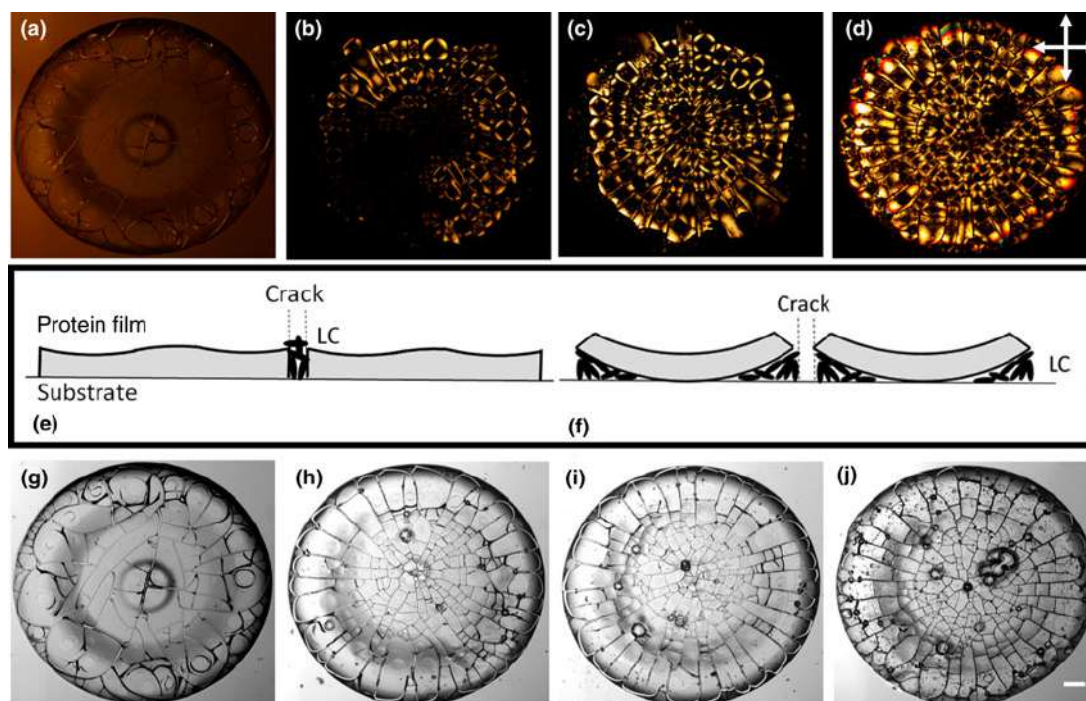


Figure 2. The morphology of drops after 24 h. Top panel: Drops imaged in crossed polarizing configuration. The initial concentration of LC droplets (\varnothing in wt%) is (a) 0, (b) 0.23, (c) 0.46, and (d) 0.91. The drop without LC droplets (\varnothing of 0 wt%) showed very weak birefringence; therefore, lamp intensity was increased for clear visualization. Middle panel: (e) and (f) show a proposed mechanism for the evolution of the unique patterns. Bottom panel: Gray scaled drops imaged in bright field configuration, where \varnothing in wt% is (g) 0, (h) 0.23, (i) 0.46, and (j) 0.91. The scale bar corresponds to 0.15 mm.

Morphological study in dried drops

The available stress in the dried drops (after visible evaporation) was relieved by the increase in the number of cracks. Also, the flow of LC droplets was found to be affected in the drops [Fig. 1(f) which was taken after visible evaporation and Fig. 2(d) which was taken after 24 h at the concentration of LC droplets (\emptyset) of 0.91 wt%]. We observed that some regions in the dried drop initially had more LC droplets (bright regions) and then, uniformly distributed toward the end of the day. Hence, all the dried samples were imaged after 24 h.

Figures 2(a)–2(d) show the images of the dried lysozyme drops with and without LC droplets imaged in the crossed polarizing configuration. The lamp intensity of the dried lysozyme drop without any LC droplets [concentration of LC droplets (\emptyset) of 0 wt%] was increased for a clear visualization. It is well known that lysozyme in crystal form shows birefringence and scatter light depending on the domain size.^[24] However, our perception is that only the evaporation process (the loss of water) from the lysozyme solution without LC droplets may not be able to form crystals completely. The scattering of light was mostly visible near the crack lines once the lamp intensity was increased to maximum. These lines were the areas without any lysozyme particles or 5CB droplets and were just the bare coverslips leaking the light from the microscope probably. Hence, comparing \emptyset of 0 wt% to other concentrations, it could be inferred that lysozyme–water system exhibits a very weak birefringence. This indicates that, the optical activity in cross-polarizing imaging was mostly due to the activities of the LC droplets. Contrary to the lysozyme–water system, LC–lysozyme systems showed a dark region in the interior and bright regions at each corner of every crack domains. In this context, a physical mechanism is proposed to understand the self-assembled patterns in the lysozyme drops due to phase separation of LC droplets [Figs. 2(e) and 2(f)]. During the convective flow of the drying process, most of the lysozyme particles were distributed on the coverslip and resulted in a protein film. However, it is possible to have some LC droplets to get trapped in the film or to be on the top of the lysozyme film. The external stress increased due to solvent loss and the drop cracked resulting in different sized interconnected domains. A simultaneous process of buckling in every domain took place. Two scenarios were possible; (i) the presence of the LC droplets was on the top of the lysozyme film; and/or (ii) the presence of these droplets was underneath the film. It was found in Figs. 1(d)–(f) that LC droplets were following the crack lines (channels) for their distributions in every domain, starting from the drop edge. Moreover, after completing the visible evaporation, the LC droplets distributed in the crack lines depicted by bright color [Fig. 1(f)], but within 24 h the crack lines became dark [Fig. 2(d)]. If the LC droplets were present on the top of the film, then their flowing through the crack lines would not be possible because the protein film is at a greater height near the drop edge (compared with the central region). The change of the bright crack lines into dark

within 24 h would also be baffling. In addition to this, the air–LC interface is known to have weak homeotropic anchoring; hence, all the domains would have shown a radial point defect in the form of the Maltese cross (a cross always lining up with the polarizer and analyzer); but here, that was not the case. The dried drops in the presence of LC droplets showed a dark region which is likely to be the attached lysozyme film to the coverslip (substrate) and most of the bright regions were the randomly oriented LC droplets underneath the protein film; suggesting being the second scenario (mentioned above). Within 24 h, the lysozyme domains were more uplifted (buckled) and the LC droplets flowed inside the domains from the crack lines through the capillary action. The representative of most of the domains in the dried drops with LC droplets show randomly oriented LC droplets in the bright regions. However, in some of the domains, a perfect radial configuration (Maltese cross) was observed probably due to the presence of the LC droplets at the air–LC interface. On the other hand, some of the crosses often seem to align with what was likely a radial flow during the drying process. In addition to this, most of the crack domains contained a single dark region at the center, some were found to be off-centered probably due to the domain shape and the unstable buckling mode. The centered configuration would evolve from that off-centering when buckling start to develop fully.^[25,26] To ensure that each of the domain had a distribution of LC droplets with random orientations, the domains were rotated with a sample angle for a complete revolution, and we did not observe any optical change in the patterns. All crack lines appeared dark even when the sample angle was varied for a complete revolution and no uniformed angular dependence with the intensity was found when compared among different domains.

In Figs. 2(b) and 2(c), an uncertainty arose in the count of the bright regions in the drop as LC droplets were partially soluble in the water. But these drops were the most repetitive ones and we concluded that LC droplets were not enough to fill the whole surface of the drop. The LC concentration up to 0.91 wt% was chosen which was just enough to fill the whole drop of radius ~ 1 mm. It was also observed that further increase of LC concentration (for, e.g., 1.82 wt%, or more) made bright blob-like structures which restricted the smooth flow of LC droplets within the drop.

A minute observation of Figs. 2(c) and 2(d) confirmed the presence of ripples in some dark regions of the domains. These were formed because of an air gap between the protein film and packing of LC droplets. These domains had a non-uniform thickness and these small (unavoidable) variations were depicted by different colors (reddish, yellowish, greenish) in the drops.^[27,28]

In the bright field imaging, the gray images with and without LC droplets were shown in Figs. 2(g)–2(j). Following the observation of the morphology at \emptyset of 0 wt% [Fig. 2(g)], it could be argued that the stress was built not only along the fluid front movement, but applied from all directions. The gradient in the protein-film thickness (a thick sheet in rim, a thin

sheet in the center, and an extremely thin sheet in between the regions) resulted in a chaotic system. Therefore, it could be concluded that a random (chaotic) crack is a response to the lack of dominant stress in any specific direction. Unlike Fig. 2(g), the presence of viscous, denser particles (here LC droplets) enabled the cracks to experience mostly azimuthal tensile stress (the stress along the fluid front), leading to radial and highly ordered cracks. Fine radial, regularly spaced cracks appeared first near the drop edge (rim), then the big LC droplets tried to fill in the large crack domains, and a further flaw was developed with the propagation of desiccation. Due to these flaws, the long and large radial cracks were developed throughout the drop. However, the orthoradial cracks appeared in the rim to release the available local strain energy in the domains created by the radial cracks. This helped the cracks to curve and join the consecutive radial cracks. Furthermore, both orthoradial and radial cracks continuously appeared in the central region to release the remaining stress in the drop resulted in forming the small domains (when compared with the domains in the rim). Further, a prominent “mound”-like structure in the central region of the drop in the absence of LC droplets (\emptyset of 0 wt%) was observed; however, the presence of LC droplets was likely to prevent or disturb this formation. This structure was likely to be “free” lysozyme particles that were light enough for the fluid front to carry to the center.^[18] The out-of-equilibrium drying of this system and the increased viscosity, density and surface tension gradients (LC–coverslip, LC–lysozyme, lysozyme–coverslip interfaces) helped in the protein aggregation throughout the whole drop. In addition to this, LC droplets were affected in forming the small domains in the central region and big domains (highly ordered, uniform radial cracks) in the rim. The perception is that LC droplets in the central region did not get to relax to a smooth uniform state owing to the in-homogeneous, fast fluid front movement as soon as the front part touched the big LC droplets while propagating from drop edge. On the other hand, in the rim, the

absence of big LC droplets helped the fluid front to move in a uniform way. As a result, the smaller LC droplets gathered enough time to anneal into the homogeneous structures, resulting in the big domains.^[10] Moreover, in all systems, the curved and wavy-ring patterns were found near the drop edge possibly due to the stress originating from the boundaries created by the radial cracks.^[29] A minute observation of Figs. 2(h)–2(j) showed a gelation between central and rim regions in the presence of LC droplets. This region believed to be a transition region in the protein film thickness and we conclude that the dispersion of LC droplets within the film trapped some water during the fluid front movement and formed this gelation.

Interestingly, no rim width dependence was observed with varying concentration of LC droplets (\emptyset). This expanded our knowledge that the rim was only affected by the concentration of protein particles and not from the added amount of LC droplets. The independence of rim width on \emptyset (due to the dispersion of LC droplets into different crack domains) supported the physical mechanism proposed in this paper.

Textural analysis in dried drops

FOS depends on the pixel distribution of the selected ROI, whereas GLCM depends on the interpixel relations. Though these are complimentary measurements to evaluate drop texture, interestingly all the parameters followed a simple exponential law when varied with the concentration of LC droplets (\emptyset).^[16] The equation stated as:

$$\delta = \delta_0 e^{-\frac{\emptyset}{k}} + \delta_s,$$

where δ is the textural parameter, δ_0 is an initial textural parameter, δ_s is the saturated parameter and k is the characteristic concentration at which the parameter diminishes by the $1/e$ factor.

The variation of \emptyset affected the textural patterns (morphology) in the dried drops (Fig. 2). The top panel of Fig. 3 showed FOS parameters in which the mean determines the intensity per

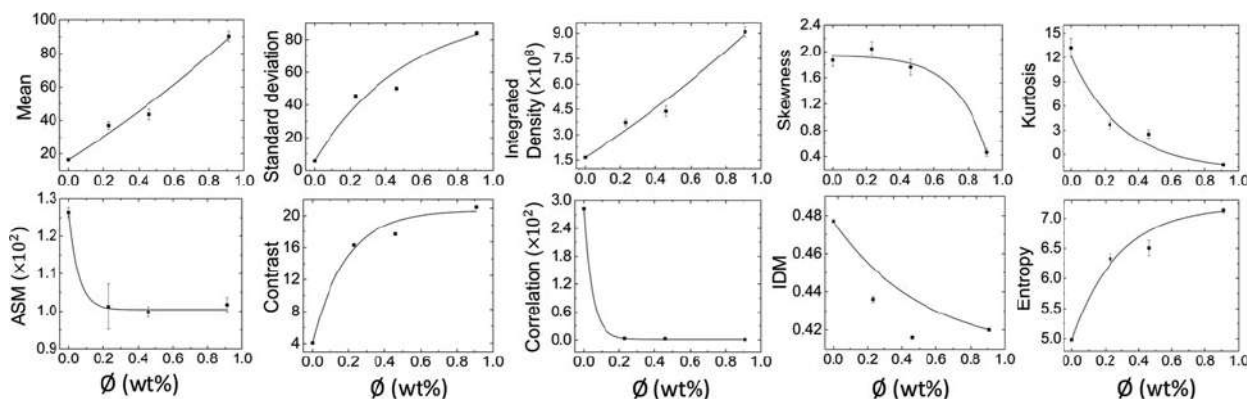


Figure 3. Texture analysis of dried drops. Top panel: First-order statistics (FOS) reveals the pixel distribution through mean, standard deviation, integrated density, skewness, and kurtosis. Bottom panel: Gray level co-occurrence matrix (GLCM) reveals the interpixel relations through ASM (angular second moment), contrast, correlation, IDM (inverse difference moment), and entropy. The exponential fit for the curves are shown in each graph. The error bars correspond to the standard error.

pixel of the selected ROI within the drop, standard deviation determines the variation around the mean values relating to the roughness of the image texture, and integrated density determines the total pixel intensity of the ROI. All grew exponentially due to the increase of LC-dominating regions resulting in an increase of the brightness (hence, the pixel intensity of the image).^[16] Both the skewness and kurtosis, in contrast, decreased with the increase of LC-dominating regions possibly due to the intensity distribution (histograms changed from asymmetrical to symmetrical tailed). The lowest values of skewness and kurtosis were found at the highest ϕ . The bottom panel of Fig. 3 showed GLCM parameters varying with ϕ , i.e., ASM measures global homogeneity in the texture, correlation measures the degree of similarity in a row or column direction of the image texture and IDM measures local homogeneity of the selected ROI. All these displayed an exponential decrease due to the decrease in the uniformity of the texture with the increase of ϕ . On the other hand, contrast and entropy increased in terms of the number of pixels and the heterogeneous regions formed. An increase in the diversity of the self-assembled structures occurred when ϕ was varied through the increase of bright LC-dominating regions in the dried textures.^[16]

It can be hypothesized that these analyses (FOS and/or GLCM) in the final deposits of any drying drops will follow simple exponential laws. Our perception is that these structural changes following the exponential laws are not due to any contribution of external salts, as our experiments were conducted by varying LC concentrations only.

Statistical analysis of crack patterns

The visual observations showed the differences in terms of crack spacing between two different regions at each concentration of LC droplets (ϕ). However, the visual observations may not be able to distinguish the data fluctuations borne out due to the experimental conditions or quantify the trend of \bar{x}_c with increasing ϕ . We observed that the aggregated data in different regions at each ϕ was not normally distributed (positively skewed). Therefore, we conducted a non-parametric Mann–Whitney U test using SPSS (version 22.0). The difference is said to be statistically significant if $P \leq 0.05$. The “region” was kept as the categorical factor (independent factor, with two levels: rim and central) and “ x_c ” as the dependent variable. The yellow dashed line in the binary image depicts an example separating the drop into rim and central regions (top panel of Fig. 4). The comparison of \bar{x}_c between the regions at different ϕ is shown in the bottom panel of Fig. 4. The statistical test quantified the morphologic observations that \bar{x}_c in two regions were almost identical in the absence of LC droplets, but their presence made two regions significantly different. \bar{x}_c was not found to be significantly different, i.e., ~ 0.20 mm in the rim and ~ 0.18 mm in central regions at ϕ of 0 wt%. It significantly decreased from ~ 0.20 to ~ 0.12 mm in the rim and to ~ 0.07 mm in the central region as ϕ increased in the presence of LC droplets. The central region was found to contain small domains, resulting in a smaller value in \bar{x}_c when compared

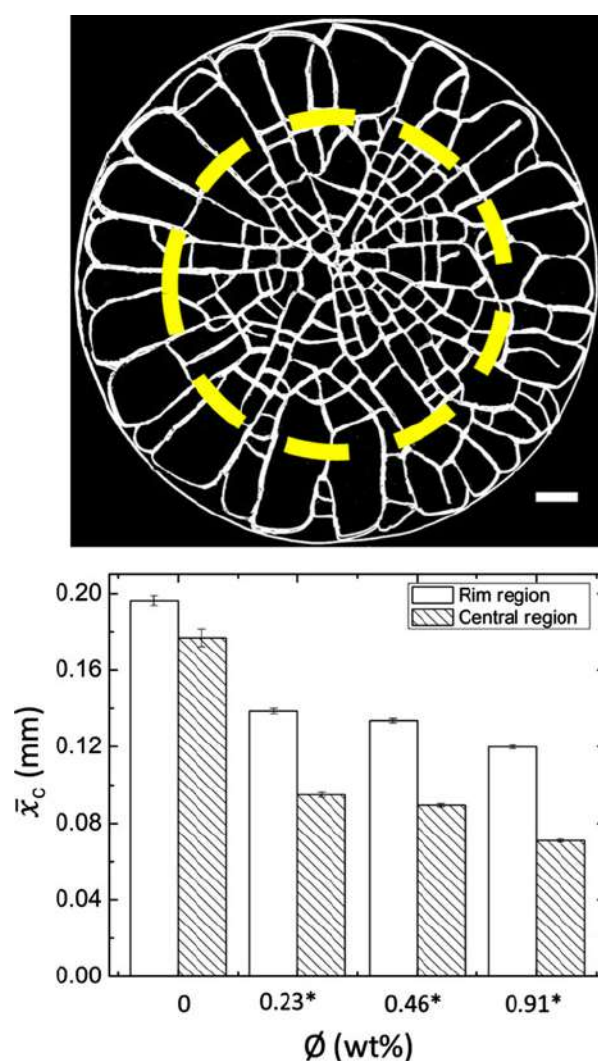


Figure 4. Top panel: An example of a binary image of a dried drop at ϕ of 0.23 wt%. The scale bar corresponds to 0.15 mm. The yellow dashed line separates the drop into rim and central regions. Bottom panel: The histogram depicting the comparison of mean crack spacing between the regions at different ϕ . Significant pairs are marked with an asterisk [*]. The error bars correspond to standard error.

with that of the rim in the presence of LC droplets. The absence of LC droplets enabled the stress to act from all the directions resulting in similar cracks in both the regions. The “mound”-like structure further facilitated the crack to propagate from all the directions. The presence of LC droplets produced the uniform and radial cracks in the rim (big domains) resulting in larger \bar{x}_c values. Many radial and orthoradial cracks were observed leading to small domains in the central region of the drop. These were possibly due to the presence of the thin sheet of the protein film in the central region resulting in smaller \bar{x}_c values. The presence of LC droplets and their partial phase-separation facilitated the uniform crack formation in the

rim region (the reason is explained in detail in the previous section). Moreover, \bar{x}_c was decreased with the increase of \emptyset in both the regions. It was because the number of LC droplets increased with the increase of \emptyset , resulting in more stress, more cracks, and subsequently resulted in a decrease in the mean crack spacing, \bar{x}_c . The results of the statistical test were found to be consistent with the visual observations and the differences in \bar{x}_c between the regions of a drop were derived by varying the concentration of LC droplets.

Conclusions

This paper showed the evolution of the unique patterns of the self-assembling lysozyme in which each domain showed a central dark region surrounded by bright regions. The bright regions were randomly oriented LC droplets present underneath the lysozyme sheet. The major finding of this study is that, these patterns evolved through phase separation of bulk LC and self-assembly of protein (lysozyme) induced by evaporation of the solvent (de-ionized water) only. The presence of LC droplets did not affect the width of the rim (a “coffee-ring” effect)^[30] in the drop. The intensity study during the drying process revealed three regimes: a slow increase, a transition phase, and a saturation of the intensity in the presence of LC droplets, whereas no variation was observed when the LC droplets were absent. A simple exponential law was followed by FOS and GLCM analyses conducted on the final deposits. The crack spacing in the presence of LC droplets was statistically different in central (small but chaotic domains) and rim (large but highly ordered domains) regions, whereas no difference was found in the absence of LC droplets in the drop.

This work does not follow the conventional way of quantifying the LC textures, for example, birefringence study in the crossed polarizing configuration, and hence, provides a new way of extracting the information about the self-assembled structures. There are many important contributing factors affecting the drying process such as pH, contact angle, mass-loss, etc., and we intend to focus on those in our future work. A ternary phase diagram is required to understand the phase separation of LC droplets in the three-component mixture. The miscibility of these components is the key to determine how the inclusion of a small fraction of LC droplets into protein solution alters the crack patterns in the drying drops which is an interesting finding of this study.

Supplementary material

The supplementary material for this article can be found at <https://doi.org/10.1557/mrc.2019.18>.

References

1. T. Kato: Self-assembly of phase-segregated liquid crystal structures. *Science* **295**, 2414 (2002).
2. Q.Z. Hu and C.H. Jang: Imaging trypsin activity through changes in the orientation of liquid crystals coupled to the interactions between a polyelectrolyte and a phospholipid layer. *Appl. Mater. Interfaces* **4**, 1791 (2012).
3. Q.Z. Hu and C.H. Jang: A simple strategy to monitor lipase activity using liquid crystal-based sensors. *Talanta* **99**, 36 (2012).
4. D. Liu, Q.Z. Hu, and C.H. Jang: Orientational behaviors of liquid crystals coupled to chitosan-disrupted phospholipid membranes at the aqueous-liquid crystal interface. *Colloids Surf. B* **108**, 142 (2013).
5. L. Marin, M.C. Popescu, A. Zabolica, H. Uji, and E. Fron: Chitosan as matrix for biopolymer dispersed liquid crystal systems. *Carbohydr. Polym.* **95**, 16 (2013).
6. M.A. Shehzad, D.H. Tien, M.W. Iqbal, J. Eom, J.H. Park, C. Hwang, and Y. Seo: Nematic liquid crystal on a two dimensional hexagonal lattice and its application. *Sci. Rep.* **5**, 13331 (2015).
7. M.J. Lee, C.H. Chang, and W. Lee: Label-free protein sensing by employing blue phase liquid crystal. *Biomed. Opt. Express* **8**, 1712 (2017).
8. S.A. Ryu, J.Y. Kim, S.Y. Kim, and B.M. Weon: Drying-mediated patterns in colloid-polymer suspensions. *Sci. Rep.* **7**, 1079 (2017).
9. Y.J. Carreón, J. González-Gutiérrez, M.I. Pérez-Camacho, and H. Mercado-Urbe: Patterns produced by dried droplets of protein binary mixtures suspended in water. *Colloids Surf. B* **161**, 103 (2018).
10. Z.S. Davidson, Y. Huang, A. Gross, A. Martinez, T. Still, C. Zhou, P.J. Collings, R.D. Kamien, and A.G. Yodh: Deposition and drying dynamics of liquid crystal droplets. *Nat. Commun.* **8**, 15642 (2017).
11. G. Chu and E. Zussman: From chaos to order: evaporative assembly and collective behavior in drying liquid crystal droplets. *J. Phys. Chem. Lett.* **9**, 4795 (2018).
12. C. Querner, M.D. Fischbein, P.A. Heiney, and M. Drndić: Millimeter-scale assembly of CdSe nanorods into smectic superstructures by solvent drying kinetics. *Adv. Mater.* **20**, 2308 (2008).
13. C. Nobile, L. Carbone, A. Fiore, R. Cingolani, L. Manna, and R. Krahne: Self-assembly of highly fluorescent semiconductor nanorods into large scale smectic liquid crystal structures by coffee stain evaporation dynamics. *J. Phys.* **21**, 264013 (2009).
14. G. Chu, R. Vilensky, G. Vasilyev, P. Martin, R. Zhang, and E. Zussman: Structure evolution and drying dynamics in sliding cholesteric cellulose nanocrystals. *J. Phys. Chem. Lett.* **9**, 1845 (2018).
15. D. Brutin and V. Starov: Recent advances in droplet wetting and evaporation. *Chem. Soc. Rev.* **47**, 558 (2018).
16. Y.J. Carreón, M. Ríos-Ramírez, R.E. Moctezuma, and J. González-Gutiérrez: Texture analysis of protein deposits produced by droplet evaporation. *Sci. Rep.* **8**, 9580 (2018).
17. H.M. Gorr, J.M. Zueger, and J.A. Barnard: Lysozyme pattern formation in evaporating drops. *Langmuir* **28**, 4039 (2012).
18. A. Pal, A. Gope, and G.S. Iannacchione: A Comparative Study of the Phase Separation of a Nematic Liquid Crystal in the Self-assembling Drying Protein Drops, Submitted to *MRS Advances* (Under Review process).
19. M.D. Abràmoff, P.J. Magalhães, and S.J. Ram: Image processing with ImageJ. *Biophoton. Int.* **11**, 36 (2004).
20. S. Preibisch, S. Saalfeld, and P. Tomancak: Globally optimal stitching of tiled 3D microscopic image acquisitions. *Bioinformatics.* **25**, 1463 (2009).
21. J. Jeong, A. Gross, W.S. Wei, F. Tu, D. Lee, P.J. Collings, and A.G. Yodh: Liquid crystal Janus emulsion droplets: preparation, tumbling, and swimming. *Soft Matter* **11**, 6747 (2015).
22. S. Paul, D. Paul, T. Basova, and A.K. Ray: Studies of adsorption and viscoelastic properties of proteins onto liquid crystal phthalocyanine surface using quartz crystal microbalance with dissipation technique. *J. Phys. Chem. C* **112**, 11822 (2008).
23. J. Prost: *The Physics of Liquid Crystals* (Oxford University Press, New York, USA, 1995), p. 83.
24. W. Singer, T.A. Nieminen, U.J. Gibson, N.R. Heckenberg, and H. Rubinsztein-Dunlop: Orientation of optically trapped nonspherical birefringent particles. *Phys. Rev. E* **73**, 021911 (2006).
25. M.F. Islam, M. Nobili, F. Ye, T.C. Lubensky, and A.G. Yodh: Cracks and topological defects in lyotropic nematic gels. *Phys. Rev. Lett.* **95**, 148301 (2005).
26. J. Zou and J. Fang: Director configuration of liquid-crystal droplets encapsulated by polyelectrolytes. *Langmuir* **26**, 7025 (2009).

27. I.S. Heo and S.Y. Park: Smart shell membrane prepared by microfluidics with reactive nematic liquid crystal mixture. *Sens. Actuat. B.* **251**, 658 (2017).
28. T. Ohzono, K. Katoh, C. Wang, A. Fukazawa, S. Yamaguchi, and J.I. Fukuda: Uncovering different states of topological defects in Schlieren textures of a nematic liquid crystal. *Sci. Rep.* **7**, 16814 (2017).
29. M. Gao, X. Huang, and Y. Zhao: Formation of wavy-ring crack in drying droplet of protein solutions. *Sci. China Technol. Sci.* **61**, 949 (2018).
30. Robert D. Deegan: Pattern formation in drying drops. *Phys. Rev. E* **61**, 475 (2000).



A Comparative Study of the Phase Separation of a Nematic Liquid Crystal in the Self-assembling Drying Protein Drops

Anusuya Pal¹, Amalesh Gope², and Germano S. Iannacchione¹

¹*Order-Disorder Phenomena Laboratory, Department of Physics, Worcester Polytechnic Institute, Worcester, MA, 01609, USA*

²*Department of English and Foreign Languages, Tezpur University, Tezpur, Assam, 784028, India*

ABSTRACT

The drying process, self-assembly of the proteins and the phase separation of a thermotropic liquid crystal (LC) from an initial aqueous solution represent a rich area of study. A focus of this work is to compare the behavior of two different proteins, bovine serum albumin [BSA] and lysozyme [Lys] in the ternary system through optical microscopy. During the drying process, the intensity profile shows three regimes in the presence of LC whereas no intensity variation is observed in its absence in both protein drops. The striking outcome is the presence of an umbilical defect of [+1] strength in every domain near the edge of BSA drop, whereas, each domain has a central dark region surrounded by a bright region in the dried Lys drop. Finally, the crack spacing in the dried Lys drop is reduced in the presence of LC whereas, no significant difference is found in the dried BSA drop.

INTRODUCTION

Pattern formation in drying drops has the potential in many technological applications including printing, microfluidics, medical diagnostics and forensics [1]. To date, majority of the drying experiments explored the drying process of various polymers, nanoparticles, proteins, biological fluid, etc. [2,3]. Of late, the findings of drying droplets attracted the attention of the liquid crystal (LC) communities. For example, in a recent study, a lyotropic LC (a dye Sunset Yellow FCF or SSY) is examined in which distinct LC phases are observed during the drying process [4]. In another study, the self-assembly of a thermotropic LC, i.e. 5CB (4-cyano-4'-pentyl-

biphenyl) is studied as a drying drop in a surfactant-stabilized system. And, the radial and bipolar orientations of 5CB are observed when transiting from chaotic to organized patterns [5].

This paper will report the drying process of the ternary system at the morphological level. The samples were prepared using two well-studied, water soluble proteins, bovine serum albumin (BSA) and lysozyme (Lys), dissolved in de-ionized water with a small fraction of a thermotropic, nematic LC. The LC (5CB) is partially soluble in water but incompatible with proteins when water is absent. The core findings of this paper include a temporal study that provides a qualitative description of BSA particles and the LC droplets during the drying process. The intensity profile of BSA-LC and Lys-LC drops could be divided in three distinct regimes- (a) the first regime starts with a slow increase; (a) a rapid rise could be observed in the second transition period, and; (c) the third regime ends with a saturation of the intensity. We further observed that, the dried BSA drop exhibits umbilical defects (a strength of [+1] in the presence of LC near the edge of different domains, however, all the domains in the dried Lys drop form a central dark region encircled by bright areas at the corners. These observations indicate that each Lys domain is buckled from the corner and LC droplets flow into the gap due to capillary action. In contrast, LC droplets form a layer on top of the BSA film revealing a radial director configuration. Finally, the cracks in two different protein drops with and without LC are quantified using a non-parametric statistical test. It is found that the crack spacing in the dried Lys is reduced in the presence of LC whereas, no significant difference is found in the dried BSA when compared these drops with and without LC.

EXPERIMENTAL METHODS

The BSA and Lys contain a molecular mass of ~66.5 and ~14.3 kDa respectively. The dimensions of BSA and Lys are $4.0 \times 4.0 \times 14.0 \text{ nm}^3$ and $3.0 \times 3.0 \times 4.5 \text{ nm}^3$ [6]. We obtained the commercial lyophilized BSA and Lys (A2153 and L6876 respectively) from the Sigma Aldrich, USA. Each protein of 100 mg was massed and dissolved in 1 ml of de-ionized water (Millipore, with a resistivity of $18.2 \text{ M}\Omega\cdot\text{cm}$, density of 0.9970 g/ml at $25 \text{ }^\circ\text{C}$) and two distinct protein solutions were prepared. The liquid crystal, 4-cyano-4'-pentyl-biphenyl (5CB, Sigma Aldrich, USA, 328510) has a nematic to isotropic phase transition temperature at $35 \text{ }^\circ\text{C}$. To attain the isotropic phase, 5CB is heated to a temperature of ($>35 \text{ }^\circ\text{C}$), and subsequently a volume of $\sim 10 \text{ }\mu\text{l}$ was added to the protein solutions to prepare LC concentration 0.91 wt%. This concentration was found to fill the whole Lys drop [7]. In the next step, all the samples were ultrasonicated and a circular drop of volume $\sim 1.3 \text{ }\mu\text{l}$ was deposited on the coverslip and let it dry under ambient conditions (room temperature of $25 \text{ }^\circ\text{C}$ and a relative humidity of 30 %).

All the drops were observed using a polarizing microscopy (Leitz Wetzlar, Germany) comprising a $5\times$ objective lens (the angular study was done with a $10\times$ objective lens). The lens contains an 8-bit digital camera (Amscope MU300) and a resolution of 2048×1536 pixels. The captured images were analyzed using ImageJ software [8]. The time lapsed images of the drying process were taken in the crossed polarizing configuration. A circular region of interest (ROI) was drawn on every time-lapsed image with *Oval tool*, and the intensity per pixel was determined for sample drop and coverslip. All the images were calibrated with the coverslip, and the corrected intensity for each sample (I_c) was measured. Drops from the same sample were deposited three times keeping a fixed lamp intensity, and an averaged intensity (\bar{I}_c) was plotted against time. Both the crossed polarizing and bright field configurations of the dried

drops were considered to observe the morphology. *Stitching plugin* of ImageJ was used to obtain the complete image of the dried drops. The stitched bright field images were further converted into gray, filtered and processed into 8-bit binary image (255 for pixels depicting the crack lines and 0 for pixels elsewhere else) for quantifying the cracks. We used the *Oval Profile plugin* to draw three circular cut-lines near the drop edge (rim). The intensity values were plotted as a function of arc-length along each circle at every 0.1° . The positions of maximum intensity values were determined with '*Array.findMaxima.*' The consecutive maxima difference provided an estimate of crack spacing (x_c). A threshold of ± 0.005 mm was used as standard range and x_c values outside this range was recorded and aggregated to obtain an average (\bar{x}_c) [7].

RESULTS AND DISCUSSIONS

Time Evolution of the Drying Drops

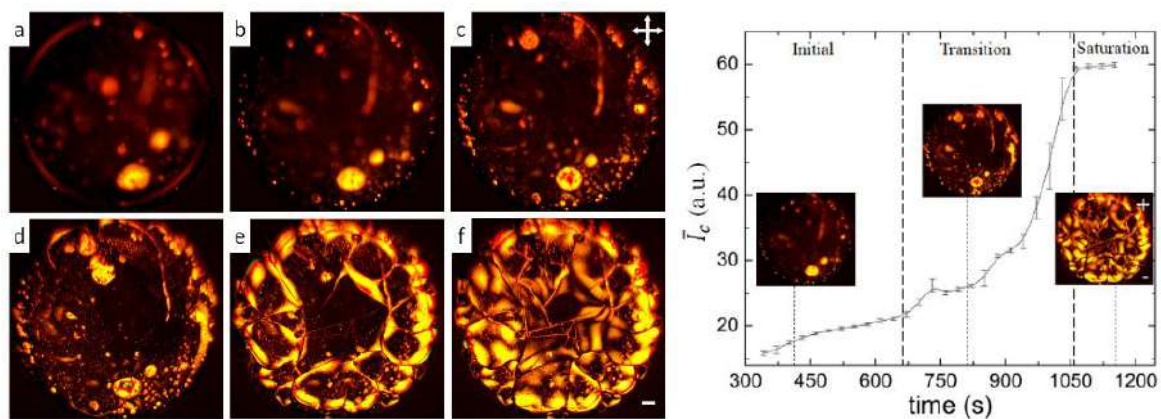


Figure 1. Left panel: Time lapsed drying images of BSA-LC drop in crossed polarizing configuration (crossed double arrows) at a) 117 s, b) 421 s, c) 677 s, d) 941 s, e) 1007 s and f) 1149 s. The white color is a scale bar of 0.20 mm. Right panel: Intensity variation of BSA-LC drop with drying time indicates three distinct regimes. The error bars correspond to the standard deviation. The microscopic images in the initial, transition and saturation regimes are taken at 415, 805 and 1149 s respectively.

The left panel of Figure 1 shows the drying evolution of the deposited drop containing BSA, water, and LC in the crossed polarizing configuration. In the first regime, the drop got pinned on the substrate (coverslip) and the contact angle started decreasing. The transformation of the intensity (from blur to prominent spots, Figure 1a-c) indicates a decreased contact angle. During this regime, the convective and radial flow of both BSA particles and tiny LC droplets were observed (see Figure 1a, b) in the time span of ~ 11 minutes. This resulted in depositing most of the BSA particles near the edge displaying a ‘coffee-ring’ effect [9]. A few big LC (clustered small LC) droplets merged with other droplets, whereas, a few LC droplets popped up, and spread individually (Figure 1b, c). The concentration of these droplets and BSA particles were mostly observed near the edge (Figure 1d). The mechanical stress was built as not much water was left and the drop started cracking to relieve the available stress. The filling of LC droplets took place in the crack lines and started spreading on the domains created by the cracks. Most of the LC droplets were spread near the boundary of each domain in the drop (Figure 1e, f) showing the morphology after the visible evaporation (Figure 1f).

The right panel of Figure 1 depicts the intensity profile of the drying process. The profile started with a slow increase of the intensity due to spherical- ‘cap’ shape of the drop, an initial regime up to ~ 670 s. Once the contact angle reached the minimum,

the LC droplets became prominent, and a rapid rise of the intensity was found in the transition regime. It raised from ~ 22 to ~ 54 a.u. and found till ~ 1030 s, i.e., for ~ 6 minutes. Finally, it saturated when the drop completed the process. This intensity profile was only possible due to the birefringence nature of LC droplets, and so the protein drops without LC didn't show any variation. Though the activities of LC droplets in Lys were different from BSA, the intensity variation couldn't account the minor details and revealed three regimes (initial, transition and saturation) like BSA-LC [7].

Birefringence of the Dried Drops

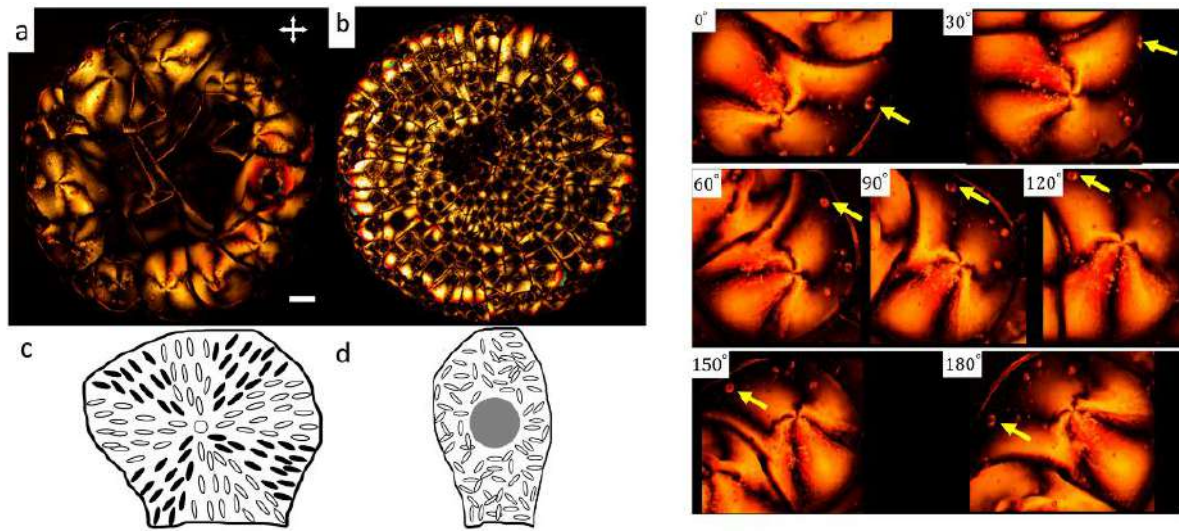


Figure 2. Left panel: The morphology of the dried drops imaged in crossed polarizing configuration (crossed double arrows) after 24 hours: a) BSA-LC, b) Lys-LC with a scale bar of 0.15 mm. The orientation of LC droplets in each domain is shown in c) BSA-LC and d) Lys-LC. Right panel: One particular domain of the BSA-LC sample is rotated under crossed polarizers at a magnification of $10\times$. The yellow arrow indicates a reference point with respect to the four-fan brushes confirming the rotation of the patterns and reveals an *umbilical defect* with a strength of $[+1]$.

It is to be noted that LC droplets (bright regions) in BSA-LC drop redistributed themselves in each domain towards the end of the day (Figure 1f and 2a). As most of the LC droplets were present near the edge after visible drying process, each domain in the rim showed four-fan like structures and bright crack lines in the central region of the dried BSA-LC drop are observed (Figure 2a). In contrast, all the domains were bright at the corners and dark in the center, separated by dark crack lines in the dried Lys-LC drop (Figure 2b). This observed behavior may be due to the protein-LC interactions that affects the wettability of the LC droplets during the drying process. Lys is a more compact, stable and four times lighter protein particle compared to BSA. The viscous nature of the LC droplets allows those to prefer beneath the Lys protein film. The (initial) process of cracking induces the flow of these droplets through the crack lines. Each domain attached to the coverslip buckled (uplifted) from the corner to the central region (dark in the morphology). The randomly distributed droplets (bright in the morphology) were rearranged by the capillary action [7] (Figure 2d). On the other hand, in case of BSA-LC, the droplets were present at every corner of the domains and spread over each BSA domain for 24 hours.

Between crossed polarizers, the characteristic fourfold brushes (lines of extinction) with a defect core appeared in BSA-LC drop after 24 hours. The distribution of LC droplets as the radial director configuration is illustrated in Figure 2c. A typical texture of the unaligned nematic phase under crossed polarizers is the *Schlieren defect* which exhibits two and fourfold brushes. Here, only the fourfold brushes were observed

and termed as *umbilical defect* [10] where each self-assembled protein domain contains only one defect. The four dark brushes in the BSA-LC drop indicated that the director of the LC nearly matches either the polarizer or analyzer in the crossed polarizing configuration. When the sample was rotated in an anti-clockwise direction (the yellow arrows shown in the right panel of Figure 2 provided a reference point) keeping the polarizer and the analyzer fixed, the brushes were observed to rotate in the same direction, whereas the defect core of the brushes continued in a fixed position indicating a [+1] strength defect.

The droplets were found to be aligned anisotropically with respect to the shape of the domains as a minimum energy configuration. The domain boundary confines these droplets and the preferred alignment of the LC droplets considers the shape of the domain and whether the anchoring energy and the domain size are large enough to accommodate their elastic energy [10]. Ideally, the core defect should be observed to be at the highest height and in the middle of the domain. However, the distortion of the brushes provides the evidence that the nematic director follows the contour in each protein domain. Based on these observations, it can be inferred that most of the LC droplets form a layer on the top of the BSA film revealing a radial defect in each domain at the air-LC interface, with some droplets trapped in the film during the drying process.

Crack Morphology of the Dried Drops

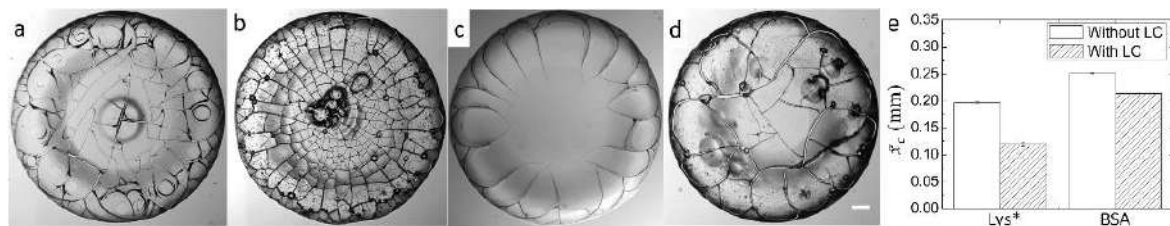


Figure 3. Dried drops imaged in bright field configuration after 24 hours: a) Lys without LC, b) Lys with LC, c) BSA without LC, d) BSA with LC. The scale bar represents 0.15 mm. e) A histogram depicting the comparison of mean crack spacing \pm standard error in the protein drops with and without LC. Significant pairs are marked with an asterisk [*].

The bright field images of each protein drop with and without LC are shown in Figure 3 a-d. The common feature noticed in all the drops is the presence of the rim at a higher height compared to the central region confirming the favored ‘coffee-ring’ effect in the drops. Nonetheless, the presence of LC droplets made the surface of the drops rough probably due to phase separation during the drying process. The inclusion of LC droplets also increased the stress in the drops resulting in increasing the number of cracks. The comparison of Lys drop with and without LC revealed that the ‘mound’-like structure was disturbed; the presence of LC droplets enabled ordered cracks in the rim (discussed in detail in our previous article [7]). The comparison of BSA drop with and without LC (Figure 3c and 3d) revealed that the cracks were only present in the rim in the absence of these droplets. Moreover, most of the cracks were not connected at their terminals in BSA drop without LC. In contrast, cracks are seen to be connected with other resulting in the formation of the domains and spread in the whole BSA drop with LC. The comparison of Lys and BSA drops with LC (Figure 3b and 3d) indicates a smaller domain size of Lys than that of BSA. Hence, it could be inferred that the domain size in BSA drop with LC was probably one of the reasons which provided the necessary criteria to form radial director configuration.

An appropriate statistical test was conducted to quantify the cracks concerning mean crack spacing (\bar{x}_c) in the rim region of the drop. The non-normal distribution of the

\bar{x}_c values enabled a subsequent non-parametric Mann-Whitney U test (SPSS version 22.0). The 'Lys' ('BSA') was kept as a categorical factor with two levels, without and with LC and ' x_c ' as a dependent variable. The comparison of \bar{x}_c with and without LC for different proteins was shown in Figure 3e. In Lys drop without LC, \bar{x}_c was found to be ~ 0.20 and reduced to ~ 0.12 mm in the presence of LC droplets. The Mann-Whitney U test indicates a significant interaction in Lys. A large crack spacing is observed in Lys without LC (depicted by [*]), agreeing to the morphological observations. In contrast, no significant difference in terms of x_c was observed in BSA drop with and without LC. \bar{x}_c without LC was found to be ~ 0.25 and ~ 0.21 mm with LC. This indicates a non-significant interaction in BSA providing an extra dimension not clearly observed morphologically. Hence, it could be concluded that LC droplets drastically affected the crack formation in Lys drop since most of these droplets were beneath the Lys film. On the other hand, LC didn't alter the crack spacing in BSA drop significantly supporting our claims that most of these droplets were present on the top of the BSA film.

CONCLUSIONS

This paper explores the drying process of different protein-liquid crystal drops driven by the evaporation-induced flow. The intensity profile of both the drops in the presence of LC droplets showed three regimes- a slow increase, a rapid rise and the final regime- that ends with a saturated intensity. The dried BSA drop showed *umbilical defects* with a strength of [+1] in different domains and is observed only near the edge. In contrast, each domain of the dried Lys drop appeared to be bright with dark central regions. Furthermore, the crack spacing (pattern) in the dried Lys drop is found to be significantly reduced in the presence of LC whereas no significant difference in terms of the crack spacing is observed in the dried BSA drop with and without LC.

This work has a potential application in the bulk liquid crystal-based biomolecule detectors. The ultimate goal of this paper is to examine the rate of the drying process (fluid front movement) with varying LC concentration. We are undertaking an extensive study to explore and correlate different morphologies of LC concentration.

ACKNOWLEDGMENTS

This work is supported by the Department of Physics at WPI. The authors would like to thank the Women's Research and Mentoring Program (WRAMP) sponsored by the Women Impact Network (WIN) at WPI for the financial assistance.

REFERENCES

1. D. Brutin and V. Starov, Chem. Soc. Rev. 47, 558 (2018).
2. S.A. Ryu, J.Y. Kim, S.Y. Kim and B.M. Weon, Sci. Rep. 7, 1079 (2017).
3. Y.J. Carreón, J. González-Gutiérrez, M.I. Pérez-Camacho and H. Mercado-Urbe, Colloids Surf. B 161, 103 (2018).
4. Z.S. Davidson, Y. Huang, A. Gross, A. Martinez, T. Still, C. Zhou, P.J. Collings, R.D. Kamien and A.G. Yodh, Nat. Commun. 8, 15642 (2017).
5. G. Chu and E. Zussman, J. Phys. Chem. Lett. 9, 4795 (2018).
6. M. Vasilescu, D. Angelescu, M. Almgren and A. Valstar, Langmuir 15, 2635 (1999).
7. A. Pal, A. Gope, R. Kafle and G.S. Iannacchione, MRS Communications, 9, 1 (2019).
8. M.D. Abramoff, P.J. Magalhães and S.J. Ram, Biophotonics Intern. 11, 36 (2004).
9. R.D. Deegan, Phys. Rev. E 61, 475 (2000).
10. I. Dierking, O. Marshall, J. Wright and N. Bulleid, Phys. Rev. E 71, 061709 (2005).



OPEN

Concentration-driven phase transition and self-assembly in drying droplets of diluting whole blood

Anusuya Pal^{1✉}, Amalesh Gope², John D. Obayemi^{3,4} & Germano S. Iannacchione¹

Multi-colloidal systems exhibit a variety of structural and functional complexity owing to their ability to interact amongst different components into self-assembled structures. This paper presents experimental confirmations that reveal an interesting sharp phase transition during the drying state and in the dried film as a function of diluting concentrations ranging from 100% (undiluted whole blood) to 12.5% (diluted concentrations). An additional complementary contact angle measurement exhibits a monotonic decrease with a peak as a function of drying. This peak is related to a change in visco-elasticity that decreases with dilution, and disappears at the dilution concentration for the observed phase transition equivalent to 62% (v/v). This unique behavior is clearly commensurate with the optical image statistics and morphological analysis; and it is driven by the decrease in the interactions between various components within this bio-colloid. The implications of these phenomenal systems may address many open-ended questions of complex hierarchical structures.

Phase transition refers to a physical process where a substance experiences a state transformation¹. The alteration of ice (solid) to water (liquid) and eventually to vapor (gas) due to heat is a typical example of the phase transition. Besides, the appearance of zero electrical resistivity in the superconductivity state, or the transformation of the liquid crystalline into the crystalline phase are just a few other well-studied phase transition examples in the field of condensed matter physics^{1,2}. In a similar way, the state of phase transitions in the biological systems equally attracted considerable research attention, where the ideas of statistical mechanics have been applied on many applications, including order parameters, fluctuations, and universality classes. For example, the phase transition of various biomolecules (from a liquid crystalline to gel state) such as lipids, cholesterol, proteins, etc. is found to play an essential role in the selective trafficking and signaling activities across the cell plasma membrane^{3,4}. Another vital instance of phase transition includes the sol-gel transformation that modifies the assembling mechanism of the platelets (one of the cellular components of the whole blood) and various fibrin proteins. This particular transition state of the sol-gel is considered to be crucial to healing an injury during the process of blood clotting⁵. Furthermore, the ion-selectivity in nerve fibers alters their structures from the swollen to the shrinking state and influences the process of nerve excitation and conduction. All these biological phase transitioning examples are at the cellular or the molecular level and are driven by both physical and chemical processes^{6,7}.

Understanding the drying phases of a multi-component bio-colloidal droplet, such as the whole human blood has attracted many researchers. For example, the spreading, the wetting and the cracking phenomena of the drying droplets of blood (varying in different parameters including substrate, wetting, relative humidity, etc.) have been examined in detail to develop an understanding of the evolving patterns^{8–13}. The presence of various cells [red blood cells (RBCs or erythrocytes), white blood cells (WBCs or leukocytes), and platelets (thrombocytes)] make the whole blood a complex bio-colloidal fluid¹⁴. These cells are suspended in the blood plasma and usually contains water (92% by volume) along with a minute amount of plasma proteins, ions, and hormones in them¹⁵. The process of drying evolution of the blood droplet starts as soon as a droplet gets deposited on a substrate. The constituent components are dispersed uniformly in the droplet that defines an initial equilibrium state. As the solvent (water) starts evaporating from the droplet, the drying process drives the system out of the equilibrium.

¹Order-Disorder Phenomena Laboratory, Department of Physics, Worcester Polytechnic Institute, Worcester 01609, USA. ²Department of English, Tezpur University, Tezpur 784028, India. ³Department of Mechanical Engineering, Worcester Polytechnic Institute, Worcester 01609, USA. ⁴Department of Biomedical Engineering, Worcester Polytechnic Institute, Worcester 01609, USA. ✉email: apal@wpi.edu

The wetting conditions on the substrate enables the evaporation-driven convective flow. Further, water-loss in the droplet concentrates the components facilitating their self-assembling interactions. A signature pattern evolves, and the droplet reaches a new equilibrium state as soon as the drying process is completed.

Recently, diluted blood samples (into different concentration ranges) have shown insightful drying patterns in blood pattern analysis (BPA)^{16–19}. Sen et al.²⁰, in a different study, examined the effects of diluted blood droplets at a fixed saline concentration by changing the substrate conditions. The study concluded that the transition of the cracking to the non-cracking regime exists for the droplets deposited on the hydrophilic substrate. On the other hand, when the droplet dries on the hydrophobic substrate, the buckling regime is merged to this transition phase. The study primarily focused on the decrease of the RBCs in diluted blood samples, and how the reduction of RBCs affects the mechanical stress developed due to the water loss. Despite the intense research on drying blood droplets, the range of dilution and the use of several experimental techniques (optical microscopy detailing the drying evolution and the final morphology, scanning electron microscopy exploring the deformed blood structures in the dried samples, contact angle measurements giving the idea of the wetting) do not reveal any concentration-driven phase transition region for these diluted blood droplets. In fact, no study is performed on the diluted blood samples to understand the characteristic changes and aim to examine the fundamental understanding of such phase transition and self-assembly²¹ during their drying process and the resulting morphology. The implication of diluted blood samples is crucial and makes this paper different from others' report. The diluted blood samples lead to changes in the initial equilibrium state that results in reducing the interaction between various components as well as minimizing the biological activities within such multi-colloidal system.

This paper reveals a unique mesoscopic phase transition that is solely driven by the physical process, drying at different concentrations. Exploring the phase transition and the self-assembly patterns in such a multi-component system may reveal much significant information. Keeping these notions in mind, this article aims to address the following vital questions: (1) What are the factors those stimulate a phase transition in the drying droplet of the whole blood? (2) What are the different drying mechanisms leading to the phase transition? (3) Is it possible to explain the complexity of the microscopic structures of the cellular components following the phase transition? If so, to what extent is it possible to do so? And finally, (4) How do the wettability and the interfacial properties of the droplets influence the different environment during the drying process?

Furthermore, the outcome of this research also has the potentiality in applications related to disease diagnosis^{22–29}. Several studies have revealed that the resulting final patterns of the drying droplets appear correlated to the initial state^{11,12}. Researchers also concluded that patients with chronic kidney disease usually suffer from overhydration or an overload of extracellular water³⁰. Moreover, patients in receipt of hemodialysis (a therapy for patients with poorly functioning kidneys) often continue to have low cellular counts after treatments^{31,32}. In some cases, this therapy tends to create a low supply of RBCs, which in turn leads to possible anemia cases. Thus, the initial concentration of the whole blood (whether diluted or concentrated) is an important parameter correlated to these pathologies. The conventional method includes the complete blood count (CBC) of almost every patient; however, this alternative drying process proposed in this paper may reflect the (actual) different stages of critical diseases in a more convenient way in the near future. Our proposed method is an initiative to explore their physiological activities.

We attempted to investigate the drying process of the whole blood macroscopically (mm scale) using a bright-field optical microscopy and a contact angle goniometer of the droplet. The statistical image parameters of the microscopy, such as the first-order statistics (mean and standard deviation) are characterized during the drying process^{33,34}. The morphological quantities of the final dried state such as the crack width, spacing, etc. are extracted from the optical images at the end of the drying process. Besides, different regions of the morphology of the dried film such as the periphery, the corona (between the periphery and the center), and the central regions are examined in detail (μm scale) using a scanning electron microscopy (SEM).

Results

Drying evolution of the blood droplets. Figure 1(I–II) shows the time evolution of the blood droplets diluted at different concentration levels (ϕ) ranging from 85 to 12.5% (v/v) in respect to the original concentration of the whole blood ($\phi = 100\%$). The texture of this first image appears to be dark within the concentration range of 100 to 62% (v/v) (Fig. 1(I)a). However, the dark texture eventually turns out to be gray following the increase of dilution levels (Fig. 1(I–II)a). The physical mechanism of its occurrence is explained in the discussion section. Moreover, a thick peripheral band is observed from 100 to 62% (v/v) (Fig. 1(I)a), which becomes thinner with further dilution from 50 to 12.5% (v/v) (Fig. 1(II)a). Subsequently, a fluid front starts receding from the periphery towards the central region (Fig. 1(I–II)b). As time progresses, the central region becomes devoid of water. The appearance of the light gray texture confirms the evaporation of the water in the central region. This (light gray) texture is prominently observed in samples from 100 to 75% (v/v) dilution; however, it cannot be clearly differentiated in samples from 62 to 12.5% (v/v). This is because the texture of the first image is already light gray at this range of ϕ , and there is not enough contrast between the two (Fig. 1(II)a,b).

The evaporation of the water and the concentration/assembly of the constituent components promotes the build up of internal stress as the droplet periphery is still pinned to the substrate (coverslip). Figure 1(I–II)c marks the evolution of the cracks (similar to the prior observations discussed in^{14,35,36}). The green dashed circular lines separate the corona from the central regions at each ϕ . The random (small and large) cracks in the central region are first observed from 100 to 75% (v/v). Some of these radial cracks begin propagating towards the periphery, and some towards central regions at ϕ of 100 to 62% (v/v) [the points A–E in Fig. 1(I–II)c]. In contrast, their propagation from the periphery towards the central regions is predominantly observed in the diluted samples ranging from 62 to 12.5% (v/v) [the points F–J in Fig. 1(I–II)c]. The radial cracks separate the film into large domains in the corona region as the remaining water evaporates from the droplet during the final

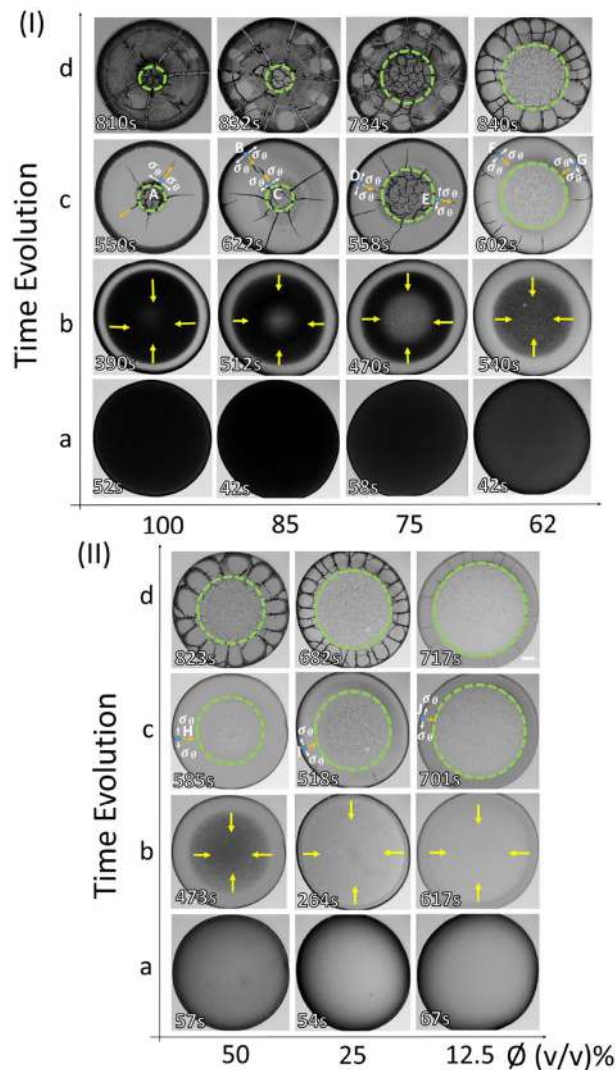


Figure 1. Time-lapse images of the blood droplets with different diluting concentration (ϕ) are captured during the drying process. These images dictate different stages: (I) from 100 to 62% (v/v), and (II) from 50 to 12.5% (v/v) (in respect to the original volume of the whole blood). The first image was captured at 40–70 s after depositing the droplet on the coverslip. The diluted samples lead to a textural change (from dark to light gray) in the images shown in (a). The evolution of the fluid front is indicated with yellow arrows in (b). It depicts the second stage of the drying process. This stage occurs at 390–620 s. The appearance of the radial cracks occurs in the third stage that lasts for 500–700 s and is outlined with the orange arrows in (c). The respective stress notions (σ_θ) are illustrated using white arrows at the A–J points. The morphology of the dried film at the end of the drying process is exhibited in (d), where the green dashed circular line separates the corona from the central region at each ϕ . The scale bar corresponds to 0.2 mm.

drying stage, as shown for ϕ from 100 to 75% (v/v) (Fig. 1(I)c). Subsequently, some micro-cracks start originating from these radial cracks in the corona region. However, these micro-cracks cannot propagate in rejoining the dominant cracks in responding to the dominant orthoradial stress field (σ_θ). These domains start then begin separating from each other and widening of the radial cracks are observed (Fig. 1(I)d). This process indicated how the film domains detach (delaminate) from the substrate. At this point in the process, the sliding of these films in the radial direction indicates that the energy to adhere to the film is costlier than the sliding energy. This process is predominantly observed from ϕ of 100 to 75% (v/v); however, with more dilution, the film adheres more strongly to the substrate. Moreover, the domains which are formed by these radial cracks become narrower with the dilution. The central region of the dried films is found to have the random small crack domains, which are observed for samples from 100 to 50% (v/v). For 25 and 12.5% (v/v), no cracks are detected by the optical microscope (under $5\times$ magnification) in the central region, where these radial cracks are mostly observed in the corona (Fig. 1(I–II)d). A comparison of these dried films textures at each ϕ indicates that the whole corona region is of dark gray at ϕ of 100% (v/v), whereas, this region is only partially covered by dark gray at ϕ of 85 and 75% (v/v). Furthermore, the texture is observed to be of light gray at ϕ of 62 to 12.5% (v/v). It should be noted that the optical microscope illumination was nearly constant during the experiments. During this time,

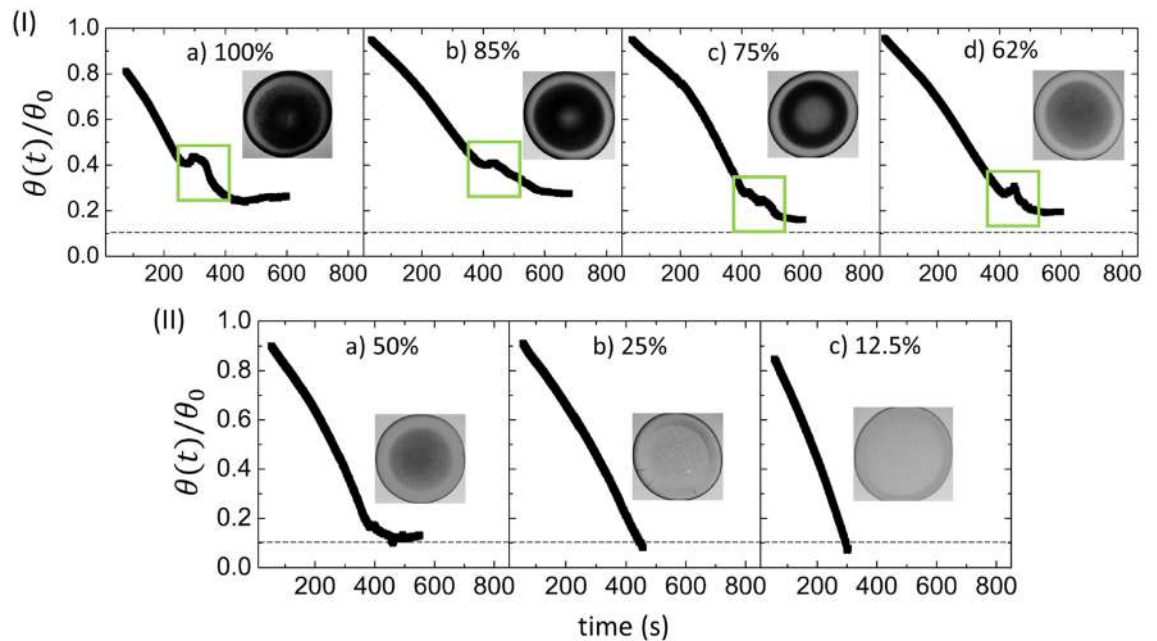


Figure 2. Variations of the normalized contact angle ($\theta(t)/\theta_0$) during the drying process of the blood droplets at different ϕ ranging (I) from 100 to 62% (v/v), and (II) 50 to 12.5% (v/v) are shown. The normalization of $\theta(t)$ is done by dividing it with the angle at $t = 0$ (θ_0). A monotonic decrease in the contact angle measurements is associated with the presence of a peak-like feature (outlined with a green rectangle) is observed in (I). The disappearance of this feature in these measurements is depicted in (II). The macroscopic images are displayed at different time points (in s) points from 100 to 12.5% (v/v) [321 s, 512 s, 470 s, 460 s, 473 s, 518 s, and 617 s respectively for different ϕ]. The instrumental limit is illustrated with dashed lines.

the width of the corona region decreases with increasing dilution (decreasing ϕ). The “coffee-ring” behavior³⁷ (similar to what is typically observed in other protein aqueous solutions³⁸) becomes evident in samples from ϕ of 62 to 12.5% (v/v). V1-V7 in the Supplementary Information show movies of the drying droplet for samples from 100 to 12.5% (v/v), respectively.

Figure 2(I-II) depicts the time evolution of the normalized contact angle of the blood droplets. The normalization of the contact angle ($\theta(t)$) is done in respect to the angle at $t = 0$ (θ_0). The θ_0 is determined by a linear extrapolation of the first 200 s of θ varying with time, where it appears linear. The y -intercept provides the normalization in θ . The average slope of this linear extrapolation of the contact angle for all ϕ are computed and found to be $-0.14^\circ/\text{s}$ with $R^2 = 0.996$ with very little variation between the samples. The contact angle then shows non-monotonic behavior after 200 s that exhibits a peak marked by a green rectangle in Fig. 2(I)a–d before saturating to a nearly constant with increasing dilution (decreasing ϕ) from 100 to 62% (v/v). The peak decreases in magnitude and shifts to a later time from 100 to 62% (v/v). No peak is observed with further dilution from 50 to 12.5% (v/v) (Fig. 2(II)a–c). Similar saturation and monotonic behavior are commonly observed in the aqueous protein solutions³⁸. The peak is observed from 250 to 400 s at $\phi = 100\%$ (v/v) (Fig. 2(I)a); and from 400 to 500 s for ϕ varying from 85 to 62% (v/v) (Fig. 2(I)b–d) (denoted with vertical dashed lines). The corresponding macroscopic images during the emergence of this peak are displayed in Fig. 2(I)a–d. The images indicate that the peak originates during the appearance of the fluid front or the gray texture from the periphery and it continues to evolve when the texture starts growing in the central region. In contrast, this peak is not observed for samples from 50 to 12.5% (v/v). The macroscopic images in Fig. 2(II)a–c are captured once the contact angle advances to steadiness. It is to note that the contact angle becomes constant when it is $\sim 25\%$ for ϕ of 100 and 85% (v/v), $\sim 15\%$ for ϕ of 75 and 62% (v/v), $\sim 10\%$ for ϕ of 50% (v/v), and $< \sim 10\%$ of the total value for ϕ of 25 and 12.5% (v/v). This suggests that the thickness of the film at the end of the drying process decreases with the diluting concentration (ϕ).

To validate the peak’s appearance is only specific to the blood samples diluted with de-ionized water, the physiological and environmental conditions were varied to measure the contact angles during the drying process. Different sample batches, and substrate types were taken into account. The diluent was also varied from the de-ionized water to the phosphate buffer saline (PBS) to observe any other possible patterns. The results show that these peaks are present in the diluted blood samples ranging from 100 and 62% (v/v) (Figs. S1-S3 in the supplementary section) for these different setups. However, it is assumed that the nature (shape, size, and time) of these peaks are affected due to these different conditions.

Figure 3(I-II) illustrates the parameters of the first-order statistics (FOS). The left y -axis of the graph shows the mean intensity ($\frac{1}{N} \sum_{i,j=0}^N I_{ij}$) and its right y -axis exhibits the standard deviation ($\sqrt{\frac{\sum_{i,j=0}^N (I_{ij}-\mu)^2}{N-1}}$), where, (i, j) , I_{ij} , and N are the gray values in a matrix, the pixel matrix of an image, and the number of pixels in the image, respectively. These parameters are extracted from the captured time-lapse images of the droplets at different ϕ

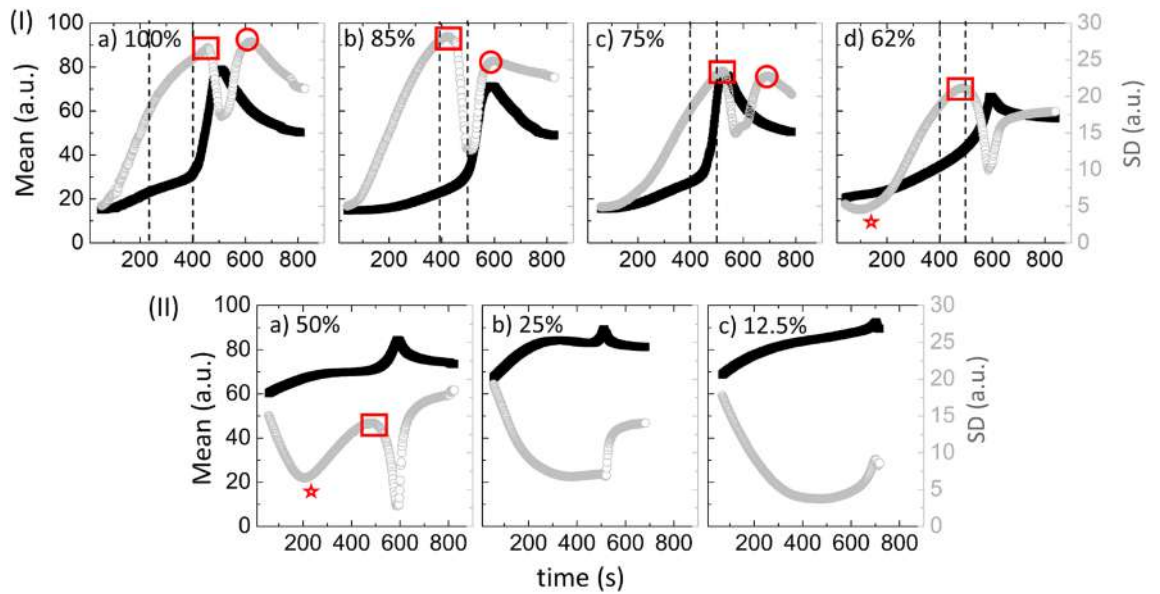


Figure 3. Statistical image analysis of the blood droplets at different ϕ from 100 to 12.5% (v/v) during the drying process. (I) and (II) show the drying evolution of the first order statistics (FOS) parameters (the mean on the left y-axis and the standard deviation (SD) on the right y-axis of the graph). The dashed lines in (I) display the time duration of the presence of the peak-like feature in the contact angle measurements from ϕ of 100 to 62% (v/v). The red rectangle and the red circle illustrate the first and the second peaks respectively in the SD. The star introduces the initial dip in the SD values observed from 62% (v/v) onwards.

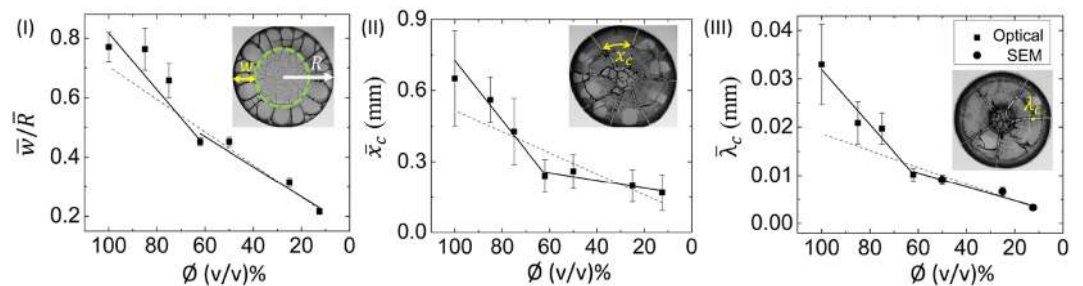


Figure 4. Variation of the averaged corona width (\bar{w} measured in mm) is normalized to the averaged radius of the droplet (\bar{R} measured in mm). It is plotted in (I), the averaged crack spacing (\bar{x}_c) is depicted in (II), and the averaged crack width ($\bar{\lambda}_c$) is exhibited in (III) at different diluting concentrations (ϕ). The dashed line shows the linear fit for the whole range of ϕ from 100 to 12.5% (v/v). The solid lines display two linear fits—first one for the range from 100 to 62% (v/v); and the second one for 62 to 12.5% (v/v). The error bars correspond to the standard deviation. The macroscopic images illustrate the width of the corona (w), the radius of the droplet (R), the distance between the consecutive radial cracks (x_c), and the width between the consecutive radial cracks (λ_c). The dashed green circular line separates the corona from the central region in the droplet.

during the drying process. The dashed lines of Fig. 3(I–II) denote the time range of the peak-like feature in the contact angle measurements. Note that the mean intensity shown in Fig. 3(I–II) depends on the average pixel distribution of the images. These data display three distinct phases—a slow increase, a rapid rise, and a saturation from ϕ of 100 to 75% (v/v). The first and second of these three phases; however, could not be distinguished in the 62 to 12.5% (v/v) samples. The large area under the peak is observed in the mean intensity at about 600 seconds for 100% sample, which continuously decreases with increasing dilution, nearly disappearing in the 12.5% (v/v) sample. The SD measurement [gray circles in Fig. 3(I–II)] depends on the global heterogeneity of the images, and is a measure of the image complexity. It exhibits an initial dip (outlined by a red-colored star) from 62% (v/v) onwards. The behavior of these FOS (the mean intensity and especially the SD) parameters changes abruptly at about 62% (v/v) dilution.

Morphology of the dried blood film. Figure 4(I) illustrates the variation of the averaged corona width (\bar{w}) that is normalized to the averaged radius of the droplet (\bar{R}). The macroscopic image in Fig. 4(I) illustrates the width of the corona (w) and the radius of the droplet (R). The increased dilution [ϕ from 100 to 12.5% (v/v)] systematically decreases the corona width. The \bar{w}/\bar{R} is plotted for the whole range of ϕ , i.e., from 100 to 12.5%

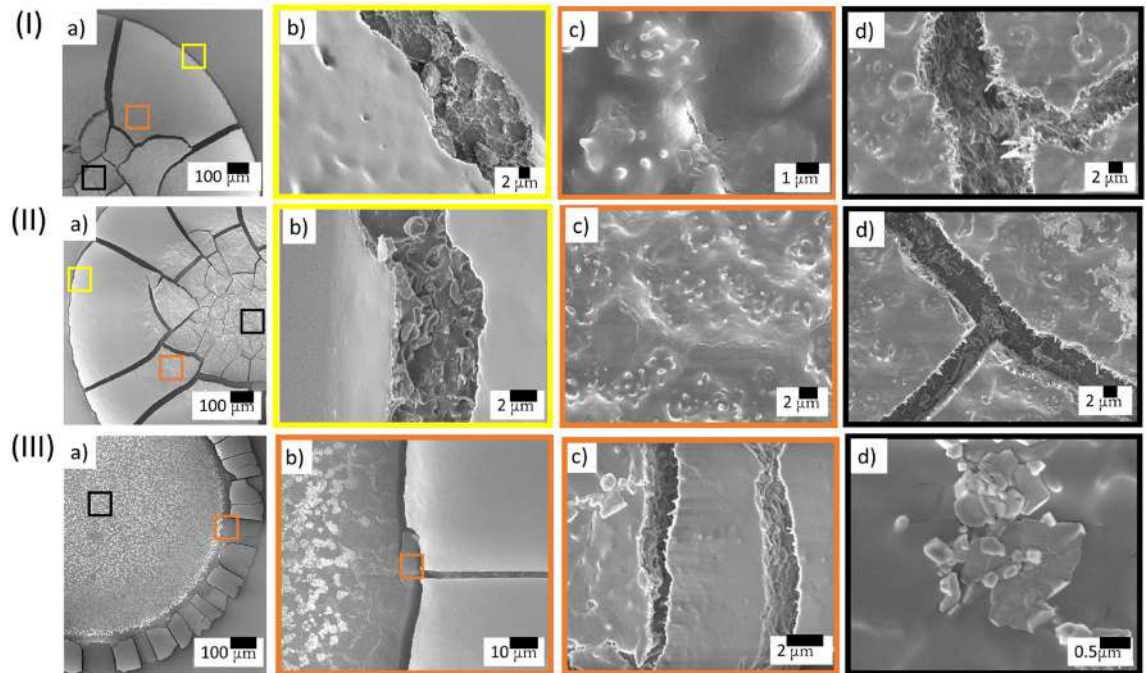


Figure 5. SEM images illustrating the microscopic structures of dried blood droplet at different length scales. The images at ϕ of 100, 75 and 12.5% (v/v) are, respectively, depicted in (I–III). The yellow, orange and black squares represent the blood structures at the periphery and corona, the transition of the corona and central regions, and the central region, respectively.

(v/v). The slope value (m) is found to be $0.0055 \pm 0.0006 \phi^{-1}$ with $R^2 = 0.931$. A first linear curve is fixed from 100 to 62% (v/v). Subsequently, a second curve is fitted from 62 to 12.5% (v/v). The slope value of the first linear fit (m_1) is found to be $0.0095 \pm 0.0019 \phi^{-1}$, with $R^2 = 0.894$. In contrast, the slope value of the second linear fit (m_2) is $0.0051 \pm 0.0008 \phi^{-1}$, with $R^2 = 0.928$. The variation of the averaged crack spacing (\bar{x}_c) with ϕ is shown in Fig. 4(II). The distance between the consecutive radial cracks (x_c) is illustrated in the macroscopic image. The parameter, m [the slope value of the linear fit for the range of 100 to 12.5% (v/v)], m_1 [the slope value of the linear fit for the range of 100 to 62% (v/v)], and m_2 [the slope value of the linear fit for the range of 62 to 12.5% (v/v)] are found to be $0.0045 \pm 0.0012 \text{ mm } \phi^{-1}$ with $R^2 = 0.668$, $0.013 \pm 0.0014 \text{ mm } \phi^{-1}$ with $R^2 = 0.965$, and $0.0016 \pm 0.0005 \text{ mm } \phi^{-1}$ with $R^2 = 0.736$ respectively. Fig. 4(III) displays the averaged crack width ($\bar{\lambda}_c$) variations of each ϕ . The width between the consecutive radial cracks (λ_c) is exhibited in the macroscopic image. The optical microscopy at $5\times$ magnification has the resolution to measure the $\bar{\lambda}_c$ down to the 62% (v/v) sample. For the $\bar{\lambda}_c$, the m_1 is extracted as $0.00057 \pm 0.00008 \text{ mm } \phi^{-1}$ (with $R^2 = 0.938$). To overcome the limitations of the optical microscopy, the SEM images are used to calculate λ_c for ϕ from 50 to 12.5% (v/v), where m_2 at this range yields $0.00014 \pm 0.00002 \text{ mm } \phi^{-1}$ (with $R^2 = 0.920$). Finally, over the whole range of ϕ , the slope (m) for $\bar{\lambda}_c$ is $0.00017 \pm 0.00003 \text{ mm } \phi^{-1}$ (with $R^2 = 0.835$).

Figure 5(I–III)a shows the regions of interest at ϕ of 100, 75, and 12.5% (v/v) respectively. The yellow, the orange, and the black squares display the zoomed view at the periphery and the corona, the interface of the corona and the central regions, and the central region, respectively. Fig. 5(I–III)b exhibits a smooth film in the corona region, and becomes more uniform with the increasing dilution of the blood sample. The cracks of the peripheral region at ϕ of 100 and 75% (v/v) [Fig. 5(I–II)b] consist of some ellipsoidal structures which lead to inhomogeneity within the cracks, whereas no such peripheral region is found at ϕ of 12.5% (v/v) (Fig. 5(III)a–b). At the interface of the corona and the central regions, some irregular troughs and ridges are revealed from the images of Fig. 5(I–II)c,d. A complex image is visible in Fig. 5(I–II)d, where the crack lines are not sharp and contain hair-like structures, which smoothly diminish in appearance in the diluted blood sample. Interestingly, these results show that the dilution at ϕ of 75% (v/v) [Fig. 5(II)] doesn't exhibit any significant changes in the distribution of these structures from the whole blood [Fig. 5(I)]. However, a marked difference can be seen at 12.5% (v/v) [Fig. 5(III)]. Unlike other concentrations, some unique blunt spicules are present on the film (Fig. 5(III) b–c), and some aggregated sickle or oblate shaped structures are observed in the central region in Fig. 5(III)d.

Discussion

Microscopic structures of dried blood film. The SEM images in Fig. 5(I–III) allow us to determine the distribution of various components in the dried film. The components that can be distinguished from these images are plasma proteins, red blood cells (RBCs), white blood cells (WBCs), and platelets. The periphery of the film and the textures within the cracks indicate that the plasma proteins interact with the substrate and form a plasma-rich layer as soon as the droplet is deposited.

Most of these cracks in the peripheral region consist of fragmented or ellipsoidal RBCs (Fig. 5(I–II)b). None of the samples [ϕ of 100, 75, and 12.5% (v/v)] show any blunt spicules (which resembles echinocyte, a deformed structural form of RBCs reported in³⁹) in these cracks. This indicates that RBCs do not interact with the substrate directly; however, it does with the plasma-rich layer. Had these RBCs adsorbed on this substrate, their membranes would have different electrostatic interactions and might have led to the echinocytes, which are not (obviously) observed here. At the upper film surface, the corona region reveals smooth fragmented sheets. This suggests that the RBCs are stacked in a packed fashion such that their membranes form this sheet, a similar phenomenon reported in⁴⁰. The compressed RBCs are ruptured, as could be seen in the crack walls due to the mechanical stress curving the cracks (shown in Fig. 5(I–II)b).

Close observation of the film from the thin periphery region across the corona and into the central region indicates that the RBCs are predominantly in the corona. Any of these platelets and WBCs are not present in the periphery and in the corona. Moving from the corona to the central region, we see the concentration of the WBCs, the platelets and some residual RBCs. Fig. 5(I–II)c displays the irregular troughs and ridges which would resemble the different functional forms of the WBCs (microvilli structures reported in^{41,42}) and some of the residual echinocytes. The crowdedness of the RBCs, the WBCs, and the plasma proteins is clearly illustrated by the fact that the dried film at ϕ of 100% (v/v) [Fig. 5(I)a] contains $\sim 500 \times 10^4$ of RBCs, $\sim 1 \times 10^4$ of WBCs, and $\sim 40 \times 10^4$ of platelets, in addition to the initial salts and other molecular blood factors¹⁴. The crack lines are not sharp enough and contain hairy structures. These hairy structures are believed to be the activated form (a spreading structure with extended filopodia mentioned in⁴³) of the platelets (Fig. 5(I–II)d). It confirms the existence of a complex combination of interactions among these components which can activate these platelets in response to the mechanical stress.

At ϕ of 12.5% (v/v), the film only contains $\sim 60 \times 10^4$ of RBCs, $\sim 0.12 \times 10^4$ of WBCs, and $\sim 5 \times 10^4$ of platelets, a decrease of about a factor of 10. This significant reduction in their counts influences the morphology of the film, and is denoted in Fig. 5(III)a. The peripheral region does not appear in these images. Furthermore, the fragmented sheets in the corona region appear to be smoother, and its width gets reduced compared to other ϕ . Some spicule-like structures are identified in the transitional region from the corona to the central regions (Fig. 5(III)b–c); and, some sickle and oblate-shaped structures are observed near the center (Fig. 5(III)d). The reduction (of RBCs, WBCs and platelets) concentrations decreases their interaction among themselves and with each other such that different functional forms of these components are observed. Moreover, as dilution increases, any interaction among the components within blood becomes negligible such that the inactivated form of these platelets are preserved, mostly observed in the central region.

Concentration-driven phase transition in the drying droplets and the dried films. The outcome of three experimental observations support the presence of concentration-driven phase separation in the samples of a multi-colloid self-interacting solution, such as the whole blood. Our observations (drawn based on these three experimental outcomes) are independent of each other and facilitate measuring different aspects of the drying process including the final dried film morphology.

The first observation is related to the contact angle (θ) measurements as a function of time during the drying process. The θ is found to decrease monotonically. Subsequently, a peak is observed for the whole blood. This pattern is observed in the dilution ranging from 100 to 62% (v/v) [Figs. 2(I) and S1–S3(I)]. The peak, however, starts disappearing in the diluted samples starting from 50 to 12.5% (v/v) [Figs. 2(II) and S1–S3(II)]. During this stage, θ exhibits a steep monotonic decrease. The third independent measurement is done on the morphology of the dried film. The mean width of the corona (\bar{w}), the mean crack spacing (\bar{x}_c) and the mean crack widening ($\bar{\lambda}_c$) are found to be the highest for the whole blood [$\phi = 100\%$ (v/v)]. All these parameters; however, are reduced as the initial concentration of the blood sample is diluted [Fig. 4(I–III)]. Interestingly, a smooth gradual decrease in these extracted parameters (\bar{w}/\bar{R} , \bar{x}_c , and $\bar{\lambda}_c$) is not observed when varying with ϕ . Had that been the case it could have assumed that the droplets experience a universal mechanism throughout the drying process, which is not the case here. Instead, a pronounced break in the trends of the parameters is seen at about 62% (v/v). Comparing the R-squared values for the double linear fits with a single linear fit clearly favors the use of two linear fits—one from 100 to 62% (v/v) samples, and, the other for 62 to 12.5% (v/v). This behavior for the parameter \bar{w}/\bar{R} is found to be weakest, but still present, and is likely due to the fact that the width formation is the result of the deposition of the components during the convective flow, especially in the early stages of drying. Dilution of the whole blood (whether DI water or PBS) lowers the number of the components, and so reduces the corona's width. Moreover, the formation of the corona is strongly influenced by the drying-driven fluid circulation, the droplet geometry, and its wetting. It is; however, not so dependent on the type of the components, but just the amount. In contrast, \bar{x}_c and $\bar{\lambda}_c$ show a much stronger break and evidence for two linear regimes from 100 to 12.5% (v/v).

All these three measurements indicate that there are two classes of the mechanisms involved. These mechanisms could be interpreted in the following way. A large number of components (such as RBCs, WBCs, platelets, proteins, etc.) are present in ~ 2 mm diameter droplet at $\phi = 100\%$ (v/v) [the whole blood]. These components are randomly distributed as soon as the droplet of the whole blood is deposited on the substrate [Fig. 6(I)]. In this *initial phase*, the evaporation rate is observed to be highest near the three-phase contact line [indicated with solid arrows in Fig. 6(I)]. A capillary flow [marked with dotted lines in Fig. 6(I)] is observed to develop and most of these components are carried towards the periphery. Subsequently, a plasma-rich layer is developed on the substrate. Soon after, all these components start moving closer to each other, which indicates the beginning of the *middle phase* in Fig. 6(II). In this phase, these components experience compression, or stretch, and shear at the same time near the periphery. The concentration of these components within the droplet increases as the water constantly evaporates. The confinement in the droplet diameter and the presence of the huge number of these components is likely to influence the activity of one component on others. Such interactions may result

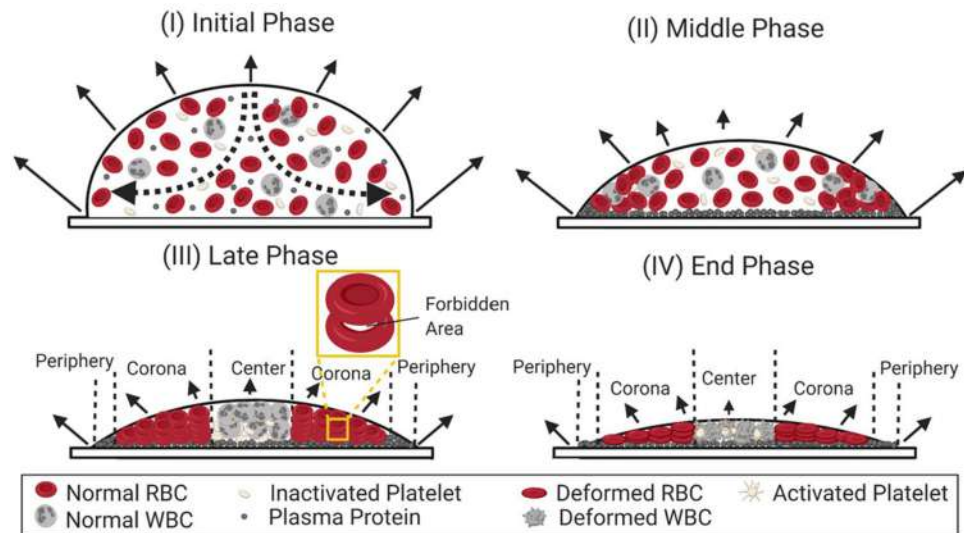


Figure 6. Side view of the self-assembling mechanism in the whole blood ($\phi = 100\%$) during the drying evolution: (I) The *initial phase* starts when the droplet is deposited on the substrate. The evaporation rate is highest near the three-phase contact line (depicted with solid arrows). The components (RBCs, WBCs, platelets, and proteins) are distributed randomly. A dotted line indicates that a capillary flow is developed in the droplet. (II) The *middle phase* begins when these components are carried towards the periphery. These components initiate interactions as soon as they come in contact with each other. Meanwhile, a plasma-rich layer is developed on the substrate. (III) The segregation of these components takes place as the water continually evaporates from the droplet. During the *late phase*, the three distinct regions (the periphery, the corona, and the center) are developed. The proteins are mostly present in the periphery. The WBCs and the platelets are pushed towards the central region. The RBCs are stacked in the corona region. The trapped water in between two RBCs is marked as the “forbidden area”. (IV) The deformation of the RBC and the WBC structures and the activation of the platelets take place during the *end phase*.

in a strong, complex combination of the potential chemicals amongst these various components. For example, a few of these components may try to arrange themselves in their original shape (elastic behavior); however, their arrangement would then create negative stress on other components. These other components may then rearrange (viscous behavior) themselves to accompany the accumulated stress. The elastic behavior can be modeled as $\sigma = E\epsilon$ where σ , E , and ϵ is the stress, averaged elastic modulus resulted from the arrangements of these components and the strain which occurs under the accumulated stress respectively. The visco-elastic behavior can be re-modeled by adding the Kelvin-Voigt element, i.e., $\sigma = E\epsilon + \eta\dot{\epsilon}$, where, η is the viscosity, and $\dot{\epsilon}$ is the change of strain in respect to time t . This speculated viscous behavior is most likely governed by the interacting capabilities of the WBCs (with the other components viz., the RBCs and the platelets) owing to its largest size ($\sim 15\mu\text{m}$) compared to the other components (the RBCs and the platelets are of $\sim 7\mu\text{m}$, and $\sim 2\mu\text{m}$ respectively). The large peak that was noticed at ϕ of 100% (v/v) [Figs. 2(I) and S1-S3(I)], the presence of a similar peak has also been reported in²⁰, may have some correlation to this viscous behavior during the drying process. However, the experiments reported in²⁰ did not concentrate on diverse ranges of dilution; and hence the study failed to observe the transition at 62%. The current study, thus, contributes a crucial information related to phase transition. It would be interesting to conduct an in-situ rheology and mass measurements to directly probe these mechanisms; however, this is beyond the scope of the paper. The segregation of these components takes place during the *late phase* of the drying process [Fig. 6(III)]. The confinement of their sizes does not allow both the RBCs and the WBCs to be present within the periphery [evident from the SEM results shown in Fig. 5(I)a–b]. Most of the RBCs are organized in stacks in the corona region, and the WBCs and the platelets are pushed towards the central region [Fig. 6(III)]. There is a possibility that some of the water is trapped between two RBCs during the stacking of the RBCs, [marked as the “forbidden areas” in Fig. 6(III)]. The change of the texture from the light to dark gray texture (Fig. 1(I)c–d) might be related to the final evaporation of this entrapped water. The loss of water in these droplets during the drying process creates a hypotonic environment to the cellular components present in the blood. The blood cells are more likely to undergo hemolysis inducing a fundamental change in their composition. Furthermore, the developing mechanical stress evolved due to the loss of the water from the droplet deforms the structures of RBCs and the WBCs in the *end phase* [Fig. 6(IV)]. The inactive platelets are activated in response to the mechanical stress and are observed as the hairy structures along the crack lines (indicated in Fig. 5(I)d).

As mentioned already, the whole blood sample is diluted by adding different volumes of de-ionized water. Obviously, the initial concentration of these components in the diluted blood samples [ϕ ranging from 85 to 12.5% (v/v)] becomes less compared to the whole blood. The addition of de-ionized water rather than PBS (the buffered saline) is likely to trigger a hypotonic environment to these cellular components prior to the drying process. However, it is to be noted that the changes (if any) occur in the initial mixtures before deposition but

may be balanced as the water evaporates. Exploring this effect would be interesting but is beyond the scope of this paper. Additional measurements were carried out in a parallel way but diluting with PBS, in order to maintain the native environment of the cells and the fundamental changes (hemolysis) in the blood composition (from intact to fragments) could be avoided. These results appear consistent with the DI water dilution and so minimizes this mechanism. However, it is worth mentioning that the dilution of the blood by PBS (at its fixed concentration) will increase the appearance of salts residues or crystals²⁰, which influences the statistics derived from the optical images, and lead to artifacts in the scanning electron microscopy images.

The drying process of the diluted blood samples exhibits similar phases [from *initial* to the *end phase* shown in Fig. 6(I–IV)]. Figure 1(I–II)a indicates a change in the texture (from dark to light gray) as soon as the first image during the drying process is captured. The normalized plot in Fig S4(I–II)a shown in the supplementary information directly illustrates this change in the texture. At ϕ from 100 to 62% (v/v), the mean intensity value of the first image is $\sim 20\%$ of the total value, further dilutions of the concentration leads the mean intensity to be at $\sim 80\%$ of the total value. It is to be noted that RBCs contain hemoglobin protein (which is responsible for the redness). The change of texture, or the rise in the normalized plot, indicates that the number of RBCs reduces with the diluted concentrations. The decrease of RBCs also ensures that the other components will also minimize to maintain their relative initial concentrations. The number of these components gradually decreases with the diluted concentrations [in ϕ ranging from 85 to 62% (v/v)] and leads to a reduction in the chemical potential amongst them. The shrinkage and disappearance of peak in the contact angle measurements supports this mechanism. In addition, the observed shift in the peak to the later time (depicted by green rectangles in Fig. 2(I) a–d) indicates that these diluted samples require more time (greater concentration and assembly) to reach the visco-elastic tipping point of the system. Furthermore, the wetting angle peak at the concentration range of 100 to 62% (v/v) is found to be present in spite of varying the physiological and environmental conditions. The blood diluted with PBS [see Fig. S1(I)], and the new blood batch deposited on different substrates [see Figs. S2–S3(I)] have been examined. We noticed a similar peak in the contact angle measurements. Nonetheless, the nature of the peaks varies, i.e., in some cases, the peak is delayed, while in some other cases, the peak is broadened or reduced, depending on the wettability of these droplets. This systematic study of diluted samples (ranging between 100 and 12.5% (v/v) that include all the possible variations in terms of physiology and environments firmly establish a very important point, i.e., the observed peak is not specific to the blood (samples) diluted with de-ionized water only; rather it confirms that the peak is a trademark that establishes a general phenomenon of the concentration-driven self-assembly.

The presence of WBCs also seems to act as a mediator which favors the interactions between various components, rather than the interaction between these components and the substrate. This process results in sliding of the cracked domains over the attachment of these domains with the substrate in the samples ranging from 100 to 62% (v/v). Furthermore, this process shows a sharp decrease in \bar{x}_c and $\bar{\lambda}_c$. In contrast, for ϕ from 50 to 12.5% (v/v), the number of these various components is reduced enough that the chemical potential related to WBCs becomes negligible. This results in the switching of the mechanism from the visco-elastic to elastic behavior. No peak observed at this concentration range in the contact angle measurements [Figs. 2(II) and S1–S3(II)]. Moreover, the attachment of the film to the substrate becomes stronger, the sliding of the crack domains stops, and more radial cracks appear on the film surface [Fig. 1(II)].

Our findings, thus, clearly establish the existence of a sharp phase transition in the whole blood through a simple physical drying process. This transition relied on the concentration of the various components present in the droplet. It reveals essential information about the self-assembling mechanism in a multi-component bio-colloid, such as the whole human blood. Our systematic study of the dilution range also ensures that the concentration-driven phase transition is not specific to the blood-water system only; rather it is a general phenomenon of drying-driven diluting blood droplets. Finally, this study demands theoretical attention for such a multifaceted phase transition that relies on the complex combination of interacting chemical potentials for unearthing the hierarchical structures present in nature.

Methods

Materials and sample preparation. A 1 μL of whole blood contains 400 to 500 $\times 10^4$ of RBCs, 0.5 to 1 $\times 10^4$ of WBCs, 14 to 40 $\times 10^4$ of platelets, depending on the pathological condition of a donor, along with a small amount of plasma proteins (fibrinogen, immunoglobulins, albumin) and salt ions¹⁴. The typical size of RBCs, WBCs, and platelets are 6 to 8 μm , $\sim 15 \mu\text{m}$, and 2 to 3 μm respectively¹⁴. The RBCs are red in color due to the presence of the iron-containing protein, hemoglobin. Furthermore, RBCs contain a membrane as well. A membrane is made of 19.5% water, 39.6% proteins, 35.1% lipids and 5.8% (w/w) carbohydrates⁴⁴. These cellular components in the blood can alter their shapes in response to the toxicity or pH or shear stress⁴³.

For example, the healthy RBCs are of bi-concave or discoid shape; however, these transform into different forms such as ellipsoidal, echinocyte (a round shape with short blunt spicules), sickle (crescent moon), teardrop, etc⁴⁴. The WBCs, on the other hand, are white in color, and generally contain irregular and nucleated structure. These structures are capable of transforming themselves into different functional forms, irregular troughs and ridges (microvilli structures)^{41,42}. The platelet, when inactivated, follows a discoid and an anuclear structure, but, changes into its spread form with extended filopodia on its activation. The cytoskeleton of platelets is composed of actin and actin-binding proteins; these can polymerize and activate those platelets in response to the environmental or chemical signals⁴³.

The whole human blood used in this study was purchased from Lampire Biological Laboratories, USA⁴⁵ and mixed with Na-Citrate anticoagulant (Catalog number 7203706). These samples are used in our experiments without any further chemical processing, except for dilution with DI water or PBS. The anticoagulants inhibit most of the platelets to aggregate, and prevent the coagulation of the blood.

Different concentrations (ϕ) of blood were prepared from 85 to 12.5% (v/v) by adding de-ionized water (Millipore, 18.2 M Ω cm at $\sim 25^\circ\text{C}$). A volume of $\sim 1\ \mu\text{L}$ of sample was pipetted on a fresh microscopic coverslip (Catalog number 48366-045, VWR, USA) to form a circular droplet of radius $\sim 1\ \text{mm}$ at the room temperature of $\sim 25^\circ\text{C}$, and relative humidity of $\sim 50\%$. This procedure ensured that every droplet is precisely exposed to the same substrate conditions, and environmental conditions, and helped achieve uniform reproducibility of 3–4 repetitions. The time-point when the droplets are deposited on the coverslip is marked as the start-time of image acquisition. It is to be noted that the samples are prepared immediately before imaging.

A few experiments were carried out separately by varying environmental and physiological conditions to ensure the wettability of these droplets. One such experiment includes the concentration of the whole blood (100% by volume) from the same batch that is diluted by adding 1 \times phosphate buffer saline (PBS, BP243820, Fisher BioReagents, USA). 1 \times PBS has a concentration of 0.137M NaCl, 0.0027M KCl, and 0.119M phosphates that maintains a pH of 7.3–7.5. Similarly, different concentrations of diluted blood samples using PBS (ϕ_p) were prepared that include the range of 75 to 12.5% (by volume). A new blood batch from the same company (Catalog number 7203706, Lampire Biological Laboratories, USA) was ordered and exactly the same procedure was followed to dilute the blood by adding de-ionized water. The wettability of these diluted blood droplets is measured under two substrate conditions. The initial contact angle of these droplets is found to be $\sim 55^\circ$ and $\sim 85^\circ$ when deposited on various coverslips, Catalogs no. 48366-045, VWR, USA and 4867-100, R & D Systems, USA, respectively.

Image acquisition. The time-lapse images are captured at every two seconds in bright field microscopy (Amscope, USA) using a 5 \times objective lens. An 8-bit digital camera (MU300, Amscope, USA) attached to the microscope captured images at a fixed resolution of 3664 \times 2748 pixels. The pixels to real-space length scale was changed by using a calibration slide. The lamp intensity was kept fixed throughout the experiment to minimize the fluctuations in the background (coverslip) intensity. All the images were converted to the gray shade for clear visualization.

The contact angle of the prepared samples was measured during the drying process by the contact angle goniometer (Model 90, Ramé-hart Instrument Company, USA) to check the wettability of these droplets. Each experiment was repeated twice to ensure the reproducibility.

The microstructural analysis of the dried films was performed using scanning electron microscopy (JEOL-7000F, JEOL Inc. MA, USA). Prior to this, the dried films were sputter-coated with a $\sim 4\ \text{nm}$ thick layer of gold nanoparticles using EMS sputter coater to improve the quality of the sample surface's conductivity. The SEM analysis was conducted using secondary electron at an accelerating voltage of 3 kV and probe current of 5 mA.

Image analysis. Different parameters of the images were measured using ImageJ⁴⁶. A circular region of interest (ROI) of the droplet image was selected by an *oval tool* in ImageJ. The mean and the standard deviation parameters of the first-order statistics (FOS) was extracted. No pre-processing of the images was required since the blood samples contain a high contrast difference compared to the background (coverslip). Furthermore, a 2-D plot profile was computed by selecting a rectangle along the horizontal diameter of the droplet, ρ . The width of the corona region was measured five times to compute the averaged width (\bar{w}). It was normalized by dividing it with the averaged radius (\bar{R}). The parameter, \bar{w}/\bar{R} is then plotted at a function of ϕ . To estimate the crack width (λ_c) and the crack spacing (x_c), a circular line was drawn, and their averaged values were also determined at each ϕ . The detailed procedure of x_c measurements can be found in⁴⁷.

Received: 24 July 2020; Accepted: 23 October 2020

Published online: 03 November 2020

References

- Landau, L. D. & Lifshitz, E. M. *Course of Theoretical Physics* (Elsevier, Amsterdam, 2013).
- Singh, S. Phase transitions in liquid crystals. *Phys. Rep.* **324**, 107–269 (2000).
- Simons, K. & Ikonen, E. Functional rafts in cell membranes. *Nature* **387**, 569–572 (1997).
- Boeynaems, S. *et al.* Protein phase separation: a new phase in cell biology. *Trends Cell Biol.* **28**, 420–435 (2018).
- Tablin, F., Oliver, A. E., Walker, N. J., Crowe, L. M. & Crowe, J. H. Membrane phase transition of intact human platelets: correlation with cold-induced activation. *J. Cell. Physiol.* **168**, 305–313 (1996).
- Jacobs, W. M. & Frenkel, D. Phase transitions in biological systems with many components. *Biophys. J.* **112**, 683–691 (2017).
- Pollack, G. H. & Chin, W.-C. *Phase Transitions in Cell Biology* (Springer, Berlin, 2008).
- Brutin, D., Sobac, B. & Nicloux, C. Influence of substrate nature on the evaporation of a sessile drop of blood. *J. Heat Transf.* **134**, 061101 (2012).
- Zeid, W. B., Vicente, J. & Brutin, D. Influence of evaporation rate on cracks' formation of a drying drop of whole blood. *Colloids Surf. A Physicochem. Eng. Asp.* **432**, 139–146 (2013).
- Bou-Zeid, W. & Brutin, D. Effect of relative humidity on the spreading dynamics of sessile drops of blood. *Colloids Surf. A Physicochem. Eng. Asp.* **456**, 273–285 (2014).
- Sobac, B. & Brutin, D. Desiccation of a sessile drop of blood: cracks, folds formation and delamination. *Colloids Surf. A Physicochem. Eng. Asp.* **448**, 34–44 (2014).
- Chen, R., Zhang, L., Zang, D. & Shen, W. Blood drop patterns: formation and applications. *Adv. Colloid Interface Sci.* **231**, 1–14 (2016).
- Chen, R., Zhang, L. & Shen, W. Controlling the contact angle of biological sessile drops for study of their desiccated cracking patterns. *J. Mater. Chem. B* **6**, 5867–5875 (2018).
- Brutin, D., Sobac, B., Loquet, B. & Sampol, J. Pattern formation in drying drops of blood. *J. Fluid Mech.* **667**, 85–95 (2011).
- Sobac, B. & Brutin, D. Structural and evaporative evolutions in desiccating sessile drops of blood. *Phys. Rev. E* **84**, 011603 (2011).

16. Ramsthaler, F., Schlote, J., Wagner, C., Fiscina, J. & Kettner, M. The ring phenomenon of diluted blood droplets. *Int. J. Legal Med.* **130**, 731–736 (2016).
17. Ramsthaler, F., Kröll, A.-K., Verhoff, M., Birngruber, C. G. & Kettner, M. Effect of anticoagulation therapy on drying times in bloodstain pattern analysis. *Int. J. Legal Med.* **131**, 955–961 (2017).
18. Van den Berge, M., De Vries, F., Van der Scheer, M., Sijen, T. & Meijrink, L. Determining how diluted bloodstains were derived: inferring distinctive characteristics and formulating a guideline. *Forensic Sci. Int.* **302**, 109918 (2019).
19. San Pietro, D. & Steelberg, R. A preliminary assessment of the correlation of drying time and the peripheral rim thickness of perimeter bloodstains. *J. Forensic Res.* **10**, 2 (2019).
20. Iqbal, R., Shen, A. Q. & Sen, A. Understanding of the role of dilution on evaporative deposition patterns of blood droplets over hydrophilic and hydrophobic substrates. *J. Colloid Interface Sci.* **579**, 541–550 (2020).
21. Whitesides, G. M. & Grzybowski, B. Self-assembly at all scales. *Science* **295**, 2418–2421 (2002).
22. Rapis, E. A change in the physical state of a nonequilibrium blood plasma protein film in patients with carcinoma. *Tech. Phys.* **47**, 510–512 (2002).
23. Yakhno, T., Sedova, O., Sanin, A. & Pelyushenko, A. On the existence of regular structures in liquid human blood serum (plasma) and phase transitions in the course of its drying. *Tech. Phys.* **48**, 399–403 (2003).
24. Yakhno, T. A. *et al.* The informative-capacity phenomenon of drying drops. *IEEE Eng. Med. Biol. Mag.* **24**, 96–104 (2005).
25. Yakhno, T. A. *et al.* Drying drop technology as a possible tool for detection leukemia and tuberculosis in cattle. *J. Biomed. Sci. Eng.* **8**, 1 (2015).
26. Tarasevich, Y. Y. Mechanisms and models of the dehydration self-organization in biological fluids. *Phys. Uspekhi* **47**, 717–728 (2004).
27. Muravlyova, L. *et al.* Structure-forming properties of blood plasma of patients with interstitial lung diseases. *World J. Med. Sci.* **10**, 478–483 (2014).
28. Bel'skaya, L. V., Sarf, E. A. & Solonenko, A. P. Morphology of dried drop patterns of saliva from a healthy individual depending on the dynamics of its surface tension. *Surfaces* **2**, 395–414 (2019).
29. Mukhopadhyay, M. *et al.* Interfacial energy driven distinctive pattern formation during the drying of blood droplets. *J. Colloid Interface Sci.* **573**, 307–316 (2020).
30. Onofriescu, M. *et al.* Overhydration, cardiac function and survival in hemodialysis patients. *PLoS ONE* **10**, e0135691 (2015).
31. Hsieh, M. M. *et al.* Allogeneic hematopoietic stem-cell transplantation for sickle cell disease. *N. Engl. J. Med.* **361**, 2309–2317 (2009).
32. Hung, S.-C. *et al.* Volume overload correlates with cardiovascular risk factors in patients with chronic kidney disease. *Kidney Int.* **85**, 703–709 (2014).
33. Pal, A., Gope, A., Kafle, R. & Iannacchione, G. S. Phase separation of a nematic liquid crystal in the self-assembly of lysozyme in a drying aqueous solution drop. *MRS Commun.* **9**, 150–158 (2019).
34. Pal, A., Gope, A. & Iannacchione, G. S. A comparative study of the phase separation of a nematic liquid crystal in the self-assembling drying protein drops. *MRS Adv.* **4**, 1309–1314 (2019).
35. Lanotte, L., Laux, D., Charlot, B. & Abkarian, M. Role of red cells and plasma composition on blood sessile droplet evaporation. *Phys. Rev. E* **96**, 053114 (2017).
36. Smith, F. & Brutin, D. Wetting and spreading of human blood: recent advances and applications. *Curr. Opin. Colloid Interface Sci.* **36**, 78–83 (2018).
37. Deegan, R. D. *et al.* Capillary flow as the cause of ring stains from dried liquid drops. *Nature* **389**, 827 (1997).
38. Pal, A., Gope, A., Athair, A. S. & Iannacchione, G. S. A comparative study of the drying evolution and dried morphology of two globular proteins in de-ionized water solutions. *RSC Adv.* **10**, 16906–16916 (2020).
39. Mukhopadhyay, M., Ghosh, U. U., Sarkar, D. & DasGupta, S. Surface property induced morphological alterations of human erythrocytes. *Soft Matter* **14**, 7335–7346 (2018).
40. Chen, R., Zhang, L., Zang, D. & Shen, W. Understanding desiccation patterns of blood sessile drops. *J. Mater. Chem. B* **5**, 8991–8998 (2017).
41. Newell, D., Roath, S. & Smith, J. The scanning electron microscopy of normal human peripheral blood lymphocytes. *Br. J. Haematol.* **32**, 309–316 (1976).
42. Yang, S. Scanning electron microscopy of normal human peripheral blood cells. *Taiwan yi xue hui za zhi J. Formos. Med. Assoc.* **88**, 1128–1132 (1989).
43. Gregory, S., Stevens, M. & Fraser, J. F. *Mechanical Circulatory and Respiratory Support* (Academic Press, Cambridge, 2017).
44. Yawata, Y. *Cell Membrane: The Red Blood Cell as a Model* (Wiley, New York, 2006).
45. *Normal Human Whole blood, Gender Unspecified, Anticoagulant Na-Citrate*, Lampire Biological Laboratories, Inc. P.O. Box 270 Pipersville, PA 18947, USA (Catalog No 7203706).
46. Abràmoff, M. D., Magalhães, P. J. & Ram, S. J. Image processing with imagej. *Biophotonics Int.* **11**, 36–42 (2004).
47. Pal, A., Gope, A. & Iannacchione, G. S. Image-based analysis of patterns formed in drying drops. In *Pattern Recognition and Machine Intelligence* (eds Deka, B. *et al.*) 567–574 (Springer, Cham, 2019).

Acknowledgements

This work is supported by the Department of Physics at WPI. We would like to express our gratitude to Professor Christopher R. Lambert for allowing us to perform the contact angle experiments in his lab. We are indebted to WPI Tinkerbox program sponsored by WIN (Women Impact Network) for awarding us the essential funding to conduct all the experiments.

Author contributions

All the authors are actively involved in preparing the final manuscript. All the experiments were crafted and performed by A.P. The interpretation of the results (except the SEM analysis) were done by both A.P. and G.I. A.P. and J.O. did the SEM analysis. The images were drawn, quantified, and computed by A.G. and A.P. A.G. also edited the final version of the manuscript. All the authors have read and approved the final manuscript.

Competing interests

The authors declare no competing interests.

Additional information

Supplementary information is available for this paper at <https://doi.org/10.1038/s41598-020-76082-6>.

Correspondence and requests for materials should be addressed to A.P.

Reprints and permissions information is available at www.nature.com/reprints.

Publisher's note Springer Nature remains neutral with regard to jurisdictional claims in published maps and institutional affiliations.



Open Access This article is licensed under a Creative Commons Attribution 4.0 International License, which permits use, sharing, adaptation, distribution and reproduction in any medium or format, as long as you give appropriate credit to the original author(s) and the source, provide a link to the Creative Commons licence, and indicate if changes were made. The images or other third party material in this article are included in the article's Creative Commons licence, unless indicated otherwise in a credit line to the material. If material is not included in the article's Creative Commons licence and your intended use is not permitted by statutory regulation or exceeds the permitted use, you will need to obtain permission directly from the copyright holder. To view a copy of this licence, visit <http://creativecommons.org/licenses/by/4.0/>.

© The Author(s) 2020

Article

Temperature and Concentration Dependence of Human Whole Blood and Protein Drying Droplets

Anusuya Pal ^{1,*} , Amalesh Gope ²  and Germano Iannacchione ¹ 

¹ Order-Disorder Phenomena Laboratory, Department of Physics, Worcester Polytechnic Institute, Worcester, MA 01609, USA; gsiannac@wpi.edu

² Department of English, Tezpur University, Tezpur 784028, Assam, India; amalesh@tezu.ernet.in

* Correspondence: apal@wpi.edu

Abstract: The drying of bio-colloidal droplets can be used in many medical and forensic applications. The whole human blood is the most complex bio-colloid system, whereas bovine serum albumin (BSA) is the simplest. This paper focuses on the drying characteristics and the final morphology of these two bio-colloids. The experiments were conducted by varying their initial concentrations, and the solutions were dried under various controlled substrate temperatures using optical and scanning electron microscopy. The droplet parameters (the contact angle, the fluid front, and the first-order image statistics) reveal the drying process's unique features. Interestingly, both BSA and blood drying droplets' contact angle measurements show evidence of a concentration-driven transition as the behavior changes from non-monotonic to monotonic decrease. This result indicates that this transition behavior is not limited to multi-component bio-colloid (blood) only, but may be a phenomenon of a bio-colloidal solution containing a large number of interacting components. The high dilution of blood behaves like the BSA solution. The ring-like deposition, the crack morphology, and the microstructures suggest that the components have enough time to segregate and deposit onto the substrate under ambient conditions. However, there is insufficient time for evaporative-driven segregation to occur at elevated temperatures, as expected.

Keywords: drying droplet; colloid; protein; blood; self-assembly



Citation: Pal, A.; Gope, A.; Iannacchione, G. Temperature and Concentration Dependence of Human Whole Blood and Protein Drying Droplets. *Biomolecules* **2021**, *11*, 231. <https://doi.org/10.3390/biom11020231>

Academic Editor: Eric B. Kmieciak
Received: 29 November 2020
Accepted: 1 February 2021
Published: 5 February 2021

Publisher's Note: MDPI stays neutral with regard to jurisdictional claims in published maps and institutional affiliations.



Copyright: © 2021 by the authors. Licensee MDPI, Basel, Switzerland. This article is an open access article distributed under the terms and conditions of the Creative Commons Attribution (CC BY) license (<https://creativecommons.org/licenses/by/4.0/>).

1. Introduction

The whole human blood is a complex bio-colloidal fluid consisting of cellular components [red blood cells (RBCs or erythrocytes), white blood cells (WBCs or leukocytes), and platelets (thrombocytes)] and plasma [1]. On the other hand, the plasma is made of water, and minute amounts of ions, salts, and albumin proteins [2]. The human blood solution, thus, comprises a successive hierarchy levels, representing just one facet of its complexity and various functions. Note that a pure protein solution, while a simple system, can be thought of as the dilute limit of whole blood, which is the most complex bio-fluid.

During the past decade, significant progress has been observed in the drying droplets of bio-colloids, such as [bovine serum albumin (BSA), and lysozyme] protein [3–6], plasma [7], DNA [8], serum [9], blood [10], etc., due to biomedical and forensic applications [9,11–15]. The coupling between the droplet and the substrate, the surrounding environment, and the constituent particles show a wide variability range [16]. This wide range leads to multiple questions that many researchers attempted to answer in recent years [17–20]. For example, is the droplet pinned to the substrate? If so, what is the effect on the droplet once it dries up? How does the morphological pattern relate to the initial state of constituent particles? Why does the droplet form cracks? How does the initial contact angle affect the morphology of the droplet? Despite the intense research at each hierarchy level, for example, blood, plasma, and protein, a few studies are conducted to understand such levels' connection in terms of drying droplets. Manouk et al. [21] have investigated how the blood, plasma, and the plasma's molecular components (especially BSA) influence the

drying evolution and morphological patterns. They concluded that each hierarchy level has a role in deciding the physical mechanism involved during the drying process. Though this work provides preliminary information, many crucial questions were unanswered. For example, does the hierarchy influence the wettability of the droplets? How do the microstructures at each level get affected? How does the droplet at each hierarchy behave in different environmental conditions?

Pal et al. [22] conducted a systematic study on the most complex bio-colloid, blood, to understand the self-assembling mechanisms during the drying process. The study reveals a concentration-driven phase transition when the blood is precisely diluted in de-ionized water. The analysis of three different independent measurements (textural analysis, contact angle measurements, and the morphology) confirmed that the complex combinations of the chemical potentials among the cellular components are responsible for such origin. The progress made by Pal et al. [22] on the drying evolution, and the resulting morphological patterns in the diluted blood samples lead to some consequent exciting questions: what happens to the phase transition when a one-component system replaces the multi-component? What kind of interactions plays a role in this type of transition? Does the wettability of the droplet change for a one-component system? How does it change during the drying process? Does the temperature affect differently for one and multi-component drying droplets?

To address these questions, the present study attempts to explore the drying evolution and final morphology of a complex (whole human blood) and a simple (BSA) droplets by varying the initial concentrations at different controlled substrate temperatures. Bright-field optical microscopy is used to capture images during the drying process and of the final dried films. The wetting properties of these droplets are investigated by measuring their contact angles through the drying process. Finally, scanning electron microscopy is used on the final dried morphology to illuminate structural information. The comparison between these two systems reveals the influence of multiple components' interactions versus features that depend on single-molecule self-interactions.

2. Materials and Methods

A volume of 1 μL whole human blood of a healthy donor contains a few cellular components such as 400 to 500 $\times 10^4$ of RBCs, 0.5 to 1 $\times 10^4$ of WBCs, 14 to 40 $\times 10^4$ of platelets, along with a small amount of proteins, salt ions, etc. [1]. The bovine serum albumin (BSA) present in the cows' blood is chemically identical to the globular protein present in human blood [23]. Each BSA comprises a molecular mass of ~ 66.5 kDa, and a prolate ellipsoid shape [24,25].

The anti-coagulant (Na-Citrate) mixed whole human blood (Catalog number 7203706) was purchased from Lampire Biological Laboratories (Campbell, CA, USA). The blood is diluted by adding different volumes of de-ionized water (Millipore, 18.2 $\text{M}\Omega\cdot\text{cm}$ at ~ 25 $^\circ\text{C}$) to prepare a different range of initial blood concentrations (ϕ_b) of 75, 62, 50, 25, and 12.5% (v/v). It must be noted that the diluent (de-ionized water) in the whole blood could change the native environment of the blood's components. It is beyond the scope of this paper if any changes in their structures happen prior to the drying process. Therefore, the images are captured soon after the sample preparation to avoid further complications (if any). The various amounts of BSA protein powder (Catalog no. A2153, Sigma Aldrich, St. Louis, MO, USA) was dissolved in 1 mL of de-ionized water to prepare the initial protein concentration (ϕ_p) of 20, 9, 5, 3, and 1 wt%. It can be argued that the usage of buffered saline instead of the de-ionized water will ensure maintaining the native states of the cellular components in the blood and the BSA particles' conformations. However, one of the primary concerns of this article is to explore the drying mechanism and its effects on their behavior without adding any external salts.

A volume of ~ 1 μL of each sample is pipetted on a coverslip (Catalog number 48366-045, VWR, USA) to form a ~ 2 mm diameter droplet under ambient conditions (room temperature of ~ 25 $^\circ\text{C}$ and relative humidity of $\sim 50\%$). The coverslip is transferred to the

hot stage attached to the bright-field optical microscope (Leitz Wetzlar, Germany) within ~ 45 s. The temperature controller was set at different temperatures (T) of 25, 35, and 45 °C to run the blood samples' experiments. Besides these temperatures, $T = 55$ °C is added for the BSA samples. It is worthwhile to mention that the T should be less than the denaturing temperature (T_d) of the sample as their structures and functions might get transformed above T_d . The T_d of the human blood and the BSA is ~ 45 °C [26] and ~ 65 °C [27].

The time-lapse images were recorded under a $5\times$ magnification every two seconds. An 8-bit digital camera (Amscope MU300) and a fixed resolution of 2048×1536 pixels were used for acquiring those images. The images of the dried samples were captured within 24 h. All of the experiments were repeated three times at each concentration and temperature to ensure the outcomes' consistency. The samples show high reproducibility.

An image processing technique is adopted (using ImageJ [28]) to conduct the quantitative analysis of the images captured during the drying process. The oval tool in ImageJ was used to select the region of the droplet. The statistical mean and the standard deviation of the images are computed. The radius of the fluid front (r) is measured five times at each time (t). The time evolution of the averaged radius ($\bar{r}(t)$) is obtained during the drying process. Finally, the averaged radius of the droplets (\bar{R}) is also calculated at each concentration. The parameter, $\bar{r}(t)/\bar{R}$, is plotted as a function of time. The averaged ring width (\bar{w}) of the dried film is also measured. The crack spacing (x_c) is computed by drawing a circular line at each crack domain. The detailed procedure can be found in our previous papers [29,30]. The \bar{w}/\bar{R} and \bar{x}_c are plotted as a function of the initial concentration at each temperature.

The contact angle measurements are done under ambient conditions (temperature of ~ 25 °C and relative humidity of $\sim 50\%$) using the contact angle goniometer (Model 90, Ramé-hart Instrument Company, Succasunna, NJ, USA). The scanning electron microscopy (JEOL-7000F, JEOL Inc., Peabody, MA, USA) is used for the microstructural analysis of the dried films. The sputter-coating with a 4 nm layer of gold nanoparticles at the accelerating voltage of 3 kV and the probe current of 5 mA.

3. Results

3.1. Qualitative Analysis

3.1.1. Whole Human Blood: The Most Complex Bio-Colloid

Figure 1 shows the morphology of the whole human blood droplet dried during 24 h at different substrate temperatures (T) ranging from 25 to 45 °C. The various initial concentrations of blood (ϕ_b) from 100 (undiluted whole blood) to 12.5% (v/v) (diluted whole blood) are also studied at this temperature range. The whole blood texture changes from dark (at ϕ_b of 100%) to light gray (at ϕ_b of 12.5%) as we dilute its initial concentration. A ring-like feature is found at all ϕ_b at $T = 25$ °C; however, it can be prominently observed at ϕ_b of 50 to 12.5% (v/v). It is to be noted that the ring (or the rim) terminology is the same as the blood's corona in this study. The ring's width (w) decreases, and the central region's width increases as ϕ_b is diluted. Both of these regions are found in all the samples except 100% (v/v) at $T = 35$ and 45 °C as well as 75% (v/v) at $T = 45$ °C. A uniform dark-gray texture is found in both of these regions for the samples ranging from 100 to 62% (v/v). The difference in their textures gets visible from 50 to 12.5% (v/v). The central region becomes lighter than the ring at this range. It indicates that the ring and the central regions are at different heights from 50 to 12.5% (v/v) [22]. Interestingly, the elevated temperatures (T of 35 and 45 °C) show a sharp-edged ring compared to $T = 25$ °C, independent of their initial concentration.

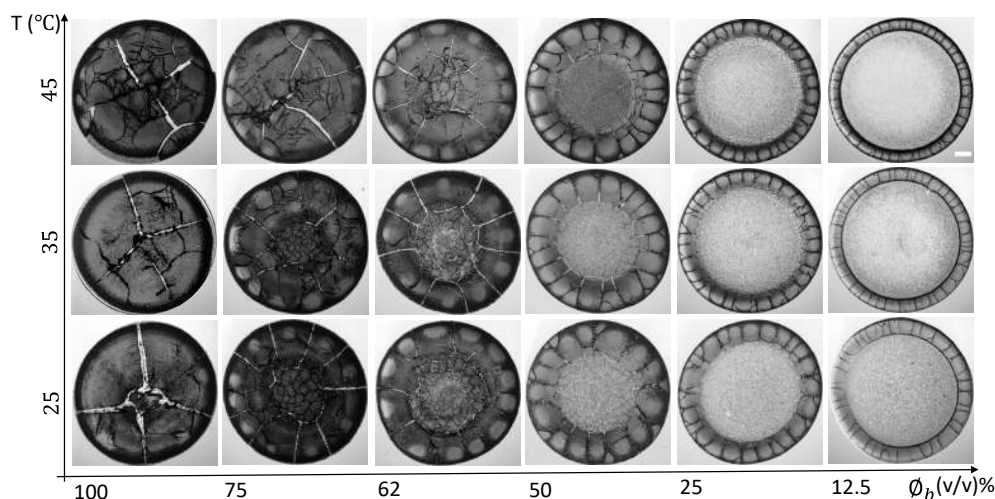


Figure 1. Morphology of the whole human blood film during 24 h at different initial concentrations (ϕ_b) ranging from 100 to 12.5% (v/v) that are dried at various substrate temperatures (T) of 45, 35, and 25 °C. The scale bar of length 0.2 mm is represented by the white rectangle in the top-right panel.

The ϕ_b of 100% (v/v) at $T = 25$ °C has four radial cracks. These cracks divide the ring (or the corona) into large-sized domains (a similar behavior is observed in [1,19]). Some of the micro-flaws are noticed in these domains. The crack lines are thick. The number of these cracks is increased as we dilute the sample. It is to be noted that the length of these cracks is directly proportional to the ring's width. The thick crack lines become thin as the sample is diluted. Looking around the edges at ϕ_b of 100% (v/v) suggests that these cracked domains are not firmly attached to the substrate. Some of these domain sheets are moved towards the center, and some are away. These misplaced sheets are profoundly exhibited at $T = 45$ °C. These dried films' high magnified images display that these films firmly adhere to the substrate (coverslip) at ϕ_b of 50 to 12.5% (v/v). The small-sized random cracks in the central region are only seen at ϕ_b of 100 to 62% (v/v) under our study's present resolution. Surprisingly, the blood samples' crack morphology does not significantly change at the elevated temperatures (T of 35 and 45 °C).

Figure 2(I,II)a–f examines the drying evolution of the blood droplet at ϕ_b of 100 and 12.5% (v/v), respectively, at the substrate temperature (T) of 45 and 25 °C. The first image is captured within ~ 70 s after the droplet's deposition on the substrate (Figure 2(I,II)a). The images at 12.5% (v/v) are lighter than 100% (v/v) under ambient and elevated temperatures. The first stage of the drying process started when the fluid front moves from the periphery towards the central region exhibited in Figure 2(I,II)b,c. The light gray texture starts appearing as the front moves, which is observed predominantly at 100% (v/v). However, the change of the texture is not notable at 12.5% (v/v) as the first captured image is already of light gray shade (Figure 2(I,II)a,b). Soon after this movement, the droplet is found to have two distinct regions, the ring (or the corona) and the central regions at $T = 25$ °C. Interestingly, the corona's edge is found to be sharp at $T = 45$ °C.

The second stage of the drying process marks the propagation of the cracks. The morphological difference between the undiluted and the diluted blood droplets begins from this stage (Figure 2(I,II)c,d). The cracks propagate radially from the center to the periphery in the undiluted blood sample [100% (v/v)]. In contrast, these cracks move from the periphery to the corona (or the ring) at $\phi_b = 12.5$ % (v/v). Subsequently, the cracked domains get detached from the substrate, whereas the central region still adheres to the substrate at ϕ_b of 100% (v/v) and $T = 25$ °C. The radial cracks propagate throughout the droplet at $T = 45$ °C, leading to the absence of the central region. The increased number of the micro-flaws and an additional sliding of the sheets are also observed at $T = 45$ °C (Figure 2(I)e,f).

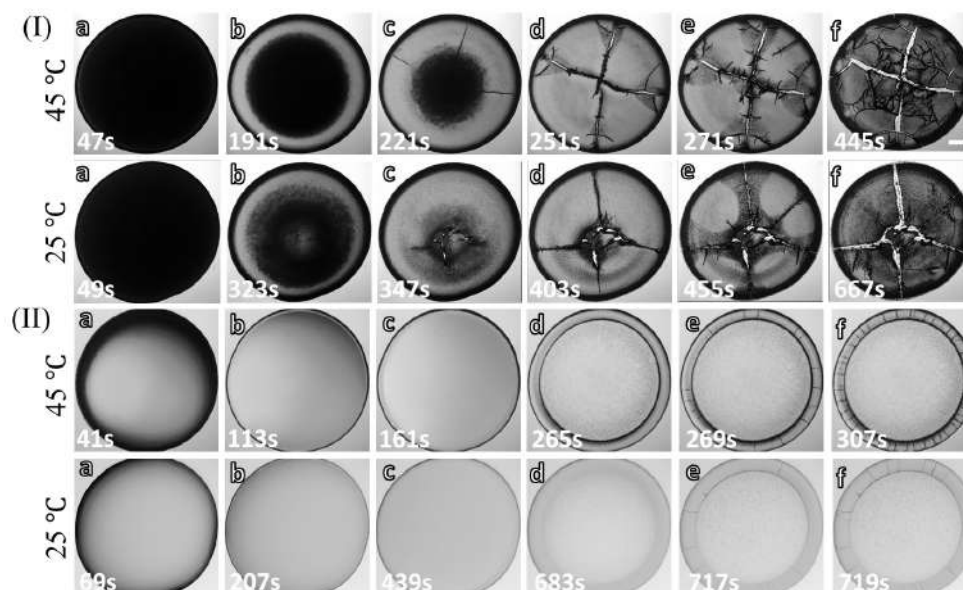


Figure 2. Time evolution of the blood droplets during the drying process: (a–f) display the drying stages at the substrate temperature (T) of 45 and 25 °C at the initial concentration (ϕ_b) of 100% (v/v) in (I) and 12.5% (v/v) in (II). The scale bar of length 0.2 mm is represented with the white rectangle in the top-right panel.

The third stage involves changing the texture (from the light to the dark gray), the appearance of the micro flaws from these radial cracks, and the widening of these radial cracks. However, this stage is found to be absent at 12.5% (v/v) [Figure 2(II)e,f].

3.1.2. Bovine Serum Albumin Protein: The Simplest Bio-Colloid

Figure 3 shows the morphology of the bovine serum albumin (BSA) droplet dried for 24 h at different substrate temperatures (T) of 25 to 55 °C and various initial concentrations (ϕ_p) ranging from 20 to 1 wt%. Unlike the blood sample (Figure 1), all BSA's dried films show a uniform light gray texture. The “coffee-ring” [31] like behavior is seen at every ϕ_p [25,32]. These films exhibit a shadowy dark texture around the inner edge of the ring. This texture differentiates the film into two separate regions, the rim (or the ring), and the central regions. It also indicates that the ring is at a higher height than the central region. The shadowy texture is prominent at 20 as compared to 1 wt%. This suggests that their heights' differences are more profound with the increase of BSA's initial concentration. A peripheral dark band is noticed at $\phi_p = 20$ wt% and minimized as we dilute the samples to 1 wt%. Similar to the whole blood dried film (Figure 1), the ring's width (w) is found to be dependent (decreased) as ϕ_p is diluted from 20 to 1 wt% at every temperature.

Furthermore, the sharp-edged ring is found at elevated temperatures (T from 35 to 55 °C). Unlike the blood samples, the cracks in BSA films are mostly observed in the ring. These cracks intervene from the ring to the central regions at ϕ_p of 20 and 9 wt%. No cracks are found in the central region from 5 to 1 wt%. Most of the cracks are radial, dividing the ring into large-sized domains. The orthoradial cracks are mainly observed to join the consecutive radial cracks (reported in our paper, [25]). Interestingly, the number of radial cracks in the blood increases, whereas its number reduces as the BSA's initial concentration is diluted. In contrast, the radial cracks' length reduces in both the blood and the BSA samples with dilution. Interestingly, some curved flaws are noticed around the corners of these domains at ϕ_p of 20 wt% and $T = 55$ °C.

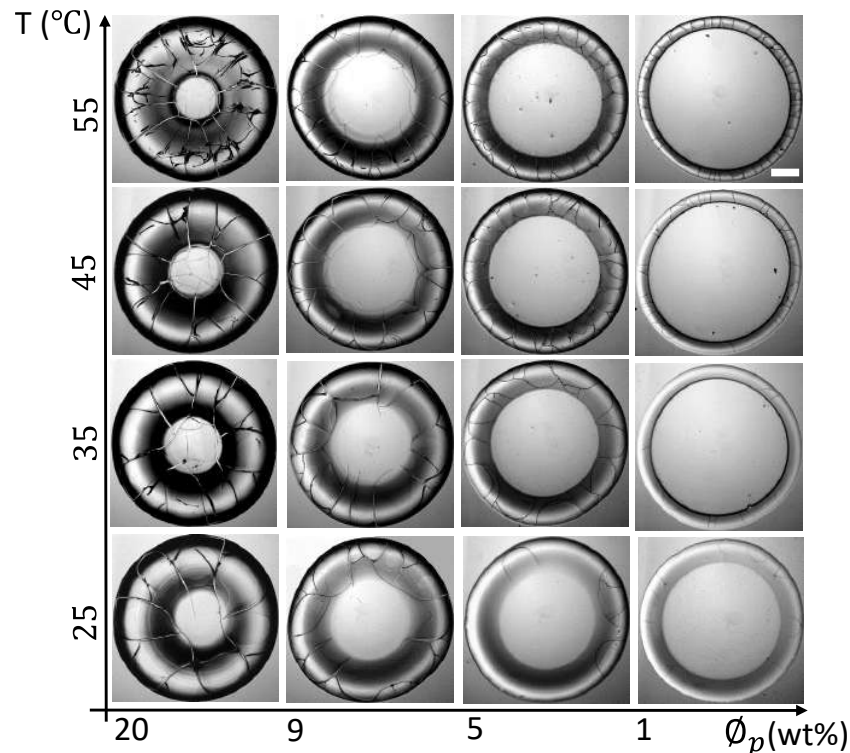


Figure 3. BSA film's morphology during the 24 h at different initial concentrations (ϕ_p) ranging from 20 to 1 wt% dried at various substrate temperatures (T) of 55, 45, 35, and 25 °C. The scale bar of length 0.3 mm is represented with the white rectangle in the top-right panel.

Figure 4(I,II)a–f illustrates the various stages of the BSA droplets' drying process. The concentrated (ϕ_p of 20 wt% in Figure 4(I)a–f and the most diluted (1 wt% in Figure 4(II)a–f) samples are selected for studying the drying evolution at T of 55, and 25 °C. After the droplets are pipetted (Figure 4(I,II)a), the fluid front recedes from the periphery towards the central region (Figure 4(I,II)b–d); similar to what is also observed in the blood droplets (Figure 2(I,II)b,c) [22,25]. This indicates that the first stage is a characteristic of a drying bio-colloidal droplet, which does not depend on the constituent particles' type. Along with the fluid front movement, a prominent dark peripheral band is observed at $\phi_p = 20$ wt%. No such band is found in 1 wt% at T = 25 °C; however, a thin dark circular line is exhibited at T = 55 °C. The distinct regions (the ring and the central) are noticed as the fluid front movement approaches its end. Simultaneously, the cracks propagate from the periphery towards the central region like the diluted blood droplet at ϕ_b of 12.5% (v/v). The cracks mostly appear in all the samples except for ϕ_p of 1 wt% and T = 25 °C. The long radial cracks generate, and, subsequently, the orthoradial cracks join these radial cracks (Figure 4(I,II)d–f). Some of the curved flaws also start forming at ϕ_p of 20 wt% and T = 55 °C. The ϕ_p of 1 wt% at T = 55 °C shows that the cracks do not propagate in the central region, whereas these cracks intervene at 20 wt%. The different observations in the blood and the protein samples are detailed in the next section.

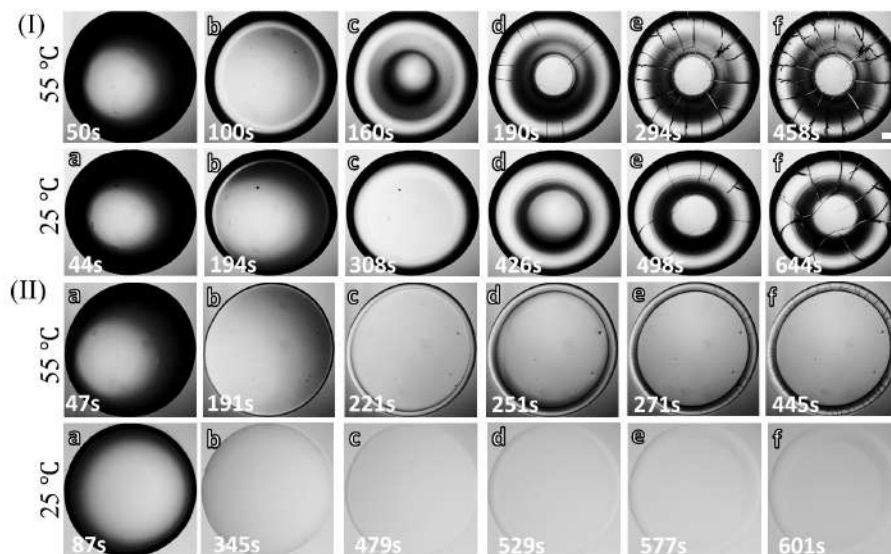


Figure 4. Time evolution of BSA droplets at different substrate temperature (T) during the drying process: (a–f) display different stages at the initial concentration (ϕ_p) of (I) 20 wt% for T of 55 and 25 °C, and (II) 1 wt% at T of 55 and 25 °C. The scale bar (0.2 mm length) is shown with the white rectangle in the top-right panel.

3.2. Quantitative Analysis

3.2.1. Drying Evolution of the Complex Bio-Colloid

Figures 5a–f and 6a–f show the drying evolution of the statistical image parameters, the mean and the standard deviation [in arbitrary units, (a.u.)] of the blood droplets at the different initial concentrations (ϕ_b) of 100 to 12.5% (v/v), respectively. The substrate temperature (T) of 45 °C is presented in the left y-axis, and T = 25 °C is displayed in the right y-axis. The x-axis exhibits the drying times in seconds for both temperatures.

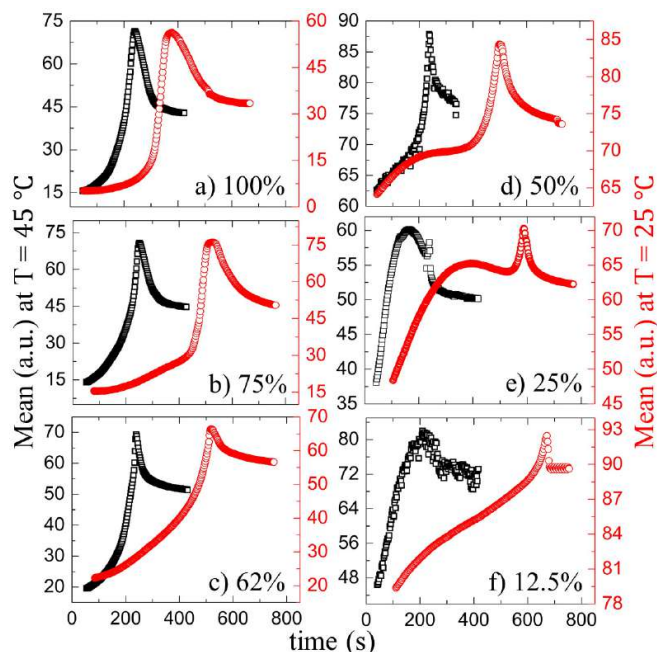


Figure 5. Time evolution of the statistical image parameter, the mean [in arbitrary units, (a.u.)] of the blood droplets at the different initial concentrations (ϕ_b) of 100 to 12.5% (v/v), respectively, in (a–f). The black and the red colors represent the mean at 45 and 25 °C respectively.

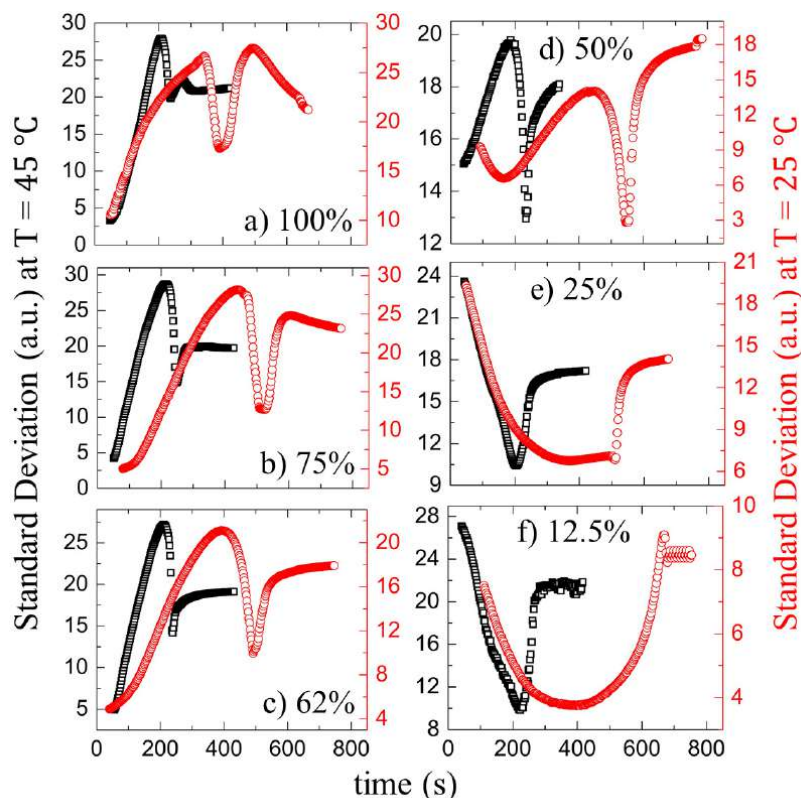


Figure 6. Time evolution of the statistical image parameter, the standard deviation [in arbitrary units, (a.u.)] of the blood droplets at the different initial concentrations (ϕ_b) of 100 to 12.5% (v/v), respectively, in (a–f). The black and the red colors represent the standard deviation at 45 and 25 °C respectively.

The mean is defined as the sum of the pixel values divided by the number of the pixels [30,33]. The mean shows three distinct phases: a rapid rise follows the initial increase, after which a peak appears and, finally, decreases to reach the saturation stage. The initial rise of the mean is when the fluid front starts moving from the periphery to the central region. When the gray texture starts appearing significantly, the pixel values increase, resulting in the mean rapid rise (Figures 5a,f and 2(I,II)a–f). Soon after reaching the maximum values, the mean begins to decrease when the cracks propagate. The standard deviation (SD) ranges from 100 to 50% (v/v) at both temperatures starts with a rapid rise, followed by a dip. Finally, it increases to reach saturation. The SD measuring the image texture's complexity can capture the finer textural details [30,33]. The uniformity of the image after the deposition of the droplet is the highest. The dark gray texture of the image for the range from 100 to 62% (v/v) signifies the low value of the SD. It follows a rise and a dip when the mean increases. The pixel values increase (the mean expands) in the process of changing the texture; however, the image's uniformity is reduced (or the complexity is escalated). As soon as the front progresses significantly, it results in a dip of the SD values. The growth of these cracks breaks the uniformity, and the SD shoots up.

Interestingly, the SD starts with a high value and reduces at ϕ_b of 25 and 12.5% (v/v) (Figure 6e,f). The uniformity of the images deteriorates due to the presence of the lower pixel values in the light gray textured images at this concentration range. It exhibits a broad dip during the fluid front movement. The crack propagation leads to an increase in their values. In addition, finally, it gets saturated at every ϕ_b as the drying process ends. It is to be noted that the substrate temperature does not induce any significant changes in their behavior (Figures 5 and 6).

Figure 7(I,II) shows the time evolution of the averaged fluid front radius [$\bar{r}(t)$] that is normalized with the averaged radius of the droplet (\bar{R}) at different diluting concentrations

(ϕ_b) ranging from 100 to 12.5% (v/v). The parameter, $\bar{r}(t)/\bar{R}$, is plotted at T of 45 °C in Figure 7(I) and 25 °C in Figure 7(II). The $\bar{r}(t)/\bar{R}$ at 45 °C shows an initial slow linear and a later fast nonlinear regime. The averaged fluid front radius [$\bar{r}(t)$] is plotted as a function of time at both temperatures. Subsequently, the velocity (or the slope) of the fluid front is analyzed. The initial slope values (m_1) are calculated when a linear fit is done in the linear regime. The m_1 is found to be weakly dependent on the initial concentration (ϕ_b). It varies from $-1.3 \mu\text{m s}^{-1}$ to $-0.4 \mu\text{m s}^{-1}$. The negative sign indicates that the radius of the fluid front reduces with the drying time. The final slope values (m_2) are extracted by doing a linear fit in the nonlinear regime. A strong dependency of m_2 on ϕ_b is found. It reduces from $-8.8 \mu\text{m s}^{-1}$ to $-1.0 \mu\text{m s}^{-1}$ as ϕ_b is diluted [inset of Figure 7(I)]. The average value of m_2 is $-5.4 \pm 3.1 \mu\text{m s}^{-1}$. On the other hand, the parameter $\bar{r}(t)/\bar{R}$ shows a weak nonlinearity in the later time at T = 25 °C. Therefore, the slope values (m) are determined from the whole range. The average value of m is $-0.5 \pm 0.2 \mu\text{m s}^{-1}$, which is weakly dependent on ϕ_b . It is to be noted that the radius of the fluid front could only be measured when it covers $\sim 20\%$ of the whole droplet at 25 °C, whereas it covers $\sim 60\%$ of the total droplet area at 45 °C.

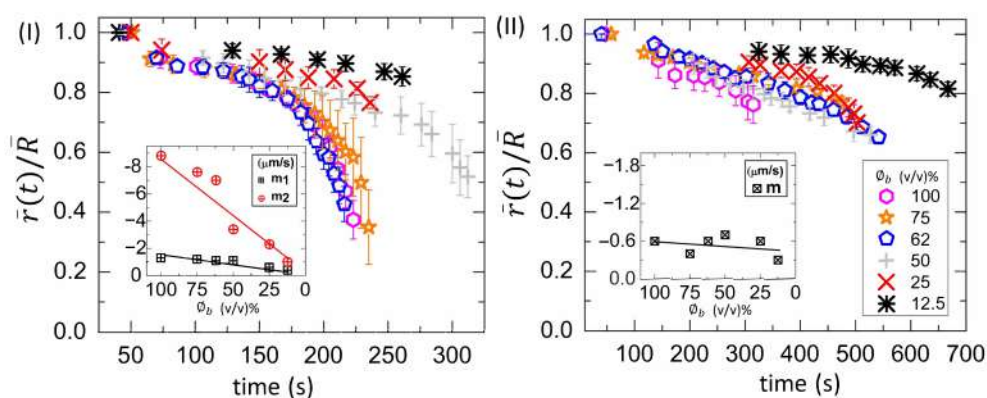


Figure 7. Time evolution of the normalized fluid front radius ($\bar{r}(t)/\bar{R}$) at different initial concentration (ϕ_b) ranging from 100 to 12.5% (v/v) in the whole blood droplets at various substrate temperatures (T) of 45 °C in (I) and 25 °C in (II). The initial (m_1) and final (m_2) slope values are calculated from ($\bar{r}(t)$) measurements in each region at T = 45 °C, whereas the slope values (m) are determined from the whole range at T = 25 °C. The variation of the slope with ϕ_b is displayed in the insets of (I) and (II).

The wettability of these blood droplets at T = 25 °C is examined by measuring the contact angle during the drying process [Figure 8(I,II)]. The contact angle is the angle formed by the interfaces of substrate–blood, blood–air, and substrate–air [2]. It shows the drying evolution of the normalized contact angle ($\theta(t)/\Theta$) at different initial concentrations (ϕ_b) ranging from 100 to 62% (v/v) in Figure 8(I) and from 50 to 12.5% (v/v) in Figure 8(II). The Θ is determined by a linear extrapolation of the contact angle [$\theta(t)$] varying with time, where it appears linear (till ~ 200 s). The normalization is done by dividing $\theta(t)$ with Θ . The presence of a peak-like feature in Figure 8(I) makes the contact angle variation non-monotonic. The range from 320 to 570 s is highlighted in the inset of Figure 8(I) at ϕ_b of 75 and 62% (v/v). The value of 0.05 is added to the $\theta(t)/\Theta$ of 62% (v/v) [inset of Figure 8(I)] for the clear visualization. The peak is broad and observed during 200–300 s at $\phi_b = 100\%$ (v/v). This peak becomes small and gets delayed as ϕ_b is diluted. It is found during 400–500 s at 75 and 62% (v/v). This peak becomes absent, and a monotonic decrease of the contact angle is found from 50 to 12.5% (v/v) [Figure 8(II)]. Furthermore, the $\theta(t)$ is plotted as a function of time, and the velocity (or the slope) of the contact angle is measured. The slope for 25 and 12.5% (v/v) is found to be $-0.1351 \pm 0.0008 \text{ s}^{-1}$ (with $R^2 = 0.994$) and $-0.1971 \pm 0.0012 \text{ s}^{-1}$ (with $R^2 = 0.996$), respectively. Its increased value from ~ 0.14 to $\sim 0.20 \text{ s}^{-1}$ suggests that the angle gets steeper as ϕ_b is diluted. The negative sign indicates that the angle reduces with time.

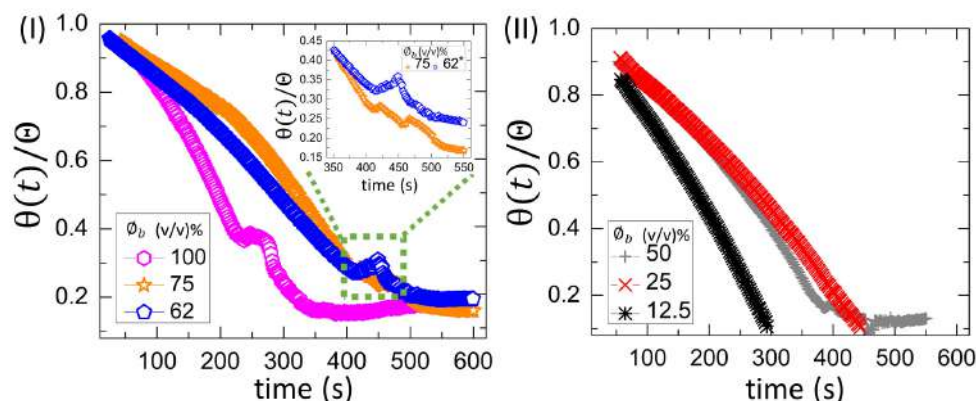


Figure 8. Time evolution of the normalized contact angle ($\theta(t)/\Theta$) in the whole blood droplets for $T = 25^\circ\text{C}$ at different initial concentrations (ϕ_b) ranging from 100 to 62% (v/v) in (I) and from 50 to 12.5% (v/v) in (II). The range from 320 to 570 s is zoomed in the inset of (I) at ϕ_b of 75 and 62% (v/v). The value of 0.05 is added to $\theta(t)/\Theta$ of 62% (v/v) (illustrated with an asterisk mark) for the clear visualization.

A comparison between Figures 7(II) and 8(I,II) reveals that both the contact angle and the fluid front radius move simultaneously at all ϕ_b except 12.5% (v/v) initially. It is to be noted that $\bar{r}(t)/\bar{R}$ is computed up to ~ 0.6 [shown in Figure 7(II)], which means that the front still moves with the time until it becomes zero. In contrast, no simultaneous movement of the contact angle and the radius is found at $\phi_b = 12.5\%$ (v/v). The contact angle reaches a minimum constant value, and, subsequently, the fluid front changes.

3.2.2. Drying Evolution of the Simplest Bio-Colloid

Figure 9(I,II) shows the drying evolution of the normalized contact angle ($\theta(t)/\Theta$) in the BSA droplets at the different initial concentration (ϕ_p) of 20 wt% in Figure 9(I) and from 9 to 1 wt% in Figure 9(II). It shows a non-monotonic decrease with a small peak at 20 wt% [Figure 9(I)]. The peak occurs from ~ 350 to ~ 450 s during the contact angle movement. It is found that this duration is the time when the fluid front moves from the periphery towards the central region [Figure 4(I)a–f]. The monotonic decrease (without the presence of any peak) is found at ϕ_p of 9 to 1 wt% (also reported in [25]). The $\theta(t)$ is plotted as a function of time, and the velocity (or the slope) of the contact angle is measured. The slope for 9, 5, and 1 wt% is found to be $-0.0731 \pm 0.0002^\circ\text{ s}^{-1}$ (with $R^2 = 0.998$), $-0.0876 \pm 0.0004^\circ\text{ s}^{-1}$ (with $R^2 = 0.996$), and $-0.0674 \pm 0.0001^\circ\text{ s}^{-1}$ (with $R^2 = 0.999$), respectively. Interestingly, the contact angle varies monotonically for both the blood droplets at ϕ_b of 50 to 12.5% (v/v) and the BSA droplets at ϕ_p of 9 to 1 wt%. However, their slope values differ, suggesting that the variation is steeper in the blood rather than the BSA droplets.

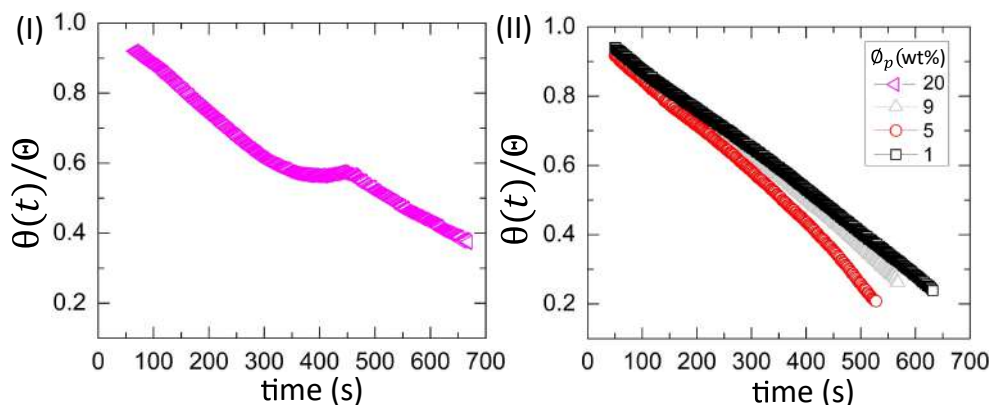


Figure 9. Time evolution of the normalized contact angle ($\theta(t)/\Theta$) in the BSA droplets at the different initial concentrations (ϕ_p) of 20 wt% in (I) and from 9 to 1 wt% in (II) for $T = 25^\circ\text{C}$.

Figure 10(I,II) shows the time evolution of the normalized fluid front radius [$\bar{r}(t)/\bar{R}$] at ϕ_p ranging from 20 to 1 wt% in the BSA droplets at a different substrate temperature (T) of 55 °C in Figure 10(I) and 25 °C in Figure 10(II). The slope values (m) are calculated from the whole range by plotting the time evolution of the $\bar{r}(t)$. The variation of m with ϕ_p is exhibited in the insets of Figure 10(I,II). The m decreases from $-4.6 \mu\text{m s}^{-1}$ to $-1.4 \mu\text{m s}^{-1}$ at $T = 55 \text{ }^\circ\text{C}$. The average value of m is $-1.3 \pm 0.3 \mu\text{m s}^{-1}$ at $T = 25 \text{ }^\circ\text{C}$.

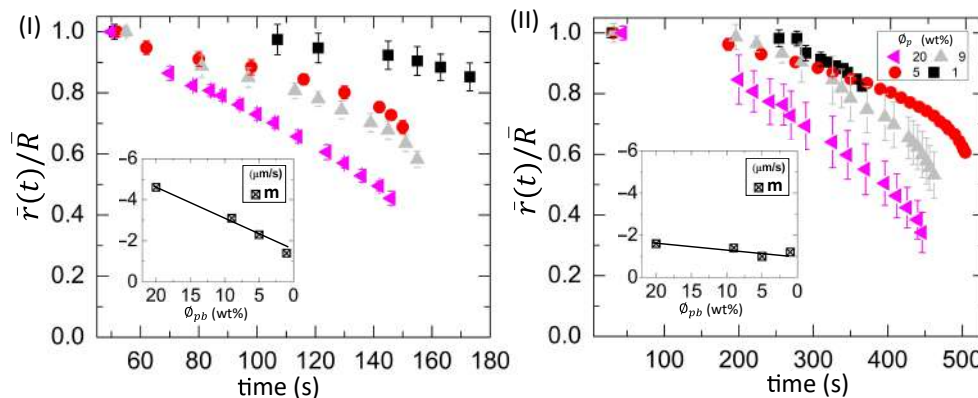


Figure 10. Time evolution of the averaged fluid front radius ($\bar{r}(t)$) that is normalized with the averaged radius of the droplet (\bar{R}) at the different initial concentration (ϕ_p) ranging from 20 to 1 wt% in the BSA droplets at different substrate temperature (T) of 55 °C in (I) and 25 °C in (II). The slope values (m) are calculated from the whole range by plotting the $\bar{r}(t)$ vs. time. The variation of m with ϕ_p is exhibited in the insets of (I) and (II).

The mapping of the contact angle [Figure 9(I,II)] and the fluid front radius [Figure 10(II)] of the BSA droplets reveals that all ϕ_p show a similar trend, unlike blood droplets. Only the contact angle reduces without any fluid front movement in the initial ~ 200 s, whereas the simultaneous movement of both the contact angle and the fluid front is found afterward.

3.2.3. Morphological Patterns of the Dried Films

Figure 11(I–III) shows the normalized ring width (\bar{w}/\bar{R}) of the blood film as a function of ϕ_b at T of 45 to 25 °C. The solid line depicts the linear fit over the whole range from 100 to 12.5% (v/v). The dotted and dash-dotted lines show the linear fit from 100 to 62, and 62 to 12.5% (v/v). It is to be noted that the linear fits for the range from 100 to 12.5% and from 100 to 62% (v/v) are not possible at $T = 45 \text{ }^\circ\text{C}$. Therefore, a dashed line is drawn for the guide to our eyes. The slope values were extracted for the different ranges of ϕ_b . The slope for the range 100 to 12.5, 100 to 62, and 62 to 12.5% (v/v) is denoted by m , m_1 , and m_2 . The m is found to be $0.0096 \pm 0.0003 \phi_b^{-1}$ ($R^2 = 0.995$) and $0.0054 \pm 0.0006 \phi_b^{-1}$ ($R^2 = 0.936$), respectively at $T = 35$ and $25 \text{ }^\circ\text{C}$. On the other hand, the m_1 is $0.0123 \pm 0.0002 \phi_b^{-1}$ ($R^2 = 0.999$), and $0.0089 \pm 0.0021 \phi_b^{-1}$ ($R^2 = 0.891$), respectively, at $T = 35$ and $25 \text{ }^\circ\text{C}$. In addition, m_2 is $0.0094 \pm 0.0020 \phi_b^{-1}$ ($R^2 = 0.873$), $0.0067 \pm 0.0006 \phi_b^{-1}$ ($R^2 = 0.999$), and $0.0051 \pm 0.0008 \phi_b^{-1}$ ($R^2 = 0.928$), respectively, at $T = 45, 35,$ and $25 \text{ }^\circ\text{C}$. The higher R^2 value of m compared to that of m_1 and m_2 indicates that the linear fit is better suited for the whole range of ϕ_b instead of splitting the fits at 62% (v/v).

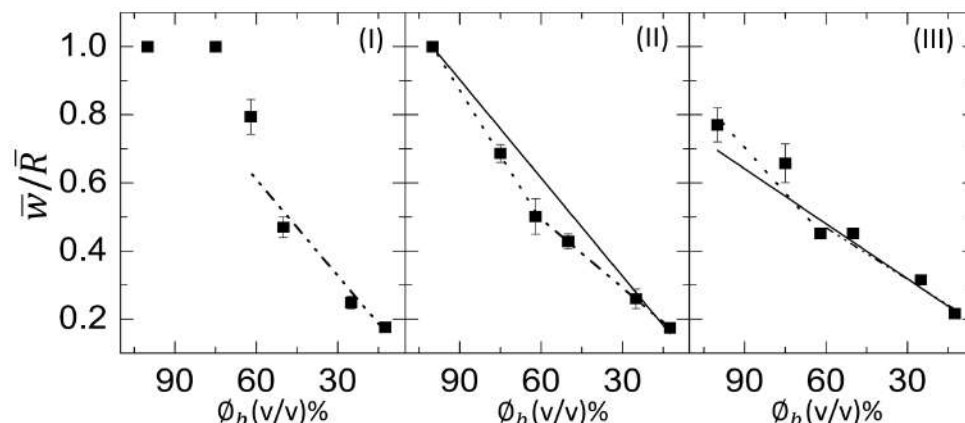


Figure 11. Concentration dependence of the normalized ring width (\bar{w}/\bar{R}) of the whole human blood film at different substrate temperatures (T) at (I) 45 °C, (II) 35 °C, and (III) 25 °C. The solid line depicts the linear fit over the whole range from 100 to 12.5% (v/v). The dotted and dash-dotted lines show the linear fit from 100 to 62%, and 62 to 12.5% (v/v), respectively. The dashed line at $T = 45$ °C is a line drawn to guide our eyes.

The variation of the averaged crack spacing (\bar{x}_c) of the blood film as a function of ϕ_b at 45, 35, and 25 °C is presented in Figure 12(I–III), respectively. Similar to Figure 11(I–III), the slope values (m , m_1 , and m_2) are extracted for various concentration ranges. The m is found to be $0.0056 \pm 0.0006 \text{ mm } \phi_b^{-1}$ ($R^2 = 0.942$) at $T = 45$ °C. As we decrease the temperature to 35 °C, the m reduces and is observed to be $0.0049 \pm 0.0013 \text{ mm } \phi_b^{-1}$ ($R^2 = 0.721$). Finally, the m becomes $0.0034 \pm 0.0012 \text{ mm } \phi_b^{-1}$ ($R^2 = 0.579$) at room temperature of 25 °C. In contrast, the m_1 is $0.0081 \pm 0.0008 \text{ mm } \phi_b^{-1}$ ($R^2 = 0.982$), and $0.0081 \pm 0.0015 \text{ mm } \phi_b^{-1}$ ($R^2 = 0.934$) at the elevated temperatures, 45 and 35 °C, respectively. At $T = 25$ °C, the m_1 is $0.0011 \pm 0.0015 \text{ mm } \phi_b^{-1}$ ($R^2 = 0.960$). The m_2 is $0.0039 \pm 0.0005 \text{ mm } \phi_b^{-1}$ ($R^2 = 0.958$), $0.0029 \pm 0.0007 \text{ mm } \phi_b^{-1}$ ($R^2 = 0.844$), and $0.0016 \pm 0.0005 \text{ mm } \phi_b^{-1}$ ($R^2 = 0.736$), respectively, at $T = 45, 35,$ and 25 °C. Unlike the \bar{w}/\bar{R} , R^2 values of m_1 and m_2 at all temperatures increases compared to m when \bar{x}_c is plotted as a function of ϕ_b . The slope values change for different ranges of the linear fits done from 100 to 62, and 62 to 12.5% (v/v). A kink is observed at 62% (v/v) in all temperatures; however, it reduces with the increase of the temperature [oval line in Figure 12(I–III)].

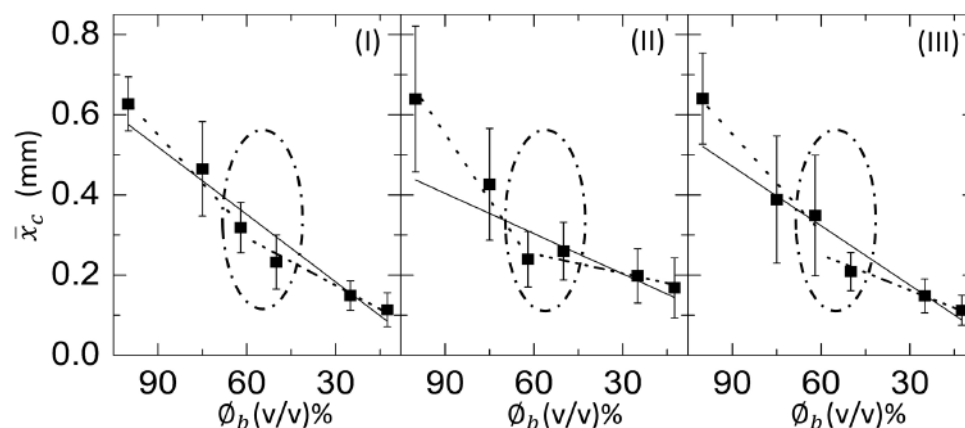


Figure 12. Concentration dependence of the averaged crack spacing (\bar{x}_c) of the whole human blood film at different substrate temperatures (T) at (I) 45 °C, (II) 35 °C, and (III) 25 °C. The solid green line depicts the linear fit done over the whole range from 100 to 12.5%. The dotted and dash-dotted lines show the linear fit from 100 to 62, and 62 to 12.5% (v/v). The oval line highlights a kink at 62% (v/v).

Figure 13(I,II) shows the variation of the normalized ring width (\bar{w}/\bar{R}) and the averaged crack spacing (\bar{x}_c), respectively, as a function of ϕ_p in the BSA film at T ranging from 55 to 25 °C. The green solid line depicts that the width of the ring decreases with the dilution. The slope values of \bar{w}/\bar{R} at T = 55, 45, 35, and 25 °C are $0.033 \pm 0.004 \phi_p^{-1}$ ($R^2 = 0.960$), $0.029 \pm 0.006 \phi_p^{-1}$ ($R^2 = 0.893$), $0.033 \pm 0.007 \phi_p^{-1}$ ($R^2 = 0.866$), and $0.026 \pm 0.004 \phi_p^{-1}$ ($R^2 = 0.945$), respectively. These values indicate that the \bar{w}/\bar{R} is independent on the temperature. In contrast, the \bar{x}_c exhibits a strong dependency on the temperature. The different colored dashed lines guide us to understand the variation of the \bar{x}_c with the substrate temperature. The straight line of \bar{x}_c suggests that it is nearly independent of ϕ_p at T = 55 °C. As T decreases from 55 to 25 °C, the \bar{x}_c reduces from ~ 0.45 mm to ~ 0.21 mm.

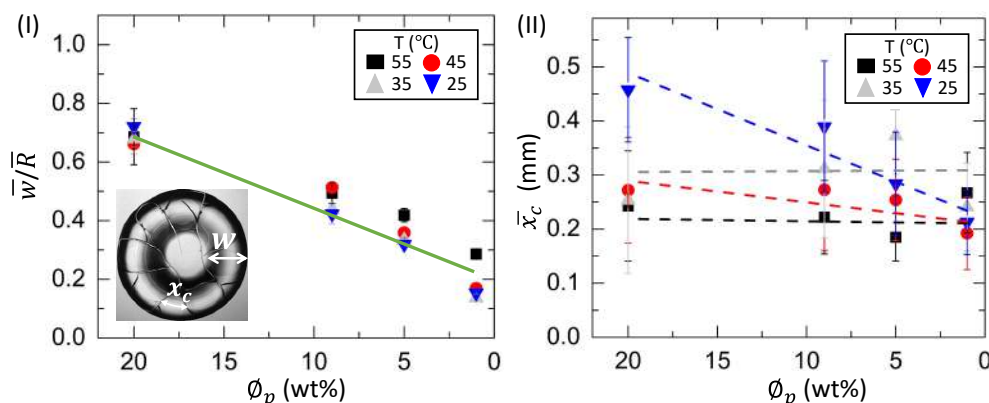


Figure 13. (I) Concentration dependence of the normalized width of the ring (\bar{w}/\bar{R}) of the BSA film at different substrate temperatures (T) from 55 to 25 °C. The green solid line shows a master linear fit. (II) Concentration dependence of the averaged crack spacing (\bar{x}_c) of the BSA film at different T from 55 to 25 °C. The different colored dashed lines at different temperatures are drawn to guide our eyes. The x_c and w are shown on the dried BSA film at ϕ_p of 20 wt% and T = 25 °C.

4. Discussion

Figures 14(I,II)a–c and 15(I,II)a–c show the physical mechanism of both the blood and BSA droplets (please refer to our previous publications [22,25] for further details in this regard). The capillary flow (Figures 14(I,II)a and 15(I,II)a) drives the particles towards the droplet periphery. As time progresses, a BSA-rich layer is observed to form in the one-component system (aqueous BSA solution in (Figure 15(I,II)b). On the other hand, a plasma protein-rich layer develops in the multi-component system (diluted whole blood droplets in Figure 14(I,II)b). With the advancement of time, more water starts evaporating from these droplets, leading to an interaction of the droplet particles. The BSA particles interact in the protein droplets, whereas the cellular components (WBCs, RBCs, and platelets) (significantly) interact in the blood droplets. We assumed that many of these particles and their interactions near the periphery disturb the contact angle measurements. For example, the non-monotonic decrease of the contact angle is observed at ϕ_b of 100 to 62% (v/v) in blood droplets and at ϕ_p of 20 wt% in the BSA droplets [Figures 8(I) and 9(I)]. Please refer to [22] for a detailed discussion on the origin of such non-monotonic property. The drying mechanism of the one component (simplest) and the multi-component (complex) bio-colloidal droplets discussed in this paper firmly establishes the fact that the non-monotonic property (i.e., the presence of the peak-like feature) is indeed a universal property that can be observed across any high-concentrated colloidal samples. A similar observation (i.e., the presence of such non-monotonic property) has recently been reported in the polymeric system [34] that further supports our claims.

A comparison amongst the macroscopic images of the drying process (Figures 2(I,II)a–f and 4(I,II)a–f) confirms that the peak-like feature obtained from the contact angle measurements (non-monotonic property) appears only during the fluid front movement. This indicates that a sufficient amount of water is still present in the droplet to preserve these

particles' native states. Both these droplets, however, experience mechanical stress as soon as the water reduces significantly. This (mechanical) stress affects the native states of RBCs and WBCs and alters the platelets' biological activity in the blood droplet. The microstructural analysis of the dried films at 100% (v/v) reveals a uniform texture (also reported in [19,22]) in the ring (marked with a black arrow in Figure 14(I)c). The RBC membranes create this uniform layer, and some deformed RBCs are observed in the cracked peripheral region (indicated with a white arrow in Figure 14(I)c). The central region is crammed with mostly WBCs (the ridges and troughs-like structures) and the platelets (the spread structure with extended filopodia). Some spicule-shaped RBCs are found near the ring's inner edge at 12.5% (v/v) (within the orange rectangle in Figure 14(II)c). The sickle-shaped RBCs and the discoid-shaped inactivated platelets are observed in the central region (marked with the blue rectangle in Figure 14(II)c). Please refer to [22] for a detailed microstructural discussion. Interestingly, BSA dried films' micrographs show a uniform texture (Figure 15(I,II)c). This indicates that these protein structures are at a shallow length scale (unlike blood dried films), and the magnification is not enough to analyze at those length scales.

It is worth mentioning that the morphological texture and the (crack) patterns significantly affect the blood droplets (Figures 1 and 2), but not the BSA droplets (Figures 3 and 4). The sliding of the cracked films is observed at ϕ_b of 100 to 62% (v/v); it is, however, absent at ϕ_b of 50 to 12.5% (v/v) [Figure 1, reported in [22]]. On the other hand, all the samples of BSA show that the dried films firmly adhere to the substrate (Figure 3, reported in [25]). Contrary to these blood samples, the \bar{x}_c is found to have a weak concentration dependence in the BSA films (Figure 13(II)). The crack patterns are similar in all the protein samples, which is possibly due to the absence of different-sized components. Furthermore, the ring's height is higher than the central region at $\phi_p = 20$ wt%, and it reduces as we dilute ϕ_p to 1 wt% (Figure 15(I,II)c). The corona region of the blood film at the highest dilution [ϕ_b of 12.5% (v/v)] nearly mimics the homogeneous texture of the BSA blood films [Figures 14(II)c and 15(II)c]. The dried films of both simplest and complex bio-colloidal films show a gradual decrease when the ring's normalized width is plotted with the initial concentration [Figures 11(I–III) and 13(I)]. This trend indicates that the width of the ring measures the deposition of the particles. When the number of particles is high, the ring's width is more (reported in one of our papers in [25]). As the number reduces, the ring's width decreases; however, the self-assembling mechanism is different during their deposition. The different self-interacting mechanism (of a large number of components) is observed for other complex multi-component systems [29,32,33], not specifically to the blood.

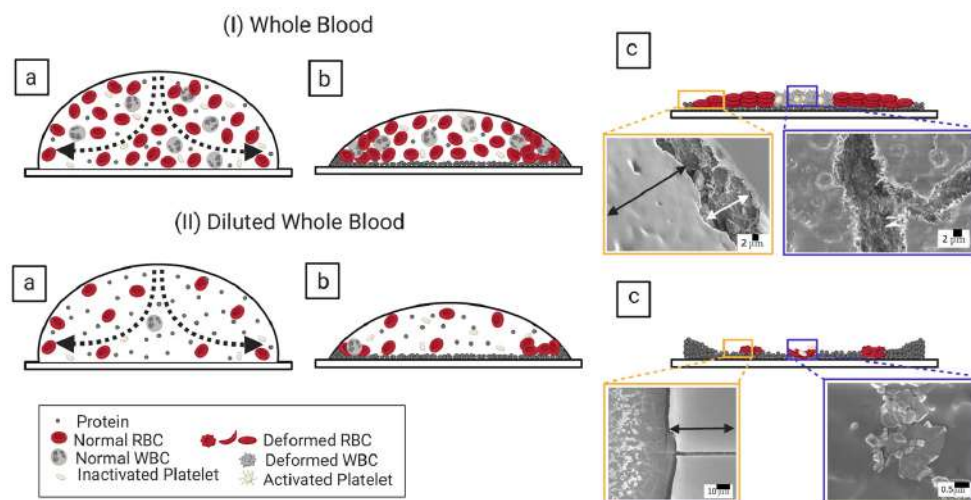


Figure 14. Self-assembling mechanism of the undiluted and the diluted blood droplets during the drying process. The ϕ_b of 100% (v/v) is displayed in ((I)a–c), and the 12.5% (v/v) is exhibited in ((II)a–c). The dotted arrows in ((I,II)a) indicates the capillary flow of the fluid. The blue rectangles in ((I,II)c) display the central region’s microstructures for both 100 and 12.5% (v/v). The orange rectangle in ((I)c) illustrates the periphery and the corona (or the ring) regions at $\phi_b = 100%$ (v/v). The corona and the central regions are presented within the orange rectangle in ((II)c). The white arrow reveals the peripheral region, whereas the black arrow demonstrates the ring.

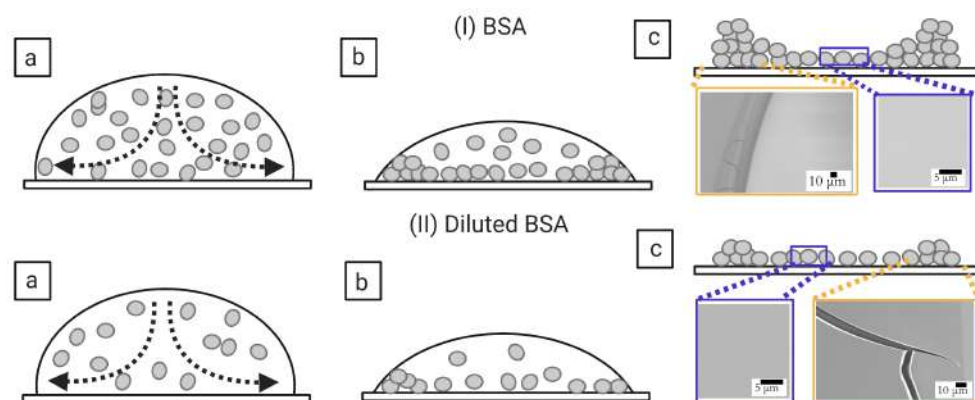


Figure 15. The BSA droplet’s physical mechanism during the drying process at $\phi_p = 20$ wt% in ((I)a–c) and at $\phi_p = 1$ wt% in ((II)a–c). The capillary flow is indicated with the dotted arrows in ((I,II)a). The blue and the orange rectangles in ((I,II)c) display the microstructures in the central and the rim regions (both 20 and 1 wt%).

We really appreciate the idea proposed by one of the reviewers to changing the ratio of blood components and plasma proteins by decreasing RBCs’ concentration using the centrifugation method instead of diluting it with de-ionized water. This particular method is used to study the morphological alteration of RBCs recently [35]. While we understand that a systematic study is required to understand how each cellular component behaves and contributes to the drying process, we must admit that this is beyond the scope of the current paper. The visco-elastic to elastic transition is developed during the drying process when the concentration of the blood components increases. Therefore, starting with the different initial concentrations, i.e., changing the ratio of blood components and plasma proteins, will affect the transition concentration reported in this manuscript. We look forward to examining those aspects in our future work.

In addition to the concentration study, the substrate temperature (T) is varied. The sample is pipetted on the substrate under ambient conditions. The substrate is transferred to the hot stage within ~ 45 s. This means that a temperature gradient forms between the apex of the droplet and the fluid–substrate interface. This gradient can generate thermally induced Marangoni flow in addition to the capillary flow in the droplets at the elevated temperatures. The images captured during the drying process and the dried films of both the BSA and the whole blood show that the morphological (crack) patterns are not significantly different from those captured under the ambient temperature (Figures 1–4). The statistical mean and the standard deviation extracted from these images confirm that the temperature only reduces the drying time (Figures 5 and 6). The fluid front measurements indicate that the fluid’s velocity gets increased with the increase of the temperature [Figures 7(I,II) and 10(I,II)]. The mean crack spacing (\bar{x}_c) shows a gradual decrease in the BSA samples [Figure 13(II)]. A kink at 62% (v/v) gets reduced as the temperature is increased in blood samples [Figure 12(I–III)]. The sharp-edged “coffee-ring” ring is predominantly observed in all the dried films at elevated temperatures [Figures 11(I–III) and 13(I)]. These observations suggest that the particles in both the blood and the BSA droplets have enough time to segregate and deposit their particles onto the substrate under ambient conditions. There is insufficient time for them to segregate fully. Despite having the same stages, the accelerated drying at the elevated temperatures exhibits a weak influence of the thermal Marangoni flow, which is partially counteracted by the particles’ enhanced edge aggregation in such droplets.

It will also be interesting to examine the effects of the relative humidity and/or its coupling with the temperature on the pattern formation of such diluted bio-colloidal droplets since relative humidity directly affects the drying mechanism.

5. Conclusions

This paper explored the physical phenomena of different patterns formed during different phases of the drying process in one of the most complex (whole human blood) and a simplest (aqueous solution of the globular protein, BSA) bio-colloidal droplets. The captured images, the statistical image analysis, the fluid front, the contact angle measurements during the drying process, and the dried films’ microstructural sketches are described for both the blood and the BSA samples. These indicate that the samples’ visco-elasticity depends on the self-interacting mechanism of large number of components, not specifically to the blood. The sample prepared by extreme dilution of the whole blood behaves like the BSA droplet. The substrate temperature only increases the rate of the drying process, and does not influence the states of the blood’s components. This current study therefore initiates a theoretical effort to examine how the dilution and the substrate temperature interplay in characterizing these bio-colloidal droplets. This study offers new macroscopic and microscopic insights connecting the hierarchical structures that are evolved as the drying process advances through a new phase transition mechanism.

Author Contributions: All the authors have actively participated in this project. A.P. did the conceptualization and literature survey. The methodology, validation, and formal analysis are conducted by A.P., and A.G.; A.P. also initiated the funding acquisition to meet the costs of experimental materials. The original draft is prepared by A.P. The final draft is reviewed and edited by A.G.; This whole project is supervised and administrated by G.I. All authors have read and agreed to the published version of the manuscript.

Funding: This research received no external funding.

Institutional Review Board Statement: Not applicable.

Informed Consent Statement: Not applicable.

Data Availability Statement: Not applicable.

Acknowledgments: The Department of Physics, WPI, supports this project. The authors are indebted to Christopher R. Lambert for allowing access to his lab for the contact angle measurements.

Conflicts of Interest: The authors declare no conflict of interest.

References

1. Brutin, D.; Sobac, B.; Loquet, B.; Sampol, J. Pattern formation in drying drops of blood. *J. Fluid Mech.* **2011**, *667*, 85–95. [[CrossRef](#)]
2. Brutin, D. *Droplet Wetting and Evaporation: From Pure to Complex Fluids*; Academic Press: Cambridge, MA, USA, 2015.
3. Annarelli, C.; Reyes, L.; Fornazero, J.; Bert, J.; Cohen, R.; Coleman, A.W. Ion and molecular recognition effects on the crystallisation of bovine serum albumin—Salt mixtures. *Cryst. Eng.* **2000**, *3*, 173–194. [[CrossRef](#)]
4. Yakhno, T. Salt-induced protein phase transitions in drying drops. *J. Colloid Interface Sci.* **2008**, *318*, 225–230. [[CrossRef](#)]
5. Chen, G.; Mohamed, G.J. Complex protein patterns formation via salt-induced self-assembly and droplet evaporation. *Eur. Phys. J. E* **2010**, *33*, 19–26. [[CrossRef](#)]
6. Gorr, H.M.; Zueger, J.M.; Barnard, J.A. Lysozyme pattern formation in evaporating drops. *Langmuir* **2012**, *28*, 4039–4042. [[CrossRef](#)]
7. Chen, R.; Zhang, L.; He, H.; Shen, W. Desiccation patterns of plasma sessile drops. *ACS Sens.* **2019**, *4*, 1701–1709. [[CrossRef](#)]
8. Schena, M.; Shalon, D.; Davis, R.W.; Brown, P.O. Quantitative monitoring of gene expression patterns with a complementary DNA microarray. *Science* **1995**, *270*, 467–470. [[CrossRef](#)]
9. Bel'skaya, L.V.; Sarf, E.A.; Solonenko, A.P. Morphology of dried drop patterns of saliva from a healthy individual depending on the dynamics of its surface tension. *Surfaces* **2019**, *2*, 395–414. [[CrossRef](#)]
10. Iqbal, R.; Shen, A.Q.; Sen, A.K. Understanding of the role of dilution on evaporative deposition patterns of blood droplets over hydrophilic and hydrophobic substrates. *J. Colloid Interface Sci.* **2020**, *579*, 541–550. [[CrossRef](#)]
11. Rapis, E. A change in the physical state of a nonequilibrium blood plasma protein film in patients with carcinoma. *Tech. Phys.* **2002**, *47*, 510–512. [[CrossRef](#)]
12. Muravlyova, L.; Molotov-Luchanskiy, V.B.; Bakirova, R.Y.; Zakharova, Y.E.; Klyuyev, D.A.; Bakenova, P.A.; Demidchik, L.A.; Suleimenova, S.B. Structure-forming properties of blood plasma of patients with interstitial lung diseases. *World J. Med. Sci.* **2014**, *10*, 478–483.
13. Yakhno, T.A.; Sanin, A.A.; Ilyazov, R.G.; Vildanova, G.V.; Khamzin, R.A.; Astascheva, N.P.; Markovsky, M.G.; Bashirov, V.D.; Yakhno, V.G. Drying drop technology as a possible tool for detection leukemia and tuberculosis in cattle. *J. Biomed. Sci. Eng.* **2015**, *8*, 1. [[CrossRef](#)]
14. González-Gutiérrez, J.; Pérez-Isidoro, R.; Ruiz-Suárez, J. A technique based on droplet evaporation to recognize alcoholic drinks. *Rev. Sci. Instrum.* **2017**, *88*, 074101. [[CrossRef](#)]
15. Mukhopadhyay, M.; Ray, R.; Ayushman, M.; Sood, P.; Bhattacharyya, M.; Sarkar, D.; Dasgupta, S. Interfacial energy driven distinctive pattern formation during the drying of blood droplets. *J. Colloid Interface Sci.* **2020**, *573*, 307–316. [[CrossRef](#)]
16. Chen, R.; Zhang, L.; Zang, D.; Shen, W. Blood drop patterns: Formation and applications. *Adv. Colloid Interface Sci.* **2016**, *231*, 1–14. [[CrossRef](#)] [[PubMed](#)]
17. Brutin, D.; Sobac, B.; Nicloux, C. Influence of substrate nature on the evaporation of a sessile drop of blood. *J. Heat Transf.* **2012**, *134*, 061101. [[CrossRef](#)]
18. Sobac, B.; Brutin, D. Desiccation of a sessile drop of blood: Cracks, folds formation and delamination. *Colloids Surf. A Physicochem. Eng. Asp.* **2014**, *448*, 34–44. [[CrossRef](#)]
19. Chen, R.; Zhang, L.; Zang, D.; Shen, W. Understanding desiccation patterns of blood sessile drops. *J. Mater. Chem. B* **2017**, *5*, 8991–8998. [[CrossRef](#)]
20. Chen, R.; Zhang, L.; Shen, W. Controlling the contact angle of biological sessile drops for study of their desiccated cracking patterns. *J. Mater. Chem. B* **2018**, *6*, 5867–5875. [[CrossRef](#)]
21. Lanotte, L.; Laux, D.; Charlot, B.; Abkarian, M. Role of red cells and plasma composition on blood sessile droplet evaporation. *Phys. Rev. E* **2017**, *96*, 053114. [[CrossRef](#)]
22. Pal, A.; Gope, A.; Obayemi, J.D.; Iannacchione, G.S. Concentration-driven phase transition and self-assembly in drying droplets of diluting whole blood. *Sci. Rep.* **2020**, *10*, 1–12. [[CrossRef](#)] [[PubMed](#)]
23. Carter, D.C.; Ho, J.X. Structure of serum albumin. In *Advances in Protein Chemistry*; Elsevier: Amsterdam, The Netherlands, 1994; Volume 45, pp. 153–203.
24. Pal, A.; Gope, A.; Iannacchione, G.S. A Comparative Study of the Phase Separation of a Nematic Liquid Crystal in the Self-assembling Drying Protein Drops. *MRS Adv.* **2019**, *4*, 1309–1314. [[CrossRef](#)]
25. Pal, A.; Gope, A.; Athair, A.S.; Iannacchione, G.S. A comparative study of the drying evolution and dried morphology of two globular proteins in de-ionized water solutions. *RSC Adv.* **2020**, *10*, 16906–16916. [[CrossRef](#)]
26. Huang, L.H.; Lin, P.H.; Tsai, K.W.; Wang, L.J.; Huang, Y.H.; Kuo, H.C.; Li, S.C. The effects of storage temperature and duration of blood samples on DNA and RNA qualities. *PLoS ONE* **2017**, *12*, e0184692. [[CrossRef](#)]
27. Giancola, C.; De Sena, C.; Fessas, D.; Graziano, G.; Barone, G. DSC studies on bovine serum albumin denaturation effects of ionic strength and SDS concentration. *Int. J. Biol. Macromol.* **1997**, *20*, 193–204. [[CrossRef](#)]
28. Abramoff, M.D.; Magalhães, P.J.; Ram, S.J. Image processing with ImageJ. *Biophotonics Int.* **2004**, *11*, 36–42.

29. Pal, A.; Gope, A.; Kafle, R.; Iannacchione, G.S. Phase separation of a nematic liquid crystal in the self-assembly of lysozyme in a drying aqueous solution drop. *MRS Commun.* **2019**, *9*, 150–158. [[CrossRef](#)]
30. Pal, A.; Gope, A.; Iannacchione, G.S. Image-Based Analysis of Patterns Formed in Drying Drops. In *Pattern Recognition and Machine Intelligence*; Deka, B., Maji, P., Mitra, S., Bhattacharyya, D.K., Bora, P.K., Pal, S.K., Eds.; Springer International Publishing: Cham, Switzerland, 2019; pp. 567–574.
31. Deegan, R.D.; Bakajin, O.; Dupont, T.F.; Huber, G.; Nagel, S.R.; Witten, T.A. Capillary flow as the cause of ring stains from dried liquid drops. *Nature* **1997**, *389*, 827. [[CrossRef](#)]
32. Carreón, Y.J.; González-Gutiérrez, J.; Pérez-Camacho, M.; Mercado-Uribe, H. Patterns produced by dried droplets of protein binary mixtures suspended in water. *Colloids Surf. B Biointerfaces* **2018**, *161*, 103–110. [[CrossRef](#)]
33. Carreón, Y.J.; Ríos-Ramírez, M.; Moctezuma, R.; González-Gutiérrez, J. Texture analysis of protein deposits produced by droplet evaporation. *Sci. Rep.* **2018**, *8*, 1–12. [[CrossRef](#)]
34. Kumar, S.; Katz, J.S.; Schroeder, C.M. Heterogeneous drying and nonmonotonic contact angle dynamics in concentrated film-forming latex drops. *Phys. Rev. Fluids* **2017**, *2*, 114304. [[CrossRef](#)]
35. Mukhopadhyay, M.; Ghosh, U.U.; Sarkar, D.; DasGupta, S. Surface property induced morphological alterations of human erythrocytes. *Soft Matter* **2018**, *14*, 7335–7346. [[CrossRef](#)]